COMPARISON OF METHODS FOR DETECTION OF ARSENIC IN SKIN USING XRF

COMPARISON OF METHODS FOR DETECTION OF ARSENIC IN SKIN USING XRF

By

ELSTAN DESOUZA, B.Sc.

A Thesis

Submitted to the School of Graduate Studies

in Partial Fulfillment of the Requirements

for the Degree
Doctor of Philosophy

McMaster University ©
Copyright by Elstan Desouza, February 2014

DOCTOR OF PHILISOPHY (2014) McMaster University
(Medical Physics) Hamilton, Ontario

TITLE: COMPARISON OF METHODS FOR DETECTION OF ARSENIC IN SKIN USING XRF

AUTHOR: Elstan D. Desouza, B.Sc. (York University)

SUPERVISOR: Dr. Fiona E. McNeill

NUMBER OF PAGES: xii, 300

Abstract

Arsenic (As) is an element that is well known for its toxic capabilities. It is odorless and colorless and is known to contaminate the drinking water of populations in several parts of the world. Routine monitoring of arsenic exposure is usually performed with urine, hair or nail, where samples are collected for laboratory analysis. Arsenic's strong affinity to keratin rich tissues make skin another possible measurement site, in addition to the latter two tissues mentioned above. In some cases, skin samples are extracted for analysis. This is painful and invasive and is not ideal for *in vivo* monitoring of arsenic. The ability to quantify elemental concentration non-destructively is the major calling card of x-ray fluorescence (XRF). To that end, work was started on development of XRF detection systems for arsenic. The technique has shown promise for other elements and dramatic improvements in As detection capabilities were previously found when going from a radioisotope-based x-ray source to an x-ray tube based approach.

This thesis documents the comparison of three x-ray tube based detection systems intended for the measurement of arsenic in skin. Two benchtop systems were used, with a) extended development of the previously assembled system and b) the first use of a separate detection system. Two handheld x-ray analyzers (portable detection systems) were also investigated in stand mode, where they were attached to a purpose-built mounting stand, provided by the manufacturer, during all analysis. Polyester resin phantoms were used to model arsenic in skin and a nylon backing was used to represent as bulk tissue behind skin. During the course of the work, modifications were made to the laboratory setup associated with the benchtop approaches.

A benchtop polychromatic Mo anode x-ray tube based x-ray fluorescence (XRF) detection system was the first system used in this work. Through modifications to the existing design of the system, the lowest minimum detection limit (MDL) achievable was found to be (0.611±0.001) ppm normalized to gross scatter, where ppm is μg of arsenic per gram of dry weight (resin). The measurement time was ~1800 seconds real time. The equivalent (skin) and whole body effective doses delivered were (19±3) mSv and (163±47) μSv respectively. The corresponding direct (un-normalized) MDL was (0.499±0.002) ppm, in agreement with that found previously. Modifications to the system allowed a reduction in the localized effective dose delivered, to achieve this MDL, from (0.64±0.03) μSv previously to (0.14±0.04) μSv here.

Next, the current work investigated two handheld x-ray analyzers provided by InnovX. A PiN diode detector based Alpha 4000S model unit (W anode x-ray tube) and a Silicon Drift Detector (SDD) based Delta model (Au anode x-ray tube). Both units were operated in benchtop mode: they were mounted in a stand and a phantom was placed on a kapton exit window. The lowest gross-scatter normalized and direct detection limit with the Alpha 4000S unit was (1.649±0.002) ppm and (1.651±0.002) ppm respectively. The equivalent and whole body effective doses delivered were found to be (9.4±2.2) mSv and (94±22) μSv respectively. The localized effective dose was (6.4±1.5) X 10^{-3} μSv. By

comparison, the Delta unit produced a gross-scatter and direct normalized detection limit of (0.570±0.002) ppm and (0.558±0.002) ppm respectively. The equivalent dose delivered was found to be (19.0±9.0) mSv. The corresponding localized and whole body effective doses delivered were (9.7±4.6) X 10^{-3} μSv and (190±90) μSv respectively.

The last system used in the current research was a monochromatic Ag anode x-ray tube based XRF setup. A doubly curved crystal (DCC) was used to select the Ag Kα line and focused the beam to a spot size of <1 X 1 mm^2 at the focal length. The phantoms were placed at a farther distance where the beam had expanded to a larger area. The lowest Compton scatter normalized detection limit with the Si(Li) detector was found to be (0.696±0.002) ppm. After characterizing its performance in a range of energies, a silicon drift detector was also used on this system. It had the benefit of higher throughput capabilities and superior resolution. The housing of the detector was sufficiently small that it could be placed closer to the phantom surface than the Si(Li) detector. The lowest Compton-scatter normalized detection limit with the SDD was (0.441±0.003) ppm in 1800 seconds real time. The equivalent dose was found to be (11±2) mSv and the localized and whole body effective doses were found to be (3.92±0.87) X 10^{-3} μSv and (110±23) μSv respectively. A significantly lower system dead time was observed with the SDD. Finally, Monte Carlo simulations of the system were performed to evaluate the performance of three ratios when their phantom measurement values were compared against simulations of skin. Results were found to be in agreement to within <10% for Compton scatter normalized results with the Si(Li) detector. This work allowed for an evaluation of the efficacy of the system calibration using resin phantoms and was used to establish an upper bound on the difference between phantom-based concentration and *in vivo* concentration of arsenic in skin (ICRP).

Finally, EDXRF measurements were performed on bulk cores of skin, *ex vivo*. While it was not possible to detect arsenic in the samples, due to the samples being collected from members of the public as opposed to an exposed population, a depth profile of numerous skin samples, starting from the surface and running straight down, was obtained for calcium, iron and copper.

Acknowledgements

I would like to express my gratitude towards my supervisor Dr. Fiona E McNeill, who has offered invaluable support to me during my time at McMaster. Discussions with her were extremely constructive. Her knowledge of the topic and ability to guide me and assist with troubleshooting numerous problems I experienced was a tremendous asset to me during my time here. Her ability to maintain calm has been a tremendous asset to me during the numerous moments of frustration that I experienced. Finally, her belief in me and the work I was doing, at all times, made it an honor for me to work for her.

I would also like to extend my heartfelt thank you to Dr. Ana Pejovic-Milic from Ryerson University for allowing me uninterrupted access to numerous pieces of laboratory equipment for use in this thesis. It should be underlined that all of the work performed here would not have been possible without her kind generosity.

I must acknowledge the contributions from my supervisory committee who have offered me invaluable support and guided me along. Dr. David Chettle has been a tremendous resource, very often in times of desperate need on my part, and his contributions through the step-by-step delving through intricate problems and breakdown of misunderstandings is highly appreciated. Dr. David Fleming's knowledge of both the handheld equipment I used and with the discussions about benchtop xrf as well as crucial input on the wording and re-wording of various drafts has been of vital importance to me. Dr. Michael Farquharson has offered invaluable support for work performed at the synchrotron in Saskatoon and has been able to offer insight into my benchtop (lab-related) work as well.

I would like to thank Dr. Bruce Wainman for the wealth of resources opened up to me regarding the biology of skin, something I wasn't particularly knowledgeable about prior to meeting him. His assistance with obtaining ethics for the ex vivo work was crucial in moving ahead with that part of my project and is greatly appreciated. I would also like to extend my gratitude to Dr. Soo Hyun Byun for his help with experimental simulations performed over the course of my time at McMaster. Additionally, Dr. Colin Weber was able to offer me good advice during the early stages of my work, and for this I am thankful.

I am very grateful to Scott McMaster, Jason Falladown and Justin Bennett who offered all the technical assistance I required and acted as a sounding board for numerous design ideas that were implemented over the duration of my time at McMaster. I would like to extend my gratitude to Mihai Gherase and Mark LeBlanc from Mount Allison University for their assistance with the data acquisition there and subsequent interpretation. I would also like to thank Dr. Joanne O'Meara from University of Guelph, for allowing access to her equipment at McMaster University. I am thankful to Alice Pidruczny for assistance with neutron activation work in the McMaster Reactor. Finally, I am thankful to Glen

Oomen, Mary Jo Smith and Mary Brunni, from Hamilton Health Sciences, for help with preparation of biological (skin) samples.

I would like to thank numerous graduate students and post-doctoral fellows in the Medical Physics and Applied Radiation Sciences Department, both past and present, for assistance with various aspects of the work done, in particular I acknowledge Eric DaSilva, James Grafe, Witold Matysiak, Lesley Egden, Sepideh Behinaein, Jovica Atanackovic, Chris Heirwegh, Andrei Hanu, Ibrahim Abu Atiya, James Harrington, Alia Al-Ebraheem and Mira Sibai for their assistance and various helpful discussions I had with them.

I am also grateful for the family support I have received over the course of this work. Their sacrifices have allowed me the opportunity to pursue so much through their words of encouragement. Their efforts have helped make the sleepless nights and long frustrating weekends worth the time and effort.

Table of Contents

List of Figures

List of Tables

Chapter 1 Introduction:

1.1 Arsenic:

Arsenic is the thirty-third element in the periodic table. It has a density of 5.37 g/cm^3 (Berger et al., 2005). It does not have a distinguishing colour or odour and is well-known for its toxic capabilities.

1.1.1 Sources of Arsenic:

As a component of mineral ores, arsenic sulphides contaminate the environment through weathering of rocks (Kabata-Pendias and Pendias, 1984) and by dissolving in waters of rivers and wells, rainwater and as dust. The main sources of human exposure are soil and sediment (Gulbrandsen, 1966; Hiller et al., 2012; Onishi, 1969; Patel et al., 2005; Razo et al., 2004; Tourtelot, 1964), water (Hopenhayn, 2006; Parvez et al., 2013), air (Hughes et al., 2011; Maud and Rumsby, 2008), plants (Gulz et al., 2005) and animals (Nachman et al., 2012). For example, when rocks move, arsenic salts are displaced (Irgolic et al., 1995) causing erosion to contaminate streams and rivers, affecting humans depending on water sources. High concentrations of arsenic are also found in hot springs (Hirner et al., 1998).

Some microbes grow in arsenic-rich environments by transforming low toxic arsenate into higher toxic arsenite (Laverman et al., 1995; Saltikov and Olson, 2002). In rice, wheat and peas, arsenite uptake occurs across the plasma membrane into cells via acquaporins. Paddy rice and wheat, irrigated with contaminated groundwater in Bangladesh, expose people to high levels of toxicity (Abedin et al., 2002). Poisoning through consumption of plants is not likely since plants will decease before toxic As levels are reached (Finnegan and Chen, 2012). The strongest sources of arsenic, through diet, are in the form of shellfish, seaweed and fish. Overall, drinking water is the primary source of arsenic (Nakajima et al., 2006; Ratnaike, 2003).

Human activities such as mining, agriculutural fertilization, pesticide usage and waste disposal are also sources of arsenic. Mining releases arsenic from oxidized sulphide minerals into soil and groundwater affecting vegetation (Azcue et al., 1994; Smedley and Kinniburgh, 2002). Droughts influence seasonal levels of arsenic uptake and water concentrations (Andreae, 1979; Savage et al., 2000).
Medicinal and Poisonous uses:

1.1.2 Medicinal and Poisonous uses:

Medicinal and poisonous uses of arsenic have been well documented (Nevens et al., 1990; Waxman, 2001; Zhang et al., 2010). Napolean Bonaparte's death was speculated as being for political reasons (Cullen, 2008). Passed off for cholera or pneumonia, displaying similar symptoms like nausea, vomiting and diarrhea (Agency for Toxic Substances and Disease Registry (ATSDR), 2007), arsenic was likely added to

food and drinks (Leslie and Smith, 1978). A compound consisting of high levels of lead and arsenic was also identified as the likely source of poisoning of the Portuguese king D. Joao VI (Carvalho et al., 2002). Acute As poisoning symptoms include diarrhea, seizures, vomiting, nausea, respiratory and renal failure, psychosis or death in 1-4 days (Ratnaike, 2003). Chronic exposure leads to peripheral neuropathy, headaches, fatigue, muscle weakness, hyper-pigmentation, diabetes mellitus and weakening of nails. Inhibition of DNA replication, disruption of cell division and alteration of gene expression and phosphate substitution are examples of how arsenic toxicity is experienced by the human body (Abernathy et al., 1999; Guha Mazumder, 2008; Ratnaike, 2003). Fowler's solution (1% potassium arsenite) was used to treat malaria, syphilis, eczema and psoriasis (Scheindlin, 2005), until evidence emerged of it's toxicity (Antman, 2001). Currently, arsenic trioxide is used in chemotherapeutic treatment of chronic promyelocytic leukemia (Rust, 2001) and is being explored as a probable drug for treatment of other cancers (Sekeres, 2007). Medical supplements and alternative forms of medicine are sources of arsenic uptake (Jha and Agarwal, 2008; van der Voet et al., 2008).

1.1.3 Methylated forms of Arsenic:

Arsine gas is the most toxic form of arsenic (Danielson et al., 2006; Winski et al., 1997). Organic arsenic is generally non-toxic (Nakajima et al., 2006; Ratnaike, 2003) and as much as 1 mg is consumed by humans through fish (Cullen and Reimer, 1989). Metabolism in the liver involves methylation of arsenic. Species of methylated arsenic are dimethylarsinic acid (DMA) and monomethylarsonic acid (MMA) (Gadd, 1993). At normal ingestion levels *in vivo*, about 60 % DMA is excreted unchanged through urine, 20 % is in the form of organic arsenic which is methylated to MMA and DMA and the last 20 % is in the form of MMA and is methylated, after absorption, to DMA (Buchet et al., 1981; Vahter et al., 1984). Oxidation states of MMA are MMA^{V} (pentavelent, called arsenate) and MMA^{III} (trivalent, called arsenite) respectively, and similarly for DMA (Feng et al., 2001). DMA is known to be an important factor in carcinogenesis caused by inorganic arsenic (Kenyon and Hughes, 2001). Through the process of methylation, and oxidation and reduction in plasma during circulation, *in vivo* arsenic is converted from arsenate to arsenite (Mandal and Suzuki, 2002). The toxicity of arsenic species increases from arsenate to arsenite to inorganic arsenic (Francesconi and Kuehnelt, 2004; Hughes et al., 2011). Studies have reported pentavelent states to be reduced to trivalent states and excreted renally (Brown et al., 1990; Vahter and Envall, 1983).

Thioredoxin reductase is responsible for catalysis of thioredoxin (Mustacich and Powis, 2000), which is the protein that acts as an antioxidant (Holmgren, 1989; Nordberg and Arnér, 2001). In *in vitro* studies, MMA^{III} was found to have a 100 times stronger ability to inhibit thioredoxin reductase than inorganic As^{III} (Lin et al., 1999). Methylation generates metabolites which affect the detoxification process (Vega et al., 2001a). MMA^{III} has also been found to be more toxic than iAs^{III} (inorganic As^{III}) and iAs^{V}, in human keratinocytes in the epidermis, hepatocytes in the liver and epithelial cells in the bronchi (Styblo et al., 2000, 1997). The proposed methylation process, listing steps involved is explained in the literature (Rossman, 2003), but a clear understanding of the

method-of-action of arsenic remains to be determined, with debate over dose-response unsettled (Druwe and Vaillancourt, 2010; Kitchin and Conolly, 2010; Kitchin and Wallace, 2008; Kumagai and Sumi, 2007).

1.1.4 Arsenic exposure to the body and its metabolism:

The main transporters of arsenic resulting in exposure *in vivo* are air, food and water. Arsenic enters the human body through ingestion and inhalation (Ouypornkochagorn and Feldmann, 2010). This is carried by the blood to various organs. Elemental arsenic is eliminated through excretion without being changed (Duker et al., 2005). After absorption in the small intestine, arsenic is metabolized to DMA and MMA in the liver. After chronic exposure, accumulation also occurs in the liver, kidney, gastrointestinal tract and heart. Nearly half of the arsenic in the body is excreted via renal function in ~5 days. Extended chronic exposure leads to deposition in nails, skin and hair (Kitchin, 2001; Ratnaike, 2003). Methylation in the liver has been shown to increase the toxicity of arsenic (Petrick et al., 2001; Styblo et al., 2000).

Chronic exposure affects the skin, respiratory organs, heart, liver and kidney from mild to carcinogenic effects. A comparison of levels between infants and adults showed arsenic in infant tissue at 0.0099 µg/g and adults at 0.048 µg/g dry weight suggesting that it accumulates in tissue with age (Raie, 1996) in agreement with findings in animal studies (Marafante et al., 1982). Due to its low permeability, dermal exposure to arsenate (a pentavalent arsenic species) is not well-known (Bernstam et al., 2002; Wester et al., 1993). Only prolonged exposure to As-contaminated water appeared relevant to dermal exposure as has been documented in countries in Asia (Wester et al., 2004; Williams et al., 2006). Arsenate uptake is of greater concern in rice (van Geen et al., 2006). In a recent study in skin, the rate of penetration of various arsenic species was found to differ by more than an order of magnitude, with arsenite found to be nearly 60 times faster than arsenate (Ouypornkochagorn and Feldmann, 2010). In the liver, arsenate methylates with the enzymes and converts to arsenite. The rate of absorption is related to the source from where it was drawn into food or water that was consumed and interaction with other food constituents (WHO, 2001).

1.1.5 Arsenic diseases:

In vivo arsenic undergoes oxidation and reduction in plasma during circulation (Mandal and Suzuki, 2002). Arsenic also affects a host of organs as it is absorbed, accumulates and is excreted by the body, as well as the cardiovascular system (Balakumar and Kaur, 2009), gastrointestinal tract (Gorby, 1988; Hindmarsh and McCurdy, 1986; Krieger et al., 2001), liver (Tchounwou et al., 1999), lungs (Enterline et al., 1987; Lee-Feldstein, 1986) and kidney (Winship, 1984). Drinking water induced arsenic disorders include skin cancer (Smith et al., 1992), vascular disease (Balakumar and Kaur, 2009; Tseng et al., 1996), desquamation (Amster et al., 2007) and hair loss (Saha et al., 1999), hyperkeratosis, dermal lesions (Mitra et al., 2004; Saha, 2003) and peripheral neuropathy (Barton and McLean, 2013). Due to its affinity for sulfhydryl groups in keratin, it also affects the skin where skin lesions are the most prevalent

symptom of arsenic exposure (Kitchin, 2001). Skin cancers such as squamous cell carcinoma in-situ and basal cell carcinoma are induced by chronic exposure to arsenic (Shneidman and Belizaire, 1986; Tseng et al., 1968). Cardiovascular and circulatory diseases including cerebrovascular, ischemic heart and blackfoot diseases are linked to arsenic in drinking water (Ch'i and Blackwell, 1968; Chen et al., 1996; Chiou, Huang, et al., 1997). Non-malignant respiratory diseases, bronchiectasis and diabetes are also linked to arsenic exposure (Mazumder et al., 2005; Milton and Rahman, 2002; Rahman et al., 1998; Tseng et al., 2000).

1.1.6 Skin toxicity and diseases caused by arsenic – studies in the literature:

Skin lesions, keratoses and increase in bladder cells (biomarker for bladder cancer) have been found due to prolonged exposure to arsenic contaminated drinking water in Chile (Biggs et al., 1997). Cases of pigmentation and keratoses were also well documented in countries such as Bangladesh, India and Argentina (Guha Mazumder et al., 1998; Smedley et al., 2005; Tseng et al., 1968).

Premalignant skin lesions appear a few years after exposure and are characterized by a change in skin pigmentation (melanosis) which progresses to a thickening of the palms and soles (hyperkeratosis) and then leads to the development of basal and squamous cell skin cancers (Alain et al., 1993; Liu et al., 2002). One of the consequences of prolonged exposure is in the form of skin lesions mainly on the hands, feet and trunk of the body (Kao, 1990). In a study of skin, liver and urine human samples collected in West Bengal, India, skin lesions were found to appear almost 5-10 years after arsenic exposure. Urine samples, skin scales and liver tissue showed 5 to 40 µg As per day in urine, 3.05-4.26 µg/g (ppm) in skin scales and 1.41-2.20 µg/g in liver tissues respectively (Das et al., 1995). Other studies have corroborated that exposure through drinking water and medicines were among the earliest known cases of arsenic toxicity related to dermal changes, resulted from and manifested as hyperkeratosis and basal and squamous cell carcinomas of the skin (Marafante et al., 1982; Nagvi et al., 1994; Raie, 1996).

1.1.7 Levels in Drinking water:

By 2006, millions of people were exposed to arsenic in drinking water, with about 3 million in the United States and 70 million in Bangladesh and India. This prompted various epidemiological studies to validate the then permissble level of <50 µg/L in water. Recommended levels of 10µg/L arsenic concentration in drinking water as determined by WHO, were subsequently made and later reviewed after evidence of outcomes associated with moderate arsenic exposure were published (WHO, 2011, 2010). Studies in Taiwan and Bangladesh have demonstrated that the risk of fatalities from cardiovascular effects can result from long term exposure to contaminated drinking water (Chiou, Chen, et al., 1997). Skin disorders were reported with arsenic content in water of up to 2 mg/L As in Bangladesh (Tondel et al., 1999), where about half the population is exposed to the risk of arsenic in drinking water (Smith et al., 2000). Access to well water concentrations of ~50 µg/L were documented in nearly half of a cohort studied in Araihazar, Bangladesh – nearly 5 times higher than the WHO limit. Nearly

20% of deaths reported were believed to be caused by chronic exposure to arsenic levels greater than 10 μg/L (Argos et al., 2010).

In studies of dose-response relationship in Bangladesh it was revealed that people were exposed to risk of skin lesions at levels <50 μg/L of water. With every increase of 10 μg/L, there was a 1.22 times higher risk of developing skin lesions (Ahsan et al., 2006). A very recently developed model of arsenic exposure in China estimated that almost 20 million people are affected due to groundwater (Rodriguez-Lado et al., 2013).

In Canada, the population is at risk due to exposure caused naturally and anthropologicaly from erosion, mining, discharge from coal plant activities, wood preservation, pesticide usage and waste disposal plants (McGuigan et al., 2010; Wang and Mulligan, 2006). Levels are largely <5μg/L except in regions dependant on wells for drinking water, where levels can be >10 μg/L. In the Appalachian region, where concentration in bedrock, soil and water is naturally higher, there is an added risk of exposure. In Nova Scotia, arsenic levels range from <10 μg/L–5000 μg/L due to dependancy on ground water sources for drinking water (McGuigan et al., 2010). In the US, arsenic concentration in hair, another keratin-rich tissue, was found to be as high as nearly 0.7 ppm and postulated as a possible source of an increase in gestational diabetes in women, near a former zinc and lead mine (Ettinger et al., 2009). Health risks were associated with low to moderate levels of arsenic in Michigan (10–100μg/L) and New Hampshire reported arsenic concentrations in drinking water ranging from 1 μg/L to 180 μg/L (Haack and Treccani, 2000; Kolker et al., 2003).

1.1.8 Arsenic in the skin:

Since arsenic is not eliminated as quickly from skin as it is through other organs, it is one of the primary tissues where arsenic accumulates over time (Schoolmeester and White, 1980). Clinical testing has confirmed pathological changes that are distinguishable by altered pigmentation (melanosis), followed by hyperpigmentation in which distinct darker spots appear. As keratosis sets in, the skin of palms and soles thicken and tiny protusions or nodes may appear (Guha et al 1998). Arsenical lesions, called arsenical keratoses, are the most common way to identify the presence of long-term arsenic expopsure. Keratosis is characterized by features including squamous cell carcinoma *in situ*, pigmentation, hyperkeratosis and basal cell carcinoma (Kao, 1990).

The structure of the skin was examined as it relates to melanin, hemoglobin and carotenoids (e.g. zeaxanthin, lutein, its metabolites, which are products of its metabolism, etc.) in skin that are responsible for its colouration (Alaluf et al., 2002; Peng et al., 1993; Wingerath et al., 1998) and are known to be susceptible to attack by free radicals (Chen and Djuric, 2001). Knowing that carotenoids are 3-6 times higher in concentration in the epidermis than the dermis (Lee et al., 1975; Vahlquist et al., 1982), two punch biopsies 2-3 mm in diameter were taken from the epidermis of arsenic afflicted patients and single biopsies from normal people. Lutien was found to be several times lower in concentration in diffuse dark brown spots. This is lower than in the case of a normal epidermis.

1.1.9 Layers of skin:

The skin is an organ in a constant state of renewal occuring as keratinization in which epithelial cells change as they move through each of the layers of the epidermis. The epidermis is the outermost layer of the skin. Five sub-layers are the stratum corneum, stratum lucidum, stratum granulosum, stratum spinosum and the stratum basale (Forslind and Lindberg, 2004). Cells proliferate in the basal layer and move upwards towards the stratum granulosum. The basal layer also contains melanocytes that produce melanin, the yellow-brown to black pigment that determines the colour of the epidermis. Melanosis and hyperpigmentation are irregularities in melanin contained in this layer and have been used as cutaneous evidence of internal arsenic exposure. In the next layer, the stratum granulosum, cell proliferation continues. With the absorption of toxins like arsenic, cells may proliferate at a higher rate here, disrupting the differentiation process such that they do not lose their nuclei as they move to the stratum lucidum. The cells in the stratum lucidum produce keratin, a water resistant protein, and a key component of skin that is especially concentrated in the feet and palms. Toxins such as arsenic can affect the cell production of keratin in this layer (Centeno et al., 2002). Cells eventually lose their nutrient supply, get denucleated and move towards the stratum corneum. Here, the cells which are packed with keratin die or get cornified (Madison, 2003; Palmer et al., 2006; Proksch et al., 2008).

Cell differentiation leads to the production of a layer of dead cells that represents the epidermis, with the layered skin structure a result of various stages of the differentiation process in the epidermis bulk. Cells lost due to desquamation (removal of keratinocytes from cornified layer) must be balanced against cells produced (proliferation) (Poumay and Coquette, 2007). Carcinogenesis can prevent differentiation at the epidermal-dermal boundary and lead to a constant state of proliferation (growth due to cell division). This change in proportionality in the two processes is crucial to the onset of carcinogesis (Perez et al., 2003). Arsenic is assumed to enhance carcinogesis since it acts against DNA repair, keratinization and chromosome breakage and enhancement of cell proliferation (Germolec et al., 1996; Vega et al., 2001b; Vogt, 2001). The end result of arsenic exposure, is enhanced proliferation and lower differentiation and has been suggested in the literature (Bae, 2001; Perez et al., 2003). When human keratinocytes were exposed to As^V from 500-1000 µg/L, keratinocyte differentiation process was affected and cells appeared flattened with thick membranes. Epidermal strata distinctly changed. Lesser changes were observed at 250 µg/L and 10–100 µg/L. In paraffin, as keratinocytes were exposed to increasing doses of As^V, basal strata lost their structure of cuboid-shaped cells in a distinct structure until they were completely disintergrated. At 1000 µg/L, degenerative changes could be attributed to toxicity and permeability differences of the two types of arsenic in the skin: the stratification and cornification with As(V) and cell loss with As(III) (Bernstam et al., 2002).

Traditional monitoring of arsenic in skin is done *ex vivo* through skin scales (Das et al., 1995; Samanta et al., 2004) or painful punch biopsies. Hair contamination, through washing with arsenic contaminated water, is undesired due to the presence of exogenous

arsenic. Since urine is a short term indicator of arsenic and skin, is comparatively more biologically relevant than hair or nails, a non-invasive method of *in vivo* quantification in skin is sought.

1.2 Basis of X-Ray Fluorescence – Photoelectric Effect:

The technique of x-ray fluorescence has been applied to the in vivo quantification of numerous elements. The method is attractive due to its non invasive nature. Using XRF *in vivo* involves its application to estimation of levels directly in human subjects as opposed to a tissue, bone or organ sample that has been extracted from a human or cadaver (*ex vivo*). Over the past three decades or so, numerous applications of XRF to development and use *in vivo* appear in the literature. A brief list of in vivo applications of x-ray fluorescence includes quantification and extensive detection system and source development quantification of lead in bone (Nie et al., 2006, 2004; Somervaille et al., 1985; Todd, 2000), strontium in bone (Heirwegh et al., 2012; Moise et al., 2012; Pejović-Milić et al., 2004; Zamburlini et al., 2006), uranium in bone (O'Meara et al., 2001), arsenic in skin (Studinski et al., 2006, 2005), platinum in head and neck tumors (Jonson et al., 1988) and cadmium in kidneys (Ahlgren and Mattsson, 1981).

1.2.1 Photoelectric Effect:

X-Ray Fluorescence is based on the photoelectric effect. The orbital shell structure of an atom is shown in figure 1.1.

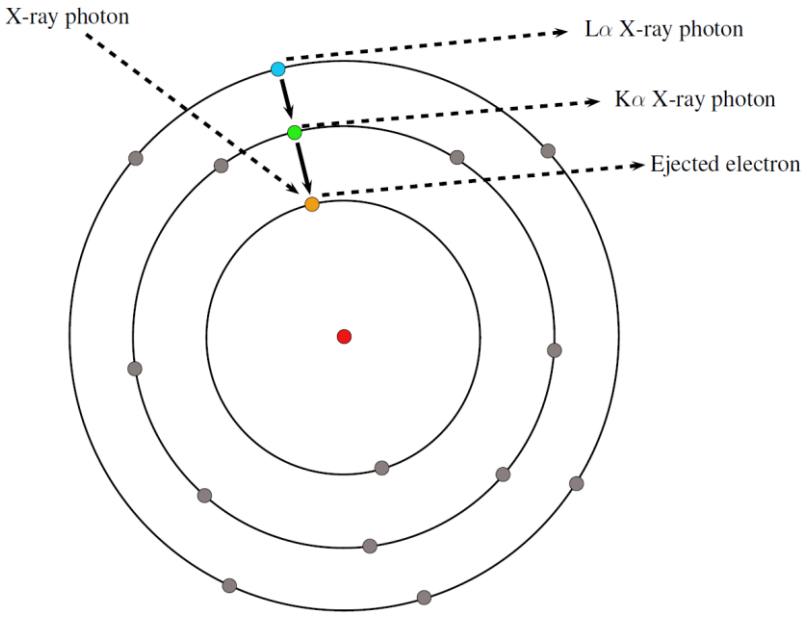

Figure 1.1: Shell diagram of an atom, depicting orbiting electrons. The inner most shell is called the K shell (n = 1), the next shell is called the L shell (n = 2) and so on. The inner most shell is the most tightly bound shell in the atom.

In this process, an incident photon interacts with an atom of a sample material. Photons of energy greater than the binding energy of an electron shell in the atom will lead to ejection of the electron from that orbital shell. An electron from a higher energy shell will then replace the ejected electron thereby filling the resulting gap or vacancy in that orbital. The emitted electron is known as a photoelectron and this process is known as the photoelectric interaction. In order to conserve energy, this process is accompanied by the emission of a characteristic x-ray photon or an Auger electron from a higher energy shell. Characteristic x-ray emission accounts for the excess energy resulting from the change in orbital by the electron that has filled the vacancy. The difference in shell binding energies is equal to the energy of the emitted characteristic x-rays. If the extra energy is not released in the form of a photon, but is transferred to another electron thereby ejecting it from the atom, then this electron is called an Auger electron. The probability of characteristic x-ray emission is higher for high Z atoms, while that for Auger emission dominates for low Z atoms. The percentage of de-excitation processes resulting in K-shell arsenic characteristic x-ray emission is 57% (Robinson, 1991).

De-excitation of an electron from the L or M shells of the atom to the K shell produces a Kα or Kβ x-ray respectively. The K-absorption edge, or simply the K-edge, refers to the energy that must be provided to eject an electron from the K-shell, by overcoming the shell's binding energy. The intensity and energy of arsenic characteristic x-rays is presented in table 1.1.

Table 1.1: Arsenic K-shell characteristic x-rays and their associated intensities which are listed per 100 K-shell vacancies (Firestone, 2005).

Line	E (keV)	Intensity (%)
$\mathbf{K\alpha_1}$	10.544	32.7
$\mathbf{K\alpha_2}$	10.508	16.8
$\mathbf{K\beta_1}$	11.726	4.25
$\mathbf{K\beta_3}$	11.72	2.19

When emitted characteristic x-rays are detected, their energy can be used to identify the elemental content of the sample that they originate from. This is referred to as Energy Dispersive X-Ray Fluorescence (EDXRF) and is characterized by a spectrum of energies corresponding to various x-rays. The area under a particular energy peak is used to quantify the elemental concentration in the sample being studied via EDXRF.

1.2.2 Scattering:

In addition to the photoelectric interaction (absorption of incident photon), there are also possible photon interactions through scattering, that will be detected. The two types of scattering are coherent (elastic) scattering and Compton (inelastic) scattering.

1.2.2.1 Compton scattering:

In inelastic (or Compton) scattering, the photon of incident energy E_1 strikes an electron in the atom and is scattered through an angle θ, relative to the incident photon

direction, with a change in energy. The energy is transferred to an outer shell electron, which is emitted from the atom and the scattered photon energy is given by E_2 where

$$E_2 = \frac{E_1}{1 + \frac{E_1}{m_0 c^2}(1 - \cos\theta)} \tag{1}$$

where m_0c^2 = 511 keV (Jenkins, 1995). This indicates that a single well-defined energy E2 exists, however, due to the fact that the electrons are not initially at rest they have some initial momentum and so the peak in the detected spectrum associated with the Compton feature is broadened since a distribution of energies is detected due to Doppler broadening and the scattering being observed over multiple angles complicating its appearance in an energy spectrum (Vincze et al., 1999) and making an analytical description very cumbersome (Van Dyck and Van Grieken, 1983). In practice, this scattering is characterized by a differential cross-section given by

$$\frac{d\sigma}{d\Omega} = \frac{1/2 {r_0}^2 (1 + cos^2\theta)}{\left(1 + 2\frac{E_1}{m_0 c^2}\sin^2\theta/2\right)^2}\left[1 + \frac{4\frac{E_1}{m_0 c^2} sin^2\theta/2}{(1 + \cos^2\theta)(1 + 2\frac{E_1}{m_0 c^2} sin^2\theta/2)}\right] \tag{2}$$

named the Klein-Nishina cross section after Oskar Klein and Yoshio Nishina who were the first to calculate it (Klein and Nishina, 1929), where r_0 is the classical electron radius and the equation indicates the probability that a photon is scattered in $d\Omega = 2\pi\sin\theta d\theta$.

1.2.2.2 Coherent (Rayleigh) scattering:

Consider a photon, with energy E_1, incident on a target atom. In elastic (or coherent) scattering, the photon strikes the atom and is scattered without a change in its energy. Recoil vibration of the atom is required for conservation of momentum but since the photon energy is so small compared to that of the atom, the recoil energy is negligible and the initial and final atomic states are the same. The differential coherent scattering cross section is given by (Hubbell et al., 1975)

$$\left(\frac{d\sigma}{d\Omega}\right) = \frac{{r_0}^2}{2}(1 + \cos^2\theta) f(x, Z) \tag{3}$$

where f(x,Z) is the atomic form factor and $(d\sigma/d\Omega)_T$ is the differential cross section for Thompson scattering given by

$$\left(\frac{d\sigma}{d\Omega}\right)_T = \frac{{r_0}^2}{2}(1 + \cos^2\theta) \tag{4}$$

A detailed description of the benefits of normalization to coherent scattering and the conditions to be met for its use were presented for XRF analysis of lead in bone (Somervaille et al., 1985; Todd, 2000).

Given the energy resolution capabilities of semiconductor radiation detectors, such as those used in this work, it will not be possible to distinguish the two Kα lines from each other and similarly for the Kβ lines. While the two sets of lines will be better resolved with a SDD, the resolution is still not good enough to visualize them separately and a single merged Kα1,2 line, estimated by a weighted average of the two Kα lines, will be observed in an x-ray spectrum and similarly for the Kβ lines. An incident energy just above the K-edge would be ideal since photoelectric absorption will be most probable. However, the detector's resolution and the position of the two scatter peaks must be considered. Compton and coherent scatter cross sections are shown in figure 1.2, for various materials.

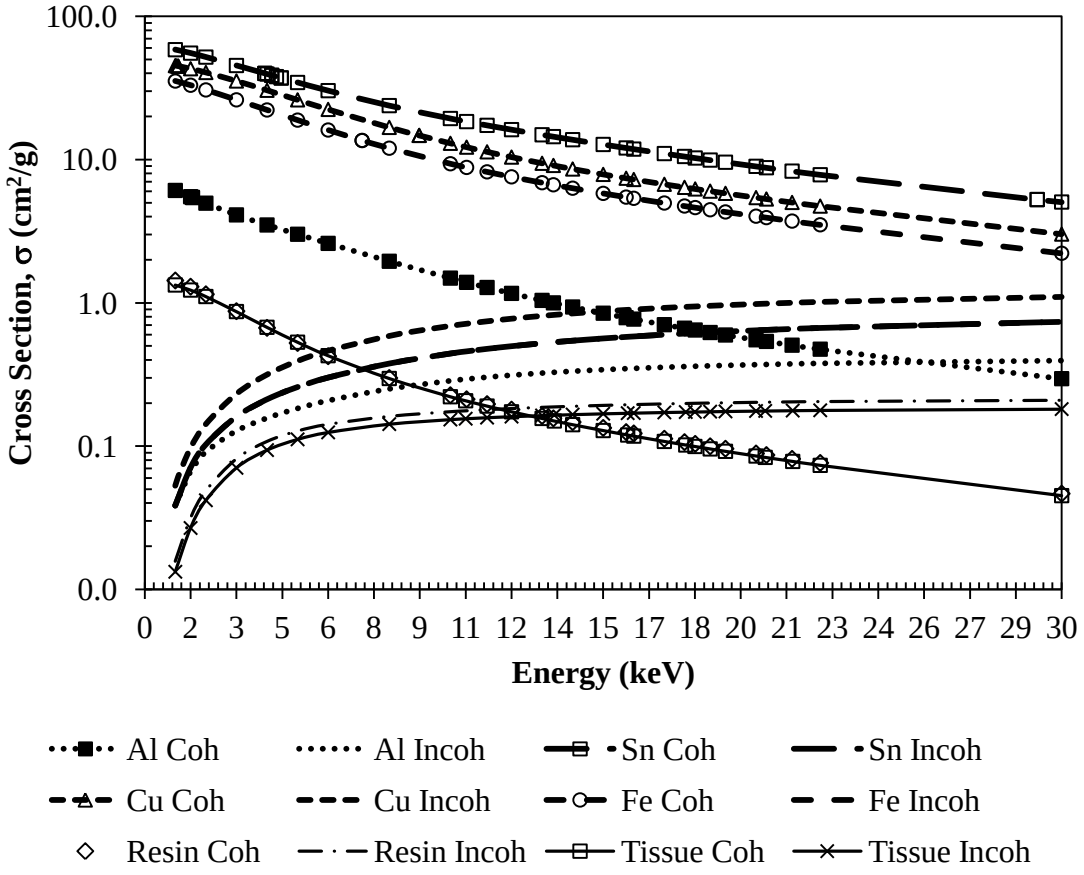

Figure 1.2: Compton (incoherent) and coherent scattering, in various materials, for energies ranging from 0-30 keV. Vertical axis is shown on a log scale in order to clearly visualize the difference between the two curves corresponding to each material (Berger et al., 2010).

The Klein-Nishina equation is valid in the energy region where the Compton cross section dominates as a total proportion of the total cross section. Due to the low-Z (atomic number) nature of human tissue, Compton scatter dominates coherent scatter in the range of energies that would be suitable choices for a source of incident x-rays to excite the characteristic x-ray lines tabulated above. In fact the majority of elements in the body are low-Z (atomic number) indicating that Compton scattering will dominate coherent scattering in the range of energies being investigated in the current work. This means that the low energy side of the continuum of the Compton feature will contribute to the background under the characteristic x-ray peaks. This is not the case for metallic samples, which are an example of a high Z material. Radiative corrections and an adjustment for a double Compton effect (Mork, 1971) are required for lower Z high energy combinations (Brown and Feynman, 1952), although these aren't relevant to the current work. Ensuring that the coherent and, more importantly, the Compton scatter peaks are sufficiently far away from the characteristic x-ray peaks, taking the detector's resolution into account, is important to minimize the background under the characteristic x-ray peaks and the uncertainty in separating them from their background. This means that the incident energy selected must be higher than what is ideally desired as per the K-edge requirement.

The mean free path of several elements' characteristic x-rays in tissue (ICRU four-component, ICRP) and skin (ICRP) is shown in table 1.2.

Table 1.2: Mean free path of characteristic x-rays in two models of soft tissue – ICRU four-component and ICRP. The mean free path is defined as $\langle x \rangle = 1/\mu$, where $\mu = (\mu/\rho)*\rho$. The characteristic x-ray energies shown are calculated as a weighted mean of the individual $K_{\alpha 1,2}$ and $K_{\beta 1,3}$ lines as these are estimated energies that can be detected with a radiation detector. The values for μ/ρ and ρ were obtained from NIST (NIST, 2005) and the tissue model compositions were acquired from ICRU (ICRU, 1989).

Line	**E (keV)**	**<x>_tissue[1], (mm)**	**<x>_tissue[2], (mm)**	**<x>_skin[3], (mm)**
As Kα	10.53	2.3574	2.3810	2.2130
As Kβ	11.72	3.2248	3.2499	3.0192
Se Kα	11.21	2.8233	2.8474	2.6466
Se Kβ	12.49	3.4459	3.4710	3.2272
Rb Kα	13.37	4.6816	4.7059	4.3748
Rb Kβ	14.96	5.3191	5.3419	4.9650
Zr Kα	15.75	7.3046	7.3206	6.7995
Zr Kβ	17.66	9.7752	9.7847	9.0818

[1]ρ = 1.00 g/cm^3 (ICRU 4-Comp), [2]ρ = 1.00 g/cm^3 (ICRP), [3]ρ = 1.10 g/cm^3 (ICRP)

This lists the depth into tissue from where an x-ray can originate, traverse a path perpendicular to the surface of the tissue, thereby being attenuated in the bulk, and still be

detected. If the path travelled is larger than the mean free path, given as $\langle x \rangle = 1/\mu$, then self attenuation inside the bulk will reduce the intensity of the emerging x-rays. This places a limitation on the thickness of a skin sample that can be analyzed using this technique. Sites located deeper in the body will thus not produce x-rays that can be measured by this technique and alternative approaches, such as neutron activation analysis may be considered and have been documented in previous work (Studinski, 2005). By comparison, the skin thickness measured by ultrasound during previous *in vivo* skin work with arsenic was in the range of 1.0-2.5 mm (Studinski et al., 2005).

1.2.3 Continuous Radiation (Bremsstrahlung):

The emission of x-rays over a wide range of energies is known as Bremsstrahlung (bremsen – to brake, in German, and strahlung – radiation). Transmission of charged particles (electrons) through a material produces Bremsstrahlung radiation when they are slowed down in the material – it is the phenomenon of loss of energy of highly energetic electrons in such an interaction. Highly energetic electrons are produced by the electric potential between the two electrodes of an x-ray tube producing characteristic x-rays and Bremsstrauhlung. The accelerating potential across the electrodes determines the photon's maximum energy – 40 kVp produces photons with energies not exceeding 40 keV. The maximum energy of the continuous Bramsstrahlung feature would be 40 keV. A continuous energy distribution of photon energies is produced due to the absence of discrete energy transitions. Thus, the accelerating potential determines the maximum photon energy. The majority of an x-ray tube's energy goes towards production of heat with only a minor fraction involved in x-ray production (Ahmed, 2007).

Due to a larger variation in electron direction, brought about by the need for multiple collisions to decelerate the electrons, a smaller directional dependence describes Bremsstrahlung from thick, as opposed to thin, targets. A peak in the energy distribution is noted at 90-degrees to the incident electron beam for various x-ray tube voltage settings with a minor offset at higher potential settings, with more bremsstrahlung given off by some x-ray tube anode materials than others. With x-ray tubes, until the kVp is increased past the K-edge corresponding to the x-ray tube target material, it is the bremsstrahlung radiation and not the anode's characteristic K-shell x-rays that will serve as the excitation source. The L or M shell characteristic x-rays will be present as kVp is increased past the L or M edge. In an x-ray tube spectrum, bremsstrahlung appears as a hump at higher energies since the lower energy contribution is absorbed by the detector's entrance window or in the sample. Incoherent and coherent scattering drive continuum generation in XRF leading to increasingly complicated shapes based on the source and sample being studied (Van Grieken and Markowicz, 2002) with additional complications brought about by multiple scattering in the sample.

1.3 Alternate type of x-ray fluorescence:

Placing the radiation detector at a specific angle relative to the sample allows for collection of characteristic x-rays that are emitted in that direction and of a signature wavelength. Either scanning the detector through a range of angles (time consuming) or

placing a series of detectors at different angles covers a spread of directions in which x-rays, of various wavelengths (driving up costs), that are emitted. A diffraction crystal is used to facilitate the scatter of x-rays emitted from the sample being studied. This is referred to as Wavelength Dispersive X-Ray Fluorescence (WDXRF). Due to these optic components, the efficiency of WDXRF is quite low and so a high-powered x-ray source is required, such as an x-ray tube with a power rating on the order of kilowatts. This work only covers EDXRF and does not cover WDXRF and so the term XRF, when used here, refers to the energy dispersive variant of the XRF technique.

1.4 Minimum Detection Limit (MDL):

The calibration of an EDXRF detection system involves counting a calibration phantom with that system and extracting the area under the peak of interest in the energy spectrum discussed earlier. These areas are then plotted against concentration of the calibration phantom to give a system calibration line. Next a minimum detectable limit is calculated from the resulting peak areas and the slope and intercept of the calibration line. The conventionally used formula for calculation of the Minimum Detection Limit (MDL) is given by,

$$\mathrm{MDL} = 2\,\frac{\sigma_{Area_{0ppm}}}{m} \tag{5}$$

where m is the slope of a linear least–squares calibration line, y = mx + b, obtained using a set of calibration standards (in this case, phantoms) and fit to a plot of peak area versus concentration. Here, $\sigma[\mathrm{Area}_{0\mathrm{ppm}}]$ is the standard uncertainty in the area of the 0 ppm (blank) calibration standard (or phantom) used as part of this set. However, this equation does not account for the non-zero uncertainty in the intercept, b, of this calibration line. A treatment of all the related uncertainties should be utilized to calculate the MDL as all of these will make a contribution to the MDL. The results of such an approach to calculating the MDL (which was then subsequently applied to results collected to date) are presented here.

1.4.1 System of equations and error propagation:

For a linear fitting function y = mx + b, the fitting parameters m and b can be obtained by minimizing

$$\mathrm{R}^2 = \sum_{i=1}^{N} [y_i - (mx_i + b)]^2 \tag{6}$$

where N is the number of data points to be fit to the function y = mx + b. This equation represents sum of squares of deviations of a set of points from the line y = mx + b. The

minimum of the above equation can be used to obtain the parameters m and b, by making use of the partial derivative of R^2 with respect to m and b respectively, giving

$$\frac{\partial(\mathrm{R}^2)}{\partial \mathrm{m}} = -2\sum_{i=1}^{N}[y_i - (mx_i + b)](x_i) = 0 \tag{7}$$

and

$$\frac{\partial(\mathrm{R}^2)}{\partial \mathrm{b}} = -2\sum_{i=1}^{N}[y_i - (mx_i + b)](1) = 0 \tag{8}$$

Bringing the constants outside the summations and evaluating any summations over unity, gives

$$\sum_{i=1}^{N} y_i - m\sum_{i=1}^{N} x_i - bN = 0 \tag{9}$$

$$\sum_{i=1}^{N} y_i - bN - m\sum_{i=1}^{N} x_i = 0 \tag{10}$$

and

$$\sum_{i=1}^{N} x_i y_i - m\sum_{i=1}^{N} {x_i}^2 - b\sum_{i=1}^{N} x_i = 0 \tag{11}$$

$$m\sum_{i=1}^{N} {x_i}^2 + b\sum_{i=1}^{N} x_i = \sum_{i=1}^{N} x_i y_i \tag{12}$$

respectively. Rearranging these gives

$$bN + m\sum_{i=1}^{N} x_i = \sum_{i=1}^{N} y_i \tag{13}$$

and

$$b\sum_{i=1}^{N} x_i + m\sum_{i=1}^{N} {x_i}^2 = \sum_{i=1}^{N} x_i y_i \tag{14}$$

respectively. This is a system of two equations with two unknowns, m and b, and can be solved for m by taking –N (14) + $\sum_{i=1}^{N} x_i$ (13) and –$\sum_{i=1}^{N} {x_i}^2$ (13) + $\sum_{i=1}^{N} x_i$ (14), giving m and b respectively as shown below

$$0 + m\sum_{i=1}^{N} x_i \left(\sum_{i=1}^{N} x_i\right) - Nm\sum_{i=1}^{N} {x_i}^2 = \sum_{i=1}^{N} x_i \sum_{i=1}^{N} y_i - N\sum_{i=1}^{N} x_i y_i \tag{15}$$

$$m\left(\sum_{i=1}^{N} x_i\right)^2 - Nm\sum_{i=1}^{N} {x_i}^2 = \sum_{i=1}^{N} x_i \sum_{i=1}^{N} y_i - N\sum_{i=1}^{N} x_i y_i$$

$$m = \frac{\sum_{i=1}^{N} x_i \sum_{i=1}^{N} y_i - N\sum_{i=1}^{N} x_i y_i}{(\sum_{i=1}^{N} x_i)^2 - N\sum_{i=1}^{N} {x_i}^2}$$

$$m = \frac{\sum_{i=1}^{N} x_i \sum_{i=1}^{N} y_i - N\sum_{i=1}^{N} x_i y_i}{N\sum_{i=1}^{N} {x_i}^2 - (\sum_{i=1}^{N} x_i)^2}$$

$$m = \frac{N\sum_{i=1}^{N} x_i y_i - \sum_{i=1}^{N} x_i \sum_{i=1}^{N} y_i}{\Delta} \tag{16}$$

where $\Delta = N\sum_{i=1}^{N} {x_i}^2 - (\sum_{i=1}^{N} x_i)^2$, and

$$-Nb\sum_{i=1}^{N} {x_i}^2 + b\left(\sum_{i=1}^{N} x_i\right)^2 + 0 = -\sum_{i=1}^{N} {x_i}^2 \sum_{i=1}^{N} y_i + \sum_{i=1}^{N} x_i \left(\sum_{i=1}^{N} x_i y_i\right)$$

$$b\left[\left(\sum_{i=1}^{N} x_i\right)^2 - N\sum_{i=1}^{N} {x_i}^2\right] = \sum_{i=1}^{N} x_i \left(\sum_{i=1}^{N} x_i y_i\right) - \sum_{i=1}^{N} {x_i}^2 \sum_{i=1}^{N} y_i$$

$$b = \frac{\sum_{i=1}^{N} x_i (\sum_{i=1}^{N} x_i y_i) - \sum_{i=1}^{N} {x_i}^2 \sum_{i=1}^{N} y_i}{(\sum_{i=1}^{N} x_i)^2 - N\sum_{i=1}^{N} {x_i}^2}$$

$$b = \frac{\sum_{i=1}^{N} x_i{}^2 \sum_{i=1}^{N} y_i - \sum_{i=1}^{N} x_i \left(\sum_{i=1}^{N} x_i y_i\right)}{N \sum_{i=1}^{N} x_i{}^2 - \left(\sum_{i=1}^{N} x_i\right)^2}$$

$$b = \frac{\sum_{i=1}^{N} x_i{}^2 \sum_{i=1}^{N} y_i - \sum_{i=1}^{N} x_i \left(\sum_{i=1}^{N} x_i y_i\right)}{\Delta} \tag{17}$$

for b. Though not shown here, the uncertainties in the parameters m and b can then be determined using the error propagation equation

$$\sigma_h{}^2 = \left(\frac{\partial h}{\partial m}\right)^2 \sigma_m{}^2 + \left(\frac{\partial h}{\partial b}\right)^2 \sigma_b{}^2 \tag{18}$$

where h = mx + b is replaced by y = mx + b, to give

$$\sigma_m{}^2 = \frac{\sigma_y{}^2 N}{\Delta} \tag{19}$$

and

$$\sigma_b{}^2 = \frac{\sigma_y{}^2 \sum_{i=1}^{N} x_i{}^2}{\Delta} \tag{20}$$

where the variance in y (the linear fit variance) is given by

$$\sigma_y{}^2 = \frac{\sum_{i=1}^{N} [y_i - (mx_i + b)]^2}{N - 2} \tag{21}$$

using the sum of squares terminology mentioned earlier (Taylor, 1997).

For the application being considered here, the line $y_{exp} = mx_{exp} + b$ represents a calibration line, obtained using a set of calibration standards, that will eventually be used to determine the value of an unknown x_{exp}, where $x_{exp} = (y_{exp} - b)/m$ and y_{exp} has been measured for that specific unknown x_{exp}. Here y_{exp} has its own uncertainty and so do b and m, so the variance of x_{exp} then includes the variances of y_{exp}, m and b with the last two contributions coming from the liner least squares fit. In addition the covariance of b and m must also be added to these three terms (Taylor, 1997). Thus, the variance of x_{exp}, as obtained from a calibration line, is then given by adding the covariance and y_{meas} variance terms to equation 18, giving

$$\sigma_{x_{exp}}{}^2 = \left(\frac{\partial x_{exp}}{\partial y_{exp}}\right)^2 \sigma_{y_{exp}}{}^2 + \left(\frac{\partial x_{exp}}{\partial b}\right)^2 \sigma_b{}^2 + \left(\frac{\partial x_{exp}}{\partial m}\right)^2 \sigma_m{}^2 + 2\frac{\partial x_{exp}}{\partial m}\frac{\partial x_{exp}}{\partial b}\sigma_{m,b}{}^2 \quad (22)$$

where $\sigma_{m,b}{}^2$ is the covariance of m and b, given by (Harris, 2006)

$$\sigma_{m,b}{}^2 = -\frac{\sigma_y{}^2 \sum_{i=1}^{N} x_i}{\Delta} \quad (23)$$

The partial derivatives in equation 22 become

$$\frac{\partial x_{exp}}{\partial b} = -\frac{1}{m}, \frac{\partial x_{exp}}{\partial m} = -\frac{(y_{exp} - b)}{m^2} = \frac{(b - y_{exp})}{m^2}, \frac{\partial x_{exp}}{\partial y_{exp}} = \frac{1}{m} \quad (24)$$

giving

$$\sigma_{x_{exp}}{}^2 = \left(\frac{1}{m}\right)^2 \sigma_{y_{exp}}{}^2 + \left(-\frac{1}{m}\right)^2 \sigma_b{}^2 + \left(\frac{b - y_{exp}}{m^2}\right)^2 \sigma_m{}^2 + 2\left(\frac{-1}{m}\right)\left(\frac{b - y_{exp}}{m^2}\right)\left(-\frac{\sigma_y{}^2 \sum_{i=1}^{N} x_i}{\Delta}\right)$$

$$\sigma_{x_{exp}}{}^2 = \left(\frac{\sigma_{y_{exp}}}{m}\right)^2 + \left(\frac{\sigma_b}{m}\right)^2 + \frac{\sigma_m{}^2 (b - y_{exp})^2}{m^4} + 2\left(\frac{y_{exp} - b}{m^3}\right)\left(-\frac{\sigma_y{}^2 \sum_{i=1}^{N} x_i}{\Delta}\right) \quad (25)$$

For the calibration line application (in the context of the MDL), being used here, $y_{exp} \pm \sigma_{y[exp]}$ would be the net peak area of a blank (0 ppm) calibration standard. When each standard is measured n times, this equation can be written with appropriate indexing as

$$\sigma_{x_{exp,j}}{}^2 = \left(\frac{\sigma_{y_{exp,j}}}{m}\right)^2 + \left(\frac{\sigma_b}{m}\right)^2 + \frac{\sigma_m{}^2 (b - y_{exp,j})^2}{m^4} + 2\left(\frac{y_{exp,j} - b}{m^3}\right)\left(-\frac{\sigma_y{}^2 \sum_{i=1}^{N} x_i}{\Delta}\right) \quad (26)$$

for j = [1, n]. The standard deviation of an average $\sigma_{x[exp]}$ is then given by (Kotulski, 2010)

$$SDOM_{\bar{\sigma}_{x_{exp}}} = \sum_{j=1}^{n} \frac{(\bar{\sigma}_{x_{exp}} - \sigma_{x_{exp,j}})^2}{(n-1)(n-2)} \tag{27}$$

Then, the Minimum Detection Limit (MDL) is then determined as

$$MDL = 2\,(\bar{\sigma}_{x_{exp}} \pm SDOM_{\bar{\sigma}_{x_{exp}}}) \tag{28}$$

where SDOM = StdDev/$n^{1/2}$ and StdDev is the standard deviation.

1.4.2 Variance-covariance matrix approach:

A matrix-based formulation for $\sigma_{x[exp]}^2$, as shown in equation 26, can be obtained without the need for solving the system of equations. This approach will be discussed here and reconciled with equation 26.

Recall the system of equations that were solved to determine the fit parameters b and m

$$bN + m\sum_{i=1}^{N} x_i = \sum_{i=1}^{N} y_i$$

and

$$b\sum_{i=1}^{N} x_i + m\sum_{i=1}^{N} {x_i}^2 = \sum_{i=1}^{N} x_i y_i$$

These can be written in matrix notation as

$$\begin{bmatrix} \mathrm{N} & \sum_{i=1}^{N} x_i \\ \sum_{i=1}^{N} x_i & \sum_{i=1}^{N} {x_i}^2 \end{bmatrix} \begin{bmatrix} b \\ m \end{bmatrix} = \begin{bmatrix} \sum_{i=1}^{N} y_i \\ \sum_{i=1}^{N} x_i y_i \end{bmatrix} \tag{29}$$

which can be represented by $\boldsymbol{S}\,\boldsymbol{c} = \boldsymbol{y}$ and solved using $\boldsymbol{S^{-1}}\,\boldsymbol{S}\,\boldsymbol{c} = \boldsymbol{S^{-1}}\,\boldsymbol{y}$ to give

$$\boldsymbol{c} = \frac{1}{D}\begin{bmatrix} \sum_{i=1}^{N} {x_i}^2 & -\sum_{i=1}^{N} x_i \\ -\sum_{i=1}^{N} x_i & N \end{bmatrix}\begin{bmatrix} \sum_{i=1}^{N} y_i \\ \sum_{i=1}^{N} x_i y_i \end{bmatrix} \tag{30}$$

where D is the determinant of **S** and is given by

$$D = N\sum_{i=1}^{N} {x_i}^2 - \left(\sum_{i=1}^{N} x_i\right)^2 \tag{31}$$

D is the same as Δ from earlier. For the variance of a fit given by

$${\sigma_y}^2 = \frac{\sum_{i=1}^{N}[y_i - (mx_i + b)]^2}{N - 2} \tag{32}$$

the variance-covariance matrix can then be written as **VC** where

$$\boldsymbol{VC} = {\sigma_y}^2 S^{-1} = \frac{{\sigma_y}^2}{D}\begin{bmatrix} \sum_{i=1}^{N} {x_i}^2 & -\sum_{i=1}^{N} x_i \\ -\sum_{i=1}^{N} x_i & N \end{bmatrix} \tag{33}$$

The variances in m and b and the covariance term then fall out of this matrix as

$${\sigma_m}^2 = \frac{{\sigma_y}^2 N}{D} \tag{34}$$

and

$${\sigma_b}^2 = \frac{{\sigma_y}^2 \sum_{i=1}^{N} {x_i}^2}{D} \tag{35}$$

which are terms VC_{22} and VC_{11} respectively. The covariance is given by VC_{12} or VC_{21}, where D = Δ. In matrix notation, the variance of x_{exp} in a calibration line equation $x_{exp} = (y_{exp} - b)/m$ is then given by (Salter, 2000)

$$\sigma_{x_{exp}}{}^2 = \left(\frac{\partial x_{exp}}{\partial y_{exp}}\right)^2 \sigma_{y_{exp}}{}^2 + \begin{bmatrix}\frac{\partial x_{exp}}{\partial b} & \frac{\partial x_{exp}}{\partial m}\end{bmatrix} VC \begin{bmatrix}\frac{\partial x_{exp}}{\partial b} \\ \frac{\partial x_{exp}}{\partial m}\end{bmatrix} \tag{36}$$

where the first term is the variance from y_{exp} and the second term is the variance from the linear least squares fit. Substituting in **VC** and performing the matrix multiplications gives

$$\sigma_{x_{exp}}{}^2 = \left(\frac{\partial x_{exp}}{\partial y_{exp}}\right)^2 \sigma_{y_{exp}}{}^2 + \begin{bmatrix}\frac{\partial x_{exp}}{\partial b} & \frac{\partial x_{exp}}{\partial m}\end{bmatrix} \frac{\sigma_y{}^2}{D} \begin{bmatrix}\sum_{i=1}^{N} x_i{}^2 & -\sum_{i=1}^{N} x_i \\ -\sum_{i=1}^{N} x_i & N\end{bmatrix} \begin{bmatrix}\frac{\partial x_{exp}}{\partial b} \\ \frac{\partial x_{exp}}{\partial m}\end{bmatrix} \tag{37}$$

$$\sigma_{x_{exp}}{}^2 = \left(\frac{\partial x_{exp}}{\partial y_{exp}}\right)^2 \sigma_{y_{exp}}{}^2 + \frac{\sigma_y{}^2}{D}\begin{bmatrix}\frac{\partial x_{exp}}{\partial b}\sum_{i=1}^{N} x_i{}^2 - \frac{\partial x_{exp}}{\partial m}\sum_{i=1}^{N} x_i & \frac{\partial x_{exp}}{\partial b}\sum_{i=1}^{N} x_i + \frac{\partial x_{exp}}{\partial m}N\end{bmatrix}\begin{bmatrix}\frac{\partial x_{exp}}{\partial b} \\ \frac{\partial x_{exp}}{\partial m}\end{bmatrix}$$

$$\sigma_{x_{exp}}{}^2 = \left(\frac{\partial x_{exp}}{\partial y_{exp}}\right)^2 \sigma_{y_{exp}}{}^2 + \frac{\sigma_y{}^2}{D}\begin{bmatrix}\frac{-\sum_{i=1}^{N} x_i{}^2}{m} + \frac{(y_{exp}-b)\sum_{i=1}^{N} x_i}{m^2} & \frac{\sum_{i=1}^{N} x_i}{m} + N\frac{(b-y_{exp})}{m^2}\end{bmatrix}\begin{bmatrix}\frac{-1}{m} \\ \frac{b-y_{exp}}{m^2}\end{bmatrix}$$

$$\sigma_{x_{exp}}{}^2 = \left(\frac{1}{m}\right)^2 \sigma_{y_{exp}}{}^2 + \frac{\sigma_y{}^2}{D}\left[\frac{\sum_{i=1}^{N} x_i{}^2}{m^2} + \frac{(b - y_{exp})\sum_{i=1}^{N} x_i}{m^3} + \frac{(b - y_{exp})\sum_{i=1}^{N} x_i}{m^3} + N\frac{(b - y_{exp})^2}{m^4}\right]$$

$$\sigma_{x_{exp}}{}^2 = \left(\frac{\sigma_{y_{exp}}}{m}\right)^2 + \frac{\sigma_y{}^2}{D}\left[\frac{\sum_{i=1}^{N} x_i{}^2}{m^2} + 2\frac{(b - y_{exp})\sum_{i=1}^{N} x_i}{m^3} + N\frac{(b - y_{exp})^2 N}{m^4}\right] \quad (38)$$

Then, multiplying $\sigma_y{}^2/D$ through the right hand bracket, gathering the components of $\sigma_y{}^2$, $\sigma_m{}^2$ and $\sigma_{m,b}{}^2$ and rearranging the result gives

$$\sigma_{x_{exp}}{}^2 = \left(\frac{\sigma_{y_{exp}}}{m}\right)^2 + \frac{\sigma_y{}^2}{D}\left[N\frac{(b - y_{exp})^2}{m^4} - 2\frac{(y_{exp} - b)\sum_{i=1}^{N} x_i}{m^3} + \frac{\sum_{i=1}^{N} x_i{}^2}{m^2}\right]$$

$$\sigma_{x_{exp}}{}^2 = \left(\frac{\sigma_{y_{exp}}}{m}\right)^2 + N\frac{\sigma_y{}^2}{D}\frac{(b - y_{exp})^2}{m^4} - 2\frac{\sigma_y{}^2}{D}\frac{(y_{exp} - b)\sum_{i=1}^{N} x_i}{m^3} + \frac{\sigma_y{}^2}{D}\frac{\sum_{i=1}^{N} x_i{}^2}{m^2}$$

$$\sigma_{x_{exp}}{}^2 = \left(\frac{\sigma_{y_{exp}}}{m}\right)^2 + \sigma_m{}^2\frac{(b - y_{exp})^2}{m^4} + \frac{2\sigma_{m,b}{}^2(y_{exp} - b)}{m^3} + \frac{\sigma_b{}^2}{m^2}$$

$$\sigma_{x_{exp}}{}^2 = \left(\frac{\sigma_{y_{exp}}}{m}\right)^2 + \left(\frac{\sigma_b}{m}\right)^2 + \frac{\sigma_m{}^2(b - y_{exp})^2}{m^4} + 2\left(\frac{y_{exp} - b}{m^3}\right)\sigma_{m,b}{}^2 \quad (39)$$

Finally, substituting in the expression for $\sigma_{m,b}{}^2$ gives

$$\sigma_{x_{exp}}{}^2 = \left(\frac{\sigma_{y_{exp}}}{m}\right)^2 + \left(\frac{\sigma_b}{m}\right)^2 + \frac{\sigma_m{}^2(b - y_{exp})^2}{m^4} + 2\left(\frac{y_{exp} - b}{m^3}\right)\left(-\frac{\sigma_y{}^2\sum_{i=1}^{N} x_i}{D}\right) \quad (40)$$

which is the same as equation 26 from earlier, with D = Δ.

1.5 Electronics – Detectors and Pulse Processing:

The detection and display of the results of the counts emitted by a calibration phantom or sample requires the use of a suitable radiation detector and supporting electronics. Over the range of x-ray detection systems used in the current work, a number of different types of x-ray detectors are used. Their principles differ in important ways and it is thus worth discussing each detector type in some detail.

The semiconductor-based radiation detector used to record x-rays in a meaningful manner is an important component of an XRF system. Choosing an appropriate detector is important to the overall performance of the system. A semiconductor radiation detector works on the principle of collecting charge carriers that were generated by the interaction of radiation incident on the detector's active volume. Amplification of charge carrier-induced electrode signal gives energy information about the incident radiation. The basic principles of the working of a semiconductor detector and associated electronics are discussed below.

1.5.1 n and p type semiconductor materials and pn junctions:

A brief description of purity of semiconductor crystals is provided, since it is an important feature in distinguishing different detector types used in this work from each other. The presence of varying amounts of impurities in a intrinsic (pure) semiconductor material's crystal lattice is able to change their conductive properties since the number of charge carriers [electrons and (electron) holes, the latter being the exact opposite of an electron with slower mobility due to higher effective mass] can be changed by applying a bias voltage across the material. Introducing these impurities into the material is known as doping and gives rise to two different types of conductor materials – n-type which contains a larger number of electrons and p-type which contains a larger number of holes; holes and electrons are referred to as charge carriers. The conductivity is determined by the amount of impurity added. The boundary between the two is known as a pn junction. A pn junction is fabricated out of a single crystal, due to the requirement of excellent thermodynamic contact between the two regions (n and p-type) in order to allow charge carriers to migrate efficiently across the junction. The diffusion of charge carriers across the junction, from high to low concentration regions, results in a change in impurity across the junction. This produces a net positive charge on the n-type material and a net negative charge on the p-type material. For the n-type material, removal of electrons (negative charge) leaves in a region with a net stationary positive charge here and, similarly, for a p-type material a region with a net stationary negative charge is established. With mobile charge carriers removed, those remaining ionized donor impurities (n-type) or acceptor impurities (p-type) cannot produce a current. This region is called a depletion region.

1.5.2 Semiconductor detector principles:

Photon detection by conventional semiconductor detectors makes use of a large reverse-biased (n-type to terminal of power source and p-type to positive terminal, $V_{cathode} > V_{anode}$) pn junction.. A transverse electric potential field is established across the silicon thickness (the bulk of the detector) by means of electrodes on the front and back surfaces. A simple schematic of this is shown in figure 1.3.

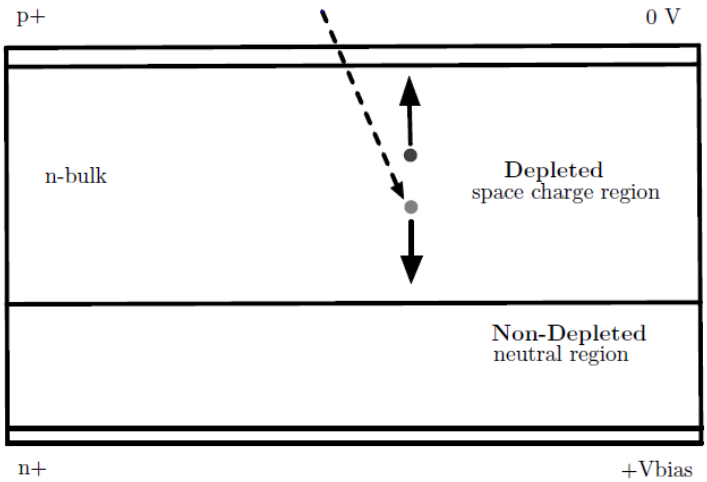

Figure 1.3: Setup of semiconductor diode structure

The interaction of ionizing radiation in the semiconductor crystal produces electrons and holes in numbers which depend on the incident x-ray energy. The potential field separates the free electrons and holes and sweeps them to the electrodes. An electron-hole pair requires 3.6 eV photon energy, for silicon (Si). The collected charge is then amplified and the resulting voltage pulse amplitude is related to the incident photon energy.

Mobility of charge carriers in some semiconductor materials is vastly different for electrons and holes. For carriers that are trapped and recombined later along the incident particle path, the detected signal is not indicative of the entire original charge produced by incoming radiation, as not all of these charges are collected. The fraction of the detected signal will grow as the electric field is ramped up and the escaping fraction is reduced. Full energy peaks are spread out on the low-energy side since the degree of trapping depends on the charge carrier path to collection electrodes (Knoll, 1999). Sensitivity to trapped carriers is reduced with smaller electrodes and carefully chosen pulse-shaping (pulse processing) parameters. This spread is referred to as a low energy tail and has been modeled in simulations and analytically (Barrett et al., 1995; Eskin et al., 1996; Kasap, 2000; Luke, 1994; Ruzin and Nemirovsky, 1997). Semiconductor detectors are one of the fastest (pulse processing time) types of radiation detectors, with the pulse rise time being contributed to by i) time required for charge carriers to travel across the region of the electric field, ii) in the case of incident alpha particles or nuclear fission products, the time for dispersion to the point of facilitating charge collection and iii) time constant of the preamplifier (pulse processing) input circuitry (Knoll, 1999).

1.5.3 Reverse biasing pn junction:

Charge carrier motion is not possible with a low electric field which is the result if using an unbiased pn junction. Current flows fluidly when a forward bias voltage is applied to the junction, but is not the case for a reverse biased junction. Conductivity is enhanced if the p-side is made positive relative to the n-side driving electrons from the n-side and holes from the p-side across the pn junction as both are the majority (more

abundant) charge carriers on those respective sides. A low forward bias voltage is required for this excellent charge carrier conductivity. For reverse biasing, the low concentration of minority charge carriers which are driven across the junction produces a comparatively low current. The higher resistivity of the junction, than either material type, means that all the applied voltage appears across it. Space charge will increase and cover a larger distance on both sides of the pn junction, beneficially increasing the volume of the depletion region that will collect charge carriers. This width of the depletion region is called the active volume of the detector. Arbitrarily increasing the bias voltage will cause diode breakdown and so the reverse bias voltage must be maintained below that specified by detector manufacturers (Knoll, 1999). For the Si(Li) detector used in this work, a high voltage of -1000 V was used.

1.5.4 Detector material:

Two semiconductor detector materials can be considered for use in the energy range being considered with the current work. A 16 mm thick silicon (Si) lithium (Li) drifted, Si(Li), detector was used in previous work with arsenic in skin (Studinski, 2005). In addition to silicon, germanium (Ge) is another commonly used semiconductor detector material and an array of four 10 mm thick HpGe (hyperpure germanium) detectors was used for *in vivo* quantification of lead in bone (Behinaein et al., 2011). Both deserve consideration and a discussion of the interactions in each material offers insight into spectral lines observed in XRF at energies comparable to those used in this work.

Absorption in the bulk of each of these detector materials is shown in figure 1.4, with specific energies highlighted.

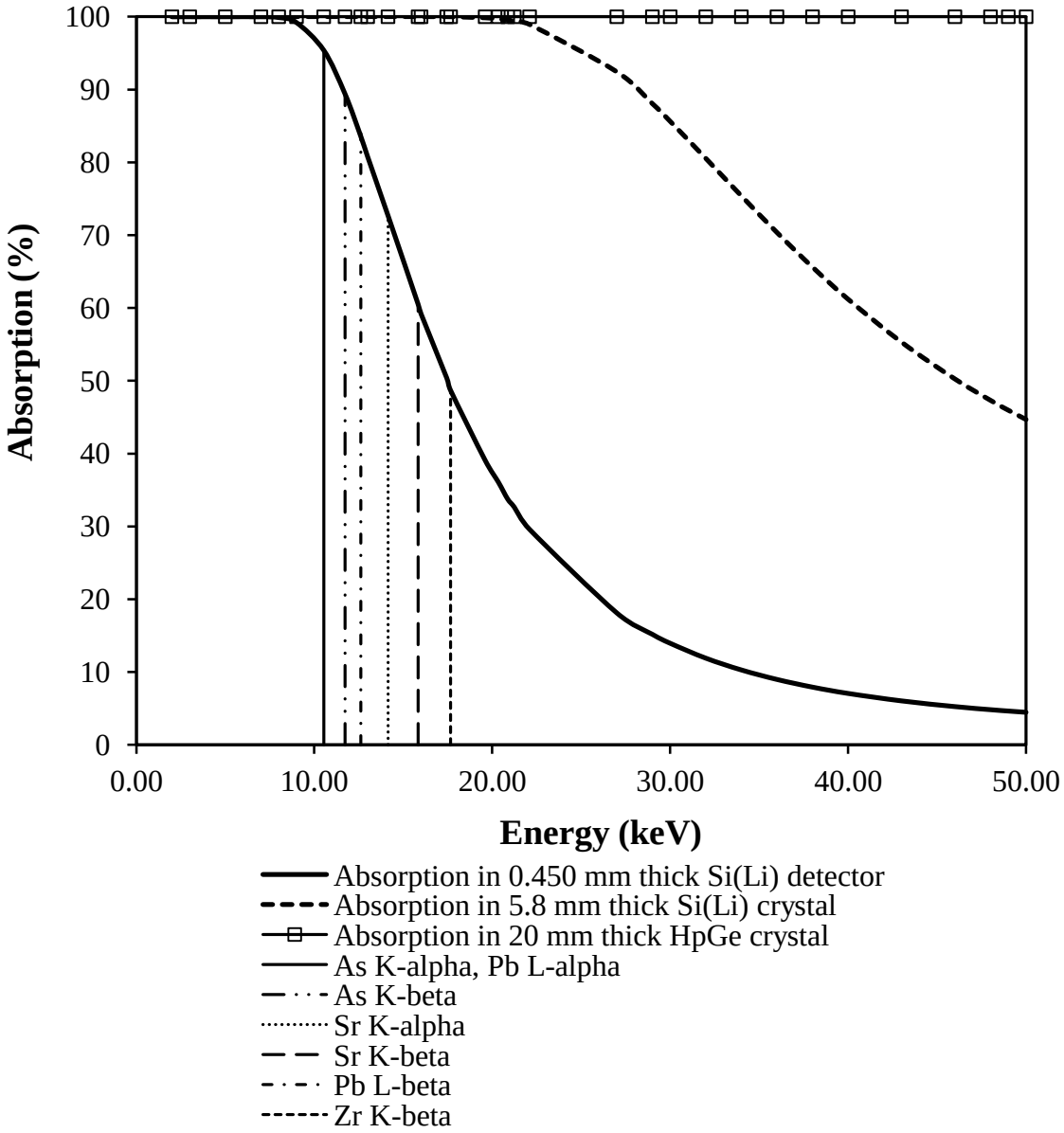

Figure 1.4: Absorption in various detector materials and thicknesses. Selected characteristic x-ray energies are highlighted on the plots.

In order to maximize absorption, it is clear that HpGe is the better choice due to the thickness of the detector being larger than that for a Si(Li) detector. For the characteristic x-ray energies investigated in this work, a Si(Li) detector with a thickness of a few ~5 mm (as indicated in the graph) would be an equally suitable choice. There are, however, other considerations that must be taken into account. The cross sections for different interactions (photoelectric absorption, coherent and incoherent scattering) are shown in figure 1.5, in both Si and Ge.

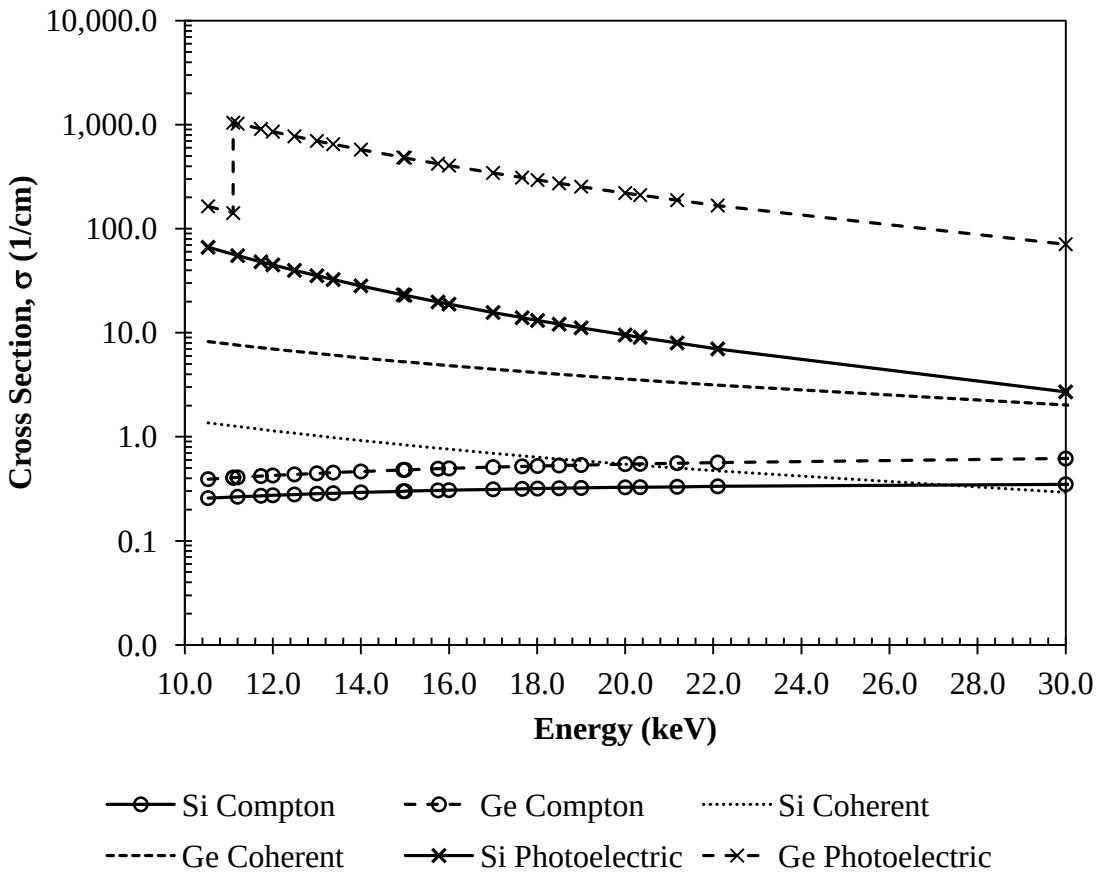

Figure 1.5: Compton (incoherent) and coherent scattering, in Ge and Si, for energies ranging from 10-30 keV. Vertical axis is shown on a log scale in order to clearly visualize the difference between the two curves corresponding to each material (Berger et al., 2010).

It is seen that for both Ge and Si, in the range of energies relevant to this work, the photoelectric absorption cross-section is larger than the Compton or coherent scattering cross sections. In fact, complete energy deposition in the bulk of the crystal by means of photoelectron absorption is particularly dominant for lower energies. The presence of a K-edge in Ge at an energy of 11.104 keV, which is just below the arsenic K_β translates to a higher efficiency in it than in Si. The fluorescence yields (K-shell) for Ge and Si are 54.5% and 5% respectively (Firestone, 2005). This indicates that there is a much higher probability that an interaction will result in characteristic x-ray production, as opposed to Auger electrons, in Ge than in Si. The characteristic x-rays of Ge will then be detected in addition to x-rays from the sample being studied. This presents two problems: characteristic x-ray and detector escape peak overlap, with lines of interest that are produced by the sample. Characteristic x-ray peaks from the two detector materials are shown in table 1.3.

Table 1.3: Ge and Si K-shell characteristic x-rays and their associated intensities which are listed per 100 K-shell vacancies (Firestone, 2005).

	Germanium		Silicon	
	E (keV)	**Intensity (%)**	**E (keV)**	**Intensity (%)**
$K_{\alpha,1}$	9.886	31.3	1.74	3.3
$K_{\alpha,2}$	9.855	16.1	1.739	1.64
$K_{\beta,1}$	10.982	3.98	1.836	0.056
$K_{\beta,3}$	10.975	2.05	1.836	0.028

For an incident energy of 22 keV, escape peaks lie at ~11.0-12.1 keV and overlap the with Arsenic characteristic x-ray peaks. Similarly for 17 keV, they would be 6.5-7.5 keV and are not a concern for this incident energy. Despite their relatively lower intensities than the Kα, the Ge Kβ lines are a clear concern for detecting arsenic. This is not the case for Si, where the lines are at a much lower energy. Si Kα and Kβ x-rays would appear in the x-ray spectrum at energies of 1.74 keV and 1.84 keV and thus have a negligible impact on the measurements. Thus it is straightforward to see a benefit in using it as opposed to Ge for measuring arsenic. For elements starting at Br (11.924 keV $K_{\alpha,1}$), and moving to higher energies, Ge escape peaks should not be a concern. The resolution of the HpGe detector is such that the Ge K_{β} may just lead to overlap with Se (11.222 keV $K_{\alpha,1}$), which is guaranteed to be cleared by Si characteristic x-rays. Attention must next be focused on the escape peaks. These are caused by incomplete energy deposition inside the detector crystal with the excess contributing to the exciting of electrons located to the conduction band. If the photon escapes without depositing this excess energy then a peak will be observed in the x-ray spectrum provided this process occurs often. The probability of escape peaks is highest at the detector's surface since incident x-rays will produce Si K-shell x-rays deeper but, due to self attenuation, these won't emerge through the crystal's surface. Of course, if the photon doesn't escape it will add on the incident photon's accumulated charge. Escape peaks for Ge would occur at ~ 10 keV below the full energy peaks and if the source energy is chosen to be less than ~25 keV, then this can lead to the appearance of Ge escape peaks at energies overlapping with the energies of interest here. The mean free path of incident x-rays in both detector materials is shown in table 1.4.

Table 1.4: Mean free path of characteristic x-rays in Si and Ge. The characteristic x-ray energies shown are calculated as a weighted mean of the individual $K_{\alpha 1,2}$ and $K_{\beta 1,3}$ lines as these are estimated energies that can be detected with a radiation detector. The values for μ/ρ and ρ were obtained from NIST (NIST, 2005) and the tissue model compositions were acquired from ICRU (ICRU, 1989).

Line	E (keV)	<x>_Si[1], (mm)	<x>_Ge[2], (mm)
As Kα	10.53	0.1473	0.0578
As Kβ	11.72	0.2017	0.0109
Se Kα	11.21	0.1763	0.0097
Se Kβ	12.49	0.2158	0.0116
Rb Kα	13.37	0.2962	0.0152
Rb Kβ	14.96	0.3390	0.0172
Zr Kα	15.75	0.4791	0.0234
Zr Kβ	17.66	0.6698	0.0317
	18.01	0.7093	0.0335
	18.50	0.7669	0.0360
Source	19.00	0.8287	0.0387
Energies	20.34	1.0096	0.0466
	21.18	1.1342	0.0520
	22.10	1.2811	0.0585

[1]ρ = 2.33 g/cm^3, [2]ρ = 5.323 g/cm^3

When compared to Si, shallower interaction sites in Ge are due to its higher Z. Combined with the higher energy of Ge characteristic x-rays, this results in a higher probability that escape peaks will be observed because the scattered photon has to escape from a depth in the crystal that is closer to the surface. The problem of Ge escape peaks was documented for XRF of Sr in bone using an I-125 source which produced a Ag Kβ escape peak at 15.06 keV between the Sr Kα and Kβ peaks (Pejović-Milić et al., 2004). For arsenic, in particular, in addition to escape peaks coming from a source of slightly lower incident photon energy than the Ag Kβ x-ray in I-125, the Ge Kβ characteristic x-ray line itself would overlap with both the As Kα and Kβ characteristic x-ray peaks. Thus, due to these two problems, Ge is not a viable detector material for use in this work and was not considered in previous work either (Studinski, 2005).

1.5.5 Processing signal generated in a detector:

The voltage pulse produced by the above mentioned pulse-type radiation detectors (integrating charge over total capacitance of detector and other pulse-processing components such as coupling capacitor between it and the first component in the pulse processing chain) is too small to work with and must be amplified before it can be further processed. The link between an amplifier and the detector is called a preamplifier.

1.5.5.1 Preamplifier:

It does not perform any amplification but its main tasks are to minimize capacitance and be a low source of impedance to the next component, which is a shaping amplifier. A minimal capacitance is achieved for a single cable coupling the detector with the preamplifier; the application of bias voltage and collection of detector signal are achieved with this cable. Voltage sensitive preamplifiers are used with a feedback resistor. Capacitors and resistors are common choices for achieving feedback. Capacitance is normally fixed for most detectors, making the preamplifier sensitive to charge collected which then gives the voltage of the input pulse. The problem of a changing capacitance, as could be the case when the detector's operating parameters are adjusted, thereby leads to a breakdown of this relationship, and is remedied in charge rather than the voltage-sensitive sensitive preamplifiers described above.

In a resistive charge-sensitive feedback preamplifier layout, the detector pulse is integrated through accumulation of charge, and thereby voltage, on the feedback capacitor. If the capacitor's time constant (required in order to reset it and accept more pulses) is longer than the input pulse duration, then the proportionality between voltage and current exists. Changing capacitance has a minimal influence on output voltage, in this configuration. The preamplifier (output) signal has a fast rise immediately followed by a long decay time. Non-ideal electrical contact to the active region of the detector or undepleted semiconductor region resistance will influence the duration of the rise time in addition to the detector's charge collection time. With a long decay time, pulses will pile up, for high counting rates, drive the preamplifier and distort its output since DC voltages limit the preamplifier's divergence from baseline. Minimizing the feedback resistance helps with this but leads to an increase in noise.

If the resistor is removed, charge (and so voltage) piles up in a staircase pattern on the feedback capacitor. When the maximum acceptable voltage is reached, the preamplifier has to be reset. Such preamplifiers are called transistor reset or pulsed optical feedback preamplifiers. The latter were not used in this work and so are not discussed. The transistor reset approach uses active circuitry with a transistor to achieve the required sudden drop in output voltage. The problem with this sudden drop is overloading, when followed by an amplifier (as is typically the case), so an inhibit out signal blocks signals when it is turned on prior to the reset beginning. The dead time for transistor reset preamplifiers is on the order of a few microseconds. Transistor reset designs result in higher noise levels than pulse optical feedback approach but for detectors with high capacitance, it offers a lower-noise option (Landis et al., 1982).

1.5.5.2 Amplifier:

A shaping amplifier amplifies and shapes the preamplifier output. This allows for accurately counting the pulses, of different pulse heights, and performing subsequent analysis. When the detector signal is passed through a shaping amplifier, it is converted into an (analog) voltage pulse with its amplitude increased from a few mV to < 10 V. The finite decay of resistive feedback preamplifier pulses means input pulses from it are not

step voltage pulses. Zero crossover, called undershoot, will result and, although it gets back to zero, the long decay of the preamplifier pulses means a subsequent pulse's amplitude could be erroneous if it occurs during this time. A pole zero cancellation will fix this problem (Sherman and Roddick, 1970) and allows for good resolution. Since an infinite decay time is observed with active reset circuitry, the pole-zero adjustment is not required here.

1.5.5.3 ADC and MCA:

An analog-to-digital converter (ADC) converts the detector's analog pulse height into a digital number, where the value of the number will change based on the height of the pulse. ADC output, comprising pulses of various heights in a digitized format, is then represented on a computer in a histogram of input pulse height, where the ADC-histogram display combination is called a multichannel analyzer (MCA). In modern pulse processing systems, this combination is housed in a single commercially available unit. This pulse typically has a triangular shape. A series of detected photons would result in a series of triangular peaks. The pulse peaking time, τ_P, is the time between the beginning of the voltage pulse and the peak of the voltage pulse. When this voltage pulse is amplified, it is shaped so as to eliminate noise. The shaping time is given by T_S where $\tau_P \sim 2T_S$. Shorter peaking times make it possible to collect more counts (pulses) in a particular amount of time and the detector's "dead" (or processing) time is minimized as (voltage) pulse pile-up is greatly reduced. Piled up voltage pulses can cause saturation during amplification and result in spectral distortions (Knoll 1999). The bench top pulse processing systems used in this work are discussed later.

1.5.6 Detector types:

1.5.6.1 Lithium Drifted Silicon Detector [Si(Li)]:

For a long time, Si(Li) detectors have been the benchmark for lower energy dispersive x-ray detection. Lithium has good mobility in silicon and is a donor atom. The pn junction required for this detector is accomplished by diffusing Li into p-type Si. After diffusion, gold ohmic contacts are attached to either side of the junction. These detectors allow for a depletion depth of ~5-10 mm, by drifting lithium which is accomplished by simultaneously heating the junction while reverse biasing it, thereby creating a nearly intrinsic region. The thickness of the active region is proportional to the time over which the drifting is performed (Tsoulfanidis et al., 2011). This was the main detector used in this work and was also used in previous work involving elements (Fe, As, Sr) covering energies ranging from 6 – 16 keV, in skin, bone and teeth (Abu Atiya, 2012; Da Silva et al., 2008; Heirwegh et al., 2012; Studinski et al., 2006; Zamburlini et al., 2008).

1.5.6.2 Silicon Drift Detector (SDD):

Silicon Drift Detectors are a comparatively modern type of detector compared to Si(Li) and Hp(Ge) detectors, which have been around since 1962 and 1970 respectively (Theodórsson, 1996), and PiN diodes, which were invented by Jun-ichi Nishizawa in 1950 (Kleinman, 1956). The concept of SDDs was first introduced by Emilio Gatti, an engineer at the Polytechnic Institute of Milan, and Pavel Rehak, a physicist at

Brookhaven National Laboratory at the European Symposium on Semiconductor Detectors in 1984 (Gatti and Rehak, 1984) and the first design specific to measuring energy soon followed (Rehak et al., 1985). The SDD is made up of a 450 μm thick detector chip of high-resistivity Si, often called a Si wafer because of its order of magnitude reduction in thickness compared to conventional Si(Li) detector bulk sizes. The SDD wafer is fully depleted by means of a negative bias voltage applied to both of its sides – a translationally invariant thin pn junction on the side facing incoming radiation and an array of p+ drift rings (electrodes) on the other side – until full depletion is achieved. On one side, the voltage is gradually increased using drift rings (electrodes are of progressively higher bias voltage), producing a strong transverse and radial electric field within the disc that then acts like a guide/pathway, for charge carriers, ending at a small collection anode. Charge carriers generated due to absorption of ionizing radiation, will drift towards the n+ collection anode.

A lower detector capacitance allows for the benefit of usability with higher count rate applications because electronic noise is reduced, thereby allowing for shorter shaping times to be used in the pulse processing system. The avoidance of stray capacitances (long bonding wires and connection pads) is firstly achieved by connecting the anode to the first transistor required in the amplification process by means of a small metal strip. This is possible by integrating a JFET (junction gate field-effect transistor used to convert current to voltage) directly into the charge-collecting anode (Lechner et al., 1996; Radeka et al., 1989), thereby reducing electronic noise between the FET and the collection anode. It should be noted that there is no need for an external reset pulse because the transistor has its own auto-correcting means of discharge. The built-in reset mechanism enables pulsed-reset operation and this translates into lower detector dead times, allowing SDDs to be used in applications involving very high count rates (Fiorini and Lechner, 1999; Strüder and Soltau, 1995). Second, since capacitance is directly proportional to area, a small area collection anode is used. Next, since electron loss may result from direct exposure of the anode-FET combination to incoming radiation leading to an increase in low energy background (Lechner et al., 1996), the JFET may be moved to the edge of the wafer as opposed to the center. This allows the anode-FET combination to be shielded from direct irradiation by means of a circular shaped collimator (Lechner et al., 2004). Since this means that the anode only collects electrons from one side, its size can be further reduced. Finally, the integrated FET layout also reduces mechanical vibration, reducing microphony further reducing noise. These measures to reduce capacitance allow for a drop in electronic noise improving the resolution. With suitable pulse processing systems, this resolution can be maintained for high count rates. An extremely thin 25 μm Be entrance window separates the detector's sensitive area from the ambient atmosphere, guaranteeing excellent transmission for low energy x-rays. Due to the use of high purity Si (low leakage current) in the manufacturing of the SDD, LN_2 cooling is not required, making possible a compact design for the detector's housing and straightforward accommodation of the SDD in tight spaces and previously unrealizable geometries.

At high energies, an SDD's efficiency is related to the amount of depletion of the 450 μm silicon wafer. X-ray absorption in the silicon bulk is 95.4% for energies up to ~10 keV (close to the As Kα energy) and ~50 % at 20 keV and this is shown graphically in figure 1. Absorption is proportional to thickness so a 5.8 mm thick crystal would have greater absorption than the 450 μm thick SDD wafer. Since the SDD wafer is much thinner, the transverse distance that any charge is required to travel is significantly reduced. This indicates that, at the As Kα energy, nearly 95% of all incident particles deposit all their energy in the Si wafer; this number is reduced to 72.7% for the Sr Kα energy, 60.6% for the Sr Kβ and Zr Kα energy, 48.7% for the Zr Kβ energy and ~29.6% for the Ag Kα energy. The significant drop-off in absorption at the Zr energies is the reason why this element is often used as an internal Si wafer collimator material in SDDs, as most SDD applications do not investigate such high energies. For the higher energies (Zr at 17.67 keV, Ag at 22.10 keV) a large fraction of x-rays pass through the detector material without full energy deposition meaning that there is a possibility of detecting their corresponding 180-degree Compton backscatter off the backing of the housing of the head of the SDD, producing energies of 16.52 keV for Zr Kα and 20.34 keV for Ag Kα.

1.5.6.3 PiN diode detector:

PiN diode detectors have been around for almost as long as Si(Li) detectors and are another approach towards meeting the need of "faster" detectors which minimize capacitance. In a PiN diode configuration, a nearly intrinsic (i) region (undoped) is inserted between n-type and p-type doped semiconductors and filled with charge carriers from those two regions. Current flows when electron-hole equilibrium is established. The size of the depletion region is thus increased in this way. Forward biasing the PiN diode leads to a very strong charge carrier flow rate, as explained earlier, requiring an electric field covering almost the entire intrinsic region. The field-induced high flow rate leads to fast operation of the detector. The pulse shaping time required is thus shorter than that for a Si(Li) detector (Knoll, 1999) and the capacitance can be less than 2 pF for smaller diode sizes (Ramírez-Jiménez et al., 2006). With a thickness of a couple of millimeters the absorption at ~15 keV would make such a detector applicable for x-ray spectroscopy applications involving energies close to it. Since a large number of electron-hole pairs are not produced by low energy photons, noise reduction is important and is achieved by means of a thermoelectric (Peltier) cooling mechanism, which uses the Peltier effect to function as a heat pump.

1.5.7 Pulse processing systems used in the current work:

1.5.7.1 Lithium Drifted Silicon Detector [(Si(Li)] DSPECPLUS system:

The Si(Li) detector system was made up of an Ortec SLP1080 Si(Li) detector (Ortec, Oak Ridge, TN, USA) coupled to an Ortec DSPEC PLUS MCA box. The diameter of the Si(Li) detector crystal was 16 mm and the crystal's sensitive thickness was 5.8 mm. Output pulses from the transistor-reset preamplifier were processed as described earlier. In the current work, communication with the host PC was accomplished

using an Ethernet BNC connector, although a 9-pin RS-232-C connector was also available. As with the Canberra DSA 1000, the trapezoidal pulse parameters – rise time and flat top – can be adjusted. The DSPEC PLUS unit allows 115 rise time choices, ranging from 0.2 to 23 μs, and 22 flat top widths ranging from 0.4 to 2.4 μs. The rise time and flat top were set to 12 μs and 0.9 μs respectively, as per previous work where the ORTEC recommended parameters were found to work best (Studinski, 2005). The DSPEC PLUS MCA was controlled using Ortec's MAESTRO-32 MCA software. This software was also used to control the high voltage required for the Si(Li) detector, which was -1000 V. The conversion gain (number of channels or number of bins in histogram) was set to 2048 and the effective linear gain was chosen empirically to allow energies up to ~30 keV to be displayed.

1.5.7.2 Silicon Drift Detector (SDD) DSA 1000 system:

The SDD system was comprised of a AXAS-A (Analytical X-Ray Acquisition System-Analog) module comprising an 80 mm^2 active area Vitus H80 single-element SDD (KETEK GmbH, Munich, Germany), preamplifier and shaping amplifier. A KETEK analog ADC and MCA were provided in a separate unit that can be connected via a USB port to a host PC on which MCA software is installed and also functions as a power supply. A resistor feedback preamplifier was coupled to the SDD. For the current work, the AXAS-A preamplifier output was coupled to an advanced DSP-capable Canberra Digital Spectrum Analyzer (DSA1000) MCA unit (Canberra Inc., Meriden, Connecticut, USA). With the DSA1000, or the ORTEC DSPEC described above, preamplifier signal digitization is performed at the beginning of the pulse processing sequence as detailed earlier. Analog-based functions in the filtering process are thus minimized in the DSA1000. Digitized signals were then filtered to produce a trapezoidal pulse shape that cannot be achieved with traditional analog pulse processing. The DSA 1000 allows for a choice of up to 40 trapezoidal rise times range from 0 to 48 μs and up to 21 flat top settings ranging from 0 to 3 μs. The rise time was chosen to be 4.0 μs and the flat top was set at 0.8 μs, giving a shaping time that matched that provided by the SDD's internal shaper (Ketek, 2011). With digital shaping capabilities, peak stability is superior to that possible with analog techniques. A USB interface was used for communication with the host at 12 Mbits/sec. An RS232 serial port was also available but not used in the current work. The DSA1000 MCA was controlled via a host PC with Canberra's Genie2K software installed. Shaping time parameters could be adjusted through the software. The conversion gain was set to 4096 and the effective linear gain was chosen empirically to allow for energies up to 40 keV to be displayed as this was the highest energy that the manufacturer allowed to be accessed with the detector.

1.5.7.3 Si PiN diode detector system:

A PiN diode detector was used with an Innov-X Alpha 4000S portable handheld x-ray analyzer system (Innov-X Systems (Mississauga, ON, Can). The analyzer was developed for use in soil sampling since it could be taken into the field with the ability to perform instantaneous data analysis. It ran on Li-ion batteries (8 hour battery life) but also had an AC adapter available to plug it into a wall socket for lab based work. The

analyzer was operated by engaging a trigger, which generated x-rays. The x-ray tube and detector were contained within the analyzer unit. A Hewlett Packard (Palo Alto, CA) handheld iPaq personal data assistant (PDA) was provided to record the spectra when the trigger was engaged and set irradiation times. The detection system parameters that could be changed were the collection time and number of consecutive trials that could be run. Other MCA parameters, such as shaping time, effective and conversion gain settings, were not accessible and the preamplifier type was not indicated.

The system was programmed, by the manufacturer, with the ability to identify twenty-five elements, with the ability for the user to add elements. This capability was built into the analyzer, eliminating the need for additional computing hardware or software. This provided a benefit of using the system, in field work, since it eliminated the need to transport the detector and pulse processing electronics to the field site. The PDA ran Microsoft Windows CE (portable system) operating system and was designed for touch-screen use, enabling the user to communicate with a built-in MCA and manually input/vary parameters such as counting time and number of trials. The MCA software was designed to display the collected spectrum and perform analysis without the need for calibrating the device on-site. Instead, the calibration was performed empirically. Data protection was ensured by accumulating the results in a base-2 number (binary) system. When synched with a printer, the software was capable of printing out data reports (Innov-X, 2005).

Chapter 2 Measurements with conventional x-ray tube benchtop system:

2.1 Introduction to article draft 1:

Draft I documents phantom calibration work performed on a molybdenum (Mo) anode x-ray tube based XRF detection system. The system was designed for quantification of arsenic in skin and previous phantom calibration work was performed and published after the initial completion of its construction. The current work documents the results of phantom calibration studies performed after extensive modifications were made to the housing of the detection system. Characterization of the calibration performance and dosimetry is reported for the after modification system with the emphasis on extending the methodology of previous research.

The benefits of a tight geometry for x-ray fluorescence work allow for improvements in the performance of the spectrometer. The effect of such modifications must be investigated both qualitatively and quantitatively. In terms of this current system the main metric of this evaluation is minimum detection limit (MDL). In addition to measuring MDL through system modifications, this chapter investigates methods for normalization of extracted fluorescence peak areas. Tube aging and variations in source strength can make interpretation of MDL, based exclusively on such signals, risky. Small changes in system dead time can affect MDL by altering the variance structure involved in the experiment. MDLs from scatter-based normalizations are compared to a dead time correction factor and normalization against real time (for a fixed live time). Application of these sorts of corrections are required to make a fair comparison between results obtained at different dead times. Other benefits of normalization include correction against variation in phantom or sample size and positioning, both of which can be expected to be present when the system is used *in vivo*. Adjustment of pulse rise time is also investigated as a means of reducing dead time and improving MDL. Finally, dosimetry was performed to map the distribution of dose over the area of the incident x-ray beam.

2.2 Draft for article 1 follows:

Extended development of a 50 W tube based K-shell XRF measurement system for detection of arsenic in soft tissue mimicking polyester resin

E. D. Desouza[1], D. R. Chettle[1], D. E. B. Fleming[2], Ana-Pejovic Milic[3] and F. E. McNeill[1]

[1] Department of Medical Physics and Applied Radiation Sciences, McMaster University, Hamilton, ON, L8S 4K1, Canada
[2] Department of Physics, Mount Allison University, Sackville, NB, E4L 1E6, Canada
[3] Department of Physics, Ryerson University, Toronto, ON, M5B 2K3, Canada

Author to check proofs:

Elstan Desouza
Department of Medical Physics and Applied Radiation Sciences
McMaster University
Tanden Accelerator Building Room 104/D
Hamilton, ON
Canada
L8S 4K1
Tel.: 905-525-9140 Ext. 21757
Email: desouze@mcmaster.ca

Short title: Quantitative XRF analysis of arsenic using phantoms
Keywords: Arsenic, x-ray fluorescence, K-edge filter, Dead time, Normalization

Manuscript will be submitted: X-Ray Spect. 2013

Author contributions:
Elstan Desouza was responsible for experimental setup, data acquisition and analysis.
Ana Pejovic-Milic offered unrestricted use of equipment.
David Chettle and David Fleming assisted in interpretation of data.
Elstan Desouza was responsible for preparation of the draft manuscript.
Fiona McNeill supervised and guided the research.

Improvements to the geometry of an x-ray tube-based system for the measurement of skin arsenic concentrations are reported in terms of its ability to measure arsenic in 2.8±0.1 mm thick skin tissue-mimicking resin phantoms and using a 50 W x-ray tube with a Molybdenum (Mo) anode. For a rise time of 12 μs, a system dead time of ~41 μs was found, using a Si(Li) detector. For a fixed percent dead time of ~30%, the benefits of an absorption edge filter were demonstrated through a factor of 5 enhancement in total throughput per unit current. Scatter normalization was found to be more feasible with the filtered spectrum and this was found to produce a MDL that is (17±5) % lower than that obtained without any normalization. Reproducibility in the detection limit was shown to be similar to that found in previous work. Best detection limits with the system are ~0.5 ppm, which are comparable to those found in previous work. However, the current work is able to report these detection limits, with either an absorption edge filter or a regenerative monochromatic filter (RMF), for lower voltage and current settings than previously. An improvement of ~0.05 ppm was noted in MDL, for a shorter rise time of 8 μs. Improvements in detection limit from ~0.9 ppm to 0.7 ppm and ~0.8 ppm to 0.5 ppm were found by reducing the source-phantom or phantom-detector distance respectively. The effective dose delivered to the palm of the hand ranged from (0.04±0.01 – 0.20±0.04) μSv for the exposures required to obtain listed MDLs. The whole body dose ranged from (42±12) μSv to (658±124) μSv. The corresponding equivalent (skin) dose delivered ranged from (5±1) mSv to (113±27) mSv.

1. Introduction and Background

1.1 Arsenic and its toxicity

Arsenic (As) is an element known to be naturally occurring everywhere on the planet (Fishbein, 1981). A form of cancer (Blackfoot disease) has been found to originate in areas with a high As concentration in water, drawn from artesian wells (Chen et al., 1985) and an excess incidence of cancer related deaths may have resulted from As contaminated drinking water in the United States (Morales et al., 2000). Symptoms of skin cancers have been linked to the consumption of arsenic in medicines and drinking water (Mandal and Suzuki, 2002).

1.2. Techniques for measurement of Arsenic

Arsenic is retained by skin, leading to its accumulation at a superficial skin depth, indicating that skin would be an appropriate organ for the investigation of arsenic exposure (Schwartz, 1997). High As concentrations, on the order of several ppm (parts per million unit mass), have been found in skin scales and nails (Das et al., 1995) but hair and nails soaked in radiolabelled arsenite have been found to be somewhat unsatisfactory for use as a biomarker for its presence (Maes and Pate, 1977) because of contamination issues. In addition, repeated measurement of As content at the same target site would not be feasible with nails and hair due to their rapid turnover.

The implications of the structure of skin suggest that As is contained in the epidermal layer and that its distribution would be directly proportional to the concentration of keratin. That is, arsenic concentrations are greatest for layers with high amounts of keratin (Misbahuddin et al., 2008). In addition, skin is not only a site of As accumulation but also, by comparison with other organs, an organ at an elevated threat of As related lesions. Thus, for this study, skin was chosen as an appropriate target site for measurement of accumulation (and ideally long term exposure) of As. Repeatable non-invasive measurements that determine arsenic levels in the directly affected organ are desirable. X-Ray Fluorescence (XRF) is an example of a method that may permit such non-invasive repeatable measurements.

1.3. X-Ray Fluorescence

X-ray energy can be transferred to tissue by inelastic scattering and photoelectric absorption. It is possible for a characteristic x-ray, with energy equal to the difference in the binding energies of the ejected and transferred electrons, to be emitted or for one or more Auger electrons to be released. For As the probability of characteristic x-ray emission per photoelectric interaction, the fluorescence yield with a K-shell electron, is 57% (Robinson, 1991).

Over the years, XRF has been used for *in vivo* XRF measurement, for example of Pt in head and neck tumors (Jonson et al., 1988) and Fe in skin (Abu Atiya, 2012; Farquharson and Bradley, 1999). A technique for detection of As was developed, with a ^{109}Cd source and As doped polyester resin with a nylon backing as a skin phantom, giving an instrumental minimum detection limit (MDL) of 3.5±0.2 μg As/g of resin

(ppm) and a dose of 5.8 mGy (Studinski et al., 2005). Using a 50 W x-ray tube (Mo filter, ~40% dead time) as the source, the MDL was improved to 0.40±0.06 ppm, using 2.8±0.1 mm thick resin phantoms (50 mm diameter) and a considerably reduced exposure dose of 0.64±0.03 μSv (Studinski et al., 2006). Another research group found an MDL of 0.446±0.006 ppm for a measurement time of 120 s using a portable x-ray tube and a Si PiN diode radiation detector. The phantoms were thicker (8 mm) but smaller (42 mm diameter) with no nylon backing (Fleming and Gherase, 2007). Such a "portable" system offers an advantage of significantly lower exposure time and measurement mobility.

1.4. Motivation for current work:

Previous work documented experimental work on a 50 W polychromatic molybdenum (Mo) anode x-ray tube based XRF system, following simulations into appropriate operating conditions. The experimental layout has since been modified so as to allow different experimental setups to be realized. Specifically, the copper shielding cabinet that contains the source has been changed to allow the detector to be placed closer to the surface of the phantom. The benefit is that comparable MDL performance may be achievable for a lower source strength since a larger fraction of the fluorescence is being captured. The cabinet has also been altered so as to allow the detector and phantom to be placed closer to the source. A $\sim 1/r^2$ drop-off in source strength is expected when working at a larger distance away from the source; the MDL system performance at a shorter source-phantom distance may be able to match that at a longer distance while using a lower accelerating voltage and current. This would be beneficial since the dose delivered *in vivo* could be reduced.

A meaningful comparison of results acquired for different source strengths, i.e. different tube voltage, current or system dead time, is crucial when investigating the effect of hardware changes such as those documented above. The x-ray tube output cannot be monitored during a single phantom measurement, or later *in vivo*, without interfering with the XRF measurement. Thus, an in-spectrum correction for fluctuations in source strength is required. Coherent normalization has been used by coworkers studying lead and strontium in bone (Heirwegh et al., 2012; Somervaille et al., 1985; Todd, 2000; Zamburlini et al., 2008). The XRF-related scatter components have been explored for *in vivo* XRF to provide a correction factor for variations in tissue. Advantages of employing such a correction to *in vivo* concentrations would be to account for inter-subject variations in the target volume and differing thicknesses of skin between the measurement site and excitation source. In the case of lead in bone, due to coherent scattered and characteristic x-ray energies being very close to each other, both of these quantities (involved in a coherent normalization procedure) are equally affected by skin thickness and bone shape. Thus different anatomic features between different individuals are accounted for by this normalization procedure and a further correction is not necessary. Likewise, despite a larger difference in the aforementioned energies involved, this approach was found to work for *in vivo* uranium in bone via XRF with a Co-57 source (O'Meara et al., 2001). Due to the composition of bone, it is much more likely that strontium x-rays will be absorbed in soft tissue than the coherently scattered photons and

that a means of utilizing the coherent scatter signal to account for a different thickness of soft tissue overlying the bone being studied is not possible. Thus, the effectiveness of the normalization depends on the application. At the Mo Kα incident energy, nearly 70% of incident photons will pass through resin, or skin, without full energy deposition and so scatter normalization cannot be expected to correct for variations in arsenic depth distribution in skin. However, a scatter-based normalization may be able to correct for differences in shape and size of the target measurement site since these will provide different system dead times. Furthermore, variations in positioning and x-ray tube output may be corrected for, using such normalization.

As a first step, the current work looks into normalization for the molybdenum (Mo) anode polychromatic x-ray tube based XRF setup after modifications. An investigation of Compton and coherent scatter normalization approaches is performed, in terms of their effect on the minimum detection limit of arsenic in resin skin phantoms. These normalization approaches are compared to an empirically determined dead time correction factor, total scatter contribution (gross counts under the scatter region of the spectrum) and normalization to real (clock) time (recall that, with this system, live time is fixed at 1000 seconds). Finally, the dose delivered is calculated using an array of thermoluminiscent dosimetry chips. Previously, this was recorded at a single position. An array of dosimetry chips allows for a map of the x-ray dose at the surface of the phantom. This is the location where the subject's hand will be placed during *in vivo* work. Hot spots in the incident x-ray beam can thus be identified.

2. Theory – Paralyzable Model for dead time:

The arsenic x-ray tube detection system has been used in previous and current work with both high and low dead times ranging from 15-40%. One approach to making a fair comparison of results acquired under such different conditions would involve applying a dead time correction to all data, where the correction factor is determined based on the specific system dead time, or input count rate, used.

For spectra collected from a steady-state source (where counting rate is not expected to change during the spectrum-acquisition time, ex. a long lived isotope), the detector dead time is given by

$$m = ne^{-n\tau} \tag{1}$$

where m is the observed (or recorded) counting rate, n is the true event rate and τ is the dead time. During the detector's "live" or active period, a specific τ is known to succeed an individual event recorded by the detector. The detector is the entire detection system, comprising a solid state detector and associated pulse processing electronics. The events occurring during τ are not recorded, or are said to be lost, by the detection system.

Through a series of measurements of m and n, τ can be determined since an exact solution to equation 1 does not exist.

The true interaction rate n_i for a specific measurement can be represented as $n_{ref}x_i$, where n_{ref} is the true interaction rate for some reference measurement and x_i is an associated scaling factor between n_{ref} and n_i.i.e. $n_i = n_{ref}x_i$. Then equation 1 can be written as

$$m_i = n_{ref} x_i e^{-n_{ref} x_i \tau} \tag{2}$$

Taking the ln of both sides of equation 2 and re-arranging gives

$$\frac{m_i}{x_i} = n_{ref} e^{-n_{ref} x_i \tau} \tag{3}$$

$$ln\left(\frac{m_i}{x_i}\right) = -n_{ref}\tau x_i + ln\left(n_{ref}\right) \tag{4}$$

which is of the form y = mx + b where m = $-n_{ref}\tau$ and b = $\ln(n_{ref})$. Isolating for n_{ref} from the two expressions and then combining the results gives $\tau = -m/e^b$. Thus, plotting $\ln(m/x_i)$ as a function of τ, and fitting to a straight line, allows the dead time to be determined from the slope and intercept. A source with the ability to offer increasing incoming counting rates would allow for the scaling factor x_i to be determined and the above method could be followed to determine the detection system's dead time. An x-ray tube with an adjustable tube current offers the ability to do this.

3. Method:

3.1. Phantoms

Standards were prepared using a mixture of polyester resin (Bondo Corp., Atlanta, GA) and Arsenic Atomic Absorption Solution (AAAS) containing As_20_5. A hardening catalyst was added to the mixture, which was left to dry producing a solid block and then cut into slices that were used as phantoms. An additional slice was produced to allow verification of As concentrations in each block, by neutron activation analysis at the McMaster Nuclear Reactor (Hamilton, Canada). The preparation and verification of concentrations was documented in earlier work (Studinski et al., 2005).

3.2. X-ray tube and detector:

The system made use of an XTF5011 50 W Mo target x-ray tube from Oxford Instruments (Scotts Valley, CA, USA). The tube allowed a maximum voltage and current of 50 kV and 1 mA respectively. Tube output was filtered, to allow for reasonable dead

times of <40 %. Filters were purchased from ESPI Metals (Ashland, Oregon, USA). The tube was encased in a copper shielding box to keep the dose rate outside the box to within required regulatory limits. The box was divided into two sections, separated by a solenoid-controlled shutter, allowing radiation either to be restricted into one section or to irradiate the entire box. The tube was placed in one section and holes were drilled in the second section allowing for insertion of the detector and phantoms. A copper flight tube was used to connect both sections of the box. A plastic ring, placed around the detector's trunk, engaged a security interlock switch. A similar switch was placed near the phantom opening. Tube operation was allowed only when both switches were engaged. Shielding cabinet dimensions are presented in earlier work (Studinski et al., 2006).

An EG&G Ortec (Oak Ridge, USA) silicon lithium [Si(Li)] drifted detector, with a 16 mm active diameter crystal (200 mm^2 active area) was used to record the fluorescence. The FWHM at 5.9 keV was quoted as 220 eV. An Ortec DSPEC PLUS MCA with MAESTRO spectrum software was used to set irradiation and shaping time and record spectra. With modifications to the housing of the shielding cabinet, the phantom-detector distance was fixed at (3.0±0.2) cm for the majority of this work. A foil was placed at the end of the flight tube primarily to reduce the system dead time. Molybdenum, silver, niobium, zirconium and palladium foils used in this work are 3N8, 5N, 3N, 3N and 3N5 purity respectively. The exact composition was not reported by the manufacturer in the associated certificate of analyses and so trace contamination due to manufacturing of foils is not available. The experimental setup is shown in figure 1.

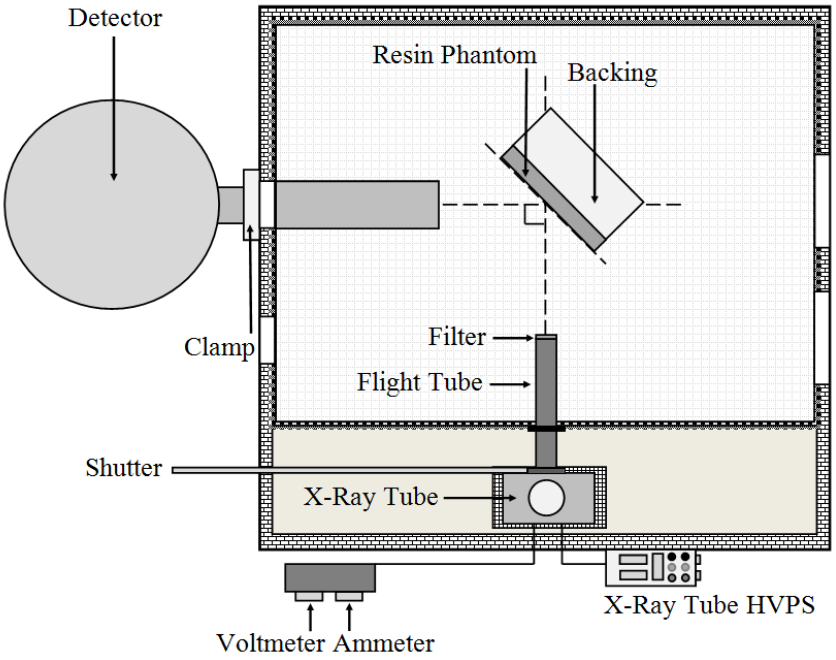

Figure 1. Top view of experimental setup for this system.

3.3. Dead Time correction factor:

The x-ray tube used with the arsenic x-ray tube detection system was used for dead time calculation with a 60 ppm arsenic phantom was oriented in standard 45-degree geometry. The Si(Li) detector was coupled to an Ortec DSPEC PLUS MCA box whose MCA software, MAESTRO, offers an Input Count Rate (ICR) feature. This is not the number of processed pulses (or counts) coming from the unit's ADC. Instead, this gives the actual counts that appear at the input, in units of cps, which is what is required by n_i (in the previously described dead time equation). Spectra and the ICR were recorded over 600 seconds real (clock) time, as the tube current was increased. The true event rate n_i scales with I_i and so it can be represented by $n_i = n_{ref}x_i$, where n_i is represented by the product of some reference true count rate n_{ref} and a current scaling factor x_i, with $x_i = x_{ii}/x_{ref}$ for tube current x_{ii} and some non-zero reference tube current, x_{ref}. x_{ref} is chosen to produce a dead time of no more than ~10% where the measured and input count rate curves are still nearly overlapping each other, i.e. a drop-off in measured count rate has not yet taken effect.

Part of the motivation behind determining a dead time correction factor was to compare meaningfully the MDLs acquired at different system dead times. The dead time is used to calculate the correction factor given by $CF = n_i/m_i$, which can be expressed, in terms of the experimentally determined dead time to be $CF = \exp(n_i\tau)$, where n_i is taken as the ICR. For a specific set of tube conditions, n_i is recorded so the dead time correction factor, and its uncertainty, were determined and used to correct phantom fitted peak areas that are discussed in the results section. Many MCAs provide a number for dead time, but we were not confident of the algorithim used. This method allowed us to calculate dead time via a straightforward and simple method which only relied on input count data.

3.4. Experimental procedure for phantom calibration, using MDL, and dosimetry:

Phantom measurements were performed over 1000 seconds live time. With the tube running, a radiation shutter was closed and phantoms were inserted and removed through a side door in the copper cabinet. Each phantom was measured three times, for a total of 15 phantom measurements covering five arsenic concentrations – 0 – 100 ppm. A nylon backing (1.3±0.2 cm thick) was placed behind the phantom to replicate bulk tissue behind skin.

Dosimetry was performed using an array of dosimeters, to map out the x-ray beam at the plane of interaction with the phantom. This will indicate the dose delivered by exposures corresponding to various experimentally used arrangements. Lithium Fluoride Li(F) thermoluminescent dosimetry (TLD) chips, from Global Dosimetry Services (Irvine, CA, USA), were used. Individual TLD chip dimensions were (3.2 X 3.2 X 0.89) mm^3. The chips are sensitive to absorbed doses ranging from 0.02 Gy to 5 kGy. Calibration was performed by Global Dosimetry, with appropriate in-house corrections applied based on the incident energy used here – Mo Kα (see text later for discussion of this). The response of the chips will fade by about 10% over the course of a year. This

was not an issue for the current work, since the chips were shipped back for reading (Zamburlini et al., 2007), shortly after exposure.

The chips were attached to the surface of the nylon block. For system calibration work, the resin skin phantom was placed against the nylon backing. Here, the phantoms were considered as the representation of skin and so were placed in front of the nylon backing. However, since the dose was required in skin, the chips replaced the resin skin phantoms. i.e. the chips, with a similar properties to soft tissue or skin, represented skin during dosimetry work. Thus, the resin phantom was not used in dosimetry work in front of the backing. In order to position the chips accurately on the block, a piece of gafchromic EBT2 (dosimetry) film (ISP Dosimetry) was used to image the x-ray beam. The beam was found to be elliptical in shape (discussed later). The film is intended for use in radiotherapy dosimetry calculations at MV potentials (Aland et al., 2011; Devic et al., 2004; Nakano et al., 2012; Niroomand-Rad et al., 1998; Reinhardt et al., 2012). For the current application, uncalibrated film was used to position the phantom or TLD chips in the center of the x-ray beam. Based on its position on the block, the chips were arranged in an array as shown in figure 2.

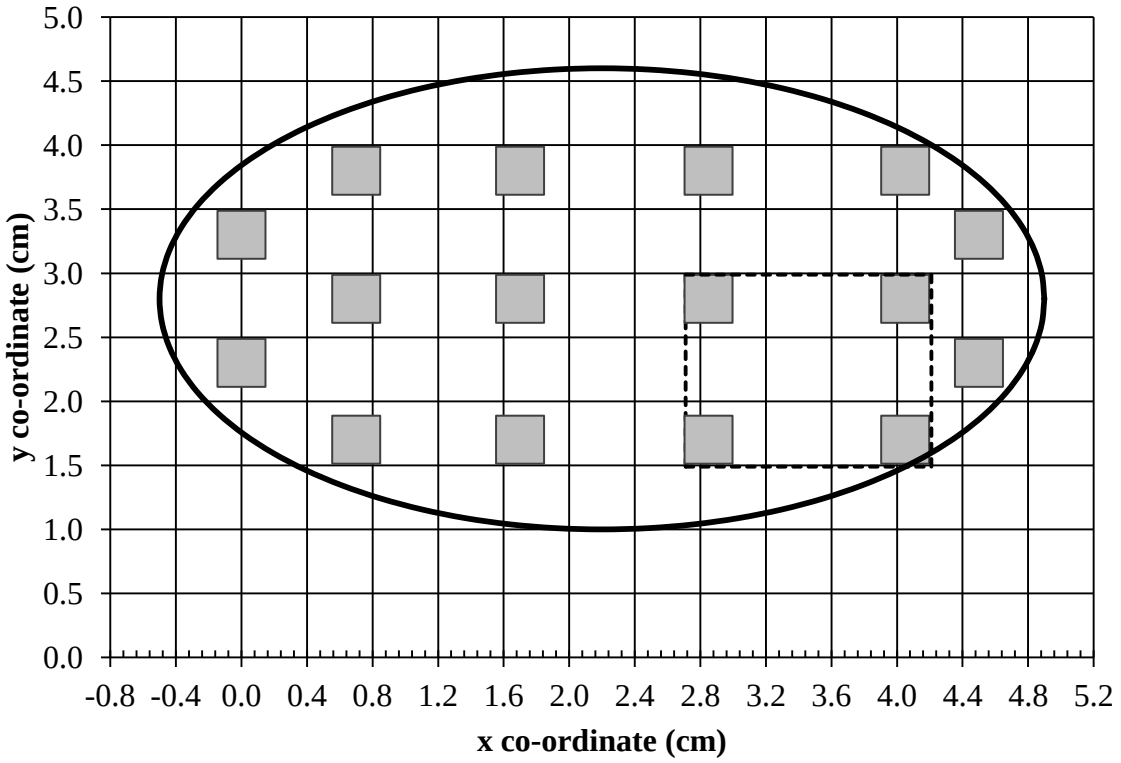

Figure 2: Schematic of TLD layout used in dosimetry exposures at longer source-phantom distance – Mo 100 μm and Mo 200 μm filters. Dashed box shows area selected for calculation of equivalent skin dose. See text in results section for beam size at both

distances and chosen box size. Note that co-ordinate system was chosen based on position of first column of TLD chips on the nylon backing. TLD chip sizes are slightly enlarged for clarity. A similar array was used for shorter source-phantom distance.

The TLDs were only sensitive for doses higher than 20 mGy. In order to determine the dose delivered to achieve a certain MDL, the chips were exposed to a higher tube current, voltage and real time. The dose readings were then scaled down to those utilized for MDL measurements. This would ensure that the minimum dose threshold of the TLD was met. With the chips in this arrangement, the tube was powered up to a voltage of 35.0 kVp and a current 0.5 mA and the TLDs were irradiated for a period of ~16 or 36 hours (real time) depending on the filter thickness. The chips were then returned to Global Dosimetry for reading.

3.5. Data Analysis:

Spectra were analyzed using a non-linear fitting technique – the Levenberg-Marquardt least squares routine (Bevington and Robinson, 2003; Marquardt, 1963) – in Microcal Origin 8.5 peak fitting software, to fit the desired peak to a Gaussian function on a linear background, with tailing (Campbell et al., 2001; Jorch and Campbell, 1977; Uher et al., 2010) included as required. Best estimates for peak width and centroid were obtained using high concentration phantoms. This assisted in reduced χ^2 minimization for fitting the lower concentration phantoms. Scatter normalization was performed for comparison to the real time (RT) and dead time corrected MDLs. The Compton and coherent scatter signals were obtained by integrating over the range of energies covering these peaks in the spectrum. The total scatter region was also used separately for normalization, as a comparison. After peak-fitting, the peak areas were corrected using the dead time correction factor or normalized using either the RT or scatter contributions, with uncertainties calculated through error propagation. A phantom calibration line was produced and the detection system's Minimum Detection Limit (MDL) was calculated using MDL = 2σ, where σ is given by

$$\sigma_{x_{exp}}{}^2 = \left(\frac{\sigma_{y_{exp}}}{m}\right)^2 + \left(\frac{\sigma_b}{m}\right)^2 + \frac{\sigma_m{}^2(b - y_{exp})^2}{m^4} + 2\left(\frac{y_{exp} - b}{m^3}\right)\left(-\frac{\sigma_y{}^2 \sum_{i=1}^{N} x_i}{D}\right) \qquad (5)$$

Here, the four variance terms are due to (from left to right): experimental calibration curve (variance derived from the data point corresponding to the 0 ppm calibration phantom), calibration curve intercept, calibration curve slope and covariance of slope and intercept. The approach is based on the variance-covariance matrix-based formulation typically used in analytical chemistry (Harris, 2006; Salter, 2000; Shoemaker et al., 1989). Three trials were performed per phantom and one value of σ was calculated per trial (per 0 ppm area). The trials were then combined using Avg±SDOM, where SDOM = StdDev/$n^{1/2}$. Previous work on the quantification of arsenic using this detection system used MDL = 2σ/M where M represents the calibration line slope and σ is given by the

uncertainty in the 0 ppm calibration phantom peak area (Arnold et al., 2002; Da Silva et al., 2008; Graham and O'Meara, 2004; Grinyer et al., 2007, 2005; Studinski et al., 2006, 2004). This definition does not include the last three terms in the variance-based equation shown above. If these 3 terms are negligible, then the equation reduces to $2\sigma/M$, in agreement with the previously used definition of MDL.

4. Results:

4.1. Observed spectrum, calibration line and system dead time:

A typical spectrum observed with a Mo 100 μm filter is shown in figure 3.

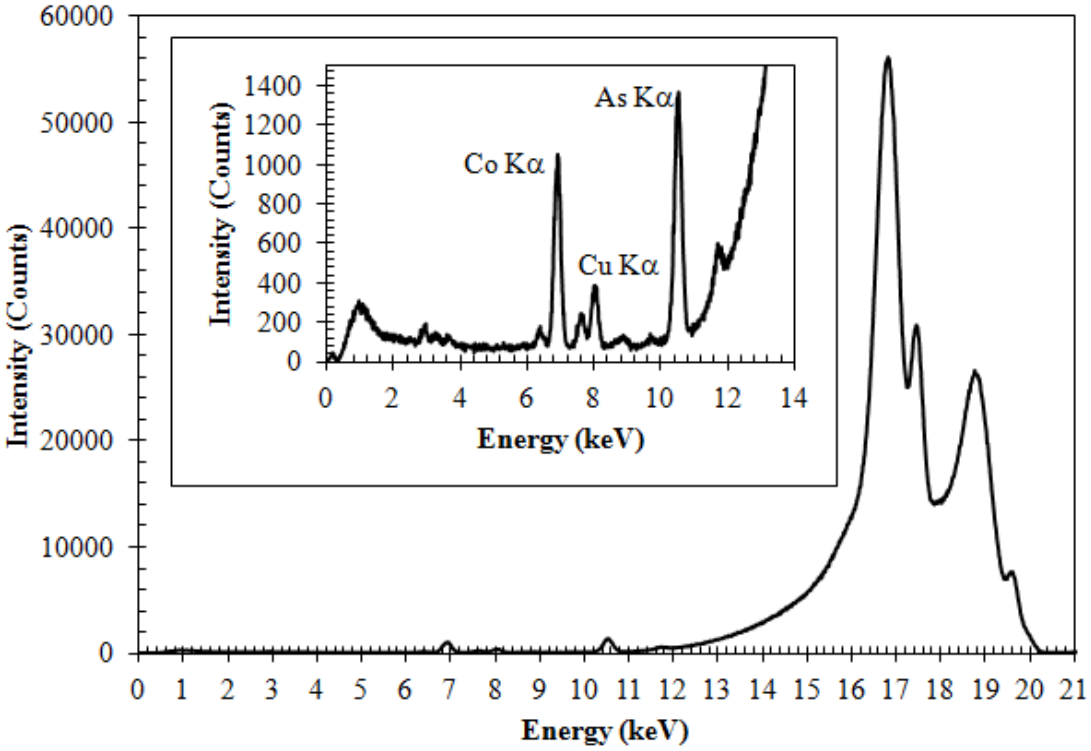

Figure 3: A spectrum collected from the 60 ppm resin phantom using a Mo 100 μm filter at 30 kVp and 20 μA.

Direct and Compton normalized calibration lines are shown, for a Nb 200 μm filter at 30 kVp and 120 μA, in figure 4.

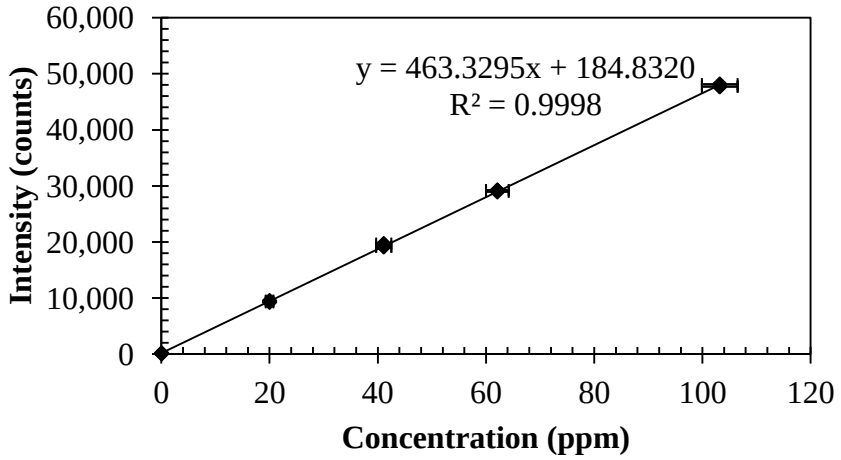

(a)

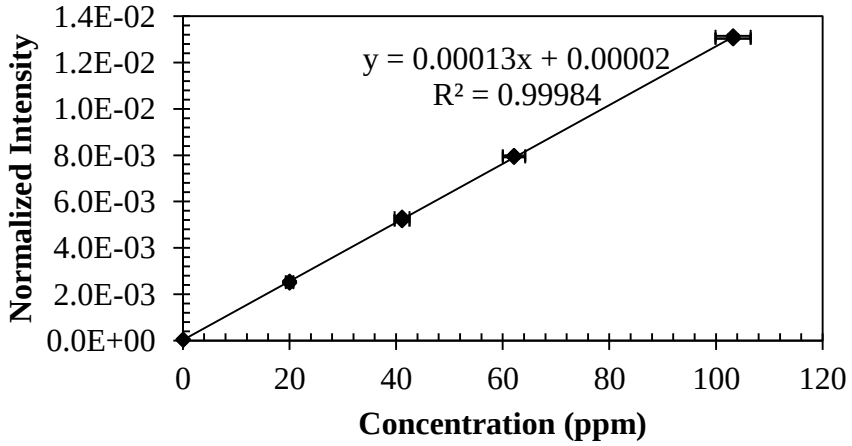

(b)

Figure 4: Representative (a) direct and (b) Compton normalized calibration lines with a Nb 200 μm filter.

Nickel, cobalt, copper and zinc are seen in all spectra. The cobalt is likely originating from the hardening catalyst. Nickel and zinc are originating in the phantom and may also be partially attributed to the catalyst. The copper peak comes mainly from the shielding material. There are two Au Lβ peaks at ~9.7 and 11.5 keV. These originate in the detector contacts and so only the As Kα peak was analyzed in the current work. The Mo Kα and Mo Kβ coherent and 90^0 Compton scatter peaks are also seen. It is worth noting the non-uniform tailing on the low-energy side of the Mo Kα Compton scatter peak, suggesting the presence of structure in this feature. More will be said about this later. The

arsenic Kα peak is also seen. The As Kβ peak is just situated at the onset of the Mo Kα Compton tail. The As Kα peak narrowly avoids this tail. The calibration lines show all 15 data points from a set of five calibration phantoms, where three trials were performed per phantom. The concentration on the horizontal axis is that obtained through neutron activation analysis (NAA) and the full approach was documented in earlier work referenced above. The vertical error bars are too small to be clearly seen. The R^2 is noted for either the direct or normalized calibration lines.

For dead time testing, after plotting $\ln(m/x_i)$ as a function of x_i, the intercept and slope of the linear fit were found to be (8.37±0.01) and (-0.177±0.003) respectively, which can then be combined to calculate a dead time of 41.17 μs (rise time used was 12 μs). In $n_i = n_{ref}x_i$ used earlier, the intercept was assumed to be equal to zero; experimentally, it was found to be within 2σ of zero and may reflect either minor irregularities with the design of the current meter or small amounts of noise entering into the system for zero tube current. A dead time correction factor for specific tube conditions was calculated by combining this dead time with the recorded count rate n_i for those chosen conditions. Additionally, normalization was separately performed by dividing fitted As Kα peak areas by (a) real time: since live time was fixed, this would change with the photon fluence rate at the phantom (or *in vivo*) measurement site, (b) gross Compton peak area, (c) gross coherent scatter peak area and (d) total scatter peak area.

4.2. Effect of changing source conditions on detection limit:

As mentioned earlier, a more inclusive version of variance was used in calculating the MDL. Consequently, MDLs were slightly higher than the lowest MDLs found in previous work. The main difference is that the variance in the intercept is now included in the overall σ. All work performed here resulted in a variance in (a) the 0 ppm phantom area (term 1) and (b) the calibration line intercept (term 2) that dominated the other two terms. If the second term is excluded from the MDL, the MDL equation shown earlier would include term 1, which is the only term used in previous MDL calculations, and terms 3 and 4 which were negligible. It is reassuring that, if term 2 is excluded, the MDLs are still found to be on the same order of magnitude as when it is retained. However, when using the phantom-based calibration line to calculate the arsenic concentration of an unknown sample, both slope and intercept will be used to determine the unknown ppm level and its error. Thus, the current work indicates that the detection system performs worse than one would predict based on ignoring the variance in the intercept.

The results of changes in MDL due to varying the accelerating voltage and current are shown in table 1.

I (μA)	DT	Slope	Direct (ppm)	ICR (ppm)	RT (ppm)
50	32.06	489	0.4994 ± 0.0024	0.4887 ± 0.0085	0.5150 ± 0.0080
40	26.80	394	0.7383 ± 0.0038	0.6157 ± 0.0007	0.6503 ± 0.0005
30	21.39	293	0.8458 ± 0.0038	0.9062 ± 0.0004	0.7894 ± 0.0007
20	15.59	199	0.9032 ± 0.0038	0.9073 ± 0.0038	0.8741 ± 0.0039

(a)

I (μA)	Compton (ppm)	Coherent (ppm)	Total (ppm)
50	0.6114 ± 0.0009	0.6284 ± 0.0010	0.6138 ± 0.0010
40	0.8515 ± 0.0031	0.8492 ± 0.0030	0.8435 ± 0.0030
30	0.7116 ± 0.0051	0.7047 ± 0.0048	0.7106 ± 0.0050
20	0.7316 ± 0.0046	0.7009 ± 0.0047	0.7141 ± 0.0046

(b)

V (kVp)	DT	Slope	Direct (ppm)	ICR (ppm)	RT (ppm)
23	10.67	133	1.109 ± 0.006	1.111 ± 0.001	1.055 ± 0.001
25	15.59	199	0.903 ± 0.004	0.907 ± 0.004	0.874 ± 0.004
28	23.84	315	0.906 ± 0.005	0.878 ± 0.001	0.716 ± 0.001
30	29.38	396	0.800 ± 0.003	0.851 ± 0.001	0.691 ± 0.001

(c)

V (kVp)	Compton (ppm)	Coherent (ppm)	Total (ppm)
23	1.1234 ± 0.0053	1.1076 ± 0.0048	1.1158 ± 0.0054
25	0.7316 ± 0.0046	0.7009 ± 0.0047	0.7141 ± 0.0046
28	0.6406 ± 0.0068	0.665 ± 0.0064	0.6332 ± 0.0069
30	0.5865 ± 0.0048	0.5624 ± 0.0052	0.5822 ± 0.0048

(d)

Table 1: Effect of changing x-ray tube (a) current for a fixed voltage of 25 kVp and (c) voltage (fixed current of 20 μA) on detection limit. A Mo 100 μm filter was placed between the tube and phantom. Units of dead time (DT) and slope are % and counts/ppm. Note that tables (b) and (d) and continuations of tables (a) and (c).

As the voltage is increased, the electron energy is eventually increased past the anode material's K-edge. If this were not the case, then the anode's characteristic x-rays

will not serve as the excitation source – instead, the bremsstrahlung continuum will be representative of the incident spectrum. For the investigation of changing current, the voltage was fixed at 25 kVp. This choice was limited by the system dead time. The highest energy photons produced will be 25 keV, which is just above the Molybdenum K-edge of 20 keV (Deslattes et al., 2003) and will thus be able to excite Mo characteristic x-rays. They will quickly start to dominate the incident excitation spectrum. Previous work also reported on sub-1 ppm detection limits with 25 kVp (Studinski et al., 2006). In *in vivo* work, scatter and dead time considerations will play a part in determining the choice of voltage setting. These are both expected to be stronger than for phantom calibration measurements and may limit the maximum voltage, however 25 kVp is almost certain to be a bare minimum recommendation for this setting or else bremsstrahlung will dominate the incident excitation spectrum meaning that (a) scatter-based normalization will not be possible because the Mo characteristic x-rays are missing and (b) As peaks may be overcome by the bremsstrahlung continuum.

The MDL and calibration line slope improve as the voltage or current are increased. Increasing either will improve the sensitivity of the system to small changes in concentration. As the voltage is increased, the maximum energy (penetration) of incident photons is increased. Arbitrarily ramping up voltage, and hence incident energy, reduces the average As photoelectric cross section in the phantom material. The current determines the number of incident photons. Increasing the current would improve the tube's photon fluence rate and produce better counting statistics in fluorescence peaks located below the incident energy. Both tube settings affect detector dead time. As the source output is ramped up, the system dead time is also increased. The direct, normalized and corrected MDLs improve as either voltage or current are increased. In previous work, the lowest arsenic MDL (~0.40 ppm) was found at 35 kVp with a Mo 200 μm filter, at a phantom-detector distance of (11.0±0.2) cm (Studinski et al., 2006). Since a thinner filter (100 μm) was used here, and the phantom-detector distance is greatly reduced, the dead time requirements dictate that a lower voltage be used. Hence, the maximum voltage used was 30 kVp. A lower current would be an alternative, but the change in dead time with current was not observed to be as great as when the voltage was adjusted. As the range of voltage settings investigated were not largely different, the increase in voltage is likely not large enough to see a worsening in MDL. The benefit of using a lower voltage-thinner filter combination than that used in previous work is the reduction in subject dose delivered *in vivo*. Also, x-ray tube aging should be considered. Rough anode surfaces have been found to have a minor affect on spectra but they alter a tube's inherent filtration (Meghzifene et al., 2006; Nowotny and Meghzifene, 2002), which would affect output. X-ray tubes have a limited heat loading capacity and the performance of a "new" tube is dependent on how it is run. It is unknown how much the output of the tube's signal will drop with usage but this depends on whether or not the power supply overshoots the maximum filament specification, which many do if only for milliseconds. The lowest MDL found here is ~0.50 ppm and is obtained for a lower dead time – ~30% here, versus 40% previously – with a thinner filter and lower voltage-

current combination that those used previously. The main reason is that a higher fraction of the emitted fluorescence is captured due to the reduced phantom-detector distance.

4.3. Comparison of direct and normalized MDLs:

Various factors contribute the changes in the total counts recorded in a spectrum, over a full set of phantom measurements. The detector head, x-ray tube and shielding cabinet are fixed in position. Source output stability and phantom positioning are, thus, the two most important factors that will affect the exact dead time during a single phantom measurement and the variation in this over a full set. Changes in source output (x-ray tube) and phantom positioning will be governed by random statistics if: (a) source strength does not rise or drop over time and (b) the phantom is not intentionally mis-positioned. If these assumptions are valid, then the change between the means of the normalized and direct MDLs, as voltage or current is increased, will not be statistically different from each other.

If the normalization or dead time correction is not affecting the set of MDLs, then the percent difference (PD) between the MDLs calculated with and without normalization or correction should be very small and not statistically different. Small changes may be expected due to statistical fluctuations. The comparisons are shown, for all sets, in table 2.

	PD relative to Direct MDL (%)				
I (μA)	**ICR**	**RT**	**Comp**	**Coh**	**Total**
50	-2.14	3.13	22.44	25.84	22.91
40	-16.61	-11.91	15.33	15.03	14.25
30	7.13	-6.67	-15.87	-16.68	-15.99
20	0.45	-3.22	-19.00	-22.40	-20.93

(a)

	PD relative to Direct MDL (%)				
V (kVp)	**ICR**	**RT**	**Comp**	**Coh**	**Total**
23	0.12	-4.85	1.27	-0.15	0.59
25	0.45	-3.22	-19.00	-22.40	-20.93
28	-3.15	-20.97	-29.33	-26.63	-30.14
30	6.39	-13.60	-26.70	-29.71	-27.24

(b)

Table 2: Changes in normalized or corrected detection limits compared to direct (un-normalized) detection limits as (a) current and (b) voltage is changed. Changes performed

using a Mo 100 μm filter at the shortest possible phantom-detector separation of (3.0±0.2) cm. Negative sign indicates that MDL is lower than direct MDL and vice versa for positive change.

It is clear that normalization is not as effective as either ICR or RT corrections, when accounting for source strength changes due to changes in tube settings. The larger PD indicates that a larger difference in MDLs was observed after normalization than those found due to ICR or RT corrections. As mentioned earlier, if the changes in dead time are due to statistical fluctuations then one would not expect a large change in MDL as a result of the normalization process. After normalization, the 4 individual variance terms change by a sufficiently large extent that they are affecting the overall MDL. In the case of the Compton, coherent or total scatter normalizations, this may mainly be caused by the presence of several peaks built into these contributions. These features may be affected differently by the changes in source conditions. For example, different amounts of scatter off the shielding cabinet may result in the appearance of multiple Compton scatter peaks in addition to those due to the Mo anode Kα and Kβ lines. These features are not always visible and the intensity of the additional Compton features is likely to change as source conditions are adjusted. This makes a reliable deconvolution harder. This is also the limitation of integrating over these three regions of the spectrum – Compton, coherent and total scatter. The affect on the variances is large enough that the expected improvement in normalized MDL with increasing tube current, due to superior counting statistics, is negated.

The effectiveness of the three scatter normalizations to correct against variations in tube voltage is worse, by comparison to changing tube current. This is seen from the PD results. This may be attributed to the non-linear relationship between x-ray tube energy fluence rate and accelerating voltage, compared to the expected linear relationship between tube photon fluence rate and current. Voltage also changes the amount of backscatter coming from the nylon backing. Since higher energy photons are produced as voltage is increased, multiple backscatters are also possible. Additionally, the detector head is another source of multiple Compton scatter peaks.

As mentioned earlier, a small range of voltage settings was used and so a large difference in MDLs would not be expected here. For the range of voltages used, the Bremsstrahlung would peak at an energy that is sufficiently far away from the scatter region to suggest that its effect here may be minimal. However, in the absence of full scatter deconvolution, the range of PDs suggests that it is not possible to rely on the three scatter normalizations as way of correcting against variations in tube voltage or current. A simplification of the scatter region, such as using a monochromator, may be useful to remedy this. Since the live time is fixed at 1000 seconds, the preferred option here would appear to be normalizing to real time or applying a dead time correction factor using the ICR.

4.4. Reproducibility testing:

Finally, three full sets of phantom measurements were performed (3 trials per set) for reproducibility testing and the results are shown in table 3.

	DT (%)	Slope	Direct (ppm)	ICR (ppm)	RT (ppm)
R 1	32.51	394.27	0.6190 ± 0.0005	0.6617 ± 0.0004	0.5969 ± 0.0006
	32.44	386.66	0.6788 ± 0.0008	0.7390 ± 0.0011	0.6307 ± 0.0009
	32.41	387.02	0.6879 ± 0.0002	0.6696 ± 0.0002	0.7087 ± 0.0002
R 2	30.80	394.27	0.5046 ± 0.0012	0.5825 ± 0.0010	0.4934 ± 0.0012
	31.05	386.66	0.5952 ± 0.0003	0.5688 ± 0.0004	0.5816 ± 0.0003
	30.71	387.02	0.5623 ± 0.0002	0.5157 ± 0.0002	0.6013 ± 0.0004

(a)

	Compton (ppm)	Coherent (ppm)	Total (ppm)
R 1	0.5278 ± 0.0010	0.5010 ± 0.0011	0.5342 ± 0.0009
	0.4665 ± 0.0014	0.4633 ± 0.0016	0.4660 ± 0.0015
	0.6996 ± 0.0002	0.6669 ± 0.0002	0.7034 ± 0.0002
R 2	0.4460 ± 0.0013	0.4275 ± 0.0012	0.4492 ± 0.0012
	0.5471 ± 0.0002	0.5255 ± 0.0003	0.5431 ± 0.0003
	0.6647 ± 0.0006	0.6551 ± 0.0005	0.6462 ± 0.0005

(b)

PD_1 (%)	ICR	RT	Compton	Coherent	Total
R 1	6.90	-3.57	-14.74	-19.07	-13.70
	8.86	-7.08	-31.28	-31.75	-31.35
	-2.65	3.02	1.70	-3.04	2.26
R 2	15.43	-2.22	-11.62	-15.28	-10.99
	-4.43	-2.30	-8.09	-11.72	-8.76
	-8.29	6.94	18.21	16.50	14.92

(c)

PD_2 (%)	Direct	ICR	RT	Compton	Coherent	Total
				-		
R 1	9.66	11.67	5.66	-11.61	-7.53	-12.77
	11.12	1.19	18.71	32.55	33.13	31.67
				-		
R 2	17.96	-2.34	17.87	22.68	22.91	20.91
	11.43	-11.47	21.87	49.05	46.90	10.94

(d)

Table 3: (a) and (b) Reproducibility testing on MDLs with two separate filter and voltage-current combinations. (c) Comparison of normalization approaches using PD relative to direct (un-normalized) measurements. (d) Evaluation of PD between repeated measurements sets, relative to first measurement in each set. A Mo 200 μm filter was used for the first set of trials (top half, R1) and a Zr 300 μm filter was used for the second set (bottom half, R2).

The PDs over the three sets were larger for the scatter normalized MDLs. This repeatability was tested using a Mo 200 μm filter for repeat 1. Due to the thickness of the filter, a higher voltage and current setting was possible. A different filter was chosen for the second test of repeatability – Zr 300 μm – and a higher voltage-current combination was also possible here. Excluding scatter normalization, a percent difference of as high as ~20 % can be expected, with this detection system, between repeated measurements. This compares to ~15% obtained in a similar test in the previous work at a larger phantom-detector distance (Studinski et al., 2006). Reproducible MDL results are possible, to this extent, with this system. As with variation of tube settings, scatter normalization cannot be verified as a means of correcting for variations in source output between individual trials and further evaluation of the scatter region is sought. It is reassuring that the order of magnitude of the MDLs does not change. The smaller spread of PDs with the Zr filter speaks to the possibility of a choice of filter material and will be explored later.

4.5. System rise time – study of MDLs:

The rise time of the Si(Li) detector is chosen as 12 μs based on earlier work; the flat top was found to have minimal impact on uncertainty in peak areas (Studinski, 2005). A similar choice of rise time is used for bone Sr work with the same Si(Li) detector (Pejović-Milić et al., 2004). The current work studied the effect of changing rise time on the As MDL. A reduction in rise time will produce a larger peak FWHM and higher count rate. However, the arsenic photopeak is a very small feature of the total spectrum. Since this count rate is spread out over the entire spectrum of energies, the gain in arsenic peak count rate may be minimal. These throughput and resolution performance-related properties are seen from table 4.

RisT (μs)	Thpt.* (counts)	Thpt. (counts)	Pk-Total Ratio (%)	FWHM (eV)	Tail-Peak Area (%)	DT (%)	Red. χ^2
12	59,231	1.19E+07	0.50	248.97	9.11	38.66	0.95 ± 0.11
8	62,151	1.22E+07	0.51	273.04	10.37	29.08	1.07 ± 0.20
4	61,401	1.76E+07	0.35	336.07	7.38	17.43	1.03 ± 0.09
3	56,695	2.90E+07	0.20	367.48	21.46	14.04	1.22 ± 0.17
12	60,751	1.22E+07	0.50	248.97	8.09	38.97	1.04 ± 0.14
8	62,278	1.24E+07	0.50	272.08	7.43	29.12	1.02 ± 0.13
4	60,941	1.79E+07	0.34	335.64	10.03	17.47	1.15 ± 0.12

* throughput and FWHM for As Kα peak; As Kα precision = (0.44±0.01) %

Table 4: Performance of varying rise time with Si(Li) detector. Results correspond to high concentration phantom (100 ppm) positioned in usual 90^0 arrangement. Precision is calculated as avg±StdDev over all rise times. A Nb 200 μm filter was used between x-ray tube and phantom. The second set of measurements are repeats of same shaping times and source conditions used in the top half of the table, but the lower half was generated after the Si(Li) detector was removed and re-inserted into the detection system at a later time.

Over all conditions tested in this work, including use of various rise times, the arsenic Kα tail-peak area is (9±3) % (average±StdDev). The tail-peak areas for rise times of 12, 8 and 4 μs fall in this range. Tail-peak area and peak precision were determined from three high concentration (100 ppm) As phantoms. The tailing for 3 μs is nearly twice as high, while the peak's FWHM is ~1.5 times higher. Since the As Kα peak precision and throughput are nearly identical, as rise time is changed, the change in MDL is expected to be very small.

The results of varying rise time are shown, in terms of MDL, in table 5.

RisT (μs)	Slope	Direct (ppm)	ICR (ppm)	RT (ppm)
12	577	0.5129 ± 0.0006	0.5108 ± 0.0006	0.5807 ± 0.0006
8	602	0.4652 ± 0.0005	0.4785 ± 0.0005	0.4754 ± 0.0005
4	592	0.5067 ± 0.0008	0.5087 ± 0.0007	0.4964 ± 0.0008
3	553	0.6824 ± 0.0003	0.6950 ± 0.0004	0.6680 ± 0.0003
12	586	0.7112 ± 0.0002	0.7114 ± 0.0001	0.6651 ± 0.0002
8	599	0.6563 ± 0.0004	0.6661 ± 0.0004	0.6508 ± 0.0004
4	593	0.7097 ± 0.0006	0.7256 ± 0.0006	0.6791 ± 0.0006

(a)

RisT (μs)	Compton (ppm)	Coherent (ppm)	Total (ppm)
12	0.6359 ± 0.0005	0.6983 ± 0.0005	0.6445 ± 0.0005
8	0.4265 ± 0.0005	0.4108 ± 0.0004	0.4221 ± 0.0005
4	0.4772 ± 0.0009	0.4680 ± 0.0009	0.4737 ± 0.0009
3	0.5495 ± 0.0003	0.4871 ± 0.0003	0.5522 ± 0.0003
12	0.6063 ± 0.0002	0.6391 ± 0.0002	0.6083 ± 0.0002
8	0.6180 ± 0.0004	0.6120 ± 0.0004	0.6203 ± 0.0004
4	0.5379 ± 0.0005	0.5535 ± 0.0005	0.5376 ± 0.0005

(b)

Table 5: Effect of changing detector rise time on detection limit. Units of slope are counts/ppm. V = 31 kVp (full table), I = 13 μA (top) and 18 μA (bottom).

The second trial (bottom half of table) was performed at a larger phantom-detector separation of (3.7±0.2) cm and thus a 20% increase in tube current, due to the larger distance, was required to match the dead times. As the rise time is reduced, the MDL changes for the second set (larger phantom-detector separation, bottom half of table) appear to be smaller than for the first set. The minimal impact on the arsenic peak area or precision suggests that the source of the variation lies in the scatter region of the spectrum. Noise in the MCA electronics circuitry may have led to greater fluctuations in perceived tube output at the lower current (trial 1) than for a higher current setting (trial 2). Finally, the scattered photons, from the shielding material and detector head, reaching the detector would contribute to the scatter region of the spectrum. For the longer phantom-detector distance, this component may be altered compared to the shorter distance, thus changing the relative intensities of the scatter components and the background of the Compton tail under the As Kα peak. Additionally, as the detector was powered down and physically removed from the system between measurements, identical detector operating conditions were not possible. Regardless of the normalization or correction method used, the MDL is found to initially experience a small change and then experience a large increase at the lowest chosen rise time. At best, the improvement in MDL (without normalization), by reducing rise time, is minimal. A case can be made for 8 μs rise time, but the reliability of scatter normalization needs further evaluation because the detector's resolution is worse than at 12 μs. The presence of a Au L peak at ~9.8 keV is motivation for using a higher rise time.

4.6. Investigation of various filter materials:

As mentioned earlier, a filter was placed in the path of the beam, before the x-ray tube was powered up. With no additional filtration preceding it, this filter serves as a primary beam filter for the detection system. This was done to reduce the system dead time to a manageable level of ~30-40%. In previous work, a so-called K-edge filter was determined to be the best for use with the detection system (detector-phantom distance =

~11 cm). Spectral deconvolution is extremely complicated due to the presence of numerous features in the scatter region of the spectrum. Normalization to Compton or coherent scatter is unreliable without significantly reducing observed features in the scatter region of the spectrum. Removal of the Mo Kβ lines and the associated Compton scatter and escape peaks facilitate this normalization and would reduce dose. Thus, there is motivation to investigate the effect of various filter materials on MDL with the current layout of the system (detector-phantom distance = ~3 cm).

The type of filter studied here is an absorption edge filter. The filter removes energies higher than its absorption edge. For the current work the x-ray tube anode's K-absorption edge is relevant and so K-edge filters are used. The present application requires that some of the Mo energies (Kα) be kept, while others (Kβ) be removed. Typically an absorption-edge filter would remove features above its absorption-edge. Here, the objective is to remove one line (Mo Kβ) while keeping the second, Mo Kα. Thus the filter material needs to be chosen so that its edge is higher than the Mo Kα but lower than the Mo Kβ. Candidate filter materials are niobium (Nb) and zirconium (Zr). K-edge filters have been extensively used in diagnostic radiology as a means of reducing patient dose (Gislason-Lee et al., 2013; McKinley et al., 2005; Nagel, 1989; Williamson and van Doorn, 1994; Yamaguchi et al., 1983; Zentai, 2011). If the filter material is chosen to be the same as the tube anode, then this is sometimes called a regenerative monochromatic filter (RMF) (Potts et al., 1986; Van Grieken and Markowicz, 2002). In the current work, a Mo filter was also examined.

Measurements, by varying filter material and thickness, were performed and representative spectra are shown in figure 5.

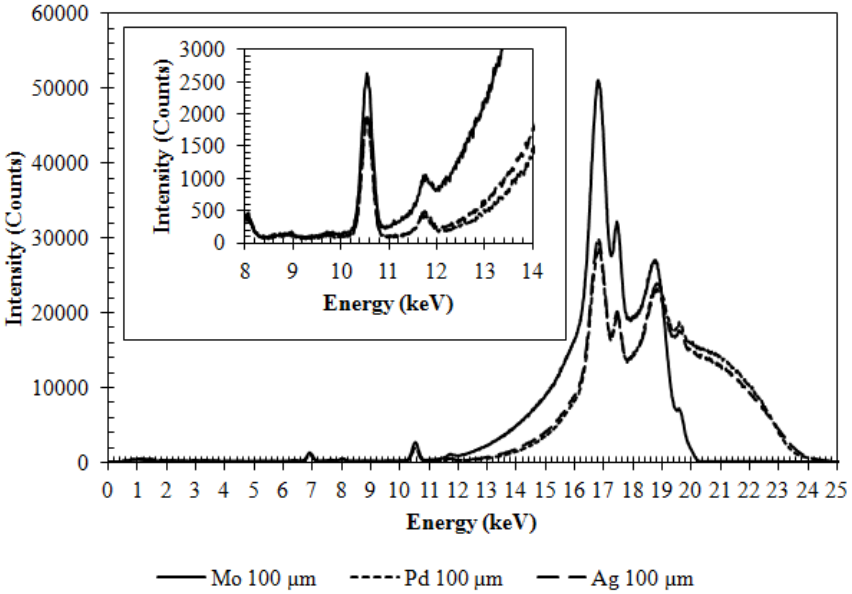

(a)

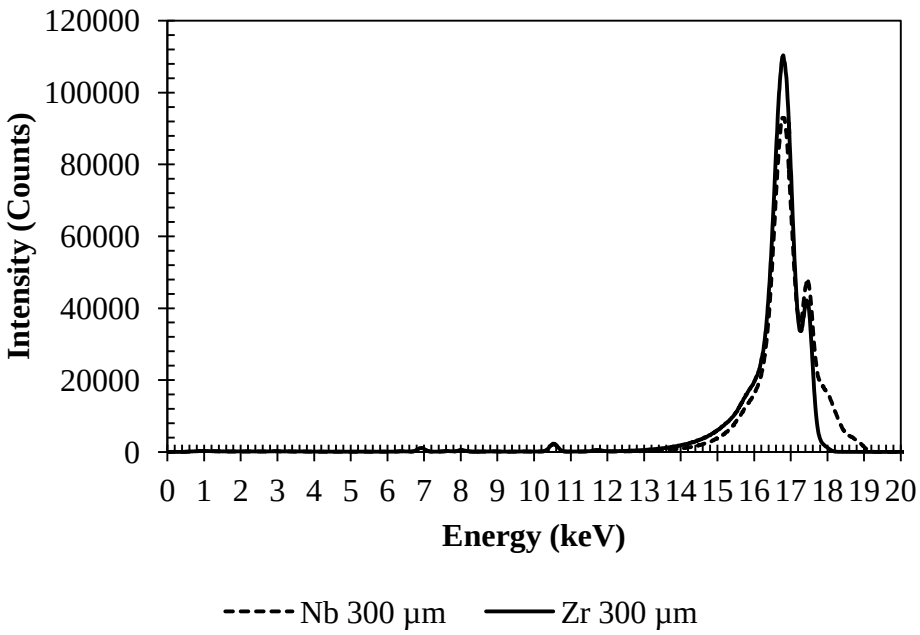

(b)

Figure 5: Spectra obtained with (a) RMF and other filter materials and (b) K-edge filters.

Palladium (Pd) and silver (Ag) have energies (Kα: 21.1 and 22.1 keV; K-edge: 24.4 and 25.5 keV) that are well past the K-edge of molybdenum (20.0 keV). These do not function as K-edge filters. By comparison, the K-edge for Zr (18.0 keV) and Nb (19.0 keV) are lower than the Mo K-edge and Mo Kβ (19.6 keV). These would remove the Kβ while preserving the Mo Kα energy. Due to immediate availability, Rh (K-edge at 23.2 keV) could not be tested. Niobium or zirconium would serve as K-edge filters for a Mo anode x-ray tube. The benefit of using a K-edge filter is clearly seen in the spectra. The Mo Kβ peak, and its associated Compton scatter, is completely removed with Zr. The Nb filter heavily attenuates these energies. The demands of the present application require the removal of Mo Kβ energy and its associated Compton scatter so as to simplify the Mo Kα scatter portion of the spectrum. Qualitatively, the K-edge filters served their purpose in that they were able to eliminate the Mo Kβ anode energy, its Compton scatter and two associated escape peaks in the scatter region of the spectrum. The end result is a pseudo-monochromatic spectrum. However, these filter materials fluoresce their own characteristic x-rays and so these as well as their associated Compton scatter and escape peaks appear in the scatter region of the spectrum. The identifiable Nb Kβ peaks indicate that the intensity of the Nb Kα peaks is just large enough that it will interfere with the Mo Kα Compton scatter peak. This tradeoff means that only the Mo Kβ section of the spectrum has been simplified. Spectral deconvolution is, thus, still complicated mainly by the insertion of the filter's characteristic x-rays and their associated Compton scatter and

escape peaks. Attempts at peak-fitting produced very strong tailing on the Mo Kα Compton and coherent peaks suggesting the presence of additional features, in that structure, than just the tailing caused by incomplete charge collection. This is a disadvantage of using an absorption-edge filter for the current application since the Mo Kα Compton scatter peak is of interest.

Quantitatively, the K-edge filters help to reduce the dead time. The extent of scattering off the shielding cabinet is seen in the total counts in the scatter region. The filter will reduce the total intensity since some energies are removed. For matching dead times, the counts in the scatter region should be reduced. This suggests that a higher tube current will be required to match dead times. However, it was found that a lower current would be needed for this. The introduction of the filter's characteristic x-rays into the lower energy part of the scatter region is driving up the total counts. Thus, current was reduced in order to match the system dead time reported with the Mo filter. The problem of additional features appearing in the scatter region of the spectrum, due to the shielding cabinet, is thus likely unresolved because features still appear below the Mo Kα. The results of detection limits and various other metrics are shown in table 6.

Filter (μm)	**V (kvp)**	**I (μA)**	**Total Scatter (counts)**	**Pk*-Total Ratio (%)**	**Total Thpt. (counts/μA)**	**Total Thpt. (counts)**
Mo 100	25	50	9,113,727	5.39E-03	186,804	9,340,186
Pd 100		90	7,065,912	3.72E-03	106,992	9,629,323
Ag 100		70	7,086,307	3.90E-03	135,837	9,508,623
Mo 300	35	570	8,664,896	3.79E-03	15,469	8,817,428
Nb 300		310	8,547,807	4.82E-03	28,135	8,721,917
Zr 300		115	8,568,870	4.97E-03	76,480	8,795,221
Zr 300	30	100	8,846,432	3.29E-03	N/A**	9,007,705
Zr 300	35	52	8,746,977	2.96E-03		8,925,544

* peak-total area ratio for As Kα peak
** changing voltage and current

(a)

Filter (μm)	**MDL (RT) (ppm)**	**Slope (counts/ppm)**
Mo 100	0.5150 ± 0.0080	751

Pd 100	0.8317	±	0.0002	527
Ag 100	0.7137	±	0.0003	550
Mo 300	0.5449	±	0.0002	478
Nb 300	0.4543	±	0.0008	596
Zr 300	0.4934	±	0.0012	624
Zr 300	0.6986		0.0009	425
Zr 300	0.6752		0.0011	384

(b)

Table 6: List of MDLs and spectral properties for various filter materials and types.

In rows 1, 5 and 6 do not follow the trend of improving MDL with increasing slope. For the particular choice of MDL, the variance in slope is the smaller term while that in the intercept is the larger term. These contributions to the overall MDL must be considered. The second term, being larger, negates some of the benefit of increasing slope. Using MDL = $2\sigma/M$, the MDLs improve with slope but the variance in intercept is assumed to be negligible here. As discussed earlier, both terms are needed when using the calibration line to determine an uknown sample's concentration with MDL = 2σ. The first section of both tables shows the disadvantage of choosing a filter with a K-edge higher than that of the anode material – Pd or Ag. A severe drop is observed in counts in the scatter region, throughput per unit current and peak-total ratio. However, for the same dead time, total throughput is nearly unchanged since the filters fluoresce their own characteristic x-rays at higher energies than the Mo K-edge. The filters attenuate exciting energies and reduce the calibration line slope. This leads to worse sensitivity to small changes in concentration and, hence, significantly worse detection limits are observed.

The second half of the tables looks into the effect of the K-edge filter. For the nearly fixed dead time, nearly the same total throughput is observed with the Mo filter compared to the K-edge filters – for the Mo filter, they are, however, spread out over a larger range of energies. The dead time was matched by adjusting tube current. The peak-total ratio is also somewhat improved with the K-edge filters. Total throughput per unit current is much higher for the K-edge filters than for the Mo filter (RMF), mainly due to the introduction of filter material's characteristic x-ray peaks. This required a lower current, as mentioned earlier. Consequently, this reduces the dose delivered. The MDL is lower for Nb but increases for Zr as the background under the As peaks is higher.

Considering all filter materials, the benefit of the K-edge filter is seen in the achievable MDL. The choice of the thicker K-edge filter is preferred due to the need for reducing the Compton-tailing background under the arsenic peaks. As mentioned earlier, thicker absorption-edge filters will offer greater Compton-tailing background reduction than thinner ones. Since the K-edge filter is able to achieve a superior reduction in

background and deliver a lower dose (by eliminating the Mo Kβ), it may be the preferred choice for the present application. *In vivo* measurements are likely to generate greater scattering than that observed in phantom-based work because a subject's entire hand will represent the sample. Although exposure of the palm of the hand will be performed, exposure to and scatter off the forearm are unavoidable. This will be caused by scatter coming from the walls of the copper shielding cabinet and is believed to be partly contributing to the low-energy tail on the Mo Kα Compton scatter peak. Thus, normalization is performed more reliably with the K-edge filter but, due to the continued interference of several features, a dependable deconvolution remains complicated. It still cannot be said that such normalization is based only on the Mo Kα Compton or coherent scatter produced by the resin phantoms.

The first test of reproducibility, shown earlier, made use of a thicker filter (RMF), which would allow the Compton tailing-background reduction for the arsenic peaks, but MDLs weren't substantially lower than those in the above table (second half) and dose is contributed by comparatively higher energies (RMF filter) than those shown in this section with a K-edge filter. With the K-edge filter (second part of above table), the three scatter normalized MDLs were found to be (17±5) % lower than associated un-normalized MDLs, and they were obtained through spectral integration as was the case before. A more refined spectral deconvolution, accounting for all Compton and coherent scatter lines as well as characteristic x-ray and escape peaks and their associated tailing, may reduce this percentage difference. It should be noted that although combinations of filters can also be used, this is likely to further complicate the scatter region making deconvolution and normalization harder.

4.7. Investigation of changing distances:

Finally, the phantom-detector and tube-phantom distances were varied separately. These were made possible through modifications to the shielding cabinet and results are shown in table 7.

Ph-det (cm)	Slope	DT (%)	Thpt. (counts)	Direct (ppm)	RT (ppm)
3.0	463	32	9.40E+06	0.4911 ± 0.0007	0.4979 ± 0.0007
4.1	273	22	5.87E+06	0.7061 ± 0.0008	0.7181 ± 0.0007
5.6	176	16	4.07E+06	0.8175 ± 0.0009	0.8044 ± 0.0009

(a)

Sou-Ph (cm)	Slope	DT (%)	Thpt. (counts)	Direct (ppm)	RT (ppm)
LONG	199	16	3.81E+06	0.9032 ± 0.0038	0.8741 ± 0.0039
SHORT	340	29	9.08E+06	0.7075 ± 0.0010	0.6742 ± 0.0009

(b)

Table **7**: Result of changing (a) phantom-to-detector (30 kVp, 120 μA) and (b) source-to-phantom (25 kVp, 0.20 μA) distances, using a Mo 100 μm filter.

First the detector was moved closer to the phantom than the previously used distance of ~11 cm. The voltage and current were held fixed and a Mo 100 μm filter was used. Reducing the phantom-detector distance allows for the capture of a higher percentage of the fluorescence signal, resulting in lower dose required to produce the same signal. Higher sensitivity and lower detection limit are produced. Detection limits are calculated using a more thorough definition of σ and are <0.1 ppm higher than those found previously at a greater source-phantom distance and the dose delivered is reduced due to the lower voltage and current settings needed. The benefits of the reduced distances are clearly visible.

Adjusting the source phantom distance affects (a) the tube output required to achieve the equivalent signal and (b) the pattern of scatter off the x-ray tube. Representative spectra are shown in figure 6

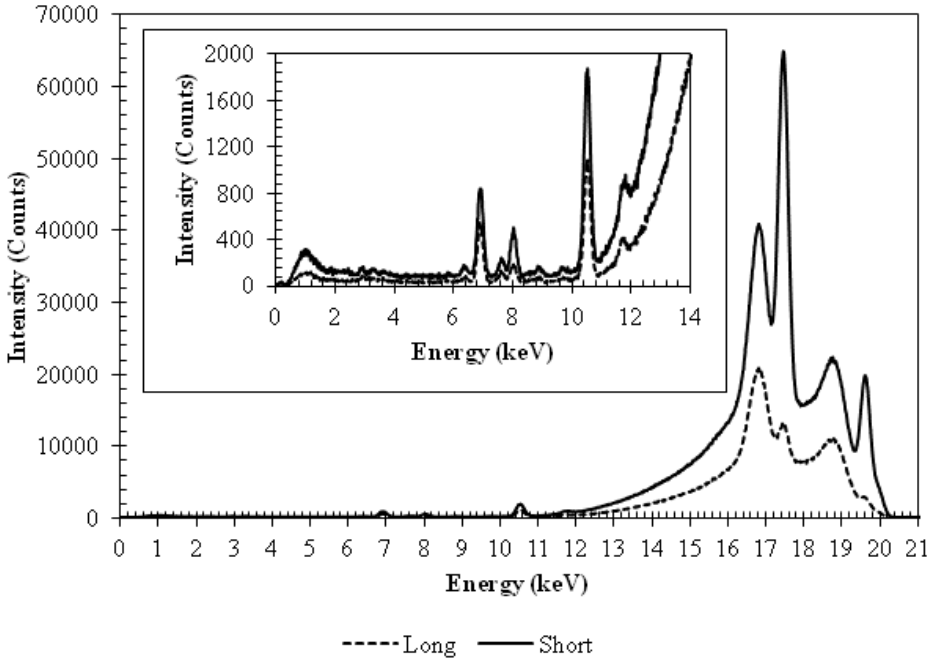

Figure 6: Comparison of 100 ppm As spectra at different source-phantom distances for unchanged source and acquisition conditions.

As with the previous arrangement, the voltage and current were fixed and a Mo 100 μm filter was placed in front of the x-ray tube. It was decided to perform the exposure at the shorter distance using a fixed current rather than matching dead time. The greater flux at the phantom suggests that a lower current would allow for matching dead time with that at the larger distance. The drop-off in performance expected from using a lower current matching dead time at the shorter distance was not known and so the current was left unchanged. It is likely that a lower voltage or current can be used to match system dead time and MDL, however the objective is to improve on the detection limit compared to that found at the longer distance. Such a comparison would be more naturally made under the same source conditions. Since the tube settings are held fixed, the sensitivity at the shorter distance is dramatically increased driving down the detection limit. Despite the improvement in sensitivity, the MDL is still higher than those attainable at the longer distance for a comparable level of DT, with either a K-edge filter or RMF arrangement. Scatter off the Mo filter itself reaches the detector adding to the Mo Kα and Kα intensities. This drives up the background under the As peaks. This overcomes the gain in sensitivity leading to a higher MDL. An additional disadvantage of the shorter distance is that the dose delivered for the same source strength is higher and remains to be investigated. Since distances are changing, a higher dose is expected for the same source strength and so dose needs to be incorporated into a comparison of system performance here.

4.8. Raw data (TLD chip readings) corresponding to absorbed dose:

Dosimetry on three exposure conditions was performed using a Mo filter: (a) 100 μm thickness, with TLD chips placed at longer source-phantom distance, (b) 100 μm, shorter source-phantom distance and (c) 200 μm, longer source-phantom distance. This filter was chosen because some of the lowest MDLs found here were produced with this filter material, and they were found for lower tube settings than other materials. Additionally, the filter was used for comparison of changing source-phantom distance and tube voltage and current so dose can be incorporated into those investigations. The experimental conditions, including all apparatus (phantom holder), are unchanged between experiments for b) above. For a) and c), the changes made are: (i) moving detector closer to x-ray tube and (ii) reducing length of flight tube. The image of the beam on the gafchromic film and surface maps corresponding to un-corrected absorbed dose readings for the shorter source-phantom distance are shown in figure 7.

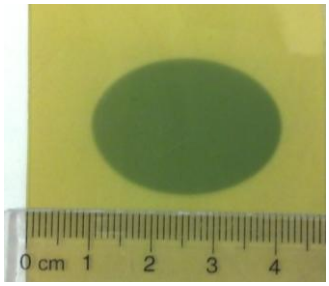

(a)

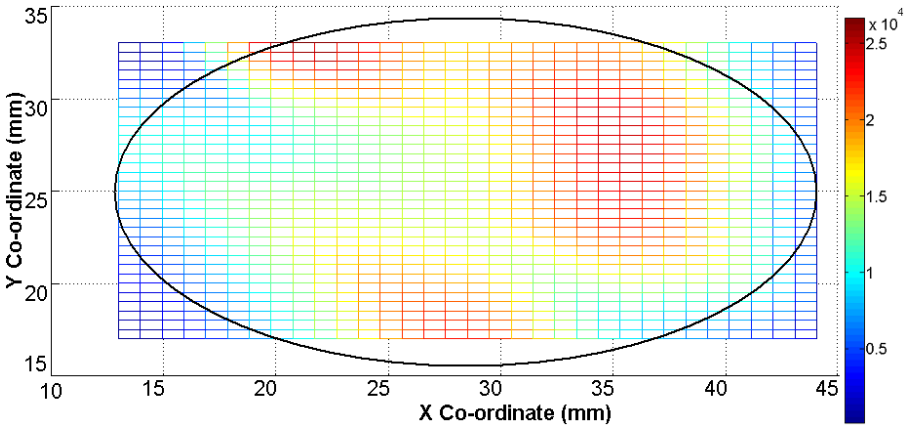

(b)

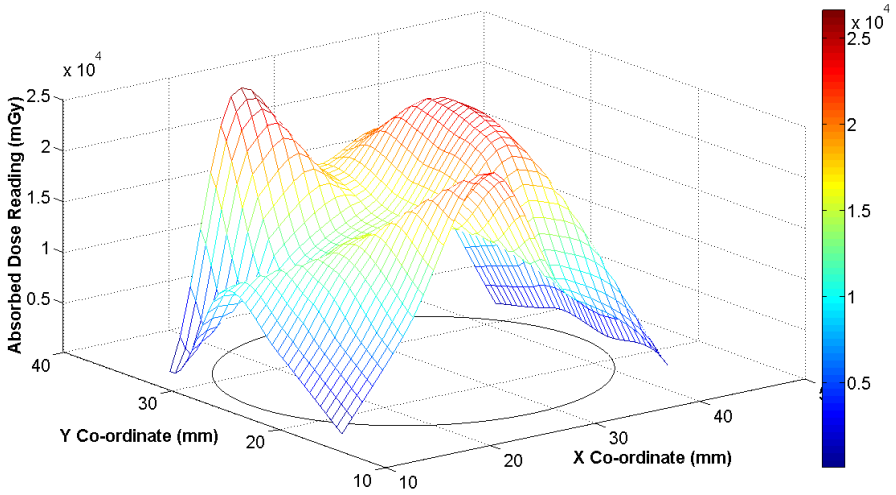

(c)

Figure 7: (a) Representative image of beam at location of phantom, obtained using gafchromic film, (b) array corresponding 2D mesh grid showing uncorrected absorbed dose as a function of x and y co-ordinate of TLD chip in array (ellipse depicts x-ray beam position and size) and (c) rotated version of 2D mesh grid from b) showing dose plotted on the z-axis (ellipse indicates position and size of x-ray beam as per gafchromic film). Image and graphs correspond to shorter source-phantom distance layout.

Using the beam image recorded on the gafchromic film, the x-ray beam's semi-major and semi-minor axis dimensions were found to be (1.6±0.2) cm by (1.1±0.2) cm and (2.5±0.2) cm by (1.8±0.2) cm, at the shorter and longer source-phantom distances respectively. The respective beam areas were found to be (5±1) cm^2 and (15±2) cm^2. Chips selected for averaging, covered (1.1±0.2) cm (horizontal) by (0.8±0.2) cm (vertical) for the shorter distance and (1.5±0.2) cm (horizontal) by (1.4±0.2) cm (vertical) for the longer distance. These dimensions are larger than 1 cm but the chips lying in these sections (dashed boxes) were those that were in the strongest part of the beam. Maps of uncorrected dose absorbed readings were produced using custom written Mathworks Matrix Laboratory (MATLAB) R2012a code with cubic interpolation between discrete data points. These maps corroborated the choice of chips used for calculating the equivalent dose. For all three distances, the maps show that variations were present in dose readings that may reflect backscatter from the nylon backing, scatter from the shielding and detector housing and scatter off the filter. Although it may be possible to select chips in a weaker part of the beam, that covered a length and width closer to 1 cm, the chosen chips represent a more realistic selection from the point of view of potential for harmful (skin) dose delivered over this localized area.

The raw absorbed dose readings for all three exposures are reported in table 8.

D (mGy)	Short	Long	Short*
Min	127	708	143
AVG	11,130	1,531	281
SDOM	1,990	110	16
Stdev	8,899	438	61
Max	26,226	2,444	369
Range	26,099	1,736	226
RSD	80	29	22

* Mo 200 μm

Table 8: Table showing results of raw dose absorbed readings returned, for each of the three exposures performed.

The maximum delivered absorbed dose of ~26 Gy is well below the usable maximum dose for these Li(F) dosimeters of 5 kGy. The dose at the two source-phantom distances are compared using the expected $\sim 1/r^2$ drop-off in source strength. As per this relationship, the average absorbed dose rate at the shorter distance is predicted to be 0.11 mGy/s. The measured dose rate is (0.23±0.19) mGy/s, which is twice the expected dose. For these two dosimetry measurements, the tube settings were fixed at 35 kVp and 0.5 mA and the same phantom-detector distance was used. Thus, the scatter off the metallic shielding cabinet, the filter itself and backscatter from the nylon backing must be considered here. Backscatter is to be expected *in vivo*. The larger than predicted dose indicates that a greater amount of scatter from the shielding and off the filter may be present at the shorter distance. Non-zero dose due to scatter from a tin shielding box was documented with a handheld XRF analyzer, using a tungsten anode x-ray tube (Gherase et al., 2010). With the current system, the shielding scatter would mainly be caused from the walls of the copper shielding cabinet with some also coming from the stand where the phantom was placed. Additionally, when the phantom and detector are moved closer to the source, the detector head is closer to the x-ray tube and so it is a source of relatively increased scatter than at the longer distance. All these secondary sources of radiation contribute dose. In the small confines of the shielding cabinet, there is not enough space for the intensity of the shielding scatter to disperse, and so the scatter from the increased beam size at the longer distance is less than the scatter reaching the detector due to photon interactions with the sample at the shorter distance. Thus, the dose at the shorter distance is much larger than the predicted value.

4.9. Corrected Absorbed Dose Calculation:

Correction factors need to be applied in order to account for differences between TLD irradiation conditions and the conditions under which the MDLs were acquired. A correction would be required for differences in attenuating material - Li(F) vs soft tissue (ST). The time of exposure and operating current are linearly related to dose delivered and so the ratio of the times used for TLD and MDL measurements would represent another such factor. A similar factor would account for the difference between the

operating voltage-current setting used in these two measurements; x-ray intensity (and subsequently dose) is proportional to the square of voltage and linearly proportional to the current (Evans, 1955; Johns and Cunningham, 1983). Taking these factors into account, the corrected absorbed dose is given by

$$D_{tissue} = D_{avg} \frac{\left(\mu_{en}/\rho\right)_{ST}}{\left(\mu_{en}/\rho\right)_{Li(F)}} \frac{T_{MDL}}{T_{Li(F)}} \frac{I_{MDL}}{I_{Li(F)}} \left[\frac{V_{MDL}}{V_{Li(F)}}\right]^2 \quad (6)$$

where D_{tissue} is the corrected absorbed dose, D_{avg} is the averaged absorbed dose over all the chips calculated as D_{avg}±SDOM, T_{TLD} is the time for which the TLD chips were exposed with V_{TLD} and I_{TLD} being the tube's operating conditions for these exposures (35.0 kV, 0.5 mA), T_{MDL}, I_{MDL} and V_{MDL} are the real time, operating current and voltage used in the associated MDL measurements performed with each of these filters respectively and the mass energy attenuation coefficients, $\mu(en)/\rho$, are values for soft tissue, assuming the soft tissue composition listed in the NIST database (Berger et al., 2005), and Li(F) at the desired energy – Mo Kα (17.44 keV). When bremsstrahlung is the dominant source of the incident photons, the well-known hump is roughly triangular in shape. The maximum energy corresponds to the voltage setting in kVp. If the voltage is increased by a factor of 3, the area under this continuum of energies goes up by a factor of ~9. When characteristic x-rays are considered as the driving source of incident radiation, electron and secondary photon production are proportional to the detected intensity. A trivial connection between such production rates and intensity may be optimistic and a detailed Monte Carlo simulation of the process would be required to correctly establish the theoretical relationship. For characteristic x-rays, a modified version of the square-law relationship has been used (Bushberg, 2002; Pella et al., 1985; Tertian and Broll, 1984) and so the power may be slightly higher or lower than 2. In the current case, an experimental measurement of this relationship may be performed with a HpGe detector, where the efficiency at such energies (>17 keV) is 100%, compared to a Si(Li) detector where the efficiency starts to drops off at around 20-25 keV. Nonetheless, the square law governing intensity with respect to x-ray tube voltage is well-referenced in x-ray spectrometry, as seen above. In the absence of a direct measurement of tube output, it offers an estimate of the relationship involved and is used in the current work.

The mass attenuation coefficients were found to be 1.1417 cm^2/g and 0.9937 cm^2/g at the weighted average Mo K$\alpha_{1,2}$ energy of 17.44 keV (Deslattes et al., 2003), for Li(F) and soft tissue respectively (Hubbell and Seltzer, 2004). The listed coefficients were obtained through interpolation from the raw NIST data. The incident energy was assumed to be a weighted average of the Mo K$\alpha_{1,2}$ energies. Thus, the soft tissue-Li(F) ratio of μ_{en}/ρ was calculated for this energy ignoring the Mo Kβ. As this energy is present in the incident spectrum emitted by the tube, it's effect on the ratio of μ_{en}/ρ is briefly investigated here. An averaged mass-energy attenuation coefficient was calculated using

$$\left(\frac{\mu_{en}}{\rho}\right)_{AVG} = \sum_{i=1}^{n} \left(\frac{\mu_{en}}{\rho}\right)_{E_i} E_i I_i \quad (7)$$

for soft tissue and Li(F). Here, E_i is the individual published energy for each Kα and Kβ line, $(\mu_{en}/\rho)_{Ei}$ is the NIST mass-energy coefficient for energy E_i, I_i is the intensity per 100 K-shell vacancies at E_i (Firestone, 2005). Then the ratio of the averaged coefficients was calculated and compared to the ratio using only the weighted average Mo $K\alpha_{1,2}$ energy. It was found that the ratio was 0.37% higher using all the energies than just the Mo $K\alpha_{1,2}$ lines. Alternatively, if the value for μ_{en}/ρ was calculated by combining coefficients for each Kα energy separately using a weighted average, with I_i as the weights, then this gives a ratio that is 0.48 % higher ratio than that used. Since these differences are very small, the weighted average of the $K\alpha_{1,2}$ energy is used to determine one value for (μ_{en}/ρ) for soft tissue and Li(F) and this is used in subsequent calculations. In order to avoid this, a single energy was assumed as listed above. The average of all the absorbed dose readings in the array was found to be (1,531±438) mGy, (11,130±2,098) mGy and (281±36) mGy for the longer distance, shorter distance and thicker filter (longer distance) respectively. The respective corrected readings were (5±1) – (19±3) mGy, (113±27) mGy and 0.9±0.1 mGy. These doses correspond to the varying voltage-current conditions, shorter distance and repeatability (R1) measurements presented earlier.

4.10. Effective Dose Calculation:

In the current design of the shielding cabinet, the palm of the right hand would be the only part of the body that could be subjected to the x-ray tube exposure at a 45-degree angle. The exposures performed with this detection system do not involve whole body irradiation. Thus, the effective dose offers a means of comparing the dose delivered to this localized area of skin, in order to obtain the listed MDLs, with the ICRP effective dose limit to members of the public. With the corrected absorbed dose determined, the effective dose to the area of the skin that is exposed would then be given by

$$\mathrm{E} = \mathrm{D}_{\mathrm{tissue}} \frac{\mathrm{V}_{\mathrm{IRR}}}{\mathrm{V}_{\mathrm{T}}} \omega_{\mathrm{R}} \omega_{\mathrm{T}} \quad (8)$$

where $V_{IRR} = A_{IRR}$ (0.2 cm), $V_T = A_T$ (0.2 cm) where the average thickness of skin was assumed to be 0.2 cm and A_T is the ICRP area of the whole body skin surface, which is 18000 cm^2 (ICRP 23) and A_{IRR} is the measured beam area in cm^2. ω_R and ω_T are the radiation and tissue weighting factors for photons (1) and soft-tissue (0.01) respectively. Under all the irradiation conditions tested, the effective dose delivered ranged from (0.007±0.001) – (0.20±0.04) μSv. Quoted effective doses typically correspond to whole-body exposure, without geometry scaling for the area of exposure. Although the exposed area here is much smaller than the whole body, it is useful to also calculate the dose without scaling for volume of skin exposed. The respective whole body effective dose

readings, without this correction, were found to cover the range of (42±12) – (163±47) μSv, (658±124) μSv and (7.88±1.01) – (7.90±1.01) μSv for the longer distance, shorter distance and thicker filter (longer distance) respectively. These ranges were calculated for the measurement conditions used for phantom measurements reported earlier – changing voltage and current for Mo 100 μm at longer distance, shorter source-phantom distance with same filter and Mo 200 μm repeatability test (R 2) for longer distance. All these effective doses are within the 1 mSv ICRP effective dose limit to members of the public (ICRP 60). They are also very similar to or less than the NCRP and UNSCEAR reported effective doses of 0.6 mSv delivered by typical medical procedures (Mettler et al., 2009). By comparison, the dose due to naturally occurring background radiation is listed at 2.4 mSv (NCRP, 2009).

4.11. Equivalent Dose Calculation.

The dose delivered to a 1 cm^2 sub-section of the beam area (highly localized dose) is also of importance to the biological consequences of an exposure required to achieve an observed MDL. The average of uncorrected absorbed dose readings, covering these chips (inside dashed box) earlier, was (1,555±269) mGy, (16,687±3977) mGy and (267±37) mGy for the longer distance, shorter distance and thicker filter (longer distance) respectively. These are very similar to the average absorbed dose of the full array of chips, as calculated in the previous section. This is because the average of chips inside the dashed box (strongest part of beam, 1555±269 mGy for longer distance) is very similar to the average of chips in the entire array (1531±438 mGy for longer distance). This is true for all three filter conditions tested. This subset of chips (covering the strongest dose) can be used to calculate the equivalent dose to the skin using

$$H = D_{tissue1}\omega_R \tag{9}$$

where $D_{tissue1} = D_{avg1} \pm SDOM_1$. The equivalent dose is an important quantity since the effective dose will not offer an indication of skin protection against deterministic effects that could be induced by the exposure. The ICRP recommends an annual limit of 50 mSv, over a 1 cm^2 area of skin. Using a radiation weighting factor of 1, the equivalent dose and a Figure of Merit (FOM), are shown in table 9, for all MDL phantom calibration work performed here, where FOM = $MDL\sqrt{E}$ (Davis et al., 2008; Grinyer et al., 2005; Studinski et al., 2008), using the localized effective dose in μSv.

Condition	V (kVp)	I (μA)	MDL (RT) (ppm)	H (mSv)	E (μSv)

Chng I* (decreasing)	25	500	0.5150	±	0.0080	19	±	3	0.14	±	0.04
		400	0.6503	±	0.0005	14	±	2	0.10	±	0.03
		300	0.7894	±	0.0007	10	±	2	0.07	±	0.02
		200	0.8741	±	0.0039	6	±	1	0.04	±	0.01
Chng V* (increasing)	23	200	1.0554	±	0.0008	5	±	1	0.04	±	0.01
	25		0.8741	±	0.0039	6	±	1	0.04	±	0.01
	28		0.7164	±	0.0006	8	±	1	0.06	±	0.02
	30		0.6913	±	0.0007	11	±	2	0.08	±	0.03
R 1**	30	145	0.5969	±	0.0006	0.9	±	0.1	0.007	±	0.001
			0.6307	±	0.0009	0.9	±	0.1	0.007	±	0.001
			0.7087	±	0.0002	0.9	±	0.11	0.007	±	0.001
SHORT***	25	22	0.8044	±	0.0009	113	±	27	0.20	±	0.04
MAX 1*	50	1000	N/A			1,864	±	322	14	±	4
MAX 2**						147	±	21	1.1	±	0.1
MAX 3***						2,564	±	611	4.4	±	0.8

(a)

Condition	**FOM (ppm$\sqrt{\text{µSv}}$)**		
Chng I* (decreasing)	0.19	±	0.03
	0.21	±	0.03
	0.21	±	0.03
	0.18	±	0.03
Chng V* (increasing)	0.20	±	0.03
	0.18	±	0.03
	0.18	±	0.03
	0.19	±	0.03
R 1**	0.049	±	0.003
	0.05	±	0.01
	0.06	±	0.01
SHORT***	0.36	±	0.03

(b)

Table 9: (a) Effective and equivalent doses delivered during exposure conditions used for MDL phantom work with Mo filters, for various voltage-current settings and (b) corresponding Figure-of-Merit (FOM). *Mo 100 μm filter at longer source-phantom distance, R 1** Mo 200 μm filter at longer source-phantom distance (conditions of first

repeatability test shown earlier, indicating as much as ~16% overall variability), SHORT*** Mo 100 μm filter at shorter source-phantom distance. Note: MAX corresponds to 1800 seconds real time exposure, using maximum tube settings of 50 kVp, 1.00 mA (1000 μA).

Except for the dose at the shorter distance, all equivalent (skin) doses listed in table 9a are within the ICRP limit recommended for members of the general public (50 mSv). Thus, localized skin exposure is not a concern for MDL measurements performed over ~1800 seconds at the longer distance. Scatter will make a contribution to the dose at the shorter distance. A way of reducing this dose is to reduce the scatter by increasing the size of the shielding cabinet. It should be noted that the maximum effective and equivalent doses that can be delivered (assuming full power 50W exposure for 1800 seconds) have the potential to do harmful damage to the subject. However, these exposures are almost certain to be unrealizable due to the system dead time likely being very close to saturation. Finally, the first three sections of table 9b show FOM results. When making a comparison, while also taking dose into account, between the performance of the various setups used, as well as between the different x-ray tube systems used, a figure of merit (FOM) can be calculated (Davis et al., 2008; Grinyer et al., 2005). The lower the FOM corresponding to a particular setup, the better the performance of that setup. These FOMs compare favorably with those for previous work on this system - 0.47 or higher. The improvement in dose, due to lower tube operating conditions, is the main reason for this. FOM does not change much for varying voltage or current conditions separately. This is expected since the lower MDL is facilitated by increasing the tube setting, which drives up the dose delivered. Nearly matching FOMs indicates that the gain in MDL is offset by the higher dose delivered. The main difference in FOM in the third section of this table is due to MDL. This listed the FOM for the repeatability testing. Three separate phantom trials were performed under the same conditions, giving separate MDLs, while only one TLD exposure was performed and interpolated to these conditions. In terms of dose, the thicker Mo filtration setup was found to be better. In terms of FOM, there is a similarly large difference between the 100 μm or 200 μm filters due to the significant reduction in dose. Given that the doses are quite low, more emphasis may be placed on the MDL than the FOM. Finally, the FOM at the larger distances show a benefit over the shorter distance. The MDL and dose are both higher (worse) at the shorter distance.

The shielding cabinet was completely closed for the entire duration of the TLD array exposures. These exposures were conducted over a much longer time interval than that those required for individual phantom counting times (< 1800 seconds). Thus, consistency of x-ray tube output over such a lengthy interval and resulting sporadic spikes/dips that may be caused by RF interference could not be accounted for. If such anomalies were to occur during a phantom measurement, a clear jump in the dead time would have occurred thus extending the real time beyond 1800 seconds – it would thus be clear that such an irregularity had affected the phantom measurement and the spectrum would have to be re-acquired. This, however, is not visible in the significantly lengthier

TLD exposures. With the currently required interlock system, opening the shielding cabinet to insert an ionization chamber and periodically monitor tube performance is not possible since the dosimeter array would be blocked if the ion chamber were placed directly in the path of the incident beam. Such equipment was not used in the current work, however, the TLD exposures were performed after regular lab operating hours and so the possibility of interference would be minimal due to reduced lab activity.

5. Conclusions

The current work investigated the effect of modifications to the setup of a 50 W x-ray tube based system in terms of its ability to detect arsenic levels in calibration phantoms. The need for realizing reliable scatter normalization was the motivation for using filtration to clean up some of the x-ray tube's characteristic x-rays. However, the results show that a K-edge filter's perceived benefit of removal of Mo Kβ is somewhat offset by fluorescing of the filter's own characteristic x-rays. For the current application, this results in unwanted complication of the scatter portion of the spectrum. An additional source of fluorescence of the filter's characteristic x-ray lines is scatter that originates off the shielding cabinet used with the detection system. A dead time correction factor or normalization to real (clock) time represents an alternative, as a way of comparing results obtained at different dead times. The limitation of voltage and current chosen in the current work is that they were based on dead time observed with polyester resin phantoms. Greater scatter will be observed when a subject's entire arm is inserted into the shielding cabinet instead of the phantom. The choice of tube strength will, thus, be expected to change *in vivo*. With the exception of this limitation, the MDL benefits of larger source-phantom and shorter phantom-detector distances were clearly demonstrated. These were found to lower the MDL and improve system sensitivity to small changes in concentration (slope of calibration line). Through modifications allowing such reductions, the lowest detection limit achievable is similar to those reported previously at larger distances. However, the current results were (a) calculated using a more extensive definition of MDL and (b) found for a lower tube voltage and/or current than previously, thereby reducing the dose delivered to the subject. The population expected to offer best possibilities of arsenic detection *in vivo* is expected to be one which has a known exposure to arsenic. The system-wide improvements reported here are able to offer these detection capabilities at a lower dose to the subject. Dose delivered by the system indicates that, even full body effective dose, is within the ICRP limit. A more realistic metric is the effective dose to the palm of the hand and this is several orders of magnitude below the limit. The skin dose is also within regulatory limits and so the system's current layout is not capable of delivering a dose that exceeds the ICRP recommended limits to members of the general public.

Acknowledgments

Funding was provided by the Natural Sciences and Engineering Research Council of Canada (NSERC), Research Tools and Instruments grants. F. E. McNeill, D. R. Chettle and D. E. B. Fleming gratefully acknowledge receipt of NSERC Discovery grants. The authors would also like to thank Jason Falladown, Scott McMaster and Steve Staniek for

their help in modifying and verifying the design of the cabinet assembly for the x-ray tube.

References:

Abu Atiya, I., 2012. In-Vivo X-Ray Fluorescence Assessment of Iron Levels in the Skin for β-Thalassemia Patients. Open Access Diss. Theses.

Aland, T., Kairn, T., Kenny, J., 2011. Evaluation of a Gafchromic EBT2 film dosimetry system for radiotherapy quality assurance. Australas. Phys. Eng. Sci. Med. 34, 251–60.

Arnold, M.L., McNeill, F.E., Stronach, I.M., Pejovic-Milic, A., Chettle, D.R., Waker, A., 2002. An accelerator based system for in vivo neutron activation analysis measurements of manganese in human hand bones. Med. Phys. 29, 2718.

Berger, M.J., Coursey, J.S., Zucker, M.A., Chang, J., 2005. ESTAR, PSTAR, and ASTAR: Computer Programs for Calculating Stopping-Power and Range Tables for Electrons, Protons, and Helium Ions (version 1.2.3) (Gaithersburg, MD: National Institute of Standards and Technology) [WWW Document]. URL http://www.nist.gov/pml/data/star/index.cfm

Bevington, P.R., Robinson, D.K., 2003. Data reduction and error analysis for the physical sciences, 3rd ed. McGraw-Hill, Boston, USA.

Campbell, J.L., McDonald, L., Hopman, T., Papp, T., 2001. Simulations of Si(Li) x-ray detector response. X-Ray Spectrom. 30, 230–241.

Chen, C.J., Chuang, Y.C., Lin, T.M., Wu, H.Y., 1985. Malignant neoplasms among residents of a blackfoot disease-endemic area in Taiwan: high-arsenic artesian well water and cancers. Cancer Res. 45, 5895–9.

Da Silva, E., Pejović-Milić, A., Heyd, D. V., 2008. The use of teeth as the site for the in vivo or ex vivo quantification of skeletal strontium by energy-dispersive X-ray fluorescence spectrometry: A feasibility study. J. Anal. At. Spectrom. 23, 527–534.

Das, D., Chatterjee, a, Mandal, B.K., Samanta, G., Chakraborti, D., Chanda, B., 1995. Arsenic in ground water in six districts of West Bengal, India: the biggest arsenic calamity in the world. Part 2. Arsenic concentration in drinking water, hair, nails, urine, skin-scale and liver tissue (biopsy) of the affected people. Analyst 120, 917–24.

Davis, K., Pejović-Milić, A., Chettle, D.R., 2008. In vivo measurement of bone aluminum in population living in southern Ontario, Canada. Med. Phys. 35, 5115.

Deslattes, R., Kessler, E., Indelicato, P., de Billy, L., Lindroth, E., Anton, J., 2003. X-ray transition energies: new approach to a comprehensive evaluation. Rev. Mod. Phys. 75, 35–99.

Devic, S., Seuntjens, J., Hegyi, G., Podgorsak, E.B., Soares, C.G., Kirov, A.S., Ali, I., Williamson, J.F., Elizondo, A., 2004. Dosimetric properties of improved GafChromic films for seven different digitizers. Med. Phys. 31, 2392.

Evans, R.D., 1955. The atomic nucleus. McGraw-Hill, New York, USA.

Farquharson, M.J., Bradley, D. A, 1999. The feasibility of a sensitive low-dose method for the in vivo evaluation of Fe in skin using K-shell x-ray fluorescence (XRF). Phys. Med. Biol. 44, 955–65.

Firestone, R., 2005. LBNL Isotopes Project Nuclear Data Dissemination Home Page. Ernest Orlando Lawrence Berkeley National Laboratory, Berkeley, U.S.A. Retrieved: October 2011 from http://ie.lbl.gov/toi.html [WWW Document].

Fishbein, L., 1981. Sources, transport and alterations of metal compounds: an overview. I. Arsenic, beryllium, cadmium, chromium, and nickel. Environ. Health Perspect. 40, 43–64.

Fleming, D.E.B., Gherase, M.R., 2007. A rapid, high sensitivity technique for measuring arsenic in skin phantoms using a portable x-ray tube and detector. Phys. Med. Biol. 52, N459–65.

Gherase, M.R., Mader, J.E., Fleming, D.E.B., 2010. The radiation dose from a proposed measurement of arsenic and selenium in human skin. Phys. Med. Biol. 55, 5499–5514.

Gislason-Lee, A.J., McMillan, C., Cowen, A.R., Davies, A.G., 2013. Dose optimization in cardiac x-ray imaging. Med. Phys. 40, 091911.

Graham, S.A., O'Meara, J.M., 2004. The feasibility of measuring silver concentrations in vivo with x-ray fluorescence. Phys. Med. Biol. 49, N259–N266.

Grinyer, J., Atanackovic, J., Byun, S.H., Chettle, D.R., 2007. Phantom studies of Cd, Hg and Cl by prompt gamma neutron activation analysis using a 238Pu–Be neutron source. Nucl. Instruments Methods Phys. Res. Sect. B 263, 262–265.

Grinyer, J., Byun, S.H., Chettle, D.R., 2005. In vivo prompt gamma neutron activation analysis of cadmium in the kidney and liver. Appl. Radiat. Isot. 63, 475–9.

Harris, D.C., 2006. Quantitative chemical analysis, 7th ed. W. H. Freeman, New York, USA.

Heirwegh, C.M., Chettle, D.R., Pejovic-Milic, A, 2012. Ex vivo evaluation of a coherent normalization procedure to quantify in vivo finger strontium XRS measurements. Med. Phys. 39, 832–41.

Hubbell, J.H., Seltzer, S.M., 2004. Tables of X-Ray Mass Attenuation Coefficients and Mass Energy-Absorption Coefficients (version 1.4) (Gaithersburg, MD: National Institute of Standards and Technology) [WWW Document]. URL http://www.nist.gov/pml/data/xraycoef/index.cfm
International Commission on Radiological Protection, Publication 23, 1975. Rep. Task Gr. Ref. Man. Pergamon, Oxford, pp. 480.
International Commission on Radiological Protection, Publication 60, 1990. Recomm. Int. Comm. Radiol. Prot. Pergamon, Oxford.
Johns, H.E., Cunningham, J.R., 1983. The physics of radiology, 2nd ed. Charles C. Thomas, Springfield, Ill., U.S.A.
Jonson, R., Mattsson, S., Unsgaard, B., 1988. A method for in vivo analysis of platinum after chemotherapy with cisplatin. Phys. Med. Biol. 33, 847–57.
Jorch, H.H., Campbell, J.L., 1977. On the analytic fitting of full energy peaks from Ge(Li) and Si(Li) photon detectors. Nucl. Instruments Methods 143, 551–559.
Maes, D., Pate, B.D., 1977. The absorption of arsenic into single human head hairs. J. Forensic Sci. 22, 89–94.
Mandal, B.K., Suzuki, K.T., 2002. Arsenic round the world: a review. Talanta 58, 201–235.
Marquardt, D.W., 1963. An Algorithm for Least-Squares Estimation of Nonlinear Parameters. J. Soc. Ind. Appl. Math. 11, 431–441.
McKinley, R.L., Tornai, M.P., Samei, E., Bradshaw, M.L., 2005. Initial study of quasi-monochromatic X-ray beam performance for X-ray computed mammotomography. IEEE Trans. Nucl. Sci. 52, 1243–1250.
Meghzifene, K., Aiginger, H., Nowotny, R., 2006. A fit method for the determination of inherent filtration with diagnostic x-ray units. Phys. Med. Biol. 51, 2585–97.
Mettler, F.A., Bhargavan, M., Faulkner, K., Gilley, D.B., Gray, J.E., Ibbott, G.S., Lipoti, J.A., Mahesh, M., McCrohan, J.L., Stabin, M.G., Thomadsen, B.R., Yoshizumi, T.T., 2009. Radiologic and nuclear medicine studies in the United States and worldwide: frequency, radiation dose, and comparison with other radiation sources--1950-2007. Radiology 253, 520–31.
Misbahuddin, M., Momin, A, Al-Amin, M., 2008. All-E lutein and 3'-epilutein in the epidermis of chronic arsenic poisoning. Clin. Toxicol. (Phila). 46, 176–80.
Morales, K.H., Ryan, L., Kuo, T.L., Wu, M.M., Chen, C.J., 2000. Risk of internal cancers from arsenic in drinking water. Environ. Health Perspect. 108, 655–61.
Nagel, H.D., 1989. Comparison of performance characteristics of conventional and K-edge filters in general diagnostic radiology. Phys. Med. Biol. 34, 1269–1287.
Nakano, M., Hill, R.F., Whitaker, M., Kim, J.-H., Kuncic, Z., 2012. A study of surface dosimetry for breast cancer radiotherapy treatments using Gafchromic EBT2 film. J. Appl. Clin. Med. Phys. 13, 3727.
NCRP, 2009. National Council on Radiation Protection and Measurements. Ionizing radiation exposure of the population of the United States: 2006. NCRP report no. 160., Journal of Radiological Protection.
Niroomand-Rad, A., Blackwell, C.R., Coursey, B.M., Gall, K.P., Galvin, J.M., McLaughlin, W.L., Meigooni, A.S., Nath, R., Rodgers, J.E., Soares, C.G., 1998. Radiochromic film dosimetry: Recommendations of AAPM Radiation Therapy Committee Task Group 55. Med. Phys. 25, 2093.
Nowotny, R., Meghzifene, K., 2002. Simulation of the effect of anode surface roughness on diagnostic x-ray spectra. Phys. Med. Biol. 47, 3973–83.
O'Meara, J.M., Börjesson, J., Chettle, D.R., Mattsson, S., 2001. Normalisation with coherent scatter signal: improvements in the calibration procedure of the 57Co-based in vivo XRF bone-Pb measurement. Appl. Radiat. Isot. 54, 319–25.
Pejović-Milić, A., Stronach, I.M., Gyorffy, J., Webber, C.E., Chettle, D.R., 2004. Quantification of bone strontium levels in humans by in vivo x-ray fluorescence. Med. Phys. 31, 528–38.
Potts, P.J., Webb, P.C., Watson, J.S., 1986. Silicate rock analysis by energy-dispersive X-ray fluorescence using a cobalt anode X-ray tube. Part I. Optimisation of excitation conditions for chromium, vanadium, barium and the major elements. J. Anal. At. Spectrom. 1, 467.
Reinhardt, S., Hillbrand, M., Wilkens, J.J., Assmann, W., 2012. Comparison of Gafchromic EBT2 and EBT3 films for clinical photon and proton beams. Med. Phys. 39, 5257–62.
Robinson, J.W., 1991. Practical Handbook of Spectroscopy. CRC Press, Boca Raton, FL, USA.
Salter, C., 2000. Error Analysis Using the Variance-Covariance Matrix. J. Chem. Educ. 77, 1239.
Schwartz, R.A., 1997. Arsenic and the skin. Int. J. Dermatol. 36, 241–50.
Shoemaker, D.P., Garland, C.W., Nibler, J.W., 1989. Experiments in Physical Chemistry, 5th ed. McGraw-Hill.
Somervaille, L.J., Chettle, D.R., Scott, M.C., 1985. In vivo measurement of lead in bone using x-ray fluorescence. Phys. Med. Biol. 30, 929–43.
Studinski, R.C.N., 2005. Development of an in vivo method of measuring arsenic with radiation.
Studinski, R.C.N., McNeill, F.E., Chettle, D.R., O'Meara, J.M., 2004. XRF analysis of arsenic-doped skin phantoms. X-Ray Spectrom. 33, 285–288.

Studinski, R.C.N., McNeill, F.E., Chettle, D.R., O'Meara, J.M., 2005. Estimation of a method detection limit for an in vivo XRF arsenic detection system. Phys. Med. Biol. 50, 521–530.
Studinski, R.C.N., McNeill, F.E., O'Meara, J.M., Chettle, D.R., 2006. A method detection limit for potential in vivo arsenic measurements with a 50 W x-ray tube. Phys. Med. Biol. 51, N381–7.
Todd, A.C., 2000. Coherent scattering and matrix correction in bone-lead measurements. Phys. Med. Biol. 45, 1953–63.
Uher, J., Roach, G., Tickner, J., 2010. Peak fitting and identification software library for high resolution gamma-ray spectra. Nucl. Instruments Methods Phys. Res. Sect. A Accel. Spectrometers, Detect. Assoc. Equip. 619, 457–459.
Van Grieken, R.E., Markowicz, A.A., 2002. Handbook of X-Ray Spectrometry. Marcel Dekker Inc., New York, USA.
Williamson, B.D., van Doorn, T., 1994. The efficacy of K-edge filters in diagnostic radiology. Australas. Phys. Eng. Sci. Med. 17, 162–74.
Yamaguchi, C., Yamamoto, T., Terada, H., Akisada, M., 1983. Effect of tungsten absorption edge filter on diagnostic x-ray spectra, image quality and absorbed dose to the patient. Phys. Med. Biol. 28, 223–232.
Zamburlini, M., Pejović-Milić, A., Chettle, D.R., 2008. Coherent normalization of finger strontium XRF measurements: feasibility and limitations. Phys. Med. Biol. 53, N307–13.
Zamburlini, M., Pejović-Milić, A., Chettle, D.R., Webber, C.E., Gyorffy, J., 2007. In vivo study of an x-ray fluorescence system to detect bone strontium non-invasively. Phys. Med. Biol. 52, 2107–22.
Zentai, G., 2011. X-ray imaging using K-edge filters. In: Kundu, T. (Ed.), Proc. SPIE 7984, Health Monitoring of Structural and Biological Systems 2011. International Society for Optics and Photonics, San Diego, California, USA, pp. 798418–798418–10.

2.3 Additional results from x-ray tube based calculation of dead time correction factor:

The software-recorded ICR is plotted, as a function of tube current, in figure 2.1.

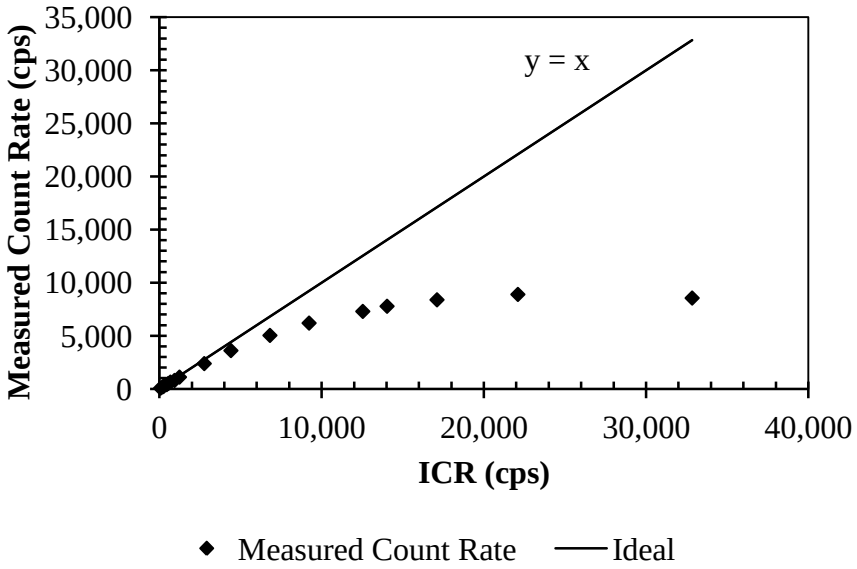

Figure 2.1: Plot of ICR as the x-ray tube current is increased. Also shown is the ideal case where Measured Count Rate = ICR.

The measured count rate corresponding to the above graph is plotted as a function of ICR in figure 2.2.

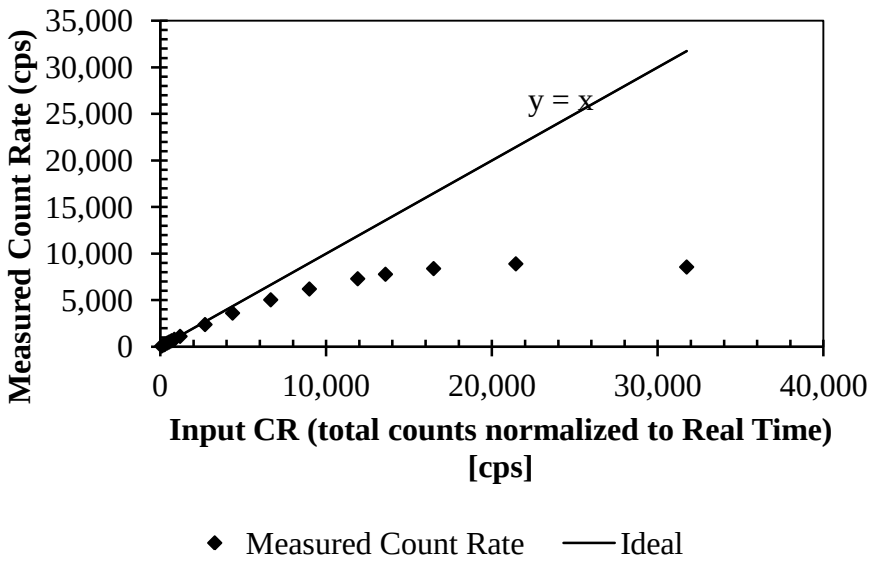

Figure 2.2: Measured count rate (total recorded counts/real, or clock, time) versus input count rate (ICR). Also shown is the ideal scenario where measured and input count rates are equal. The rise time was fixed at 12 μs here and in figure 2.1.

The expected drop-off in measured count rate is observed here beyond a certain ICR value. This figure looks very similar to figure 2.1, except that measured count rate is normalized to real time here. The largest difference is that the maximum ICR drops from ~33 kcps (figure 2.1) to ~32 kcps (here). Although ICR was used in the calculations, this count rate (normalized to real time) would also be suitable. With this data set, $\ln(m/x_i)$ was plotted as a function of x_i as per equation 8 and is plotted along with the resulting linear fit in figure 2.3.

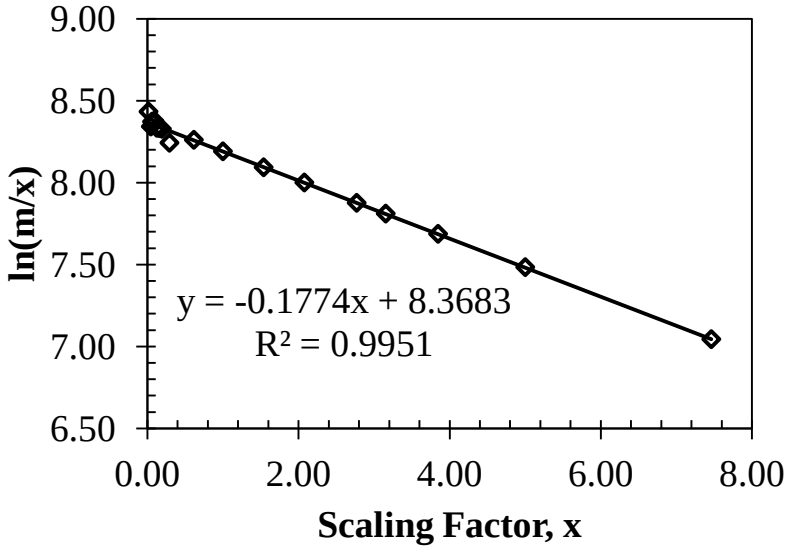

Figure 2.3: Plot of $\ln(m_i/x_i)$ versus x_i, obtained by increasing the tube current.

The intercept and slope of the linear fit were found to be (8.37±0.01) and (-0.177±0.003) respectively, which can then be combined to give a dead time of 41.17 μs.

2.4 Calculation of dead time correction factor – multi-method comparison:

Additional approaches to calculation of a dead-time correction factor are documented here. The first method for this calculation was presented earlier. Here, variations on the approach are documented, followed by a comparison of these methods.

2.4.1 X-Ray Tube based approaches:

Method 2:

Taking the ln of both sides of $m = ne^{-n\tau}$ gives

$$ln(m_i) = ln\,(n_i e^{-n_i\tau}) \quad (1)$$

$$ln(m_i) = ln(n_i) + ln(e^{-n_i\tau}) \quad (2)$$

$$ln(m_i) = ln(n_i) - n_i\tau \quad (3)$$

$$ln(m_i) = -n_i\tau + ln(n_i) \quad (4)$$

$$ln(m_i) = -\tau n_i + ln(n_i) \quad (5)$$

Equation 5 is of the form

$$y = cx + d \quad (6)$$

where the dead time is found from the slope to be

$$\tau = -c \quad (7)$$

Using the same data set as that shown above, but this time ignoring the tube current, the ln of the measured count rate representing m_i (total recorded counts/real time) was plotted against the ICR (n_i) as shown in figure 2.4.

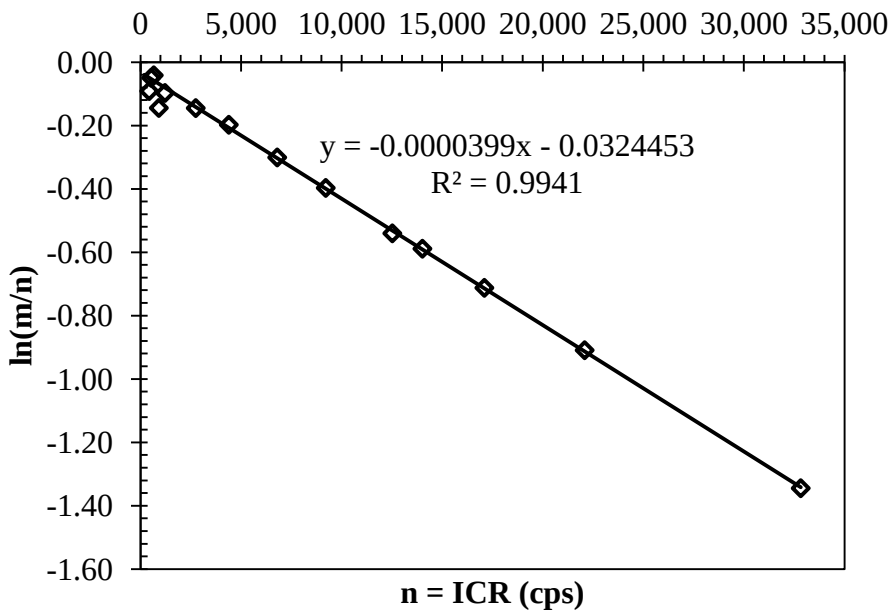

Figure 2.4: Plot of $\ln(m_i/n_i)$ versus n_i (where n_i = ICR).

The slope and intercept of the linear fit were found to be ($-0.0000399 \pm 8.24493 \times 10^{-7}$) and ($-0.0324453 \pm 0.010042092$) respectively. The negative of the slope gives the dead time to be 39.89 μs.

Method 2.1:
The live time of the detection system is the time when it is not busy processing but actively accepting pulses and is the difference between real time and dead time, where real (clock) time is the elapsed time. If the true count rate is not taken as the ICR provided by the DSPEC PLUS MCA software (MAESTRO) but instead by

$$n_i = \frac{Total\ Recorded\ Counts}{Live\ Time} \tag{8}$$

then the formulation in method 2 can still be used, with

$$m_i = \frac{Total\ Recorded\ Counts}{Real\ Time} \tag{9}$$

the same as what was used in methods 1 and 2 and m_i is plotted against n_i as shown in figure 2.5.

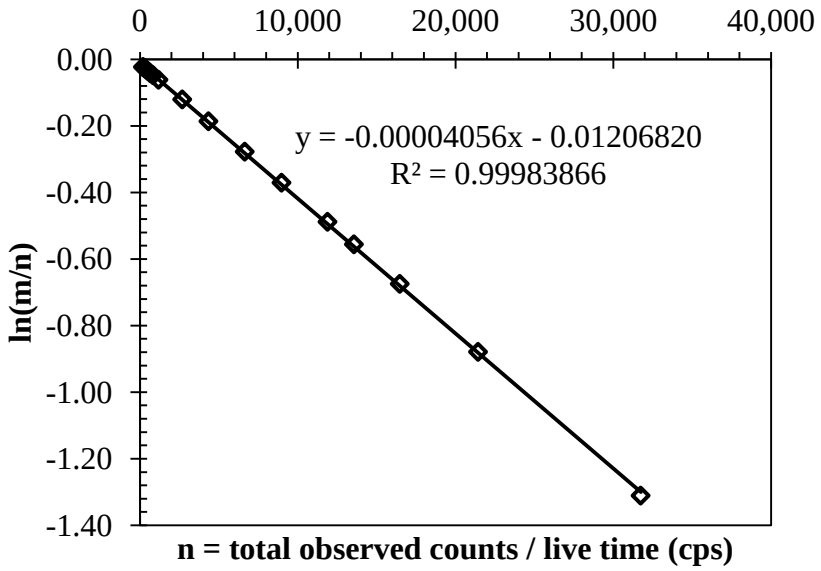

Figure 2.5: Plot of $\ln(m_i/n_i)$ versus n_i.

The slope and intercept of the linear fit were found to be ($-0.0000406 \pm 1.37704 \times 10^{-7}$) and ($-0.0120682 \pm 0.00162152$) respectively. The negative of the slope gives the dead time to be 40.56 μs.

2.4.2 Dead Time Correction Factor for methods 2 and 2.1:

The intention of this work was to determine the dead time correction factor. The dead time is used to calculate the correction factor (CF) which is given by

$$CF = \frac{n_i}{m_i} \tag{10}$$

which can be expressed, in terms of the experimentally determined dead time, from equation 1 to be

$$CF = e^{n_i \tau} \tag{11}$$

where n_i is taken as either the ICR or given by total recorded counts/live time. For a specific tube current, either version of n_i is known (ICR is recorded, for methods 1 and 2, and n_i, can be calculated from the recorded spectrum), so the dead time correction factor

can be determined. Full error analysis is shown in Appendix A. For a count rate (ICR) of 17,103 cps (dead time of 49.09 %), the correction factors are found to be

CF_1 = 2.02193±0.02855 (using current scaling factor)
CF_2 = 1.97828±0.02790 (using n = ICR)
$CF_{2.1}$ = 1.95087±0.00446 (using n = total observed counts / live time)

This correction factor can then be compared to the ratio n_i/m_i, as shown in equation 26, which is obtained independent of the experimentally determined dead time τ. Instead, either choice of n_i is divided by the measured count rate m_i as shown below

$$CF = \frac{n_i}{m_i} \tag{12}$$

with the uncertainty given by

$$\frac{\delta(CF)}{CF} = \sqrt{\left(\frac{\delta n}{n}\right)^2 + \left(\frac{\delta m}{m}\right)^2} \tag{13}$$

When using n = ICR, this becomes

$$\frac{\delta(CF)}{CF} = \sqrt{\left(\frac{\delta m}{m}\right)^2} \tag{14}$$

$$\delta(CF) = CF\frac{\delta m}{m} \tag{15}$$

$$\delta(CF) = \frac{n}{m}\frac{\delta m}{m} \tag{16}$$

$$\delta(CF) = \frac{n}{m^2}\delta m \tag{17}$$

When using n = total recorded counts / live time, this becomes

$$\delta(CF) = CF\sqrt{\left(\frac{\sqrt{total\ recded\ cnts}}{LT}\right)^2 + \left(\frac{\sqrt{total\ recded\ cnts}}{RT}\right)^2} \tag{18}$$

Using this approach:
$CF_{n=ICR}$ = 2.03890±0.00088, which can be compared to CF_1 (2.02193±0.02855) and CF_2 (1.97828±0.02790) above. Also, $CF_{n=\text{total observed counts/LT}}$ = 1.96412±0.00124, which can be compared to $CF_{2.1}$ (1.95087±0.00446) above. The correction factors almost agree, within uncertainty.

The above set of results corresponds to the dataset collected using the x-ray tube with a Nb 200 μm filter in place. The dead time of the detection system will not change from filter to filter, since the filter materials produce fluorescence spectra that are very similar to each other. The procedure was repeated with 5 other filters, and the results are shown in table 2.1.

Table 2.1: Results of dead time and dead time correction factor calculations for set of five filters that were used individually with the x-ray tube.

Method	Filter (μm)	ICR	CF	CF using n/m	τ (μs)
1			2.022 ± 0.029		41.17
2	Nb (200)	17,103	1.978 ± 0.028	2.039 ± 0.001	39.89
2.1			1.951 ± 0.004	1.964 ± 0.001	40.56
1			1.871 ± 0.019		42.06
2	Mo (200)	14,893	1.887 ± 0.026	1.844 ± 0.001	42.62
2.1			1.820 ± 0.014	1.813 ± 0.001	40.91
1			1.915 ± 0.020		41.80
2	Nb (100)	15,540	1.859 ± 0.011	1.940 ± 0.001	39.90
2.1			1.843 ± 0.004	1.850 ± 0.001	41.27
1			1.872 ± 0.017		41.45
2	Mo (100)	15,129	1.827 ± 0.014	1.903 ± 0.001	39.83
2.1			1.801 ± 0.003	1.809 ± 0.001	40.90
1			1.893 ± 0.017		41.06
2	Ag (100)	15,546	1.879 ± 0.014	1.905 ± 0.001	40.58
2.1			1.851 ± 0.004	1.859 ± 0.001	40.58
1			1.895 ± 0.047		40.96
2	Ag (50)	15,603	1.843 ± 0.025	1.925 ± 0.001	39.18
2.1			1.851 ± 0.015	1.875 ± 0.001	40.50

The dead time correction factor is the ratio of the true interaction rate, n, to the measured counting rate, m. For low counting rates, which give long enough time between the detected events so that dead time between successive pulses may be ignored, the correction factor would be close to 1.00. Here, the measured counting rate would be approximately equal to the true interaction rate. For high counting rates, the measured counting rate would be lower than the true interaction rate and so the correction factor

would be higher than 1.00. This is the case here. As expected, the dead time is nearly unchanged from one filter-based setup to the next. Also, for each filter, the correction factors with methods 1, 2 and 2.1 are very close to the values determined using n/m. When the ICR values are very close to each other [(Nb 100 μm, Ag 100 μm, Ag 50 μm) or (Mo 200 μm, Mo 100 μm)], the correction factors nearly agree within uncertainty.

2.4.3 Source of known count rate:

Method 3:

With this method, the underlying principle was that if a known count rate was supplied (from a source that does not pile-up) to the detection system, then the measured count rate should be equal to this known value; if a second source (which suffers from pulse pile-up) is then mixed in with this fixed count rate source, then the observed decrease in measured count rate (i.e. deviation from the ideal case) could be used to determine the dead time correction factor. Unlike the other three methods, this method would not yield the system dead time directly, but rather just a ratio of expected to measured count rates which is the dead time correction factor. The results of such an approach to calculating the correction factor are presented here.

A fixed count rate of 215 cps, provided by a BNC Pulser, was fed into the Ortec DSPEC PLUS MCA by connecting a coaxial cable from the pulser output to a "T" connector attached to the MCA's Input BNC connector where the Si(Li) detector's amplifier output is normally attached. The other end of the "T" was initially left unconnected, in order to collect a pure signal from the pulser without pileup, and subsequently connected to the detector output. This was done in order to mix sources with and without pileup. With the same setup as that used for the other methods (x-ray tube with standard 45-degree 60 ppm arsenic phantom setup), the pulser peak was positioned to overlap the arsenic K-alpha peak in the recorded spectrum. Thus, this As peak would have two contributions: one (larger) from the x-ray tube (as the tube current is ramped up) and one (smaller) from the pulser. The reasons for choosing a larger and smaller contribution are explained in the following paragraph. Ideally, neither the larger nor the smaller contribution would suffer from pile-up and so a measured count rate of 215 cps would always be observed. In reality, the larger (detection system based) contribution would suffer from pile-up and dominate the overall signal giving measured count rates that are lower than the expected (ideal) count rate. In terms of the spectra recorded here, in the absence of pulse pile-up, the measured arsenic Kα peak count rate (arsenic Kα peak area/real time) should always be equal to the known count rate that is fed in – 215 cps; in the presence of pulse pile-up, the measured count rate would be less than that observed in the ideal scenario and the ratio of expected to measured count rates would provide the dead time correction factor.

Since pulses added by the pulser do not pile up, these pulses cannot dominate the input signal, since this would not be a realistic representation of experimental conditions. These pulses must only cover a very small range of count rates. The interval between random (in this case, the detector's) pulses is governed by Poisson statistics and so if the

pulser signal dominates, then statistics are no longer valid. This leads to a requirement that the added pulser count rate not be much higher than the photopeak count rate induced by the other source (x-ray tube) alone. Thus, it was decided that the pulser count rate would not exceed more than 10-12% of the lowest non-zero value of the ICR reading recorded as the tube current was increased; this fraction would be smaller for the other (higher) current readings.

With this setup, a set of 10 spectra were acquired, for increasing tube current and the resulting pulser count rate (recall this is the arsenic Kα peak only) is plotted as a function of ICR in figure 2.6.

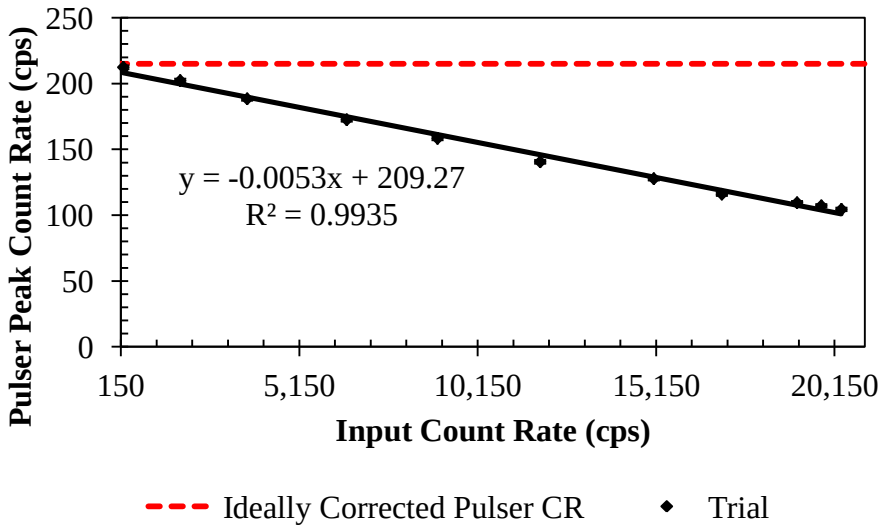

Figure 2.6: Plot of expected (ideal) and observed (trial) count rates, obtained with pulser method of calculating dead time correction factor.

The fitted equation is of the form y = ex + f where e and f are the slope (dimensionless) and intercept (cps) of the straight line. It is clear that, as the ICR (or, tube current) is increased, pulse pile-up starts to dominate and the measured count rate begins to drop. For a particular recorded ICR (corresponding to a specific tube current), m_{obs} = ex + f gives the associated correction factor by

$$CF = \frac{m_{expct}}{m_{obs}} \tag{19}$$

where

$$\delta m_{obs} = \sqrt{\left(\frac{\partial m_{obs}}{\partial e}\delta e\right)^2 + \left(\frac{\partial m_{obs}}{\partial f}\delta f\right)^2} \quad (20)$$

and

$$\delta m_{obs} = \sqrt{(x\delta e)^2 + (1\delta f)^2} \quad (21)$$

$$\delta m_{obs} = \sqrt{(x\delta e)^2 + (\delta f)^2} \quad (22)$$

for x = ICR, giving m_{obs} in dimensions of cps, and m_{expct} is the expected count rate (taken from the ICR reading in MAESTRO of 215 cps). The correction factors obtained for the full set of filters used earlier is shown in table 2.2, along with a comparison to the CF values from method 1, for the same ICR value.

Table 2.2: Comparison of correction factors obtained with methods 1, 2 and 2.1. Average percent difference (PD) is 8.05%.

ICR (cps)	Method 1			Method 3			PD (%)
17,103	2.02	±	0.02	1.88	±	0.02	6.87
	2.03	±	0.02	1.84	±	0.01	9.44
	2.04	±	0.02	1.89	±	0.02	7.42
	2.01	±	0.05	1.87	±	0.02	7.06
	2.05	±	0.02	1.89	±	0.02	7.71
	2.02	±	0.03	1.82	±	0.01	9.80

For a fixed ICR (i.e. for a fixed tube current), the methods produce values for the correction factor that are very close to each other. The correction factor from method 1 is used to correct the peak area and uncertainty, in phantom-related work in this chapter, and the scaled up (corrected) peak areas are then used to determine the MDL.

This method was intended to be a way to validate the approaches used earlier (1, 2, 2.1). Its calculation of the dead time correction factor is independent of the other three methods. While it has served this purpose, the >5% difference in correction factors obtained with earlier methods is a bit disappointing. It may be attributed to the tube-phantom spectra containing several other peaks, besides the chosen arsenic K-alpha peak. An alternate (mono-energetic) source may have been a better choice. Additionally, methods 1, 2 and 2.1 also provide the detection system dead time in addition to the correction factor, while only the latter is obtained with this pulser method.

It was found that, due to a problem with the BNC pulser, the output count rate produced was not as indicated on the pulser's digital meter and so a reading of 200 cps produced 215 cps in reality. This was verified both from the ICR reading in the DSPEC PLUS MAESTRO software and also by displaying the output pulse on an oscilloscope and using the oscilloscope's cursor menu to calculate its frequency. The pulser manufacturer indicated that, since no other confounding symptoms were noticed, the pulser was showing the effects of time and that a re-calibration would be required to fix this problem. This is not very important here, since this method was only utilized for verifying three other methods. If this method is to be pursued in future more rigorous work, a full repair and certified calibration of the pulser must be performed before this feature is used.

2.5 Calibration line intercepts with thick filters:

All the 300 μm filters have 0 ppm areas and calibration line intercepts that are >2σ away from 0. These are significantly different from zero at the 95% confidence level. The origin is in the foil itself as quoted purity from the manufacturer listed trace levels of lead (Pb), which has an L line at 10.55 keV. This is just about overlapping with the As energy at 10.53 keV. In the absence of scatter, this may not be a concern however, the system's current layout is conducive to shielding-based scattering. As the shielding cabinet is made exclusively of copper, care was taken to ensure that Pb was not present in the housing. So, Pb peaks are originating from (a) the incident (source) radiation as it passes through filters and (b) scatter off the foil itself. The problem was also observed for the shorter distance work. A 100-200 μm filter is relatively cleaner in this regard, strictly from a manufacturing perspective. These are advantageous for either RMF or K-edge layouts.

Chapter 3 Measurements with portable x-ray system:

The second type of x-ray fluorescence system studied in this thesis was a portable (handheld) XRF system. Two units were investigated: an Innov-X Alpha 4000S portable x-ray analyzer and an Innov-X Delta Premium model, from Innov-X Systems (Mississauga, ON, Can). Both were developed for use in applications including scrap recycling, soil sampling, archaeomtery and metal analysis. With such a diverse application set, the units had to be assembled in a highly portable form with the ability to perform instantaneous data analysis. Arsenic phantom calibration work and dosimetry were performed on both systems.

3.1 System components – X-Ray tube, Detector and Electronics:

The analyzers run on Li-ion batteries but also had an AC adapter available to plug it into a wall socket for lab based applications – test mode (used in the current work, for both units). The Alpha 4000S unit used a built-in Si PiN diode detector, utilizing peltier-cooling, and the voltage and current were fixed at 40 kV and 20 μA respectively for a tungsten (W) target x-ray tube, which was used as the x-ray source (no focusing or collimation). Internal aluminum filtration of 2 mm (fixed) was present between the tube and kapton window. A kapton [2.64% H, 69.11% C, 7.33% N, 20.92% O; $\rho = 1.42$ g/cm^3 (NIST, 2005)], window is a thin heat/chemically impervious window typically <0.5 mm allowing for >99% photon transmission at >6 keV. An internal aluminum filter was present inside the unit, but its exact orientation is unknown. Since the device is targeted at industrial/agricultural users, times of a couple of minutes are more than sufficient for obtaining quality data for those applications. The Delta unit recorded the fluorescence with a SDD detector, with a gold (Au) anode x-ray tube (unfocused and no collimation), as the excitation source, having variable voltage, current and internal aluminum filtration. The details of the SDD are part of the manufacturer's proprietary information and thus are not available. The Delta unit employed three experimental conditions referred to as beams: (1) 40 kVp and automatically chosen current of ~37 μA, (2) 40 kVp, automatically chosen current of ~17 μA and (3) 15 kV with a current of ~5 μA – beam 3 was designed for lighter elements. In any of these three setups, the current could not be manually specified. Internal Al filtration was present with this system as well. Beams 1 and 2 used different filtration. Both units were intended for operation, in either test (stand) or handheld modes, by engaging a trigger, which generated x-rays. The x-ray tube and detector were contained within the analyzer unit, with the beam emerging through a thin kapton window, interacting with the sample and the fluorescence/scatter being detected in a $<90^0$ phantom-detector geometry.

The Alpha 4000S analyzer was available for handheld use in either a fully enclosed waterproof layout or a second arrangement where the spectrum display device could be

detached from the main analyzer unit itself. An iPaq handheld personal data assistant (Hewlett Packard, Palo Alto, California, USA) was provided to record the spectra and set irradiation times. The PDA was designed for touch-screen use, enabling the user to input/vary parameters such as counting time and number of trials. The Delta unit did not allow for a removable PDA and experimental parameters, as well as spectrum acquisition, were controlled with manufacturer-provided PC software. With the delta unit, only a single trial could be set up (1, 2 or 3 beams) for use.

Since the analyzers were developed for use in the field (job-site), they were pre-programmed with the ability to quantify more than twenty elements and the ability for the user to add elements. This capability was built into the analyzer, eliminating the need for expensive computing hardware or software and it operated as a standalone handheld unit intended for use in the field. As mentioned earlier, x-ray fluorescence is a non-destructive technique. This provided a benefit of using the system, in field work, since it eliminated the need to transport delicate soil or rock samples to a laboratory for analysis. The software was designed to display the collected spectrum and perform analysis without the need for calibrating the device on-site. Instead, the calibration was performed empirically using a NIST standard provided with each of the systems. Finally, the electronically cooled detectors avoided transport of bulky LN_2 dewars, facilitating the units' use in handheld mode in a truly portable manner.

For the phantom measurements and dosimetry performed in this work, the analyzer unit was mounted on a specially designed stand, in test mode, with a metallic lid. The purpose of the lid was to prevent leakage radiation from escaping into the surrounding air. A safety light was mounted on the lid and connected to the trigger; the light turned on when the lid was closed. With the safety light on, the analyzer could generate x-rays. This setup was used for both systems.

3.2 Experimental Setup and Procedure:

With both systems in a test (stand) mode arrangement, the phantoms were placed horizontally on the kapton window, and so the source-to-phantom and phantom-to-detector distances were fixed, as seen in figure 3.1.

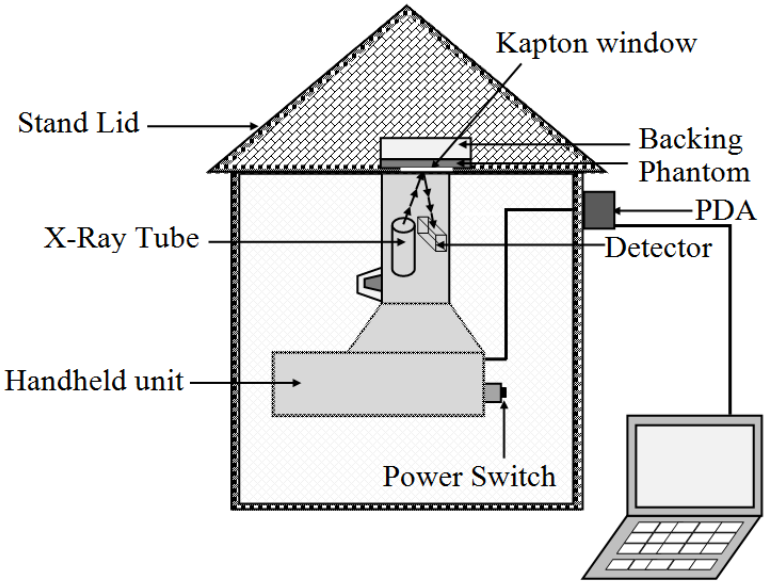

Figure 3.1: Experimental setup used for phantom measurements with portable x-ray analyzer.

Also, since the unit was securely mounted onto a rigid base, the position of the analyzer, relative to the phantom and detector was fixed. In both systems, the analyzer was clamped to the base of the stand and aimed upward.

For the Alpha 4000S unit, the PDA and PDA holder were removed from the handheld component and attached to the mounting stand. For the purposes of this work, the PDA software was only used to set the counting time, number of successive trials to be performed and to record and save the spectra. The PDA was connected to the analyzer unit. This allowed the PDA to control the trigger of the x-ray tube, enabling the user to set irradiation times and save the recorded spectra through the PDA. The PDA was programmed to perform five successive 120-second trials per phantom, with each trial set to automatically start upon the completion of the previous one. At the end of the fifth trial, all five spectra were saved to the PDA and this procedure was then repeated for the other phantoms. This procedure was performed with phantom sets from both McMaster University (2.8±0.1 mm thickness, 50.0±0.1 mm diameter) and Mount Allison University (thickness = 2.6±0.2 mm, diameter of 42.0±0.1 mm). The work on the Alpha 4000S unit was performed at Mount Allison University. The thicker (McMaster University) phantom set was also used with the other (benchtop) systems documented in this work. For each phantom set, the measurements were performed with and without the (1.3±0.1) cm nylon backing in place giving a total of four data sets. The PDA was then synched with a PC, allowing the spectrum data to be transferred over and saved for analysis.

For the Delta model work, the supplied software was used to set the exposure conditions. Beams 1 and 2 were used for 120 second exposures and 5 successive trials per phantom. This work was done with a single set of phantoms (2.8±0.1 mm thickness as

above), with and without the nylon backing in place giving a total of two datasets. The spectra were saved on the host PC's hard-drive and were transferred, using a USB 2.0 thumb drive, for further analysis.

3.3 Beam Shape:

An image of the beam produced by each of the portable x-ray systems was obtained using a piece of gafchromic film. The film was placed on the surface of the kapton window. The resulting beam image, for the Alpha 4000S unit, is shown in figure 3.2.

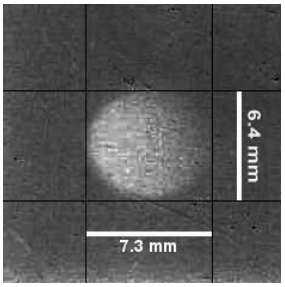

Figure 3.2: Image of beam obtained using gafchromic film with the Innov-X Alpha 4000S system.

As can be seen, the Alpha 4000S beam is nearly circular in shape, with a horizontal diameter of (7.40±0.2) mm, a vertical diameter of (6.44±0.2) mm and the beam area was found to be (37.43±1.54) mm^2. The left part of the beam appears to be the strongest, gradually decreasing along the horizontal diameter, as seen by the strongest darkening at the right hand side of the image, suggesting that the dose delivered by the left side of the beam will be higher. This largely confirms the numeric results from previous dosimetry work on this unit, where a sub-set of chips were found to report higher doses than others (Gherase, Mader, & Fleming, 2010). It should be noted that these are images of the beam at the location of the kapton window and not that of the beam at the sampling (exit) window of the x-ray tube. The beam is somewhat widened as it spreads over the distance between these two positions. This corresponds to the beam image at the location where the phantoms were be placed for phantom measurements. The beam's center is also the center of where the phantoms were placed on the kapton window. The Delta unit's beam is also elliptical with a semi-major axis diameter of (7.0±0.2) mm and a semi-minor axis diameter of (6.0±0.2) mm, giving a beam area of (30.63±1.39) mm^2 (Shehab, Haya: Personal communication). The uniformity of the Delta unit beam image appeared more uniform. Two factors are likely to account for this: a) the angle of the filter in front of the tube would alter the relative uniformity ofthe beam intensity and b) differences in the shape of the lid would produced varying amounts of scatter at the film (no backing used during imaging) surface and change the relative distribution.

3.4 Innov-X Alpha 4000S system:

3.4.1 Spectra and Minimum Detection Limits:

The output file produced by this system lists count-rate as opposed to counts. This had to be converted to counts before the peak-fitting was performed. It is not correct to convert to counts from count rate by multiplying with the acquisition (real) time. Instead, this is done by multiplying with the live time which had to be recorded separately for each run. The approach of choosing live time is correct because live times are smaller than acquisition times, particularly for larger samples that give off more back scatter photons, and produce a larger dead time. The reason for this conversion to number of counts is to use the Poisson statistics for each point, and thus, have a realistic reduced chi-square value (i.e. ~ 1.00, on average). One can fit spectra with count rate on the y-axis, however, the goodness-of-fit expressed by the reduced chi-squared would be much smaller than 1.00 because of the lack of error for each channel value. The conversion gain utilized by the Alpha 4000S pulse processing system was 1980, corresponding to the number of channels.

3.4.1.1 Spectra for thick and thin phantom sets – with and without backing:

By way of example, the spectrum obtained with the 20 ppm phantom in the thicker phantom set (with backing), is shown in figure 3.3.

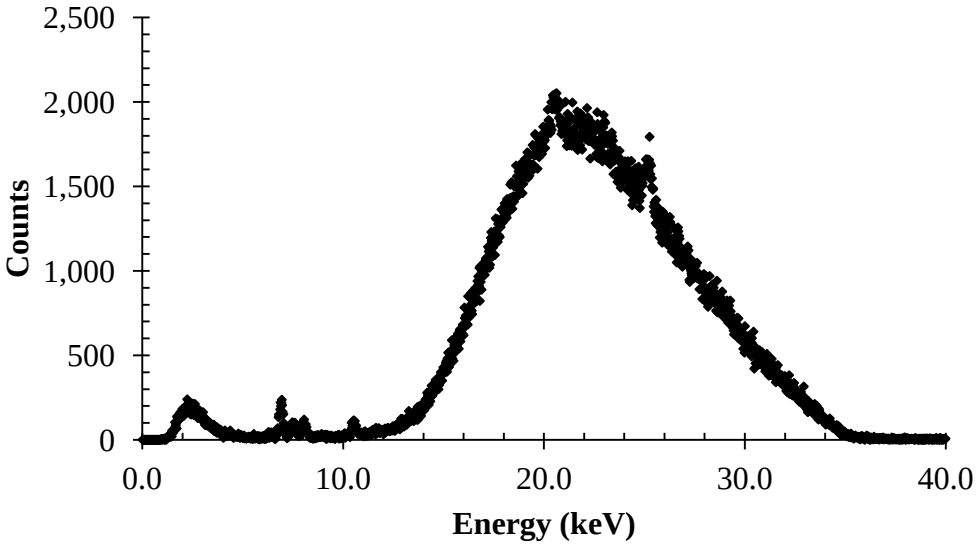

Figure 3.3: Spectrum obtained using 20 ppm As phantom from the 2.8 mm thick phantom set, with nylon backing.

Two separate sections are visible. The higher energy region shows a broad continuum feature with peaks from tin (Sn) in the shielding lid material. This has been noted elsewhere (Fleming & Gherase, 2007; Roy, Gherase, & Fleming, 2010). A view of only the lower energy portion of the spectrum is shown in figure 3.4.

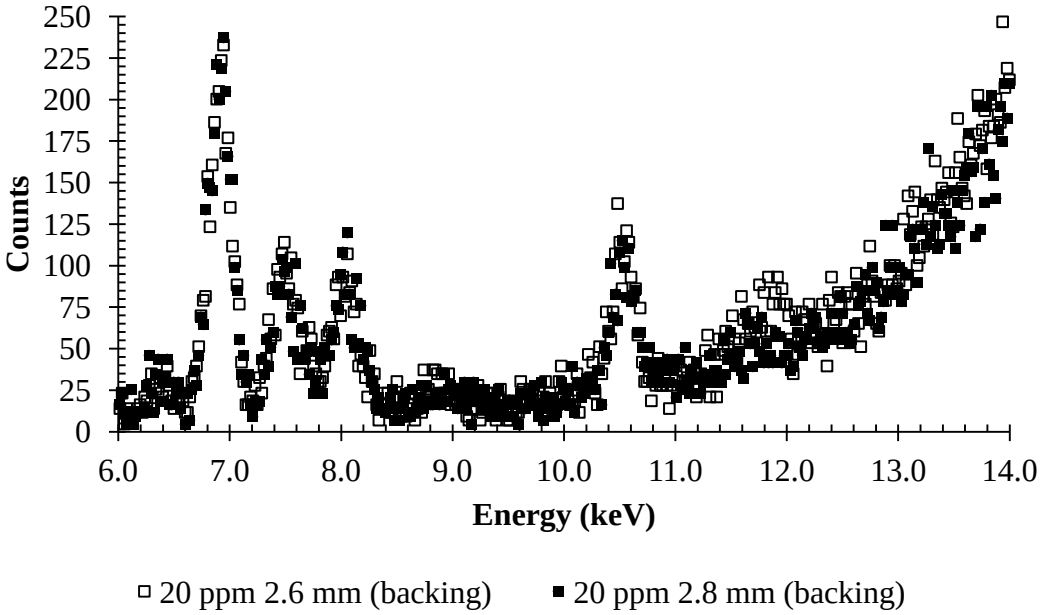

Figure 3.4: Low-energy section of spectra obtained from 2.6 mm thick and 2.8 mm thick 20 ppm As phantoms, both with the nylon backing.

The peaks at 6.93 keV (Co Kα), 7.48 keV (Ni Kα), 8.0 keV (Cu Kα) and 8.9 keV (Cu Kβ) originate in the phantom/resin and have been observed in other work on this system (Fleming & Gherase, 2007; Gherase, Mader, et al., 2010; Gherase, Vallee, & Fleming, 2010). The arsenic Kα and Kβ peaks are also present. When considering the 2.6 mm and 2.8 mm thick spectra, a stronger difference appears in the As Kβ peak than the Kα peak. This is partly due to higher noise that elevates the background under the Kβ, for the thinner set, when compared to the background for the thicker set in this energy region.

In the absence of the nylon backing, the result will be less Compton backscatter which produces a reduction in the observed background and manifests itself as a smaller uncertainty in the fitted peak areas and lower reduced chi-squared value. The spectra obtained using the 20 ppm phantom, from the thicker phantom set, with and without the nylon backing, are shown in figure 3.5.

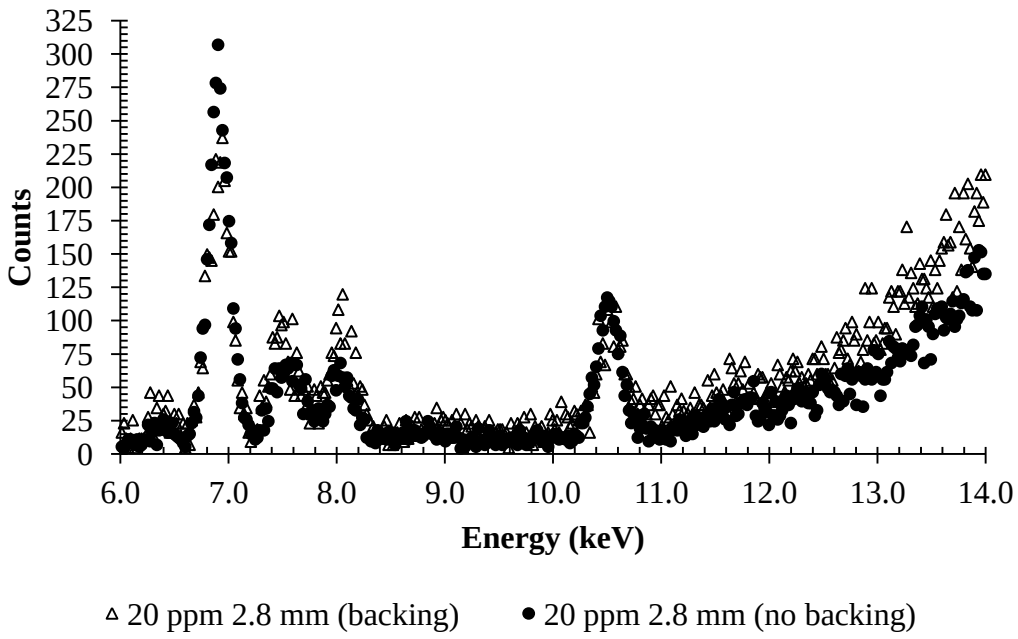

Figure 3.5: Spectra obtained using portable x-ray analyzer with 2.8 mm thick phantom set (20 ppm As), with nylon backing (open triangles) and without nylon backing (closed circles).

A larger background and higher scatter of data points can be seen with the backing in place than without the backing. Of note are the inability to visualize clearly a low-energy tail on the As Kα (observed with or without backing), when the backing is used. Due to the absence of Au in the detector contacts, contrary to that observed with the conventional desktop system used at McMaster University, in the absence of the nylon backing, both the As Kα and Kβ peaks could be fit in the thicker (higher maximum concentration) phantom set with the intention of investigating the As Kα:Kβ ratio. The ratios were found to range from 4.10-7.92 with a mean at 6.29±1.05 (mean±StdDev) with backing. A range of 4.89-6.80 was noted without backing with a mean of 5.82±0.57. These are in agreement with their expected value of ~5.8 at this thickness of resin (comparable to the expected ratio for skin). However, the large range of ratios obtained precludes its use in a combined inverse variance-weighted Kα:Kβ MDL or as a gauge of skin thickness for *in vivo* studies. The 2.6 mm thick phantom set (without backing) had a maximum concentration of 30 ppm where the As Kβ peak was not very visible and so this set was not included in the ratio calculation. Additionally, a comparatively greater scatter of points caused a more pronounced interference with the As Kβ peak. Thus, with backing, a fitting function consisting of a single gaussian on a linear background was used to fit all the spectra acquired with this portable system.

The live times for the various conditions tested are listed in table 3.1.

Table 3.1: List of live times for all setups and phantom types, used to convert cps to counts.

Live Time (s)	2.6 mm with	2.6 mm w/out	2.8 mm with	2.8 mm w/out
Minimum	56.1000	74.5700	57.5300	70.3900
Average	60.5420	75.0480	58.9720	73.8700
StdDev	3.2861	0.6129	1.3468	1.9502
Maximum	65.3500	76.0400	60.5000	74.9500

The two phantom sets' average live times agree with each other, within standard deviation. For a further comparison of the sets of live times, a two-tailed student's t-test was also used. For either thickness, the comparison of live times with versus without backing produced a difference that was statistically significant based on the t-value ($p = 0.05$). By comparison, the difference was not significant ($p = 0.05$) for a comparison between thicknesses, when the live times with or without backing were treated separately. However, as mentioned above, there is a significant difference in live time introduced by including the nylon backing. The live times would indicate that backscatter off the lid does not result in as high a dead time as that coming directly off the nylon backing block placed immediately above the phantom. This results in a longer live time without the backing than with it. As seen in above spectra, the higher dead times (with backing) produce a greater scatter of points than without backing.

3.4.1.2 Minimum Detection Limits:

Sample peak-fitting results are shown in figure 3.6.

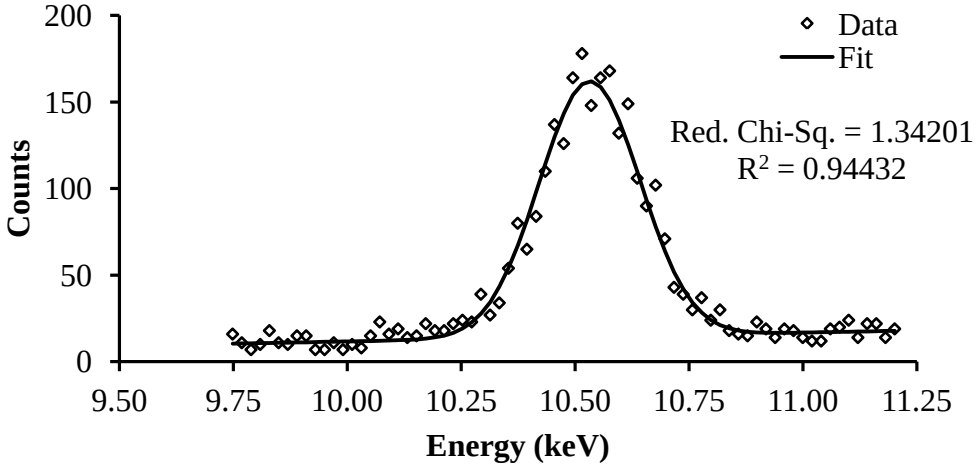

(a)

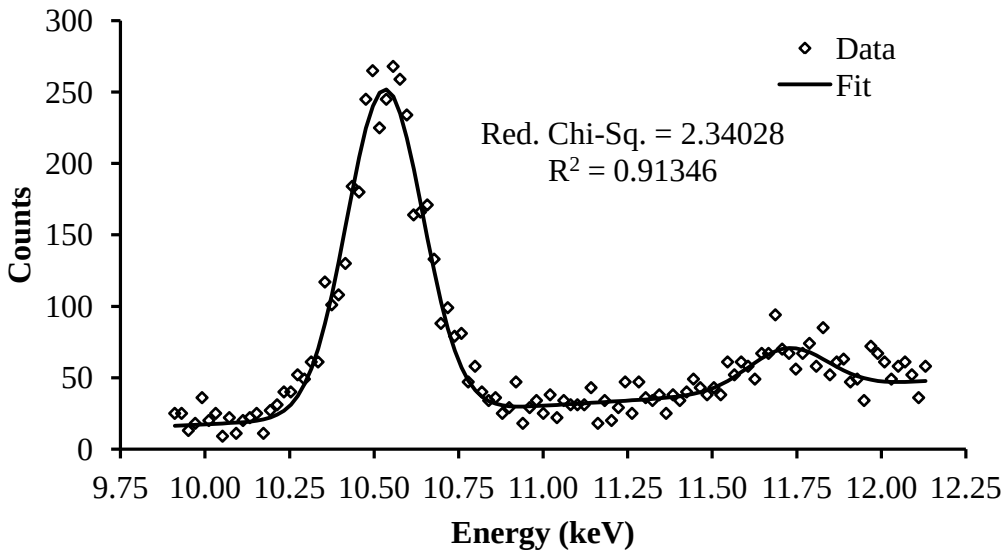

Figure 3.6: Peak-fitting curves compared to raw data for (a) 30 ppm (2.6 mm thick, without backing) and (b) 40 ppm (2.8 mm thick, with backing) phantoms.

(b)

The As Kα FWHM was found to be 261.5±1.7 eV (2.8 mm without backing), 262.6±7.3 eV (2.6 mm without backing), 264.3±7.8 eV (2.8 mm with backing) and 250.7±6.1 eV (2.6 mm with backing). All results are mean±StDev over 5 trials, where the mean is the arithmetic mean. As with the other detection systems, after fitting the 5 high concentration phantom trials separately and determining the mean fitting parameters (ex. As Kα peak centroid and width), these parameters were then entered into the fitting function as fixed parameters rather than fitting variables since peak position and FWHM would not be expected to change with concentration in the absence of systematic drift. The fitting function was then used to fit the full set of phantoms with a reduced number of unknowns and this reduced the uncertainties in the fitted peak areas. If the FWHM were kept free, as a fitting-variable to be optimized, it was found that the fitted Gaussian forced it to a lower value than the mean results listed above. Since the lower concentration phantom would return a lower-than-average FWHM, calculating the mean FWHM over the full dataset (all concentrations) would then give an artificially lower value than if it were held fixed based only on the highest concentration phantom where the counting statistics were superior to any other phantom.

The larger scatter of points, in the presence of the nylon backing, is driving up the reduced chi-squared value for the associated fits. The possible presence of low-intensity peaks on the low-energy side of the As Kα and high energy side of the As Kβ peaks may be the reason for this but are extremely hard to identify clearly, due to such a large scatter on the points. Backscatter off the backing material may further backscatter after passing through the detector material resulting in peaks due to the detector collimator and could

be the cause of these additional peaks. This would appear to indicate that, without the backing, more scatter is noted off the lid. The lid-originating photons would be able to penetrate through the resin phantom and would further complicate the recorded spectra. With the backing lid, photon intensity reaching the resin phantom is reduced because of attenuation in the backing. Separately, regarding thinner and thicker phantoms, primary beam scatter is greater for the thicker phantoms since there is more phantom material to scatter off. Here, the scatter from the lid is reduced compared to the scatter for thinner phantoms. All these factors contribute to differences in the chi-squared under different conditions.

The calibration line parameters and MDLs are reported in table 3.2.

Table 3.2: List of calibration line parameters and first two terms of MDL. Below each sub-table is reduced $\chi 2$ (avg±StdDev) over all phantoms, calibration line intercept and slope.

Conditions	Term 1	Term 2	MDL
2.6 with	0.227 0.251 0.218 0.266 0.252	0.213	1.3448 ± 0.0167
χ^2=2.53±0.78, 27.35±25.29, 54.78±1.40			

Conditions	Term 1	Term 2	MDL
2.6 without	0.038 0.046 0.041 0.036 0.043	0.055	0.6139 ± 0.0046
χ^2 = 1.51±0.37, -26.79±16.85, 71.68±0.94			

Conditions	Term 1	Term 2	MDL
2.8 with	0.239 0.304 0.218 0.266 0.246	0.422	1.6510 ± 0.0160
χ^2 = 2.65±0.43, 57.80±32.04, 49.33±0.56			

Conditions	Term 1	Term 2	MDL
2.8 without	0.090 0.081 0.083 0.087 0.103	0.162	1.0105 ± 0.0063
χ^2 = 1.49±0.33, 42.86±24.75, 61.42±0.43			

As indicated by the longer live times, and resulting smaller degree of scatter, the datasets acquired without backing produce lower MDLs than those with the backing in place. For the most part, the two terms in the definition of MDL are very similar to each other in magnitude and the 2.6 mm detection limits are in the sub-ppm range as was found in previous work (Fleming & Gherase, 2007). However, the differences in live time are of concern when comparing datasets. A fair comparison requires a correction for variations in system dead time.

Correcting for the live time produces slopes of 0.8365±0.0094 and 0.8314±0.0058, for the 2.8 mm thick phantom set, with and without backing respectively, which differ by 0.61%. By comparison, the 2.6 mm thick phantom set produces corrected slopes of 0.904±0.023 and 0.955±0.012 with and without backing, which differ by 5.6%. The live time correction was made by dividing each phantom's fitted peak area by the live time associated with that phantom. Here, the uncertainty in the live time is assumed to be small enough that it can be ignored. The live time correction works quite well. The larger difference for the thinner set of phantoms is likely due to greater differences in the individual phantom thicknesses with this set, than those for the thicker phantom set.

Next, the two thickness were combined together to investigate whether the difference in thickness is significantly affecting the slope of the calibration line. The combined datasets produced a slope and intercept of 61.39±0.50 (slope) and 92.75±19.87 (intercept) without backing (R^2 = 0.99615) and 49.26±0.46 and 87.77±18.22 with backing (R^2 = 0.99498). For the live time corrected calibration lines, the respective slopes and intercepts are 0.84±0.01 and 1.26±0.29 (R^2 = 0.99570) with backing and 0.83±0.01 and 1.10±0.25 (R^2 = 0.99679) without backing. Within uncertainty, the slope of the 2.8 mm and 2.6 mm thickness combined calibration line is in agreement with the slope of the 2.8 mm dataset. This is true with or without the live time correction. These results would appear to indicate that the higher concentrations are having a greater impact on the overall calibration line slope than the lower concentrations. The R^2 values indicate that the difference in thickness, whether the live time correction is applied or not, may not be significant enough to warrant separating the two datasets. It should be noted that the elevation in the intercept, which would be used when determining the concentration of an unknown sample, of the combined 2.6 mm and 2.8 mm calibration line would result in a

difference in calculated concentration since the intercepts (combined 2.8/2.6 mm line versus 2.8 mm line) do not agree, within uncertainty, unless the live time correction is applied. This also requires that the calculation of unknown concentration be performed using count rate, as opposed to counts. The benefit of using the higher concentration phantom set (2.8 mm thickness) is the ability to obtain a better estimate of the fitting parameters such as peak position and width, which can then be fixed for fitting of the lower concentrations.

Normalizing to the coherent or Compton scatter component would serve as another way to account for the difference in dead time, as the scatter component would be proportional to the dead time. As the individual coherent or Compton scatter peaks aren't visible here, the As Kα peaks were normalized to the gross counts under the full continuum contribution (excluding range of energies covering the two Sn peaks) and the results are shown in table 3.3.

Table 3.3: List of continuum-normalized calibration line parameters and first two terms of normalized MDL.

Conditions	Term 1	Term 2	MDL
2.6 with	0.268 0.290 0.253 0.311 0.294	0.220	1.4098 ± 0.0179
b = (2.55±2.61) X 10^{-5}, m = 5.58±0.15 X 10^{-5}			

Conditions	Term 1	Term 2	MDL
2.6 without	0.114 0.138 0.123 0.107 0.130	0.058	0.8426 ± 0.0112
b = (-9.83±3.67) X 10^{-5}, m = 1.52±0.20 X 10^{-4}			

Conditions	Term 1	Term 2	MDL
2.8 with	0.242 0.306 0.216 0.264 0.249	0.419	1.6486 ± 0.0167
b = (5.73±3.29) X 10^{-5}, m = 5.09±0.06 X 10^{-5}			

Conditions	Term 1	Term 2	MDL
2.8 without	0.081 0.073 0.075 0.078 0.092	0.123	0.9029 ± 0.0065
b = (2.54±4.46) X 10^{-5}, m = 1.272±0.008 X 10^{-4}			

Of the four datasets, the sets acquired without backing experience the largest changes in MDL as a result of the normalization, with term 1 experiencing the largest change in one case and term 2 in the other. While the MDLs with backing are essentially unchanged (4.84% higher for 2.6 mm and 0.15% lower for 2.8 mm), the larger uncertainty of the stronger hump observed without backing appears to be the cause of a 37.25% increase (2.6 mm) and 10.65% decrease (2.8 mm) in MDLs without backing. However, due to the complex nature of this region, there are several contributions present – two Sn peaks also with their own tail features. A gross sum over all these includes several peak overlaps that should be treated separately. The greater degree of variability in normalized versus direct MDLs, without the backing, suggests that the influence of the two Sn peaks, which were found to be stronger in this setup, may also be countering the benefits of the normalization procedure and a more accurate method of extracting their areas should be sought.

Previous results with this system reported (un-normalized) MDLs of (0.446±0.006) ppm in 120 seconds (real time), with 8 mm thick resin phantoms ranging from 0-30 ppm (without backing) (Fleming & Gherase, 2007). These were reported using MDL = 2σ/M, where σ represents the uncertainty in area of a blank resin phantom and M is the slope of the calibration line. The current work reports an MDL of (0.40±0.01) ppm using this definition, in 120 seconds (real time) with the same arsenic concentrations. It should be noted that the previous work reported fitted peak areas in counts per second, while the current work reports peak areas in units of counts. The currently reported MDL above was calculated in counts and then divided by system live time, before calculating MDL. The mean free path of arsenic Kα x-rays in resin is 2.74 mm and so a phantom

thickness of 8 mm would produce more arsenic signal, from deeper in the resin phantom, than one of 2.6 mm thickness. However, ~52% of this arsenic signal would be attenuated in the resin alone before reaching the detector. Thus, the benefit of deeper arsenic signal, in a thicker resin phantom, is reduced compared to the phantom thickness used in the current work. Also, a physiologically relevant phantom thickness of ~2.8 mm acts as a superior model of the intended *in vivo* site.

The effectiveness of the normalization procedure, in terms of correcting for differences in phantom thickness, can be evaluated by comparing the slopes and MDLs of the 2.8 mm and 2.6 mm datasets when the with and without backing conditions are treated separately. The normalized slope for the 2.6 mm thick phantom set are 9.57% and 19.41% higher than the 2.8 mm set, with and without backing respectively. By comparison, the corresponding normalized MDLs are 14.49% and 6.68% lower, with and without backing respectively. Given the large number of unknown features included in the normalization procedure, it is not surprising that the normalized MDLs, for the two thicknesses used, do not agree with each other. With so many features contributing, it is hard to establish which of those makes the largest contribution to this discrepancy. The limitation of the normalization is more clearly seen in its inability to correct for the presence of the backing material, as evidenced by the disagreement between the normalized slopes (63.29% and 59.99% for 2.6 mm and 2.8 mm respectively) and MDLs (67.32% and 82.59% for 2.6 mm and 2.8 mm respectively) with backing relative to without backing, indicating the highly variable nature of the scatter off the metallic lid. The normalization is required in order to make a comparison across datasets acquired over different live times (system dead times) and phantom thicknesses. Although it does not fully provide a correction against thickness of phantoms, its effectiveness at correcting for differences in backing is far less effective than the corresponding correction for phantom thickness. Of course, during an *in vivo* trial, the lid would not be in place and the shape of the scatter region would likely be greatly changed potentially allowing for the scatter peaks to be resolved.

3.4.2 Dosimetry:

As with the conventional arsenic system, dosimetry on the Alpha 4000S unit was performed using an array of Li(F) TLD chips. The TLD chips were calibrated by the manufacturer – Global Dosimetry (California, USA) – with appropriate in-house corrections applied based on the incident energy used here, which is estimated to be 20 keV (Gherase, Mader, et al., 2010). The TLD chips were arranged flat on the surface of the kapton window. It was not possible to place the chips over the entire area of the kapton window while simultaneously ensuring that each chip was placed fully on the window. Given the small size of the window, it was decided to place 8 chips over the window in the arrangement shown in figure 3.7.

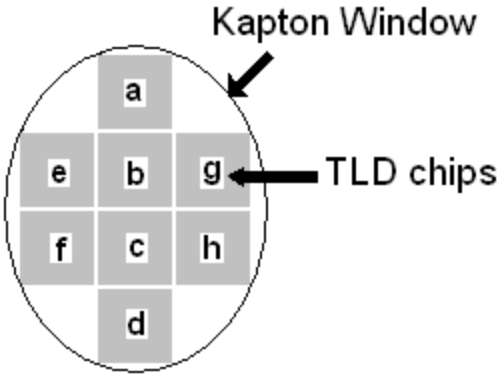

Figure 3.7: Array of TLD chips over the surface of the kapton window of the portable system.

With the chips in this arrangement, the stand lid was closed and the tube was turned on. As with the conventional system, it was decided to irradiate the chips for longer than 2 minutes and then scale down the results, with time. Using the timing controls on the PDA, the chips were first irradiated for 5 minutes and then, a separate set of chips was irradiated for 10 minutes. The exposures were performed separately with and without backing. The position of each chip in the array was recorded, so as to obtain a map of the dose. The TLD chips were then sent to Global Dosimetry Services to extract the absorbed dose readings in Li(F).

The returned absorbed dose, after correction for mass-energy attenuation and time of exposure, is given by

$$D_{tissue} = D_{avg} \frac{\left(\mu_{en}/\rho\right)_{ST}}{\left(\mu_{en}/\rho\right)_{Li(F)}} \frac{T_{MAX}}{T_{TLD}} \quad (1)$$

where D_{tissue} is the corrected absorbed dose, D_{avg} is the averaged absorbed dose over all the chips calculated as D_{avg}±SDOM, T_{TLD} is the time for which the TLD chips were exposed (5 or 10 minutes) and T_{MAX} is the real time in a phantom measurement (120 seconds). The mass attenuation coefficients, $\mu(en)/\rho$, are values for soft tissue, assuming a tissue composition listed in the NIST database (Berger, Coursey, Zucker, & Chang, 2005), and Li(F). These are taken at the average energy of the portable analyzer – 20 keV (Hubbell & Seltzer, 2004). It should be noted that the incident energy chosen here, 20 keV, is an estimate of the average energy. Over a range of ~17.5-30 keV, the ratio of $\mu(en)/\rho$ for soft tissue-Li(F) changes by 1.68%. However, the intensity of energies lower and higher than ~20 keV would be comparatively reduced due to their lower intensity

based on the recorded phantom spectra. If these energies are present in the incident spectrum, they would make a non-zero contribution to the scaling factor and ultimately dose, albeit with a weaker intensity. Note that the K-shell energies of the tube anode are likely heavily attenuated by the inherent aluminum filtration and very low incident energies (< 3 keV) would likely be completely removed. Thus, the primary excitation source would be continuum hump like feature observed in the phantom spectra. Also, the exact energies present might change, when going from phantom measurements to *in vivo*. For example, scatter off the metallic lid would be removed due to attenuation in the hand/palm of the subject, however backscatter would remain and secondary sources of incident radiation would be introduced from other components of the face (exit window) of the portable analyzer. eg. aluminum plate holding kapton window, base plate below this, etc. The average incident energy of ~20 keV is used here since it is the most intense, but a separate investigation of the contribution of the additional dominant incident energies may be warranted if a better representation of a) the incident spectrum from the x-ray tube and b) scattered spectrum of energies (including all secondary sources of excitation) are accounted for.

3.4.2.1 Raw TLD chip readings:

The absorbed dose readings, returned by Global Dosimetry Services, are listed in table 3.4.

Table 3.4: Summary of absorbed dose readings, returned by Global Dosimetry Services, for tld chip irradiations using portable system, showing (a) 5 minute trials with backing, (b) 10 minute trials with backing, (c) 5 minute trials without backing and (d) 10 minute trials without backing.

E (nb, 5) (mGy)		
	5.527	
23.114	48.937	8.532
39.829	75.206	7.048
	13.497	

(a)

E (b, 5) (mGy)		
	4.346	
19.298	40.606	9.784
22.013	52.926	18.730
	9.065	

(b)

E (nb, 10) (mGy)		
	17.790	
101.059	131.456	34.052
104.625	175.257	36.469
	25.813	

(c)

E (b, 10) (mGy)		
	14.530	
41.704	60.635	25.058
56.140	103.816	32.559
	17.896	

(d)

The highest dose is delivered by the left hemisphere of the beam, as predicted by the image of the beam, with the single chip on the top and bottom most rows mainly picking up scatter since only a smaller part of them lies directly in the path of the beam. Higher dose readings were observed without backing than with backing. The absence of the nylon backing allows for x-rays passing through the chips to scatter off the stand lid and be absorbed by the chips, thus delivering a higher dose than if this contribution was to be stopped by the nylon block. This was also discussed when examining the spectra and system calibration work. When the backing was in place, a larger fraction of photons will Compton backscatter off the backing than what will backscatter off the lid. Compton backscatter off the backing is then weaker than scatter coming from the lid due to the high-Z content of the lid material (tin). Additionally, since the chips did not entirely cover the kapton window, some of the incident x-rays would strike the lid un-attenuated and result in further scattering and deposition of a dose into the chips. When the readings of the 10 minute runs (tables b and d) are examined, all the TLD chip readings are higher without backing than with backing, indicating that the scatter contribution off the lid is more observable over longer times of irradiation. Chips that were not fully in the path of the beam would have picked up dose primarily from the scatter. In the absence of backing, the raw (absorbed) dose delivered in 10 minutes is more than twice the dose delivered in 5 minutes. Since dose would be expected to increase linearly with time, this result is unexpected. This difference in 5 and 10 minute absorbed doses is reduced when backing is used. Higher scatter, without backing, has been noted in other dosimetry work done on this system with smaller TLD chips (Gherase, Mader, et al., 2010). Variability in scatter results in non-linear time scaling in equivalent and effective dose, when going from 10 minutes to 5 minutes. This can be attributed to more scatter being produced by the lid than the by the nylon backing (lid has higher Z materials) thus delivering a higher dose to the chips over 10 minutes than over a 5 minute exposure. The ratio of dose delivered with no backing to that with backing, in 10 minutes, is greater than the ratio of

dose delivered with no backing to backing in 5 minutes. The increase is due to enhanced scatter from the higher Z material in the lid (Sn) than that in the backing (nylon). The ratio of no backing in 10 minutes to no backing in 5 minutes is also greater than the ratio using the dose readings collected with backing. A larger amount of lid-originating scatter is produced in the longer exposure time than in the shorter one due to the higher Z number of the lid material. The difficulty in establishing exact trends with these readings is due to the change in the distribution of dose delivered under all four tested conditions. The main reason for this is likely to be small differences in the positioning of the array of TLDs, within all four trials. This was also postulated in the above mentioned work, when comparing the doses with and without a polyethylene holder in place.

3.4.2.2 Equivalent and Effective Dose:

The raw readings correspond to the absorbed dose over a period of 5 or 10 minutes. Since the MDL exposures lasted only 2 minutes (120 seconds), corrections for time need to be made here in order to obtain a meaningful absorbed dose. Since the x-ray tube's voltage and current are fixed, correction factors for these are not required. Correcting for exposure times gives absorbed dose readings corresponding to 2 minute exposures. The equivalent dose is thus given by

$$H = D_{tissue}\omega_R \tag{2}$$

where ω_R is the radiation weighting factor of 1 for photons. With this correction made, the conversion to equivalent (skin) dose can be performed. The skin dose is of greatest significance when determining whether or not the system produces exposures that are within ICRP limits, since the beam spot size is much smaller than that produced with the conventional desktop system at a larger distance away from the source. It may be that a large dose is concentrated over a small site on the skin and this could result in localized radiation-induced skin damage. The chips covered an area of 1.2288 cm^2, with a length of 1.28 cm and a width of 0.96 cm, in comparison to the ICRP dose which is quoted for a 1 X 1 cm^2 area of skin. The ratio of mass energy absorption coefficient of tissue to LiF was applied to the time-scaled absorbed dose readings. The 2-minute scaled equivalent doses, determined from 5 and 10 minute exposures, are (9.38±2.51) mSv and (9.35±2.21) mSv respectively with backing and (11.77±3.75) mSv and (16.63±4.36) mSv respectively (mean±SDOM) without backing. The large values for SDOM are due to the average over the entire beam, which is necessary to make up the area suitable for comparison to the ICRP limit. These results are on the same order of magnitude to the equivalent dose of 13.2 mSv found in other work (Gherase, Mader, et al., 2010) and to the ICRP equivalent dose limit of 50 mSv for members of the public per year. The argument for choosing ideal exposure conditions, in terms of dosimetry and radiation safety, must take the following two points into account: (a) although less than the regulated limit, the doses delivered are all of the same order-of-magnitude as it and so a significant increase in exposure time would produce a higher equivalent dose; (b) countering this is the fact that *in vivo* work with such a system would not require use of the unit in test (stand) mode but instead in handheld mode where the metallic shielding lid is not required, thereby

reducing scatter and driving the dose down. Speculating as to which of these factors will dominate may be misleading and cannot be verified unless the analyzer is employed in an actual *in vivo* situation.i.e. without the shielding lid. Future work may look into construction of a hand, rather than skin, phantom with (cylindrical) bone encased by overlying soft-tissue to further investigate this.

Finally, the effective dose is determined using

$$E = D_{tissue} \frac{V_{IRR}}{V_T} \omega_R \omega_T \quad (3)$$

where A_{IRR} is the beam size, $V_{IRR} = A_{IRR}$ * ICRP skin thickness (ICRP skin thickness = 0.2 cm), A_T is the total ICRP skin surface area of 18000 cm^2 ICRP 23). This gives V_T = 3600 cm^3. The radiation weighting factor is 1 for photons and the tissue weighting factor, given by ω_T, is 0.01 for soft tissue. This accounts for the fact that the intended use of this system for *in vivo* trials would not result in a whole body dose. The equivalent dose is scaled by the tissue weighting factor and the ratio of exposed (area covered by the chips of 0.96 cm X 1.28 cm X thickness) to ICRP whole body skin volume (18000 cm^2 X thickness). The skin thickness was chosen as 0.2 cm ICRP 60). Using the 5 and 10 minute exposures, the effective dose delivered was found to be (6.41±1.71) X 10^{-3} μSv and (6.38±1.51) X 10^{-3} μSv with backing and (8.03±2.56) X 10^{-3} μSv and (11.35±2.97) X 10^{-3} μSv without backing respectively. These compare favorably with the effective dose of 6.1 X 10^{-3} μSv found in the previous dosimetry work on the system, which was done with a more advanced backing assembly placed behind the chips (Gherase, Mader, et al., 2010). By comparison, the ICRP limit for annual effective dose is 1 mSv for members of the public. It must be noted here that the beam area (0.36525 cm^2) is smaller than the area chosen for determining the effective dose (1.2288 cm^2). However, choosing only the chips lying inside the primary beam (approximated by positions b, c, e and f which cover an area of 0.64 X 0.64 cm^2 very close to the primary beam area and correspond to approximately where the beam would be centered) results in lower effective doses of (3.26±2.03) X 10^{-3} μSv and (3.17±1.94) X 10^{-3} μSv with backing and (4.52±2.81) X 10^{-3} μSv and (6.19±3.67) X 10^{-3} μSv without backing, for the 5 and 10 minute exposures respectively. Equivalent dose starts to become a concern as the area chosen is reduced in size. The effective dose results are on the same order of magnitude as that found when the larger area is chosen. This ignores the non-zero dose contribution by the other 4 chips and the contribution to the irradiated area that they would present. As a more representative *in vivo* area, the full set of chips, and the larger area that they cover, is considered in evaluating the radiation safety of this system. If one takes only the 2 central chips, then the respective equivalent doses are (19±20) mSv, (17±18) mSv, (26±27) mSv and (33±33) mSv, where the higher doses are delivered with backing. Although the latter two exceed ICRP limits, the area covered is (0.32 X 0.64 = 0.20) cm^2, which is considerably smaller than the 1 cm^2 used by ICRP and a physical meaning is

harder for the highly localized dose obtained with just the two central chips. At the other extreme, if a sufficiently large array of chips were used, it would be expected that dose would fall off in an approximately Gaussian-like shape with the peak dose delivered in the near vicinity of the kapton window. A strong drop-off is already noted in the results here and this would be expected to continue, rapidly approaching zero extra dose outside the main beam (~1 X 1 array of chips). The dose from the scattered radiation would make a non-zero contribution to an area outside this array, however such an area would be removed *in vivo* since the analyzer would be directed at the subject without using the lid. Thus the ~ 1 X 1 array of chips would be sufficient to capture the dose due to the primary (incident) beam. If the scaling factor for exposed area is not applied, then the 5 and 10-minute effective doses are (93.8±25.1) μSv and (93.5±22.1) μSv with backing and (117.7±37.5) μSv and (166.3±43.6) μSv without backing respectively. These whole body and localized effective doses are within the ICRP limit for members of the general population.

The scaled effective dose is several orders of magnitude lower than the ICRP limit and suggests that longer exposure times are afforded by this system, which would improve counting statistics. This effective dose is not an absolute indication of radiation exposure since acquisition times would be varied empirically during an *in vivo* trial based on expected arsenic concentration in the subject's skin. The unscaled (whole body) effective doses are at least one order of magnitude below the ICRP limit. The reason for evaluating the dosimetry of this system was to mitigate the risk of over-exposure to radiation during a typical *in vivo* trial. This appears to be borne out in the dosimetry results since both the equivalent and effective doses are smaller than the ICRP recommended limits.

3.5 Innov-X Delta Premium System:

3.5.1 Spectra and Minimum Detection Limits:

The Delta Premium's output file listed counts as opposed to count rate. As a result, the user does not need to determine the live time in a separate run since the live time for each spectrum is recorded in the header data of the output file. Live time is not required for spectral analysis with this system. The conversion gain used by the pulse processing electronics was 2048.

3.5.1.1 Spectra for thin and thick phantom sets – with and without backing:

The spectra obtained using the 60 ppm phantom, from the 2.8 mm thick phantom set, with and without the nylon backing, are shown in figure 3.8.

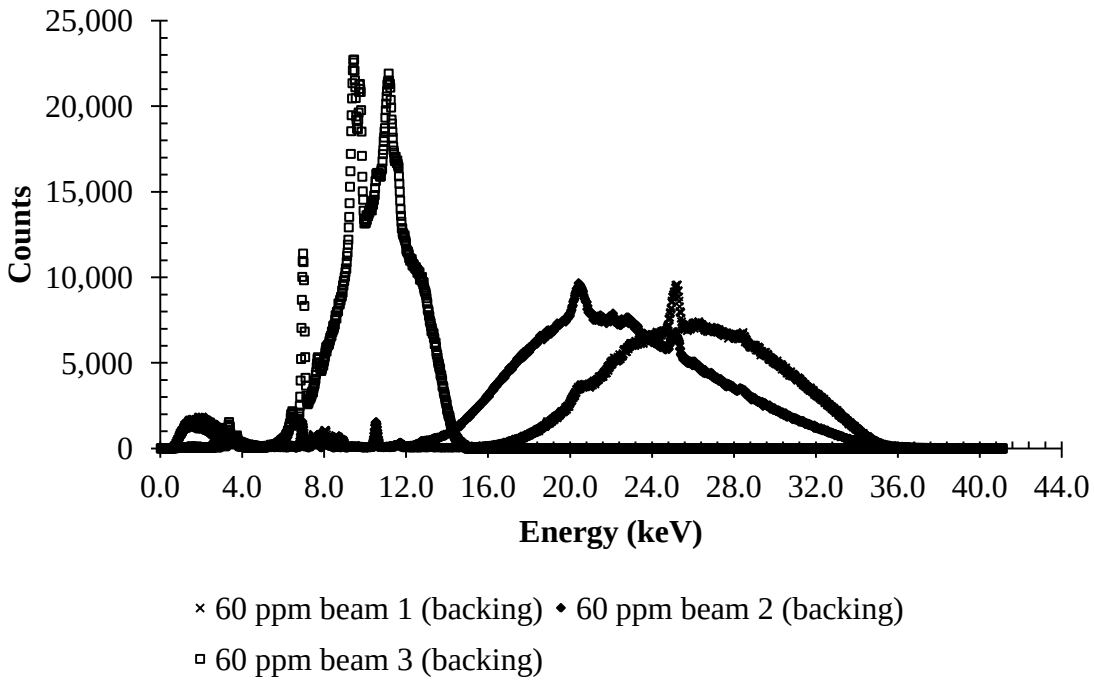

Figure 3.8: Spectra obtained using portable x-ray analyzer with the 2.8 mm thick phantom set (60 ppm As), with nylon backing, for all three beams.

The same shape of the scatter region of the spectrum is noted here as with the Alpha 4000S unit. Beam 3 was not used in analysis since the As peaks are consumed by the continuum component of the spectrum. The change in energy between beams 1 and 2 was likely due to the aforementioned pre-determined change in the internal filtration. An enlarged view of the lower energy region, for beams 1 and 2, is shown in figure 3.9.

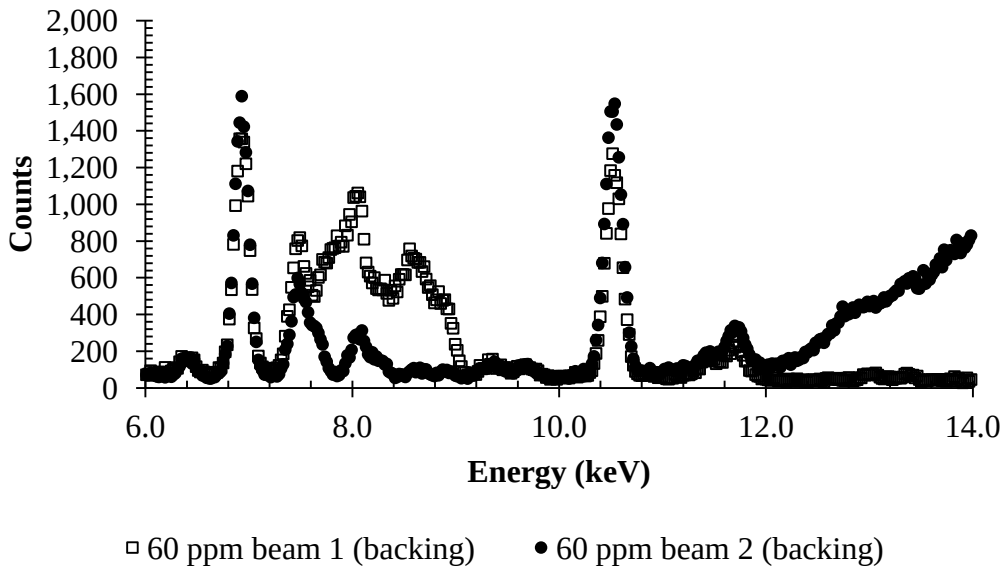

Figure 3.9: Lower energy region of 60 ppm As phantom, with nylon backing, using 2.8 mm thick phantom set. Spectra are shown for beams 1 and 2.

Peaks due to Co, Ni and Cu are once again seen, as was the case with the Alpha 4000S unit. Additional peaks at around 8 keV, for beam 3, are likely due to the filter's characteristic x-rays. The hump feature is shifted down in energy resulting in a higher background under the As Kβ peak for beam 2. The effect of the backing on the spectra is shown in figure 3.10.

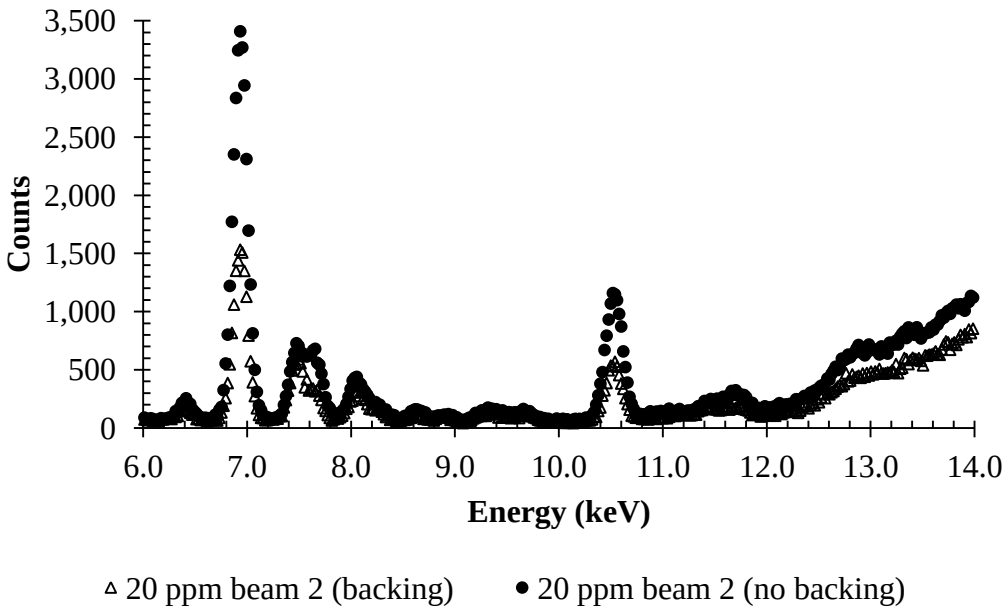

Figure 3.10: Lower energy region of spectra for beam 2, showing effect of backing on As peaks.

The absence of backing results in a large increase in total count rate with this unit, like that observed with the Alpha 4000S analyzer. The same is observed with beam 1. The live times (seconds), voltage (kVp) and current (μA) corresponding to each of the sets of exposures, sheds further light on this, and are listed in table 3.5.

Table 3.5: List of (a) live time and x-ray tube (b) current (variable) and (c) voltage (fixed) for all datasets.

Live Time (s)	With, Bm 1	With, Bm 2	Without, Bm 1	Without, Bm 2
Minimum	40.0141	32.2486	86.2698	76.9572
Average	40.8273	32.8197	87.2664	78.3864
StdDev	0.4648	0.3092	0.8308	1.1095
Maximum	41.7949	33.5738	88.4815	79.9206

(a)

Current (μA)	With, Bm 1	With, Bm 2	Without, Bm 1	Without, Bm 2
Minimum	35.9140	16.7742	72.4731	40.8602
Average	36.7484	17.2817	72.9032	40.8781
StdDev	0.4781	0.2140	0.2197	0.0878
Maximum	37.6344	17.4194	73.1183	41.2903

(b)

Voltage (kVp)	With, Bm 1	With, Bm 2	Without, Bm 1	Without, Bm 2
Minimum	40.0000	40.0000	39.9570	40.0000
Average	40.0378	40.0396	40.0340	40.0323
StdDev	0.0258	0.0119	0.0310	0.0229
Maximum	40.0860	40.0430	40.0860	40.0860

(c)

As with the Alpha 4000S unit, the live times with the backing were shorter than without, due to weaker backscatter off the lid (without backing) at a greater distance away from the window and phantom than when the backing is placed immediately on top of the resin phantom. For beams 1 and 2, the voltage is held fixed but the current and live time are both changed automatically by internal software programmed by the manufacturer thus eliminating the possibility of user control of those two settings. It can be postulated that the higher current is utilized when the dead time is found to be lower (longer live time). Without knowledge of the manufacturer's programming logic, further speculation may be misleading.

The approach to peak-fitting was the same as that listed for the Alpha 4000S unit – all 5 trials of the 100 ppm phantom (highest concentration) were fit and the average of all parameters were fixed, entered into the fitting function and then used to fit the full set of the concentrations. For beam 1, a single Gaussian was used to fit the As Kα. For beam 2, Gaussians were used to represent both As peaks for beam 2, due to the improved intensity of the As K$\beta_{1,3}$ which made it easier to fit, and one Au Lβ peak (11.478 keV, corresponding to a weighted average of the Au Lβ_1 and Au L$b_{2,15}$). A tail was used on the As Kα, but not on the As Kβ. This is because of the difficulty in modeling its parameters due to strong degree of overlap with the Au peak of its low energy side. A linear background was chosen for both beams. Sample fits are shown in figure 3.11.

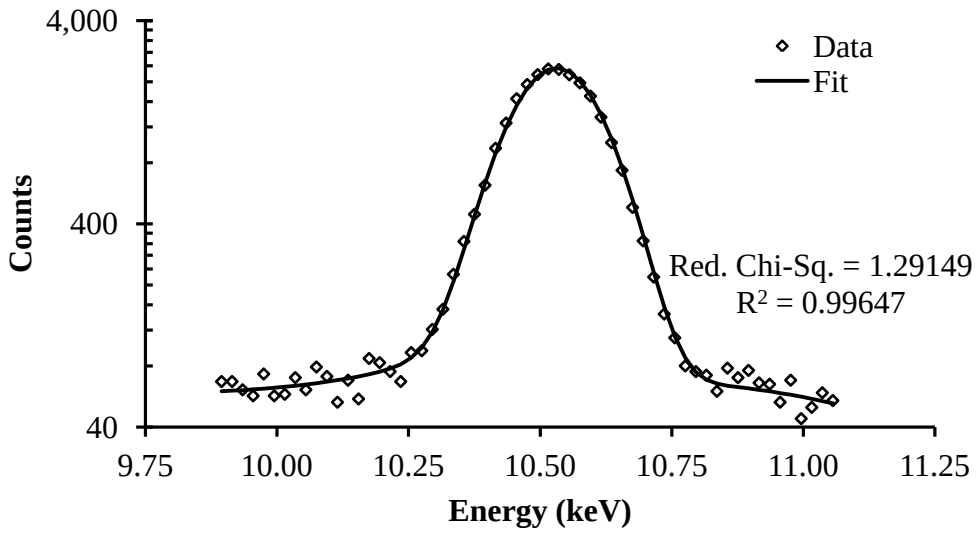

(a)

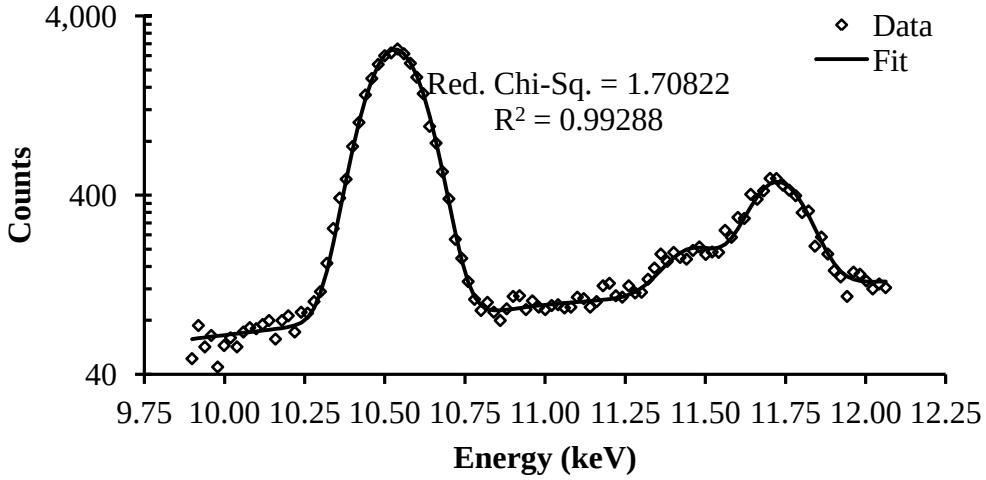

Figure 3.11: Fit shown for (a) 60 ppm phantom without backing (beam 1) and (b) 100 ppm phantom with backing (beam 2).

(b)

A small feature, likely the Au $L\beta_5$ (11.916 keV) on the high energy side of the As $K\beta_{1,3}$ (11.723 keV) and low energy side of the Au Lβ peak were hard to hard to identify and so were excluded in the fitting routine for beam 2. The As $K\beta_2$, at 11.864 keV, was not visible and so was excluded. With strong enough battery life, a long count of several hours would reveal such features in the blank and highest concentration phantoms, thereby enabling their inclusion in the fitting function. This would improve the reduced

chi-squared for beam 2. A longer count would also improve the modeling of the tail on the As Kα and would allow for a tail to be included with the As Kβ which wasn't done here. The As Kα FWHM was found to be 190.3±1.9 (with backing beam 1), 187.9±1.1 (with backing beam 2), 189.4±0.9 (without backing beam 1) and 188.8±2.3 (without backing beam 2). Finally, the As Kα:Kβ ratios (beam 2) were found to be 6.77±0.36 with backing and 6.94±0.32 without backing. These are elevated in comparison to their expected value of ~5.8 at this thickness of resin (comparable expected ratio for skin) and compared to those obtained with the Alpha 4000S unit. All results are mean±StDev over 5 trials, where the mean is the arithmetic mean. The higher-than-expected ratios suggest that the As Kβ may be underestimated, with the interference caused by the Au Lβ being the likely source of this. It should be noted that the As Kα:Kβ ratio was not corrected for absorption differences, at the two As energies, since the thickness of the Si wafer is not made available to the user. Difficulty in modeling additional features (mentioned above) would at least partially contribute to the discrepancy in this ratio. However, the main concern is the presence of the Au Lβ peak since this precludes inclusion of a tail on the As Kβ peak. The benefits of the SDD's superior resolution capabilities are clearly revealed, however this also reveals features not clearly seen with other detectors such as a Si(Li) detector or PiN diode. These features must be accurately included in order to maximize the benefit of its use. Without doing so, the As Kα:Kβ ratios may not be fully reliable. A more detailed discussion regarding this ratio is presented in the next chapter, where Au interference is absent and the intensity of the As Kβ is strong enough to include a tail feature.

3.5.1.2 Minimum Detection Limits:

As with the Alpha 4000S system, 5 trials were performed for each of five phantoms and so a single calibration line, comprising all 25 points, was produced. The calibration line parameters and MDLs are reported in table 3.6.

Table 3.6: MDL and phantom calibration line results for all datasets.

Conditions	Term 1	Term 2	MDL
With, Bm1	3.347E-02 3.355E-02 3.365E-02 3.599E-02 3.358E-02	1.911E-02	0.4615 ± 0.0020
χ^2 = 1.13±0.19, 65.26±25.20, 182.30±0.44			

Conditions	Term 1	Term 2	MDL
With, Bm2	1.929E-02 1.923E-02	5.853E-02	0.5577 ± 0.0009

	1.780E-02		
	1.923E-02		
	1.880E-02		
χ^2 = 1.66±0.33, -26.63±58.66, 242.48±1.02			

Conditions	Term 1	Term 2	MDL
	7.993E-03		
	8.028E-03		
Wout, Bm1	7.849E-03	2.790E-02	0.3796 ± 0.0001
	8.078E-03		
	7.845E-03		
χ^2 = 1.16±0.25, 113.54±60.54, 362.46±1.05			

Conditions	Term 1	Term 2	MDL
	4.780E-03		
	4.863E-03		
Wout, Bm2	4.860E-03	2.602E-02	0.3503 ± 0.0003
	4.490E-03		
	4.597E-03		
χ^2 = 1.94±0.30, -160.36±88.57, 549.13±1.54			

Although terms 3 and 4 were used in the calculation of MDL, they were several orders of magnitude weaker and so have not been reported as their contribution to the MDL was negligible. The inclusion of the As Kβ peak in the fitting routine is clearly producing a higher reduced chi-squared value (beam 2). As mentioned earlier, this may be addressed best by a series of long counts to bring out minor features in the spectrum that do not appear clearly in two minute acquisitions. Of note are that the MDLs without backing are clearly better than those with backing, as predicted by the longer live times and higher current readings. The calibration line slopes would thus not be an indicator of MDL since they correspond to varying live times. A way to correct for the differences in dead time and tube output (voltage/current) would again be required, as was the case with the Alpha 4000S unit. The continuum normalized results are shown in table 3.7.

Table 3.7: MDL and phantom calibration line results for all datasets. Terms 3 and 4, in the definition of MDL, are used in the calculation of MDL but not shown since they were several orders of magnitude weaker than terms 1 and 2.

Conditions	Term 1	Term 2	MDL
With, Bm1	3.375E-02 3.374E-02 3.369E-02 3.648E-02 3.345E-02	2.051E-02	0.4683 ± 0.0023
$b = (2.04\pm0.85) \times 10^{-5}$, $m = (5.92\pm0.01) \times 10^{-5}$			

Conditions	Term 1	Term 2	MDL
With, Bm2	1.968E-02 1.934E-02 1.795E-02 1.955E-02 1.911E-02	6.174E-02	0.5700 ± 0.0010
$b = (-0.78\pm1.53) \times 10^{-5}$, $m = (6.15\pm0.03) \times 10^{-5}$			

Conditions	Term 1	Term 2	MDL
Wout, Bm1	7.970E-03 8.023E-03 7.837E-03 8.047E-03 7.821E-03	9.513E-02	0.6504 ± 0.0002
$b = (1.45\pm0.39) \times 10^{-4}$, $m = (1.288\pm0.007) \times 10^{-4}$			

Conditions	Term 1	Term 2	MDL
Wout, Bm2	4.742E-03 4.834E-03 4.849E-03 4.475E-03 4.571E-03	5.576E-02	0.4952 ± 0.0002
$b = (4.82\pm3.14) \times 10^{-5}$, $m = (1.328\pm0.005) \times 10^{-4}$			

When each beam is treated separately, the normalized calibration line slopes (with or without backing) are on the same order of magnitude as the corresponding normalized

slopes obtained with the two 2.8 mm datasets using the Alpha 4000S unit. As with the Alpha 4000S unit, the MDLs without backing are subjected to larger changes as a result of the continuum normalization. The variation in the intercept (term 2), has grown substantially in the normalized compared to the direct results and is the reason for the elevated MDLs. The normalization is nearly correcting for the differences in the beams (live time and current) as evidenced by the near agreement of the two sets of slopes when considering beam 1 relative to beam 2 (3.69% and 2.99%, with and without backing respectively). The normalized detection limit changes (17.8% and 31.3%), as found with the attempted normalization correction for phantom thickness with the Alpha 4000S unit, are larger than the associated change in slopes. As seen with the Alpha 4000S system, normalization cannot correct for the presence of the backing behind the resin phantom. The changes in slope, with backing relative to without backing, are 54.0% and 53.7% for beams 1 and 2 respectively and their associated changes in MDLs are 28.0% and 15.1%. Numerous features are again present in the continuum region of the spectrum and these cannot be separated. The summed counts, covering all these features, may not be fully representative of a single variable that is proportional to source strength and, subsequently, system dead time. Thus, the normalization would appear to be more reliable when correcting for differences in the two beams' operating conditions when the backing is used as this minimizes the influence of the scatter off the shielding lid and produces a smaller difference in MDLs as opposed to that noted without backing.

3.5.2 InnovX Delta system dosimetry:

The chips were arranged in a 3 X 3 array, as was the case with the InnovX Alpha 4000S system. Gafchromic film was used to image the beam. For this, three successive 10-minute (real time) exposures were performed for beam 1 and beam 2 (total 6 exposures) in order to produce a clear image of the beam and the chips were positioned based on the recorded beam image obtained from the film. Based on the image position on the film, 4 strips of tape were attached to the flat mounting surface of the analyzer stand – the strips were aligned with the position of the (circular) beam circumference. Next, the chips were placed on the kapton window using the strips of tape as a guide for positioning. With the chips in position, the film was removed and the nylon backing was placed behind the chips. Finally, a single TLD exposure was performed for 10 minutes for beam 1. The chips were removed from the kapton window and placed in a light-tight bag. A second 3 X 3 array of chips was then placed on the kapton window and a 10 minute exposure was performed for beam 2. Both sets of chips were then shipped for reading the absorbed doses.

TLD exposures were performed for a longer period of time (10 minutes real time for beam 1 at 37 μA and 10 minutes real time for beam 2 at 17 μA) than phantom measurements (2 minutes each for total of 4 minutes). The absorbed dose delivered by either beam, during 2 minute exposures, was found using

$$D_{AVG} = D_{Bm1,2}\left(\frac{I_{Bm\#,MDL}}{I_{Bm,TLD}}\right)\left(\frac{T_{Bm\#,MDL}}{T_{Bm,TLD}}\right) \quad (4)$$

where $I_{Bm\#,MDL}$ is the current during beam 1 (37 μA) or 2 (17 μA) respectively delivered for $T_{Bm\#,MDL}$ (2 min for beam 1 and beam 2) which is the time over which the MDL measurements was performed, $I_{Bm,TLD}$ is the average current delivered by the TLD exposures during time $T_{Bm,TLD}$ (= 10 min for beam 1 and beam 2).

3.5.2.1 Absorbed Dose Distribution:

The energies used for beams 1 and 2 were 20 keV and 25 keV respectively as these were estimated as the mean energy of the continuum feature in the recorded scattered spectrum. The respective Li(F) and soft-tissue mass-energy absorption coefficients were 0.649 and 0.507 cm^2/g for beam 1 and 0.416 and 0.36395 cm^2/g for beam 2. It was found that the three chips in the top row (0.32 cm X 0.96 cm) produced an order of magnitude weaker readings than those in the other two rows (0.64 cm X 0.96 cm). The incident beam was likely more closely centered around the bottom two rows, due to small differences in positioning the TLD chips in the beam compared to what was suggested by the image of the beam in the film. This is shown, as well as the gafchromic film image of the x-ray beam at the kapton window, in figure 3.12.

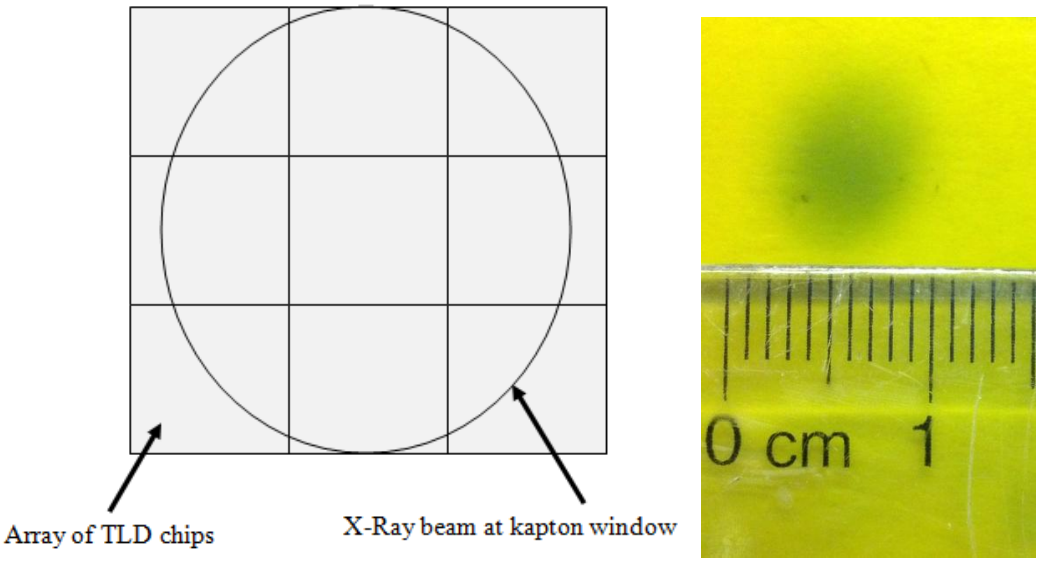

Figure 3.12: (Left) Layout of chips used and positioning of chips relative to center of incident x-ray beam, and (right) image of beam using gafchromic EBT2 film. The top row of the array would occupy the blurry part of the beam (top in right image).

Excluding the top row of chips would produce a higher average absorbed dose. If this is used in subsequent calculations of effective and equivalent dose, then each of those two quantities will give a higher delivered dose. Thus, exclusion of the top row of chips would represent a conservative estimation of dose. However, removing the chips in that

row from the calculation would produce an area of <1cm^2 and a comparison to the ICRP standard for equivalent dose, which requires 1 cm^2 area, may not be as meaningful as if this row were included (0.92 cm^2). Thus all chip readings were retained in this and subsequent calculations. Nonetheless, for comparison, the calculated effective and equivalent doses are compared to the results if this exclusion is made.

3.5.2.2 Equivalent and Effective doses delivered:

The calculation of effective (whole body and scaled versions) and equivalent dose follows those shown for the InnovX Alpha handheld unit. The equivalent doses were (13.2±3.5) mSv (average± SDOM) and (19.0±9.0) mSv (average±SDOM), for beams 1 and 2 respectively. A large spread is observed in the chip readings, with the top most row of the array making an order of magnitude smaller contribution than the other rows. Thus, the standard deviation (StdDev) and SDOM (StdDev/$n^{1/2}$) are higher when this row is included than if it is excluded (discussed later). The equivalent dose readings are within the ICRP limit of 50 mSv and are similar to those reported elsewhere with the Alpha 4000S unit (Gherase, Mader, & Fleming, 2010). The scaled effective doses were 6.8±1.8 X 10^{-3} μSv and 9.8±4.6 X 10^{-3} μSv for beams 1 and 2 respectively. These are well within the ICRP limit. The whole body effective doses were (132±35) and (190±90) μSv, for beam 1 and beam 2, respectively. These are an order of magnitude below the limit to members of the public.

Excluding the weaker part of the array (row 1), the area covered by the chips is 0.64 X 0.96 cm^2. Here, the equivalent dose was (19.0±3.0) mSv for beam 1 and (27.6±12.3) mSv for beam 2 in 120 seconds (real time). These are roughly 1.5 times larger than the effective dose delivered if the top row is included in the calculation. The corresponding localized effective doses are (9.7±1.5) X 10^{-3} μSv for beam 1 and (14.1±6.3) X 10^{-3} μSv for beam 2. The whole body effective doses are (190±30) μSv and (276±123) μSv for beam 1 and beam 2 respectively. With either set of results, all doses delivered are still within the ICRP limit of 50 mSv. TLD exposures were performed for a longer period of time (10 minutes) than phantom measurements (2 minutes). The backscatter dose contribution is also present. With these two scatter components (backscatter and shielding lid), scaling down the TLD results linearly in time, from 600 seconds to 120 seconds, may represent an under-estimation of the true correction required to account for the scatter (lid) and backscatter (nylon).

3.5.2.3 Dosimetry comparison to InnovX 4000S unit:

The dose delivered with this system is higher than that produced by the Alpha 4000S analyzer setup. The equivalent dose, including the full 3 X 3 array, is approximately twice as large as that delivered by the Alpha 4000S unit – (9.35±2.2) mSv taken from the 10 minute exposure with the Alpha 4000S unit vs (13.2±3.5) mSv for beam 1 and (19.0±9.0) mSv for beam 2 with the Delta handheld system. The effective dose is at least ~1.5 times larger – (6.38±1.51) X 10^{-3} μSv (Alpha 4000S) vs 6.8±1.8 X 10^{-3} μSv (beam 1) and 9.8±4.6 X 10^{-3} μSv (beam 2). The whole body effective doses were (94±22) μSv (Alpha 4000S) vs (132±35) and (190±90) μSv for beams 1 and 2 – a

factor of ~1.5 or 3 lower for the Alpha 4000S unit. A thinner kapton window may permit a higher incident flux and offer a partial explanation of the elevated dose readings. Differences in the exact composition of the shielding material would also contribute – higher Z materials, if present, would produce a greater amount of scatter here. Also, backscatter from the backing material will contribute to this and may be different based on the strength of the incident x-ray beam. The higher current delivered for beam 1 in the TLD work, ~37 μA (Delta) vs 20 μA (Alpha 4000S), would result in relatively greater primary beam dose, scatter dose off the lid and backscatter off the nylon backing and, thus, may dominate the cause of this difference. Inherent aluminum filtration is present with both units, however differences in the thickness of this component would affect the source photon fluence rate. For potential *in vivo* use, the lid would not be required. Dosimetry without the shielding cannot be performed currently due to x-ray shielding regulatory requirements. Removal of the lid would offer a way to estimate a) the magnitude of the scatter coming from it and b) the fraction of this to the total scattered dose delivered to the TLD chips, where the total scattered dose includes the combination of scatter from the lid and backscatter from the nylon backing.

The direct and normalized MDLs with the Delta Premium unit are in the sub-ppm range and on the same order of magnitude. Lower values for terms 1 and 2 in the MDL were noted for the Delta unit. Thus, the Delta MDLs are lower than those found with the Alpha 4000S analyzer. The higher current settings, superior resolution capabilities of the Delta model's SDD and lower degree of scatter in the energy spectrum data points are likely contributors to this. These MDLs, however, may not be fully representative of *in vivo* monitoring scenarios since the shielding lid would need to be removed and the unit would be pointed into the air horizontally, as opposed to mounted vertically in the stand. Both systems are capable of detecting arsenic in an exposed population. Improvements to the spectra are nonetheless required to the Delta Premium results to improve the fitting function for the case without backing.

Chapter 4 Characterization of SDD in suitable energy range:

4.1 Introduction to article draft II:

Draft IV documents the use of a silicon drift detector (SDD) for use with a benchtop XRF system. Work characterizing its performance in numerous aspects is documented with various x-ray sources. The use of the SDD specifically as part of the phantom-based calibration of the benchtop XRF system will documented separately.

Quality assurance standards must be in place in order to rely on quantitative analysis of spectrometry work. XRF detection system calibration may be performed using a set of calibration phantoms. The benefits of a high concentration phantom lie in its counting statistics, allowing for a deconvolution of all spectral features. Such features can be justifiably fixed in analysis of lower concentration phantoms and eventually *in vivo* as they are then characteristics of the detection system. This process demands excellent detector stability so as to avoid drift in peak position, FWHM and sensitivity from one phantom to the next. This work thus investigates the stability of a SDD. Detector properties including electronic noise (ENC) and dead time are also investigated.

4.2 Draft for article II follows:

Characterization of Silicon Drift Detector in the 5.9-17 keV energy range for *in vivo* XRF applications.

Authors
Elstan D. Desouza[a], David R. Chettle[a], Ana Pejovic-Milic[b], David E. B. Fleming[c], Fiona E. McNeill[a],

Affiliations:
[a] Department of Medical Physics and Applied Radiation Sciences, McMaster University, Canada
[b] Department of Physics, Ryerson University, Canada
[c] Department of Physics, Mount Allison University, Canada

Manuscript will be submitted: X-Ray Spect. 2013

Author contributions:
Elstan Desouza was responsible for experimental setup, data acquisition and analysis.
Ana Pejovic-Milic offered unrestricted use of equipment and her previous research documented setup, performance evaluation and optimization of the equipment.
David Chettle and David Fleming assisted in interpretation of data.
Elstan Desouza was responsible for preparation of the draft manuscript.
Fiona McNeill supervised and guided the research.

Abstract:

This work characterizes an 80 mm^2 active area Silicon Drift Detector (SDD) in terms of peak position, full width half maximum (FWHM), and sensitivity stability as a function of time. The presence of a short warm up period was observed when tracking peak position as a function of time after powering up the detector and supporting electronic components, leading to instability in peak position during this time. No such drift was noted in sensitivity or FWHM stability. As well, system dead times of (3.353±0.014) μs, (5.385±0.020) μs and (9.955±0.067) μs respectively were found for shaping times of 0.4 μs, 0.8 μs and 1.8 μs respectively. The Equivalent Noise Charge (ENC) was found to be of (7.53±0.08) e^- rms for Mn Kα, (8.33±0.09) e^- rms for Cu Kα, (11.48±0.14) e^- rms for Rb Kα and (16.75±0.12) e^- rms for Mo Kα respectively, increasing with FWHM as a function of energy. The Mn Kα FWHM was consistently found to be ~134 eV at ~5 to 6 kcps, which is good for such a large area detector. Finally, investigation of shaping times suggests that if system dead times are anticipated to lie in the range of <5%, as has been indicated from preliminary phantom calibration work with the same SDD, then FWHM may be of more importance that percent error in peak area or throughput, as the percent change in FWHM was larger than that for the latter two, when examined over the range of energies to be investigated in phantom calibration work with this SDD.

1. Introduction and Background:

1.1. Silicon Drift Detector:

A Silicon Drift Detector (SDD) is made of a 450 μm thick detector chip of high-resistivity Si, which is often called a Si wafer because of its order of magnitude reduction in thickness compared to conventional Si(Li) detector bulk crystal sizes. The SDD wafer is fully depleted by means of a negative bias voltage applied to both of its sides – a translationally invariant thin pn junction on the side facing incoming radiation and an array of p+ drift rings (electrodes) on the other side – until full depletion is achieved. On one side, the voltage is gradually increased using drift rings (electrodes are of progressively higher bias voltage), producing a strong transverse and radial electric field within the disc that then acts like a guide/pathway, for charge carriers, ending at a small collection anode. Charge carriers (electrons) generated due to absorption of ionizing radiation will drift towards the n+ collection anode.

A low detector capacitance allows this detector type to be used in high count rate applications because electronic noise is minimized, thereby allowing for short shaping times to be used in the pulse processing system. This is superior to a Si(Li) detector. The avoidance of stray capacitances (long bonding wires and connection pads) is firstly achieved by connecting the anode to the first transistor required in the amplification process by means of a small metal strip. This is possible by integrating a JFET (junction gate field-effect transistor used to convert current to voltage) directly into the charge-collecting anode (Lechner et al., 1996; Radeka et al., 1989), thereby reducing electronic noise between the FET and the collection anode. It should be noted that there is no need

for an external reset pulse because the transistor has its own auto-correcting means of discharge. The built-in reset mechanism enables pulsed-reset operation and this translates into lower detector dead times, allowing SDDs to be used in applications involving very high count rates (Fiorini and Lechner, 1999; Strüder and Soltau, 1995). Second, since capacitance is directly proportional to area, a small area collection anode is used. Next, since electron loss may result from direct exposure of the anode-FET combination to incoming radiation leading to an increase in low energy background (Lechner et al., 1996), the JFET may be moved to the edge of the wafer as opposed to the center. This allows the anode-FET combination to be shielded from direct irradiation by means of a circular shaped collimator (Lechner et al., 2004). Since this means that the anode only collects electrons from one side, its size can be further reduced. Finally, the integrated FET layout also reduces mechanical vibration, reducing microphony, further reducing noise. These measures to reduce capacitance allow for a drop in electronic noise improving the resolution. With suitable pulse processing systems, this resolution can be maintained for high count rates. An extremely thin 25 μm Be entrance window separates the detector's sensitive area from the ambient atmosphere, guaranteeing excellent transmission for low energy x-rays. Due to the use of high purity Si (low leakage current) in the manufacturing of the SDD, LN_2 cooling is not required to permit a compact design for the detector's housing and straightforward accommodation of the SDD in tight spaces and previously unrealizable geometries.

At high energies, an SDD's efficiency is related to the amount of depletion of the 450 μm silicon wafer, in this case 450 μm. X-ray absorption in the silicon bulk is 95.4% for energies up to ~10 keV (close to the As Kα energy) and ~50 % at 20 keV and this is shown graphically in figure 1.

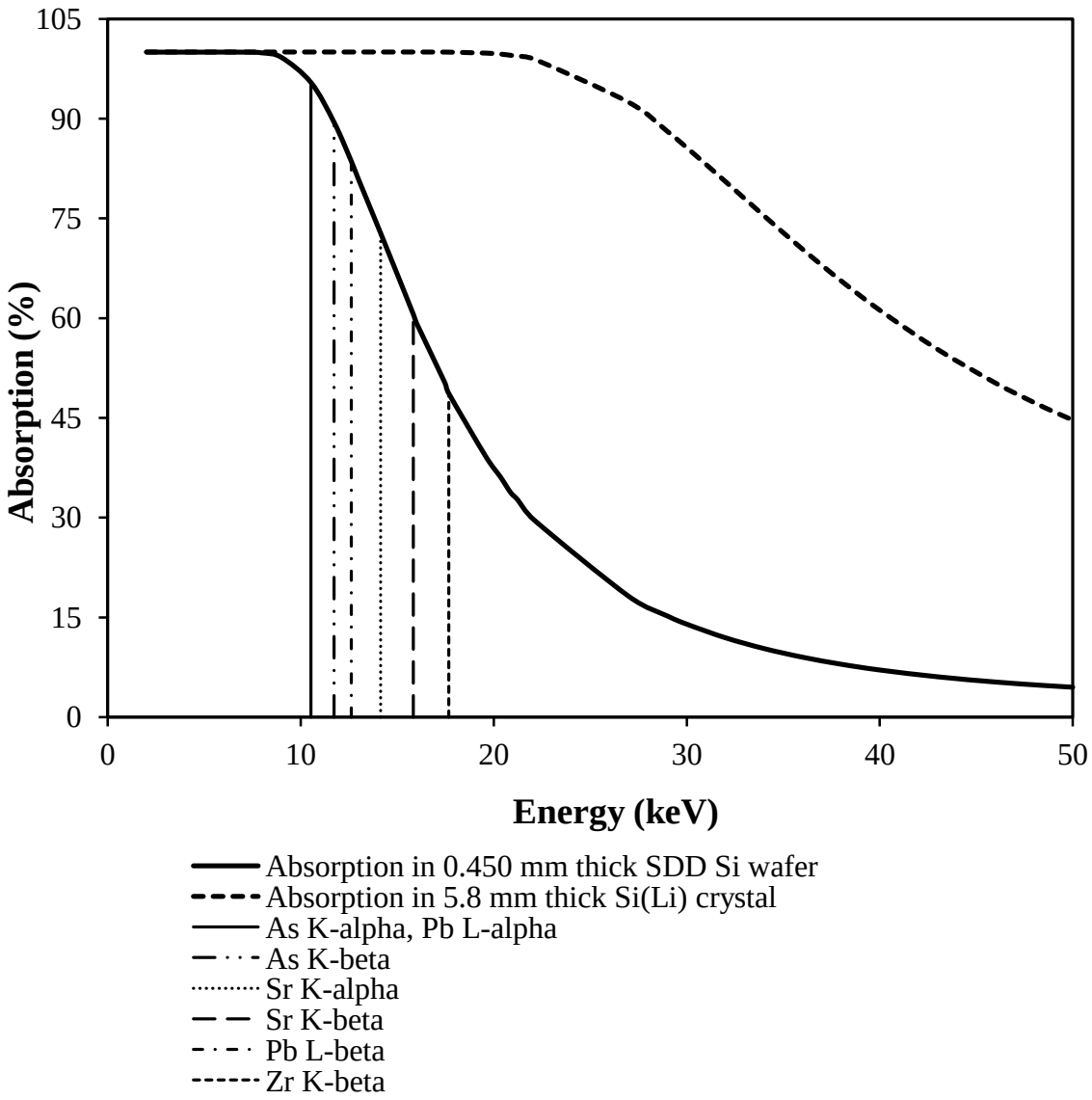

Figure 1. Differences in absorption between Si(Li) and SDD sensors due to the thickness of silicon wafer (SDD) vs silicon crystal [Si(Li)].

Absorption is exponentially proportional to thickness so a 5.8 mm thick crystal would have greater absorption than the 450 μm thick SDD wafer. Since the SDD wafer is much thinner, the transverse distance that any charge is required to travel is significantly reduced. This indicates that at the As Kα energy, nearly 95% of all incident x-rays deposit all their energy in the Si wafer; this number is reduced to 72.7% for the Sr Kα energy, 60.6% for the Sr Kβ and Zr Kα energy, 48.7% for the Zr Kβ energy and ~29.6%

for the Ag Kα energy. The significant drop-off in absorption at the Zr energies is the reason why this element is often used as an internal Si wafer collimator material in SDDs, as most SDD applications do not investigate such high energies. For the higher energies (Zr at 17.67 keV, Ag at 22.10 keV) a large fraction of x-rays pass through the detector material without full energy deposition meaning that there is a possibility of detecting their corresponding 180-degree Compton backscatter off the backing of the housing of the head of the SDD, producing energies of 16.52 keV (Zr Kα) and 20.34 keV (Ag Kα).

1.2. In vivo x-ray fluorescence (XRF):

X-Ray Fluorescence (XRF) is based on the phenomenon of the photoelectric effect. For an electron in one of the shells of an atom, an incident photon, with energy higher than the electron's binding energy, transfers its energy to the electron, ejecting it from its shell. The spot occupied by the ejected electron, known as a photoelectron, is filled by an electron from an outer (higher energy) shell. This is known as the photoelectric interaction and is the foundation for XRF. Through the excitation and detection of characteristic x-rays, at energies depending on the element being investigated, from a sample it is possible to specify and, with appropriate calibration, quantify, the elemental composition of the sample. Accompanying interactions, utilized in XRF analysis, include coherent (elastic) scattering and Compton scattering.

Over the past five decades or so, interest has been raised in the *in vivo* quantification of trace elements non-invasively using XRF. This approach offers the benefit of avoiding painful tissue or organ extraction and is achieved using low-dose x-rays to induce the fluorescence. Our research group, along with collaborators, has extensive experience with the development and implementation of *in vivo* analysis techniques including quantification of lead, strontium and uranium in bone and arsenic and silver in skin via radioisotope-induced or x-ray tube based XRF (Behinaein et al., 2011; Nie et al., 2006, 2004; O'Meara et al., 2001; Studinski et al., 2005, 2004) and accelerator (ex. aluminum and fluorine) (Byun et al., 2007; Chamberlain et al., 2012; Davis et al., 2008) as well as prompt gamma-based (cadmium, mercury, chlorine and gadolinium) (Atanackovic et al., 2007; Gräfe et al., 2012, 2011; Grinyer et al., 2007, 2005) neutron activation analysis approaches. XRF-based quantification of cadmium and platinum in the kidney have also been documented in the literature (Ahlgren and Mattsson, 1981; Jonson et al., 1988). The current work reports on the characterization of a SDD for use with of an x-ray tube based XRF system intended for application to *in vivo* analysis of strontium in bone and arsenic in skin. This detector type has not been used by researchers in our group and thus an investigation of its properties, as it pertains to the intended application, is warranted.

The purpose of this work was to characterize the detector's performance in terms of: (a) Mn Kα peak (chosen to allow for easy comparison to expected results provided by manufacturer) position and FWHM stability at the shaping time matching the internal shaper and at shorter shaping times and (b) peak position stability for a higher range of energies encompassing characteristic x-ray lines that will be accessed for *in vivo* XRF

work by members of the research group. Additionally, system dead time, sensitivity stability and electronic noise are investigated at various shaping times, for the SDD-based detection system.

1.3. Peak and FWHM stability:

For the *in vivo* application described here, detector stability is important because of the method by which we extract peak area information. When higher concentration calibration phantoms are measured, superior counting statistics in the peaks of interest are accumulated than in phantoms with a lower analyte concentration. Thus, features of the spectra that are not visible at lower analyte concentrations will be visible and can be characterized. For example, the presence of low energy tailing is a known concern for Si(Li), HpGe and Silicon Drift detectors and has been documented by various workers (Hansen et al., 1973; Lépy et al., 2000, 2003; Scholze and Procop, 2001). With poor counting statistics, as is the case for lower concentration phantoms, such features are not very visible in the spectra. However, they are observed at higher concentrations and they can then be characterized, through inclusion of a tailing feature in a peak-fitting function that is used to extract net peak areas. When lower concentration phantoms are then fit with this same function, the relevant fitting parameters can then be held fixed or within very tight upper and lower limits (i.e. within some chosen tolerance, eg. within a window of 0.5σ). This improves the extraction of peak information at lower concentrations. In order to determine reliable fitting parameters, detector stability is therefore extremely important since drift in FWHM or peak centroids, between measurements of higher and lower concentration phantoms, could produce misleading results for analysis of lower concentration phantom data. If peak drift is observed, this may be accompanied by an elevation in SDD chip temperature due to a malfunctioning cooling mechanism/circuit. Thus, tracking SDD chip temperature as a function of time is of importance for SDDs.

The discussion of peak stability applies to a fully assembled *in vivo* detection system where spectral acquisition parameters, such as counting and shaping times, are fixed. Shaping time is of importance since *in vivo* x-ray XRF is limited by measurement time. *In vivo* XRF measurements in our group are generally performed over a period of approximately 30 minutes due to subject comfort and to minimize movement of the XRF interrogation site over the duration of the measurement (Studinski et al., 2008, 2006; Zamburlini et al., 2007). Years of experience have determined that volunteers are willing and able to sit relatively still for half an hour. While various holders or mild forms of restraint are employed during an *in vivo* measurement, subject motion cannot be fully eliminated, however if it is possible to reduce this counting time, then subject motion would be reduced. As mentioned above, the default Vitus H80 SDD shaping time is 2 μs (analog), for the SDD being discussed here. If it is possible to reduce this further (while increasing the incident source signal, in order to match total incident counts between the two shaping times), without compromising the MDL, then a shorter counting time may be considered for *in vivo* trials. The current work looks into peak stability at the Mn Kα energy, which is used by detector manufacturers when quoting the FWHM that can be attained with a particular detector. Absorption in the 450 μm SDD wafer begins to drop

at ~10 keV. Thus, in addition to the Mn Kα energy, higher energies ranging from 8-17 keV, which would be of interest for SDD-based *in vivo* XRF work by our group, are also investigated for peak stability as a function of shaping time.

2. Theory:

2.1. Determination of system dead time:

Part of detector characterization involves an evaluation of the dead time that is present in the detection system. This is important for the application intended here since peak counts, in phantom trials, need to be maximized. Incident count rates are therefore set high and this, in turn, may result in relatively high dead times. A dead time correction factor would offer one way to correct for this and thus determination of system dead time is also of interest. The low noise capabilities of SDDs are well known and a comparison will be possible between the SDD system used in the current work and dead times reported in the literature. The dead time here is taken as the dead time of the entire detection system, since the detector is not used in isolation.

Assuming Poisson statistics, for spectra collected from a steady-state source (where counting rate is not expected to change during the spectrum-acquisition time, eg. a long lived isotope), the dead time (assuming a paralyzable model, discussed further below) of a solid-state detector is given by

$$m = ne^{-n\tau} \tag{1}$$

where m is the observed (or recorded) counting rate, n is the true event rate and τ is the dead time (Knoll, 1999). During the detector's "live" or active period, a specific τ is known to succeed an individual event recorded by the detector. The events occurring during τ are not recorded, or are said to be 'lost' by the detection system. These lost events also lead to another dead time interval. This is the paralyzable model of dead time, which has been used in a similar dead time calculation work (Woicik et al., 2010) and is assumed here. Dividing both sides of equation 1 by n, taking the natural logarithm and rearranging gives

$$ln\left(\frac{m}{n}\right) = -\tau n \tag{2}$$

Equation 2 is of the form y = zx+b, where the dead time is found from the slope to be τ = -z. Experimentally, the live time of a detection system is the time when it is not busy processing but is actively accepting pulses and it is the difference between real (clock) time and dead time (Carlton, 2011). Normalizing to live time will give the true count rate n, which can be written as

$$n_i = \frac{Total\ Recorded\ Counts}{Live\ Time} \tag{3}$$

which has been corrected for dead time. Conversely, normalizing to real (clock) time will give the measured count rate, m, which has not been corrected for system dead time. This can be written as

$$m_i = \frac{Total\ Recorded\ Counts}{Real\ Time} \tag{4}$$

Through a series of measurements of m and n, τ can be determined since an exact solution to equation 1 does not exist.

As a means of verifying this, an x-ray source with adjustable source strength can be used. The true interaction rate n for a specific measurement can be represented as $n_{ref}x$, where n_{ref} is the true interaction rate for some reference measurement and x is a an associated scaling factor relating n_{ref} to n. Then equation 1 can be written as

$$m = n_{ref} x e^{-n_{ref} x \tau} \tag{5}$$

Re-arranging equation 5 and taking the natural logarithm of both sides gives

$$ln\left(\frac{m}{x}\right) = -n_{ref}\tau x + ln\left(n_{ref}\right) \tag{6}$$

Equation 6 is of the form y = cx+d, where $c = -n_{ref}\tau$ and $y = \ln(n_{ref})$. Isolating these two terms for n_{ref} and combining the resulting expressions gives the dead time as $\tau = -c/e^d$. Thus, plotting ln(m/x) as a function of x, and fitting to a straight line, allows the dead time to be determined from the fitted slope and intercept. A source with the ability to offer increasing incoming counting rates, such as the adjustable current of an x-ray tube, would allow for the scaling factor x_i to be determined, for the i^{th} tube current setting, as $x_i = I_i/I_{ref}$, where I_i and I_{ref} are two tube current settings (with I_{ref} chosen for a dead time of not more than ~5%, to avoid dead time artifacts). This alternate formulation could be followed to determine the detection system's dead time. In this way an x-ray tube with an adjustable tube current offers the ability to use this approach as verification of the above technique. Alternatively, source-to-detector distance or attenuators between the source and detector can be used to obtain the scaling factor, x_i.

2.2. Sensitivity stability:

Stability in system sensitivity is vital for the intended application of the SDD since a set of calibration phantoms differs only in analyte concentration and so spectral analysis should not deviate in its approach over a set of phantoms, within some accepted tolerance, as discussed earlier. However, variations in sensitivity will affect such analytical work and can result in large deviations in spectral parameters. Evaluation of the stability of the system's sensitivity is thus important for the application of the SDD to phantom calibration studies. For a series of measurements performed under identical conditions, if spectral analysis (peak-fitting) is not performed, the total experimental uncertainty of the resulting series of peak intensities, P, can be written as

$$Unc_{EXPRMT} = \sqrt{Unc_{INSTR}{}^2 + Unc_{STAT}{}^2} \quad (7)$$

where the statistical uncertainty term is given by $Unc_{STAT} = P^{1/2}$. Peak-fitting would add to Unc_{EXPRMT}. Ideally the instrumental uncertainty term is small in comparison to the statistical uncertainty. For such a series of replicate measurements, the experimental uncertainty would be calculated as the standard deviation of the series of measurements. The instrumental uncertainty can then be isolated to give

$$Unc_{INSTR} = \sqrt{Unc_{EXPRMT}{}^2 - Unc_{STAT}{}^2} \quad (8)$$

Thus, through a series of measurements, instrumental uncertainty can be calculated. Peak instability would affect the uncertainty associated with spectral analysis. Instrumental uncertainty has been tracked, with the above approach, using an SDD dataset comprising a series of >600 acquisitions with an 8 mm^2 Canberra X-PIPS x-ray detector (500 μm Si thickness) using an Fe-55 source, to track the Mn Kα peak over a period of time spanning 90 hours (Paepen et al., 2005). In the current work, the same approach was used to determine Unc_{INSTR}, with the SDD detection system used here, to permit comparison with the above previously published work.

2.3. Electronic Noise:

The Equivalent Noise Charge (ENC) of the digital processing systems was also investigated in the current work. As with FWHM and peak stability, this was performed over a range of energies. This is the charge across the input of a detector capacitance that produces an output signal amplitude equal to the root-mean-square noise (Gatti and Manfredi, 1986; Nicholson, 1974). The FWHM measured with a detection system is given by

$$(FWHM_{total})^2 = (FWHM_{Stat})^2 + (2.35wENC)^2 \quad (9)$$

where the total (or measured) FWHM is the sum of the squares of contributing terms related to the statistical (left) and noise (right) fluctuations present in the signal processing chain. The above equation can be written out explicitly in terms of its components as

$$(FWHM_{total})^2 = (2.35\sqrt{wF_aE})^2 + (2.35wENC)^2 \quad (10)$$

where F_a is the Fano factor, w is the electron-hole pair creation energy in Silicon (w = 3.65 eV) and E is the photon energy in eV (Knoll, 1999; Metzger et al., 2004; Pinotti et al., 1995). Equation 10 can be re-arranged to give

$$(FWHM_{total})^2 = 2.35^2 wF_a E + 2.35^2 w^2 ENC^2 \quad (11)$$

$$2.35^2 w^2 ENC^2 = (FWHM_{total})^2 - 2.35^2 wF_a E \quad (12)$$

$$ENC^2 = \frac{(FWHM_{total})^2 - 2.35^2 wF_a E}{(2.35w)^2} \quad (13)$$

$$ENC^2 = \left(\frac{FWHM_{total}}{2.35w}\right)^2 - \frac{F_a E}{w} \quad (14)$$

where the ENC can now be calculated from measurements of FWHM, provided the Fano factor is known, for comparison to results in the literature.

3. Equipment setup and method:

3.1. SDD-based pulse processing system:

The base detection system provided by the manufacturer consisted of an AXAS-A (Analytical X-Ray Acquisition System-Analog) module comprising an 80 mm^2 active area Vitus H80 single-element SDD (KETEK GmBH, Munich, Germany), preamplifier and shaping amplifier. A KETEK analog ADC and MCA were provided in a separate unit that can be connected via a USB port to a host PC on which MCA software is installed and also functions as a power supply. Built into the AXAS-A box is an analog shaper having a fixed shaping time of 2.00 μs. A schematic of this setup is provided in figure 2.

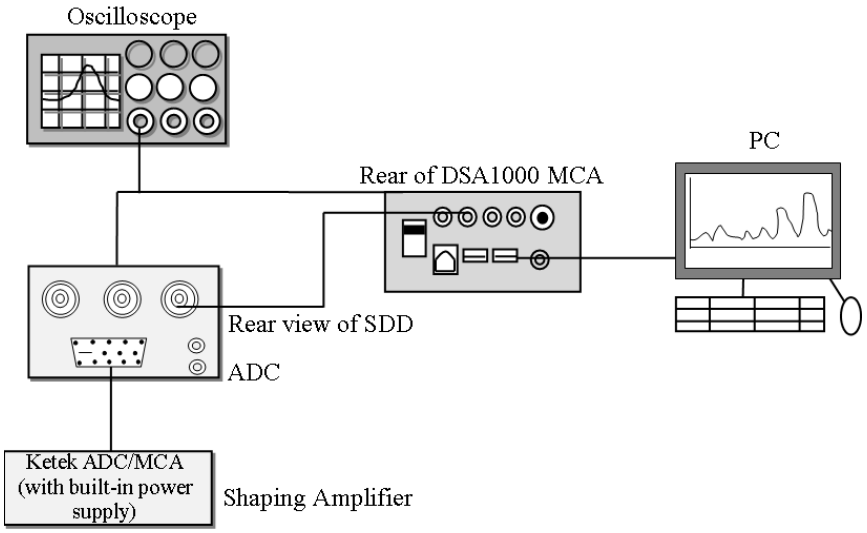

Figure 2: The three connectors on the back of the SDD (second row from top left) are labeled “Test”, “Amp(lifier)” and “Pre(amplifier)”. Two pins (red and black), just below the preamplifier connector are labelled “TEMP”.

The ability to adjust the shaping time is not possible with the manufacturer’s standard hardware setup described above. The manufacturer offers an AXAS-D system (Digital), which allows for adjustment of this and other pulse processing parameters. When using the AXAS-A system in combination with an external third-party ADC/MCA unit, the pre-amplifier output of the AXAS-A system would need to be connected to the external ADC/MCA unit. However, an external ADC/MCA does no shaping of the signal. Therefore an additional external shaping amplifier would need to be connected between the AXAS-A preamplifier output and the external ADC/MCA unit. Such a system would then offer the ability to adjust the shaping time freely. For the current work, a full-featured Canberra Digital Spectrum Analyzer (DSA1000) MCA box with up to 16K channels was used for this purpose. The conversion gain was set to 4096.

The Canberra DSA1000 is an ADC+MCA unit and is referred to as a DSP, DPP or DXP, meaning Digital Signal, Pulse or X-Ray Processor unit and it represents a more modern method of processing signals for any kind of detector. It is referred to as ADC+MCA rather than ADC/MCA to make this distinction. Functionally, it replaces the shaping amplifier, ADC and MCA units. Thus, when connecting the SDD to this external ADC+MCA unit, the AXAS-A system’s preamplifier output was directly connected to the external ADC+MCA box. In this way, the BNC preamplifier connector on the rear of the AXAS-A housing provides the user with the ability to bypass the built-in analog shaper and access the preamplifier signal using the external ADC+MCA unit. When utilized with the external ADC+MCA box, the Ketek ADC/MCA unit was only required to provide power to the SDD. A micro-usb to usb cable connecting it to the host PC would be required if the associated MCA software were to be utilized for acquiring

spectra, but was not used in the current work. With an external unit, Canberra's Genie2K MCA software was used for this purpose. The preamplifier type for the SDD was set to resistive capacitor feedback, although the DSA1000 can also handle most pulsed reset preamplifiers.

A quoted FWHM will be achieved for a specific shaping time; an external ADC+MCA-based setup allows the ability to select shorter shaping times in the event that higher count rates are desired. The manufacturer's documentation only quotes the FWHM for shaping performed by the built-in analog shaper – 2.0 μs shaping time – which would be the equivalent to ~4.0 μs rise (peaking) time. The Canberra DSA1000 DSP uses a trapezoidal filter (digital filtering), whose principle is well explained (Jordanov and Knoll, 1994; Knoll, 1999). As the counting period for *in vivo* studies is typically 30 minutes, maximizing throughput without severe degradation of spectral features is important. Thus, shaping times appreciably higher than 2.00 μs were not investigated in the current work because they would considerably limit detector throughput. The highest shaping time chosen was 2.8 μs.

3.2. External Cooling:

If the detector's external housing temperature is kept as close to +20°C (293 K) as possible, with some form of external cooling, then this will help stabilize the system and achieve the guaranteed FWHM specifications. This will also definitely help to improve the peak stability and overall performance. The AXAS-A box is aluminum covered with nickel. Nine 35 X 35 mm heat sinks (DigiKey Electronics, Mississauga, ON, Canada) were attached, using thermal adhesive, to the outer surface of the AXAS-A housing. Advanced cooling functionality (including externally attached heat sinks) is built in to a more advanced version of the manufacturer's AXAS system – AXAS-M (Modular).

3.3. Experimental Procedure:

Peak and FWHM drift monitoring was performed using a Fe-55 source (Spectrum Techniques, Oak Ridge, TN, USA). The source was placed in front of the SDD's Be window. Spectra were acquired for a short counting period of 60 seconds (real time) because longer collection times would mask the visibility of peak drift. In addition, the number of counts in the Mn Kα peak was further limited by dead time, which was chosen not to exceed ~8%. Over a period of 60 seconds, a minimum of 130,000 counts were collected in the Mn Kα peak, ensuring good statistics.

Investigation of the shaping time was performed using two separate sources to vary the energy range. The first source was the same Fe-55 source used for drift monitoring. In order to access higher energies, an Amersham variable x-ray source (Amersham, UK) was also employed. This consisted of a 10 mCi Am-241 source contained inside a steel housing. A rotating fly-wheel target holder was available inside the housing allowing for a choice of one of 6 targets – Cu, Rb, Mo, Ag, Ba or Tb. For the present work, the x-ray spectra from Cu, Rb and Mo were used from this source. The beam port was placed in

front of the SDD's Be window and spectra were acquired for 200 s, 60 s and 60 s real time for Cu, Rb and Mo respectively. The source-detector distance was adjusted so that the dead time was less than ~5%.

In the current work, system dead time was determined using the approach outlined in equations 1-4 and verified with the alternative approach with x-ray tube current as the adjustable source. The SDD was placed in front of an Ag-target (monochromator) x-ray tube (XOS, Albany, NY, USA), with adjustable accelerating voltage and current meters, and spectra were collected for 600 seconds real time. The monochromator fine-tuned the beam energy to the Ag Kα line. The source makes use of an optical focusing system to direct x-rays to a <1 μm spot size at a distance of (30.0±0.2) cm. The SDD was positioned with its Be window at this distance. Such a setup allows for the measured count rate (m_i) to be recorded as the true (input) count (n_i) rate is varied by ramping up either tube voltage or current. The maximum voltage and current settings possible with the tube were 50 kVp and 0.50 mA respectively – for this work, the current was adjusted to cover a range of dead times from ~4–75%, with the accelerating voltage held fixed at 43.4 kVp, 38.3 kVp and 34.3 kVp for shaping times of 0.4 μs, 0.8 μs and 1.8 μs respectively. It should be noted that the first in this series of measurements was performed >24 hours after the SDD was turned on and 2 hours after the x-ray tube was powered up. This was to ensure that peak drift or FWHM artifacts were not observed in the spectra during a possible warm-up period, which would likely occur immediately after powering up the detector. Also, operating during a possible warm-up period for the tube could lead to fluctuations in tube flux, which could further change while the current is ramped, as was the case here.

The detection system's sensitivity stability was evaluated using the built-in batch-acquisition features of the Genie2K MCA software. A set of fifty consecutive 60 second (LT) measurements was set up for a shaping time of 2.0 μs (0.8 μs flattop). The Fe-55 source was placed in front of the detector close enough to produce a dead time of 5.3 %, giving an integral ROI of approximately 800,000 counts under the Mn Kα peak. A custom-written Mathworks Matrix Laboratory (MATLAB) R2012a script was used to extract the integral area under a fixed ROI, for all spectra. This is equivalent to defining an ROI in the MCA software and tracking the gross counts. A correction for source-decay was then applied to this integral area. The batch-acquisition was executed 19 times successively, only during the day (no overnight acquisition), encompassing a total of 105 hours and 950 trials. The instrument uncertainty was then calculated using equation 8.

Finally, in order to measure the SDD chip operating temperature over a period of ~2 days following detector power up, the detector was exposed to an Fe-55 source and temperature readings were recorded using a FLUKE 73 Series III multi-meter in voltage mode to measure the voltage drop between the TEMP output pins on the back of the SDD housing. The multi-meter had an accuracy specification of ±0.3% for its voltage readings. The internal cooling of the detector is controlled with a temperature feedback circuit. Accordingly, a reading of 2.35V corresponds to a temperature of 235 K (- 38°C). Using

this conversion factor, the recorded voltage drop readings were used to track the temperature of the SDD chip. Room temperature was estimated to have changed by less than 2 ^{0}C over the duration of these measurements.

3.4. Data Analysis:

Spectral analysis of the Mn, Cu, Rb and Mo Kα peaks, at 5.899 keV, 8.048 keV, 13.395 keV and 17.479 keV (Deslattes et al., 2003) respectively, was performed with the non-linear least squares Marquardt-Levenberg fitting routine (Marquardt, 1963) utilizing combinations of various expressions that are commonly employed for this purpose, including

$$G(E) = \frac{A_G}{\sqrt{2\pi}s} exp\left[-\frac{(E-E_0)^2}{2s^2}\right] \quad (15)$$

$$S(E) = \frac{1}{2} H_{ST} erfc\left[\frac{(E-E_0)}{\sqrt{2}s}\right] \quad (16)$$

$$T(E) = \frac{1}{2} H_T exp\left[\frac{(E-E_0)}{\beta}\right] erfc\left[\frac{(E-E_0)}{\sqrt{2}s} + \frac{s}{\beta\sqrt{2}}\right] \quad (17)$$

where A_G is the area of the Gaussian component, H_{ST} is the height of the step feature, H_T is the height of the tail, E_0 is the Gaussian peak location (centroid), s is the Gaussian width and β is the tail shaping coefficient (Campbell et al., 2001, 1985; Jorch and Campbell, 1977; Phillips and Marlow, 1976; Uher et al., 2010; Van Gysel et al., 2003). Spectral peak-fitting was performed using Microcal Origin ver. 8.5 (Originlab, Northhampton, MA, USA). The FWHM, in eV, was calculated as FWHM = 2.35s (Knoll, 1999) with the error given by FWHM = 2.35δs and similarly for peak centroid E_0.

4. Results and Discussion:

4.1. Output signal characteristics:

Before investigating the shaping and stability properties of the detection system, a TDS1000 oscilloscope (Tektronix – Beaverton, OR, USA) was used to view the output of the system. An Fe-55 x-ray source [two x-rays emitted: 5.899 keV (Mn Kα) and 6.490 keV (Mn Kβ)], was used for irradiation of the detector and the resulting amplifier output is shown in figure 3.

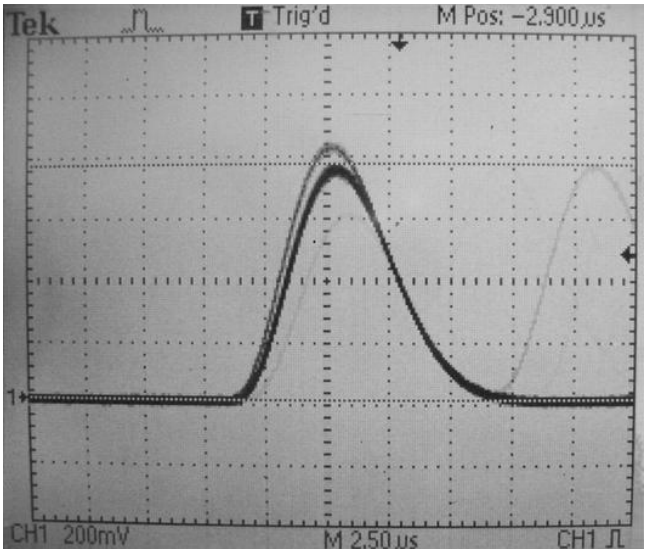

Figure 3: Oscilloscope screenshot of the amplified output signal acquired from the AXAS-A system, after passing through the internal shaper, produced by an Fe-55 source. Signal is accessed via the BNC/Shaper OUT connector on rear of AXAS-A module.

The oscilloscope screenshot shows the output pulse of the AXAS-A system. Both Mn Kα and Kβ lines are clearly separated. Pulse amplitude is proportional to x-ray energy, with the Kβ amplitude being slightly higher than the Kα as seen in the figure. The rising and falling edges of the pulse are shown in figures 4 a and 4 b, which respectively show oscilloscope screenshots depicting the rise time of approximately 260 ns (manufacturer quotes approx. 200 ns) and fall time of 196 µs (manufacturer quotes approx. 200 µs) of the pre-amplified signal acquired from the AXAS-A system via the BNC/Preamp OUT connector.

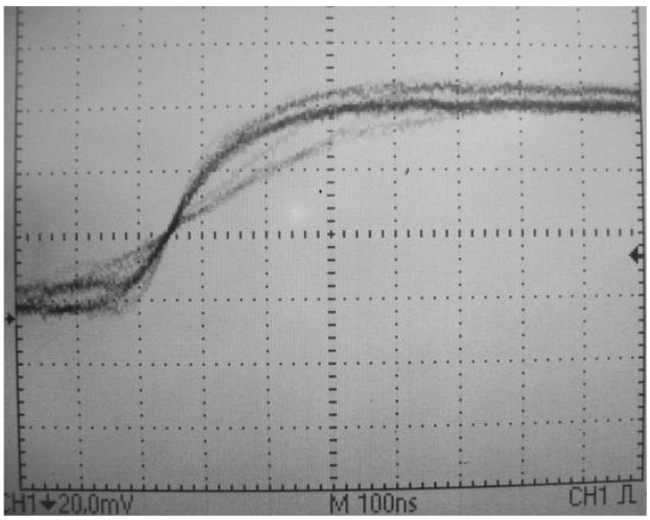

(a)

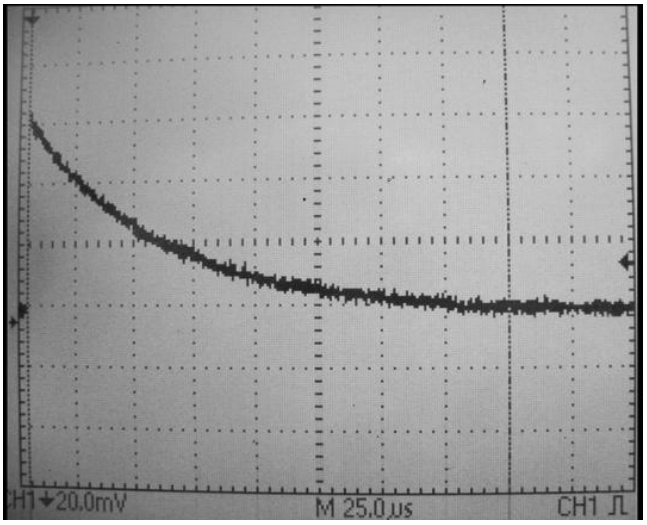

(b)

Figure 4: Oscilloscope screenshot of the pre-amplified output signal acquired from the AXAS-A system showing (a) rising edge and (b) falling edge. Pulse polarity (negative) was inverted on the oscilloscope for viewing and thus appears as positive.

4.2. Spectra from various sources:

By way of example, spectra and associated fits are shown in figure 5 a-c for various energies analyzed in this work.

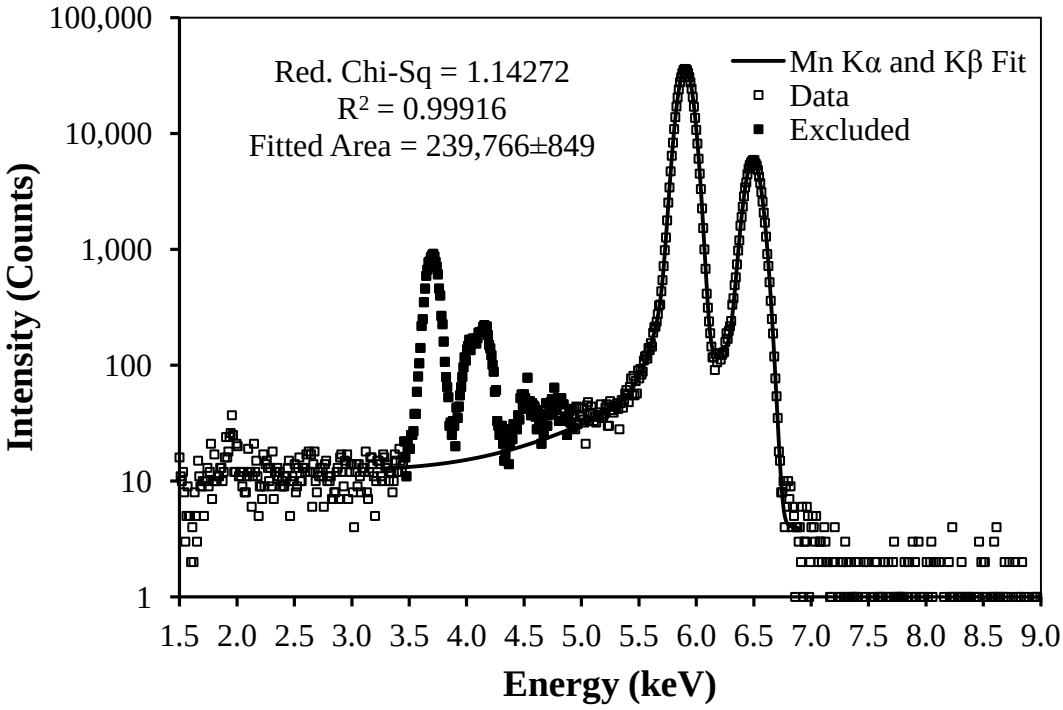
Red. Chi-Sq = 1.14272
R² = 0.99916
Fitted Area = 239,766±849
Mn Kα and Kβ Fit
Data
Excluded
Intensity (Counts)
Energy (keV)
100,000
10,000
1,000
100
10
1
1.5 2.0 2.5 3.0 3.5 4.0 4.5 5.0 5.5 6.0 6.5 7.0 7.5 8.0 8.5 9.0

(a)

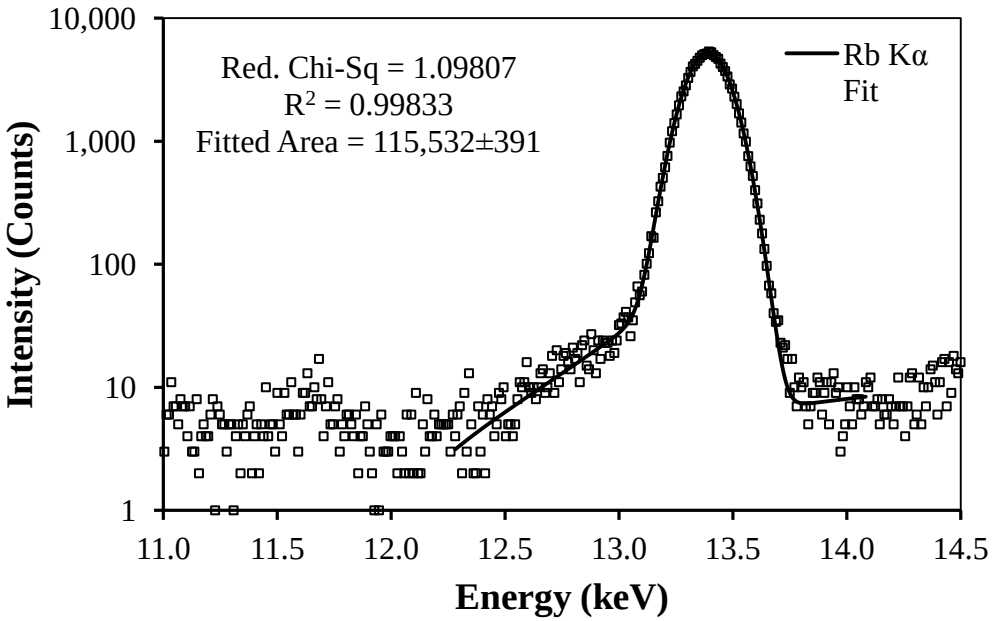
Red. Chi-Sq = 1.09807
R² = 0.99833
Fitted Area = 115,532±391
Rb Kα Fit
Intensity (Counts)
Energy (keV)
10,000
1,000
100
10
1
11.0 11.5 12.0 12.5 13.0 13.5 14.0 14.5

(b)

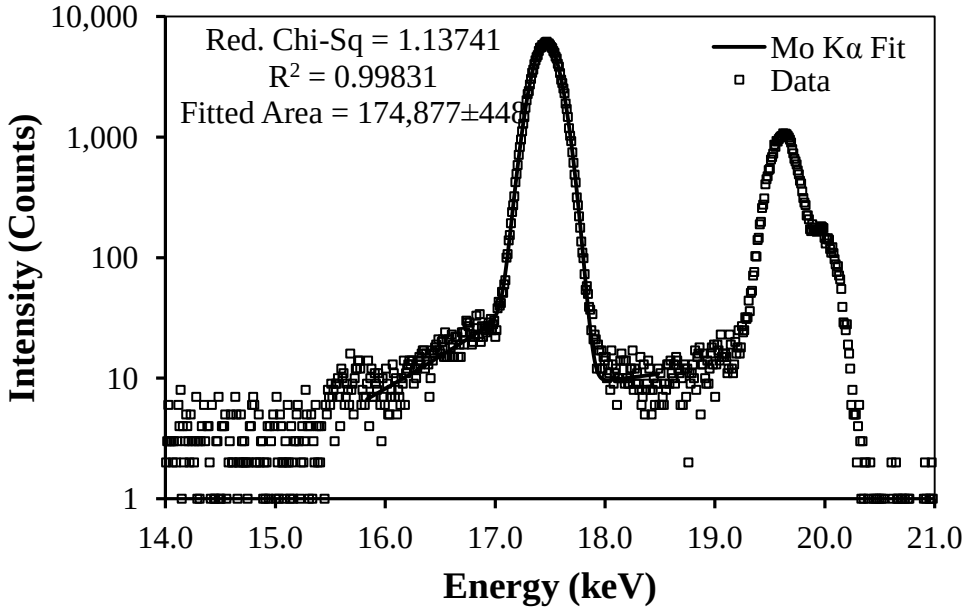
Red. Chi-Sq = 1.13741
R2 = 0.99831
Fitted Area = 174,877±448
Mo Kα Fit
Data
Intensity (Counts)
Energy (keV)
10,000
1,000
100
10
1
14.0
15.0
16.0
17.0
18.0
19.0
20.0
21.0

(c)

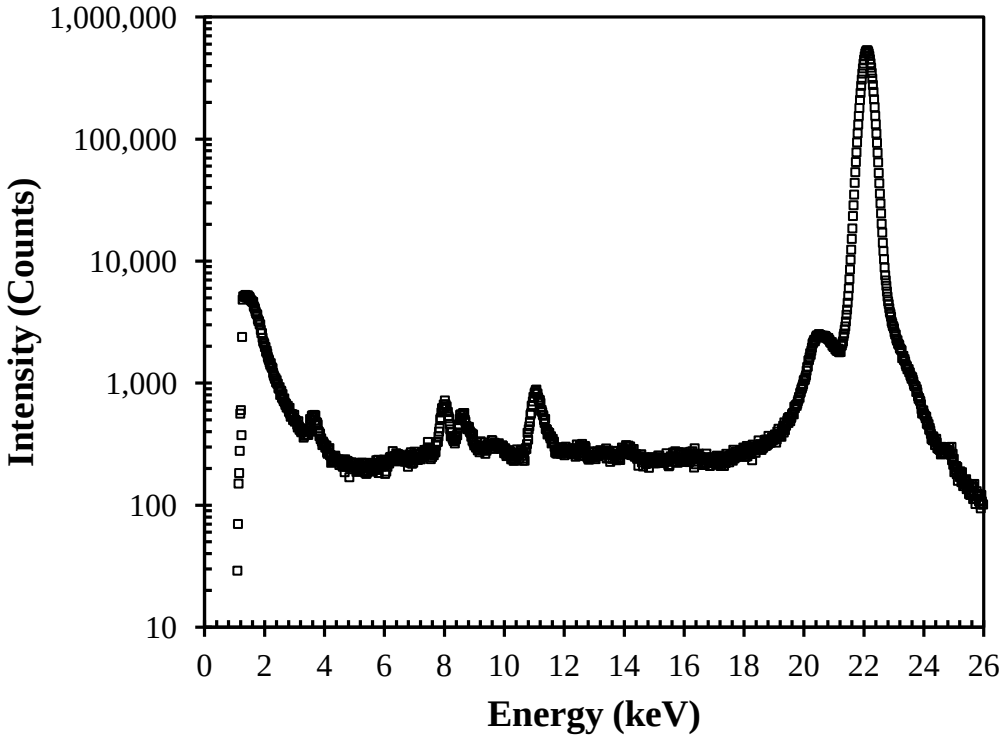
Intensity (Counts)
Energy (keV)
1,000,000
100,000
10,000
1,000
100
10
0
2
4
6
8
10
12
14
16
18
20
22
24
26

(d)

Figure 5: Spectrum corresponding to (a) Mn Kα (1.6 μs shaping time), (b) Rb Kα (0.2 μs), (c) Mo Kα (0.6 μs), all shown with DT < 10 %, and (d) x-ray tube output (2.0 μs, over a period of 300 s live time at 33.7 kVp and 0.11 mA, DT = 49.6 %) at the source-to-detector distance corresponding to the smallest spot-size for the focused monochromator tube output, used for head-on exposures of the SDD. Sample fit is shown for parts (a) – (c).

The excellent resolution of the SDD is noted in the clear separation of Kα and Kβ peaks, even for short shaping times. Silicon escape peaks are noted, for the two Mn lines, with a lower-energy features at ~3.7-4.4 keV (Ca Kα, Kβ) likely originating in the source holder material since it was not noted with other sources. For the intended XRF application of the SDD, the counting times are not more than 1800 seconds and so the strength (visibility) of low-energy tailing would be heavily reduced. However, this was still previously used in analysis of bone Sr XRF spectra with a Si(Li) detector (Da Silva et al., 2008; Zamburlini, 2008). A sample spectrum collected for a shaping time of 2.0 μs with the SDD placed head-on in front of the Ag-target x-ray tube (with monochromator), for calculation of system dead time, shows. Peaks corresponding to the anode material, Ag, and others inside the housing of the tube are visible in the range of 4-12 keV. No external collimators or possible scattering media were placed between the tube and the detector. The appearance of these low energy peaks was also noted for other source-to-detector distances and removed when a 5 mm thick Al absorber was placed between the tube and detector, verifying the source of their origin as being inside the tube housing. As expected, the dominant feature observed is the Ag Kα energy of 22.10 keV, nearly three orders of magnitude stronger than the closest feature.

4.3. Peak position, FWHM and SDD chip temperature stability performance:

The results of the peak stability tracking are shown in figure 6, for three different shaping times.

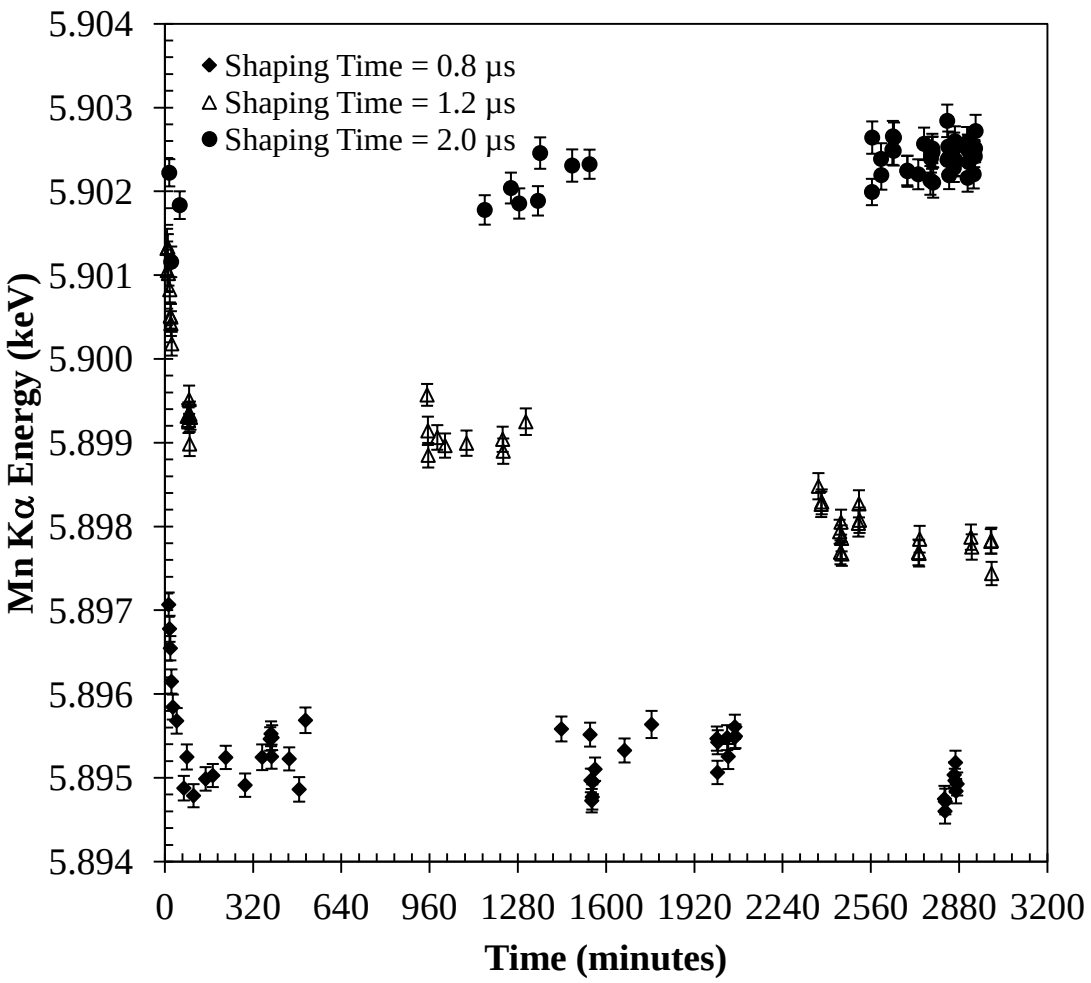

Figure 6: Results of testing stability of peak position, shown for various shaping times.

A warm-up period is clearly present over the ~50-70 minutes immediately following the powering up of the SDD. After this, excellent stability is noted as seen from the plot of absolute deviation in peak position from the average shown in figure 7.

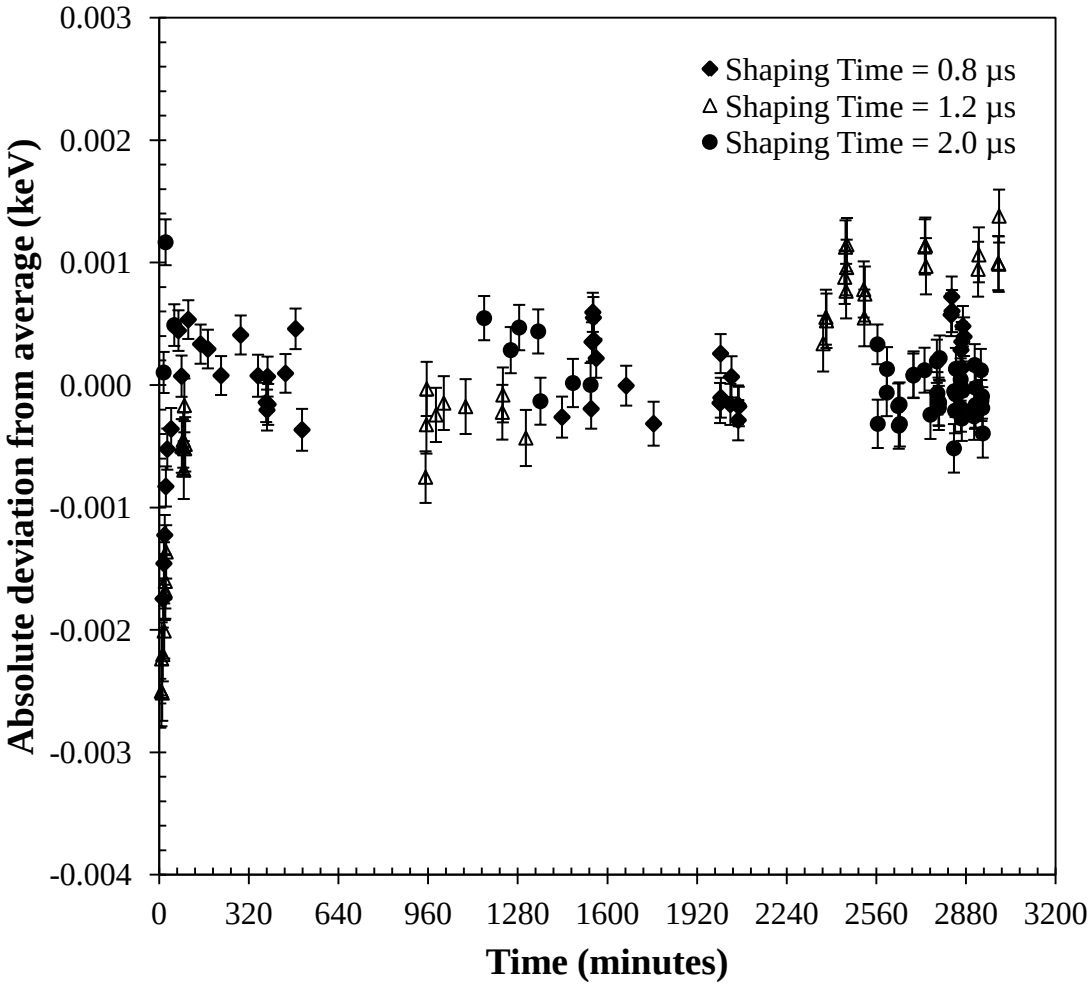

Figure 7: Tracking gain stability through absolute deviation in Mn Kα peak position, for various shaping times.

A summary of the different peak stability trials, with statistical information to quantify peak stability, is presented in table 1.

	ShpT = 0.8 μs	ShpT = 1.2 μs	ShpT = 2.0 μs
Minimum (eV)	142.55 ± 0.28	136.18 ± 0.28	132.98 ± 0.32
Avg±SDOM (eV)	143.17 ± 0.04	136.65 ± 0.04	133.96 ± 0.05
Maximum (eV)	143.73 ± 0.28	137.25 ± 0.29	134.70 ± 0.32
RSD (%)	0.18	0.18	0.24
Min Abs Dev (eV)	-0.56 ± 0.28	-0.60 ± 0.29	-0.74 ± 0.33
Max Abs Dev (eV)	0.63 ± 0.29	0.47 ± 0.28	0.98 ± 0.32
PD (%)	0.85 ± 0.29	0.77 ± 0.29	1.24 ± 0.33
R_P (%)	2.4286 ± 0.0007	2.3165 ± 0.0006	2.2695 ± 0.0008

Manfacturer quotes FWHM = 138.7 eV, Exp % Res based on manufacturer's FWHM (2.0 μs) at 5.899 keV = 2.3512 %

(a)

	ShpT = 0.8 μs	ShpT = 1.2 μs	ShpT = 2.0 μs
Minimum (keV)	5.8946 ± 0.0001	5.8973 ± 0.0001	5.9012 ± 0.0002
Avg±SDOM (keV)	5.8953 ± 0.0001	5.8988 ± 0.0002	5.9023 ± 0.0000
Maximum (keV)	5.8971 ± 0.0001	5.9013 ± 0.0002	5.9028 ± 0.0002
RSD (%)	0.0089	0.0196	0.0049
Min Abs Dev (eV)	-1.7459 ± 0.0002	-2.5149 ± 0.0003	-0.5171 ± 0.0002
Max Abs Dev (eV)	0.7204 ± 0.0002	1.5309 ± 0.0002	1.1661 ± 0.0002
PD (%)	0.0418 ± 0.0035	0.0686 ± 0.0035	0.0285 ± 0.0045

(b)

Table 1: Quantities used to quantify (a) FWHM and (b) peak position stability over time after power up. Results are shown for various shaping times.

Here, RSD is the relative standard deviation and was calculated, as a percentage, using

$$RSD_x = \frac{StdDev_x}{x_{AVG}} X\ 100 \tag{18}$$

RSD is also referred to as the coefficient of variation. The absolute deviation was calculated using (Taylor, 1997)

$$Abs\ Dev_x = x_{AVG} - x_i \tag{19}$$

where x_{AVG} is the arithmetic mean. The minimum and maximum absolute deviation values were the minimum and maximum values of the quantity x_i - x_{AVG}. The percent resolution and its error were computed using (Knoll, 1999)

$$R_P = \frac{FWHM}{E_{0,AVG}} X\ 100 \tag{20}$$

The expected percent resolution is determined using a FWHM of 138.7 eV as provided in supporting documents supplied by the manufacturer, as mentioned earlier. Since detector specifications are typically quoted for the Mn Kα line only, the comparison of measured and expected R_p only applies to an energy of 5.899 keV (Mn Kα). Errors in x_i were determined from peak-fitting and the error in Abs Dev_x and the percentage difference (PD) calculated using error propagation (Taylor, 1997). Abs Dev_x and PD offer a way to quantify the change in peak position over the period of data collection.

This formulation was then applied to the FWHM and is summarized in table 1a. Unlike peak position, the presence of a warm-up period was not observed for FWHM. The importance of choosing the short collection time (60 seconds) must be noted. If these data were acquired for longer than 60 seconds, then peak drift would have caused artificial peak-broadening because a single spectrum is being collected as the peak is drifting. This would have increased the FWHM over this time. This is not seen from the FWHM stability graph. In addition, drift in peak position would not be clearly visible as the peak would have moved significantly during the longer collection time and smaller changes would not be visible. A relative standard deviation of 0.18 %, 0.18 % and 0.24 % was observed for shaping times of 0.8 μs, 1.2 μs and 2.0 μs respectively. The maximum absolute deviation in FWHM ranged from (-0.74±0.33) eV to (0.98±0.32) eV for a shaping time of 2.0 μs. The PD values from all three shaping times are in agreement with each other, within uncertainty, meaning that large deviations in the FWHM are not present in the data. The largest absolute deviation in peak position occurred for a shaping time of 1.2 μs, where the deviation ranged from (-2.5149±0.0003) eV to (1.53092±0.00022) eV with a very low RSD of 0.02 %. These are seen from table 1b. The range of absolute deviation and the RSD value includes drift occurring during the warm up period. This indicates a very low level of drift in peak position over the ~2 days that encompassed data collection, with the majority of this occurring during a short period of time immediately after the detector is turned on.

The average Mn Kα FWHM, at a shaping time of 2.0 μs, is ~4 eV lower than the value quoted by the manufacturer. The same is true for the percent resolution calculated from the data compared to that from the FWHM quoted by the manufacturer. The manufacturer-quoted FWHM is for an input count rate of 10,000 cps. The maximum input count rate used in the measurements of Mn Kα peak and FWHM drift was ~6,000 cps. This may account for some of the noted FWHM improvement reported here.

Benefits of digital shaping may also partially account for this difference due to such features as improved filtering of noise and minimal pulse pile up and finite input response which reduces baseline shift, etc. The manufacturer has a more advanced shaping system, AXAS-M, which is intended specifically for large area SDDs such as the detector used in the current work. A factory-modified version of the AXAS-A was used here and could make a small contribution to the difference in FWHMs. Finally, the result of the SDD chip temperature stability measurement is plotted in figure 8.

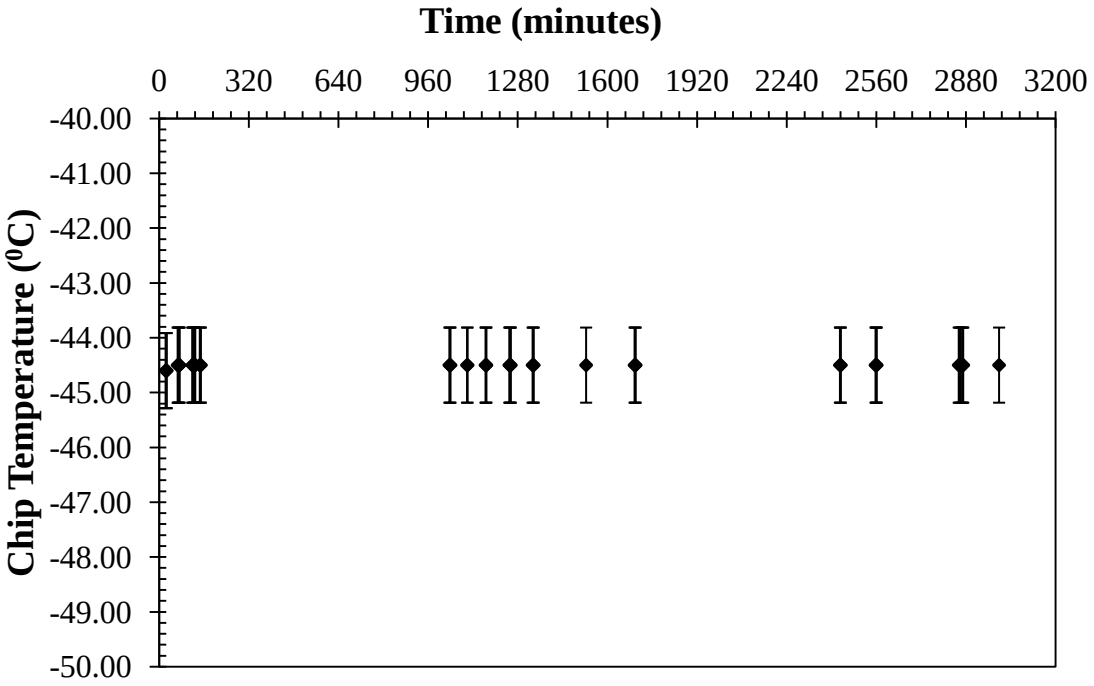

Figure 8: Stability of SDD chip temperature, recorded with a FLUKE 73 Series III multi-meter. Error bars were calculated using 0.3% V_i, as per the multi-meter manufacturer's specification.

It is clear that chip temperature stability is very good since it is essentially constant. This clearly shows that the chip is not overheating and forcing the detector to operate under non-ideal conditions. A more realistic error estimate, the multimeter readings, might be obtained through multiple readings under the same conditions.

4.4. SDD shaping parameter testing for low and high energies:

The effect of varying shaping time, for a flattop of 0.8 μs, on FWHM, is shown in figure 9, for various energies.

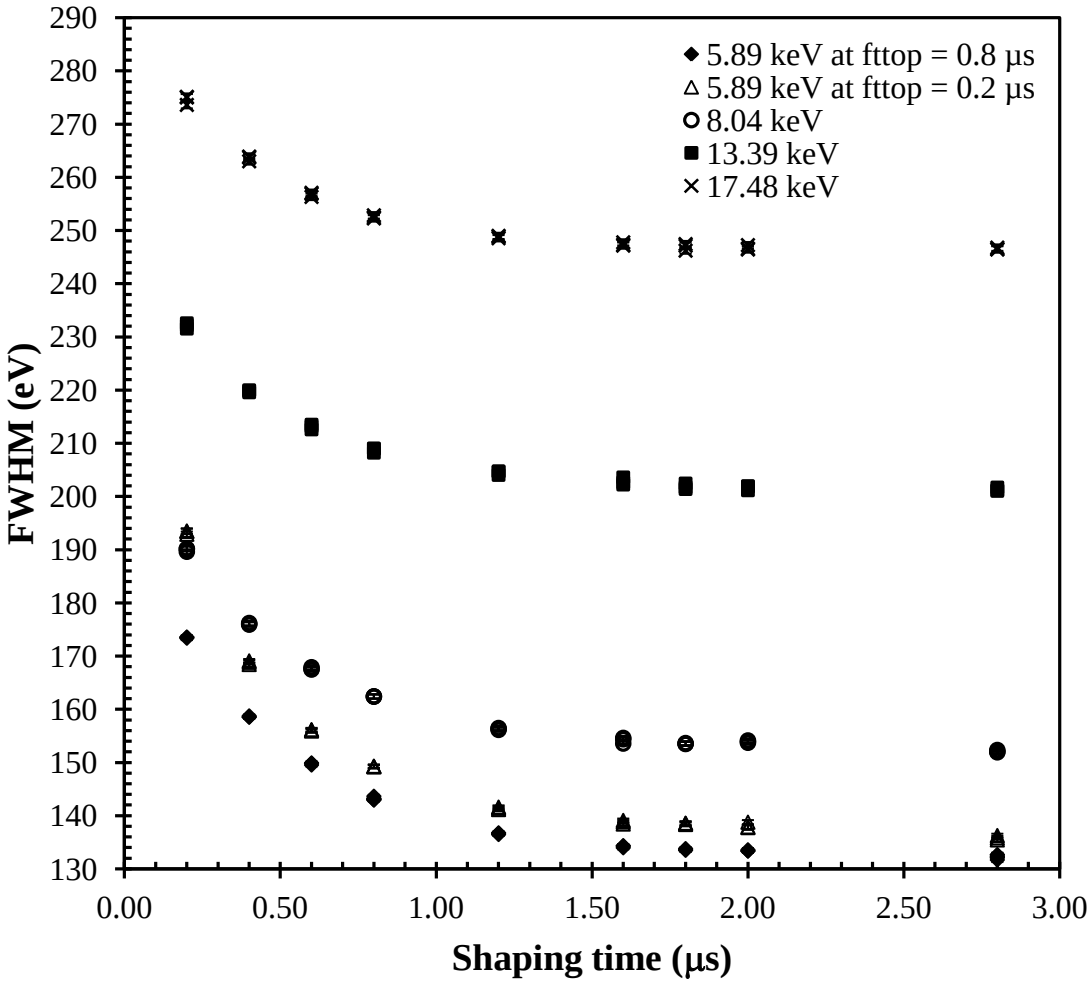

Figure 9: Results of tracking FWHM as rise time is changed, for a fixed flattop. Results are shown for various energies.

Results for changing shaping time, at a second flattop setting of 0.2 μs, are also displayed on the graph at the Mn Kα energy only. As expected, the FWHM improves with increasing shaping time. Beyond a certain shaping time, further FWHM improvement will not be noted unless throughput reduction is accepted. The onset of this is not clearly observed for the choice of short shaping times tested in the current work. Choosing higher shaping times would obviate this plateau but would reduce count rate with respect to the default shaping time of 2.00 μs. It is known that the resolution, and hence FWHM, will degrade as the energy is increased (Knoll, 1999) and this is seen in the graph. It is reassuring that similar trends in FWHM are observed as the energy is increased because a marked difference in these trends, as a function of energy, could call into question the performance of either the detector or pulse processing electronics. For the same range of shaping times (0.2 μs to 2.8 μs), using two flattop settings, it was seen that FWHM

benefits from the larger flattop. For shorter peaking times, a larger flattop component of the output pulse length (2 X rise time + flattop) is beneficial for improving collection of charge carriers (Knoll, 1999). Over shaping times ranging from 2.8 μs to 0.2 μs, the resulting FWHM range was found to change from (131.7±0.4) eV to (173.6±0.3) eV at 0.8 μs, versus (135.4±0.4) eV to (193.5±0.5) eV at 0.2 μs. Note that this figure showed a change in Mn Kα FWHM as shaping time is adjusted from 0.2 – 2.8 μs. The range of FWHMs is 132-174 eV. The previous table has listed FWHM values as part of monitoring drift. These are shown for 3 individual shaping times – 2.0 μs, 1.2 μs and 0.8 μs. The range is 133 – 143 eV. This is a smaller range since the lowest shaping time (0.8 μs) is higher than the lowest used (0.2 μs) in studying the FWHM in this figure.

Peak precision is of use for the range of energies intended in the current application of the SDD. i.e. ~ 10–15 keV, inclusive. When the shaping time was adjusted from 0.2 to 2.8 μs, for a fixed flattop of 0.8 μs, this produced a percent error in peak area (error in peak area/peak area), that ranged from i) 0.290 % to 0.292 % (total spectrum counts: 1.89-1.96 X 10^5) for Cu Kα, ii) 0.321 % to 0.359 % (1.55-1.60 X 10^5) for Rb Kα and iii) 0.252 % to 0.264 % (2.21-2.32 X 10^5) for Mo Kα. These represent a i) 0.83 % change in percent error in the Cu Kα peak area (3.83 % change in throughput; dead time range: 0.32-1.67 %, FWHM: 25.21%), ii) 11.81 % change in percent error in the Rb Kα peak area (3.19 % change in throughput; dead time range: 0.77-3.93 %, FWHM: 15.68%) and iii) 4.52 % change in percent error in the Mo Kα peak area (4.94 % change in throughput; dead times range: 1.08-5.38 %, FWHM: 11.75%). Peak position and FWHM were allowed to vary during the peak fitting process. Since the objective of this work was to track these variations, not only for shaping time but also in order to determine the presence of drift, these parameters were not fixed. In system calibration work with a set of calibration phantoms, both parameters are fixed based on their respective estimates from high concentration phantoms. This helps to lower the uncertainty in fitted peak areas and, consequently, the precision. The requirement to do this is brought about by the comparatively lower counting statistics with calibration phantoms, particularly at lower analyte concentrations, than those observed in the current work. In system calibration, a source-phantom-detector geometry is utilized; the current work reports direct exposure of the detector from the source photons. The source can be moved as close to the detector surface as physically possible, which is often not the case in system calibration work and so the incident source strength is reduced. Thus, the formulation of peak precision reported here may be limited to cases where excellent counting statistics are present (> 100,000 counts).

As the shaping time was increased, thereby lowering the FWHM, clear trends in percent error in peak area or in total count rate (total counts/live time), such as the presence of a valley, were not observed. Thus, in the energy range investigated comparable system performance is observed over a range of shaping times near to, or lower than the internal 2.00 μs analog shaper. With this in mind, the change in FWHM takes on more importance and it may be instructional to give it more weight when

choosing shaping parameters, for phantom calibration with the x-ray tube-based XRF system, than throughput or percent error in peak area. Furthermore, in the case of Sr in bone, discrepancies in the Kα:Kβ ratio have been reported (Heirwegh et al., 2012; Zamburlini et al., 2007) and are of interest since they offer a means of determination of the thickness of the soft tissue overlying bone. The presence of a Zr Kα peak underlying the Sr Kβ peaks could lead to inadequacies in the extraction of the respective peak's area since such interfering features may not be included in a fitting function (Heirwegh et al., 2012). The current work suggests that improving the FWHM, through selection of a higher shaping time, should not severely worsen total throughput and may shed light on the source of the discrepancy in the Sr Kα:Kβ ratio because it would bring out such hidden spectral features and allow for a more detailed analysis of the region of the spectrum containing these peaks.

Due to the immediate availability and ability to cover the relevant range of energies, the Amersham variable x-ray source was used in the current work. The Amersham source showed fewer counts than the Fe-55 source, which allowed a smaller range of throughput values to be accessed. The *in vivo* XRF system intended for use with this SDD is the x-ray tube with optical focusing capabilities and a silver monochromator. The tube has a maximum power of 50 W and hence is a low powered source. The spectra collected from both sources used in the current work show the Kα and much weaker Kβ lines associated with the element of interest, with minimal contribution from other energies. This is very similar to the output of the x-ray tube where a single Ag Kα peak is present with significantly weaker features present at lower energies. Thus, in both the sources used in this work and the intended source for application of the SDD, the main source of total spectrum counts is represented by a single dominant peak. Throughput trends, ought to thus be similar for both scenarios as shaping times are adjusted. From preliminary phantom calibration work (assuming a 90^0 angle between incident x-rays and SDD), the combination of this x-ray tube source with the SDD, even at high power settings, produced dead times in the range of <5% (Sibai, 2011) with Sr bone or As skin calibration phantoms that have been used elsewhere (Studinski et al., 2005; Zamburlini et al., 2006) and that will be used in the future with this XRF detection system. Thus remarkably high throughputs are not expected when this system is used for this particular XRF application and so the results for the higher energies recorded with the Amersham variable x-ray source, though collected at comparatively lower throughputs, are still relevant.

The results of testing the stability of peak position for various shaping times, at various energies, are summarized in table 2.

	ShpT (μs)		**FT (μs)**			
E (eV)	**Max**	**Min**	**Max**	**Min**	**AVG±SDOM (eV)**	**PD (%)**
5,899	2.80	0.20	0.80		5899.63 ± 0.68	0.213 ± 0.004

5,899	2.80	0.20	0.20	5908.65	±	1.55	0.447	±	0.005
5,899	0.80		0.80 0.20	5902.45	±	1.52	0.251	±	0.003
8,048	2.80	0.20	0.80	8047.21	±	0.55	0.133	±	0.004
13,395	2.80	0.20	0.80	13402.27	±	0.48	0.070	±	0.003
17,479	2.80	0.20	0.80	17474.46	±	0.83	0.078	±	0.002

Table 2: List of results for stability in peak position as shaping time is changed (through varying rise time).

It is clear that the peak position demonstrates excellent stability for the range of rise time or flattop settings used here, with the Mn Kα peak. This stability is also noted over a range of energies. At the lowest energy (Mn Kα), the absolute deviation in peak position ranged from (-5.96±0.70) eV to (6.62±0.71) eV, for shaping times ranging from 2.8 μs to 0.2 μs, with a very low RSD of 0.0660 %. At the highest energy (Mo Kα), the absolute deviation in peak position ranged from (-8.56±0.88) eV to (5.06±0.88) eV, for the same range of shaping times, with a RSD of 0.0248 %. The maximum RSD was 0.1413%, which occurred for the shorter flattop setting of 0.2 μs at the Mn Kα energy. The PD values are <0.25%, except for the result at a shorter flat top setting (row 2) which is still less than 0.5%. These results indicate that peak drift is not a concern over the range of investigated energies, as the pulse processing system's shaping time is varied.

The electronic noise was determined for various shaping times (from the data sets used to generate the graphs and tables shown in section 4 – FWHM vs rise time), and the results are shown in figure 10.

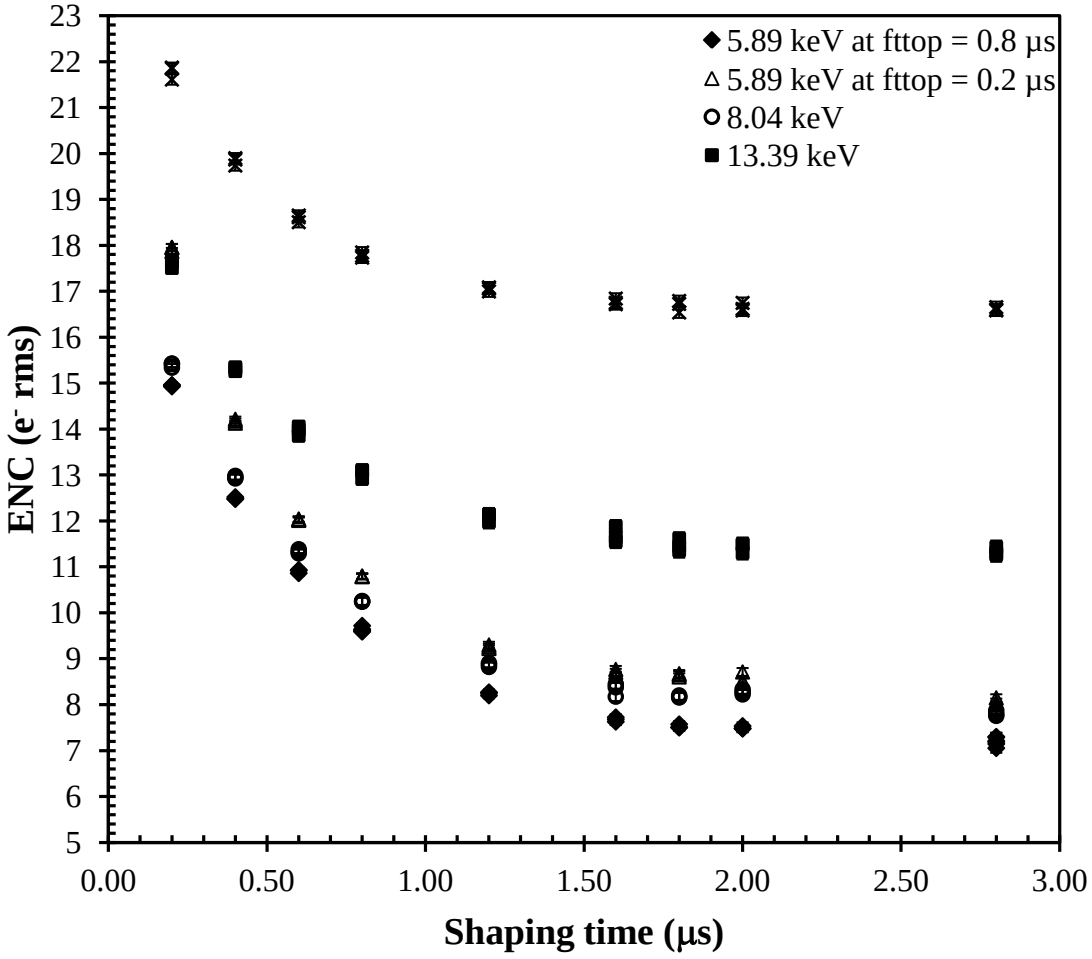

Figure 10: Electronic noise charge shown as a function of shaping time, over the energy range investigated in the current work.

This was tested over a range of energies. As expected, the noise increases with energy (rows 1, 4 – 6), seen from table 3 below, and follows the FWHM vs rise time (or shaping time) trends shown earlier. The benefit of decreasing the flattop, to improve count rate (thereby sacrificing FWHM), results in a slightly higher noise, as seen from rows 1 and 2 of the table. For a shaping time of 2.0 μs, at the Mn Kα energy, the ENC was found to be (7.53±0.08) e^- rms for a flattop of 0.8 μs and (8.71±0.09) μs for a flattop of 0.2 μs. The corresponding ENC values (at a shaping time of 2.0 μs) for higher energies were found to be (8.33±0.09) e^- rms for Cu Kα, (11.48±0.14) e^- rms for Rb Kα and (16.75±0.12) e^- rms for Mo Kα. The minimum and maximum ENC values listed in table 3 were found for shaping times of 2.8 μs and 0.2 μs respectively.

	RisT (μs)		FT (μs)				
E (eV)	**Max**	**Min**	**Max**	**Min**	**AVG±SDOM (e- rms)**		
5,899	2.80	0.20	0.8		9.36	±	0.43
5,899	2.80	0.20	0.2		10.86	±	0.64
5,899	0.80		0.80	0.20	10.20	±	0.11
8,048	2.80	0.20	0.80		10.15	±	0.48
13,395	2.80	0.20	0.80		13.10	±	0.40
17,479	2.80	0.20	0.80		17.97	±	0.33

Table 3: Summary of the electronic noise present in the detection system used, for various energies.

The literature has examples of work investigating the noise in a large area SDD. The ENC in a 100 mm^2 SDD (350 μm thick) was found to be 27 e- rms at a shaping time of 4 μs, for which a Mn Kα resolution of 159 eV was determined (Iwanczyk et al., 1999). More recent studies with approximately the same size detector (280 μm thickness) found ENC to be 14 e^- rms and a Mn Kα FWHM of 170 eV for a shaping time of 8 μs (Metzger et al., 2004). In the case of a monolithic SDD array, with a total active area of 670 mm^2, 9 e^- rms at a shaping time of 0.75 μs (FWHM = 142 eV) worsening to 15 e^- rms at a shaping time of 4 μs (Fiorini et al., 2006). In the current work, even at higher energies, all ENC values are below 20 e^- rms, at a shaping time of 2 μs. Both the FWHM and ENC results reported here compare favorably with literature results for large area SDDs.

4.5. SDD sensitivity stability performance:

The evaluation of system sensitivity stability gave statistical ($N^{1/2}$), experimental (standard deviation) and instrumental uncertainties of 912.19 (0.109%), 2147.82 (0.258%) and 1944.49 (0.233%) respectively, where the terms in brackets are uncertainties relative to the average peak integral expressed as a percentage. The average dead time over the ~100 hours of data acquisition was ~ 5.3 %. An F-test was performed to test the difference between these two sources of uncertainty and it was found to be significant ($p<0.01$). The F-test was calculated as the ratio of the two standard deviations squared and found to be 5.54397, with $F_{\alpha=0.005,949,949} = 0.76827$, indicating that there is enough evidence to reject the null hypothesis that the two standard uncertainties are equal at the $p<0.01$ significance level. The mean integral area over all 950 acquisitions was found to be 832,103 and the ratio of the i^{th} peak integral to average peak integral is shown over 105 hours in figure 11.

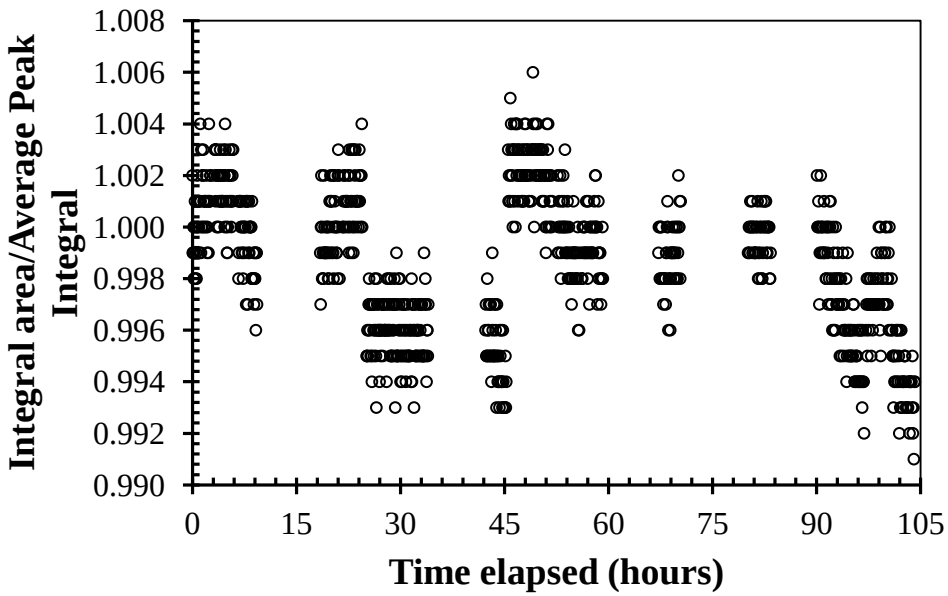

Figure 11: Tracking Peak Integral$_i$/Peak Integral$_{AVG}$ as a function of time. Blank sections correspond to breaks between executions of the programmed sequence.

A distinct drift in this ratio is not present in the data. These results compare to 880.5 (0.113 %), 1014.8 (0.131 %) and 504.5 (0.065 %) respectively, for a mean peak integral of 775,257, found in the referenced work for a dead time of 5.7 %, with an F-test revealing no significant difference between the statistical and experimental uncertainty contributions when the experiment was repeated in a room with air-conditioning (Paepen et al., 2005). Differences in the internal (peltier) cooling element of the SDD, external cooling efficiency (heatsinks, for the current work) and laboratory ventilation (air flow) in the referenced (PiN diode, 500 μm thickness) and current work could account for this difference. The laboratory conditions under which the present work was performed will match those under which the SDD will be used for phantom-based calibration purposes.

4.6. Determination of system dead time:

Figure 12 shows m as a function of n, as outlined in equations 1-4, for the three investigated shaping times.

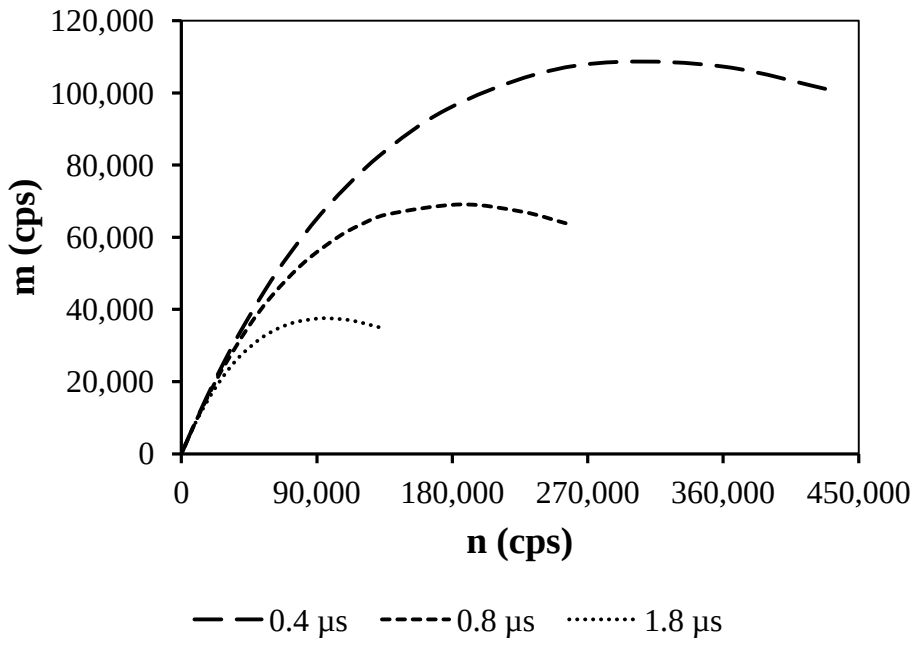

Figure 12: Measured count rate (total recorded counts/real, or clock, time) versus true count rate, shown for three SDD shaping times adjusted using the MCA software.

For each curve, the observed drop-off in measured count rate is observed here up to a limiting count rate. Beyond this limit, the system is overwhelmed by incoming counts and the performance is sufficiently reduced that the measured count rate decreases. This is in agreement with the paralyzable model of dead time. The plot of ln(m/n) as a function of n is shown in figure 13 and is used to determine τ.

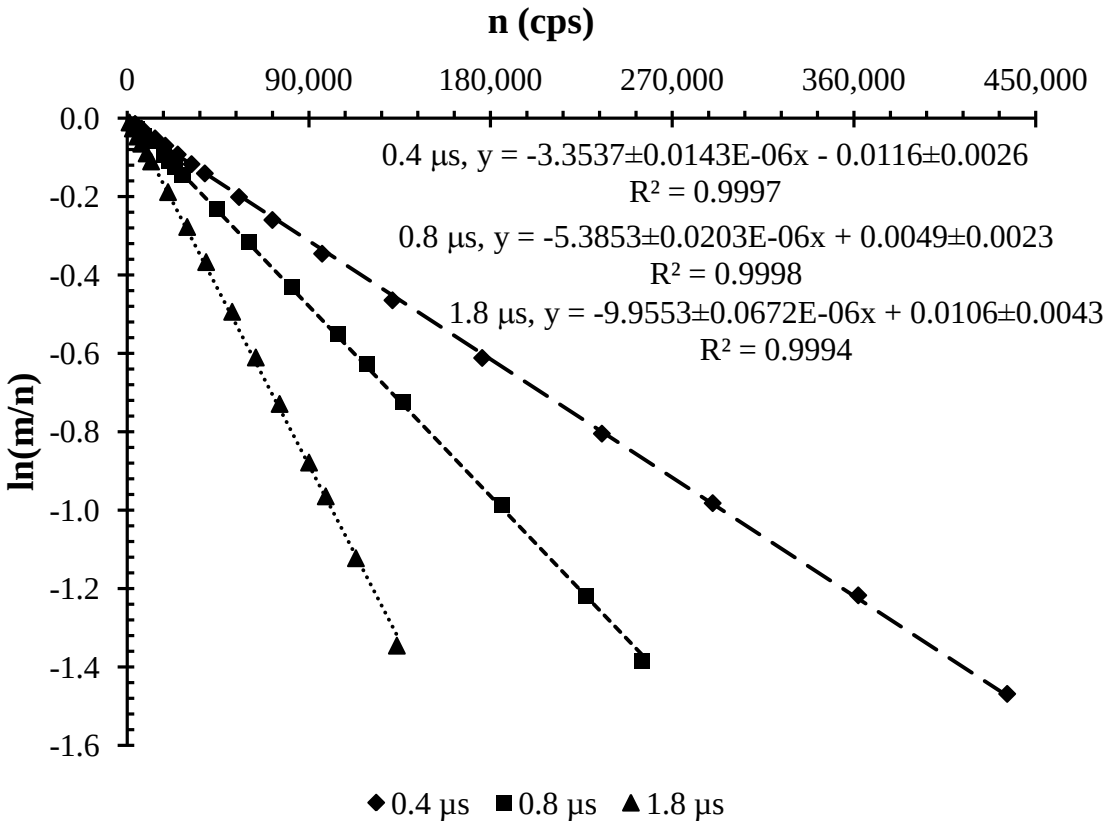

Figure 13: Plot of ln(m/n) versus n, for three shaping times.

From the slope of the line of best fit, the system dead times were found to be (3.35±0.01) μs, (5.39±0.02) μs and (9.96±0.07) μs respectively for shaping times of 0.4 μs, 0.8 μs and 1.8 μs. As expected, the dead time increases for higher shaping times. This is because increasing the shaping time will allow the detection system a longer period of time to improve the accuracy with which incoming pulses are amplified and shaped. During this processing phase, the system is not able to accept new pulses, leading to a longer dead period where the detector is inactive. The result, however, is superior accuracy in pulse shaping.

Using the approach of adjustable x-ray tube current a plot of ln(m/x) as a function of x as per equation 8 is shown, in figure 14, along with the resulting linear fit.

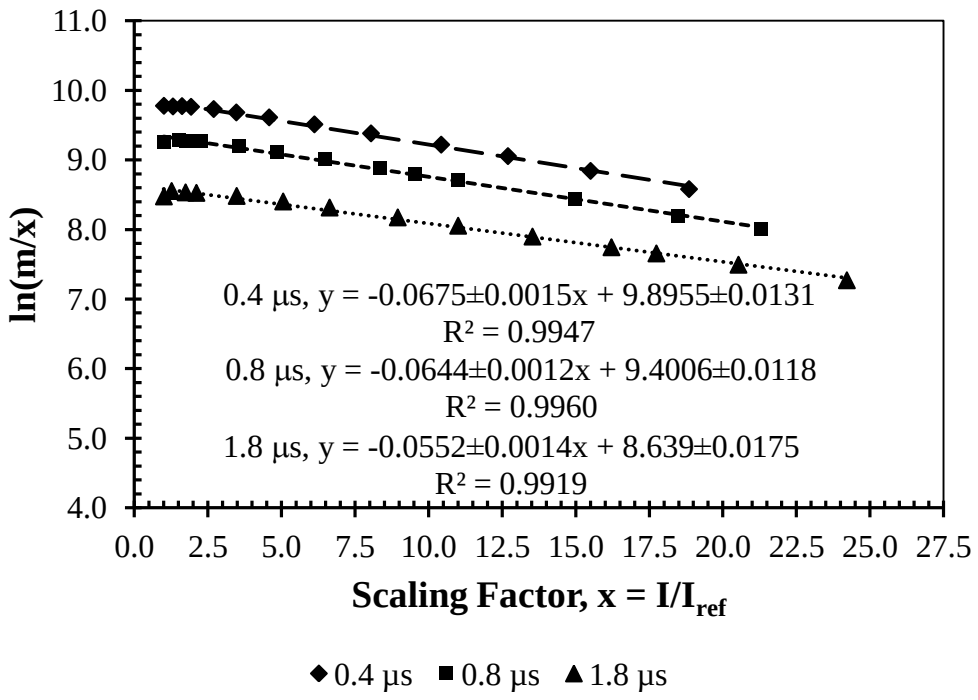

Figure 14: Plot of ln(m/x) versus x, obtained by adjusting x-ray tube current. Here I_i and I_{ref} are tube current settings. Data are shown for three shaping times.

Accordingly, the system dead times for shaping times of 0.4 μs, 0.8 μs and 1.8 μs were found using $\tau = -c/e^d$ to be (3.40±0.09) μs, (5.32±0.12) μs and (9.78±0.31) μs where c and d are the slope and intercept respectively. The error was found by propagation of uncertainties to be $\delta\tau=[(\delta c)^2 + c(\delta d)^2)]^{1/2}/e^d$. These dead times agree, within uncertainty, with those found with the previous approach. As a comparison, dead times of 2.6 μs, 5.1 μs and 7.6 μs were noted for shaping times of 0.5 μs, 1.0 μs and 2.0 μs with a 4-element SDD by SII Nanotechnologies having a total active area of ~50 mm^2 and 4 Canberra 2026x spectroscopy amplifiers, at Brookhaven National Laboratory (Woicik et al., 2010). The dead times found in the current work compare favorably with these results.

5. Conclusion:

The current work characterized an 80 mm^2 active area KETEK Vitus H80 Silicon Drift Detector for Mn Kα peak position, FWHM and sensitivity stability over a period of more than 2 days after powering up. A short warm-up period is noted immediately after powering up the detection system, resulting in peak drift during this time. After this, the absolute deviation in peak position, from the average, is ~0.002 keV (2 eV), with a maximum absolute deviation of 2.5 eV, which are not resolvable. The peak FWHM demonstrates excellent stability over this time with no evidence of drift, while good sensitivity stability was observed over a period of more than 4 days. Based on this, it can be seen that assumptions of fixed peak locations and FWHM can be made when

developing peak-fitting functions to extract net areas from a set of calibration phantoms which differ only in analyte concentration and thus qualify for this assumption. However, such a constraint can only be applied after the warm up period since the fixed FWHM will be broader than its true value to reflect motion of the centroid's channel number before peak position stability is reached. Over a range of energies covering ~5.9 – 17.5 keV, shaping times extending from 0.2 μs to 2.8 μs showed marked improvements in FWHM, for increasing shaping times, without significant degradation in observed count rate. It should be noted that throughput and error in percent peak area in isolation can have their limitations since our group's work involves calculation of minimum detection limits, to calibrate an XRF detection system, which combine errors in peak area with count rate over a series of calibration phantoms with increasing concentration. Variances in the resulting calibration curve are accounted for in determining the MDL but are not discussed in the current work. This limitation aside, the current work suggests that an improvement in FWHM may take precedence over throughput considerations since, for the anticipated range of system dead times, it exhibits a comparatively stronger variation as a function of shaping time. Detection system dead times were found to be (3.353±0.014) μs, (5.385±0.020) μs and (9.955±0.067) μs respectively for shaping times of 0.4 μs, 0.8 μs and 1.8 μs respectively, and these compare favorably with literature values. ENC results were tracked over a range of shaping times; ENCs of (7.53±0.08) e^- rms for Mn Kα, (8.33±0.09) e^- rms for Cu Kα, (11.48±0.14) e^- rms for Rb Kα and (16.75±0.12) e^- rms for Mo Kα were found for a shaping time of 2.00 μs and compare favorably to results from the literature. Both these features would benefit from a higher shaping time and, when combined with previously documented trouble in resolving and analyzing the Sr Kβ in bone phantoms, further indicate the increased importance to be placed on FWHM if percent error in peak area and total throughput are considered. Future work is planned to evaluate the performance of the SDD detection system, in comparison to a Si(Li) detection system, in terms of Sr and As MDLs, with the monochromator x-ray tube source.

Acknowledgements:
The authors would like to thank Steffen Pahlke from Ketek GmbH for assisting with the set-up of the detector and James Collins Jr. and Mathieu Morelle from Canberra and Lesley Egden from McMaster University for assistance with setting up the DSA 1000 pulse processing system and batch acquisition protocol, both via email correspondence and in person. The authors would also like to thank John Cave, Scott McMaster and Jason Falladown from McMaster University for construction of the monochromator x-ray tube-based detection system housing and implementation of its safety interlock system. The authors hold Discovery Grant funding from the Natural Sciences and Engineering Research Council of Canada which was used in partial support of this work.

References:

Ahlgren, L., Mattsson, S., 1981. Cadmium in man measured in vivo by x-ray fluorescence analysis. Phys. Med. Biol. 26, 19–26.

Atanackovic, J., Grinyer, J., Chettle, D.R., Byun, S.H., 2007. The comparison of two MCNP models used for prompt gamma in vivo detection of cadmium and mercury. Nucl. Instruments Methods Phys. Res. Sect. B Beam Interact. with Mater. Atoms 263, 169–174.

Behinaein, S., Chettle, D.R., Atanackovic, J., Egden, L.M., Fleming, D.E.B., Nie, L.H., Richard, N., Stever, S., 2011. In vivo measurement of lead in the bones of smelter workers using the four-element "clover-leaf" geometry detector system. Phys. Med. Biol. 56, 653–665.

Byun, S.H., Pejović-Milić, A., McMaster, S., Matysiak, W., Liu, Z., Watters, L.M., Prestwich, W. V, McNeill, F.E., Chettle, D.R., 2007. Dosimetric characterization of the irradiation cavity for accelerator-based in vivo neutron activation analysis. Phys. Med. Biol. 52, 1693–1703.

Campbell, J.L., McDonald, L., Hopman, T., Papp, T., 2001. Simulations of Si(Li) x-ray detector response. X-Ray Spectrom. 30, 230–241.

Campbell, J.L., Millman, B.M., Maxwell, J.A., Perujo, A., Teesdale, W.J., 1985. Analytic fitting of monoenergetic peaks from Si(Li) X-ray spectrometers. Nucl. Instruments Methods Phys. Res. Sect. B Beam Interact. with Mater. Atoms 9, 71–79.

Carlton, R.A., 2011. Pharmaceutical Microscopy (Google eBook). Springer, New York, USA.

Chamberlain, M., Gräfe, J.L., Aslam, Byun, S.-H., Chettle, D.R., Egden, L.M., Webber, C.E., McNeill, F.E., 2012. In vivo quantification of bone-fluorine by delayed neutron activation analysis: a pilot study of hand-bone-fluorine levels in a Canadian population. Physiol. Meas. 33, 375–84.

Da Silva, E., Pejović-Milić, A., Heyd, D. V., 2008. The use of teeth as the site for the in vivo or ex vivo quantification of skeletal strontium by energy-dispersive X-ray fluorescence spectrometry: A feasibility study. J. Anal. At. Spectrom. 23, 527–534.

Davis, K., Pejović-Milić, A., Chettle, D.R., 2008. In vivo measurement of bone aluminum in population living in southern Ontario, Canada. Med. Phys. 35, 5115-5123.

Deslattes, R., Kessler, E., Indelicato, P., de Billy, L., Lindroth, E., Anton, J., 2003. X-ray transition energies: new approach to a comprehensive evaluation. Rev. Mod. Phys. 75, 35–99.

Fiorini, C., Gola, A., Longoni, A., Zanchi, M., Restelli, A., Perotti, F., Lechner, P., Soltau, H., Strüder, L., 2006. A large-area monolithic array of silicon drift detectors for medical imaging. Nucl. Instruments Methods Phys. Res. Sect. A Accel. Spectrometers, Detect. Assoc. Equip. 568, 96–100.

Fiorini, C., Lechner, P., 1999. Continuous charge restoration in semiconductor detectors by means of the gate-to-drain current of the integrated front-end JFET. IEEE Trans. Nucl. Sci. 46, 761–764.

Gatti, E., Manfredi, P.F., 1986. Processing the signals from solid-state detectors in elementary-particle physics. La Riv. del Nuovo Cim. 9, 1–146.

Gräfe, J.L., McNeill, F.E., Byun, S.H., Chettle, D.R., Noseworthy, M.D., 2011. The feasibility of in vivo detection of gadolinium by prompt gamma neutron activation analysis following gadolinium-based contrast-enhanced MRI. Appl. Radiat. Isot. 69, 105–11.

Gräfe, J.L., McNeill, F.E., Chettle, D.R., Byun, S.H., 2012. Characteristic X ray emission in gadolinium following neutron capture as an improved method of in vivo measurement: A comparison between feasibility experiment and Monte–Carlo simulation. Nucl. Instruments Methods Phys. Res. Sect. B Beam Interact. with Mater. Atoms 281, 21–25.

Grinyer, J., Byun, S.H., Chettle, D.R., 2005. In vivo prompt gamma neutron activation analysis of cadmium in the kidney and liver. Appl. Radiat. Isot. 63, 475–9.

Grinyer, J., Popovic, M., Chettle, D.R., 2007. Detection of mercury in the kidney via source-excited x-ray fluorescence. X-Ray Spectrom. 36, 99–103.

Hansen, J.S., McGeorge, J.C., Nix, D., Schmidt-Ott, W.D., Unus, I., Fink, R.W., 1973. Accurate efficiency calibration and properties of semiconductor detectors for low-energy photons. Nucl. Instruments Methods 106, 365–379.

Heirwegh, C.M., Chettle, D.R., Pejovic-Milic, A., 2012. Ex vivo evaluation of a coherent normalization procedure to quantify in vivo finger strontium XRS measurements. Med. Phys. 39, 832–41.

Iwanczyk, J.S., Patt, B.E., Tull, C.R., Segal, J.D., Kenney, C.J., Bradley, J., Hedman, B., Hodgson, K.O., 1999. Large area silicon drift detectors for X-rays-new results. IEEE Trans. Nucl. Sci. 46, 284–288.

Jonson, R., Mattsson, S., Unsgaard, B., 1988. A method for in vivo analysis of platinum after chemotherapy with cisplatin. Phys. Med. Biol. 33, 847–57.

Jorch, H.H., Campbell, J.L., 1977. On the analytic fitting of full energy peaks from Ge(Li) and Si(Li) photon detectors. Nucl. Instruments Methods 143, 551–559.

Jordanov, V.T., Knoll, G.F., 1994. Digital synthesis of pulse shapes in real time for high resolution radiation spectroscopy. Nucl. Instruments Methods Phys. Res. Sect. A Accel. Spectrometers, Detect. Assoc. Equip. 345, 337–345.

Knoll, G.F., 1999. Radiation Detection and Measurement, 3rd ed. John Wiley & Sons Inc.

Lechner, P., Eckbauer, S., Hartmann, R., Krisch, S., Hauff, D., Richter, R., Soltau, H., Strüder, L., Fiorini, C., Gatti, E., Longoni, A., Sampietro, M., 1996. Silicon drift detectors for high resolution room temperature X-ray

spectroscopy. Nucl. Instruments Methods Phys. Res. Sect. A Accel. Spectrometers, Detect. Assoc. Equip. 377, 346–351.
Lechner, P., Pahlke, A., Soltau, H., 2004. Novel high-resolution silicon drift detectors. X-Ray Spectrom. 33, 256–261.
Lépy, M.C., Campbell, J.L., Laborie, J.M., Plagnard, J., Stemmler, P., Teesdale, W.J., 2000. Experimental study of the response of semiconductor detectors to low-energy photons. Nucl. Instruments Methods Phys. Res. Sect. A Accel. Spectrometers, Detect. Assoc. Equip. 439, 239–246.
Lépy, M.-C., Plagnard, J., Ferreux, L., 2003. Study of the response function of a HPGe detector for low-energy X-rays. Nucl. Instruments Methods Phys. Res. Sect. A Accel. Spectrometers, Detect. Assoc. Equip. 505, 290–293.
Marquardt, D.W., 1963. An Algorithm for Least-Squares Estimation of Nonlinear Parameters. J. Soc. Ind. Appl. Math. 11, 431–441.
Metzger, W., Engdahl, J., Rossner, W., Boslau, O., Kemmer, J., 2004. Large-area silicon drift detectors for new applications in nuclear medicine imaging. IEEE Trans. Nucl. Sci. 51, 1631–1635.
Nicholson, P.W., 1974. Nuclear electronics. Wiley, New York, USA.
Nie, H., Chettle, D., Luo, L., O'Meara, J., 2006. In vivo investigation of a new 109Cd gamma-ray induced K-XRF bone lead measurement system. Phys. Med. Biol. 51, 351–60.
Nie, H., Chettle, D., Stronach, I., Arnold, M., Huang, S., McNeill, F., O'Meara, J., 2004. A study of MDL improvement for the in vivo measurement of lead in bone. Nucl. Instruments Methods Phys. Res. Sect. B Beam Interact. with Mater. Atoms 213, 579–583.
O'Meara, J.M., Börjesson, J., Chettle, D.R., Mattsson, S., 2001. Normalisation with coherent scatter signal: improvements in the calibration procedure of the 57Co-based in vivo XRF bone-Pb measurement. Appl. Radiat. Isot. 54, 319–25.
Paepen, J., Osorio, V., Van Espen, P., Evrard, O., Van Buul, L., Keters, M., Jordanov, V.T., Burger, P., 2005. High-performance x-ray silicon detector for reliable industrial and research XRF applications. X-Ray Spectrom. 34, 417–420.
Phillips, G.W., Marlow, K.W., 1976. Automatic analysis of gamma-ray spectra from germanium detectors. Nucl. Instruments Methods 137, 525–536.
Pinotti, E., Longoni, A., Gambelli, M., Struder, L., Lechner, P., Zanthier, C.V., Kraner, H., 1995. Room temperature, high-resolution X-ray spectroscopy with silicon drift chambers. IEEE Trans. Nucl. Sci. 42, 12–16.
Radeka, V., Rahek, P., Rescia, S., Gatti, E., Longoni, A., Sampietro, M., Bertuccio, G., Holl, P., Struder, L., Kemmer, J., 1989. Implanted silicon JFET on completely depleted high-resistivity devices. IEEE Electron Device Lett. 10, 91–94.
Scholze, F., Procop, M., 2001. Measurement of detection efficiency and response functions for an Si(Li) x-ray spectrometer in the range 0.1-5 keV. X-Ray Spectrom. 30, 69–76.
Sibai, M., 2011. Second generation of the diagnostic tool for the In vivo measurement of strontium levels in human bone. Theses Diss.
Strüder, L., Soltau, H., 1995. High Resolution Silicon Detectors for Photons and Particles. Radiat Prot Dosim. 61, 39–46.
Studinski, R., O'Meara, J., McNeill, F., 2008. The feasibility of in vivo measurement of arsenic and silver by x-ray fluorescence. X-Ray Spectrom. 37, 51–57.
Studinski, R.C.N., McNeill, F.E., Chettle, D.R., O'Meara, J.M., 2004. XRF analysis of arsenic-doped skin phantoms. X-Ray Spectrom. 33, 285–288.
Studinski, R.C.N., McNeill, F.E., Chettle, D.R., O'Meara, J.M., 2005. Estimation of a method detection limit for an in vivo XRF arsenic detection system. Phys. Med. Biol. 50, 521–530.
Studinski, R.C.N., McNeill, F.E., O'Meara, J.M., Chettle, D.R., 2006. A method detection limit for potential in vivo arsenic measurements with a 50 W x-ray tube. Phys. Med. Biol. 51, N381–7.
Taylor, J.R., 1997. An Introduction Error Analysis: The Study of Uncertainties in Physical Measurements, 2nd ed. University Science Books, Sausalito, California, USA.
Uher, J., Roach, G., Tickner, J., 2010. Peak fitting and identification software library for high resolution gamma-ray spectra. Nucl. Instruments Methods Phys. Res. Sect. A Accel. Spectrometers, Detect. Assoc. Equip. 619, 457–459.
Van Gysel, M., Lemberge, P., Van Espen, P., 2003. Implementation of a spectrum fitting procedure using a robust peak model. X-Ray Spectrom. 32, 434–441.
Woicik, J.C., Ravel, B., Fischer, D.A., Newburgh, W.J., 2010. Performance of a four-element Si drift detector for X-ray absorption fine-structure spectroscopy: resolution, maximum count rate, and dead-time correction with incorporation into the ATHENA data analysis software. J. Synchrotron Radiat. 17, 409–13.
Zamburlini, M., 2008. In vivo measurement of bone strontium with x-ray fluorescence.
Zamburlini, M., Pejović-Milić, A., Chettle, D.R., 2006. Evaluation of geometries appropriate for 125I in vivo bone strontium X-ray fluorescence measurement. J. Radioanal. Nucl. Chem. 269, 625–629.

Zamburlini, M., Pejović-Milić, A., Chettle, D.R., Webber, C.E., Gyorffy, J., 2007. In vivo study of an x-ray fluorescence system to detect bone strontium non-invasively. Phys. Med. Biol. 52, 2107–22.

Chapter 5 Comparison of detector types:

Draft III investigates a performance evaluation of the silicon drift detector (SDD) against the Si(Li) detector, using a benchtop XRF system. The appraisal is performed so as to offer an indication of the capabilities of the new detector type against the existing detector technology in terms of minimum detection limit (MDL) and As Kα:Kβ ratio. The normalization against scatter peaks is also investigated with each type of detector. This is done in order to account for differences in source strength and phantom positioning (system dead time) from measurements conducted using one set of experimental conditions to those acquired under another set. The MDL application of the SDD as part of this phantom-based calibration of the benchtop XRF system is the natural follow-up to the characterization of the new detector type.

5.1 Motivation and chosen specifications:

The benefits of an SDD are due to its lower capacitance, which allows for such a detector to be used in high count-rate applications. Also, a superior energy resolution is possible and this allows for better separation of spectral features in data analysis. In the current application, the lower leakage current, due to the lower capacitance, with such a detector eliminates the need for a bulky LN_2 dewar for cooling. Peltier cooling is used instead allowing for such a detector to be positioned closer to the phantom. This allows for an enhancement in the detection system's sensitivity to small changes in concentration and allows the opportunity to improve the system's performance in terms of its reported MDL.

5.2 Draft for article III follows:

Performance appraisal of Silicon Drift Detector (SDD), in comparison to Si(Li) detector, for intended application to measure arsenic in skin using K-shell EDXRF.

Authors
Elstan D. Desouza[a] , Fiona E. McNeill[a], David R. Chettle[a], Ana Pejovic-Milic[b], David E. B. Fleming[c]

Affiliations:
[a] Department of Medical Physics and Applied Radiation Sciences, McMaster University, Canada
[b] Department of Physics, Ryerson University, Canada
[c] Department of Physics, Mount Allison University, Canada

Manuscript will be submitted: App. Rad. Isotopes. 2013

Author contributions:
Elstan Desouza was responsible for experimental setup, data acquisition and analysis.
Ana Pejovic-Milic offered unrestricted use of equipment and her previous research documented setup, performance evaluation and optimization of the equipment.
David Chettle and David Fleming assisted in interpretation of data.
Elstan Desouza was responsible for preparation of the draft manuscript.
Fiona McNeill supervised and guided the research.

Abstract:

This work compares the performance of an 80 mm^2 active area Silicon Drift Detector (SDD) with a 200 mm^2 Si(Li) detector. Full width half maximum (FWHM), minimum detection limit (MDL) of arsenic in skin phantoms, peak precision (relative error) and tail-to-peak areas were examined as a function of SDD shaping time. The MDL with each detector was investigated with the SDD offering a lower MDL than the Si(Li) detector and a lower percent dead time. Additional parameters such as scatter peak characterization and arsenic Kα:Kβ ratio were also compared for both detectors. With the exception of the lowest investigated shaping time (0.2 μs), the mean arsenic tail-to-peak area was unchanged over shaping times ranging from 0.4-2.4 μs and was very similar to that obtained with the Si(Li) detector. The FWHM was largely unchanged over 1.2-2.4 μs, with negligible improvement in total count rate suggesting that a higher shaping time may be useful for the currently available source strength. With both detectors, normalization to Compton scatter was deemed to be more appropriate for this application than coherent scatter due to a significant improvement in peak statistics under this feature, brought about by a higher absorption cross section in the skin phantoms. This choice was further motivated the presence of a deeper mean interaction depth, with both detectors, than that predicted by the chosen 90^0 source-detector geometry, nullifying the ability of coherent normalization to correct for arsenic depth variations in skin.

1. Introduction:

Arsenic (As) is an element naturally found to occur everywhere (Fishbein, 1981). A form of cancer (Blackfoot disease) originated in areas with a high As water concentration (Chen et al., 1985) and a higher incidence of cancer related deaths may have resulted from As contaminated drinking water in the United States (Morales et al., 2000). High As concentrations, on the order of several ppm (parts per million), have been observed in skin scales and nails of people exposed to As (Das et al., 1995). Other means of measuring arsenic levels involve tracking its concentration in hair and nails soaked in arsenite, but these were found to be unsatisfactory for use as a biomarker for its presence due to contamination (Maes and Pate 1977). The implications of the structure of skin suggest that arsenic is contained in the epidermal layer and that its distribution would be directly proportional to the concentration of keratin (Misbahuddin et al., 2008). Keratinocytes are found deeper in the epidermis. By comparison to hair and nails, skin is an organ with an elevated threat of As related lesions. Thus, skin is as an appropriate

target site for measurement of accumulation (and ideally long term exposure) of arsenic. It is potentially both a site of cumulative exposure and an organ-at-risk. Repeatable non-invasive measurements that determine arsenic levels in the directly affected organ are desirable. X-Ray Fluorescence (XRF) is an example of a non-invasive method that may permit such repeatable measurements.

The importance of quantifying arsenic levels in skin, via *in vivo* XRF, lie in the technique's ability to indicate long term build-up of the element in the target organ/site. A previous XRF detection system developed for this purpose made use of I-125 x-rays to excite arsenic x-rays in skin. Later an x-ray tube based approach was used with an improvement in minimum detectable limit (MDL) noted (Studinski et al., 2006), warranting its use moving forward. Also, since this time, silicon drift detector (SDD) technology has become increasingly popular due to its potential for dramatic improvements in resolution, without compromising total throughput. The above mentioned works utilized a lithium drifted silicon detector [Si(Li)], along with digital signal processing electronics, to capture the emitted characteristic x-rays for use in quantification analysis. The count rate of an element's characteristic x-rays is proportional to its concentration in the (interrogated) volume of interest if the volume is contained in the target site. eg. bone, skin, etc. This allows for a series of analyte-doped calibration phantoms to be used in determining the concentration of a particular element in that target site. Some examples of K and L XRF *in vivo* include lead in bone using Cd-109 for excitation (Behinaein et al., 2011; Nie et al., 2006, 2011), strontium in bone (Pejović-Milić et al., 2004; Zamburlini et al., 2007) and arsenic in skin using I-125 (Studinski et al., 2005) and uranium in bone using Co-57 (O'Meara et al., 1998). Strontium in bone was also measured *ex vivo*, using this technique (Heirwegh et al., 2012, 2010).

The emergence of the SDD can be traced back to the mid 1980s (Gatti and Rehak, 1984; Rehak et al., 1985) with the use of commercially available modules and testing prototypes appearing the literature in the early 1990s (Bertuccio et al., 1992; Lechner et al., 2004; Metzger et al., 2004; Strüder and Soltau, 1995). The major advantage of SDDs is that their noise, at high count rates, is heavily reduced in comparison to Si(Li) detectors. This is also true for larger area SDDs. The benefit in noise level is due to a severe reduction in capacitance, thereby driving down the lowest achievable resolution towards the theoretical value, which should allow for a higher throughput. An improved throughput should improve precision in XRF measurements and subsequently in the MDL of an *in vivo* detection system. However, there are two factors countering this advantage. First, the SDD benefits are particularly evident for low energies because the active detector thickness (depth) is reduced from a few mm, as in the case of a Si(Li) detector, to ~500 μm, and thus a relative drop-off in the performance gain may be expected at higher energies than at lower ones since full energy deposition is not possible. A detector's efficiency depends on the amount of depletion of the active volume. For a Si(Li) detector, x-ray absorption in the detector thickness of a few mm is 100% for As Kα and Kβ energies, compared to 95% and 89% respectively in the 450 μm

thick SDD wafer. Second, the maximum active area in commercially available SDDs is typically two or more times smaller than commonly available Si(Li) detectors. Longer counting times are required to offset this.

As mentioned earlier, our laboratory has projects involved in detection of strontium in bone and arsenic in skin and previous work has involved use of a Si(Li) detector. A new SDD has become available and is intended for use as a replacement detector in these and other projects in a similar energy range. Since counts scale with area, one would need to count for more than 10 times as long with, for example, a 7 mm^2 active area detector (SDD) as with a 100 mm^2 SDD. Also, the geometrical difference between the two SDDs is sufficiently large to mean that one might not be fully confident in extrapolating from one detector size (active area) to the other. So, on balance, a smaller size active area SDD with superior resolution is not close enough to this application's likely eventual requirements to be very useful. With this in mind, the largest commercially available single-element SDD was purchased from Ketek GmbH (Munich, Germany). An internal Si wafer collimator (Zr) would interfere with other applications utilizing the SDD and so a special multi-element collimator was used as a replacement and the collimated area is 80 mm^2.

The current work reports on an investigation of the SDD's performance, at various shaping times – FWHM and peak precision are compared, with the intention of choosing optimal conditions for use with arsenic calibration phantoms and subsequently *in vivo*. It reports the MDL achieved with the existing Si(Li) detector and SDD, using an x-ray tube as the exciting source so as to compare directly the SDD's performance to the currently used Si(Li) detector; a comparison of MDLs, with shaping time, is also presented. Finally, it evaluates scatter normalization and the As Kα:Kβ ratio achievable with the SDD, both of which are of relevance to the intended application of the SDD in our group.

2. Equipment setup and method:

2.1. Silicon Drift Detector (SDD) DSA 1000 system:

The SDD system comprised an AXAS-A (Analytical X-Ray Acquisition System-Analog) module comprising an 80 mm^2 active area Vitus H80 single-element SDD (KETEK GmbH, Munich, Germany), preamplifier and shaping amplifier. A KETEK analog ADC and MCA were provided in a separate unit that can be connected via a USB port to a host PC on which MCA software was installed. It also functioned as a power supply. For the current work, the AXAS-A preamplifier output was coupled to an advanced DSP-capable Canberra Digital Spectrum Analyzer (DSA1000) MCA unit (Canberra Inc., Meriden, Connecticut, USA). With the DSA1000, as with other DSPs, preamplifier signal digitization is performed at the beginning of the pulse processing sequence. Analog-based functions in the filtering process are thus minimized in the DSA1000. Digitized signals are filtered to produce a trapezoidal pulse shape that cannot be achieved with traditional analog pulse processing. The DSA 1000 allows for a choice of up to 40 trapezoidal rise times range from 0 to 38 μs and up to 21 flat top settings

ranging from 0 to 3 μs. Peak stability is superior to that possible with analog techniques. A USB interface was used for communication with the host at 12 Mbits/sec. An RS232 serial connection was also available but not used in the current work. The DSA1000 MCA was controlled via a host PC with Canberra's Genie2K software installed.

2.2. Lithium Drifted Silicon Detector [(Si(Li)] DSPEC^{PLUS} system:

The Si(Li) detector system was made up of an Ortec SLP1080 Si(Li) detector (Ortec, Oak Ridge, TN, USA) coupled to an Ortec DSPEC PLUS MCA box. Output pulses from the preamplifier are processed by this MCA box. In the current work, communication with the host PC was accomplished using an Ethernet BNC connector, although a 9-pin RS-232-C connector was also available. As with the Canberra DSA 1000, the trapezoidal pulse parameters – rise time and flat top – can be adjusted. The DSPEC PLUS unit allows 115 rise time choices, ranging from 0.8 to 23 μs, and 22 flat top widths ranging from 0.3 to 2.4 μs. The DSPEC PLUS MCA was controlled using Ortec's MAESTRO-32 MCA software. This software was also used to control the high voltage required for the Si(Li) detector, which was -1000 V.

2.3. Skin phantoms:

Arsenic measurements were performed using resin phantoms, with a detection system using the SDD DSA 1000 system and Si(Li) DSPEC PLUS system. The composition of the resin was 5% H, 35% O, 60% C (Gawdzik et al., 2001) with a measured density of 1.20 g/cm^3. The mean free path of arsenic x-rays in resin is 2.74 mm for the As Kα, 3.72 mm for the As Kβ and 17.22 mm for the Ag Kα; the corresponding mean free paths in soft tissue (ICRU-4 Component with a density of 1.00 g/cm^3, NIST) are 2.36 mm for the As Kα, 3.22 mm for the As Kβ and 16.30 mm for the Ag Kα. The composition of soft tissue (ICRU-4 Comp) is 10.1% H, 11.1% C, 2.6% N, 76.2% O. The oxygen content is more than twice as high, in soft tissue, as it is in resin, however, the model for resin contains a much carbon carbon content by comparison. Thus, despite its higher density, the mean free path in resin is higher than it is in soft tissue. By comparison, the skin thickness measured during previous arsenic *in vivo* work was found to range from 1.0-2.5 mm (Studinski et al., 2005). These give probing depths (assuming 99.999999% attenuation in the Bethe exponential decay equation) of 1.26 cm, 1.71 cm and 7.93 cm versus 1.09 cm, 1.49 cm and 7.51 cm for the As Kα, As Kβ and Ag Kα in resin and soft tissue respectively.

2.3. Experimental Procedure:

The resin phantoms were circular discs 2.8 mm thick with a diameter of (50.0±0.2) cm. The phantoms were placed in front of a silver target x-ray tube with a monochromator and optical focusing (XOS, Albany, NY, USA), with adjustable accelerating voltage and current meters. The phantoms were placed at a source-phantom distance of (78.2±0.2) cm, where the x-ray beam size was measured using radiochromic film to be ~ 8 X 8 mm^2. This distance was chosen because it is the largest source-phantom distance accessible by the Si(Li) detector and its liquid-nitrogen cooling dewar.

Each detector was used individually. The detector was placed at angle of 90^0 with respect to the incident x-ray beam. A square nylon backing (5.0 cm side) was placed behind the resin phantoms to mimic bulk tissue behind skin. The resin-nylon combination was placed at 45^0 to the incident beam. Three 1800 second (real time) measurements were performed for each phantom. The same Si(Li) detector used here was used extensively in previous work in our group, with arsenic in skin and strontium in bone, with a shaping time of 5-6 μs (Heirwegh et al., 2012; Pejović-Milić et al., 2004; Studinski et al., 2006; Zamburlini et al., 2007). Thus, the DSPEC PLUS was set to a shaping time of 6 μs, when coupled to the Si(Li) detector, as per previously chosen values. As the objective here is to evaluate the performance of the SDD detection system (new) against the Si(Li) system (existing), the Si(Li) shaping parameters were held fixed (while various SDD shaping parameters were investigated), the x-ray tube voltage and current were unchanged and the phantom-detector separation was fixed [(1.5±0.2) cm for the SDD or (2.0±0.2) cm for the Si(Li) detector with the resin phantom. These were the shortest possible phantom-detector distances and they were limited by the 45^0 geometry.

2.4. Data Analysis:

Spectral analysis was performed with the non-linear least squares Marquardt-Levenberg fitting routine (Marquardt, 1963) utilizing combinations of various expressions that are commonly employed for this purpose, including

$$G(E) = \frac{A}{\sqrt{2\pi}\sigma} exp\left[-\frac{(E-E_0)^2}{\sqrt{2}\sigma}\right] \quad (1)$$

$$T(E) = \frac{H}{2} exp\left(\frac{E-E_0}{\beta}\right) erfc\left(\frac{E-E_0}{\sqrt{2}\sigma} + \frac{\sigma}{\beta\sqrt{2}}\right) \quad (2)$$

where A is the Gaussian area, H is the tail amplitude, E_0 is the Gaussian centroid, σ is the Gaussian width and β is the tail shaping coefficient (Campbell et al., 2001; Jorch and Campbell, 1977; Uher et al., 2010). Data analysis was performed using Microcal Origin ver. 9.0 (Originlab, Northampton, MA, USA).

For the application being considered here, the line $y_{exp} = mx_{exp} + b$ represents a phantom calibration line, obtained by plotting fitted As Kα peak area versus phantom concentration. This will eventually be used to determine the arsenic concentration in ppm in an unknown sample, x_{exp}, where $x_{exp} = (y_{exp} - b)/m$ and y_{exp} is the peak area obtained from the spectrum for that specific unknown. Here y_{exp} has its own uncertainty, from peak fitting, and so do b and m, so the variance of x_{exp} then includes the variances of y_{exp}, m and b with the last two contributions coming from the linear least squares fit. In addition the covariance of b and m must also be added to these three terms (Taylor,

1997). Thus, when each phantom is measured n times, the variance of x_{exp}, as obtained from the above calibration line, is then given by

$$\sigma_{x_{exp,j}}{}^2 = \left(\frac{\sigma_{y_{exp,j}}}{m}\right)^2 + \left(\frac{\sigma_b}{m}\right)^2 + \frac{\sigma_m{}^2(b - y_{exp,j})^2}{m^4} + 2\left(\frac{y_{exp,j} - b}{m^3}\right)\left(-\frac{\sigma_y{}^2 \sum_{i=1}^{N} x_i}{\Delta}\right) \quad (3)$$

for j = [1, n] (Salter, 2000). Here, $y_{exp,j} \pm \sigma_{y[exp,j]}$ is the net peak area of a blank (0 ppm) arsenic calibration phantom, $\sigma_b{}^2$ is the variance in the y-intercept, $\sigma_m{}^2$ is the variance in the slope and $\sigma_y{}^2$ is the variance in the linear fit given by

$$\sigma_y{}^2 = \frac{\sum_{i=1}^{N}[y_i - (mx_i + b)]^2}{N - 2} \quad (4)$$

In the fourth term, the term inside the rightmost bracket is the covariance (Harris, 2006). The standard error of the mean $\sigma_{x[exp]}$ is then given by (Kotulski, 2010)

$$SDOM_{\bar{\sigma}_{x_{exp}}} = \sum_{j=1}^{n} \frac{(\bar{\sigma}_{x_{exp}} - \sigma_{x_{exp,j}})^2}{n(n-1)} \quad (5)$$

Then, the Minimum Detection Limit (MDL) is then determined as

$$MDL = 2\,(\bar{\sigma}_{x_{exp}} \pm SDOM_{\bar{\sigma}_{x_{exp}}}) \quad (6)$$

as has been previously used by numerous workers in our group (Da Silva et al., 2008; Fleming and Gherase, 2007; Grinyer et al., 2007; Pejović-Milić et al., 2004; Somervaille et al., 1985; Studinski et al., 2004).

3. Results and Discussion:

Spectra and Peak fitting:

By way of example, a spectrum collected with the SDD placed at the x-ray tube's focal length of 30.0±0.2 cm is shown for the SDD in figure 1a for a shaping time of 0.8 μs and tube settings of 30.0 kVp, 0.45 mA (dead time = 23.2%) and for the Si(Li) detector in figure 1b for a shaping time of 6 μs and tube settings of 26.3 kVp, 0.08 mA (dead time = 18.1%).

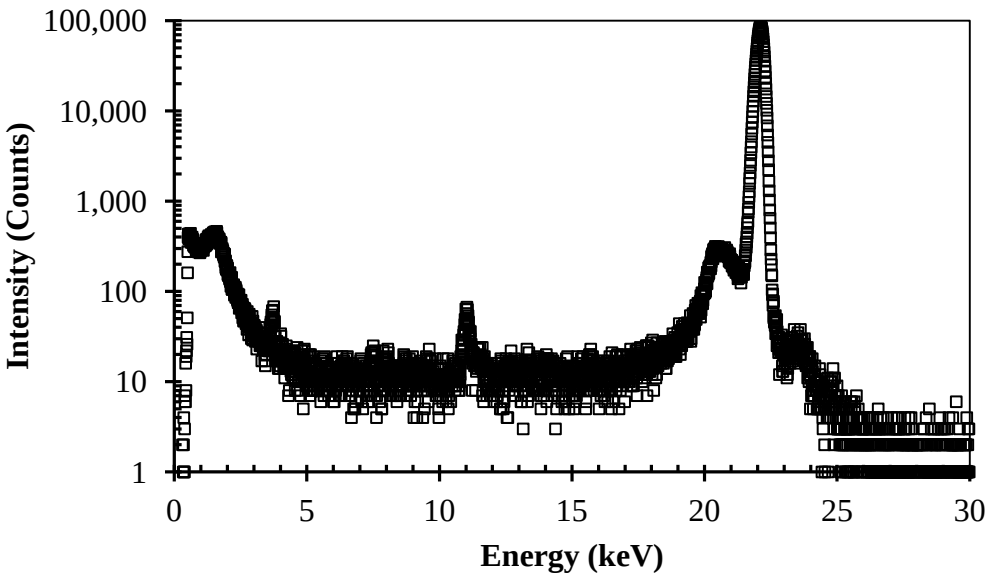

SDD - 30.0 kVp, 0.45 mA (DT = 23.2 %)

(a)

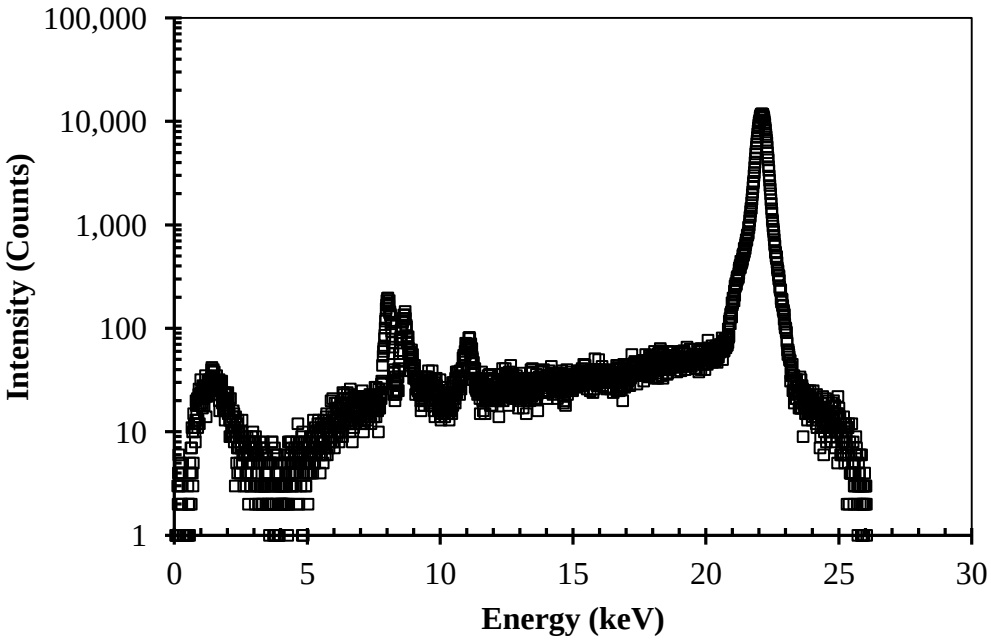

Si(Li) - 26.3 kVp, 0.08 mA (DT = 18.1 %)

(b)

Figure 1: Spectrum acquired by placing (a) SDD at (77.7±0.2) cm in front of x-ray tube and (b) Si(Li) detector at (30.0±0.2) cm in front of x-ray tube.

Copper and zinc are seen in the Si(Li) spectra, but not in the SDD. In addition, both detectors indicate the presence of a diffraction peak at 11.1 keV, which originates in the focusing optic of the x-ray tube. The SDD spectrum shows a peak at ~ 20.4 keV, which corresponds to a combination of coherent Si escape and (due to an increased width) 180^0 backscatter of the incident 22.10 keV x-rays off the interior of the detector housing. When fitting the phantom spectra (90^0 geometry), forcing a peak to be centered at this energy was not successful since the reduced chi-squared was found to be higher with its inclusion. This peak is expected to be much weaker in the phantom geometry (90^0) since it is the coherent scattered x-rays, as opposed to the incident x-rays, that will pass through the SDD wafer and backscatter. Compton backscatter, if at all present, in the Si(Li) spectra after passing through ~5 mm of Si, is much weaker by comparison to that with the SDD and the feature here is mainly due to Si escape from the detector material.

A spectrum corresponding to the 90^0 phantom geometry is shown in figure 2a for the SDD and 2b for the Si(Li) detector, with the sample arsenic peak fits shown in figures 2c and 2d.

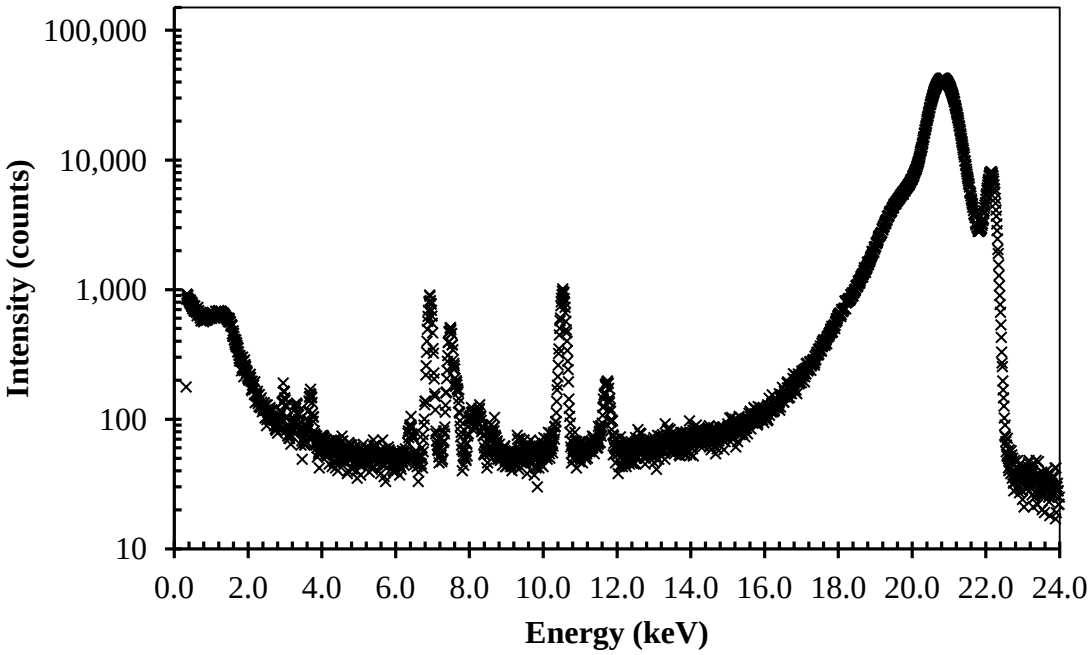

× SDD at 2.0 μs, 40.0 kVp, 0.38 mA

(a)

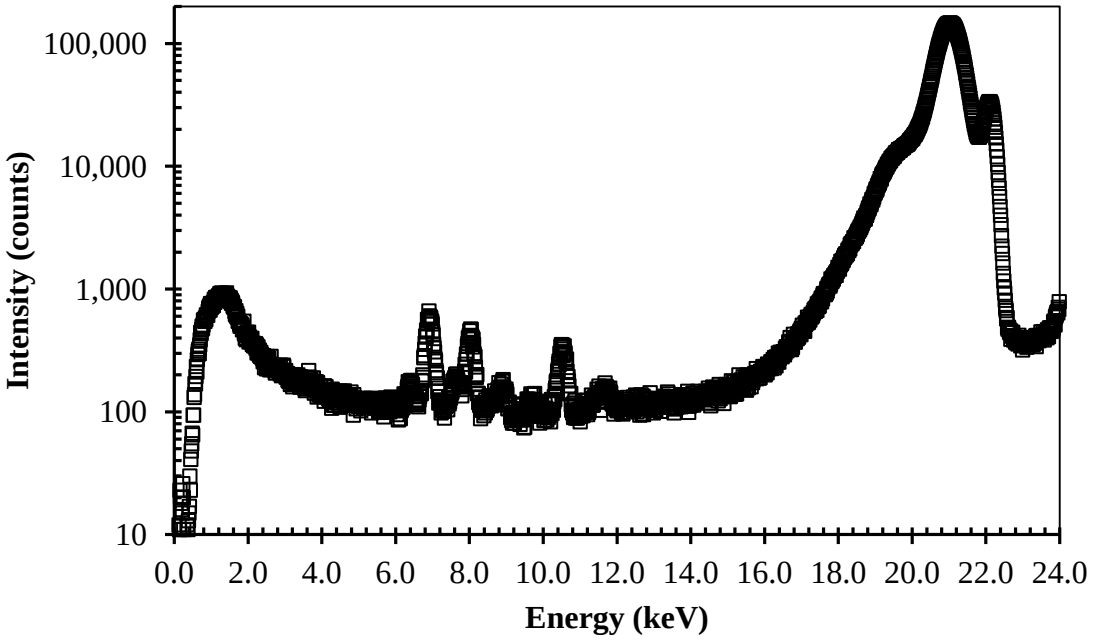
100,000
10,000
1,000
100
10
Intensity (counts)
0.0 2.0 4.0 6.0 8.0 10.0 12.0 14.0 16.0 18.0 20.0 22.0 24.0
Energy (keV)
Si(Li) at 6.0 ms, 45.0 kVp, 0.40 mA

(b)

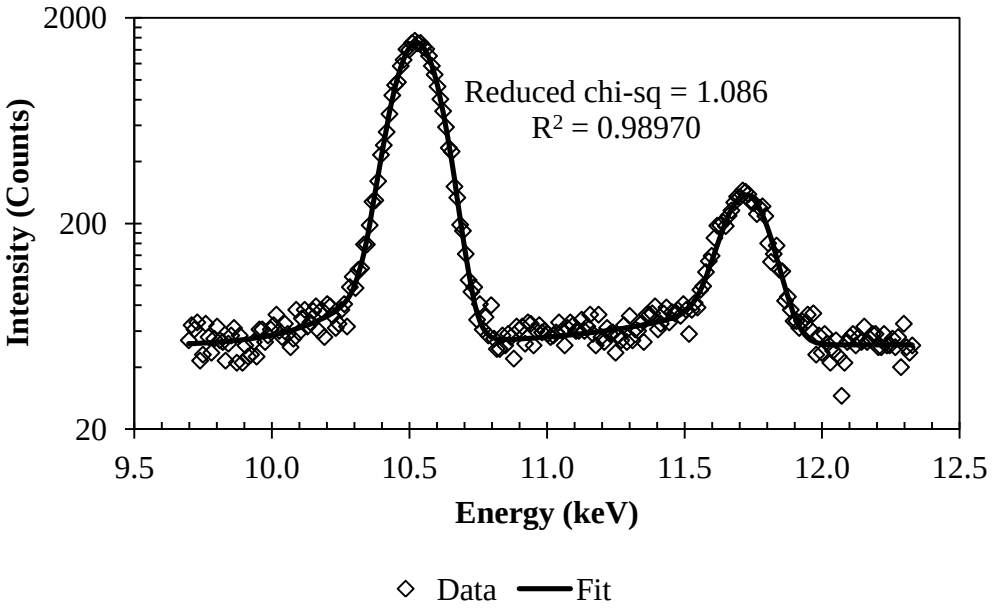
2000
200
20
Intensity (Counts)
Reduced chi-sq = 1.086
R2 = 0.98970
9.5 10.0 10.5 11.0 11.5 12.0 12.5
Energy (keV)
Data
Fit

(c)

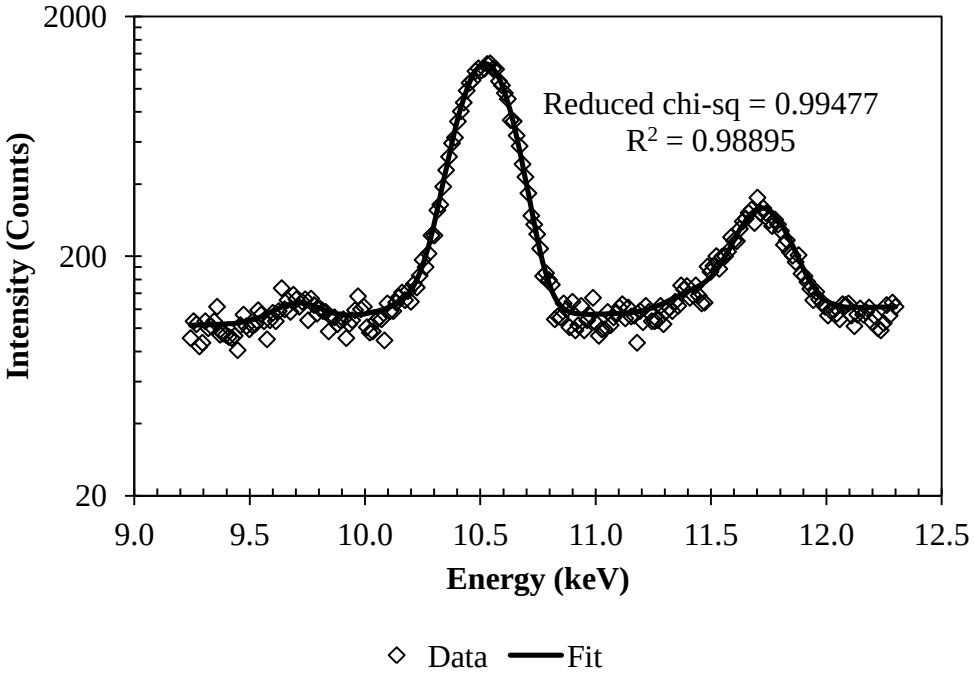

(d)

Figure 2: Sample spectrum acquired by SDD for 90^0 source-detector geometry with resin phantom in (a) SDD and (b) Si(Li) detector. Sample fits for As peaks are shown for (c) SDD and (d) Si(Li) detector – FWHMs were (175.80±0.07) and (249.59±0.23) eV over three trials for the 100 ppm phantom, with the SDD and Si(Li) detector respectively.

Peaks caused by cobalt in the phantoms are noted with both detectors and have been observed in other work (Fleming and Gherase, 2007; Roy et al., 2010; Studinski, 2005). This is attributed to cobalt used as a catalyst in the resin. From the sample fits, the need for a low energy tail is seen in both detector types. In the Si(Li) detector, the presence of gold contacts produces a peak corresponding to the Au Lα at 9.7 keV and Lβ at 11.44 keV and so four Gaussians were used to fit the two As peaks with this detector. A tail on the As Kβ was observed to produce a negative amplitude and so was omitted from the fitting function for the Si(Li) peak fitting. It must be noted that the As Kβ energy is not higher that the Au L-edge (11.92 keV) and so it cannot excite the gold in the detector. The source of the Au excitation is the scattered x-rays at 20 keV or higher. Thus, stronger amounts of arsenic will not excite a greater amount of gold in the detector and the gold signal would not be expected to grow with the arsenic concentration. The gold Lβ peak in the 0 ppm As phantom was fitted and the corresponding Gaussian parameters were fixed in subsequent peak fitting of the As peaks with other phantoms.

Effect of varying shaping time on FWHM and peak precision:

The change in the As Kα FWHM, as a function of rise time and, separately, as a function of flattop, is shown in figure 3.

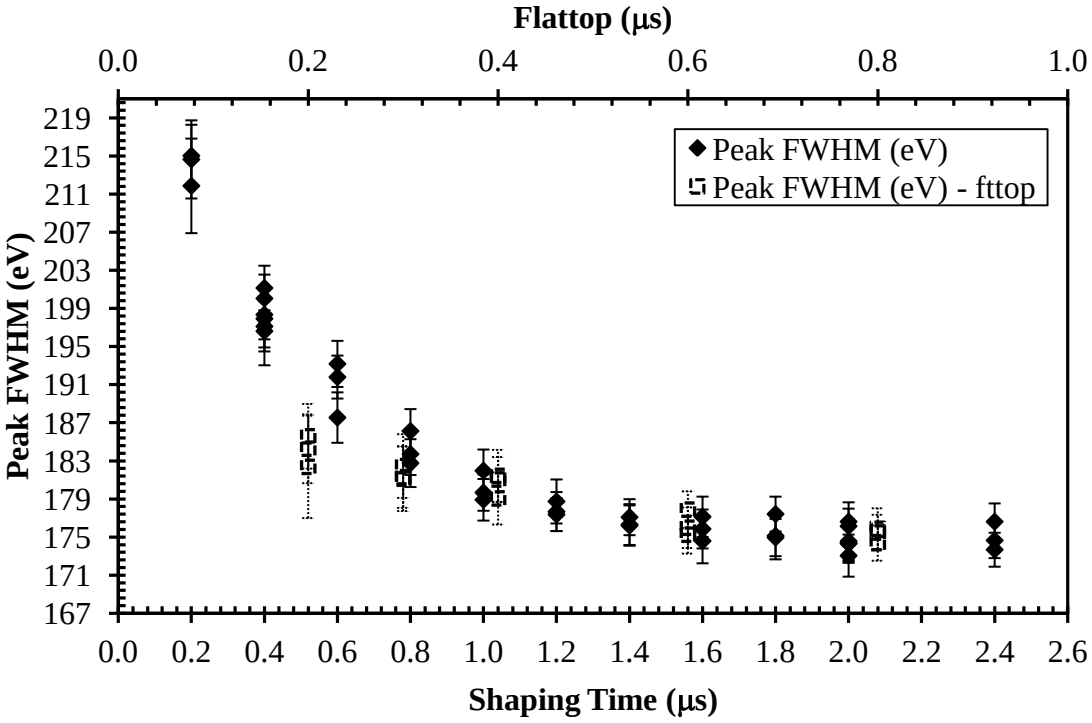

Figure 3: Variation in As Kα FWHM, in 100 ppm resin phantom, as a function of rise time time. Note that the Canberra GENIE2K software's default flattop setting of 0.8 μs was used for varying shaping times. The top axis shows a variation in flattop for a fixed shaping time of 2.0 μs.

It is clear that the As Kα FWHM worsens as the pulse shaping time is reduced. However, there is very little change in FWHM in the range of ~1.2-2.0 μs. The effect of a change in FWHM, caused by adjusting the shaping time, also requires the peak and total observed count rate (defined as peak counts/live time and total counts/live time respectively) to be considered. The variation in As Kα peak and total count rates, as a function of shaping time, are shown in figure 4.

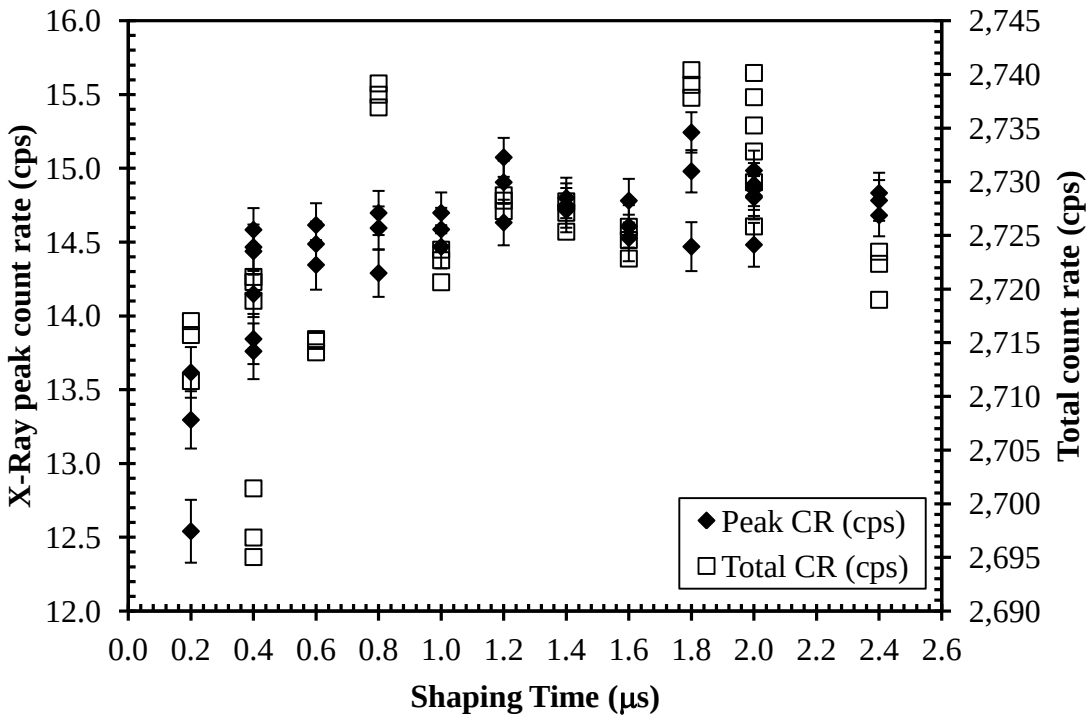

Figure 4: Variation in peak and total count rates, in 100 ppm resin phantom, as a function of shaping time for flattop setting of 0.8 μs.

Repeat trials were performed at a shaping time of 0.4 μs. One of the trials appears to produce a lower peak and total count rate. With this exception, the change in either count rate is minimal, within uncertainty. Also, dead times were not in excess of ~5% and so the incoming signal is not pushing the pulse processing system very hard. This means that the expected gain in throughput for lower shaping times is not evident in these data. A much higher counting rate is likely required to see such a change.

The results of statistics relating to this range of shaping times are shown in table 1, and complement the two figures shown above.

40.0 kVp, 0.38 mA	Total CR (cps)	Peak Area (counts)	Total Counts	Peak FWHM (eV)
Min	2695.03	22,401	4,738,723	173.07
Mean	2724.26	25,632	4,811,515	184.39
SDOM	1.79	126	4,952	1.95
Stdev	11.19	790	30,923	12.15
Max	2740.40	26,744	4,860,225	215.03
Range (Min to Max)	45.36	4,343	121,502	41.97
RSD[1]	0.411	3.080	0.643	6.590
Min Abs Dev[1]	-29.22	-3,231	-72,792	-11.33
Max Abs Dev[1]	16.14	1,112	48,710	30.64
Expected (2.0 μs)	2734.62	25,882	4,787,017	175.29
PD (%)	0.00168	0.01939	0.00256	0.02425

[1] relative to mean

(a)

40.0 kVp, 0.38 mA	Total CR (cps)	Peak Area (counts)	Total Counts	Peak FWHM (eV)
Min	2,717.94	19,759	4,758,630	174.38
AVG	2,725.62	23,955	4,779,969	179.58
SDOM	1.00	539	2,968	0.92
Stdev	3.86	2,087	11,494	3.56
Max	2,731.67	26,273	4,792,176	185.59
Range (Min to Max)	13.73	6,514	33,546	11.21
RSD[1]	0.142	8.713	0.240	1.983
Min Abs Dev[1]	-7.68	-4,197	-21,339	-5.20
Max Abs Dev[1]	6.05	2,317	12,207	6.02
Expected (0.8 μs)	2,719.05	26,073	4,760,556	175.25
PD (%)	0.00051	0.03297	0.00070	0.00643

[1] relative to mean

(b)

49.1 kVp, 0.49 mA	Total CR (cps)	Peak Area (counts)	Total Counts	Peak FWHM (eV)
Min	7202.57	61,481	11,912,337	174.26
AVG	7231.91	65,342	12,415,336	184.90
SDOM	2.99	208	46,959	2.23
Stdev	16.40	1,141	257,205	12.21
Max	7256.59	66,996	12,759,474	213.87
Range (Min to Max)	54.02	5,515	847,137	39.60
RSD[1]	0.227	1.746	2.072	6.606
Min Abs Dev[1]	-29.33	-3,861	-502,999	-10.64
Max Abs Dev[1]	24.69	1,654	344,138	28.96
Expected (2.0 μs)	7236.72	65,314	12,158,680	175.77
PD (%)	0.00075	0.00897	0.00711	0.02273

[1] relative to mean

(c)

Table 1: Statistics relating to change in As Kα peak FWHM and count rate and total count rate, over range of (a) shaping times for 40.0 kVp and 0.38 mA (flattop = 0.8 μs), (b) flattop settings for 40.0 kVp and 0.38 mA (2.0 μs shaping time) and (c) shaping time for 49.1 kVp and 0.49 mA (flattop = 0.8 μs).

Most of the quantities in the table are standard statistics, however it is should be noted that the minimum and maximum absolute deviation values were the minimum and maximum values of the quantity x_i - x_{AVG}. The percentage difference (PD) was then calculated using

$$PD = \frac{x_{MAX} - x_{MIN}}{x_{MIN}} X\ 100 \tag{7}$$

where x_{MIN} and x_{MAX} are the minimum and maximum values observed over that range of shaping times investigated. The expected results are taken for a shaping time of 2.0 μs, which was the default shaping time that the manufacturer supplied with the detector's internal shaper. The results obtained for changing the flattop setting from 0.2 – 0.8 μs are shown in table 1b. Table 1c shows the corresponding statistics for cycling through the same range of shaping times using the source (x-ray tube) at its maximum supported voltage and current. It is clear that even for the source operating at full power, combined with one type of calibration phantom with which the system is intended to be used, the change in FWHM over a range of 2.2 μs shaping times is very small (< 0.5%). The

change in this case is interpreted as a worsening of the As Kα peak FWHM as the shaping time is reduced. Accompanying this is a small improvement in total count rate, As Kα peak count rate, total counts and As Kα peak counts. The source strength is the limiting factor that causes the small change in these. Comparable results are noted for the range of flattop settings investigated, with a smaller worsening of peak FWHM noted here. For a sufficiently powerful x-ray tube, a stronger change in count rate would be observed. Thus, the benefits of a reduction in pulse shaping time, as it pertains to overall x-ray tube-SDD system performance, are expected to be minimal for the particular choice of x-ray tube used as part of the detection system investigated in the current work.

A summary of tracking tail parameters, for each of the As peaks, as a function of SDD shaping time, is shown in figures 5 a-c for the As Kα at 40.0 kVp and 0.38 mA.

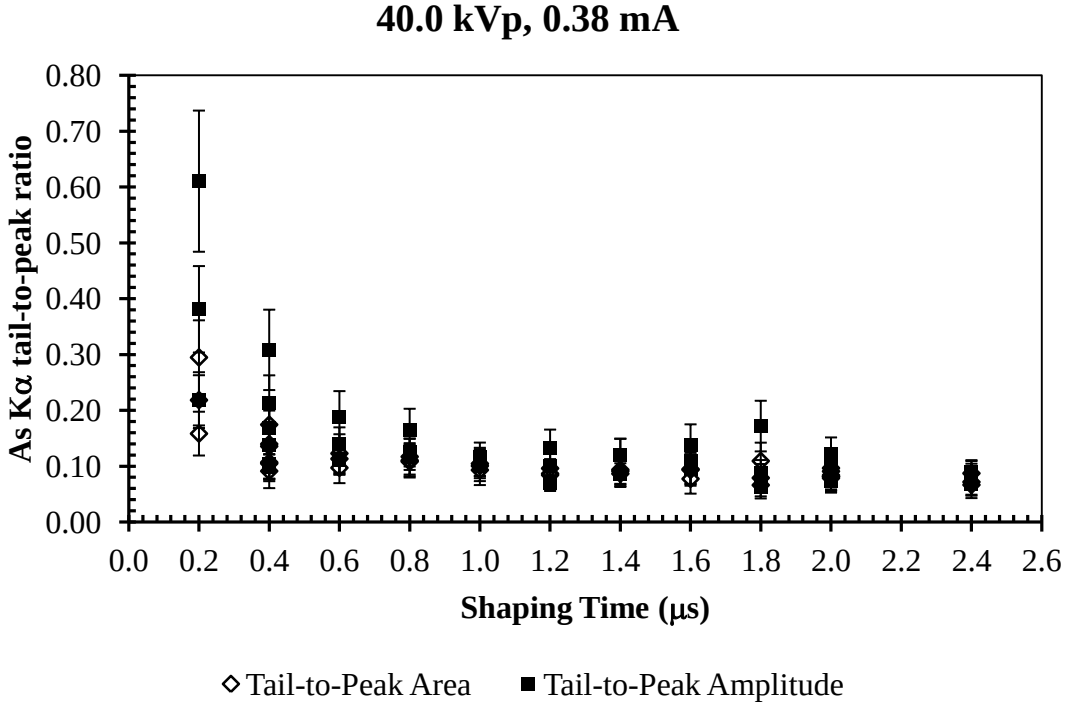

(a)

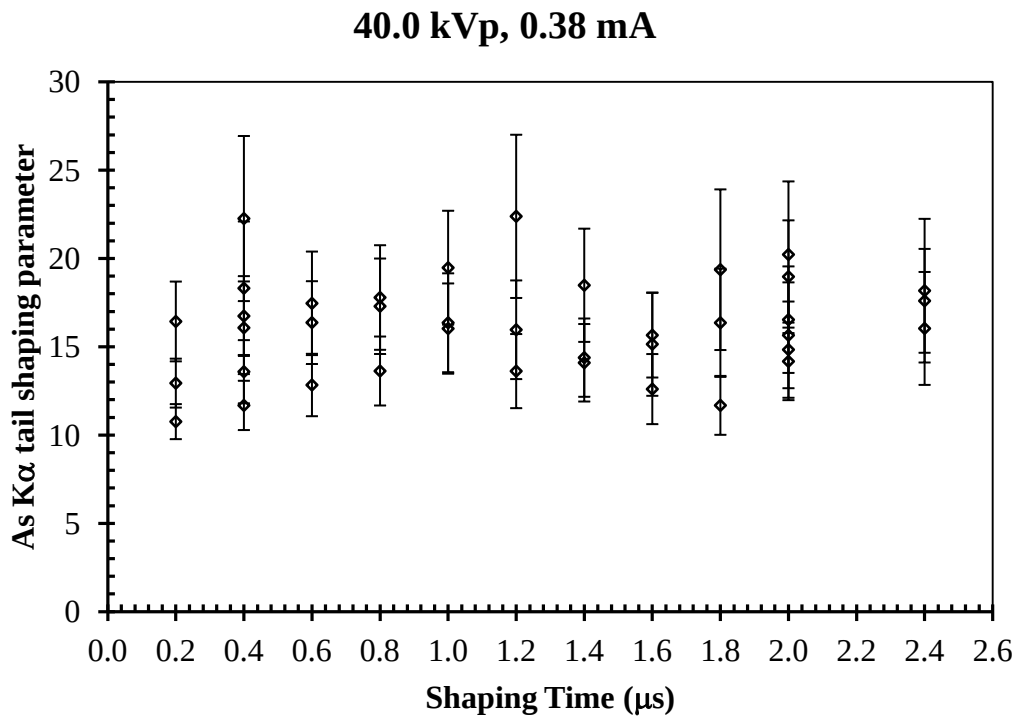

(b)

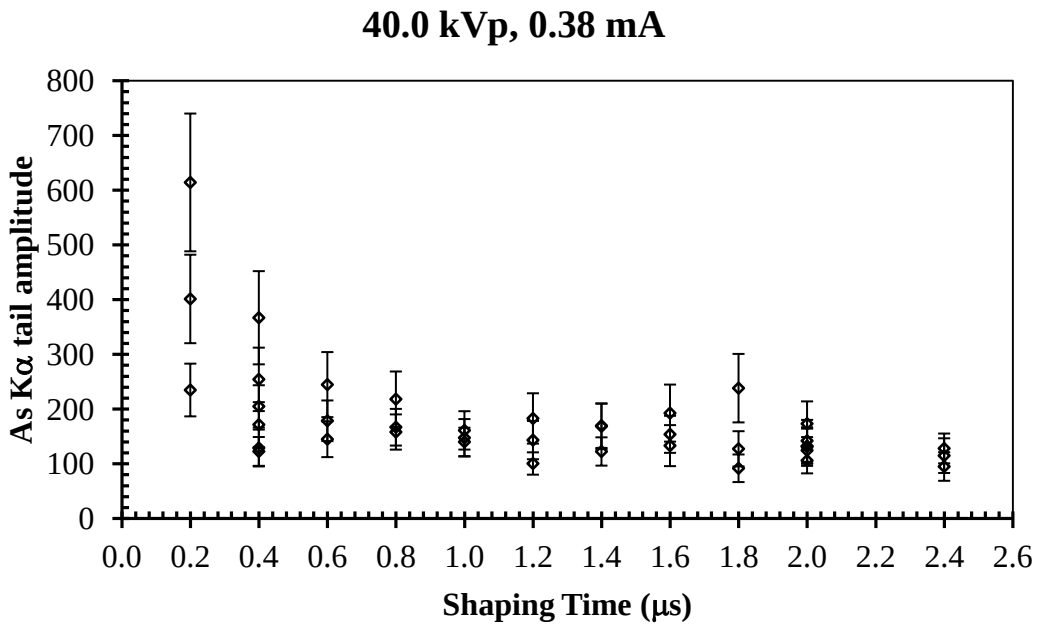

(c)

Figure 5: Change in As Kα (a) tail-to-peak ratio, (b) tail shaping parameter β and (c) tail amplitude H.

Similar trends were observed for higher tube operating conditions tested – 49.1 kVp and 0.49 mA. An average of the tail-peak area, obtained with the highest concentration phantom, was used in the final peak fitting as this parameter would not be expected to change as a function of concentration, for all other system conditions being kept the same. Due to difficulty in fitting the As Kβ peak with both a tail and a Gaussian for the Au peak, the As Kβ tail was omitted and is discussed later. No trends were observed except for an elevation in the ratio, caused by a larger tail amplitude, at the shortest shaping time chosen (0.2 μs) which is unlikely to be chosen for extended use due to the significant deterioration of FWHM. Over all shaping times, the SDD's As Kα tail-peak area ratio was 0.109±0.039 (mean±StdDev), compared to 0.119±0.073, with the Si(Li) detector.

The relative error in the As Kα and Kβ peak area is shown in figures 6a and 6b for 40.0 kVp and 0.38 mA.

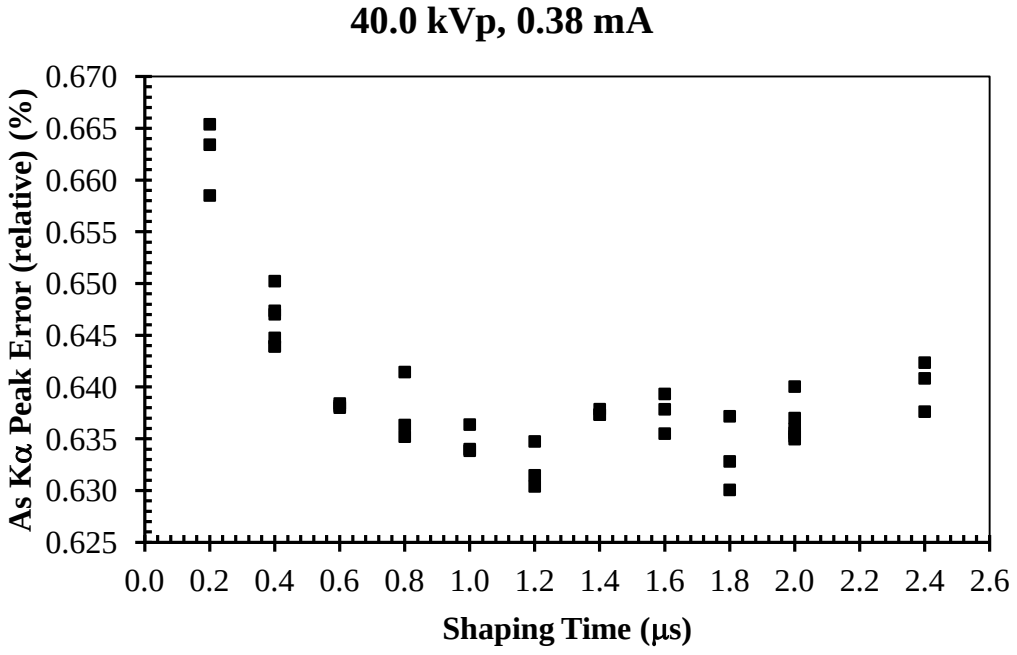

(a)

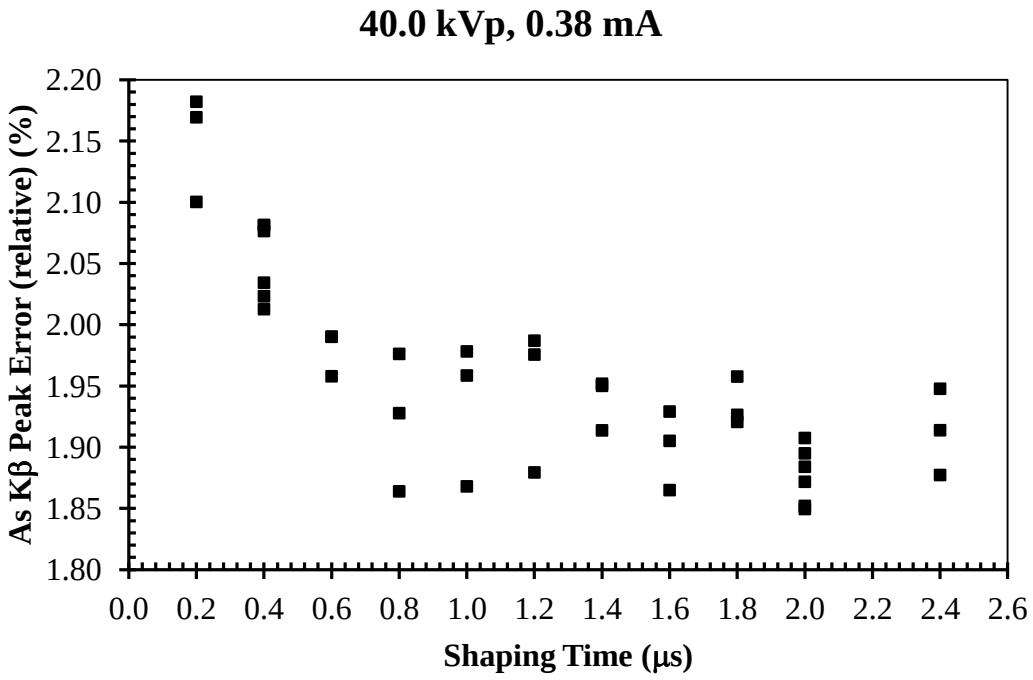

(b)

Figure 6: Effect of varying shaping time on peak precision of (a) As Kα and (b) As Kβ peaks.

The trends observed are similar to those seen for when the tube is operated at maximum voltage and current. The statistics relating to these figures are summarized in table 2a and 2b. The presence of a valley is barely observed here between 1.2-2.0 μs.

40.0 kVp, 0.38 mA[1]	As Kα Peak Err (%)	As Kβ Peak Err (%)
Min	0.630	1.850
AVG	0.640	1.960
SDOM	0.001	0.013
Stdev	0.008	0.084
Max	0.665	2.182
Range (Min to Max)	0.035	0.333
RSD	1.250	4.288
PD (%)	5.606	17.985

[1] SDD with dead time (mean ± SD) = (1.88±0.77) %, over range of rise times

(a)

49.1 kVp, 0.49 mA[2]	As Kα Peak Err (%)	As Kβ Peak Err (%)
Min	0.397	1.164
AVG	0.401	1.217
SDOM	0.001	0.009
Stdev	0.003	0.049
Max	0.411	1.350
Range (Min to Max)	0.013	0.186
RSD	0.861	4.052
PD (%)	3.357	15.934

[2] SDD with dead time (mean ± SD) = (4.63±1.88) %, over range of rise times

(b)

Table 2: Summary of statistics relating to As Ka peak precision (%) in resin phantoms for (a) 40.0 kVp, 0.38 mA and (b) 49.1 kVp, 0.49 mA.

The average reduced chi-squared value for the fits, over the same range of shaping times, was 1.108±0.128 corresponding to the lower tube settings and 1.111±0.129 corresponding to the higher tube settings (mean±StdDev). The trend in the As Kα peak relative error is caused by differences in dead time, as shaping time is adjusted, which will affect the total number of counts recorded. For the range of dead times investigated here, for either low or high tube settings, the change in shaping times brought about a very small change in system dead time and it is reassuring that this is reflected in the small percentage change (min to max) in the As Kα peak relative error (3rd last row of above table). For the As Kα peak, the absolute values of the percent error on the y-axis are <1%. The relatively weaker statistics in the As Kβ peak leads to a larger percentage change in its relative error.

SDD MDL, as function of shaping time, and versus Si(Li) detector:

The results of phantom calibration measurements, with each detector individually, are shown in table 3.

Det	ShpT (μs)	Norm	MDL_{AVG} (over three trials)[2]			$Slope_{AVG}$ (over three trials)[2]		
Si(Li)[3a]	6.0	Compton	1.14545	±	0.00154	0.0000313	±	0.0000003
		Coherent	1.21686	±	0.00047	0.0003454	±	0.0000032
		Direct[1]	1.35623	±	0.00064	150.133	±	1.548
Si(Li)[3b]	6.0	Compton	0.69579	±	0.00165	0.0000313	±	0.0000001
		Coherent	0.74904	±	0.00121	0.0003372	±	0.0000016
		Direct	0.71957	±	0.00150	222.947	±	0.977
SDD[3a]	2.0	Compton	0.44150	±	0.00260	0.0000969	±	0.0000003
		Coherent	0.43593	±	0.00247	0.0014017	±	0.0000037
		Direct	0.54266	±	0.00150	251.343	±	0.955
	1.2	Compton	0.55334	±	0.00101	0.0000963	±	0.0000004
		Coherent	0.53774	±	0.00080	0.0013895	±	0.0000053
		Direct	0.56649	±	0.00096	253.205	±	1.028
	0.8	Compton	0.55715	±	0.00106	0.0000945	±	0.0000004
		Coherent	0.52726	±	0.00148	0.0013112	±	0.0000047
		Direct	0.56745	±	0.00113	248.365	±	0.981
	0.4	Compton	0.66153	±	0.00065	0.0000959	±	0.0000005
		Coherent	0.63615	±	0.00056	0.0013555	±	0.0000062
		Direct	0.70945	±	0.00041	249.141	±	1.304
SDD[3c]	1.2	Compton	0.48273	±	0.00026	0.0001028	±	0.0000004
		Coherent	0.42849	±	0.00018	0.0015341	±	0.0000051
		Direct	0.48472	±	0.00020	634.499	±	2.430

[1]without normalization; [2]arithmetic mean ± SDOM, where SDOM = StdDev/$n^{1/2}$; [3a]40.0 kVp, 0.38 mA, [3b]45.0 kVp, 0.40 mA, [3c]49.1 kVp, 0.49 mA
*listed for a single phantom trial, for brevity, with similar results obtained for two subsequent trials

Table 3: Summary of MDLs obtained with both detectors, covering various shaping times and x-ray tube operating conditions.

The count-rate benefits produced by a decrease in shaping time are not strong enough to allow for a significant improvement in calibration line slope. The drawback of a lower shaping time is the compromised resolution. Thus, spectral factors (ex, Kα:Kβ ratio, obvious blurring of interfering peaks, etc.) should also drive this decision and not just the slope of the calibration line or MDL as the shaping time is reduced from 2.0 μs to 0.4 μs. With the exception of the second and last entries in the table, all other results correspond to data collected under matching tube conditions. Hence a comparison between the two detectors can be made from this subset. These entries show that the larger phantom-

detector distance, required with the Si(Li) detector, appears to offset its larger active area because the SDD reports superior MDLs for all shaping times than the Si(Li) detector at 6 μs. The average chi-squared value for fitting with the Si(Li) detector was 1.067±0.098 (mean±StdDev). Considering the full table, the comments about comparison between detector types remain true for the tube operated at near maximum power [dead time ~40% with Si(Li) detector vs < 10% with SDD]. For a fixed shaping time of 1.2 μs, an improvement is noted in MDL for higher voltage and current with the SDD and this is accompanied by an increase in the normalized or direct calibration line slope. Note that dosimetry, for varying tube conditions, will be addressed elsewhere. Increasing the slope improves the detection system's sensitivity to small changes in concentration and this would be expected to lower the MDL, as is observed. At full power, the SDD's higher throughput capabilities are thus clearly demonstrated. This lower dead time indicates that the SDD would work with a stronger source, to further lower the MDL. The ability of each of the two detectors to detect arsenic is influenced by the fact that they have significantly different detection volumes and different intrinsic efficiencies. A direct comparison between the results must thus bear in mind this difference between the detectors. Careful dosimetry would be required for an increase in source output – the voltage would not require adjustment for As but a tube current on the order of low mA rather than μA would be the way to achieve this. Ramping up the source strength would not offer a benefit to the Si(Li) detector–based work since that detector is already at the higher end of an acceptable range of dead time – 30-40% (Knoll, 1999).

Previous work has used a fairly common implementation of σ in calculating the MDL: MDL = 2σ/M, where σ is the uncertainty in the zero ppm phantom arsenic peak area (assumed to be equal to zero, within error). The currently used definition only converges to this if the covariance, variance in slope and variance in intercept are all nearly zero. The current work found the last of these terms was consistently making a significant contribution to the overall calculation of σ, while the first two were negligible. If this last term is ignored then the above definition of MDL is retrieved. However, when the calibration line equation is used to calculate an in vivo concentration, both the slope and intercept, and their respective errors, are employed. Thus, a conservative assumption would be to include the variance in the intercept as is typically done in analytical chemistry approaches. As such, both types of detectors report system MDLs, with calibration phantoms, that are higher than those required to detect arsenic in members of a, unexposed (general) population (Studinski et al., 2005). However, the performance of a detection system (full power) with either detector type would allow quantification of arsenic in members of an exposed population [~0.3-24 μg As/g dry weight *ex vivo* (Das et al., 1995; Samanta et al., 2004)]. The benefit of the SDD is that a lower level of arsenic loading in the subject can be quantified *in vivo*, than with a Si(Li) detector.

The main source of the discrepancy between the three types of MDLs (direct, Compton normalized, coherent normalized) is the term listing the variance in the y-intercept. Two systematic issues, that are possibly relevant to this, are now discussed. In

the MDLs in the first entry, as collected with the Si(Li) detector, are an extreme example of this. Here, a 47% and 15% change is noted between the Compton and coherent normalized MDLs and the un-normalized (direct) MDL. The scatter peak variations are shown in table 4a and b.

Variation in Compton	V-I[1]	V-I[2]	SDD 0.4 μs[3]	SDD 1.2 μs[4]	SDD 2.0 μs[3]
Min	7,121,090	4,660,260	2,595,450	6,140,400	2,591,280
AVG	7,163,985	4,955,820	2,615,207	6,162,523	2,607,783
SDOM	6,626	27,097	2,874	3,863	2,236
Stdev	25,661	104,947	11,133	14,962	8,659
Max	7,201,220	5,047,920	2,633,610	6,182,990	2,617,270
Range	80,130	387,660	38,160	42,590	25,990
RSD	0.358	2.118	0.426	0.243	0.332
Min Abs Dev	-42,895	-295,560	-19,757	-22,123	-16,503
Max Abs Dev	37,235	92,100	18,403	20,467	9,487
Rng%of expct	1.125	8.318	1.470	0.694	1.003

(a)

Variation in Coherent	V-I[1]	V-I[2]	SDD 0.4 μs[3]	SDD 1.2 μs[4]	SDD 2.0 μs[3]
Min	658,458	421,034	183,940	413,303	178,796
AVG	666,823	455,107	186,596	419,060	181,738
SDOM	1,430	3,338	513	1,056	439
Stdev	5,539	12,929	1,985	4,090	1,699
Max	676,221	466,771	189,110	425,383	184,415
Range	17,763	45,737	5,170	12,080	5,619
RSD	0.831	2.841	1.064	0.976	0.935
Min Abs Dev	-8,365	-34,073	-2,656	-10,713	-2,943
Max Abs Dev	9,398	11,664	2,515	1,367	2,676
Rng%of expct	2.698	10.863	2.811	2.923	3.143

(b)

[1]45.1 kVp, 0.40 mA (mean DT = 40.10±0.09 % at 2.0 cm); [2]40.0 kVp, 0.38 mA (mean DT = 32.29±1.09 % at 2.0 cm)
[3]40.0 kVp, 0.38 mA (mean DT = 1.88±0.77 % at 1.5 cm); [4]49.1 kVp, 0.49 mA (mean DT = 4.63±1.88 % at 1.5 cm

Table 4: Variation in (a) Compton and (b) coherent scatter peaks.

The slope increases faster than that predicted by the ratio of V^2I. The limitations of this relationship were discussed earlier. A continuous spectrum of photon arrives at the detector, after scattering off the phantom. Bremsstrahlung due to scattering in the phantom accounts for the low-energy bump. It is clear that a simple empirical relationship may underestimate the . A clear change is observed (quantified in last row) in the Compton or coherent range of peak areas relative the minimum area. Fluctuations in noise, likely caused due to poor grounding in the Ortec DSPEC MCA box or electrical interference in the laboratory building circuitry, were observed over the course of running this work with the Si(Li) detector and this produced larger variations in live time than for the other dataset acquired with the same detector. Accompanying this is an order of two times increase in the standard deviation of the coherent peak area. If source output is not changing significantly, then a) such a large change is not expected and b) electrical interference may be attributed to this. The strong variation in live time may be affecting either the low energy (characteristic x-ray) and high energy (scatter) peaks differently, which results in a different response on the scatter and un-normalized MDLs. Shifts and broadening of spectral features were not observed.

In the case of the SDD at 2.0 μs shaping time, a change of 23% in the direct and normalized MDLs is noted. The variance in the intercept was found to make a contribution here to the detection limit. This term was larger than the variance in the 0 ppm area, for shaping times of 0.4, 0.8 and 1.2 μs. For 2.0 μs, it was almost the same as the variance in the 0 ppm area. The main differences here are noted for the two normalized MDLs. Peak precision was found to be unchanged, within 1 standard deviation, as shaping time was decreased. This was true for both direct and either of the normalized peak areas. A lower average net peak area in the Compton scatter peak was observed for a shaping time of 2.0 μs. For this shaping time (2.0 μs), both scatter peaks were shifted by 20 channels (out of 4096). The same phenomenon causing this shift is likely also forcing down the scatter peak areas just enough to affect the normalization. Such a shift was not observed at other shaping times. The cause of the systematic shift was not identified but may be isolated to noise in the electrical connections or power outlet during the course of the work at this shaping time. Future work should investigate this further by intentionally counting several phantoms in a single dataset with significantly varying detector live times and determine if a similar effect is observed.

Evaluation of currently used scatter peak fitting:

In fitting the scatter peak region in addition to using two Gaussians and two tails to fit the Compton and coherent scatter peaks, two additional Gaussians were included in the SDD fitting function, while only one additional Gaussian was used for the Si(Li) detector fitting. The average chi-squared value for scatter fitting with the Si(Li) detector was 3.15±0.64 (mean±StdDev), compared to 2.12±0.39 with the SDD. The average fitted area of the Compton peak was 6.06×10^6 counts with the Si(Li), compared to 6.16×10^6 counts and 2.63×10^6 respectively, for the higher and lower x-ray tube conditions, with the SDD. As seen earlier, in the direct Si(Li) spectra out of the tube, a second peak is not

observed and its presence cannot be justified in the scatter peak-fitting. Furthermore, the reduced chi-squared increased from ~2.5 to 10 by inclusion of a second additional feature in the Si(Li) fitting. A sample fit is shown in figure 7a for the SDD and 7b for the Si(Li) detector. By way of example, for a shaping time of 2.0 μs, the first additional SDD feature was observed at an energy of 19.634±0.011 keV (mean±SD) and is representative of that observed at other shaping times.

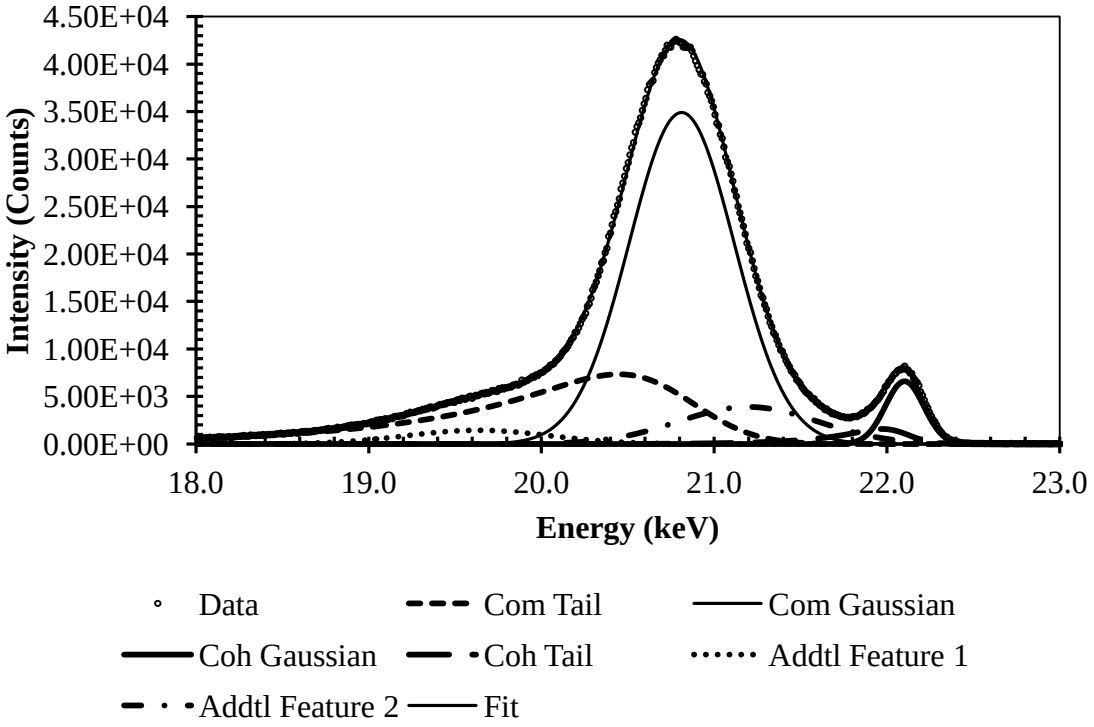

(a)

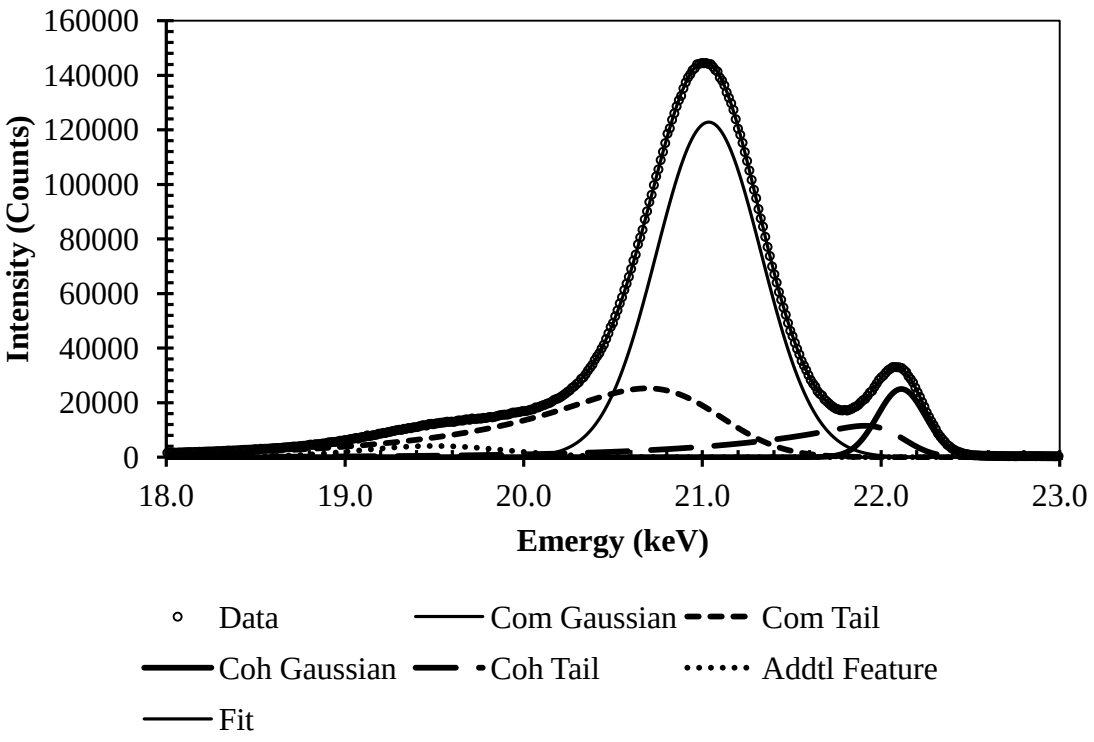

(b)

Figure 7: Sample fit shown fit scatter portion of 100 ppm spectrum acquired with (a) SDD at 2.0 μs shaping time (χ^2 = 3.05, R^2 = 0.99982) and (b) Si(Li) detector at 6.0 μs shaping time (χ^2 = 1.77, R^2 = 0.99952).

An explanation of this shifted Compton feature is offered here. A schematic of the experimental layout is shown in figure 8, focusing on the detector head, resin phantom and nylon backing.

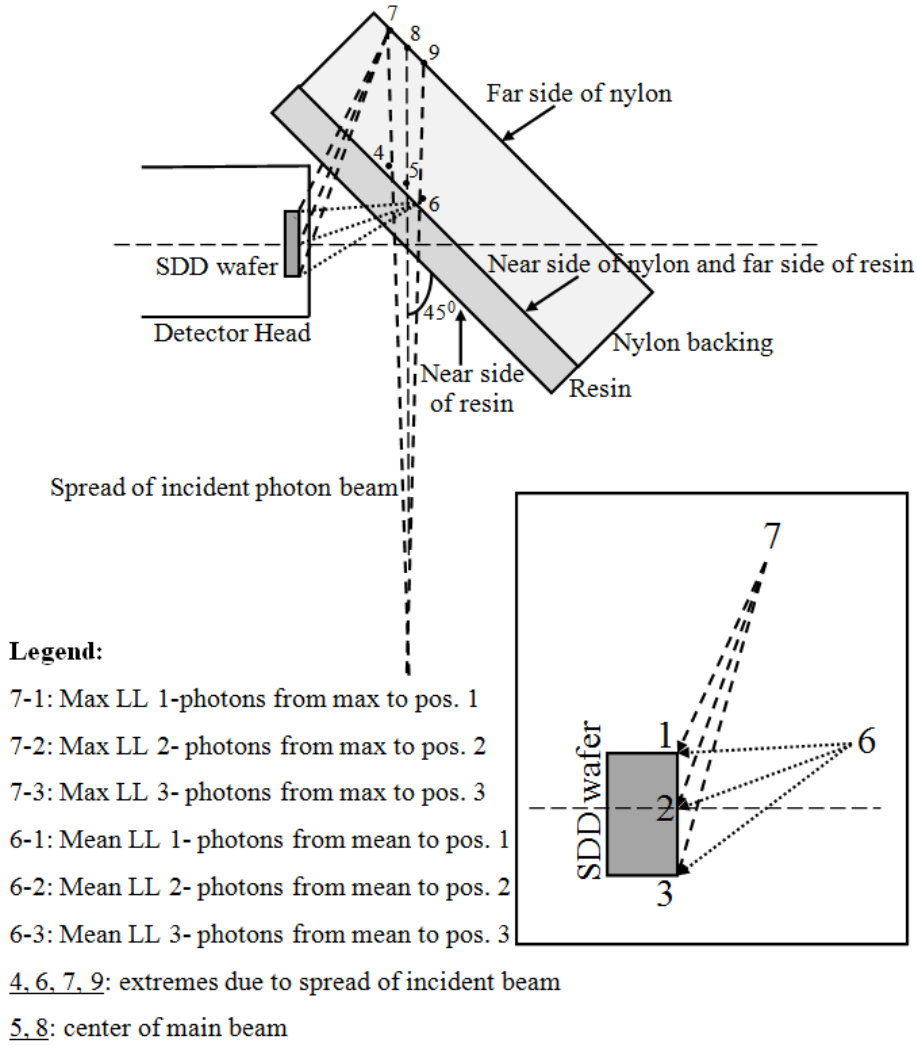

Figure 8: Schematic of experimental layout showing calculations performed in scale drawing discussed in text. This figure is not drawn to scale.

The observed mean interaction depth is shown along the center of the main beam (position 5); it occurs in the nylon backing. The mean interaction depth is based on the observed Compton scattered energy. Based on this energy, the mean Compton scattered angle of ~115^0 (90^0 + 25^0) was estimated. Using the known phantom (resin) to detector (Be window) distance, the mean interaction depth was calculated using the tangent trigonometric relationship. This was performed for the center of the incident x-ray beam and the extremes of this beam spread, which were determined using the recorded beam image with Gafchromic x-ray film. Note that the spread is sufficiently small that a line along the center of the main beam is very nearly parallel to the line created by either of the extremes due to beam spreading. The mean interaction depth is the site where the majority of Compton scatter interactions, on average, occur. As the beam energy is the

same for the center of the beam or either extreme, the same depth into the nylon was assumed there as well. The maximum possible interaction depth is at the far end of the nylon backing. This is also shown in the figure for the center of the beam and the two extremes.

Photons originating at the far end of the nylon (positions 7, 8, 9) correspond to the largest possible Compton scatter angle at the detector. These are detected at the near and far end of the surface of the Si wafer (1, 2, 3 in enlarged view) and each will make a contribution to the overall Compton scatter. In fact, there would be a spread (continuum) of features observed within the two limiting interaction positions for photons (1 and 3) on the surface of the Si wafer. Affecting the continuum is the fact that different amounts of attenuation will result through nylon, resin, air and Be (window). Similarly, interactions would be possible at all depths between the near side of the resin and the far side of the nylon. This includes at the mean interaction depth (positions 4, 5, 6). In the inset of figure, positions 6 and 7 are illustrated. For all 6 points labeled in the figure, Compton scattered photons are detected at one of 3 possible locations on the surface of the SDD wafer – 1, 2, 3. Note that only three of a continuum of interaction sites are shown graphically. Starting from each of the 6 points in the nylon and ending at each of the 3 points on the Si wafer surface, a) a Compton scatter angle was calculated and b) the propagation distance of Compton scattered photons was determined – this distance is a combination of distances through nylon, resin, air and Be (entrance window). These distances were calculated from a scale drawing of experimental layout shown in the above schematic. The intensity of the detected Compton scattered x-rays, with respect to that of the incident x-rays from the source (assumed to be 100 %), is then calculated over this distance by

$$I = I_0 exp\left[-\left(\frac{\mu}{\rho}\right)_{n1,2}\rho_{n1,2}x_{n1,2}\right] exp\left[-\left(\frac{\mu}{\rho}\right)_{r1,2}\rho_{r1,2}x_{r1,2}\right] X$$
$$exp\left[-\left(\frac{\mu}{\rho}\right)_{air}\rho_{air}x_{air}\right] exp\left[-\left(\frac{\mu}{\rho}\right)_{Be}\rho_{Be}x_{Be}\right] \quad (8)$$

where $n_{1,2}$ represents nylon and $r_{1,2}$ represents resin. The fitted compton scatter peak at 20.811±0.013 keV (mean±StdDev) over all the full datasets collected with the SDD [detector-phantom separation of 1.68 cm (1.50 cm detector to Be)] indicates that the mean interaction depth is located 0.783 cm [1.68 tan(25^0) cm] behind the surface of the resin phantom. The mean Compton peak position over the two datasets acquired with the Si(Li) detector was (21.023±0.003) keV, in comparison to the mean predicted energy of 21.187 keV. With a FWHM of ~250 eV at the As Kα energy of 10.53 keV, and increasing with energy, the mean difference of 161 eV between the fitted and predicted compton scatter energies will not be resolvable with the Si(Li) detector. Also Compton backscatter off the backing behind the Si crystal (~5 mm) is minimal due to nearly full absorption of photons of those energies in the Si crystal. This is not the case in the Si

wafer (450 mm) for the SDD. Additionally, for each of the shaping times investigated in the full datasets acquired with the SDD, the mean difference of ~365-390 eV, between predicted and expected Compton scatter energies, compares to the fitted Compton Gaussian FWHM of ~300 eV and so the shift in Compton peak positions is potentially resolvable with this detector type, necessitating further discussion.

As seen above, for a phantom thickness of 0.281 cm, the mean interaction depth would be 0.783 cm into the nylon backing, in the 45^0 orientation. The incident 22.10 keV x-ray component (along the center of the main beam) goes through a path consisting of 0.395 cm resin and ~0.39 cm nylon (0.783 cm – 0.395 cm). Then, the Compton scattered component goes through a path comprising 0.35 cm nylon, 0.25 cm resin, 1.1 cm air and $[0.0025/\cos(25^0)]$ cm in the SDD's 25 μm Be window. Including attenuation of the incident photons in resin and nylon, the fraction I/I_0 becomes ~18% at the front surface of the Si wafer (assumed vacuum between Be window and Si wafer). Similarly, the intensity of Compton scattered photons reaching the surface of the SDD wafer were calculated for all combinations of 6 points of origin in the nylon backing and 3 points of detection on the surface of the Si wafer. The results are listed in table 5.

Assumed Interaction Depth	Angle-Depth and Si wafer	Compton Scattered Energy (keV)	Scattered Only Frct Reach Front of Si	Scattered Only Frct Reach Back of Si	Incident & Scattered At front of Si Wafer	Incident & Scattered At rear of Si Wafer
Main Mean 1	11	21.025	67%	45%	15%	10%
Main Mean 2	25	20.823	71%	45%	18%	11%
Main Mean 3	37	20.671	72%	42%	19%	11%
Main Max 1	45	20.587	43%	23%	2%	1%
Main Max 2	52	20.520	40%	20%	2%	1%
Main Max 3	57	20.471	41%	18%	2%	1%
LL Mean 1	24	20.840	69%	44%	16%	10%
LL Mean 2	38	20.663	70%	41%	18%	10%
LL Mean 3	49	20.546	70%	36%	17%	9%
LL Max 1	54	20.500	42%	20%	2%	1%
LL Max 2	60	20.454	41%	17%	2%	1%
LL Max 3	64	20.424	39%	14%	2%	1%
RR Mean 1	4	21.130	64%	43%	13%	9%
RR Mean 2	17	20.928	69%	45%	16%	11%
RR Mean 3	30	20.760	72%	45%	19%	12%
RR Max 1	26	20.805	42%	26%	2%	1%
RR Max 2	45	20.579	42%	23%	2%	1%
RR Max 3	52	20.518	42%	21%	2%	1%

Table 5: List of Compton scattered intensities at two locations in the detector head – front and back of the Si wafer. The columns list 1: angle between interaction depth point (1-6) and location on Si wafer of SDD, 2: Compton scatter energy based on angle from 1, 3: intensity of Compton scattered photons reaching front surface of Si wafer, originating from interaction depth, 4: intensity of Compton scattered photons passing through Si wafer, originating from interaction depth, 5: intensity of Compton scattered photons reaching front surface of Si wafer, including reduced intensity caused by attenuation of incident beam and 6: intensity of Compton scattered photons reaching back surface of Si wafer, including reduced intensity caused by attenuation of incident beam.

In oncology applications, it is known that photons deliver a dose below the surface of tissue. Photons lose their energy and build up in the medium. Deeper depths, thus, also make a contribution to the total radiation dose delivered to a patient. An analogous situation is present in the current application. Here, photons originating at the far end of the nylon backing, correspond to the largest possible Compton scatter angle. In the limiting case, these photons are detected at the near (Main Max 1) and far (Main Max 3) end of the front surface of the Si sensitive volume and will make a contribution to the observed Compton feature. However, the mean Compton scatter feature will be associated with detection of these photons at the center (Main Max 2) of the surface of the Si wafer. Thus, Compton scattered photons originating from deeper and shallower depths must be considered.

The incident Ag photons have enough energy to fully pass through the resin and the backing. This means that along the path from the near side of the resin to the far side of the nylon backing, they will Compton scatter and the scattered photons will be detected by the detector. As seen above, these Compton scattered photons will reach the detector with a non-zero intensity (column 3 for entries Main Max 1, 2 and 3) and so they will make a contribution to the observed Compton feature. After passing through the resin (~0.39 cm), the intensity of the incident Ag photons has dropped to 79 %. As they pass through the bulk of the nylon backing, their intensity continues to drop as they Compton scatter off of the target (nylon) atoms. As a result, two factors contribute to magnitude of their observed Compton scattered feature. Scattered photons that originate close to the near side of the nylon backing are not attenuated as much as those that originate at the far side of the nylon backing. Photons from the near side do not have to travel through as much nylon and resin before reaching the detector as those from the far side. Also, the incident beam intensity is weaker at the extreme far (30 % after fully passing through resin and nylon) side than close to the near side (max. 79 %, as mentioned above). These two factors are illustrated in the above figure 8, by examining the paths shown for locations 6 (near side of resin) and 7 (far side of nylon). For these reasons, scattered photons originating at the near side have a higher intensity than those at the far side of the nylon. This is seen from the table by comparing entries for Main Max 1,2,3 to Main Mean 1,2,3. Thus, the dominant contribution to the observed Compton

scattered feature is made by scattered photons originating close to the near side of the nylon backing.

Additional Compton scatter features with energies corresponding to geometries obtained from such depths (90^0 + smaller angles between the assumed interaction depth and Si wafer) will be expected to appear in the observed spectrum and will dominate features from deeper depths (90^0 ± larger angles, the maximum angle allowed is ~57^0). This is in agreement with the observed mean interaction site (incident intensity is ~68% after all resin and some nylon). The mean interaction site is located close to the near side of the nylon backing (angle of ~25^0). For depths greater than this, a continuum of weaker Compton scatter features will be detected because the incident intensity is weaker and the scattered photons have to travel through more nylon and resin before reaching the detector.

The incident photon intensity drops by only ~20% after passing through the resin thickness of 0.395 cm (oriented at 45^0). This means that nearly 4/5ths of the incident Ag Kα photons emerge through the far side of the resin in 45^0 orientation. Thus, a greater fraction of the overall Compton scattering occurs in the bulk of the nylon than at the near side (entrance surface) of the resin. Indeed the near side of the resin and the far side of the nylon define the limits (allowable range of angles) within which the majority of the Compton scattering occurs. The smaller fraction of photons that do Compton scatter from the surface (90^0) have not been attenuated through resin or nylon and so easily pass through the Si wafer and deposit less than half of their energy (I = ~30% I_0). However, they backscatter off the housing behind the Si wafer. Note that a spread in emission of 90^0 scattered photons is possible, indicating a range of Compton angles, but they would be centered about a mean of 90^0. Compton backscatter photons corresponds to angles $>90^0$. They are also of sufficiently high intensity (see columns 4 and 6 of table) that they have the impact of significantly lowering the position (mean energy) of the dominant observed Compton scatter feature. The above also applies when incident beam spreading is taken into account since the incident energy does not change. This is shown (for the left) as LL mean and LL max and (for the right, of the spread) as RR mean and RR max, in the table. For these reasons, the dominant Compton feature in the observed spectrum corresponds to a scattering angle $>90^0$ and the additional feature at ~90^0 is weaker in intensity. Finally, if the coherent scatter peak is to be solely used for normalization purposes in skin or skin phantoms, using the Si(Li) detector, further work looking into these two features is warranted, as the coherent tail-to-peak amplitude is higher in the Si(Li) detector than in the SDD. Attempts at including an additional feature near the coherent scatter were not successful. As mentioned earlier, Compton and coherent backscatter features are comparatively reduced because of the order of magnitude thicker Si sensitive volume. Also counts in the coherent scatter peak are a full order of magnitude weaker than those under the Compton scatter peak, leading to worse precision.

Since the scattering solid angle is not well defined at such a short phantom-detector separation (required for the highest characteristic x-ray count rate), moving the

detector away from the phantom may allow for better insight into the source of the two additional features. Also, cycling the detector through a range of scattering angles, with respect to the incident x-rays, would add/remove or shift some of the observed components allowing for them to be more clearly identified.

The importance of a correction for source (tube) strength is seen by tracking the fitted Compton or coherent scatter areas over each full dataset, with either detector. This is done in two ways: (a) scatter peak areas sorted by order of acquisition, where the respective scatter areas are plotted in the order in which their corresponding phantoms were run through the detection system and (b) scatter peak areas sorted by increasing As ppm (0-100 ppm), in each of the three trials recorded per concentration. The results are shown in figure 9 a,b.

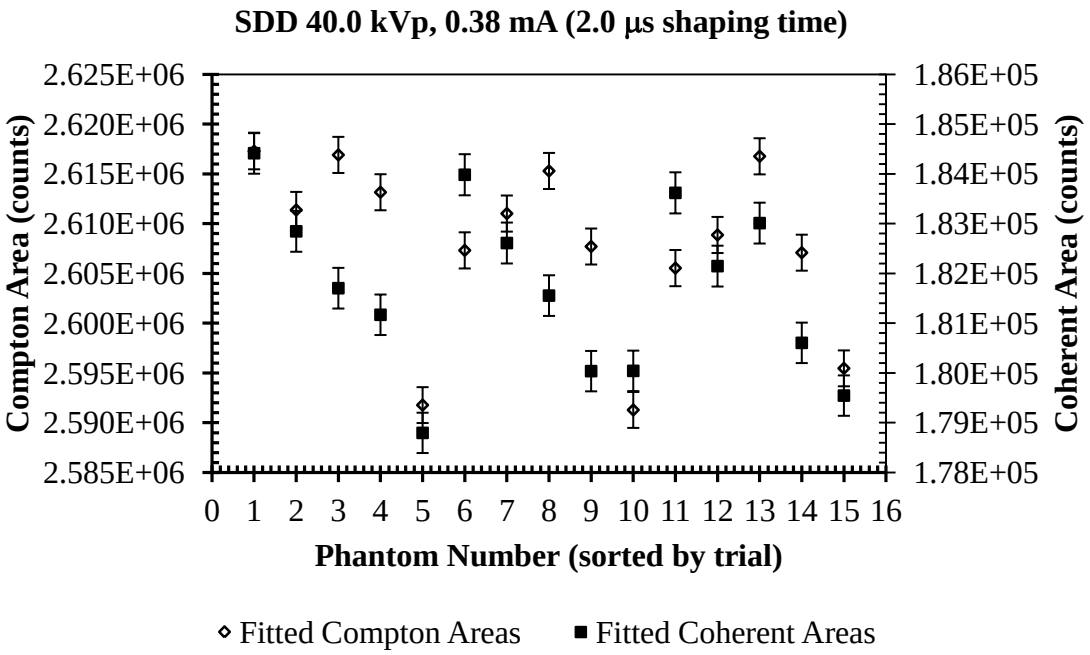

(a)

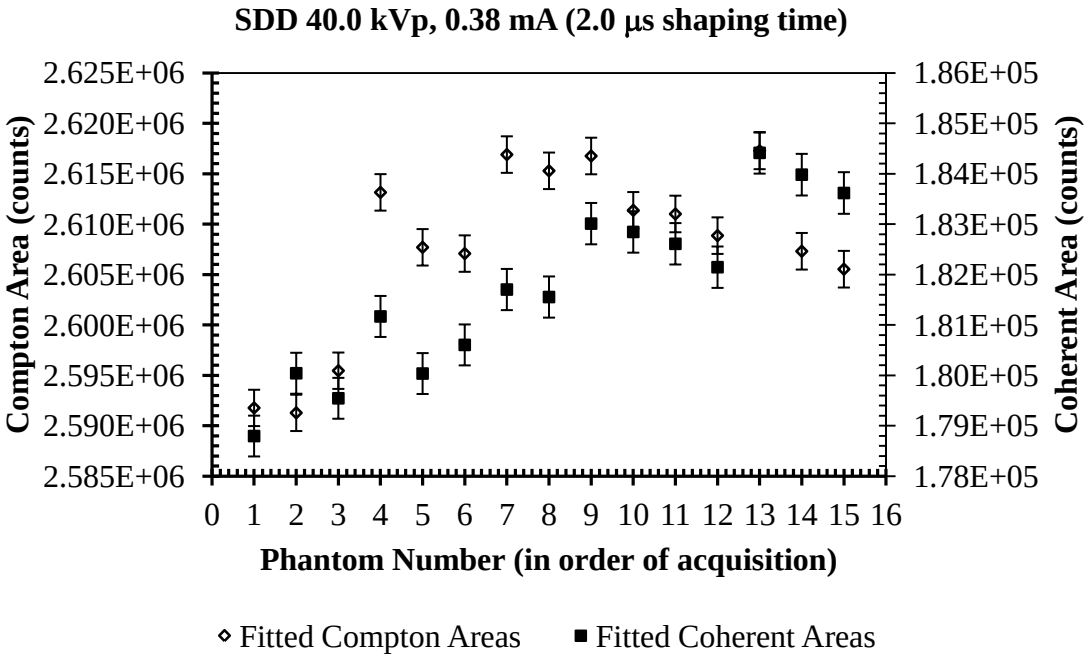
SDD 40.0 kVp, 0.38 mA (2.0 μs shaping time)
Compton Area (counts)
Coherent Area (counts)
2.625E+06
2.620E+06
2.615E+06
2.610E+06
2.605E+06
2.600E+06
2.595E+06
2.590E+06
2.585E+06
1.86E+05
1.85E+05
1.84E+05
1.83E+05
1.82E+05
1.81E+05
1.80E+05
1.79E+05
1.78E+05
0 1 2 3 4 5 6 7 8 9 10 11 12 13 14 15 16
Phantom Number (in order of acquisition)
Fitted Compton Areas
Fitted Coherent Areas

(b)

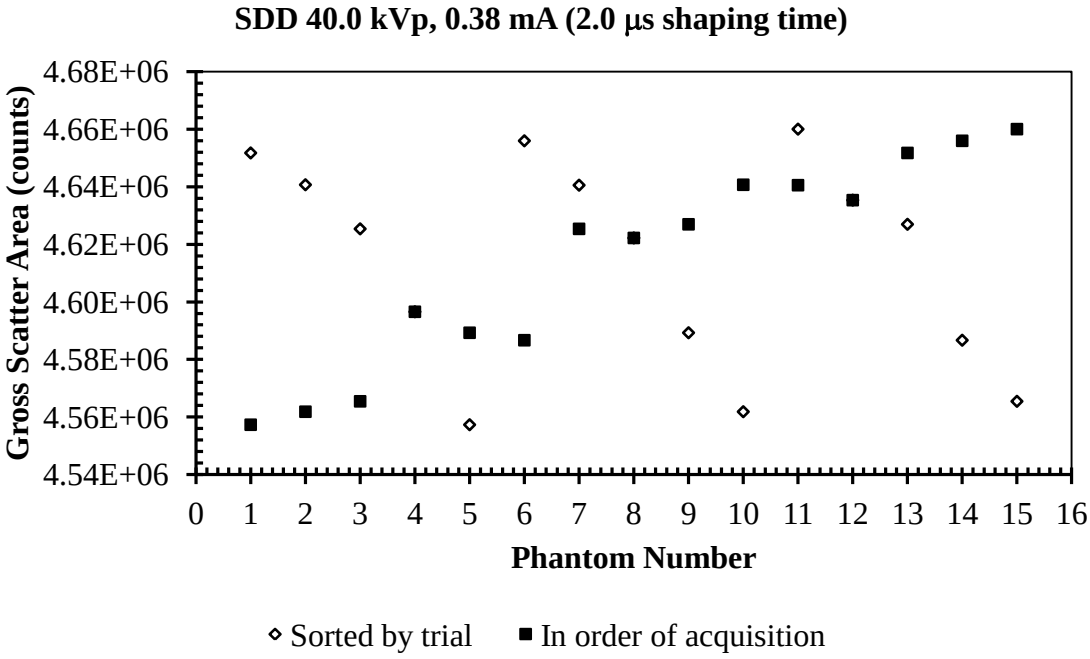
SDD 40.0 kVp, 0.38 mA (2.0 μs shaping time)
Gross Scatter Area (counts)
4.68E+06
4.66E+06
4.64E+06
4.62E+06
4.60E+06
4.58E+06
4.56E+06
4.54E+06
0 1 2 3 4 5 6 7 8 9 10 11 12 13 14 15 16
Phantom Number
Sorted by trial
In order of acquisition

(c)

Figure 9: Change in Compton and coherent peak scattered areas, (a) when sorted by trial in ascending order of concentration and (b) when sorted by order of acquisition (ascending order), (c) Change in gross scatter sorted in both ways.

A comparison to the gross scatter region, defined as the gross sum of all counts under the same region of the spectrum chosen for fitting the scatter peaks, is shown in figure 9 c and general agreement is noted here for the overall trends, when compared with figures 9a and 9b. Similar results were observed with the Si(Li) detector, and so are not included, for brevity. A change in scatter peak areas, when sorted in both ways discussed above, is clearly observed necessitating a correction to As Kα and Kβ peak areas. The drops in peak area of 0.53% (Compton), 2.70% (Coherent) and 2.25% (gross scatter) are noted when going from the first phantom in the first trial (phantom number 1) to the last phantom in the third trial (phantom number 15). For either detector, the majority of the counts in the spectrum are seen to be contained under the Compton scatter peak, which is expected given the higher absorption cross-section for skin or resin, and so it may be a better choice for normalizing to correct for source strength. Coherent normalization could not be expected to correct for variations in As concentration in skin with depth since more than two-thirds of the incident x-rays pass through resin or skin, without depositing their energy, as mentioned earlier. The mass attenuation coefficient of arsenic x-rays in resin is nearly nine times larger than that of the coherently scattered Ag x-rays. The bulk of the coherent scatter would originate deeper – in this case, in the nylon backing, or in the *in vivo* situation, bulk tissue behind skin. Also, peak precision would be higher for the Compton scatter peak; the total error in peak area includes the error due to peak-fitting. Combined with the order of magnitude reduction in the number of counts collected in the coherent peak, compared to the Compton scatter peak, with both the Si(Li) detector and the SDD. This would suggest that the Compton normalization would be a better choice for correction against variations in source strength for arsenic in skin. Work on development of the same detection system for XRF in bone (mean interaction site of both characteristic and scattered x-rays is located at the bone's surface) may require use of the coherent scatter peak due to the different matrix involved and the benefits derived from coherent normalization, as a means of correcting for bone size, have been detailed for bone Sr elsewhere (Zamburlini et al., 2008). Nonetheless, a cross-reference against the Compton peak would be advisable as a verification of a correction for source strength, due to its significantly superior statistics for the bone matrix as is the case with skin.

Monitoring arsenic Kα:Kβ ratio in resin phantoms:

In our group, previous and ongoing XRF work with Sr in bone has documented discrepancies in the Kα:Kβ ratio with the same Si(Li) detector as that used here (Heirwegh et al., 2012; Zamburlini et al., 2007). This ratio is of interest since it offers a way to examine the extent of x-ray attenuation in soft tissue overlying bone and is thus useful as an indicator of overlying tissue thickness. For the intended application of the current work, the thickness of the skin being probed could similarly be investigated. The result of tracking the Kα:Kβ ratio in the resin phantoms are shown, in comparison to the

results found with the Si(Li) detector, in table 6 as a function of shaping time for the five full SDD-based MDL datasets.

	2.0 μs	1.2 μs	0.8 μs	0.4 μs	Si(Li)	Si(Li) without Au
Min	5.440	5.631	5.848	6.325	4.108	4.794
AVG	6.135	6.331	6.481	6.840	5.033	5.792
SDOM	0.096	0.090	0.084	0.087	0.039	0.054
Stdev	0.331	0.311	0.292	0.303	0.359	0.498
Max	6.880	6.778	6.929	7.583	5.568	6.496
Range	1.440	1.148	1.082	1.258	1.460	1.702
RSD	5.399	4.915	4.513	4.426	7.127	8.598
PD (%)	26.471	20.382	18.499	19.885	35.542	35.512

Table 6: Kα:Kβ ratios with SDD (corrected), sorted by shaping time, and Si(Li) detector.

Non-zero ppm phantoms were used to calculate the ratio. The mean ratio over all shaping times and all tube conditions, is 6.881±0.392 (mean±StdDev) with the SDD and 5.033±0.359 for a shaping time of 6 μs with the Si(Li). Correcting for differences in absorption in the 450 μm thick Si wafer, at the two As energies, the mean SDD ratio improves to 6.448 ± 0.367 (mean±StdDev), which is still significantly higher than the ratio observed with the Si(Li) detector. Sorted by concentration, the mean corrected ratios (±StdDev) were 6.537±0.278, 6.492±0.199, 6.493±0.393 and 6.270±0.501 for 100 ppm, 60 ppm, 40 ppm and 20 ppm respectively and so a clear trend is not noted in ratio vs ppm. These are the same value to within uncertainties. A weak peak likely originating in the phantom or head of the detector was noted at ~11.4 keV. The diffraction peak at ~11.1 keV has been eliminated by increasing the tube voltage. This is possible with the 90^0 layout since the dead time is much lower than that for a head-on spectrum. For this additional peak between the two arsenic peaks, an accurate estimate of its position and width could not be found due to its low amplitude, meaning that it should not be expected to interfere significantly with the As Kβ peak itself. The As Kβ FWHM is ~190 eV and is located sufficiently far away from this additional peak for the As Kβ tail, as opposed to the As Kβ Gaussian, to contain the majority of the overlapping counts from the additional feature. Thus an additional Gaussian could not be fitted to model this peak and was omitted from the fitting. Sorted by shaping times, the ratios are plotted in figure 10, in comparison the Si(Li) detector ratios.

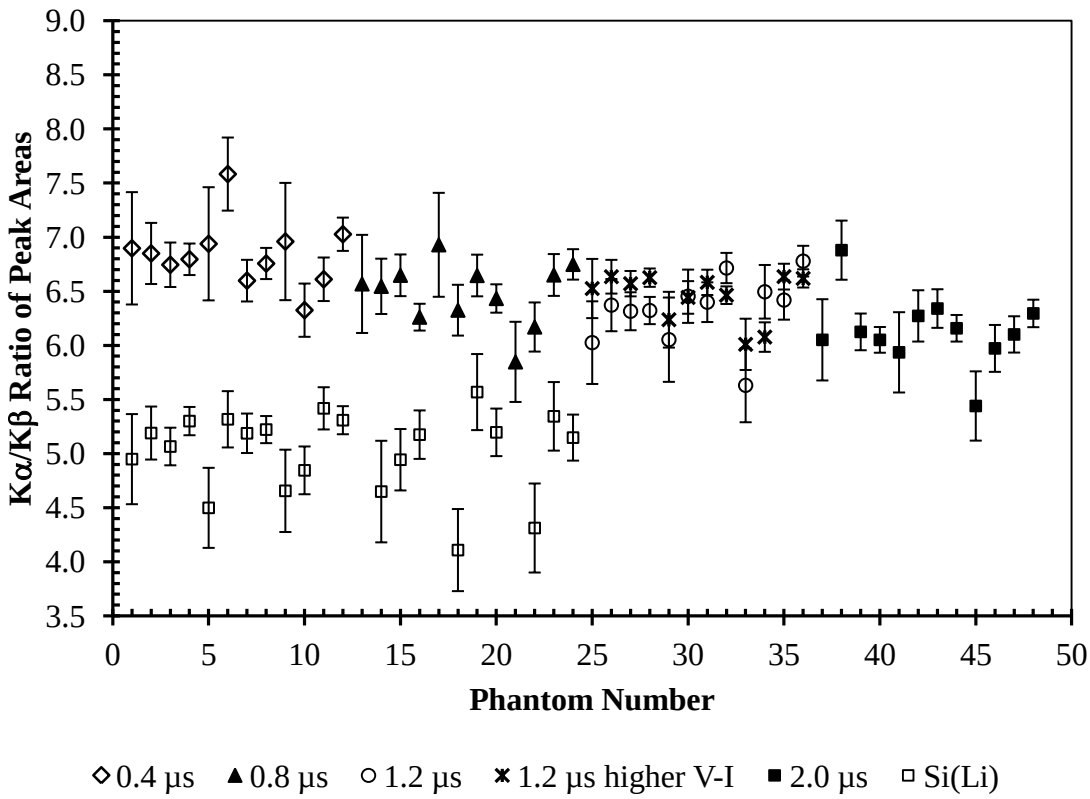

Figure 10: As Kα:Kβ peak ratios plotted per phantom number, for SDD (sorted by shaping time) and for Si(Li) detector.

The ratio is clearly improving as the SDD's shaping time is increased, to 6.135±0.331 for the highest chosen shaping time of 2.0 µs, warranting presentation of these ratios separately. At lower shaping times, the FWHM gets worse and so the interfering peak may be enhancing its contribution to the tail on the As Kβ peak, thereby reducing the counts under Kβ and driving up the As Kα:Kβ ratio. The higher shaping time allows for better resolution of the As Kβ peak and its tail from the remnants of the interfering peak at ~11.4 keV. If the additional feature cannot be modeled reliably with a Gaussian, then this may result in a comparatively better representation of counts under the As Kβ peak.

By contrast, establishing a reliable As Kα:Kβ ratio in the same counting time (1800 seconds), with the Si(Li) detector, is much more challenging due to the presence of gold in the detector contacts, as mentioned earlier. The mean Si(Li) detector ratio is 5.201±0.170 (±StdDev) using the 40, 60 and 100 ppm phantoms, 5.201±0.109 using the 60 and 100 ppm phantoms and 5.205±0.110 using only the 100 ppm phantoms. Including all the ppms, the ratio was listed earlier to be ~5.0. It is clear that the lowest ppm phantom is lowering the mean ratio substantially and should not be used for this calculation. The first factor that may contribute to this difference in ratios, between

detectors, is the gold Lβ peak at 11.44 keV, which is close to the As Kβ peak at 11.73 keV. This interference problem is greater for the Si(Li) detector than for the SDD because of the worse resolution. The degree of Au Lβ interference with the As Kβ peak area is greatest in the 20 ppm phantom, by comparison to the others and so the ratio diverges more in this phantom than in the others. The second factor affecting the ratio with the detector Si(Li) is the inability of the fitting routine to include a tail in the fitting function. With the highest concentration phantom, it was found that the tail function diverged strongly when included in fitting the As Kβ peak with the Si(Li). This was not the case with the SDD. With the Si(Li) detector, the gold peak takes up a large fraction of the counts that would normally fall under the As Kβ tail. This problem would be exaggerated at lower concentrations where the As Kβ tail would be strongly mixed with the gold peak. Excluding the tail with the Si(Li) analysis may overestimate the As Kβ peak area causing the ratio to be lower than that observed with the SDD. When the full set of Si(Li) spectra was analyzed with a tail included in the peak-fitting function, excluding the Gaussian for the Au Lβ, the average chi-squared value was found to be 1.123±0.125 and the Kα:Kβ ratio was found to be 5.79±0.49 (mean±StdDev). The elevation in standard deviation can be reduced by excluding the 20 ppm phantom results, as was done above, giving a mean ratio of 6.03±0.29. These ratios agree with the expected ratio of ~5.8 for As in resin. Both of these ratios are in agreement, within standard deviation, of the SDD Kα:Kβ ratio at the highest SDD shaping time.

While the earlier shaping time results did not reveal substantial gains in peak precision or peak and total count rates, this As Kα:Kβ ratio result along with the lower MDL suggests that the Kα:Kβ ratio should influence the choice of shaping time. Additionally, strictly speaking, exclusion of the gold peak from the fitting is not justified, however the improved agreement does indicate that a) the As Kβ area dropped, thereby increasing the Kα:Kβ ratio and b) despite the poor resolution of the Si(Li) detector, the influence of the gold Lβ peak may be more strongly influencing the As Kβ tail than it is the As Kβ Gaussian used in the peak-fitting; in turn the tail takes away counts from the Gaussian. If a tail is included in the Kα peak, then it should be retained in the As Kβ peak to account correctly for the non-Gaussian peak shapes at the lower energy side. This ratio result indicates that inclusion of the Kβ tail would produce a ratio that is closer to the theoretically predicted value. For all SDD shaping times, the tail for the As Kβ peak was found to be longer than that for the As Kα peak, suggesting that a substantial part of the ~11.4 keV peak is contained in the tail feature and not in the As Kβ Gaussian. The difficulty in fitting the As Kβ peak, with either detector, suggests reporting an As Kα-specific MDL as opposed to an inverse variance-weighted Kα-Kβ combined As MDL with this detector, as has been done elsewhere, for Sr in bone (Sibai, 2011; Zamburlini et al., 2006).

Several additional factors possibly influencing this ratio can be ruled out. The distribution of As in the resin may account for this difference, as different levels of self-

attenuation would be observed. However, all else being equal, such a factor would affect both detector types equally. Additionally, absorption in the Be window [50 μm for Si(Li) and 25 μm for SDD] is <1% in both cases and the difference in absorption of the Kα and Kβ peaks is 0.11% for the Si(Li) and 0.06 % for the SDD, eliminating the need for a correction here. The fits shown earlier extend sufficiently past the high energy side of the Kβ peak to estimate properly the background under both peaks. Previous work with resin phantoms has shown that neutron activation analysis (NAA) produced an As concentration of 0.04±0.10 ppm for blank (undoped) resin (Studinski et al., 2005), eliminating the resin as a possible source. The origin of the discrepancy of the Kα:Kβ ratio, between detector types, can thus be isolated to systematic (detector) based factor – exclusion of a tail on the As Kβ due to the presence of gold contacts in the Si(Li), not found in the SDD. Further work to examine the As Kβ fitting is warranted, if this ratio is to be used for As detection, particularly with the Si(Li) detector due to its worse energy resolution. Perhaps the best way to address this would to perform a series of long counts with the blank and 100 ppm As phantoms. The degree of possible interference with either As peak, which is not evident in 1800 seconds used in the current work, will be enhanced and can be built into the fitting function if such features are found to be present.

5. Conclusion:

This work compares the performance of an 80 mm^2 active area Silicon Drift Detector (SDD) with a 200 mm^2 Si(Li) detector. For the given source strength, the variations in As tail-to-peak areas, peak and total count rates are minimally changed as the SDD's shaping time is reduced, suggesting that another variable may be more important in driving the choice of shaping time. A weaker than desired source strength limits the true benefit of the SDD from being demonstrated in these data. This was further reflected in significantly lower dead times observed with the SDD. Despite this, the current work reports a lower As Kα MDL was noted with the SDD than with the Si(Li) detector. Except for the lowest tested shaping time of 0.4 μs, for MDL work, the MDLs with the SDD were largely unchanged as shaping time was reduced. However, the SDD's Kα:Kβ ratio was found to be in better agreement with the ratio with the Si(Li) detector at the highest tested shaping time of 2.0 μs. Thus, this shaping time should be used for future work with this detector. Results of the current work suggest that calculation of this ratio, with the Si(Li) detector, may be limited to strong As signals due to interference of a gold Lβ line with the As Kβ peak. This produced a ratio, using the lowest ppm As phantom, that was lower than that found using the three higher concentration ones. Finally, a mean interaction site located deeper than that predicted by the geometry of the setup used was observed with both detectors. Combined with an elevated degree of backscatter off the internal housing of the SDD, resulted in a larger downshift in the Compton scatter peak with this detector type compared to that with the Si(Li) detector. Future work should more closely investigate the origin of the various components of the scatter peak features observed in the spectra of both detectors since the need for their use for normalization against variations in source output is demonstrated here.

Acknowledgements:
The authors would like to acknowledge research support from the Occupational Nuclear Medicine Research Group and Nuclear Instrumentation Group within the Medical Physics and Applied Radiation Sciences Department at McMaster University. Funding through Discovery Grants from the Natural Sciences and Engineering Research Council of Canada was used in partial support of this work.

References:

Behinaein, S., Chettle, D.R., Atanackovic, J., Egden, L.M., Fleming, D.E.B., Nie, L.H., Richard, N., Stever, S., 2011. In vivo measurement of lead in the bones of smelter workers using the four-element "clover-leaf" geometry detector system. Phys. Med. Biol. 56, 653–665.

Bertuccio, G., Sampietro, M., Fazzi, A., 1992. High resolution X-ray spectroscopy with silicon drift detectors and integrated electronics. Nucl. Instruments Methods Phys. Res. Sect. A Accel. Spectrometers, Detect. Assoc. Equip. 322, 538–542.

Campbell, J.L., McDonald, L., Hopman, T., Papp, T., 2001. Simulations of Si(Li) x-ray detector response. X-Ray Spectrom. 30, 230–241.

Chen, C.J., Chuang, Y.C., Lin, T.M., Wu, H.Y., 1985. Malignant neoplasms among residents of a blackfoot disease-endemic area in Taiwan: high-arsenic artesian well water and cancers. Cancer Res. 45, 5895–9.

Da Silva, E., Pejović-Milić, A., Heyd, D. V., 2008. The use of teeth as the site for the in vivo or ex vivo quantification of skeletal strontium by energy-dispersive X-ray fluorescence spectrometry: A feasibility study. J. Anal. At. Spectrom. 23, 527–534.

Das, D., Chatterjee, a, Mandal, B.K., Samanta, G., Chakraborti, D., Chanda, B., 1995. Arsenic in ground water in six districts of West Bengal, India: the biggest arsenic calamity in the world. Part 2. Arsenic concentration in drinking water, hair, nails, urine, skin-scale and liver tissue (biopsy) of the affected people. Analyst 120, 917–24.

Fishbein, L., 1981. Sources, transport and alterations of metal compounds: an overview. I. Arsenic, beryllium, cadmium, chromium, and nickel. Environ. Health Perspect. 40, 43–64.

Fleming, D.E.B., Gherase, M.R., 2007. A rapid, high sensitivity technique for measuring arsenic in skin phantoms using a portable x-ray tube and detector. Phys. Med. Biol. 52, N459–65.

Gatti, E., Rehak, P., 1984. Semiconductor drift chamber — An application of a novel charge transport scheme. Nucl. Instruments Methods Phys. Res. 225, 608–614.

Gawdzik, B., Matynia, T., Chmielewska, E., 2001. Modification of unsaturated polyester resin with bismaleimide. J. Appl. Polym. Sci. 82, 2003–2007.

Grinyer, J., Atanackovic, J., Byun, S.H., Chettle, D.R., 2007. Phantom studies of Cd, Hg and Cl by prompt gamma neutron activation analysis using a 238Pu–Be neutron source. Nucl. Instruments Methods Phys. Res. Sect. B 263, 262–265.

Harris, D.C., 2006. Quantitative chemical analysis, 7th ed. W. H. Freeman, New York, USA.

Heirwegh, C.M., Chettle, D.R., Pejović-Milić, A, 2010. Evaluation of imaging technologies to correct for photon attenuation in the overlying tissue for in vivo bone strontium measurements. Phys. Med. Biol. 55, 1083–98.

Heirwegh, C.M., Chettle, D.R., Pejovic-Milic, A., 2012. Ex vivo evaluation of a coherent normalization procedure to quantify in vivo finger strontium XRS measurements. Med. Phys. 39, 832–41.

Jorch, H.H., Campbell, J.L., 1977. On the analytic fitting of full energy peaks from Ge(Li) and Si(Li) photon detectors. Nucl. Instruments Methods 143, 551–559.

Knoll, G.F., 1999. Radiation Detection and Measurement, 3rd ed. John Wiley & Sons Inc.

Kotulski, Z.A., 2010. Error Analysis with Applications in Engineering. Springer Science+Business Media B.V., Dordrecht.

Lechner, P., Pahlke, A., Soltau, H., 2004. Novel high-resolution silicon drift detectors. X-Ray Spectrom. 33, 256–261.

Marquardt, D.W., 1963. An Algorithm for Least-Squares Estimation of Nonlinear Parameters. J. Soc. Ind. Appl. Math. 11, 431–441.

Metzger, W., Engdahl, J., Rossner, W., Boslau, O., Kemmer, J., 2004. Large-area silicon drift detectors for new applications in nuclear medicine imaging. IEEE Trans. Nucl. Sci. 51, 1631–1635.

Misbahuddin, M., Momin, A., Al-Amin, M., 2008. All-E lutein and 3'-epilutein in the epidermis of chronic arsenic poisoning. Clin. Toxicol. 46, 176–180.

Morales, K.H., Ryan, L., Kuo, T.L., Wu, M.M., Chen, C.J., 2000. Risk of internal cancers from arsenic in drinking water. Environ. Health Perspect. 108, 655–61.

Nie, H., Chettle, D., Luo, L., O'Meara, J., 2006. In vivo investigation of a new 109Cd gamma-ray induced K-XRF bone lead measurement system. Phys. Med. Biol. 51, 351–60.

Nie, L.H., Sanchez, S., Newton, K., Grodzins, L., Cleveland, R.O., Weisskopf, M.G., 2011. In vivo quantification of lead in bone with a portable x-ray fluorescence system--methodology and feasibility. Phys. Med. Biol. 56, N39–51.
O'Meara, J.M., Chettle, D.R., McNeill, F.E., Webber, C.E., 1998. In vivo X-ray fluorescence (XRF) measurement of uranium in bone. Appl. Radiat. Isot. 49, 713–715.
Pejović-Milić, A., Stronach, I.M., Gyorffy, J., Webber, C.E., Chettle, D.R., 2004. Quantification of bone strontium levels in humans by in vivo x-ray fluorescence. Med. Phys. 31, 528–38.
Rehak, P., Gatti, E., Longoni, A., Kemmer, J., Holl, P., Klanner, R., Lutz, G., Wylie, A., 1985. Semiconductor drift chambers for position and energy measurements. Nucl. Instruments Methods Phys. Res. Sect. A Accel. Spectrometers, Detect. Assoc. Equip. 235, 224–234.
Roy, C.W., Gherase, M.R., Fleming, D.E.B., 2010. Simultaneous assessment of arsenic and selenium in human nail phantoms using a portable x-ray tube and a detector. Phys. Med. Biol. 55, N151–N159.
Salter, C., 2000. Error Analysis Using the Variance-Covariance Matrix. J. Chem. Educ. 77, 1239.
Samanta, G., Sharma, R., Roychowdhury, T., Chakraborti, D., 2004. Arsenic and other elements in hair, nails, and skin-scales of arsenic victims in West Bengal, India. Sci. Total Environ. 326, 33–47.
Sibai, M., 2011. Second generation of the diagnostic tool for the In vivo measurement of strontium levels in human bone. Theses Diss.
Somervaille, L.J., Chettle, D.R., Scott, M.C., 1985. In vivo measurement of lead in bone using x-ray fluorescence. Phys. Med. Biol. 30, 929–43.
Strüder, L., Soltau, H., 1995. High Resolution Silicon Detectors for Photons and Particles. Radiat Prot Dosim. 61, 39–46.
Studinski, R.C.N., 2005. Development of an in vivo method of measuring arsenic with radiation.
Studinski, R.C.N., McNeill, F.E., Chettle, D.R., O'Meara, J.M., 2004. XRF analysis of arsenic-doped skin phantoms. X-Ray Spectrom. 33, 285–288.
Studinski, R.C.N., McNeill, F.E., Chettle, D.R., O'Meara, J.M., 2005. Estimation of a method detection limit for an in vivo XRF arsenic detection system. Phys. Med. Biol. 50, 521–530.
Studinski, R.C.N., McNeill, F.E., O'Meara, J.M., Chettle, D.R., 2006. A method detection limit for potential in vivo arsenic measurements with a 50 W x-ray tube. Phys. Med. Biol. 51, N381–7.
Taylor, J.R., 1997. An Introduction Error Analysis: The Study of Uncertainties in Physical Measurements, 2nd ed. University Science Books, Sausalito, California, USA.
Uher, J., Roach, G., Tickner, J., 2010. Peak fitting and identification software library for high resolution gamma-ray spectra. Nucl. Instruments Methods Phys. Res. Sect. A Accel. Spectrometers, Detect. Assoc. Equip. 619, 457–459.
Zamburlini, M., Pejović-Milić, A., Chettle, D.R., 2006. Evaluation of geometries appropriate for 125I in vivo bone strontium X-ray fluorescence measurement. J. Radioanal. Nucl. Chem. 269, 625–629.
Zamburlini, M., Pejović-Milić, A., Chettle, D.R., 2008. Coherent normalization of finger strontium XRF measurements: feasibility and limitations. Phys. Med. Biol. 53, N307–13.
Zamburlini, M., Pejović-Milić, A., Chettle, D.R., Webber, C.E., Gyorffy, J., 2007. In vivo study of an x-ray fluorescence system to detect bone strontium non-invasively. Phys. Med. Biol. 52, 2107–22.

Chapter 6 Measurements with optically-focused x-ray tube system:

The last XRF system investigated for the *in vivo* measurement of arsenic in this thesis uses optics to focus the incident x-rays with the advantage of excitation using monochromatic x-rays. In the absence of monochromatic incident exciting radiation, a non-zero dose is contributed by photons that do not contribute to the detection capabilities of the element under investigation. Removal of these photons from a polychromatic source would reduce both the dose delivered and the background under the peaks of interest, with the latter possibly making those peaks visible in the recorded spectrum. The x-ray tube's energy pickoff is performed with a doubly curved crystal (DCC). Crystal bending techniques also produce a very focused beam with the benefit of better signal-to-noise ratio during measurement of secondary characteristic x-rays and reduces background without requiring high power output.

6.1 Motivation, optical focusing and chosen specifications:

The Bremsstrahlung background in a conventional XRF spectrum is produced from scattering of source radiation in the sample. Focusing x-rays allows for a reduction in the exposed area and this, in turn, decreases the background in addition to reducing the dose. Specifically, focusing the x-ray anode's characteristic x-rays, as opposed to the Bremsstrahlung, allows for comparatively superior incident intensity. Such an optically focused tube output produces a highly intense tight beam, greatly reducing scatter.

6.2 Draft for article IV follows:

The feasibility of a method for potential in vivo measurements of arsenic using optically focused x-ray fluorescence

E. D. Desouza[1], F. E. McNeill[1], D. R. Chettle[1], A. Pejovic-Milic[2], D. E. B. Fleming[3]

[1] Department of Medical Physics and Applied Radiation Sciences, McMaster University, Hamilton, ON, L8S 4K1, Canada
[2] Department of Physics, Ryerson University, 350 Victoria Street, ON, M5B 2K3, Canada
[3] Department of Physics, Mount Allison University, Sackville, NB, E4L 1E6, Canada

Manuscript will be submitted: Phys. Meas. 2013

Author contributions:
Elstan Desouza was responsible for experimental setup, data acquisition and analysis.
Ana Pejovic-Milic offered unrestricted use of equipment and her previous research documented setup, performance evaluation and optimization of the equipment.
David Chettle and David Fleming assisted in interpretation of data.
Elstan Desouza was responsible for preparation of the draft manuscript.
Fiona McNeill supervised and guided the research.

Abstract

Results of the development of an x-ray tube based system for the measurement of arsenic in skin is reported in terms of its ability to measure arsenic in 2.8 ± 0.1 mm thick skin tissue mimicking resin phantoms using a 25 W x-ray tube. The x-ray tube uses a doubly curved crystal to focus x-rays from an x-ray tube with a silver anode. The beam is focused to 0.05 mm^2 at the focal length (30.0±0.2) cm away from the tube and expands to ~0.9 mm^2 at a distance of (95.6±0.2) cm away. The performance of the XRF detection system is documented by cycling through various x-ray tube conditions and through other system parameters such as source-to-phantom and phantom-to-detector distance. A brief comparison is made between two types of radiation detectors. The lowest detection limits possible with a lithium drifted silicon detector and silicon drifted detector are ~0.8 ppm and 0.45 ppm respectively in a 30-minute measurement. These would allow the system to detect arsenic in the skin of exposed individuals. The sensitivity of the system to changing phantom-detector distance, r, was found to follow ~$1/r^2$ and is fairly stable as the beam spreads out as distance from the focal length is increased. Li(F) thermoluminescent dosimetry chips found that the maximum equivalent (skin) and whole body effective doses delivered by the system are ~8-25 mSv, depending on distance away from the radiation source, and <1 mSv respectively, for a potential 30 minute subject exposure. This is an acceptable radiation dose that does not exceed regulatory ICRP limits for members of the general population.

1. Introduction

1.1 Arsenic toxicity and monitoring

Arsenic (As) is well known to be a naturally occurring toxin and is carcinogenic to humans (WHO-IARC, 2012). Parts of China, Taiwan, Bangladesh and Chile have been found to contain drinking water with high arsenic concentrations (Chakraborti et al., 2003; Chiu et al., 2004; Ferreccio et al., 2000; Mead, 2005; Mo et al., 2006). Naturally occurring arsenic in areas of eastern Canada contributes elevated risks due to water drawn from wells with arsenic concentrations higher than 10 μg/L (Klassen, 2009; McGuigan et al., 2010), which is the WHO recommended limit (WHO, 2011, 2010). Parts of the USA have also reported elevated levels of arsenic (Ettinger et al., 2009; Lewis et al., 1999). Negative health effects such as Blackfoot disease, liver and bladder cancers and neurological disorders have been associated with arsenic contaminated water (Ch'i and Blackwell, 1968; Chen et al., 1985; Chiou et al., 1995). In the absence of contaminated water, the most potent source of inorganic arsenic is food, through crops or direct ingestion (Mead, 2005). Inhalation of arsenic from copper smelters is another source of arsenic in the body (Lubin et al., 2008).

Monitoring is commonly performed destructively using hair (Mandal et al., 2003) or nail samples (Button et al., 2009; Karagas et al., 1996; Slotnick and Nriagu, 2006). This permits some assessment of cumulative exposure. Arsenic content in urine samples offer a short-term indication of arsenic in the body (Apostoli et al., 1999; Dang et al., 1999; Hwang et al., 2002). However, it has been shown that arsenic binds to keratin

(Misbahuddin et al., 2008) and is retained in skin (Schwartz, 1997) suggesting that quantification of skin arsenic content could permit the assessment of long term arsenic exposure. In addition, skin is the most "at-risk" keratin-containing organ making a form of non-invasive measurement, such as X-Ray Fluorescence (XRF), of skin arsenic concentrations worthwhile. Skin measurements could therefore be a measure of both long term exposure and specifically of exposure to an organ-at-risk.

1.2. X-Ray Fluorescence (XRF)

1.2.1. Basics of technique and examples of in vivo application

XRF is based on the phenomenon of the photoelectric effect. For an electron in one of the shells of an atom, an incident photon, with energy higher than the electron's binding energy, can transfer its energy to the electron, ejecting it from its shell. The spot occupied by the ejected electron, known as a photoelectron, is filled by an electron from an outer shell (less tightly bound) with a lower energy. This is known as the photoelectric interaction and is the foundation of XRF. X-rays with an energy characteristic to a particular element can be emitted. A competing process can produce an Auger electron. The fraction of characteristic x-rays emitted per absorbed photons is called the fluorescence yield. For arsenic, the K-shell (innermost) fluorescence yield is 57% (Robinson, 1991). Through the excitation and subsequent detection of characteristic x-rays, at element-specific energies, from a sample it is possible to specify and quantify the elemental composition of the sample.

The XRF technique has been previously used for the *in vivo* quantification of trace element content. Strontium, uranium and lead in bone (Nie et al., 2006; O'Meara et al., 1998; Zamburlini, Pejović-Milić, et al., 2007) and cadmium in the kidney (Ahlgren and Mattsson, 1981) are some examples of *in vivo* applications of XRF. An arsenic in vivo detection limit of 2.6-5.7 ppm was previously estimated using an I-125 radioisotope as the source, from members of the general population. However, this represents the range of concentrations expected in a population that has been exposed to arsenic (Studinski et al., 2005). An order of magnitude reduction in the detection limit was subsequently obtained by using an x-ray tube with a molybdenum target (Studinski et al., 2006). Other work has reported the use of a portable (handheld) x-ray analyzer. This was used for 120 second real time irradiations with a Si PiN diode detector and obtained an MDL of 0.446 ± 0.006 ppm in 8 mm thick phantoms with no nylon backing (Fleming and Gherase, 2007).

1.2.1. Optical focusing concepts

The non-destructive applications of energy dispersive X-Ray Fluorescence (XRF), to elemental analysis, span a range of fields such as research and development and forensics and serves as the motivation behind the development of the optical focusing technology that is coupled to the x-ray tube source used in the current work. Not only does XRF allow for identification of the presence of trace elements in a sample but it also allows for their quantification. Improved accuracy and sensitivity in XRF has been achieved through a combination of XRF with focusing optics. With a highly focused

beam, trace element analysis of small sections of a sample individually is possible. The principle behind Doubly Curved Crystal (DCC) optics lies in the well-known Bragg law. Monochromatization is realized through the diffraction of an x-ray beam off a crystal, where the angle at which the diffraction occurs is given by the Bragg law: $n\lambda = 2d \sin\theta$, where θ is the angle between the x-ray beam and the crystal surface (or Bragg plane), d is the crystal plane spacing, λ is the diffracted beam's wavelength and n specifies the order of diffraction off the crystal surface. The choice of monochromator (crystal) material and grazing angle determines the excitation energy of the emitted x-rays. Diffraction planes parallel to the crystal surface satisfies the Bragg condition over a large range of angles. Such DCC optics produce a tight beam and, thus, greatly reduce scatter. Thus, a DCC focusing XRF system produces a very well focused monochromatic x-ray beam. It results in an exceptionally low background resulting in vastly improved sensitivity to small changes in sample concentration because of the removal of the background from conventional x-ray tubes (MacDonald et al., 1999). Applications have been documented in μXRF (Bjeoumikhov et al., 2005) and mammography (Sugiro et al., 2004).

In *in vivo* XRF of skin for quantifying arsenic, the palm of the hand was used in the previous work related to arsenic referenced above. In order for the measured arsenic concentration in a subject to be representative of the target organ as a whole, maximal coverage of the intended area by the incident beam is desired. Thus, the requirement for spatial resolution is not strict and exposures can be performed at distances larger than the focal length.

1.2.2. Experimental setup

A DCC focusing based XRF system has been developed by X-Ray Optical Systems (Albany, NY, USA), consisting of an X-Beam module housing the x-ray tube and built-in monochromator crystal. The X-Beam module is connected to a high voltage power supply and mounted on top of a cooling fan. It provides optical alignment preventing drift of the beam location. The monochromator crystal cannot be accessed and so the incident energy is fixed. The X-Beam used in this work made use of a silver target x-ray source. It allowed for a maximum tube operating voltage of 50.0 kVp and a maximum current of 0.50 mA.

The need to focus the produced characteristic x-rays brings into consideration the choice of x-ray tube anode material. Instrumental sensitivity could be improved if the DCC optics would have been designed as to provide a more suitable energy (~12-13 keV) for As excitation, thus improving the detection limits and minimizing the radiation exposure of subjects. This would be complicated by the overlap with the Compton scatter feature observed in XRF spectra and so a higher energy needs to be chosen. The arsenic K-edge is just below 12 keV (Deslattes et al., 2003). The available system was however originally designed for quantifying Sr in bone. Previous XRF work on that project has been done using I-125 brachytherapy seeds as the fluorescing source (Heirwegh, Chettle, & Pejovic-Milic, 2012; Moise, Adachi, Chettle, & Pejović-Milić, 2012; Zamburlini, Pejović-Milić, & Chettle, 2006; Zamburlini et al., 2007a). However, the main limitation

of using that source was due to the wide range of energies that it emitted. With such a source, the emitted energy cannot be changed. Thus, maximizing the photoelectric cross section is not possible using a radioisotope source since the average source energy cannot be moved closer to the K-edge of the element being studied. The photoelectric cross section of arsenic in resin is 34.78 cm^2/g, 44.63 cm^2/g and 66.07 cm^2/g when using silver (Ag), molybdenum (Mo) and rhodium (Rh) x-ray targets respectively (Berger et al., 2010). The benefits of choosing Rh anode are clear. In the absence of monochromatic incident exciting radiation, a non-zero dose is contributed by photons that do not contribute to the detection capabilities of the element under investigation. For the x-ray tube anode materials above, these would be Mo Kβ, Rh Kβ or Ag Kβ. Removal of these photons from a polychromatic source would reduce both dose delivered and the background under the peaks of interest.

The Bremsstrahlung background in a conventional XRF spectrum is produced from scattering of source radiation in the sample. Focusing x-rays allows for a reduction in the exposed area and this, in turn, decreases the background in addition to reducing the dose. Specifically, focusing the x-ray anode's characteristic x-rays, as opposed to the Bremsstrahlung, allows for comparatively superior incident intensity. Such an optically focused tube output produces a highly intense tight beam greatly reducing scatter. However, an x-ray tube tuned to select a single energy is limited by the anode materials that can be used as x-ray tube targets. The energy must be close enough to the element's absorption edge to maximize the photoelectric cross-section, however it cannot be so close that the photopeak being studied is influenced by a very strong continuum from the anode material's scattering peaks. The use of a silver anode was found to optimize the conditions of a bone strontium measurement (Zamburlini, 2008). The choice of anode material is clearly justified for Sr given that the 90^0 and 180^0 Compton scatter peaks are at 21.28 keV and 20.43 keV, compared to the Sr Kβ peak at 15.72 keV (Deslattes et al., 2003). The gain in cross-section by choosing Rh over Ag, in resin, is ~20%. The As Kα background contribution due to the Ag Compton tail feature is nearly constant due to the large difference in energies between Ag and As. This is reduced for Rh – the Compton scatter feature would move to a lower energy – assuming 115^0 scatter angle, 19.1 keV for Rh, as opposed to ~20.8 keV for Ag. The uncertainty in background ($N^{1/2}$) under the As Kα peak, using Rh anode, was estimated to be ~40% higher than that for an Ag anode. If a system was being designed from scratch for the *in vivo* measurement of As, the design may have been different and a different target material might have been chosen. However, the use of this system was pragmatic. It was already purchased and available and so its performance for the measurement of As *in vivo* was assessed.

2. Method

2.1 Layout and Experimental Procedure

The x-ray tube, with the DCC crystal, was mounted inside an X-Beam module and was placed inside a square shaped plexiglass cabinet. A voltage-current ramp up/control box (provided by XOS) was placed on a lab bench and connected to the tube. For radiation safety purposes, an external shutter was installed and connected to a safety

interlock system. This allowed the user to control exposure to x-rays from the tube. The shutter provided by the X-Beam, connected to the ramp-up box, was by-passed. The detector was placed on a movable base and the center of the flight tube (through which the x-ray beam emerged) above the base was aligned with the center of the detector's Be window above the base. The movable base allowed variation of the distance between the source (tube) and phantom. With the detector at 90^0 relative to the direction of the incident x-ray beam, two positioning plates (heavy-duty right angle brackets) were attached to a movable base. These allowed variation in phantom-detector distance while preserving the 90^0 orientation. The shortest phantom-detector distance possible with this layout was (4.2±0.2) cm. The largest source-detector distance possible was (78.1±0.2) cm, due to the large size of the Si(Li) detector's LN2 dewar. An overhead schematic of the setup is shown in figure 1.

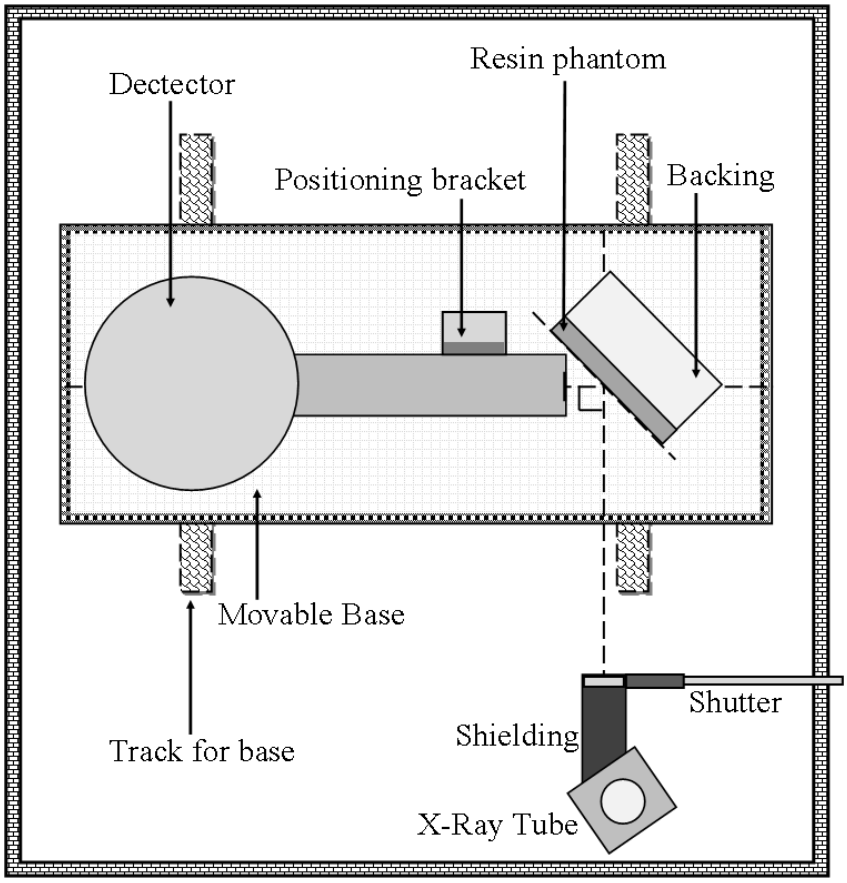

Figure 1. Overhead schematic of the experimental layout used with x-ray tube housing containing DCC optic built in.

The phantoms were prepared by mixing polyester resin with varying amounts of Arsenic Atomic Absorption Solution (AAAS) and a hardening catalyst. The resulting mixture was allowed to dry and the resulting solid blocks were then cut into slices. One

slice was used as the phantom while another was used to verify the phantom concentration and its uncertainty using neutron activation analysis following a previously described method (Studinski et al., 2005). Phantom irradiations were performed for a live time of 1000 seconds. Phantom-detector and source-phantom distances as well as detector type were varied in the current work. Each detector was used separately, with the phantom oriented such that the incident and take-off angles are 45^0 each.

Precise phantom alignment was achieved by imaging the x-ray beam using Gafchromic EBT film (ISP Dosimetry). Film exposure was performed over several hours for a sufficiently long duration that the beam image was just clear enough to identify its boundary. Through several trials, it was found that longer exposures produced clearer images of the beam but also seemed to produce a greater degree of blurring of the beam image on the film. This observation was found to be reproducible. The result is that the beam appeared to be spread out over a larger area giving the impression of a larger-than-true spot-size. In order to avoid having this effect the reported results, shorter exposures were performed such that the beam image was just visible enough to identify the boundaries and determine the area of the beam and the center of the beam. The beam area was taken as the product of beam width and height.

An ORTEC (Oak Ridge, TN, USA) SLP series Lithium Drifted Silicon [Si(Li)] detector was used to record the fluorescence. It had an active area of 200 mm^2 and a sensitive volume of 5.8 mm thick. The detector had a 50 μm Be entrance window and a resolution of 220 eV at the Mn Kα energy of 5.9 keV. The detector was coupled to an ORTEC DSPEC Plus MCA box. This unit's MCA software, MAESTRO, was used to control the data acquisition and pulse processing parameters including rise time, live time, amplifier gain and conversion gain. The rise time was set at 12 μs. The detector has been used in previous work performed on arsenic in skin and strontium in bone, with similar rise times used there (Heirwegh et al., 2012; Moise et al., 2012; Zamburlini et al., 2007b). A Silicon Drift Detector (SDD) was separately used to record the fluorescence, for a preliminary comparision of the two detector types. It had an active area of 100 mm^2, collimated to 92 mm^2, and a sensitive thickness of 450 μm. The detector head was smaller in size than the Si(Li) detector and had a Be entrance window thickness of 25 μm. The detector was connected to an Analytical X-Ray Acquisition System-Analog (AXAS-A) unit for power supply and as an ADC/MCA unit. The manufacturer's MCA software was used to acquire data through a USB connection with the AXAS-A box. It had an internal analog shaper of 2 μs. The FWHM was 139 eV at 5.9 keV.

In order to realize larger source-detector angles, the existing layout of the system had to be changed. The reliability of repositioning the detector at these angles was critical and so it was decided to upgrade the positioning of the SDD to a partial optomechanical-based layout. If the Si(Li) detector's phantom-detector angle was increased, then the phantom-detector distance would also need to be increased. This is due to the larger footprint of the Si(Li) detector. This would mean that a smaller fraction of the

fluorescence emitted from the sample would be captured. Due to the smaller physical size of the SDD, this is not a concern with that detector. Also, non-linearity in motion of the optomechanical components would be likely when the Si(Li) detector's dewar (filled with LN2) was placed on top of them since their sustainable vertical load would be exceeded. Thus, it was decided that only the SDD layout would be used in such an arrangement.

The results of the modifications are as follows: on the base of the cabinet are mounted two 107 mm long linear motion tracks (Igus, Concord, ON). One end of the track is aligned with the flight tube on the front of the housing of the x-ray tube. This is the origin or the point where the x-rays emerge; the x-rays are produced deeper into the housing of the X-Beam unit, but cannot be accessed at those depths since the housing is fully sealed and, thus, this represents the first location where x-rays emerge into the rest of the cabinet. On each track is a carriage, carrying a Thorlabs L490/M lab jack. The jack is attached to the carriage with a custom machined adapter plate. On one jack, is a Thorlabs PT1/M linear stage with a phantom holder mounted on it. The phantom holder is designed to hold the phantom, with backing, at a 45-degree angle relative to the incident beam. On the surface of this holder was a rectangular shaped opening into which the nylon backing and phantom could be inserted and held in place. This ensured that repeatable measurements could be performed without altering the orientation of the phantom relative to the incident beam. On the second jack is a rotational stage with a Newport linear stage (4" travel) mounted on it. The SDD is mounted on this stage with a custom machined adapter plate. An investigation of variation in phantom-detector angle will be reported elsewhere, but the new track-based layout was used for phantom-based system calibration with the SDD in the 90^0 geometry. When the Si(Li) detector is to be utilized instead for system calibration, the carriage on the second track is not used. The Si(Li) detector remains positioned on the movable platform, however a new positioning bracket was installed allowing for a shorter phantom-detector separation of (2.0±0.2) cm. With the modified layout, phantom irradiations were performed for a real time of 1800 seconds as is typical for *in vivo* XRF (Behinaein et al., 2011; Heirwegh et al., 2012; Nie et al., 2006; Pejović-Milić et al., 2004; Studinski et al., 2005; Zamburlini et al., 2007a).

Dosimetry was performed using Lithium Fluoride Li(F) thermoluminescent dosimetry (TLD) chips (3.2 mm X 3.2 mm X 0.89 mm) from Global Dosimetry Services (Irvine, CA). These chips have been used previously in our research group for comparable dosimetry calculations. In the previous work, I-125 brachytherapy seeds were used as the radiation source and they estimated a whole body effective dose of 64-76 X 10^{-3} μSv in 1800 seconds (Zamburlini et al., 2007a). The chips are sensitive to absorbed doses ranging from 0.02 Gy to 5 kGy. Calibration and dose extraction were performed by Global Dosimetry. Using the beam image on a piece of gafchromic film as a guide, the chips were positioned on the nylon block in an array. They were attached to the block using a light adhesive. As with the resin phantoms, the block was then placed at a 45-degree angle to the incident beam. The TLDs were only sensitive for doses higher than 20 mGy. In order to determine the maximum dose that can be delivered by the x-ray tube,

the chips were exposed to a higher tube current, voltage and real time. This would ensure that the minimum dose threshold was met. The readings were then scaled appropriately to the tube's maximum voltage-current settings. With the chips in this arrangement, the tube was powered up and the TLD array was irradiated for no less than ~10 hours. The chips were then sent back to the manufacturer for reading. Absorbed dose in Li(F) was returned for each chip in the array.

2.2 Data Analysis:

The data were fit using Microcal Origin 8.5 (Originlab, Northampton, MA, USA). The peak area was calculated by fitting a single Gaussian equation to the As Kα peak. The background model added to the Gaussian was linear of the form y = mx +b. After producing a phantom calibration line, showing peak area versus concentration, the MDL was calculated using MDL = 2σ, where σ is given by

$$\sigma_{x_{exp}}{}^2 = \left(\frac{\sigma_{y_{exp}}}{m}\right)^2 + \left(\frac{\sigma_b}{m}\right)^2 + \frac{\sigma_m{}^2(b - y_{exp})^2}{m^4} + 2\left(\frac{y_{exp} - b}{m^3}\right)\left(-\frac{\sigma_y{}^2 \sum_{i=1}^{N} x_i}{D}\right) \qquad (1)$$

where the first three terms are the variance in the experimental calibration curve taken from a blank calibration phantom, calibration curve intercept and slope respectively. The fourth term is the covariance of the slope and intercept as per the variance-covariance approach used in analytical chemistry (Harris, 2006; Salter, 2000; Shoemaker et al., 1989). The traditional approach to calculation of MDL is well documented and is calculated by MDL = 2σ/M where σ is the uncertainty of a 0 ppm calibration phantom and M is the slope of the calibration line produced by plotting peak area against phantom concentration (Arnold et al., 2002; Da Silva et al., 2008; Graham and O'Meara, 2004; Grinyer et al., 2007, 2005; Studinski et al., 2006, 2004). This simplified definition does not include the last three terms in the equation above and assumes they make a small contribution to the MDL.

3. Results and discussion

3.1. Observed Spectrum and beam dimensions

By way of example, spectra obtained with each detector are shown in figure 2.

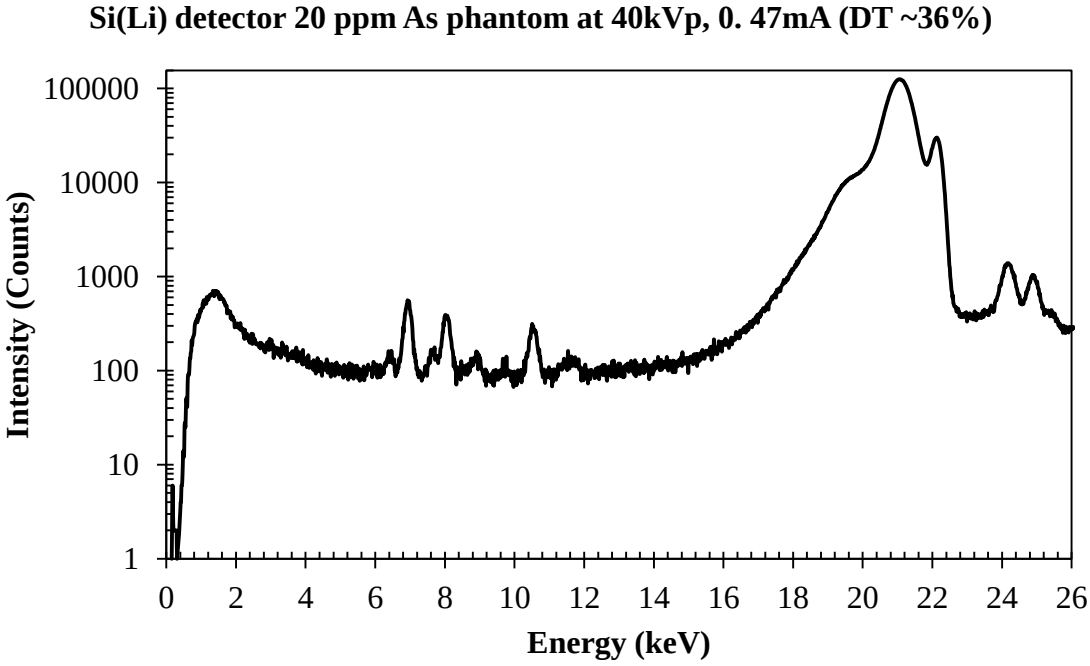
Si(Li) detector 20 ppm As phantom at 40kVp, 0. 47mA (DT ~36%)
Intensity (Counts)
100000
10000
1000
100
10
1
0
2
4
6
8
10
12
14
16
18
20
22
24
26
Energy (keV)

(a)

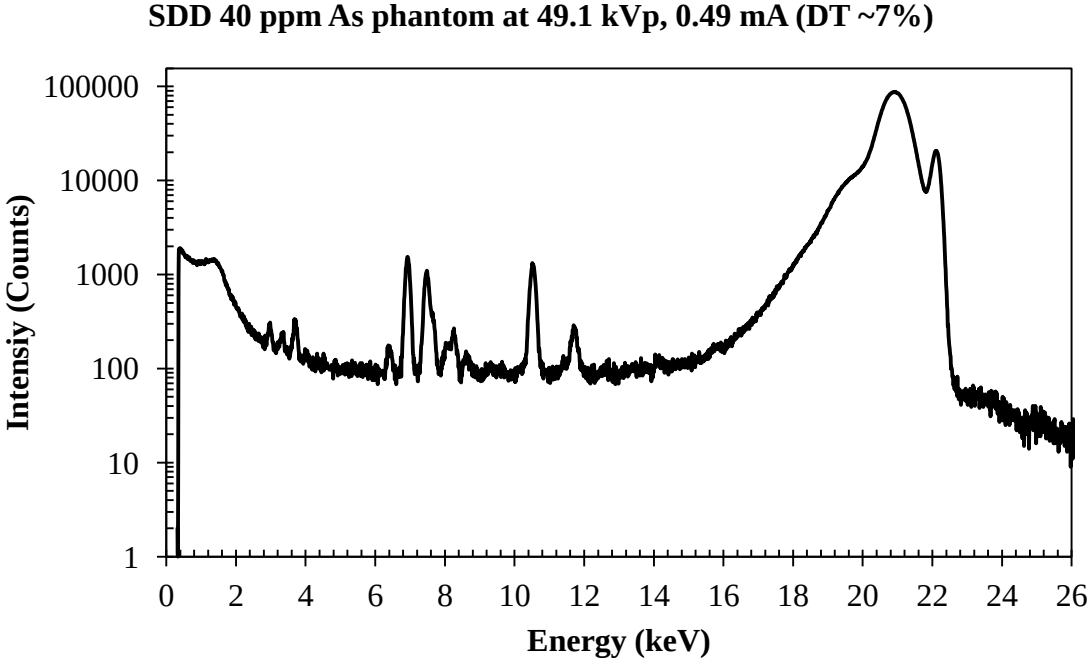
SDD 40 ppm As phantom at 49.1 kVp, 0.49 mA (DT ~7%)
Intensiy (Counts)
100000
10000
1000
100
10
1
0
2
4
6
8
10
12
14
16
18
20
22
24
26
Energy (keV)

(b)

Figure 2. Typical spectrum obtained with (a) Si(Li) detector using 20 ppm As phantom and (b) SDD using 40 ppm As phantom.

Peaks at 7.5 keV (Ni Kα), 8.0 keV (Cu Kα) and 8.9 keV (Cu Kβ) are likely due to the Si(Li) detector material. The peaks at 6.9 keV (Co Kα) and 7.6 keV (Co Kβ) originate in the resin and/or catalyst (Fleming and Gherase, 2007; Studinski, 2005). The As Kα and Kβ peaks are also clearly seen in the spectrum, at 10.5 keV and 11.7 keV respectively. The Ag Kβ appears to be breaking through the monochromator. This can be removed with a higher voltage setting as seen in the SDD spectrum.

The beam dimensions obtained with the gafchromic film are listed in table 1.

Table 1. Results of beam spot measurements recorded with gafchromic film.

Source-phantom distance (cm)*	Length (mm)**	Width (mm)**
30.0	1.0	0.5
34.6	1.0	1.0
42.6	2.0	2.0
50.0	3.0	4.0
62.8	6.0	6.5
70.1	6.0	6.5
78.2	8.0	8.0
95.6	10.0	9.0
101.5	11.0	11.0

*±0.2 cm, **±0.1 mm

The beam was confined most tightly at (30.0±0.2) cm from the tube – the focal length. As distance increases, the beam's energy is deposited over a larger area. As mentioned earlier, the focusing optic is beneficial in terms of background scatter reduction because the beam interacts with a small section of the sample (phantom). Given this condition, in order to maximize the exposed area, thereby replicating as closely as possible the area of the palm (intended *in vivo* site for arsenic measurements), the largest distance would be most appropriate for location of the phantoms. The physical dimensions of the Si(Li) detector are sufficiently large that the largest distance usable with it is (78.1±0.2) cm. By comparison, the SDD can be positioned at (95.6±0.2) cm due to its smaller housing and lack of a LN_2 dewar.

Sample images of the beam recorded at various distances away from the x-ray tube are shown in figure 3.

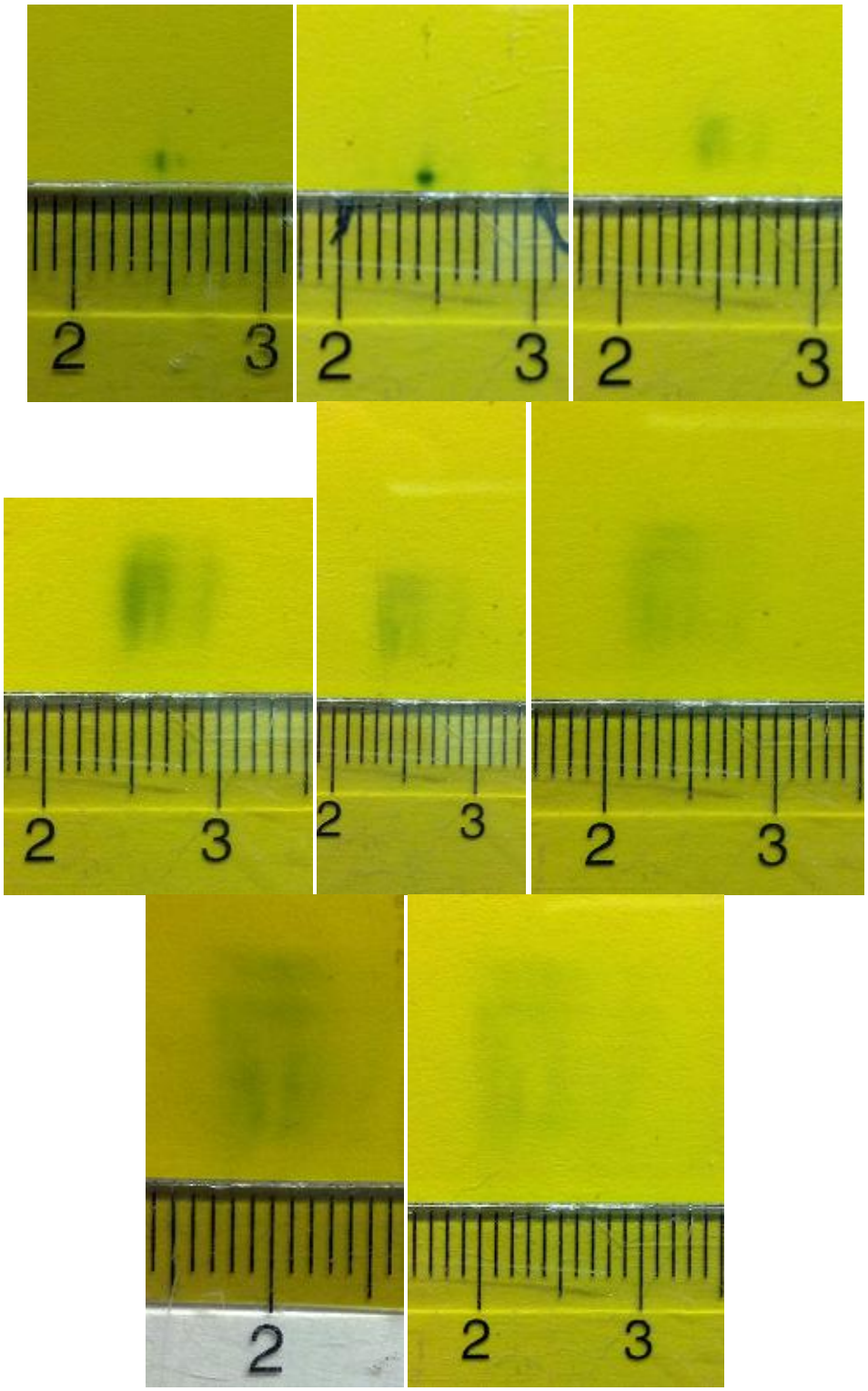
2
3
2
3
2
3
2
3
2
3
2
3
2
2
3

Figure 3. Images of beam recorded on gafchromic film, at various distances of (top row – left to right) 30.0 cm, 34.6 cm, 50.0 cm, 62.8 cm and (bottom row – left to right) 70.1 cm, 78.2 cm, 95.6 cm and 101.5 cm away from x-ray tube.

A visibly lighter secondary image was observed immediately to the right of the main beam, but was only just visible at larger distances and so would not be the main contributor to the incident x-ray beam. As the distance increased, and the beam spread out, the focusing of the optic was lost and so longer exposures were required to obtain an image. Also, the main beam became more divided into sub-areas as the distance was increased. When these were considered together, as one, the center of the resulting shape was positioned at the center of the phantom. Thus, the geometric center of the visible part of the whole beam was positioned at the center of the phantom. Enhanced image analysis is beyond the intended scope of this work. The main features were visible in the acquired images. Furthermore, determining which of these sub-areas is the strongest, and centering that spot with the phantom's center, would be an exercise limited to phantom related work. Such extensive positioning is almost certain to be impossible with *in vivo* trials since the (open) palm of a subject will move during the course of a 30-minute measurement and thus the exact positioning will the thrown off to varying degrees by this subject motion. Smaller movements would be possible with measurements performed on the lower leg/foot since the sole of the foot would be placed on a flat surface, thereby restricting its movement. By comparison, the palm of a subject cannot be forcibly kept open and fixed without introducing several additional place holders that would introduce scatter or interfering peaks into the spectrum. Smaller movements may also be possible with a finger as the measurement site.

3.2. Detection limits with Si(Li) Detector

Sample normalized calibration lines are shown, for each detector type, using each of the scatter peaks in figure 4.

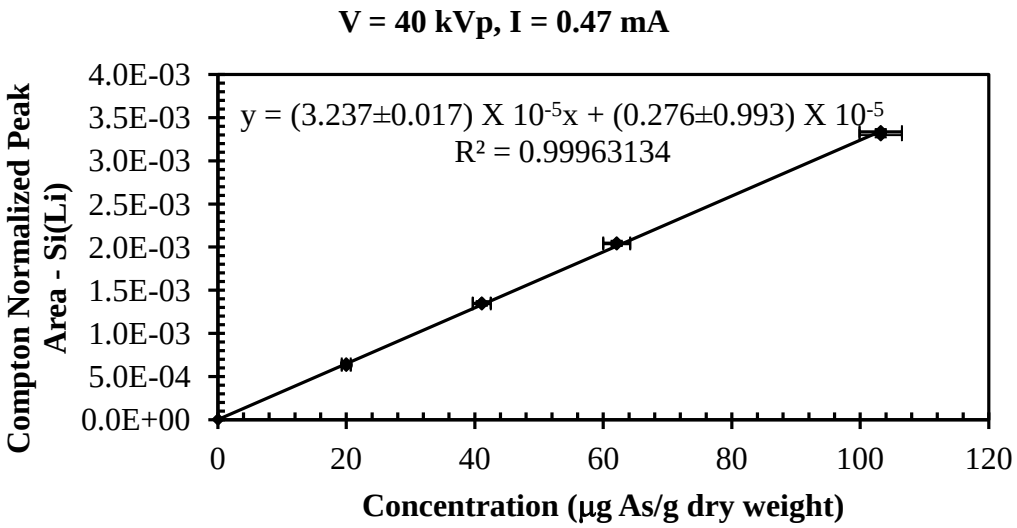
V = 40 kVp, I = 0.47 mA
Compton Normalized Peak Area - Si(Li)
4.0E-03
3.5E-03
3.0E-03
2.5E-03
2.0E-03
1.5E-03
1.0E-03
5.0E-04
0.0E+00
y = (3.237±0.017) X 10-5x + (0.276±0.993) X 10-5
R² = 0.99963134
0
20
40
60
80
100
120
Concentration (μg As/g dry weight)

(a)

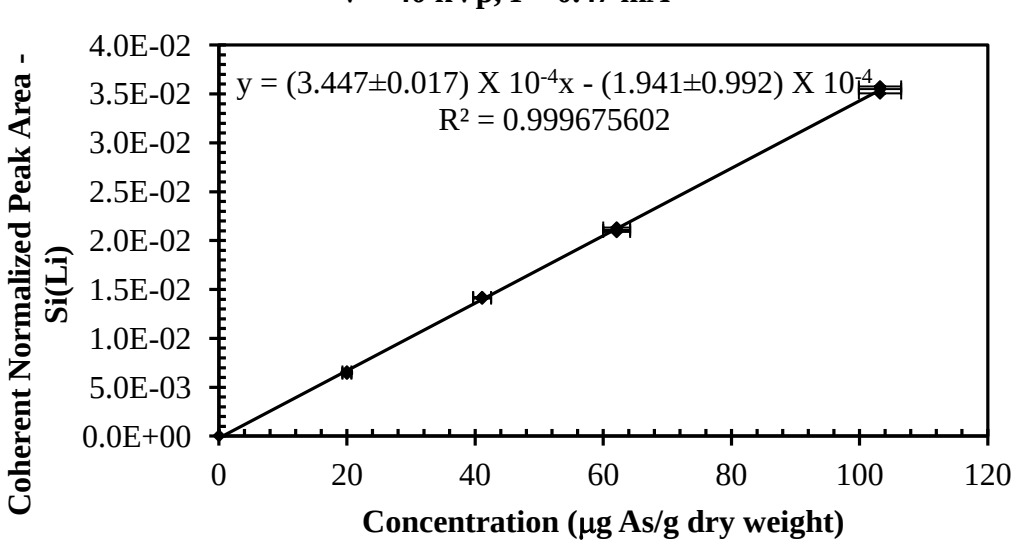
V = 40 kVp, I = 0.47 mA
Coherent Normalized Peak Area - Si(Li)
4.0E-02
3.5E-02
3.0E-02
2.5E-02
2.0E-02
1.5E-02
1.0E-02
5.0E-03
0.0E+00
y = (3.447±0.017) X 10-4x - (1.941±0.992) X 10-4
R² = 0.999675602
0
20
40
60
80
100
120
Concentration (μg As/g dry weight)

(b)

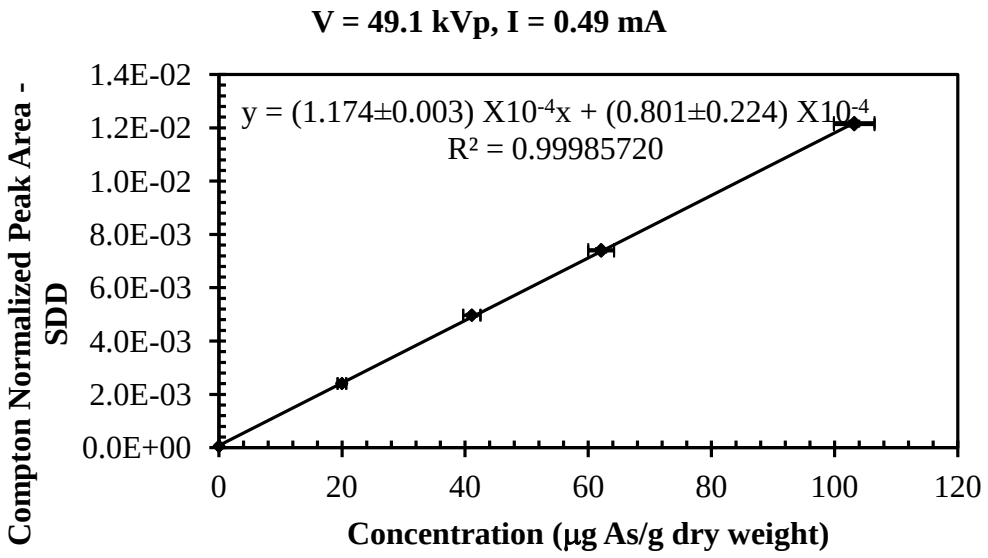

(c)

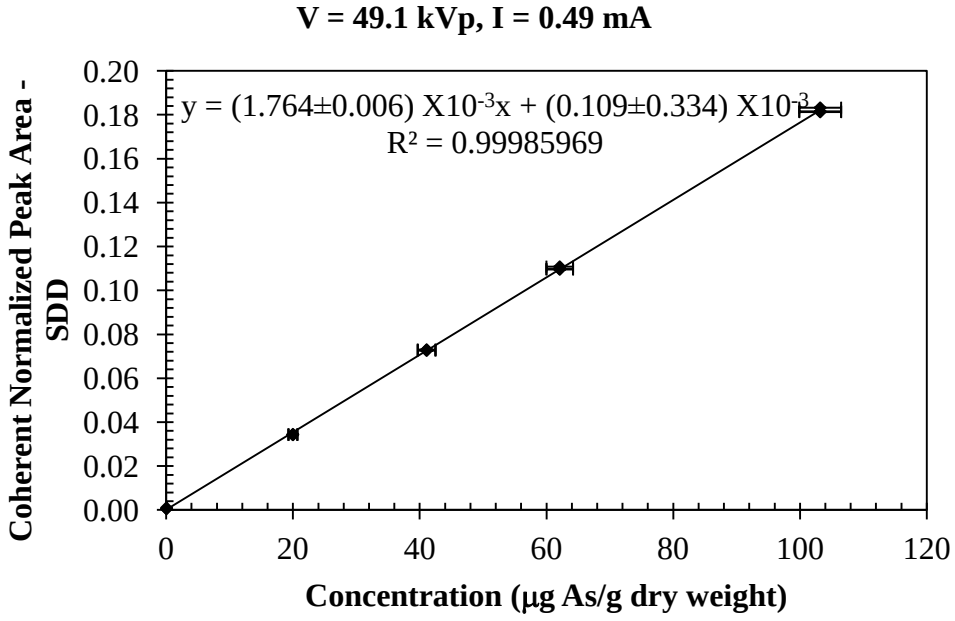

(d)

Figure 4. Normalized calibration line for arsenic in resin for Compton and coherent scatter peak respectively using (a) and (b) Si(Li) detector for 40 kVp, 0.47 mA and (c)

and (d) SDD for 49.1 kVp, 0.49 mA, with x-axis indicating arsenic concentration verified by neutron activation analysis and reported previously.

All R^2 values are greater than 0.999. A negative intercept is found for the Si(Li) coherent normalization line. These were found to be zero within uncertainty. Occasional negative areas were observed for the 0 ppm phantom. These are the result of the Marquardt Levenberg peak fitting routine. In the observed spectra, data points on either side of the fitted peak were used during peak area extraction act as an estimate of the background on top of which the peak was observed. Fitting the 0 ppm peak can result in an area that is less than background when the statistical error of each data point is taken into account. Negative peak areas have also been previously observed and discussed in the determination of Sr in bone (Pejovi´c-Mili´c *et al* 2004). The average reduced chi-squared value for work with the Si(Li) detector was 0.929±0.116, suggesting that the fitting model used was an adequate representation of the spectral shape.

MDL results acquired with the Si(Li) detector are summarized in figure 5.

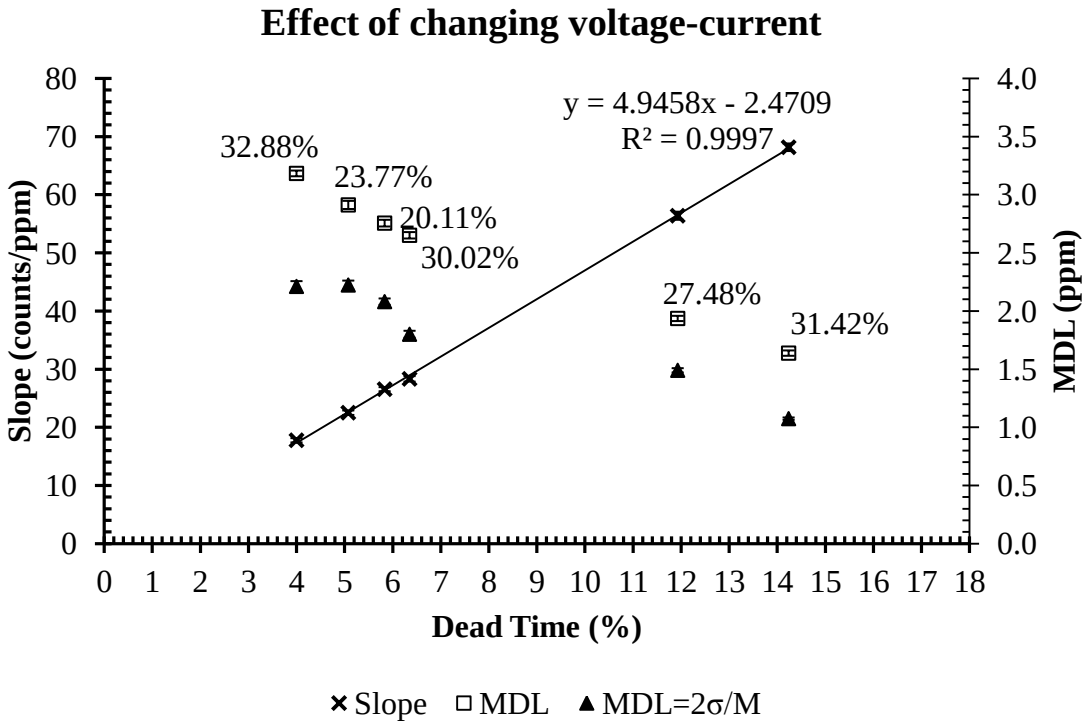

(a)

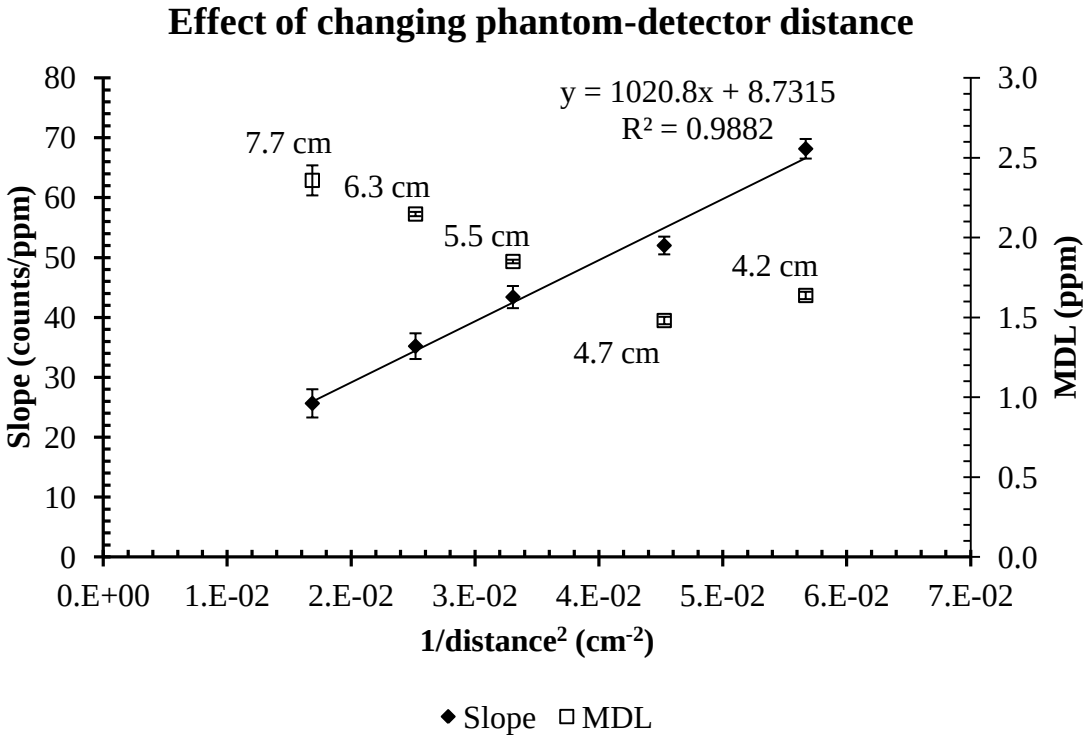
Effect of changing phantom-detector distance
y = 1020.8x + 8.7315
R² = 0.9882
7.7 cm
6.3 cm
5.5 cm
4.2 cm
4.7 cm
Slope (counts/ppm)
MDL (ppm)
1/distance² (cm⁻²)
0.E+00
1.E-02
2.E-02
3.E-02
4.E-02
5.E-02
6.E-02
7.E-02
0
10
20
30
40
50
60
70
80
0.0
0.5
1.0
1.5
2.0
2.5
3.0
Slope
MDL

(b)

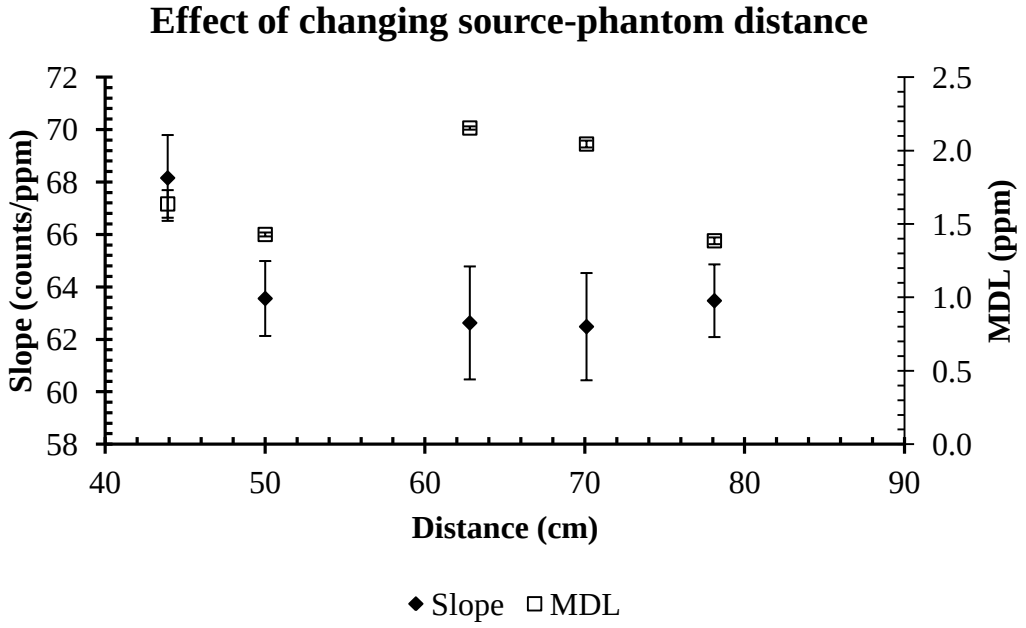
Effect of changing source-phantom distance
Slope (counts/ppm)
MDL (ppm)
Distance (cm)
40
50
60
70
80
90
58
60
62
64
66
68
70
72
0.0
0.5
1.0
1.5
2.0
2.5
Slope
MDL

(c)

Figure 5. Trends in direct slope (left) and direct MDL (right) for varying (a) system dead times caused by variations in x-ray tube voltage and current, (b) inverse squared phantom-detector distance and (c) source-phantom distance.

Figure 5a shows MDL data points with labels indicating the percent difference between the direct MDL and the conventional MDL equation ($2\sigma/M$), relative to the conventional equation. Over all the datasets with both detectors used in this layout, the percent difference relative to the variance-covariance MDL (2σ) was (30.2±10.8)%, with the conventional approach yielding lower results. The conventional MDL equation does not contain terms for covariance, variance in the slope or variance in the intercept. The last of these three was found to make the largest contribution to the overall MDL. Thus, the conventional MDL is expected to be lower and this was observed in all analyses in the current work.

In terms of system performance, the detection limit is improved as dead time increases. This change in dead time is brought about through increases in either tube voltage or current. The current is proportional to the number of photons emitted by the tube, while the voltage in kVp controls the photon energy (Johns and Cunningham, 1983). The kVp setting on the tube determines the highest energy photons produced. The voltages tested here ranged from 35-42 kVp. This work was done with a setup that allowed the Si(Li) detector to be placed no closer than (4.2±0.2) cm away from the phantom. Thus, the dead time is controlled by the phantom-detector distance and was <15%, even for the highest chosen tube operating conditions. Since dead time is proportional to the flux at the surface of the phantom, increasing it would enhance count-rates and calibration line slope, thereby lowering the MDL. The recommended maximum dead time is ~30-40%, above which a drop-off in pulse processing capabilities may hinder system performance (Knoll, 1999). However, this threshold is higher than that achievable with this arrangement. The V-I combination giving the lowest MDL here is at 80% of the tube's capacity (voltage and current settings) and improvement in both calibration line slope and MDL would be expected for higher combination settings. There is a possibility of a sub-1 ppm MDL resulting simply from an increase in the V-I setting, for dead times that do not exceed the limiting value. This limit is chosen as being the value below which models of dead time are known to be accurate. The current work is not intended to optimize the tube settings; rather it investigates the detection capabilities of the XRF system and whether it is feasible for use with arsenic *in vivo* monitoring. For the range of x-ray tube settings (voltage and current) investigated here, system detection limits in the range of ~1.5-2.5 ppm are possible.

The next two sub-figures demonstrate the effect of changing the two distances accessible with the layout of the system. Increasing the phantom-detector distance causes a $\sim 1/r^2$ drop in count rate at the detector. This leads to a higher MDL and is demonstrated in 5b. Increasing $1/r^2$ is analogous to moving the detector towards the phantom and this is seen to improve the MDL while increasing the slope of the calibration line. Figure 5c

shows the effect of moving the phantom and detector away from the x-ray tube. As the source-phantom distance is increased, the beam spreads out beyond the focal length. Since the phantom-detector distance is maintained at 4.2 cm, the un-normalized MDL is relatively unchanged. The beam area increases by a factor of ~16, over the range of distances covered (~35 cm). As the beam area increases, incident photons excite arsenic fluorescence from a larger surface area of the phantom. Thus, over this range of distances covered, the drop in incident x-ray intensity, as the beam spreads out, is not strong enough to produce a substantial difference in calibration slope. From the scatter point of view, the incident photons produce Compton scatter from a smaller area, at the focal length, than at a larger distance after the optical focusing has been relaxed. The Compton scatter peak thus has a contribution from a wider range of angles. Further complicating this is that the solid angle of detection also changes as the beam area increases. Normalization to the Compton scatter was chosen since it contains significantly more counts than the coherent scatter peak, for a tissue-equivalent material (Berger et al., 2010), and is easily the dominant feature in the energy spectrum. As a first approximation, this normalization would correct for fluctuations in detector dead time. A more in-depth investigation of the nature of the two scatter peaks will be performed in future work. A comparison across varying dead times, as is the case in this work, would require a normalization factor and the Compton scatter peak area is used for this purpose. Given that the beam area increases with increasing source-phantom distance, the largest such distance would be desired so as to maximize the measurement area and come close to matching it with the desired *in vivo* measurement site area (eg. the palm). The results here suggest that the detection limits in the range of ~1.5-2.0 ppm can be expected for this system with this experimental layout as the source-phantom distance (and hence beam size) is increased.

3.3. Detection Limits with SDD

Results obtained with the SDD are presented in table 2.

Table 2. Effect of changing tube settings on MDL acquired with SDD. Fixed live time of 1000 seconds used; rise time = 2.0 μs. The source- phantom distance is 78.1±0.2 cm; phnt.-det. distance = 1.5±0.2 cm.

V (kVp)	I (mA)	Slope (counts/ppm)			Compton-normalized MDL (ppm)		
37	0.300	97.17	±	0.66	1.038	±	0.003
37	0.350	109.87	±	0.67	1.076	±	0.002
40	0.250	109.77	±	0.89	1.076	±	0.004
40	0.350	125.27	±	0.89	1.040	±	0.003
32	0.400	54.39	±	0.52	1.307	±	0.011

The phantom-detector distance was 1.5±0.2 cm, which is the shortest possible distance at which the phantom can be safely placed from the SDD's beryllium entrance window. The

source-phantom distance was fixed at 78.1±0.2 cm. The same fitting function as that used for the Si(Li) detector was used here. The average reduced chi-squared was found to be 1.02±0.09 (±S.D.) again suggesting that the mathematical model describing the spectral shape was adequate. Varying the tube conditions reveals that MDLs are fairly consistent around 1.00 ppm with voltage settings of 37 or 40 kVp used with tube current settings ranging from 0.25-0.35 mA. The change in MDLs, as voltage-current combination is changed, is higher than that predicted by V^2I. This relationship assumes a single incident energy, as opposed to a tube which produces a continuous spectrum of energies at the detector. Also, the variation in the intercept contributes to the MDL. This term was larger than the variance in the slope and so the relationship V^2I may underestimate the change in MDLs. If both tube and distance conditions were identical and assuming that counts scaled with detector active area, one would need to count for more than 2 times as long with this SDD as with the 200 mm^2 Si(Li) detector. The SDD wafer is nearly an order of magnitude thinner than the Si(Li) detector crystal, which lowers the detection efficiency due to a smaller number of energy-depositing interactions with the sensitive area. The geometrical difference may also be sufficiently large to mean that one might not be fully confident in extrapolating from one to the other. In addition, the SDD resolution is superior due to a reduction in the noise characteristics. The lower noise also allows for higher throughput capabilities by comparison to Si(Li) detectors, due to a reduction in system dead time. These gains act against the superior detection efficiency possible with the Si(Li) detector. Perhaps the over-riding difference between the two detectors, for the current application, is the smaller form factor of the SDD. This allows the detector to be as close to the phantom as possible enhancing the detected count rate. The lowest MDL achieved with the Si(Li) detector (~4.5 cm phantom-detector separation) is improved by ~0.5 ppm with the SDD (1.5 cm away). This preliminary comparison reveals the benefit of using the SDD over the Si(Li) detector with this system. The non-ideal layout used here is clearly demonstrated, in particular for the Si(Li) detector.

3.4. Modifications to system and parameters

For the set of results above, with either detector, the real (clock) time was ~1200 seconds (fixed live time of 1000 seconds). *In vivo* XRF measurements have been typically performed for 1800 seconds real time, when using XRF *in vivo* (Moise et al., 2012; Pejović-Milić et al., 2004; Zamburlini et al., 2006; Zamburlini et al., 2007a). Anecdotal evidence is that this is a length of time that volunteers find acceptable and so has become a standard in *in vivo* studies. Using this length of time would offer an improvement in slope and better counting statistics. In addition, the phantom-detector distance is too large and needs to be reduced. Thus, modifications were made to the setup to reduce this distance, as discussed earlier. With the new setup, a small set of phantom trials were run with the Si(Li) detector at 78.1±0.2 cm and one trial for the SDD at 95.6±0.2 cm; note that the largest distance can only be accessed with the SDD due to the bulkier form factor of the Si(Li) detector. Due to interference between an internal zirconium (Zr) collimator and the Sr Kβ peak, the collimator was replaced with a multi-element collimator reducing the active area to 80 mm^2. The SDD was then coupled to a Canberra DSA1000 MCA unit with a rise time (digital) of 4 μs (2 μs analog). A

performance appraisal of the SDD, with the Canberra MCA, versus the Si(Li) detector will be performed elsewhere. Additionally, the voltage and current were ramped up for these trials, with either detector type, so as to push the x-ray tube towards it maximum output power setting of 25 W. The results of this last set of phantom trials with the Si(Li) detector is listed in table 3.

Table 3. Effect of changing tube settings on MDL acquired with Si(Li) detector with fixed real time of 1800 seconds. Fixed shaping time of 6.0 μs used. MDLs listed are Compton normalized, coherent normalized and direct (un-normalized).

V-I Settings	MDL_{AVG} (3 trials)[1]	$Slope_{AVG}$ (3 trials)[2]
35 kVp, 0.47 mA	1.0035 ± 0.0014 1.0390 ± 0.0011 1.3556 ± 0.0010	150.41 ± 1.55
37 kVp, 0.47 mA	0.7821 ± 0.0023 0.9831 ± 0.0004 0.9581 ± 0.0008	173.23 ± 1.15
40 kVp, 0.47 mA	0.8195 ± 0.0003 0.7717 ± 0.0007 1.0662 ± 0.0005	196.22 ± 1.54
42 kVp, 0.47 mA	0.9065 ± 0.0008 1.1051 ± 0.0014 0.9047 ± 0.0007	224.82 ± 1.50

[1] listed for a single phantom trial, for brevity, with very similar results obtained for two subsequent trials

[2] arithmetic mean ± SDOM, where SDOM = StdDev/$n^{1/2}$

The Compton-normalized MDL with the SDD, for a source-phantom distance of (95.6±0.2) cm at 49 kVp, 0.49 mA was found to be (0.4370±0.0004) ppm. This is an improvement of ~0.5 ppm, for either detector type. The peak-fitting was performed using two Gaussians on a linear background. The average reduced chi-sq. was 1.26±0.14 for the SDD and 1.19±0.15 with the Si(Li) detector. Tails were included for both Gaussians describing the two x-ray peaks; these were not clearly visible with the 1000 s live time acquisitions and so could not be included in the fitting model. The terms for covariance and variance in slope, as with the Si(Li) detector, were significantly smaller than the other two terms in the MDL definition. The vastly superior statistics of the Compton scatter peak help to lower slightly the normalized MDL, relative to the MDL calculated directly. Coherent normalization was not found to offer such an enhancement in two of the four cases examined. Further, nearly 70-80% of the incident Ag Kα photons will pass through the resin phantom, or skin, without depositing their energy. Thus, their mean interaction depth is located in the backing as opposed to the phantom. Coherent normalization is thus likely not able to correct for depth distribution of As in skin or

resin, although used in other normalization work to allow measurement results to be independent of factors including bone shape, mis-positioning, source strength, thickness of soft tissue overlying bone and human subject motion during an *in vivo* XRF measurement among others (Bellis et al., 2012; Hoppin et al., 1995; O'Meara et al., 2001; Somervaille et al., 1989; Todd, 2000; Zamburlini et al., 2008). Further investigation of this will be done through experiments and Monte Carlo simulations, where the theoretical basis of this normalization and the limitations of experimental work will be compared. As can be seen, the improvements in the system design and acquisition parameters significantly drive down the MDLs with either detector by ~0.5 ppm. It must be noted that a performance appraisal of the SDD compared to the Si(Li) detector will be performed in future work but these modifications appear to be quite promising as sub-ppm MDLs can now be realized through phantom-based calibration with this detection system.

3.5. Dosimetry

3.5.1. Raw data (TLD chip readings) corresponding to absorbed dose:

The absorbed dose readings returned are shown in the table 4.

Table 4. Raw TLD readings of absorbed dose.

Distance (cm)*	**Absorbed Dose, D (mGy)**			**time (min)**
30	987			723
42.6	1161	164		893
50	666	264		842
62.8	300	132		838
	228	110		
78.2	412.8	305.8	138.9	1241
	278.7	287.5	102.4	
	110.4	123	46.7	
95.6	581	273		1065
	644	292		
	547	383		
	198	109		

* readings are listed as per their position in the array of chips at each distance from the x-ray tube.

The maximum absorbed dose reading was well below 10 Gy, thus avoiding the regime where varying dose-response is observed with the dosimeters. Background dose was not included since the experiments were performed in a laboratory facility where the closest x-ray tube-based setup was not operated during the dosimetry exposures, as has also been done in other XRF tube-based work (Gherase, Mader, et al., 2010). Also, the other x-ray setups in the laboratory were heavily shielded.

Plotting the average absorbed dose, in soft tissue, delivered in 1800 seconds, at maximum tube power (50 kVp, 0.5 mA), as a function of 1/distance^2, the points on this curve were observed to follow a linear trend. The linear fit to this plot was found to be 35,856x+4.838 (R^2 = 0.998). This is as expected since dose would fall off with ~1/r^2, as the distance from the tube, r, is increased. However, a large variation in individual dosimeter readings is noted with this source. This calculation was repeated using only the highest individual reading from each distance and the R^2 was found to be 0.739. The maximum dose would indicate the strongest part of the beam, however any particular TLD chip used at one distance was not consistently placed at the same position in the array for other distances. Thus, the chip with the maximum dose may not offer the best estimate of the absorbed dose trend with distance. This trend can only be reliably established by ensuring that one chip in the array is always placed at the same position for all distances.

The likelihood of a radiation induced harmful event occurring is termed a stochastic effect and, thus, there is no specific dose limit to consider for the onset of these effects. However, deterministic effects have a limit (threshold) associated with them. The dose delivered is directly proportional to the severity of the effect. The highest individual absorbed dose chip reading in the entire set of readings observed with this x-ray tube system is 1,161 mGy delivered in 53,580 seconds, or 39 mGy delivered in 1800 seconds. By comparison, ICRP 60 lists the threshold for deterministic effects in bone marrow, which is a type of tissue, as 0.5 Gy for a single absorption. Thus, this x-ray tube does not deliver radiation at levels close to the limit for deterministic effects.

3.5.2 Corrected Dose Calculations

Correction factors need to be applied in order to account for differences between TLD irradiation conditions and the conditions corresponding to maximum tube settings, representing the worst case scenario for radiation exposure resulting from this x-ray tube during a 30-minute *in vivo* measurement. These source conditions also gave the best MDLs earlier. A correction would be required for differences in attenuating material - Li(F) vs soft tissue (ST). The time of exposure and operating current are linearly related to dose delivered and so the ratio of the times used for TLD and MDL measurements would represent another such factor. A similar factor would account for the difference between the operating voltage-current setting used in these two measurements; intensity, and subsequently dose, is proportional to the square of voltage and linearly proportional to the current (Evans, 1955; Johns and Cunningham, 1983). Taking these factors into account, the corrected absorbed dose is given by

$$D_{tissue} = D_{avg} \frac{\left(\mu_{en}/\rho\right)_{ST}}{\left(\mu_{en}/\rho\right)_{Li(F)}} \frac{T_{MAX}}{T_{TLD}} \frac{I_{MAX}}{I_{TLD}} \left(\frac{V_{MAX}}{V_{TLD}}\right)^2 \quad (2)$$

where D_{tissue} is the corrected absorbed dose, D_{avg} is the averaged absorbed dose over all the chips calculated as D_{avg}±SDOM, T_{TLD} is the time for which the TLD chips were exposed with V_{TLD} and I_{TLD} being the tube's operating conditions for these exposures (35.0 kV, 0.5 mA), T_{MAX}, I_{MAX} and V_{MAX} are the real time in an *in vivo* measurement (1800 seconds) and, as mentioned earlier, it is assumed that the tube will be operated at maximum voltage-current 50 kVp-0.50 mA. The mass attenuation coefficients, $\mu(en)/\rho$, are values for soft tissue, assuming a tissue composition listed in the NIST database (Berger et al., 2005), and Li(F) at the desired incident energy – Ag Kα (Hubbell and Seltzer, 2004).

With the current design of the shielding cabinet, the palm of the right hand would be the most easily accessible part of the body that could be subjected to the x-ray tube exposure at a 45-degree angle. The exposures performed with this detection system do not involve whole body irradiation. Thus, the effective dose offers a means of comparing the dose delivered, in order to obtain the listed MDLs, with the ICRP effective dose limit to members of the public. With the corrected absorbed dose determined, the effective dose to the area of the skin that is exposed would then be given by

$$E = D_{tissue} \frac{V_{IRR}}{V_T} \omega_R \omega_T \quad (3)$$

where A_{IRR} is the beam size giving $V_{IRR} = A_{IRR}$ * ICRP skin thickness (0.2 cm), A_T is the ICRP total skin surface area, which is 18000 cm^2 ICRP 23) giving $V_T = 3600$ cm^3. The radiation weighting factor, ω_R, is 1 for photons and the tissue weighting factor, ω_T, is 0.01 for soft tissue. The results of all three types of dose readings are presented in table 5.

Table 5. Summary of absorbed, equivalent and effective dose readings when scaled to full-power (49.1 kVp, 0.49 mA) and to their corresponding values for 1800 second *in vivo* exposures.

Distance (cm)	**D_{Corr} (mGy)**	**H (mSv)***	**E (μSv)**
30.0 ± 0.2	47.044 ± N/A	45 ± N/A	0.13×10^{-3} ± N/A
42.6 ± 0.2	24.479 ± 18.419	24.479 ± 18.419	0.54×10^{-3} ± 0.45×10^{-3}
50.0 ± 0.2	19.222 ± 7.877	18.222 ± 7.877	1.22×10^{-3} ± 0.58×10^{-3}
78.2 ± 0.2	11.018 ± 2.251	11.018 ± 2.251	3.92×10^{-3} ± 0.87×10^{-3}
95.6 ± 0.2	9.305 ± 1.625	9.305 ± 1.625	4.65×10^{-3} ± 0.88×10^{-3}

*for rows 1-4, area < 1 cm^2; for row 1, since single chip is used, uncertainty here is not reported (see text for discussion). $\mu_{en,Li(F)}/\rho$ = 0.4811 cm^2/g, $\mu_{en,ICRU\text{-}4\ Comp}/\rho$ = 0.4312 cm^2/g. For d = 30-50 and 95.6 cm, V_{TLD} = 45 kVp, I_{TLD} = 0.463 mA; for d = 78.2 cm, V_{TLD} = 35 kVp, I_{TLD} = 0.40 mA. For all settings, V_{MAX} = 50 kVp, I_{MAX} = 0.5 mA (worst

case for dosimetry) and t_{MAX} = 1800 s. The error in D_{Corr} is given as ±SDOM, with errors in H and E calculated by propagation of uncertainties.

The effective dose from the handheld XRF unit referenced above was found to be 6.1 X 10^{-3} μSv to skin, which is similar to the results obtained here. The voltage-current settings there were 40 kVp and 20 μA, compared to ~50 kVp and 0.50 mA here; a much shorter source-phantom and phantom-detector geometry arrangement, as well as inherent filtration, were used with that system. The currently-reported localized effective doses are on the same order of magnitude as those from the work with I-125 brachytherapy seeds mentioned earlier. Those doses were found to be (49.08±0.05) $X10^{-3}$ μSv and (87.32±0.09) $X10^{-3}$ μSv to the finger and tibia ankle respectively (Zamburlini, Pejović-Milić, et al., 2007). The annual background radiation is ~2.5 mSv, ranging from ~1.5-8 mSv, across various locations in the world. These are whole body doses. The effective dose readings in the last two columns of the table are scaled down based on the area of exposure.

Regardless of distance from the tube, these effective doses are within the corresponding ICRP-prescribed dose limit of 1 mSv to members of the public. As the distance from the tube is increased, the beam area spreads out and the irradiated volume of skin is increased. The beam area increases from 8X (at 42.6 cm) to 180X (at 95.6 cm), relative to the beam size at the focal length; this is an increase of 22.5. By comparison, the distance squared increases by 10.2 $(95.6\ cm/30.0\ cm)^2$. The beam area increases faster than the increase in $distance^2$. The calculation of effective dose involves a scaling factor for irradiated area of skin. Thus, the effective dose increases as the distance is increased. Comparing the effective dose, scaled down to the exposed skin volume, to the whole body dose limit is valid since the intended *in vivo* exposures with this setup will never be to the entire body of a subject. Nonetheless, the whole body effective doses (removing the scaling factor for volume of exposed skin versus volume of whole body skin), over this set of distances, were found to range from 76-450 μSv, where the highest dose was found to be at the focal length. These are still below the yearly effective dose contribution from natural background sources and below the whole body effective dose limit of 1 mSv. The current whole body effective doses are on the same order of magnitude as those produced by a Cd-109 based *in vivo* XRF system used for lead quantification in bone (Nie et al., 2007). By comparison, the corresponding whole body dose associated with a diagnostic x-ray procedure is ~0.1 mSv with various examples listing higher doses – endoscopic procedure (radiology) 4 mSv, chest CT 15 mSv, Thallium-201 chloride cardiac stress test 40.7 mSv (nuclear medical exam) (Mettler et al., 2008) with the US per-capita yearly effective dose listed at ~3.0 mSv (Mettler et al., 2009). Although it is reassuring that the whole body doses measured are within the ICRP limits, the scaled versions, correcting for exposed skin, are more appropriate and several orders of magnitude below the prescribed maximum value. With this in mind, this XRF detection system is not able to produce exposures that will exceed ICRP regulations during *in vivo* measurements. A stronger source (higher power x-ray tube) may be used

for a 30-minute measurement resulting in stronger fluorescence and better counter statistics.

The dose delivered to a 1 cm^2 sub-section of the beam area (highly localized dose) is also of importance to biological consequences of the exposure required to achieve an observed MDL. As all beam areas here are 1cm^2 or less in total area, the full array of TLD chips was selected and an average (±SDOM) was determined. This can be used to calculate the equivalent dose to the skin using

$$H = D_{tissue}\omega_R \quad (4)$$

where D_{tissue} was calculated using equation 2. The equivalent dose is an important quantity since the effective dose will not offer an indication of skin protection against deterministic effects that could be induced by the exposure. The ICRP recommends an annual limit of 50 mSv, over a 1 cm^2 area of skin, for members of the general public ICRP 60). Using a radiation weighting factor of 1, the equivalent dose was calculated and listed in the columns 5 and 6 of the above table. The equivalent dose listed at the focal length is listed without an uncertainty. The systematic uncertainty in the TLD chip reading procedure is not known, but is estimated at an upper limit of ~10% from the manufacturer. This leads to a dose of ~(45±4.5) mSv. It agrees with the ICRP recommended limit, within this error. However, a single chip was used for exposure at this distance because of the small beam size here. The small spot size (<<1 cm^2) makes interpretation of the equivalent dose harder. *In vivo* exposures to the palm of the hand for arsenic, or to the finger for strontium, are not intended for this distance. This spot size is not representative of the area being probed since the largest possible coverage of the target site will not be possible with such a small beam size. With this exception, the other equivalent dose readings are all within the limit recommended for members of the general public. The above referenced handheld unit produced an equivalent dose of 13.2 mSv; as with the effective dose, this is on the same order of magnitude as the results from this system.

4. Conclusion

We report on the development of a XRF-based detection system for quantifying of arsenic in skin *in vivo*. The lowest observed minimum detection limit, in a 30 minute phantom measurement, was found to be ~0.45 ppm. This is similar to that obtained with a 50 Watt molybdenum anode x-ray tube, but the dose delivered in the current work (25 Watts) is two orders of magnitude weaker. The ability to control the focusing of the x-rays allows the experimenter to minimize unwanted dose to skin, in the process of performing a 30-minute *in vivo* measurement. The maximum equivalent (skin) and whole body dose delivered are <25 mSv and <0.25 mSv respectively, in 30 minutes. These are within the respective ICRP recommended limits for members of the general public. Ideally, phantom detection limits as low as 0.1 ppm or lower may be required for

detection in members of the general population. Such capabilities, though, may be beyond the feasibility of the technique. In its current layout, the system is in a position to detect and quantify arsenic in subjects from an exposed population.

Acknowledgements

The authors would like to thank Jason Falladown, Scott McMaster and Frank Labonte from the McMaster accelerator laboratory for the assembly of the XBEAM and the interlock safety system. We acknowledge Steffen Pahlke, from Ketek, for his assistance with the setup of the SDD. We would like to thank Lesley Egden from the McMaster lab for assistance with setting up the Canberra DSA for use with the SDD. The authors would like to acknowledge research support from the Occupational Nuclear Medicine Research Group and Nuclear Instrumentation Group within the Medical Physics and Applied Radiation Sciences Department. Funding for the x-ray optical system was provided by the Natural Sciences and Engineering Research Council of Canada (NSERC), Research Tools and Instruments grants. F. E. McNeill, D. R. Chettle and D. E. B. Fleming gratefully acknowledge receipt of NSERC Discovery grants.

References:

Ahlgren, L., Mattsson, S., 1981. Cadmium in man measured in vivo by x-ray fluorescence analysis. Phys. Med. Biol. 26, 19–26.

Apostoli, P., Bartoli, D., Alessio, L., Buchet, J.P., 1999. Biological monitoring of occupational exposure to inorganic arsenic. Occup. Environ. Med. 56, 825–32.

Arnold, M.L., McNeill, F.E., Stronach, I.M., Pejovic-Milic, A., Chettle, D.R., Waker, A., 2002. An accelerator based system for in vivo neutron activation analysis measurements of manganese in human hand bones. Med. Phys. 29, 2718.

Behinaein, S., Chettle, D.R., Atanackovic, J., Egden, L.M., Fleming, D.E.B., Nie, L.H., Richard, N., Stever, S., 2011. In vivo measurement of lead in the bones of smelter workers using the four-element "clover-leaf" geometry detector system. Phys. Med. Biol. 56, 653–665.

Bellis, D.J., Todd, A.C., Parsons, P.J., 2012. An interlaboratory comparison of bone lead measurements via K-shell X-ray fluorescence spectrometry: validation against inductively coupled plasma mass spectrometry. J. Anal. At. Spectrom. 27, 595–603.

Berger, M.J., Coursey, J.S., Zucker, M.A., Chang, J., 2005. ESTAR, PSTAR, and ASTAR: Computer Programs for Calculating Stopping-Power and Range Tables for Electrons, Protons, and Helium Ions (version 1.2.3) (Gaithersburg, MD: National Institute of Standards and Technology) [WWW Document]. URL http://www.nist.gov/pml/data/star/index.cfm

Berger, M.J., Hubbell, J.H., Seltzer, S.M., Chang, J., Coursey, J.S., Sukumar, R., Zucker, D.S., Olsen, K., 2010. XCOM: Photon Cross Section Database (version 1.5) National Institute of Standards and Technology, Gaithersburg, MD. Retrieved: January, 2010 from http://physics.nist.gov/xcom [WWW Document]. URL http://www.nist.gov/pml/data/xcom/index.cfm

Bjeoumikhov, A., Arkadiev, V., Eggert, F., Hodoroaba, V.-D., Langhoff, N., Procop, M., Rabe, J., Wedell, R., 2005. A new microfocus x-ray source, iMOXS, for highly sensitive XRF analysis in scanning electron microscopes. X-Ray Spectrom. 34, 493–497.

Button, M., Jenkin, G.R.T., Harrington, C.F., Watts, M.J., 2009. Human toenails as a biomarker of exposure to elevated environmental arsenic. J. Environ. Monit. 11, 610–7.

Ch'i, I.-C., Blackwell, R.Q., 1968. A controlled retrospective study of Blackfoot disease, an endemic peripheral gangrene disease in Taiwan. Am. J. Epidemiol. 88, 7–24.

Chakraborti, D., Mukherjee, S.C., Pati, S., Sengupta, M.K., Rahman, M.M., Chowdhury, U.K., Lodh, D., Chanda, C.R., Chakraborti, A.K., Basu, G.K., 2003. Arsenic Groundwater Contamination in Middle Ganga Plain, Bihar, India: A Future Danger? Environ. Health Perspect. 111, 1194–1201.

Chen, C.J., Chuang, Y.C., Lin, T.M., Wu, H.Y., 1985. Malignant neoplasms among residents of a blackfoot disease-endemic area in Taiwan: high-arsenic artesian well water and cancers. Cancer Res. 45, 5895–9.

Chiou, H.Y., Hsueh, Y.M., Liaw, K.F., Horng, S.F., Chiang, M.H., Pu, Y.S., Lin, J.S., Huang, C.H., Chen, C.J., 1995. Incidence of internal cancers and ingested inorganic arsenic: a seven-year follow-up study in Taiwan. Cancer Res. 55, 1296–300.

Chiu, H.-F., Ho, S.-C., Yang, C.-Y., 2004. Lung cancer mortality reduction after installation of tap-water supply system in an arseniasis-endemic area in Southwestern Taiwan. Lung Cancer 46, 265–270.
Da Silva, E., Pejović-Milić, A., Heyd, D. V., 2008. The use of teeth as the site for the in vivo or ex vivo quantification of skeletal strontium by energy-dispersive X-ray fluorescence spectrometry: A feasibility study. J. Anal. At. Spectrom. 23, 527–534.
Dang, T.M.., Tran, Q.., Vu, K.., 1999. Determination of arsenic in urine by atomic absorption spectrophotometry for biological monitoring of occupational exposure to arsenic. Toxicol. Lett. 108, 179–183.
Deslattes, R., Kessler, E., Indelicato, P., de Billy, L., Lindroth, E., Anton, J., 2003. X-ray transition energies: new approach to a comprehensive evaluation. Rev. Mod. Phys. 75, 35–99.
Ettinger, A.S., Zota, A.R., Amarasiriwardena, C.J., Hopkins, M.R., Schwartz, J., Hu, H., Wright, R.O., 2009. Maternal arsenic exposure and impaired glucose tolerance during pregnancy. Environ. Health Perspect. 117, 1059–1064.
Evans, R.D., 1955. The atomic nucleus. McGraw-Hill, New York, USA.
Ferreccio, C., González, C., Milosavjlevic, V., Marshall, G., Sancha, A.M., Smith, A.H., 2000. Lung cancer and arsenic concentrations in drinking water in Chile. Epidemiology 11, 673–9.
Fleming, D.E.B., Gherase, M.R., 2007. A rapid, high sensitivity technique for measuring arsenic in skin phantoms using a portable x-ray tube and detector. Phys. Med. Biol. 52, N459–65.
Gherase, M.R., Mader, J.E., Fleming, D.E.B., 2010. The radiation dose from a proposed measurement of arsenic and selenium in human skin. Phys. Med. Biol. 55, 5499–5514.
Graham, S.A., O'Meara, J.M., 2004. The feasibility of measuring silver concentrations in vivo with x-ray fluorescence. Phys. Med. Biol. 49, N259–N266.
Grinyer, J., Atanackovic, J., Byun, S.H., Chettle, D.R., 2007. Phantom studies of Cd, Hg and Cl by prompt gamma neutron activation analysis using a 238Pu–Be neutron source. Nucl. Instruments Methods Phys. Res. Sect. B 263, 262–265.
Grinyer, J., Byun, S.H., Chettle, D.R., 2005. In vivo prompt gamma neutron activation analysis of cadmium in the kidney and liver. Appl. Radiat. Isot. 63, 475–9.
Harris, D.C., 2006. Quantitative chemical analysis, 7th ed. W. H. Freeman, New York, USA.
Heirwegh, C.M., Chettle, D.R., Pejovic-Milic, A., 2012. Ex vivo evaluation of a coherent normalization procedure to quantify in vivo finger strontium XRS measurements. Med. Phys. 39, 832–41.
Hoppin, J.A., Aro, A.C., Williams, P.L., Hu, H., Ryan, P.B., 1995. Validation of K-XRF bone lead measurement in young adults. Environ. Health Perspect. 103, 78–83.
Hubbell, J.H., Seltzer, S.M., 2004. Tables of X-Ray Mass Attenuation Coefficients and Mass Energy-Absorption Coefficients (version 1.4) (Gaithersburg, MD: National Institute of Standards and Technology) [WWW Document]. URL http://www.nist.gov/pml/data/xraycoef/index.cfm
Hwang, Y.-H., Lee, Z.-Y., Wang, J.-D., Hsueh, Y.-M., Lu, I.-C., Yao, W.-L., 2002. Monitoring of arsenic exposure with speciated urinary inorganic arsenic metabolites for ion implanter maintenance engineers. Environ. Res. 90, 207–216.
International Commission on Radiological Protection, Publication 23, 1975. Rep. Task Gr. Ref. Man. Pergamon, Oxford, pp. 480.
International Commission on Radiological Protection, Publication 60, 1990. Recomm. Int. Comm. Radiol. Prot. Pergamon, Oxford.
Johns, H.E., Cunningham, J.R., 1983. The physics of radiology, 2nd ed. Charles C. Thomas, Springfield, Ill., U.S.A.
Karagas, M.R., Morris, J.S., Weiss, J.E., Spate, V., Baskett, C., Greenberg, E.R., 1996. Toenail samples as an indicator of drinking water arsenic exposure. Cancer Epidemiol. Biomarkers Prev. 5, 849–52.
Klassen, R., 2009. Geoscience modelling of relative variation in natural arsenic hazard potential in New Brunswick.
Knoll, G.F., 1999. Radiation Detection and Measurement, 3rd ed. John Wiley & Sons Inc.
Lewis, D.R., Southwick, J.W., Ouellet-Hellstrom, R., Rench, J., Calderon, R.L., 1999. Drinking water arsenic in Utah: A cohort mortality study. Environ. Health Perspect. 107, 359–65.
Lubin, J.H., Moore, L.E., Fraumeni, J.F., Cantor, K.P., 2008. Respiratory cancer and inhaled inorganic arsenic in copper smelters workers: a linear relationship with cumulative exposure that increases with concentration. Environ. Health Perspect. 116, 1661–5.
MacDonald, C.A., Owens, S.M., Gibson, W.M., 1999. Polycapillary X-ray optics for microdiffraction. J. Appl. Crystallogr. 32, 160–167.
Mandal, B.K., Ogra, Y., Suzuki, K.T., 2003. Speciation of arsenic in human nail and hair from arsenic-affected area by HPLC-inductively coupled argon plasma mass spectrometry. Toxicol. Appl. Pharmacol. 189, 73–83.
McGuigan, C.F., Hamula, C.L.A., Huang, S., Gabos, S., Le, X.C., 2010. A review on arsenic concentrations in Canadian drinking water. Environ. Rev. 18, 291–307.
Mead, M.N., 2005. Arsenic: in search of an antidote to a global poison. Environ. Health Perspect. 113, A378–86.
Mettler, F.A., Bhargavan, M., Faulkner, K., Gilley, D.B., Gray, J.E., Ibbott, G.S., Lipoti, J.A., Mahesh, M., McCrohan, J.L., Stabin, M.G., Thomadsen, B.R., Yoshizumi, T.T., 2009. Radiologic and nuclear medicine studies in the United

States and worldwide: frequency, radiation dose, and comparison with other radiation sources--1950-2007. Radiology 253, 520–31.
Mettler, F.A., Huda, W., Yoshizumi, T.T., Mahesh, M., 2008. Effective doses in radiology and diagnostic nuclear medicine: a catalog. Radiology 248, 254–63.
Misbahuddin, M., Momin, A., Al-Amin, M., 2008. All-E lutein and 3'-epilutein in the epidermis of chronic arsenic poisoning. Clin. Toxicol. 46, 176–180.
Mo, J., Xia, Y., Wade, T.J., Schmitt, M., Le, X.C., Dang, R., Mumford, J.L., 2006. Chronic Arsenic Exposure and Oxidative Stress: OGG1 Expression and Arsenic Exposure, Nail Selenium, and Skin Hyperkeratosis in Inner Mongolia. Environ. Health Perspect. 114, 835–841.
Moise, H., Adachi, J.D., Chettle, D.R., Pejović-Milić, A., 2012. Monitoring bone strontium levels of an osteoporotic subject due to self-administration of strontium citrate with a novel diagnostic tool, in vivo XRF: a case study. Bone 51, 93–97.
Nie, H., Chettle, D., Luo, L., O'Meara, J., 2006. In vivo investigation of a new 109Cd gamma-ray induced K-XRF bone lead measurement system. Phys. Med. Biol. 51, 351–60.
Nie, H., Chettle, D., Luo, L., O'Meara, J., 2007. Dosimetry study for a new in vivo X-ray fluorescence (XRF) bone lead measurement system. Nucl. Instruments Methods Phys. Res. Sect. B Beam Interact. with Mater. Atoms 263, 225–230.
O'Meara, J.M., Börjesson, J., Chettle, D.R., Mattsson, S., 2001. Normalisation with coherent scatter signal: improvements in the calibration procedure of the 57Co-based in vivo XRF bone-Pb measurement. Appl. Radiat. Isot. 54, 319–25.
O'Meara, J.M., Chettle, D.R., McNeill, F.E., Webber, C.E., 1998. In vivo X-ray fluorescence (XRF) measurement of uranium in bone. Appl. Radiat. Isot. 49, 713–715.
Pejović-Milić, A., Stronach, I.M., Gyorffy, J., Webber, C.E., Chettle, D.R., 2004. Quantification of bone strontium levels in humans by in vivo x-ray fluorescence. Med. Phys. 31, 528–38.
Robinson, J.W., 1991. Practical Handbook of Spectroscopy. CRC Press, Boca Raton, FL, USA.
Salter, C., 2000. Error Analysis Using the Variance-Covariance Matrix. J. Chem. Educ. 77, 1239.
Schwartz, R.A., 1997. Arsenic and the skin. Int. J. Dermatol. 36, 241–50.
Shoemaker, D.P., Garland, C.W., Nibler, J.W., 1989. Experiments in Physical Chemistry, 5th ed. McGraw-Hill.
Slotnick, M.J., Nriagu, J.O., 2006. Validity of human nails as a biomarker of arsenic and selenium exposure: A review. Environ. Res. 102, 125–39.
Somervaille, L.J., Nilsson, U., Chettle, D.R., Tell, I., Scott, M.C., Schütz, A., Mattsson, S., Skerfving, S., 1989. In vivo measurements of bone lead--a comparison of two x-ray fluorescence techniques used at three different bone sites. Phys. Med. Biol. 34, 1833–45.
Studinski, R.C.N., 2005. Development of an in vivo method of measuring arsenic with radiation.
Studinski, R.C.N., McNeill, F.E., Chettle, D.R., O'Meara, J.M., 2004. XRF analysis of arsenic-doped skin phantoms. X-Ray Spectrom. 33, 285–288.
Studinski, R.C.N., McNeill, F.E., Chettle, D.R., O'Meara, J.M., 2005. Estimation of a method detection limit for an in vivo XRF arsenic detection system. Phys. Med. Biol. 50, 521–530.
Studinski, R.C.N., McNeill, F.E., O'Meara, J.M., Chettle, D.R., 2006. A method detection limit for potential in vivo arsenic measurements with a 50 W x-ray tube. Phys. Med. Biol. 51, N381–7.
Sugiro, F.R., Li, D., MacDonald, C. a., 2004. Beam collimation with polycapillary x-ray optics for high contrast high resolution monochromatic imaging. Med. Phys. 31, 3288.
Todd, A.C., 2000. Coherent scattering and matrix correction in bone-lead measurements. Phys. Med. Biol. 45, 1953–63.
WHO, 2010. Exposure to arsenic: a major public health concern, WHO Press, Geneva, Switzerland. World Health Organization, Geneva, Switzerland.
WHO, 2011. Guidelines for drinking-water quality, fourth edition, WHO Press, Geneva, Switzerland. World Health Organization, Geneva, Switzerland.
WHO-IARC, 2012. Arsenic, metals, fibres, and dusts: A review of human carcinogens. (International Agency Res. Cancer, WHO Press Lyon, Fr. 100C.
Zamburlini, M., Byun, S.H., Pejović-Milić, A., Prestwich, W. V., Chettle, D.R., 2007. Evaluation of MCNP5 and EGS4 for the simulation ofin vivo strontium XRF measurements. X-Ray Spectrom. 36, 76–81.
Zamburlini, M., Pejović-Milić, A., Chettle, D.R., 2006. Evaluation of geometries appropriate for 125I in vivo bone strontium X-ray fluorescence measurement. J. Radioanal. Nucl. Chem. 269, 625–629.
Zamburlini, M., Pejović-Milić, A., Chettle, D.R., 2008. Coherent normalization of finger strontium XRF measurements: feasibility and limitations. Phys. Med. Biol. 53, N307–13.
Zamburlini, M., Pejović-Milić, A., Chettle, D.R., Webber, C.E., Gyorffy, J., 2007. In vivo study of an x-ray fluorescence system to detect bone strontium non-invasively. Phys. Med. Biol. 52, 2107–22.

6.3 Draft for article V follows:

Use of experimental phantom results and Monte Carlo skin simulations to evaluate candidates for normalization for arsenic x-ray fluorescence (XRF) in skin during a potential *in vivo* measurement.

Authors
Elstan D. Desouza[a], Eric Da Silva[b], Soo Hyun Byun[a], Ana Pejovic-Milic[b], David R. Chettle[a], Fiona E. McNeill[a]

Affiliations:
[a] Department of Medical Physics and Applied Radiation Sciences, McMaster University, Canada
[b] Department of Physics, Ryerson University, Canada

Manuscript will be submitted: Nucl. Inst. Meth. B 2013

Author contributions:
Elstan Desouza was responsible for experimental setup, data acquisition, analysis, coding and running Monte Carlo simulations and extracting results from simulations.
Eric Da Silva and Soo Hyun Byun assisted with interpretation of base Monte Carlo code that was modified here.
Ana Pejovic-Milic offered unrestricted use of equipment and her previous research documented setup, performance evaluation and optimization of the equipment.
David Chettle and David Fleming assisted in interpretation of data.
Elstan Desouza was responsible for preparation of the draft manuscript.
Fiona McNeill supervised and guided the research.

Abstract

Scatter peak normalization is commonly used in x-ray fluorescence to correct for source and experimental setup-based variations. The suitability and success of the normalization is often dependent on the particular experimental layout. In this article, usage of Compton and coherent scatter normalization is investigated, experimentally and through simulations, for an x-ray tube radiation source. The range of Kα:Kβ ratios expected during an *in vivo* measurement of XRF in skin is also investigated. Normalization to the Compton scatter peak is found to offer superior correction against phantom mis-positioning than coherent normalization. Gross misalignment of the phantom, thereby changing the incident and take-off angles, can lead to a variation in the Kα:Compton ratio by as much as 20% and higher for the Kα:Coherent ratio assessed using a Si(Li) detector. Experimental resin phantom-based Kα:Compton, Kα:Coherent and Kα:Kβ ratios are higher than simulated skin values by (10.40±10.66)%, (39.45±47.14)% and (9.17±10.60)% respectively: this includes datasets collected with intentional mis-positioning. Considering only experimental datasets, including misaligned datasets, the relative standard deviation of Kα:Compton and Kα:Coherent

ratio is 7.13% and 20.43%. These compare to 4.31% and 5.89% without misalignment, showing the benefit of the former for correction against mis-positioning. An upper limit of ~20% for the percentage change in the resin phantom Kα:Kβ ratio can be expected during *in vivo* trials in skin. Based on experimental work, the range of ratios covering SDD phantom-detector angles $>90^0$ were ~9%, 20% and 7% higher than the ratio at 90^0; simulations found ranges to be 6%, 23% and 7%. The SDD Kα:Kβ ratio, through experiments and simulations, was not found to change much due to mis-positioning. As with the Si(Li) detector, the Kα:Compton ratio is less susceptible to change for incorrectly positioned phantoms than the Kα:Coherent ratio. Trends in a shift in Compton peak position were found to be consistent for both detectors in experiments and simulations. A stronger shift is noted for the SDD due to Compton backscatter inside the detector head. Finally, an evaluation of the benchmarking capabilities of the code was performed, using resin phantoms. The simulated Kα:Compton and Kα:Kβ ratios agreed within ~7% with the experiments. Inclusion of a source broadening term allowed for the Kα:coherent ratio to also fall within this range.

1. Introduction:

Monte Carlo simulations are of tremendous use in the design, development and assembly of radiation detection systems. With an accurate experimental layout, they offer the ability to simulate the performance of an experiment without running it in the laboratory. This can provide insight into the ability of commercially available laboratory equipment to meet the needs a particular experiment before it is purchased. Their ability to model transport of electrons, neutrons and photons can be used to benchmark real-life experimental results. One recent example is a simple yet powerful benchmark of a prompt gamma-neutron activation analysis based gadolinium detection system (Gräfe et al., 2010).

In recent years, EGS5 has been tested and found to be in good agreement with experimental results at high energies on the order of GeV (Nelson and Field, 2007). At low energies, discrepancies with NIST data have been observed in Geant4 (Amako et al., 2005) and *in vivo* XRF comparison against EGS4 was not found to be in good agreement with experimental results due to limitations of modeling the Compton scatter process (Al-Ghorabie et al., 2001). For low energy *ex vivo* XRF, a very promising benchmark was performed in our group for strontium (Sr) in bone using EGS5, where the bone Sr signal normalized to coherent scatter was shown to follow very closely with experimental results using cadaver fingers (Zamburlini et al., 2008). Similarly encouraging results were found prior to that against low energy XRF spectra using EGS4 where its Doppler broadening capabilities were found to be superior to that of MCNP (Zamburlini et al., 2006). In both of these latter studies, although not used, the Compton scatter peak's shape was found to broaden as expected and seen to be visibly similar to that observed in laboratory testing of the same experimental setup. This naturally warrants strong consideration for further low energy XRF Monte Carlo modeling. In addition, for bone Sr, previous work has documented the difficulty in using the Sr Kα:Kβ ratio as a method

of calculating the thickness of soft tissue that surrounds bone (Heirwegh et al., 2012; Zamburlini, Pejović-Milić, et al., 2007). Arsenic (As) is known to bind to keratin and keratinocytes are typically located deeper in the epidermis (outermost layer) of the skin. However, they do experience some diffusion towards the skin surface as evidenced by accumulation of calcium in the stratum corneum of skin (Menon et al., 1985). Thus, this ratio would be of interest to measurements of arsenic in skin as it may offer an indication of the most superficial depth at which the arsenic is being measured. This ratio can be compared to theoretical predictions using an estimation of the attenuation of the known Kα and Kβ x-ray emission intensities. However, in previous work on arsenic in skin, the ratio was found to cover a large enough range that it was not used in analysis (Studinski, 2005). Thus, a first step in its usage is to determine the range of ratios attainable experimentally and compare this to simulations.

Unpublished benchmarking of EGS4 vs EGS5 has also been performed within our group. EGS5 has superior photoelectric cross section modeling built in (Hirayama et al., 2013). In the current work, the performance of EGS5 is investigated against laboratory XRF results for arsenic in 2.8±0.1 mm thick resin phantoms with a 1.3±0.1 cm thick nylon backing placed behind in order to simulate skin and the bulk tissue behind it. The primary goals are to: (a) investigate the suitability of using one of the two scatter peaks for correction against changes in source strength and phantom misalignment, through resin phantom experiments and skin simulations and (b) evaluate the performance of EGS5 against experimental resin phantom work. Throughout this work, source strength refers to a change in photon fluence rate at the measurement site. Skin is chosen, in (a), for simulation work since it is the intended measurement site for *in vivo* arsenic measurement trials. Thus the simulations are intended to offer an indication of the effectiveness of quantification of arsenic in skin *in vivo* using resin calibration phantoms. A secondary goal is to compare the effect of changes in source strength and positioning on the skin Kα:Kβ ratio and to compare it to the ratio obtained experimentally with phantoms. Two detector types – lithium drifted silicon [Si(Li)] and silicon drifted (SDD) – were tested.

2. Setups – experimental and simulation:

2.1. Radiation Source:

The radiation source used was a 25W x-ray tube with an Ag anode. The tube was manufactured by X-Ray Optics (XOS, East Greenbush, NY, USA). The x-ray source uses a doubly curved crystal (DCC) to focus the x-rays produced by an x-ray tube. The particular choice of the crystal material is dependent on the desired monochromatic energy. Further details about the principles and selected applications of optical focusing have been published previously (Bellis et al., 2009; Chen et al., 2008; Gibson et al., 2008; MacDonald and Gibson, 2003; Wei et al., 2009). The system was intended for use with Sr in bone. In order to extract meaningful information from the Sr Kβ peak at 15.8 keV (Deslattes et al., 2003), the Compton scatter low-energy tail must not interfere with the high-energy side of the Sr peak. On-site testing at the x-ray tube manufacturer's facility revealed that an Ag anode would serve this purpose better than a Mo or Rh anode

(Zamburlini, 2008). This is the incident energy used in experiments and simulations performed here. The benefit of choosing a 90^0 source-detector layout over a backscatter (180^0 arrangement) also lends itself to lowering the background under the Sr Kβ peak. Additional details about the particular choice of optic and preliminary testing with plaster of Paris (poP) bone Sr phantoms have been documented elsewhere (Sibai, 2011).

2.2 Detector characteristics and pulse processing electronics:

The Si(Li) detector used with the current work has been used extensively in the past in our research group for both Sr in bone (Heirwegh et al., 2010; Moise et al., 2012; Zamburlini, Pejović-Milić, et al., 2007) and As in skin (Studinski et al., 2006, 2005, 2004). The detector is manufactured by EG&G ORTEC (Oak Ridge, TN, USA) and is a model SLP-16220-S unit. The detector has an active diameter of 1.6 cm with an active area of 200 mm^2 and a FWHM of 220 eV at 5.9 keV. The Be window is 50 μm thick and the detector has a volume with a sensitive thickness of 5.8 mm. The detector utilizes a transistor-reset type preamplifier and is coupled to an ORTEC DSPEC Plus MCA box. For the experimental work, the rise time was fixed at 12 μs. Liquid nitrogen cooling is utilized.

The silicon drift detector (SDD) was manufactured by KETEK GmbH (Munich, Ger). It has an active area of 100 mm^2 collimated down to 80 mm^2 using a multi-element collimator. The detector FWHM is 139 eV at 5.9 keV and it uses a reset type preamplifier. The detector housing is equipped with a 10 cm long aluminum cold finger and this contains the head of the detector. The detector has a 25 μm thick DuraBe entrance window and the detector sensitive volume is 450 μm in thickness. The detector is contained in thermally optimized housing and is cooled via Peltier cooling. It is connected to an Analog X-Ray Acquisition System-Modular (AXAS-M) power supply box and is coupled to a Canberra DSA 1000 MCA unit (digital signal processor) with a fixed pulse rise time of 4.0 μs (digital).

2.1. Experimental arrangement:

The experimental layout of the XRF detection system is shown in figure 1.

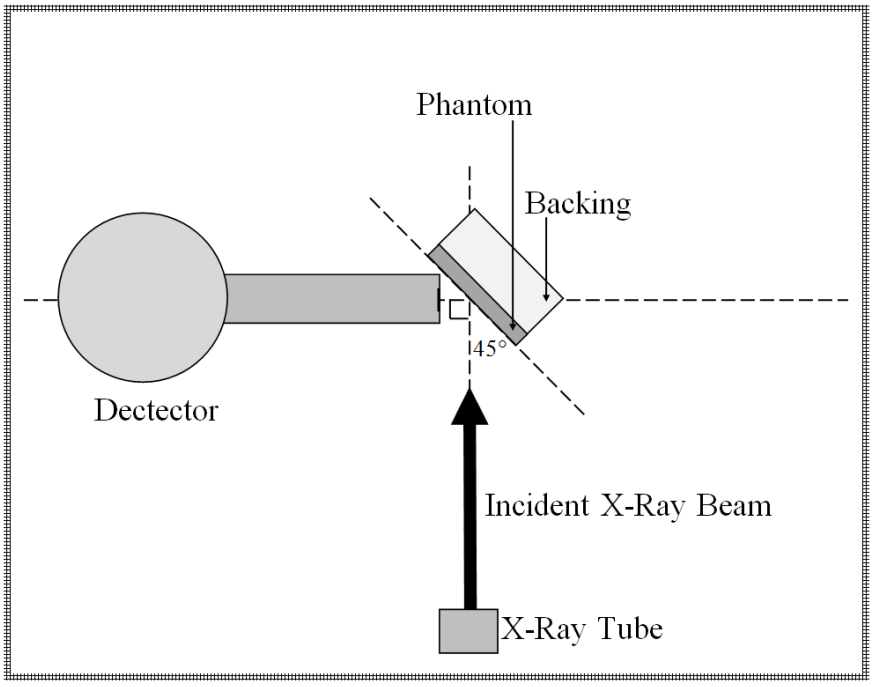

Figure 1: Schematic showing experimental layout including phantom, detector and source (x-ray tube, with built-in monochromator).

This detection system was designed for measurement of Sr in bone but is also used for As in skin. A reduction in photoelectric cross section is to be expected for As since the incident energy is moved farther away from the element's K-edge than for Sr. However, the layout allows for freedom to investigate numerous source-phantom and phantom-detector geometries and for a different detector type to be used for record the fluorescence.

Resin phantoms were prepared by adding controlled amounts of arsenic atomic absorption solution (Sigma Aldrich, Oakville, ON, Canada) to polyester resin – H 5%, C 60%, O 35% (Gawdzik et al., 2001), with a density of 1.2 g/cm^3. Phantom preparation details have been presented previously (Studinski et al., 2005) and concentrations were verified via neutron activation analysis (NAA) at the McMaster Nuclear Reactor (MNR) NAA facility (Hamilton, ON, Canada). The phantom is placed in a phantom holder at an angle of 45^0 with respect to the source and detector.

2.3. Simulated layout:

Detailed drawings provided by the detector manufacturer allowed the internal structure of the Si(Li) detector to be constructed using CGView 2.4.0. CGView is custom-written software designed to visualize the geometry constructed for simulations with EGS5, and is provided by the KEK laboratory (Tsukuba, Japan). The software allows the user to build various geometrical arrangements including a combinatorial

geometry arrangement, which was used here. The x-ray tube was represented as a point source at the focal length of the focusing optic, which was experimentally determined to occur at a distance of (30.0±0.2) cm away from the x-ray tube. Using gafchromic film to record beam size, the incident x-ray beam was allowed to expand to a larger size at the location of the phantom (48.1±0.2) cm away from the focal length. In EGS5, these distances and the beam size at the desired distance were specified based on the solid angle that they created. The limitations of this layout are that the true spot size, at the focal length, is slightly larger than a point and a focusing artifact in the gafchromic film beam image is not modeled. The artifact has a weaker intensity than the primary beam. Instead, the beam is considered to be a single spot with a beam area that includes the artifact. In the absence of optical densitometry work, the degree of this distinction cannot be made accurately as the resolution of the film is not as good as the digital camera systems typically used for this sort of application. The simulated layout is presented in figure 2.

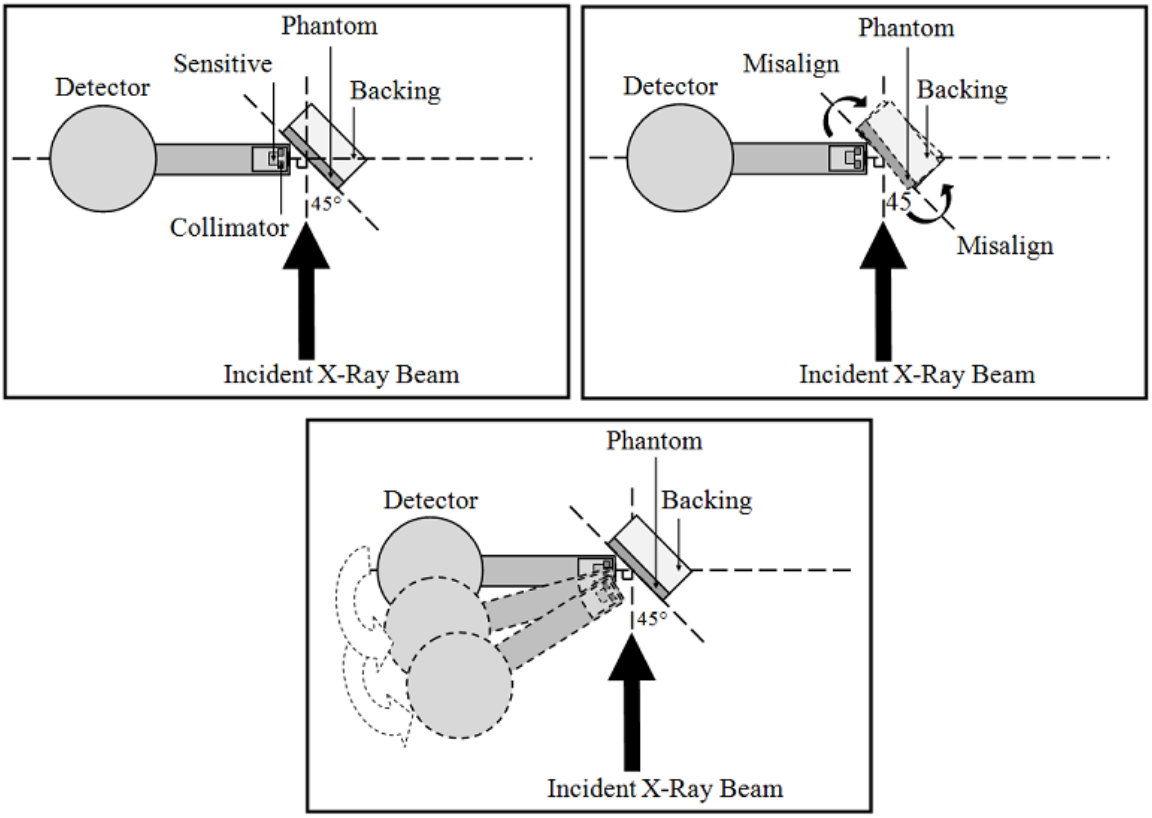

Figure 2: (top left) Standard arrangement used in simulations for either detector type, (top right) layout showing mis-positioning studied in simulations and experiments and (bottom) layout showing change in phantom-detector angle studied in simulations and experiments. The sensitive volume of each detector is shown in the sub-drawings.

The anatomical site being investigated was modeled as a cylindrical block of skin (ICRP) with a block of type 6/6 nylon backing. In addition, although resin was not listed in the EGS5 standard material database, other tissue equivalent materials – tissue-4 Comp (ICRU) and tissue (ICRP) - were modeled for comparison. The mean ionization energy for all materials listed in this database are the standardized ones (Berger et al., 2005; ICRU, 1989). Both skin and backing were of the same thickness as the resin phantom and nylon backing used in the experiments. Finally, the housing of the Si(Li) detector's front surface was placed (2.0±0.2) cm away from the measurement site. In the case of the SDD, it was placed (1.5±0.2) cm away. Both these distances represented the closest that each detector's Beryllium window could be placed safely to the surface of phantom in experiments. Finally, for both detectors, the detector head and the Beryllium entrance window were modeled, but the room, various base holders for the housing of each detector type and the sample stand were not modeled, as was the case with the previous EGS5 work. It should be noted that, unlike for the case with the Si(Li) detector, a scale drawing for all of the SDD head's interior dimensions was not available and so interpolations were made based on the information that was supplied without proprietary restrictions.

2.4. Method and data analysis:

Experimental XRF spectra were collected for real time of 1800 seconds with the phantom placed at a 45^0 angle relative to the incident beam. The take-off angle was also 45^0. The x-ray tube had a maximum voltage of 50 kVp and a maximum current of 0.50 mA. The tube was operated at a voltage of 49.0 kVp and a current of 0.49 mA. Unless indicated, three trials were performed per measurement condition. XRF spectra were recorded as .chn files and spectral reports were generated listing channels and counts.

Experimental spectral de-convolution was performed via custom non-linear least squares peak-fitting equations using Microcal Origin 8.5 (Originlab, Northampton, MA, USA), using the Levenberg-Marquardt algorithm (Bevington and Robinson, 2003; Marquardt, 1963). The peak area was calculated by fitting a two Gaussians and two tails (Campbell et al., 2001; Da Silva et al., 2008; Uher et al., 2010) equation to the As Kα and Kβ peaks, and similarly for the scatter peaks. The background model was linear of the form y = mx +b. For both detector types, the simulated As Kα:Kβ, As Kα:Compton and Kα:Coherent ratios were calculated by tallying the simulated counts in the range of energy bins covering the As Kα, As Kβ, Compton and coherent scattering peaks . Simulated uncertainties for the Kα and Kβ were thus ~1% and 2.5% respectively, while uncertainties for the scatter peaks were <1%. These ratios can be compared against results obtained in the laboratory as has been done in bone Sr EGS5 simulations mentioned above.

3. Results:

3.1. Si(Li) Detector misalignment results:

The major concern with using a 90^0 arrangement for *in vivo* trials is the ability to position the subject's hand at a 45^0 angle in the correct location. This misalignment would show up as a change in the Kα:Compton and Kα:Coherent ratios since gross misalignment would move the Compton scatter peak changing the counts accumulated under both scatter peaks. These are thus two natural choices for investigating the influence of incorrect positioning. Trials with intentional phantom misalignment were run experimentally and in simulations. The effect of intentional phantom and backing misalignment experimentally listed in table 1.

Condition	Kα:Compton	Kα:Coherent	Kα:Kβ
Small misalign L	-3.13	10.37	15.24
Large misalign L	10.77	49.87	16.00
Small misalign R	-5.18	-3.13	16.61
Large misalign R	20.30	68.92	14.76

Table 1: Percent difference in experimental Kα:Compton, Kα:Coherent and Kα:Kβ ratios relative to correctly aligned (45^0) phantom in phantom holder, using Si(Li) detector. Note that small is ~1^0 and large is ~5-6^0.

Experimentally, the misalignment was performed by rotating the phantom about its center, thus changing the angle from 45^0 by a variable amount in each trial. This change was made in a random manner. The direction of the misalignment, to the left or right of 45^0, was noted. As can be seen, the Kα:Coherent ratio is far more susceptible to changes in phantom misalignment with the source (x-ray tube) and detector than the Kα:Compton ratio. Experimental misalignment is a combination of using a phantom-detector (or source-phantom) angle that is smaller or larger than 45^0 and a vertical displacement that translates the phantom up or down such that its geometric center is no longer aligned with the incident x-ray beam. All percent difference ratios are expressed relative to the correct (45^0) phantom orientation. The smaller change in the Kα:Compton ratio indicates the benefit of choosing this ratio for normalization, against phantom mis-positioning, over the Kα:coherent ratio particularly for smaller mis-positioning. The variation in the Kα:Kβ ratio is fairly consistent suggesting that the degree and direction of the misalignment does not significantly add to or take away from the severity of the offset in this ratio. Although the percent difference is >10%, these results give an indication into what can be realistically expected during an *in vivo* measurement.

Simulations showing the effect of intentionally using the wrong phantom-detector angle, are listed in table 2.

Angle (degrees)	Kα:Compton	Kα:Coherent	Kα:Kβ
40	5.64	8.03	-4.09
42	3.72	5.92	-1.58
43	2.49	4.57	-0.21
44	0.20	2.19	-0.47
46	-3.42	-1.46	-1.71
47	-4.05	-2.04	-0.33
48	-4.70	-2.83	2.44
50	-9.47	-5.35	2.80

Table 2: Percent difference in Kα:Compton, Kα:Coherent and Kα:Kβ ratios between correctly (45-deg) and incorrectly aligned phantom in Si(Li) detector simulations, for numerous incorrect angles. The extent of the misalignment increases as the difference between the incorrect angle and 45^0 increases. Percent differences expressed as ratio relative to simulation for skin (ICRP), at 45^0.

Simulated angles less than 45^0 correspond to experimental misalignment towards the left and $>45^0$ are for misalignment towards the right. Small misalignment to the left would be closer to 45^0 and larger misalignment would be closer to 40^0. Similarly, small and large misalignments to the right would be closer to 45^0 and 50^0 respectively. Deviations from the ratios at 45^0 are not particularly large. The exact geometry of the misaligned setup cannot be simulated because the intentional offsets in phantom positioning were not performed in a controlled manner; rather these offsets were intended to reflect the sort of variation that could result in the event of gross misalignment of the intended measurement site for As in the palm of the hand (thickest skin on the body) during an *in vivo* trial. Specifically, varying amounts of lateral movement towards or away from the source may have resulted when the experimental misalignment was performed but the exact shifts are not known and so were not modeled in simulations. A lateral shift causes the mean interaction depth of the incident Ag Kα photons to move, which in turn would shift the Compton scatter peak position. This, in turn, affects the counts under both scatter peaks and the two related ratios. In the simulations, such a peak shift was not observed as the angle was varied and the well-known Compton energy equation was able to predict the simulated Compton scatter feature energy with good accuracy. In experiments, a downshifted Compton scatter energy was recorded, compared to the simulated or theoretically predicted peak position. This will be compared to simulations later; in the current context, this lower Compton scatter peak position produces a greater separation between the experimental scatter peaks than that in the simulated case. This separation would then affect the counts under the coherent scatter feature and, consequently, the Kα:Coherent ratio. Additionally, tailing was not observed in simulations as the detector's response is not built-in to the Monte Carlo coding. In practice such tailing is inevitable (Campbell et al., 1985; Knoll, 1999; Lépy et al., 2000; Scholze and Procop, 2001; Watanabe et al., 1986). Additionally, a non-zero contribution

from scatter off the internal shielding in the housing for either detector could produce a small Compton scatter contribution that could partially overlap with the tail feature on the coherent scatter peak. This too is not depicted in simulations. Finally, the incident energy is modeled as a single energy – in reality, a small spread in energies is present. This would lead to a) a wider coherent scatter peak and b) additional low intensity Compton scatter peaks as described here overlapping with the coherent scatter tail. Additional energies were not investigated here but will be discussed later. As such, the coherent scatter peak is an overestimate of the experimental scatter contribution and the simulated Kα:Coherent ratio is lower than that observed in experiments.

These lateral shifts would also influence the Kα:Kβ ratios since this ratio would be affected by the amount of attenuation of arsenic characteristic x-rays through resin. The mean free path, $\langle x \rangle = 1/\mu$, of the As Kα and Kβ x-rays through resin are ~20% higher than in skin (ICRP) at their respective energies. By comparison, the range of percentage differences between the experimental ratios and their simulation counterparts (16.00% to -4.09% and 14.76% to 2.80%) range from ~12-18%. Note that comparisons made are not exact since, for example, the large experimental phantom misalignments were likely not exactly 40^0 and 50^0 respectively. Additionally, vertical positioning misalignment was randomly present in the experimental work and variations in the arsenic distribution across the surface of the sample would result. Both of these changes could not be simulated because the vertical misalignment was randomly chosen and the variation in concentration across the resin phantom surface is unknown. Nonetheless, the difference in mean free paths between the resin phantom and skin (ICRP) suggests that this range of percentage difference in Kα:Kβ ratio between resin experiments and skin simulations is possible. Thus, this ratio would be more susceptible to change experimentally (table 1) than in the simulations (table 2). Although the extent and nature of misalignment (rotation, vertical and lateral) during an *in vivo* measurement is not likely to be known, more detailed controlled shifts in either direction combined with lateral movements should be investigated in the future for all three ratios in simulations.

3.2. Si(Li) detector – phantom experiment versus skin simulation:

Next, a comparison is made between experimental results, collected under various conditions, and a correctly aligned simulation of arsenic in skin. This was done in order to evaluate the reliability of calculating the *in vivo* As concentration using the existing resin calibration phantoms. The results are shown in table 3.

Condition	Kα:Compton	Kα:Coherent	Kα:Kβ
Small misalign L*	5.44	55.10	20.61
Large misalign L*	20.57	110.61	21.41
Small misalign R*	3.21	36.13	22.05
Large misalign R*	30.95	137.37	20.11
45.1 kVp, 0.40 mA	8.85	40.53	4.67

45.1 kVp, 0.40 mA trial 2*	16.73	47.04	21.01
40 kVp, 0.38 mA	13.23	49.62	10.12
42 kVp, 0.47 mA	6.71	37.00	6.10
35 kVp, 0.47 mA	21.47	63.99	14.74
40 kVp, 0.47 mA	14.96	46.82	7.33
37 kVp, 0.47 mA	14.50	43.48	3.46
Tissue (ICRP) Simulated	-6.47	-3.45	-0.47
Tissue-4 (ICRU) Simulated	-5.90	-4.28	-2.66

(a)

Condition	**Kα:Compton**	**Kα:Coherent**	**Kα:Kβ**
45.1 kVp, 0.40 mA	-3.87	-6.08	-4.95
45.1 kVp, 0.40 mA trial 2*	3.09	-1.72	9.89
42 kVp, 0.47 mA	-5.76	-8.43	-3.65
35 kVp, 0.47 mA	7.28	9.61	4.20
40 kVp, 0.47 mA	1.53	-1.87	-2.53
37 kVp, 0.47 mA	1.12	-4.10	-6.05

(b)

Table 3: (a) Percent difference between simulation (skin ICRP) and experiment (various conditions) in terms of Kα:Compton, Kα:Coherent and Kα:Kβ ratios. Percent differences expressed as ratio relative to simulation for skin (ICRP). (b) Percent difference between various sets of voltage-current settings and arbitrarily chosen set at 40 kVp, 0.38 mA, in terms of Kα:Compton, Kα:Coherent and Kα:Kβ ratios. Table applies to Si(Li) detector. * single trial; others are averaged over three trials. All ratios are acquired with or simulated for 100 ppm As phantom.

Table 3a compares experimental results to simulations. The two misalignment entries, with a larger percentage difference relative to the simulation, correspond to larger offsets from the intended positioning. The second entry at 45.1 kVp, 0.40 mA offers a single trial comparison. Here a single experimentally obtained ratio is compared to the simulated ratio; in the preceding row, the average over three experimental ratios is compared to the simulated ratio. Trial 2 offers an indication of what is to be expected with a single experimental result, while the row above it captures the mean of multiple experimental values. The average percentage difference relative the correctly aligned simulation of arsenic in skin is (10.69±11.10)% for the Kα:Compton, (38.56±50.77)% for the Kα:Coherent and (9.00±11.42)% for the Kα:Kβ ratios respectively. If the four experimental misalignment results (rows 1-4) are ignored, the corresponding ratios are (9.78±9.34)%, (23.62±35.64)% and (7.36±7.14)% respectively. In both cases, the

Kα:Compton and Kα:Kβ ratios are <10%, within StdDev, while the Kα:coherent ratio is not. A change of ~20% is suggested for these ratios compared to as much as ~60% for the Kα:Coherent ratio. The case for choosing the Kα:Compton ratio as a means of correcting against phantom positioning is strongly suggested by this due to its smaller average percentage difference relative to the simulated result.

To investigate further the suitability of the two scatter peak ratios, the subset of the experimental results, each with a voltage-current combination, can be examined separately. This is firstly done by considering this subset as a whole. The relative standard deviation [RSD = StdDev/Average (%)] of the experimentally obtained Kα:Compton and Kα:Coherent ratios, for this subset, is 4.31% and 5.89% respectively. Including the misaligned datasets, which were acquired under different source conditions, the RSDs are 7.13% and 20.43% respectively. The RSD for the Kα:Kβ ratio is 5.72% for correct alignment and 6.64% with misalignment. Even with misalignment, the change in the Kα:Compton ratio is <10% and again outperforms the Kα:Coherent normalization. Next, an inter-comparison between one arbitrarily chosen value from this subset and the remaining entries is examined. The percent difference relative to the ratios for a tube voltage-current setting of 45.1 kVp-0.38 mA are shown in table 3b. The average±StdDev percent difference in Kα:Compton and Kα:Coherent ratios, relative to their values under this chosen voltage-current combination, are (0.56±4.74) % and (-2.10±6.28) % respectively, both of which are equal to zero within StdDev. Based entirely on experimental phantom-based work with correct positioning, the two ratios are statistically equivalent.

Larger differences are clearly noted when comparing phantom experiments to skin simulations than inter-phantom (experimental) comparisons. This is likely to be dominated by differences between the resin phantoms and skin (ICRP). The density of resin is measured to be 1.20 g/cm^3, compared to a density of 1.10 g/cm^3 for skin (Berger et al., 2005), which is ~8% lower. The differences in elemental composition produce a mass attenuation coefficient of 0.3651 cm^2/g at the As Kα energy for resin and 0.4519 cm^2/g for skin (ICRP), which is ~35 % lower and a mean free path of 2.74 mm for resin, at the As Kα energy, compared to 2.21 mm for skin, which is ~24% higher in resin than in skin (ICRP). Differences between experiment and simulation discussed earlier also apply here. The current phantom model has been used extensively in our group for XRF of arsenic in skin (Studinski et al., 2008, 2006, 2005, 2004). It has also been used for quantifying selenium via XRF (Gherase et al., 2013; Gherase, Vallee, et al., 2010; Roy et al., 2010). Although a more appropriate comparison would be between phantom results only, the intention is to use these phantoms for *in vivo* quantification of arsenic in skin. As such, an experiment-to-simulation comparison offers a valid estimation of the feasibility of this. For this material to be used to calibrate the *in vivo* XRF system for *in vivo* quantification of arsenic, the results shown in this work represent differences that can be expected in skin during *in vivo* work.

3.3. Absolute ratios with Si(Li) detector vs simulations in skin:

The Kα:Compton, Kα:Coherent and Kα:Kβ ratios are shown graphically in figure 3.

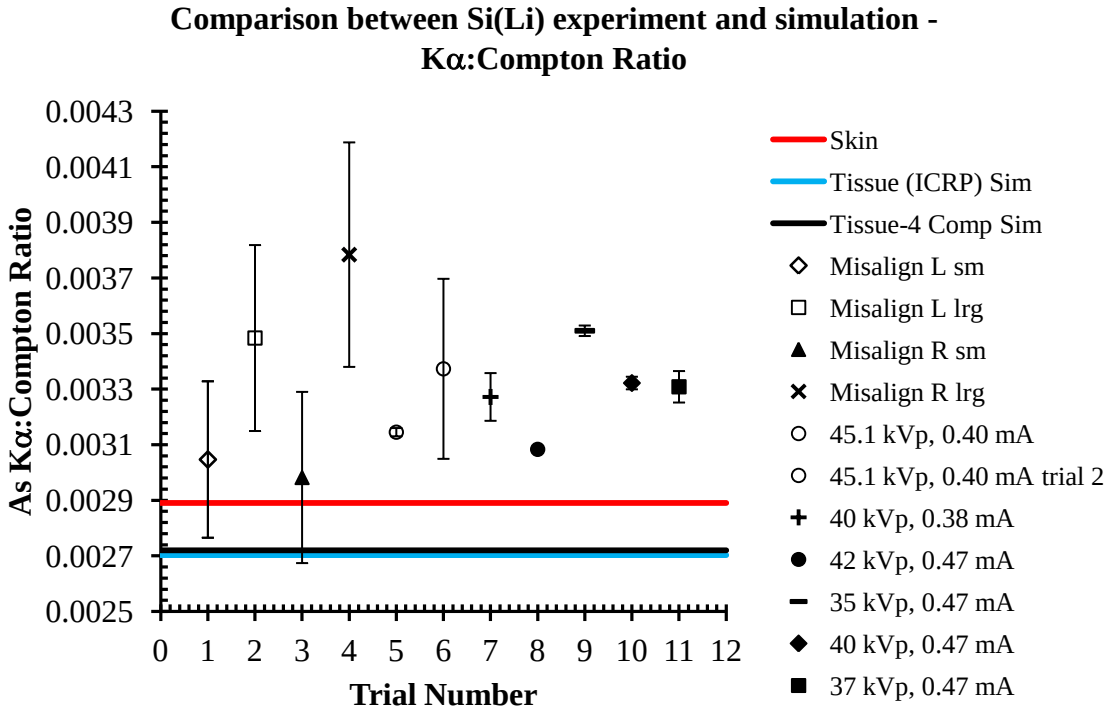

(a)

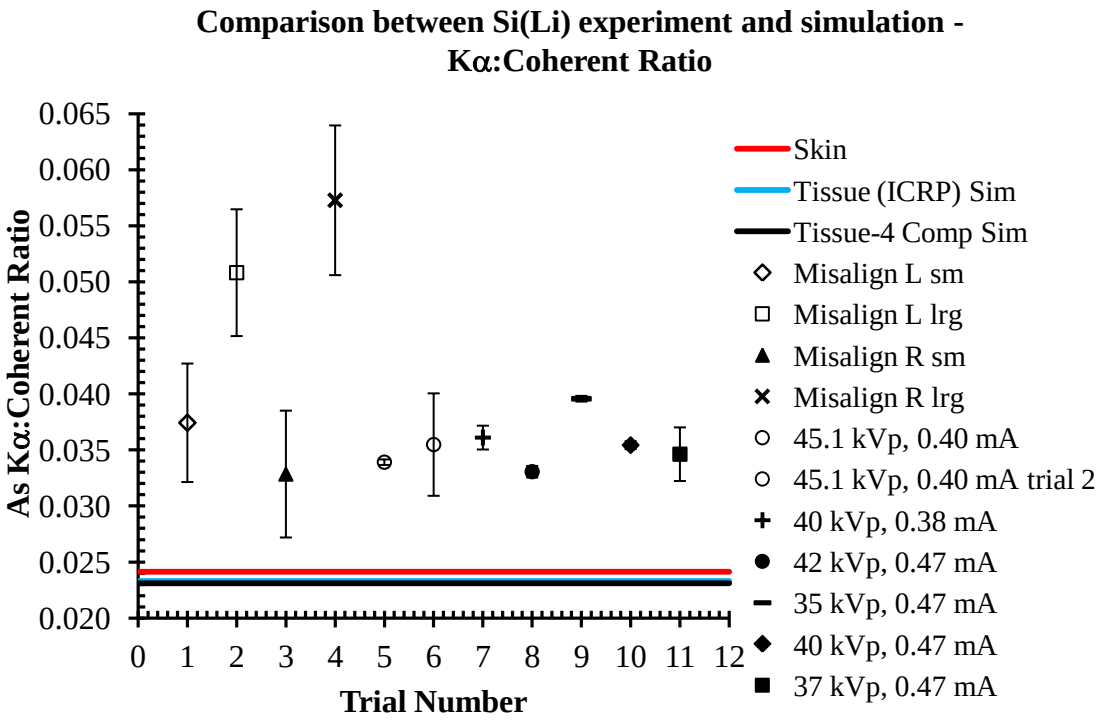
Comparison between Si(Li) experiment and simulation - Kα:Coherent Ratio
As Kα:Coherent Ratio
0.065
0.060
0.055
0.050
0.045
0.040
0.035
0.030
0.025
0.020
0 1 2 3 4 5 6 7 8 9 10 11 12
Trial Number
Skin
Tissue (ICRP) Sim
Tissue-4 Comp Sim
Misalign L sm
Misalign L lrg
Misalign R sm
Misalign R lrg
45.1 kVp, 0.40 mA
45.1 kVp, 0.40 mA trial 2
40 kVp, 0.38 mA
42 kVp, 0.47 mA
35 kVp, 0.47 mA
40 kVp, 0.47 mA
37 kVp, 0.47 mA

(b)

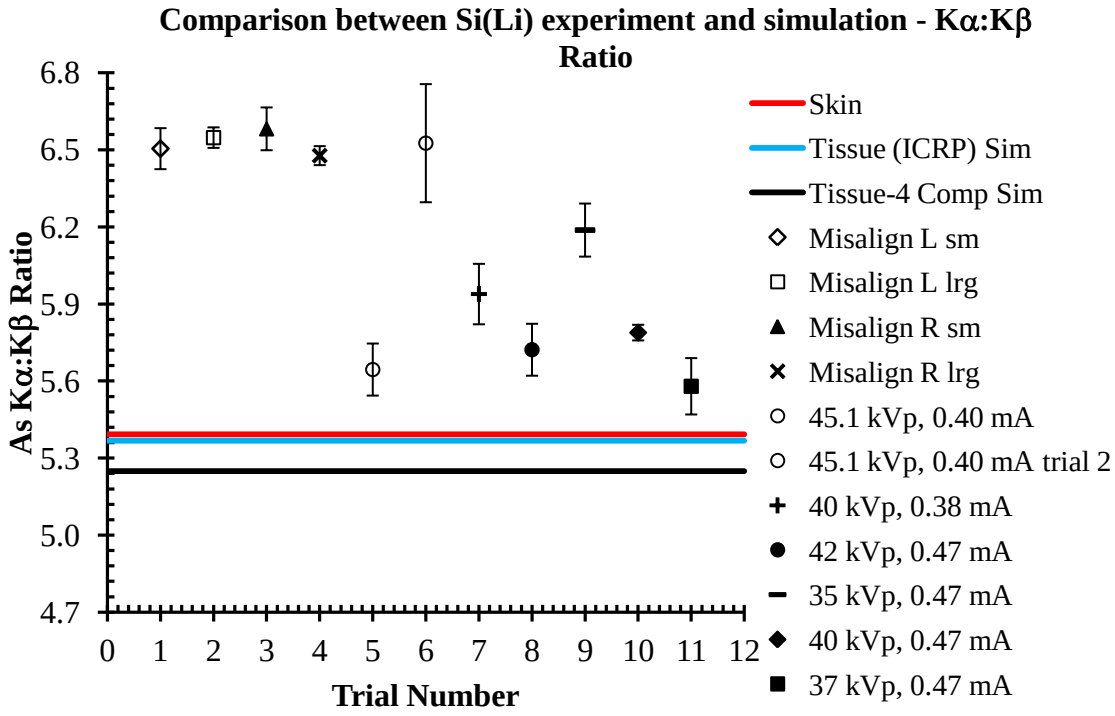

(c)

Figure 3: Plot of experimental As (a) Kα:Compton, (b) Kα:Coherent and (c) Kα:Kβ ratio in phantom measurements, under various conditions, at phantom-detector angle of 90^0, shown in comparison to results predicted by simulations in various media. Graphs apply to Si(Li) detector. Misalign L (R) small is small misalignments to the left (right) and vice-versa for Misalign L (R) lrg.

These figures demonstrate uncertainties in the absolute ratios and also show trends. Error bars in the figure are calculated as the standard deviation of multiple trials. For the point corresponding to 45.1 kVp, 0.40 mA trial 2 and the misalignment measurements, a single trial was performed, the error bars correspond to that obtained directly from propagation of uncertainties within a single trial. Proper alignment helps the Kα:Kβ ratio move closer to the simulated curves, regardless of source conditions (voltage and current), than when mis-alignment is included. Mis-positioning here changes the path length to be traversed by the arsenic characteristic x-rays and affects their attenuation through the phantom material before reaching the detector. In the absence of misalignment, nearly all the experimental Kα:Kβ ratios agree with the correctly aligned skin simulation to within 10%. With misalignment, this changes to 20% which is slightly larger than the change of ~15% (first table) for misalignment in experimental results relative to the correctly aligned experimental result. Thus, the relative change in this ratio, has an upper limit of ~20% in terms of variation expected during *in vivo* trials in skin. This encompasses

variations in chosen tube settings and inadequate positioning of a subject's hand during the measurement. For Kα:Compton and Kα:Coherent ratios, the differences are ~20% and 50% respectively and have been discussed earlier. Finally, comparing various simulated sample tissue equivalent materials, the percentage difference relative to skin (ICRP) in each of the Kα:Compton, Kα:Coherent and Kα:Kβ ratios is not more than 6.47%. This indicates that the conclusions presented, related to simulations performed, in this work are not expected to change greatly if the tissue-equivalent material's composition is changed from that of skin (ICRP).

3.4. Silicon Drift Detector – varying source-detector angle:

The experimentally obtained SDD Kα:Compton, Kα:Coherent and Kα:Kα ratios were first tracked as the phantom-detector angle was increased from 90^0. The angle was increased from 90^0 to 125^0. With the current layout, this represents the largest achievable angle while still maintaining the phantom-detector distance of (1.5±0.2) cm. Larger angles are possible but require an increase in this distance so as to avoid incident x-rays scattering off the side of the housing of the detector's cold finger. The percentage difference relative to the experimentally obtained ratio at 90^0 is shown in figure 4, on the left axis while the right axis shows the percentage difference for simulations of these geometries relative to the simulated 90^0 ratio.

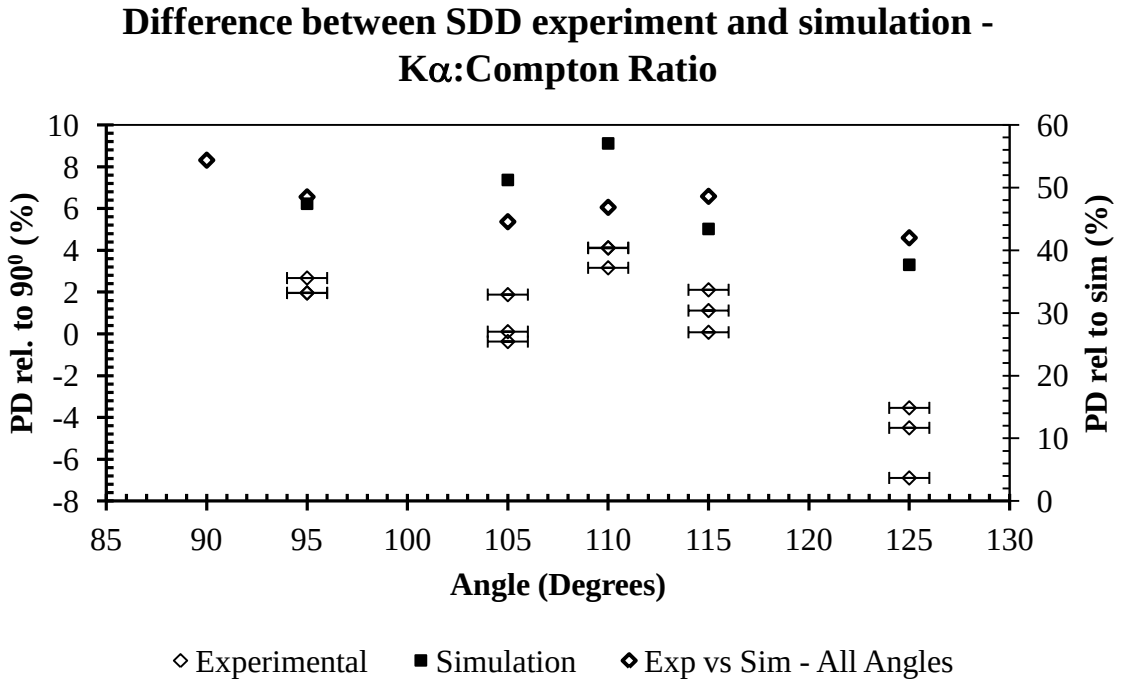

(a)

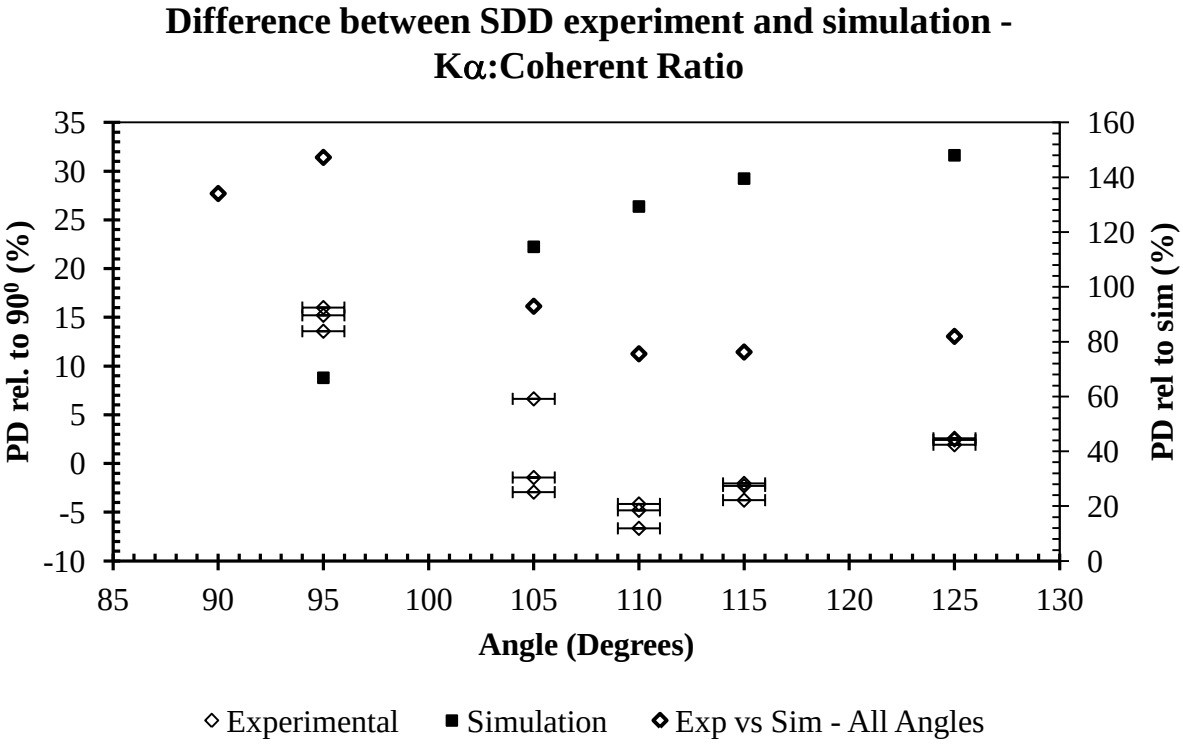
Difference between SDD experiment and simulation - Kα:Coherent Ratio
PD rel. to 90⁰ (%)
PD rel to sim (%)
Angle (Degrees)
Experimental
Simulation
Exp vs Sim - All Angles

(b)

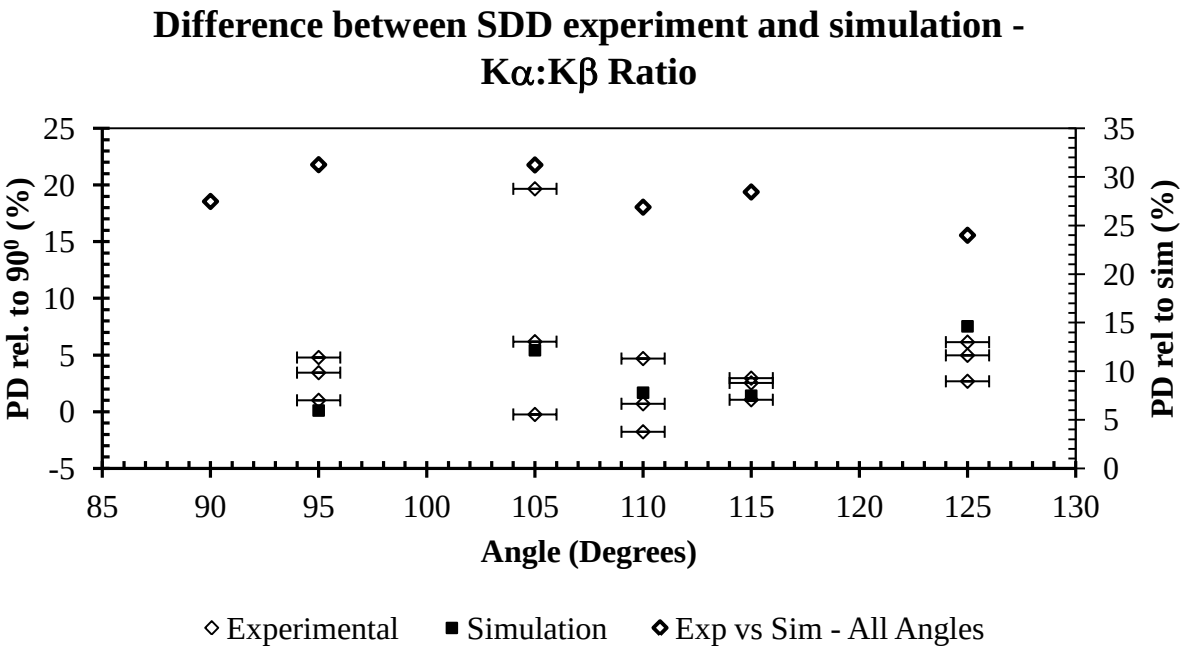
Difference between SDD experiment and simulation - Kα:Kβ Ratio
PD rel. to 90⁰ (%)
PD rel to sim (%)
Angle (Degrees)
Experimental
Simulation
Exp vs Sim - All Angles

(c)

Figure 4: Percentage difference between observed and simulated SDD (a) Kα:Compton ratio, (b) Kα:Coherent and (c) Kα:Kβ ratio as a function of phantom-detector angle, with respect to experimental ratio (left axis) and simulation (right axis) at 90 degrees.

The left axis allows a comparison of the change in the ratios based on experimental work. The average percentage difference for the experimental Kα:Compton, Kα:Coherent and Kα:Kβ ratios, relative to the experimental resin phantom ratio at 90^0, is (0.54±3.32)%, (2.02±7.79)% and (3.92±2.86)%, and all are nearly equal to zero, within standard deviation. The respective percent differences cover a range of ~9%, 20% and 7%. Simulations in skin at the same angles were then compared to the simulated ratios at 90^0 and the respective percent differences were found to be (6.21±2.21)%, (23.65±9.01)% and (3.23±3.12)%. The respective ranges were ~6%, 23% and 7%. The range of this difference is similar for experiment and simulations. In the case of the two scatter peak ratios, the range found in both sets of results indicate that the Compton scatter normalization may be more suitable for use to compare results as the phantom-detector angle is changed from 90^0.i.e. the Kα:Compton ratio shows a smaller variation in correcting against source-phantom and phantom-detector geometry, when referred to 90^0. It would thus be recommended for use *in vivo*, if a phantom-detector angle larger than 90^0 is used. For the Kα:Kβ ratio, the range is similar to that noted with the Si(Li) detector although only 90^0 was studied with that detector type. Once again, this leads the experimenter to expect a variation of ~20% in this ratio, as the phantom-detector angle is increased from 90^0.

The comparison between experiment and simulation, over the range of angles is demonstrated on the right axis. The scale of the values is quite large revealing disagreement in both experiments and simulations for all three ratios as the phantom-detector angle is increased. This was investigated by further examining 90^0 experimental results directly against skin simulations at 90^0. The results are tabulated in table 4.

PD relative to sim	**Kα:Comp**	**Kα:Coh**	**Kα:Kβ**
Trial 1	46.69	109.43	28.52
Trial 2	46.25	108.88	30.84
Trial 3	47.79	111.30	28.79
Repos 1	53.18	112.23	24.58
Repos 2	53.67	122.45	29.71
Repos 3	55.01	120.23	23.38
Repos 4	63.67	214.89	25.64
Repos 5	63.37	219.25	29.86
Repos 6	67.56	109.48	27.15
Repos 7	46.79	112.37	26.26

Min	46.25	108.88	23.38
AVG	54.40	134.05	27.47
SDOM	2.52	13.92	0.78
Stdev	7.96	44.00	2.47
Max	67.56	219.25	30.84
Range (Min to Max)	21.32	110.37	7.46
RSD	14.62	32.83	8.99

Table 4: Percent difference in Kα:Comp, Kα:Coh and Kα:Kβ ratios at 90^0 relative to skin (ICRP) simulations at 90^0, with and without re-positioning of detector and phantom holders between trials. Percent differences expressed as ratio relative to simulation for skin. Table applies to SDD. Note: SDOM = StdDev/sqrt(n).

It is clear that the simulations are not nearly as close to the experimental results as was observed with the Si(Li) detector. The discrepancy noted at larger angles is also true at a fixed angle of 90^0. The detector's multi-element collimator was chosen to be clear of interference, due to characteristic x-ray lines, in this region. Attenuation through various sub-layers in the detector housing and backscatter off the rear of the housing's interior will greatly affect the simulated results. If the detector head is not modeled accurately, this will occur through the appearance of Compton backscatter peaks. The location of these peaks will be addressed later, however, their presence would affect peak shapes and ratios in simulations. Non-zero contributions to the main Compton scatter peak will be produced at angles greater and smaller than 90^0. As mentioned earlier, not all of the exact dimensions of the interior and exterior of the SDD's housing were available. Numerous dimensions had to be obtained through interpolation from a drawing that was not to scale. This makes modeling the SDD housing much harder than with the Si(Li) detector where all dimensions were reliable. It is believed that this will be the largest contribution to the discrepancy between simulation and experiment. Thus, an absolute comparison between experiment and simulation, as tabulated here or presented in the previous figure, cannot be established.

3.5. SDD misalignment results:

The response of the Kα:Compton and Kα:Coherent ratios to small changes in positioning of the phantom are shown for experimental and simulation-based results, in table 5.

Experimental	**Kα:Comp**	**Kα:Coh**	**Kα:Kβ**
Small misalign L	63.39	-34.04	1.31
Small misalign R	-5.30	-21.14	-1.96
Large misalign L	16.51	-22.55	3.06
Large misalign R	-13.65	13.77	-2.15

(a)

Angle (degrees)	Kα:Comp	Kα:Coh	Kα:Kβ
40	7.149	7.393	-0.219
42	4.566	5.080	0.216
43	3.018	3.216	1.232
44	2.008	2.160	-1.309
46	-2.104	-1.906	0.072
47	-3.040	-2.909	0.200
48	-3.559	-3.655	3.455
50	-6.147	-6.568	2.278

(b)

Table 5: Percent difference in Kα:Compton, Kα:Coherent and Kα:Kβ ratios obtained for correctly (45-deg) and incorrectly aligned phantom in phantom holder, using SDD in (a) observations and (b) simulations. Percent difference is expressed relative to ratio when correctly aligned. Note that small is ~1^0 and large is ~5-6^0.

The experimental results in a resin calibration phantom show a larger range than the percentage difference obtained through simulations in skin. The Kα:Kβ ratio is relatively unaffected by the random mis-positioning, when compared to ratios involving the two scatter features observed in the spectrum. It is in agreement with the range of values obtained by simulations. The larger difference in the two scatter peak ratios, for the small misalignment to the left, indicates that the origin of this relatively larger deviation of experiment from simulation lies in the scatter of the incident photons. The first difference here is in the simulated and experimental misalignment. The simulated misalignments are not identical to those performed experimentally, but are believed to be close estimates. However, given the low range of energies present here, the change can be exaggerated for differences in the magnitude of the misalignment. A difference in experimental versus simulated misalignments to the left introduce additional phantom material through which incident photons have to travel. Scatter is enhanced in misalignments to the left, with additional Compton scatter features appearing at angles smaller than 90^0. For misalignment to the right, it is greater for angles larger than 90^0. This leads to a continuum of Compton scattering appearing at different angles for each of the two layouts and can be expected to contribute differently to the overall Compton scatter in one setup than in the other. The added dependence on accuracy, in the experimental and simulated layouts, is because the thinner Si sensitive thickness. This leads to Compton backscatter peaks with the SDD, which in turn are susceptible to shifts based on disagreement in the two layouts to the left or right. A difference in the experimental versus simulated misalignment, in this direction, will have a large impact on this ratio since varying amounts of skin or phantom material are introduced. Second, the extent to which this is influenced by the physical design limitations, discussed earlier. These

factors contribute to the difference between the experimental and simulated scatter peak ratios; these two factors are dependent on each other. i.e. a change in the first factor will bring about a change in the second.

The SDD head could be moved closer to the phantom than was the case with the Si(Li) detector. The solid angle of detection is larger than that for the Si(Li) detector due to this reduced distance. However, the solid angle is reduced because of the smaller diameter of the SDD's internal collimator opening. Finally, the solid angle will change differently based on differences in mis-positioning in experiments or simulations, making it susceptible to deviations in these layouts. It is likely that the SDD's collimator opening is small enough to be accepting photons within the same solid angle regardless of the mis-positioning. Additionally, a thinner Be window assists in energy deposition by more fluorescence photons than would be the case with the Si(Li) detector. These are likely contributors to the small range of As Kα:Kβ ratios in both simulations and experiments with the SDD.

As with the Si(Li) detector, the experimental percent differences for each of the scatter peaks are larger than the simulated results, likely due to unknown amounts of lateral movement during the misalignment. This is nonetheless valid since such variation in positioning is expected *in vivo*. That the magnitude of the difference between experiment and simulations is larger for the SDD, than for the Si(Li) detector, adds further credence to the notion that the physical dimensions of the SDD housing are of critical importance to accurate modeling of this type of detector for the purpose of simulations.

3.6. Compton scatter peak positioning – SDD and Si(Li) Detector:

The last comparison with simulations involves an investigation of the position of the Compton scatter peak. The results of the comparison are shown in table 6.

Predicted vs measured energy			**Percentage Difference (%)**		
Material	**Sim. (deg)**	**Obs.* (deg)**	**Obs-sim (%)**	**Obs-thry (%)**	**Sim-thry (%)**
Skin	21.15		-0.21		-0.63
Tissue	21.09	21.10	0.05	-0.84	-0.89
Tissue-4	21.09		0.05		-0.89
Skin	20.98		-0.30		-1.41
Tissue	20.98	20.92	-0.30	-1.70	-1.41
Tissue-4	20.98		-0.30		-1.41

* polyester resin phantom - H: 5% C: 60% O: 35%; Si(Li) Observed ±0.02 (StdDev), SDD Observed ±0.01 (StdDev). Note: top half of table applies to Si(Li) detector and bottom half applies to SDD. All entries apply to arrangement geometry at nominal angle of 90^0 only.

Table 6: Comparisons of observed, theoretically predicted and simulated Compton peak positions. Shown are percent difference between experiment and simulations, between experiment and theory and simulation for each detector.

The relationship between Compton-peak energy and angle is well-known and would be expected to predict accurately the observed Compton scatter peak position in the spectrum. However, a percentage difference, relative to the theory, was observed and was found to be twice as large in the case of the SDD than for the Si(Li) detector. This means that the observed Compton peak position is further away from the theoretically predicted energy for the SDD than it is for the Si(Li) detector. An increased difference between the SDD's simulation and theory also appears when comparing observations to theory. The fact that these trends are also observed with the simulated results, relative to the theory, suggests that the phenomenon bringing about this shift in peak position has been modeled reasonably well in the simulations involving the SDD. Nonetheless, the source of the shift in Compton scatter peak energy is sought. One explanation of this is backscatter inside the head of the SDD. Nearly 65-70% of the Compton and coherent scattered photons will pass through the SDD wafer, without fully depositing their energy. They will Compton backscatter off the back housing in the SDD, behind the thin sensor. These backscattered photons would also interact with the active volume of the detector and deposit some of their energy. These lead to the appearance of Compton scatter features at lower energies. This is only true for photons entering at the center of the Be window; in practice, photons within some range of solid angles will pass through the detector, depositing a fraction of their energy, leading to additional lower-energy Compton scatter features. These features may be adding up to shift the overall Compton scatter peak down in energy and produce a scatter. This factor is not relevant for the much thicker Si(Li) detector and so the discrepancies are reduced by almost 50% compared to those for the SDD.

A second factor contributing to the lower energy component is that the mean interaction depth of the incident Ag Kα x-rays is actually located in the backing material and not the resin because ~80% of incident x-rays pass through resin without full energy deposition. Thus, the source of the Compton scattered x-rays is in fact not perpendicular to the center of either detector's active diameter. A significant component of Compton scatter will be detected from this deeper location in the backing and thus from an angle which is larger than 90^0. Thus, based on this factor alone, the Compton scatter peak would be expected to appear at a lower energy than that known for a 90^0 geometry case. Future work should investigate the introduction of varying thickness of backing behind the resin phantom or skin. Improvements between SDD observations and simulations may improve with a better model of the SDD head, which would reduce the percentage difference relative to simulations to values closer to those reported for the Si(Li) detector.

The two effects causing the relatively larger downshift in the SDD Compton scatter peak warrant further investigation, given the substantial fraction of total counts under the Compton scatter peak. If the mean interaction site can be moved to the surface

of the material then the strength of the two effects can be investigated. i.e. if this shift, in mean interaction site, is accomplished, but the Compton scatter peak energy is unchanged, then the stronger effect can be identified as the backscatter inside the detector head. This test requires a change in the material being studied. Thus, in order to investigate this, several materials were tested in the same 90^0 geometry and at the same distance from the x-ray tube. The voltage-current setting chosen for all materials was 49.0 kVp, 0.49 mA. A single spectrum was acquired with all materials for 2700 seconds real time. All dead times were < 8%. The Compton peak position observed for each material is listed in table 7.

Material	**Comp (keV)**	**μ/ρ (cm^2/g)**	**ρ (g/cm^3)**	**μ (cm^{-1})**	**σ (mm)**
poP at 3.8 cm	21.20	3.56	2.32	8.26	1.21
poP at 1.5 cm	21.14				
Resin at 3.8 cm	21.09	0.48	1.20	0.57	17.42
Resin at 1.5 cm	20.94				
Polyethylene	20.96	0.40	1.17	0.47	21.12
Polycarbonate	20.97	0.43	1.20	0.51	19.43
Iron	21.23	19.16	7.87	150.87	0.07
Copper	21.15	25.34	8.96	227.05	0.04
Aluminum	21.21	2.56	2.70	6.90	1.45
Acrylic	20.99	0.47	1.19	0.56	17.92

Table 7: Shift in Compton peak position based on material chosen. Mean free path, σ, is shown for each material chosen. The theoretically predicted Compton scatter energy is 21.28 keV.

The three metals clearly have a very shallow mean free path (σ). The majority of the scattering interactions with the sample are occurring near the material's surface. The effect of this is clearly seen in the relative up-shift in the position of the Compton scatter peak compared to that observed for resin. This change in peak position suggests that the mean interaction site is making a substantial contribution to the location of the Compton scatter peak. Over all the listed materials, the Compton peak shift, caused by changing the mean interaction site, is 0.2-1.6% compared to the theoretically expected energy, depending on the material chosen. When compared to resin plus nylon, the shift is 0.1% (polyethylene)-1.42% (iron). This was further investigated by moving the SDD head away from the resin phantom. The phantom-detector distance was increased from (1.5±0.2) cm to (3.8±0.2) cm. This allows for a better defined solid angle and is shown in figure 5.

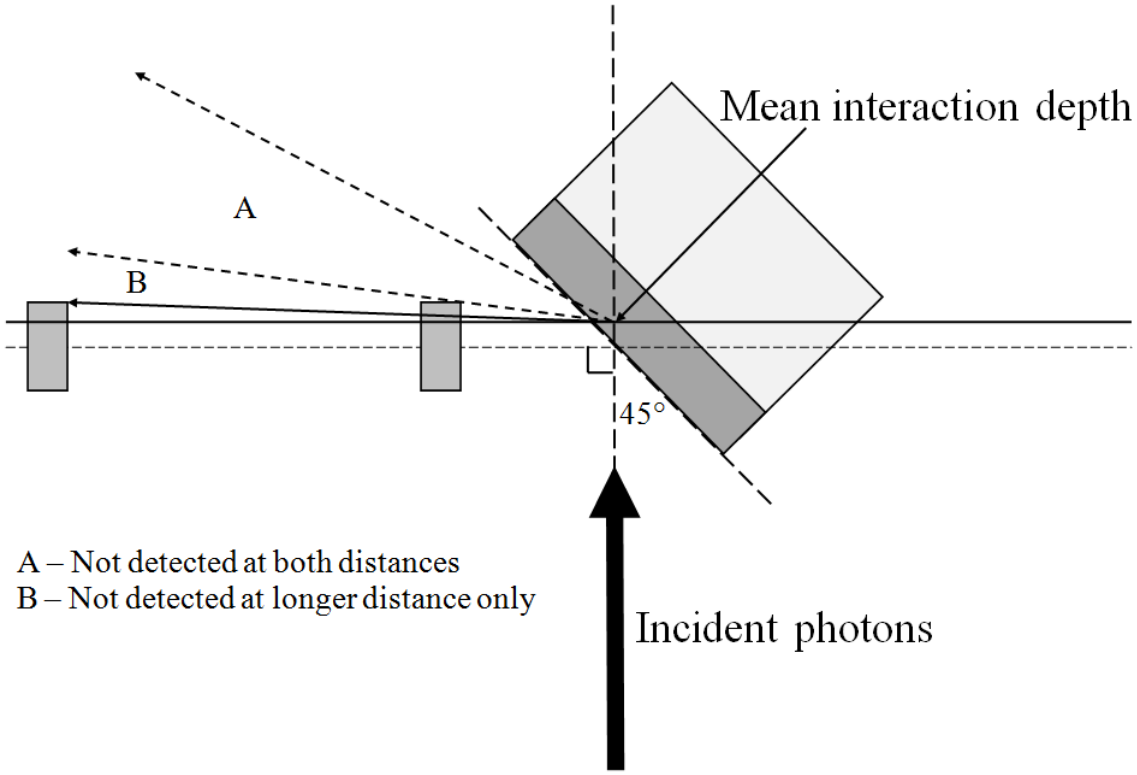

Figure 5: Influence of solid angle on fraction of scattered photons that are captured by the detector's sensitive element. Shown are fraction of scattered photons that are not captured at shorter (A) and longer (A+B) phantom-detector distances.

As seen, a larger number of photons scattered from the mean interaction depth are not detected at the longer distance (A+B) compared to those for the shorter distance (A). At the longer distance, a smaller fraction of photons scattered from deeper in the phantom will reach the detector. In this way, only those photons Compton scattered through an angle very close to 90^0 are detected at the longer distance. In addition, at the shorter phantom-detector distance, a non-zero contribution is made by scatter off the internal housing of the detector head near the edges of the detector's sensitive element. By comparison, this contribution is preferentially reduced at the larger distance. The Compton peak position shift caused by moving the detector head back is 0.74% towards the expected Compton energy, for resin. However, it is still ~1% lower than the predicted energy. For a plaster of Paris strontium bone phantom, it moves by 0.29% toward the expected energy. The shift brought about by changing the material (1.42% for Fe, 1.03% for Cu, 1.33% for Al) and forcing the interactions to occur at the surface offers a greater shift in Compton scatter peak than moving the detector head back (improving the solid angle). It should be noted that in a thin tissue-equivalent sample or resin phantom, a large fraction of incident photons will pass through sample without depositing their energy. Since the bulk behind the sample is now very thin, a small number of these photons would be scattered off backing material (if present); most of these photons would be

detected from a scatter angle close to 90^0. In this case, the Compton scatter peak would be detected closer to the predicted energy, higher than that observed in a thicker tissue-equivalent material.

3.7. Investigating effect of incident energy broadening – SDD and Si(Li) Detector:

This section is concluded by examining the influence of including the broadening of the incident energy peak. As mentioned earlier, the incident energy for the simulations was 22.2 keV, which corresponds to the Ag Kα line from the x-ray tube. However, with the x-ray tube, the incident line has intrinsic broadening and, thus, is not a delta function at a single energy. When running the simulations, the incident energy used was that of the Ag Kα line. However, it is possible to alter the incident energy distribution in EGS. The FWHM was estimated at 286 eV for the SDD and 395 eV for the Si(Li) detector, through head-on detector measurements directly out of the source. This was obtained experimentally by placing the SDD at the required distance away from the tube and recording spectra. For the Si(Li) detector, the width was obtained by placing the detector in the focal spot of the x-ray tube and recording the spectra. Due to its bulky size, it could not be placed at the maximum distance in the system's containment cabinet, as was done with the SDD. Note that since these are the recorded peak widths, they are a mixture of the intrinsic spread in the incident energy produced by the x-ray tube and the response of the detector. An in-house custom-written Matrix Laboratory (MATLAB) code (version R2012a, Mathworks, MA, USA) was used to create energy bins with this spread of energies built-in, thereby creating a small range of incident energies with a spread that was based on the estimated FWHMs above. With this setup, the simulations for both the SDD and Si(Li) detector were re-run.

For both detectors, it was found that the Kα:Kβ and Kα:Compton ratios changed by <4% relative to their values without broadening. Scatter peak positions were unchanged. This is expected since the simulated geometries were unchanged. The Kα:Coherent ratio improved by (16.47±2.28) % for the Si(Li) detector and (16.63±4.12) % for the SDD. Here, improved means that the simulated ratio increased towards the experimentally measured ratio. These are the average±StdDev over all skin (90^0 + other arrangements) and tissue models (90^0) simulated. Only minor changes were noted in trends observed in graphs presented earlier. A single incident energy was replaced with a binned layout that is determined based on the empirically measured incident peak width. This would be expected to spread the same number of counts in the incident peak over a larger range of energies. Previously, the counts fell under a single energy bin. In the case of the Compton scatter and Kα peaks, the change in number of counts were (-2.18±2.32) % and (-0.72±1.48) % relative to those under the same peaks without broadening respectively. The negative sign indicates that the peak counts without broadening were lower. However, the coherent scatter peak counts changed by (-16.47±2.28) % for the Si(Li) detector and (-16.63±4.12) % for the SDD respectively. Both changes are not equal to zero within standard deviation. Equal contributions would be made to the coherent scatter from a broader incident peak by incident to energies lying above or below the mean incident energy. Since the mean incident energy was the same, with and without

broadening, the peak counts would not be expected to change and should follow that of the other Kα and Compton scatter peaks. Since the current work is focused on changes in each of the three ratios (a relative quantity), this difference in absolute number of coherent scattered counts, with and without broadening was not further investigated. Despite this improvement, as seen earlier, the Kα:Coherent ratio remains more susceptible to geometry changes than the Kα:Compton ratio. The usability of broadening requires refinement of the calculation of the experimentally measured head-on FWHM but appears promising for the Kα:Coherent ratio, based on this investigation.

3.8. Resin phantom simulations – evaluation of potential for benchmarking code:

An evaluation of the ability of the EGS5 code in benchmarking the laboratory results at 90^0 was performed. The EGS5 input file was modified to include the composition of the resin material used. The resin phantom material was defined as per that found in the literature (Gawdzik et al., 2001) and was measured to have a density of 1.20 g/cm^3. Loss of energy between interactions by charged particles are determined in EGS5 using the standard Bethe-Bloch equation (Bethe, 1930; Bloch, 1933) combined with a Sternheimer density effect correction (Sternheimer and Peierls, 1971; Sternheimer, 1967, 1966, 1956, 1953). Since resin is not a standard mixture material listed in the database accessed by EGS5, it is recorded as a custom mixture. Thus, the Sternheimer density effect coefficients are set to their default values, as opposed to skin (ICRP) which is a standard material with specific values. Since the energies involved in the processes relevant to the Sternheimer coefficients (2 photon positron-electron annihilation and Moller scattering) are much higher than those used here, this is not expected to be a concern to the current work. For the purposes of this test, the average of each of the three experimentally obtained ratios, with the Si(Li) detector and the SDD, was calculated. This average ratio was compared against the corresponding ratios obtained in resin phantom simulations. This represents a direct comparison between arsenic resin phantom simulations and experiments.

For the Si(Li) detector, without the source broadening included, the percentage difference relative to the experimental Kα:Compton, Kα:Coherent and Kα:Kβ ratios were 2.25 %, -22.08 % and -7.62 % respectively. For the SDD, they were -21.62 %, -49.83 % and -15.57 % respectively. With broadening, they were 1.74 %, -4.84 % and -6.46 % respectively for the Si(Li) detector and -21.63 %, -41.21 % and 16.46 % respectively for the SDD. The negative sign indicates that the experimental ratios are higher than the simulated ratios. The broadened version is a better representation of what is observed experimentally and this is reflected in the associated ratios. Thus, for a comparison of simulations and experiments with both detectors, the broadening term does not change the Kα:Compton and Kα:Kβ ratios greatly, while the Kα:coherent ratio is affected to a greater extent by this term. Thus, inclusion of the source broadening is a better representation of the incident energy spectrum. Additionally, Compton scatter peak positions reported in the previous table were the same as for skin (ICRP) namely 21.15 keV for the Si(Li) detector and 20.98 keV for SDD. The observed downshift is still

observed in the resin phantom and so the previous discussion also applies here. When using the Si(Li) detector, an upper limit of ~20% for the difference between experiment and skin simulation was found earlier. A greater difference was observed when using the SDD. These are improved here with the resin phantom material, with or without source broadening, since a direct comparison of the matrix involved is being made. The application of such calibration phantoms in vivo requires a comparison to skin, not resin. However, it is reassuring that the code is able to replicate the experimental Kα:Compton and Kα:Kβ ratios to within 8% for the Si(Li) detector, better than those reported earlier in skin simulations. The larger differences for the SDD may be improved with a better physical model of the detector head.

4. Conclusion:

The present work investigated the variations from resin phantom XRF calibration measurements to be expected during *in vivo* measurement of arsenic in skin, by comparing resin phantom experiments to skin Monte Carlo simulations. The purpose was to offer guidance into the range of three specific arsenic ratios – Kα:Compton, Kα:Coherent and Kα:Kβ – when transitioning from phantom calibration to experiment. Assumptions made in the above work are that the arsenic distribution in simulated skin is uniform. This is not likely and a depth distribution in the arsenic concentration is expected. This information is currently not available and was not included in the current work. Also, the source was modeled as a point source in simulations. Bremsstrahlung from an x-ray tube was not included in the incident energy spectrum. These limitations aside, the importance of phantom mis-positioning is clearly presented for two types of detectors – Si(Li) and SDD. While phantom calibration of an XRF detection system relies on custom holders sized specifically for the phantom, this is not possible *in vivo* due to the variation in a subject's hand size. The arsenic Kα:Compton ratio was found to be preferred as a means of correcting against mis-positioning or subject motion during an *in vivo* measurement. The correction is more effective for a smaller degree of mis-positioning. Since true skin phantoms are not available, the simulations offer a useful comparison as this is the matrix that will be observed *in vivo*. The variation in the Kα:Kβ ratio with the Si(Li) detector is ~20% when mis-alignment is included and this is an *in vivo* upper bound that should be expected for this detector. A complementary and inexpensive technique to measuring skin thickness may involve performing an ultrasound measurement of the skin comprising the subject's palm. This may assist in determining the validity of an *in vivo* Kα:Kβ ratio. In the case of the SDD, the range of ratios for phantom-detector angles $>90^0$ were close to those observed from skin simulations and both revealed a small benefit to choosing the Kα:Compton ratio to correct for comparisons across various angles. Here too we found that the Kα:Compton ratio is not as affected by smaller mis-alignments as the Kα:Coherent ratio. The Kα:Kβ ratio did not change as much upon mis-alignment as with the Si(Li) detector suggesting a small acceptance solid angle. The range of this ratio for varying phantom-detector angles is very similar to that observed with the Si(Li) detector at 90^0. Compton backscatter must clearly be considered with the SDD, due to its thickness, and this was demonstrated in the

larger shift of the Compton peak position relative to theory. Changing the simulated sample composition to other tissue-equivalent materials available in the EGS5 database produced ~10% discrepancy relative to skin (ICRP) indicating that, within this level, conclusions drawn here will be valid. Finally, the evaluation of the code's benchmarking capabilities revealed the need for a source broadening term to improve agreement with the experimental Kα:coherent ratio to within 10%.

Acknowledgements:
The authors would like to acknowledge research support from the Occupational Nuclear Medicine Research Group and Nuclear Instrumentation Group within the Medical Physics and Applied Radiation Sciences department at McMaster University. We would also like to thank technical support for the experimental layout was provided by Jason Falladown, Scott McMaster and Justin Bennett. They would like to thank ORTEC for providing detailed private drawings of the interior dimensions of the Si(Li) detector. Funding through Discovery Grants from the Natural Sciences and Engineering Research Council of Canada was used in partial support of this work.

References:

Al-Ghorabie, F.H.H., Natto, S.S.A., Al-Lyhiani, S.H.A., 2001. A comparison between EGS4 and MCNP computer modeling of an in vivo X-ray fluorescence system. Comput. Biol. Med. 31, 73–83.

Amako, K., Guatelli, S., Ivanchenko, V.N., Maire, M., Mascialino, B., Murakami, K., Nieminen, P., Pandola, L., Parlati, S., Pia, M.G., Piergentili, M., Sasaki, T., Urban, L., 2005. Comparison of Geant4 electromagnetic physics models against the NIST reference data. IEEE Trans. Nucl. Sci. 52, 910–918.

Bellis, D.J., Li, D., Chen, Z., Gibson, W.M., Parsons, P.J., 2009. Measurement of the microdistribution of strontium and lead in bone via benchtop monochromatic microbeam X-ray fluorescence with a low power source. J. Anal. At. Spectrom. 24, 622–626.

Berger, M.J., Coursey, J.S., Zucker, M.A., Chang, J., 2005. ESTAR, PSTAR, and ASTAR: Computer Programs for Calculating Stopping-Power and Range Tables for Electrons, Protons, and Helium Ions (version 1.2.3) (Gaithersburg, MD: National Institute of Standards and Technology) [WWW Document]. URL http://www.nist.gov/pml/data/star/index.cfm

Bethe, H., 1930. Theory of passage of swift corpuscular rays through matter. Ann. Phys. 397, 325–400.

Bevington, P.R., Robinson, D.K., 2003. Data reduction and error analysis for the physical sciences, 3rd ed. McGraw-Hill, Boston, USA.

Bloch, F., 1933. Stopping power of atoms with several electrons. Zeitschrift fur Phys. 81, 363–376.

Campbell, J.L., McDonald, L., Hopman, T., Papp, T., 2001. Simulations of Si(Li) x-ray detector response. X-Ray Spectrom. 30, 230–241.

Campbell, J.L., Millman, B.M., Maxwell, J.A., Perujo, A., Teesdale, W.J., 1985. Analytic fitting of monoenergetic peaks from Si(Li) X-ray spectrometers. Nucl. Instruments Methods Phys. Res. Sect. B Beam Interact. with Mater. Atoms 9, 71–79.

Chen, Z.W., Gibson, W.M., Huang, H., 2008. High Definition X-Ray Fluorescence: Principles and Techniques. X-Ray Opt. Instrum. 2008, 1–10.

Da Silva, E., Pejović-Milić, A., Heyd, D. V., 2008. The use of teeth as the site for the in vivo or ex vivo quantification of skeletal strontium by energy-dispersive X-ray fluorescence spectrometry: A feasibility study. J. Anal. At. Spectrom. 23, 527–534.

Deslattes, R., Kessler, E., Indelicato, P., de Billy, L., Lindroth, E., Anton, J., 2003. X-ray transition energies: new approach to a comprehensive evaluation. Rev. Mod. Phys. 75, 35–99.

Gawdzik, B., Matynia, T., Chmielewska, E., 2001. Modification of unsaturated polyester resin with bismaleimide. J. Appl. Polym. Sci. 82, 2003–2007.

Gherase, M.R., Desouza, E.D., Farquharson, M.J., McNeill, F.E., Kim, C.-Y., Fleming, D.E.B., 2013. X-ray fluorescence measurements of arsenic micro-distribution in human nail clippings using synchrotron radiation. Physiol. Meas. 34, 1163–1177.

Gherase, M.R., Vallee, M.E., Fleming, D.E.B., 2010. Simultaneous detection of As and Se in polyester resin skin phantoms. Appl. Radiat. Isot. 68, 743–745.

Gibson, W.M., Chen, Z.W., Li, D., 2008. High-Definition X-Ray Fluorescence: Applications. X-Ray Opt. Instrum. 2008, 1–17.
Gräfe, J.L., McNeill, F.E., Byun, S.H., Chettle, D.R., Noseworthy, M.D., 2010. A benchmarked MCNP model of the in vivo detection of gadolinium by prompt gamma neutron activation analysis. Nucl. Instruments Methods Phys. Res. Sect. B Beam Interact. with Mater. Atoms 268, 2451–2457.
Heirwegh, C.M., Chettle, D.R., Pejović-Milić, a, 2010. Evaluation of imaging technologies to correct for photon attenuation in the overlying tissue for in vivo bone strontium measurements. Phys. Med. Biol. 55, 1083–98.
Heirwegh, C.M., Chettle, D.R., Pejovic-Milic, A., 2012. Ex vivo evaluation of a coherent normalization procedure to quantify in vivo finger strontium XRS measurements. Med. Phys. 39, 832–41.
Hirayama, H., Namito, Y., Bielajew, A.F., Wilderman, S.J., Nelson, W.R., 2013. The EGS5 Code System. SLAC-R-730.
ICRU, 1989. Tissue substitutes in radiation dosimetry and measurement. ICRU Report No 44. (Bethesda, MD: ICRU).
Knoll, G.F., 1999. Radiation Detection and Measurement, 3rd ed. John Wiley & Sons Inc.
Lépy, M.C., Campbell, J.L., Laborie, J.M., Plagnard, J., Stemmler, P., Teesdale, W.J., 2000. Experimental study of the response of semiconductor detectors to low-energy photons. Nucl. Instruments Methods Phys. Res. Sect. A Accel. Spectrometers, Detect. Assoc. Equip. 439, 239–246.
MacDonald, C.A., Gibson, W.M., 2003. Applications and advances in polycapillary optics. X-Ray Spectrom. 32, 258–268.
Marquardt, D.W., 1963. An Algorithm for Least-Squares Estimation of Nonlinear Parameters. J. Soc. Ind. Appl. Math. 11, 431–441.
Menon, G.K., Grayson, S., Elias, P.M., 1985. Ionic Calcium Reservoirs in Mammalian Epidermis: Ultrastructural Localization by Ion-Capture Cytochemistry. J. Invest. Dermatol. 84, 508–512.
Moise, H., Adachi, J.D., Chettle, D.R., Pejović-Milić, A., 2012. Monitoring bone strontium levels of an osteoporotic subject due to self-administration of strontium citrate with a novel diagnostic tool, in vivo XRF: a case study. Bone 51, 93–97.
Nelson, W.R., Field, C., 2007. Comparison of EGS5 simulations with experiment. Nucl. Instruments Methods Phys. Res. Sect. A Accel. Spectrometers, Detect. Assoc. Equip. 572, 1083–1093.
Roy, C.W., Gherase, M.R., Fleming, D.E.B., 2010. Simultaneous assessment of arsenic and selenium in human nail phantoms using a portable x-ray tube and a detector. Phys. Med. Biol. 55, N151–N159.
Scholze, F., Procop, M., 2001. Measurement of detection efficiency and response functions for an Si(Li) x-ray spectrometer in the range 0.1-5 keV. X-Ray Spectrom. 30, 69–76.
Sibai, M., 2011. Second generation of the diagnostic tool for the In vivo measurement of strontium levels in human bone. Theses Diss.
Sternheimer, R., 1953. The Energy Loss of a Fast Charged Particle by Čerenkov Radiation. Phys. Rev. 91, 256–265.
Sternheimer, R., 1956. Density Effect for the Ionization Loss in Various Materials. Phys. Rev. 103, 511–515.
Sternheimer, R., 1966. Density Effect for the Ionization Loss of Charged Particles. Phys. Rev. 145, 247–250.
Sternheimer, R., 1967. Density Effect for the Ionization Loss of Charged Particles. II. Phys. Rev. 164, 349–351.
Sternheimer, R., Peierls, R., 1971. General Expression for the Density Effect for the Ionization Loss of Charged Particles. Phys. Rev. B 3, 3681–3692.
Studinski, R., O'Meara, J., McNeill, F., 2008. The feasibility of in vivo measurement of arsenic and silver by x-ray fluorescence. X-Ray Spectrom. 37, 51–57.
Studinski, R.C.N., 2005. Development of an in vivo method of measuring arsenic with radiation.
Studinski, R.C.N., McNeill, F.E., Chettle, D.R., O'Meara, J.M., 2004. XRF analysis of arsenic-doped skin phantoms. X-Ray Spectrom. 33, 285–288.
Studinski, R.C.N., McNeill, F.E., Chettle, D.R., O'Meara, J.M., 2005. Estimation of a method detection limit for an in vivo XRF arsenic detection system. Phys. Med. Biol. 50, 521–530.
Studinski, R.C.N., McNeill, F.E., O'Meara, J.M., Chettle, D.R., 2006. A method detection limit for potential in vivo arsenic measurements with a 50 W x-ray tube. Phys. Med. Biol. 51, N381–7.
Uher, J., Roach, G., Tickner, J., 2010. Peak fitting and identification software library for high resolution gamma-ray spectra. Nucl. Instruments Methods Phys. Res. Sect. A Accel. Spectrometers, Detect. Assoc. Equip. 619, 457–459.
Watanabe, Y., Kubozoe, T., Mukoyama, T., 1986. Analytical functions for fitting K X-ray doublet peaks from Si(Li) detectors. Nucl. Instruments Methods Phys. Res. Sect. B Beam Interact. with Mater. Atoms 17, 81–85.
Wei, F., Chen, Z.W., Gibson, W.M., 2009. Measurement of oxidation states for transition elements with a small spot tabletop XANES instrument. X-Ray Spectrom. 38, 382–385.
Zamburlini, M., 2008. In vivo measurement of bone strontium with x-ray fluorescence.
Zamburlini, M., Pejović-Milić, A., Chettle, D.R., 2006. Evaluation of geometries appropriate for 125I in vivo bone strontium X-ray fluorescence measurement. J. Radioanal. Nucl. Chem. 269, 625–629.
Zamburlini, M., Pejović-Milić, A., Chettle, D.R., 2008. Coherent normalization of finger strontium XRF measurements: feasibility and limitations. Phys. Med. Biol. 53, N307–13.

Zamburlini, M., Pejović-Milić, A., Chettle, D.R., Webber, C.E., Gyorffy, J., 2007. In vivo study of an x-ray fluorescence system to detect bone strontium non-invasively. Phys. Med. Biol. 52, 2107–22.

6.4 Ex vivo sample – qualitative investigation :

With the system assembled and aligned, some human skin and animal bone samples were collected and run through the system. The samples were collected from cadavers donated to the Education Program in Anatomy at McMaster University. The cadavers originated from members of the general population. Details of sample collection are presented later in this thesis.

The samples were cylindrical bulk cores of skin with the fatty tissue intact. The samples were frozen until use. A 5 X 5 X 1 cm high-density polyethylene block was purchased from P&A Plastics Inc. (Hamilton, ON, Canada) and used as the holder for the samples. The holder was washed with distilled water, soaked in nitric acid for ~24 hours and then run through a VWR Model 97043-960 Ultrasonic Cleaner. Finally, the holder was placed in anhydrous ethyl alcohol (Greenfield Ethanol, Brampton, ON, Canada) until it was used. In order to avoid cross-contamination, a separate holder was used for each of the human skin samples; the cleaning procedure was performed for all three holders. In addition, a few spectra from animal bones are also shown. An intensive cleaning procedure was followed to remove the bone marrow from the bone (personal communication, Hedieh Mohseni). Due to their shape and size, a holder was not required for the bone samples. The bone marrow was placed on a cleaned aluminum lab jack such that no part of the aluminum surface was in the path of the x-ray beam. Sample spectra were acquired with the SDD at 1.5 cm away from the sample with the tube running at 49.0 kVp, 0.49 mA, at a distance of 78.1±0.2 cm away from the x-ray tube. A 2 ppm arsenic resin phantom (2.8 mm thickness, 5.0 cm diameter) was also measured under the same conditions. The phantom and skin samples were placed at 45^0, while the bone samples were positioned as close to 45^0 as possible. All spectra were acquired for 5400 seconds real time and are presented in figure 6.1.

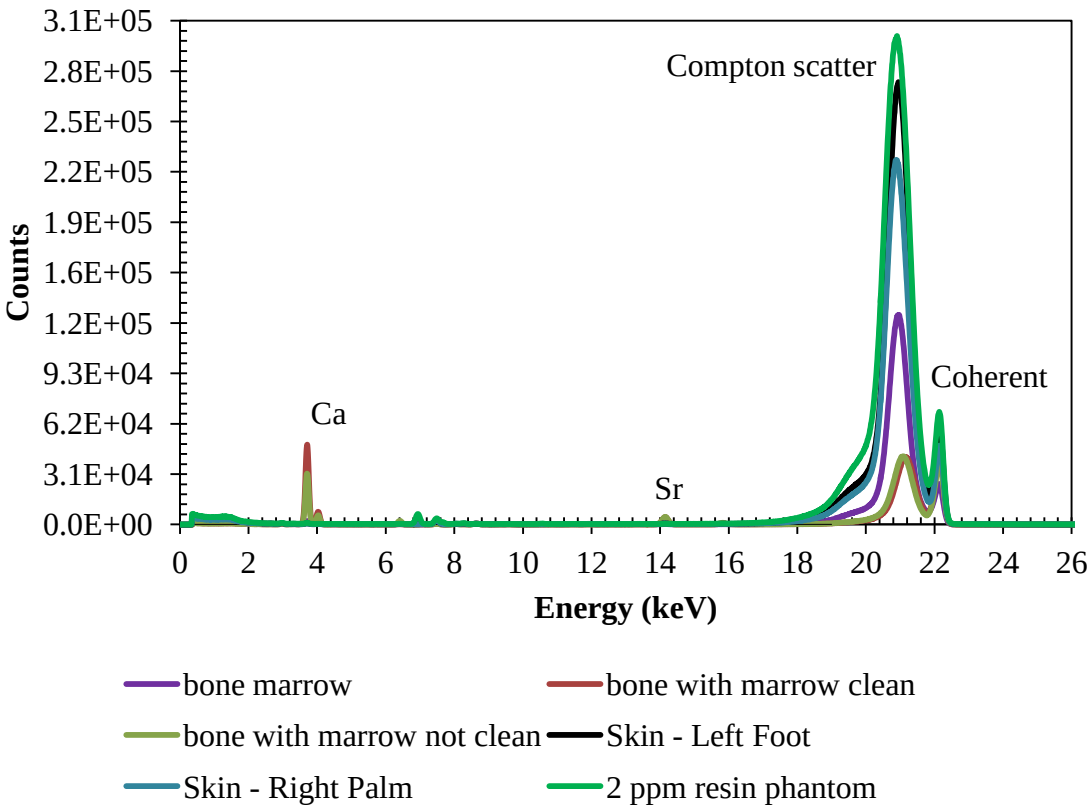

Figure 6.1: Full energy spectrum collected with skin and bone samples. Higher peak amplitudes are indicative of a lower system dead time or higher live time during which the detector is actively accepting pulses.

The full range of energies in the spectrum highlights the difference in the matrix composition of the samples. In particular, bone marrow is remarkably similar in its scatter profile to skin and to the resin phantoms. This is encouraging since bone marrow is a type of soft tissue and thus it should be possible to distinguish it experimentally from the matrix comprising bone. This is clearly borne out qualitatively in the spectra. It should be noted that shifts in the Compton scatter peaks are primarily due to the positioning and shape of the tested bone samples. An enlarged version is listed in figure 6.2.

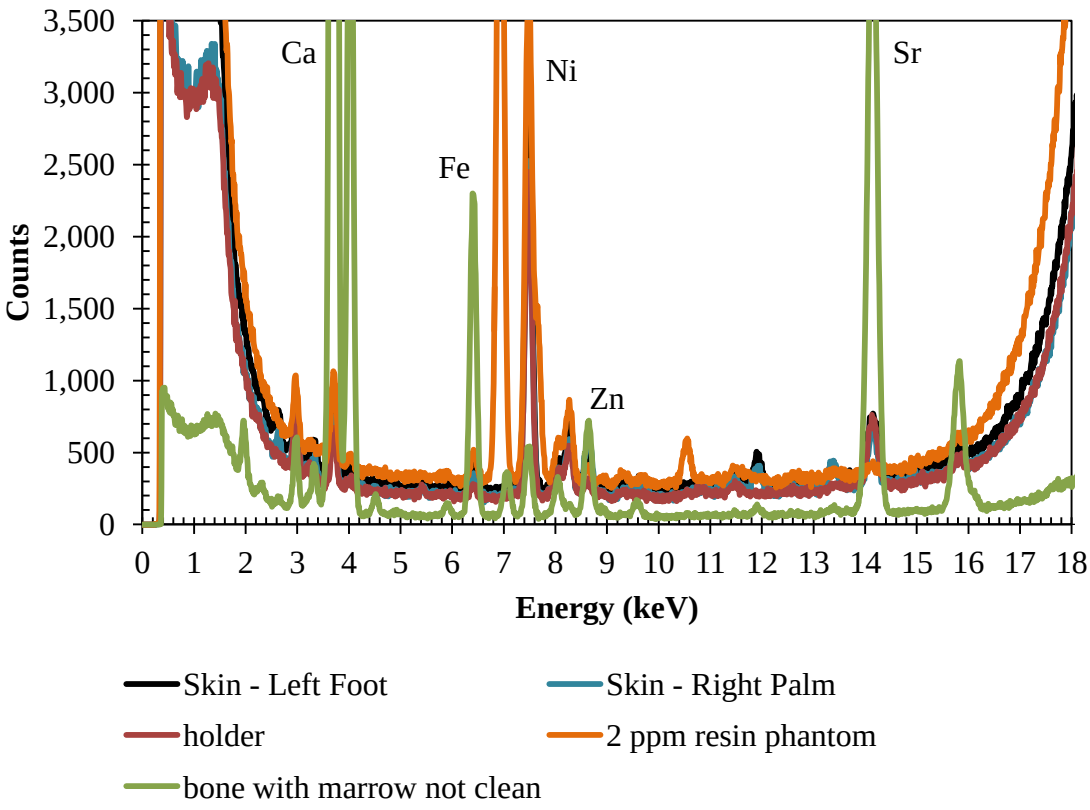

Figure 6.2: Enlarged version of select spectra collected with skin and bone samples. Dead times ranged from ~7.8% (2 ppm resin phantom) to ~12.2 % (bone with marrow not clean); all real times were fixed at 5400 seconds.

The significant difference in peak amplitudes of either the calcium or strontium Kα peaks in the bone samples is immediately noted. These are expected in bone samples and are not observed in the skin samples. Iron, zinc, rubidium and nickel are clearly identified in bone samples. An L-shell peak due to mercury may also be present, in bone and skin samples, at ~11.88 keV. The beam size at the location of the measurements was slightly larger than the diameter of the skin samples (0.8 cm) and so scatter off part of the holder was also detected. Unfortunately, this interferes with the low energy x-ray peaks in the skin sample spectra, leading to significant interference due to the holder itself. As a result, the presence of chromium or copper cannot be established in the tested skin samples and strontium is noted in the holder, likely originating from the fabrication process. A smaller beam size may have sufficed here. Nonetheless, the absence of arsenic is noted in all the skin samples tested. The presence of arsenic is clearly observed in the low concentration As phantom. With skin samples acquired from an exposed population, inspection of these spectra would appear to indicate that the system should be able to detect an arsenic signal in thick skin to ~ 2 ppm. This is considerably higher than the system's detection limit, however preparing lower concentration phantoms may well still

produce a detectable arsenic signal and could be investigated. Time-permitting, the results of such testing would have been reported.

Although the system is designed primarily for *in vivo* work, long counting times are possible with cadaver skin or bone samples since the constraints of *in vivo* work involving a human subject are released. The tested sample spectra would appear to indicate that, with a better holder material and choice of beam size, the system is capable of being used to quantify trace element content in samples acquired from cadavers with known exposure to the element of interest. With an appropriate calibration phantom set or a suitable NIST reference standard material, additional organs could also be tested and quantified.

6.5 Theoretical calculation of expected Kα:Kβ ratio for arsenic in various media:

Although the analysis of the Kβ peak area does not significantly improve the MDL, the arsenic Kα:Kβ ratio was investigated, as it may be useful in discerning As skin-depth related information. This section shows a calculation of the estimated ratio based on attenuation of theoretically known emission probabilities.

As incident photons interact with the material, they are attenuated producing fewer x-rays. Assuming a target material depth dependent decrease [exponential, eg: $I(\alpha) = I_0 \exp(-\mu x)$] in the production of As x-rays, and an incident photon fluence characterized by the Ag Kα energy, a corrected As Kα:Kβ ratio, PR(α:β), that accounts for attenuation in the desired material is found by summing x-rays emerging from all depths within the resin, for both the Kα and Kβ lines, and taking the ratio as described using

$$PR(\alpha:\beta) = \frac{\sum_{i=1}^{n} I_i * I(\alpha)}{\sum_{i=1}^{n} I_i * I(\beta)} \quad (1)$$

where I_i is the intensity of the incident energy. A certain number of discretely chosen depths in the resin are picked for sampling. For the current work n=100 depth intervals were chosen for 0-4 mm. The composition of a polyester resin, by weight, is known to be 5% H, 60% C and 35%, as mentioned in earlier sections, and this composition was assumed for resin. A certain number of discretely chosen depths in the resin is picked. Note that the mean free path of the arsenic Kα energy in resin precludes inclusion of the nylon backing, since photons from such depths are attenuated after passing through nylon followed by resin or some other tissue model. A continuum of depths is present in the resin, but for calculation purposes, a discrete number of chosen. Exponential attenuation of the incident energy intensity (assumed to be 100% at the surface) is calculated for the discretely chosen depths. At each incident depth, the corresponding output depth (distance to be travelled by arsenic Kα and Kβ characteristic x-rays) also results in

attenuation of the arsenic photons in resin. This attenuation is also calculated with the exponential attenuation law. The product of I_i*I represents the product of the incident Ag photons, after attenuation through the incident depth, and As Kα photons after attenuation through the output depth. The combined intensity exits the material and can be detected. This is repeated for the Kβ energy and the ratio is calculated.

The final step is the sum of the contribution of this ratio over all depths. When summing, as a simplification, for the first depth just beyond the surface of the resin, the contribution to the ratio is assumed to be coming from that depth alone. The alpha and beta contributions from this depth give the desired ratio at this depth into the resin. For the second discrete chosen depth, the contributions are assumed to be coming from the first two depths. For the third depth, the first three depths are assumed to be making a contribution to the ratio, and so on. At each depth, this summing procedure is performed, up to the maximum depth given by the geometry of the experimental setup - 3.95 mm (recall 45^0 geometry in chapter 5). The desired ratio occurs at the mean free path of arsenic Kα photons in resin – approximately 2.8 mm. The summed ratio at this depth will be discussed below. Using a measured resin density of 1.20±0.06 g/cm^3, the attenuation coefficient of resin, at the desired energy, was found using

$$\mu = \left[\sum_{i=1}^{3} \left(\frac{\mu}{\rho}\right)_i\right]\rho \qquad (2)$$

The incident spectrum is complicated by the nature of the source used here. The output spectrum from typical x-ray tubes includes two characteristic x-ray lines (anode material) and a bremsstrahlung hump-like feature. The incident energy used in the calculation above is thus a mixture of this feature and the characteristic x-ray lines for the anode material. Characterization of this hump requires spectra produced directly out of the x-ray tube. Due to dead time considerations, these were collected with the SDD at a voltage setting of ~33 kVp, which is lower than those used for phantom measurements. This setting suggests that the bremsstrauhlung will peak at ~11 keV, making its affect on the theoretically predicted As Ka:Kb ratio of significance. Further complicating matters is the diffraction peak (due to the optical focusing) at ~11.1 keV, in experimental results. Ideally one would model the bremsstrahlung and include a range of incident energies in the theoretical calculation. Since an accurate model is quite challenging with the current setup, the range of energies was estimated and included in the calculation of the ratio from the raw As Kα and Kβ emission probabilities. Spectra presented earlier suggest that, even for low kVp settings, bremsstrahlung will not be a concern for the system with optical focusing, but it is nonetheless useful to examine the possible impact that this feature could have on x-ray tube spectra in general. The contribution of each energy included in the bremsstrahlung model was varied. Head-on spectra with the conventional x-ray tube benchtop system could not be recorded due to shielding obstructions (see future work section) and so the estimation presented here could offer guidance into how

this ratio would change. In the current work, a depth corresponding to the thickness of the phantom – 2.8 mm – is of interest.

This calculation is intended to estimate the expected ratio, based on theoretical intensities. The limitations are that it assumes a point source pencil beam (incident photons) and a single-point infinitely thick detector. For the SDD, the detector is sufficiently thin that a contribution to arsenic Kα (~5%) and Kβ (~10%) is made by Compton backscattered photons off the internal housing of the SDD cold finger. The above calculation was performed assuming that the source is placed directly in front of the resin disc and that the detector is in a backscatter arrangement (180^0 – Detector: Source → material, where the material is resin). When the calculation was repeated for the 90^0 arrangement, the incident and output distances travelled were changed based on trigonometry relations of the 90^0 degree layout, with the phantom oriented at 45^0. Arsenic Kα and Kβ photons originating in the nylon again must pass through >2.8 mm resin and so are attenuated before exiting the bulk of the resin. Assuming this 90^0 layout and an incident energy characterized by the Mo Kα energy, the ratios at 2.8 mm, were found to be 5.934 for resin, 5.812 for skin (ICRP) and 5.861 for tissue (ICRP). These compare to 5.866 for the 180^0 (backscatter) layout for resin. At the Ag Kα incident energy, the ratios were 5.923 for resin, 5.794 for skin (ICRP) and 5.846 for tissue (ICRP). These are compared to 5.8513, in the 180^0 layout for resin. The mean free paths for as Kα photons in skin (ICRP) and tissue (ICRP) are 2.21 mm and 2.38 mm respectively.

Finally, the relative intensity of each incident energy line was investigated. Since the exact shape of the bremsstrahlung continuum will vary with kVp, a range of intensities was investigated to offer an estimate of the possible influence on the ratio. In each, case, since the bremsstrahlung energy peaks and then decreases towards that of the characteristic x-rays (anode material), the slope of the line describing this decrease is negative. Hence, for testing the influence of different intensities, the highest energy was chosen at the Ag Kα energy and the lowest energy (bremsstrahlung peak) was chosen at 15 keV, corresponding to ~45 kVp; recall that in 90^0 geometry, a higher kVp is permitted due to lower system dead time. This is comparable voltage to that used in the last three sections of this work, where the lowest detection limits were obtained. By comparison, the arsenic K-edge is located at ~12 keV. The results of changing intensities are shown in table 6.1.

Table 6.1: Results of changing relative contribution of various incident energies to ratio.

	Energy (keV)								
Material	**15**	**16**	**17**	**18**	**19**	**20**	**21**	**Ag**	**Ratio***
resin	0.40	0.35	0.30	0.25	0.20	0.15	0.10	1.00	5.9020
resin	0.80	0.68	0.57	0.45	0.33	0.22	0.10	1.00	5.9044
resin	1.50	1.27	1.03	0.80	0.57	0.33	0.10	1.00	5.9059
resin	7.00	5.85	4.70	3.55	2.40	1.25	0.10	1.00	5.9075
resin	12.00	10.02	8.03	6.05	4.07	2.08	0.30	1.00	5.9078
resin	15.00	12.52	10.03	7.55	5.07	2.58	0.30	1.00	5.9078
resin	20.00	16.68	13.37	10.05	6.73	3.42	0.30	1.00	5.9079
resin	50.00	41.68	33.37	25.05	16.73	8.42	0.50	1.00	5.9080
A-150**	50.00	41.68	33.37	25.05	16.73	8.42	0.50	1.00	5.8707
Tiss (ICRP)	50.00	41.68	33.37	25.05	16.73	8.42	0.50	1.00	5.8302
Tiss (ICRU)	50.00	41.68	33.37	25.05	16.73	8.42	0.50	1.00	5.8196
Skin (ICRP)	50.00	41.68	33.37	25.05	16.73	8.42	0.50	1.00	5.7913

As mentioned earlier, the mean free path of arsenic in skin is ~2.8 mm – this is the depth investigated here. For this depth, the influence of additional source energies closer to the K-edge of arsenic does not make a large contribution to the weighted average Kα:Kβ ratio over the energies chosen. It can be seen that changes in the intensity of the lower energies do not greatly influence the As Kα:Kβ ratio. For the depth of interest, the attenuation of the lower energies is preferentially stronger than that of the higher bremsstrahlung energies. Thus, the influence of higher intensities (lower energies) is more strongly reduced than that of the higher ones. A limitation of the chosen bremsstrahlung model is that the peak is assumed with a sudden jump in intensity (vertical line) as shown in figure 6.3.

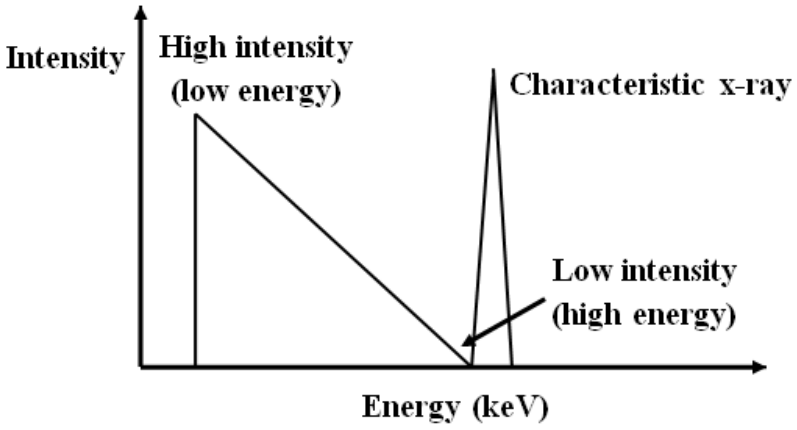

Figure 6.3: Model used to estimate bremsstrahlung continuum.

A positive slope may be leading up to the bremsstrahlung peak and is not accounted for here. This leading section of the hump may more strongly influence the ratio because it would be closer to the As K-edge. This is a limitation of the model chosen and a more detailed model of the bremsstrahlung contribution may be explored in future work. A similar range of ratios is noted, regardless of the incident energy model or the tissue model chosen – ~5.80 – 5.95. These differ by ~2.5%. With the above limitations in mind, such a ratio is expected experimentally. The comparison to experimentally obtained ratios is discussed in the third and fifth sections in this chapter. This ratio was referred to in discussions in chapter 3, but the estimated ratio to be expected with this model is 5.8-5.9.

6.6 Calibration line intercepts observed with SDD:

Calibration line intercepts with the SDD were >2σ away from 0. These are significantly different from zero at the 95% confidence level. By comparison, all intercepts with the Si(Li) detector were within 2σ of zero. Filtration of the source output was performed to investigate the origin on this. The results were found to have minimal impact on the peak areas as seen from figure 6.4.

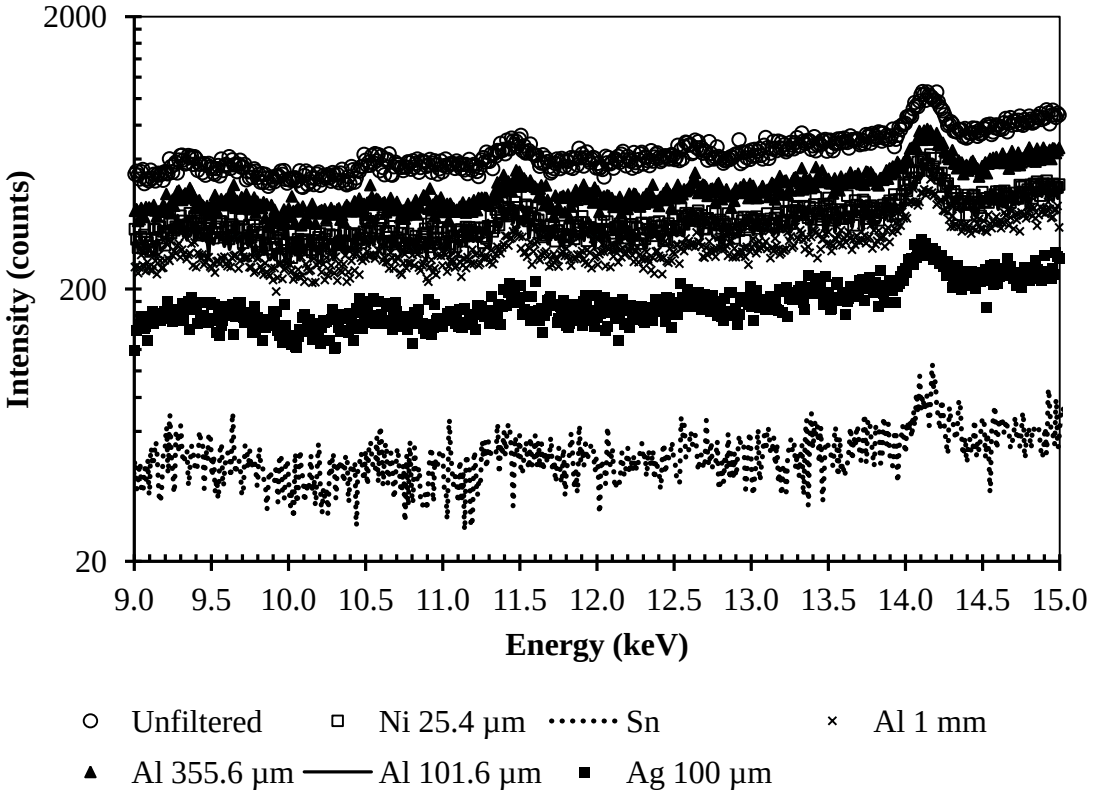

Figure 6.4: Comparison of filtered and unfiltered spectra with 0 ppm As phantom. Filters were placed at the focal spot of (30.0±0.2) cm away from the x-ray tube.

Other sources of fluorescence scatter must be examined. The lab jacks on which the phantom and detector were placed are an alloy of aluminum and unlikely to fluoresce lead, which has an L line overlapping with the As Kα energy. The As 0 ppm phantom was checked using NAA for its concentration and was found to have 0.04 ppm As. This is one order of magnitude lower than the detection capabilities of the SDD. The possibility of a Si (1.74 keV) escape peak can be ruled out since a sufficiently strong feature is not observed at ~12.3 keV for the As Kα energy at 10.53 keV. The same nylon backing was used with the Si(Li) detector. Thus, the source of the contamination is likely to be the head of the SDD – either trace levels of lead or arsenic are originating in the electronic components, wires or interior housing of the SDD. For the backing alone, it is possible that the mere gain of FWHM with the SDD is strong enough to pick up trace levels of Pb or As in it. The comparatively poorer resolution of the Si(Li) detector is why it would not have been detected with that detector type, or with the conventional benchtop system. These possible sources can be addressed with long runs. Repeating the filtration experiment, with an alternate filter holder, will confirm whether some of this contribution is present in the filter material itself or the filter holder. High density polyethylene was used as the sample holder in the *ex vivo* section (4.6) and this showed the presence of a small peak at the As Kα or Pb Lα energy as well. If the source is in the backing material used to calibrate the system for *in vivo* use, then an alternate plastic material may be warranted for use as the backing to mimic bulk tissue behind skin. A check of the level of interference can be performed by preparing a low concentration resin phantom – eg. ~1 ppm – and comparing the bare nylon spectra qualitatively and quantitatively to the spectrum with this phantom in front of it. If the source of this is the SDD itself, then this interference can be expected to appear *in vivo* as well. In this case, an external collimator may resolve the problem provided it is concentrated at the outer boundary of the detector head. If subject concentrations are higher than this level of interference, then this is not likely to be a concern. However, if they are smaller, then zero ppm phantom results may need to be subtracted from *in vivo* peak areas before determining concentration or MDL.

Finally, it should be noted that the amplitude of the observed Sr Kα peak is nearly unchanged in filtered and unfiltered spectra. It is likely that the Sr is originating after the filter. Thus, the Sr signal is likely originating in the nylon backing. It was not seen in other detection systems since the incident energies were lower and the Sr peaks were consumed by the Compton scatter tailing.

6.7 Comparison of system performance:

An inter-comparison of all the detection systems used, including this one, is shown in table 6.2.

Table 6.2: Comparison of performance of various detection systems used in current work, using FOM calculated using (a) localized effective dose and (b) whole body effective dose. Note that the Innov-X Delta unit does not have dosimetry readings without backing and so it is omitted because the FOM cannot be calculated.

System	MDL (ppm[1])	H (mSv)	E (μSv)	FOM
Conventional[2]	0.611 ± 0.001	19 ± 3	0.138 ± 0.040	0.227 ± 0.033
Alpha (wb[3])	1.649 ± 0.002	9 ± 2	0.006 ± 0.002	0.132 ± 0.016
Alpha (wout b[4])	0.903 ± 0.001	17 ± 4	0.011 ± 0.003	0.096 ± 0.013
Delta (wb[5])	0.468 ± 0.005	13 ± 3	0.007 ± 0.002	0.039 ± 0.005
Optical - Si(Li)[6]	0.696 ± 0.002	8 ± 2	0.003 ± 0.001	0.036 ± 0.004
Optical - SDD[6]	0.441 ± 0.003	12 ± 2	0.004 ± 0.001	0.028 ± 0.003

(a)

System	MDL (ppm[1])	H (mSv)	E (μSv)	FOM
Conventional[2]	0.611 ± 0.001	19 ± 3	163 ± 47	7.8 ± 1.1
Alpha (wb[3])	1.649 ± 0.002	9 ± 2	94 ± 22	15.9 ± 1.9
Alpha (wout b[4])	0.903 ± 0.001	17 ± 4	166 ± 44	11.6 ± 1.5
Delta (wb[5])	0.468 ± 0.005	13 ± 3	132 ± 35	5.4 ± 0.7
Optical - Si(Li)[6]	0.696 ± 0.002	8 ± 2	76 ± 15	6.0 ± 0.6
Optical - SDD[6]	0.441 ± 0.003	12 ± 2	117 ± 22	4.8 ± 0.5

[1] ppm = μg As/g dry weight, [2] in RMF arrangement normalized to Compton scatter, [3,4] with, without backing normalized to gross continuum, [5] with backing, beam 2, normalized to gross continuum, [6] normalized to Compton scatter

(b)

MDLs normalized to the x-ray tube anode's continuum feature were shown for the two handheld units. It was found that MDL and dosimetry differences are observed without the backing. Also, the efficiency of the normalization remains to be optimized but direct detection limits would correspond to varying levels of sensitivity and, therefore, it is hard to make a fair comparison across detection systems. It must be noted that the MDL performance of the Innov-X Alpha 4000S was found here to be lower without normalization or backing. In order to make a fair comparison for the purposes of this thesis, only normalized MDLs, collected with backing, are comparable from those listed in this table. Based on the FOM from table 4.2a, the system ranks are 6, 5, 4, 3, 2, 1 from

the first row of the table to the last row; based on table 4.2b, the corresponding ranks are 4, 6, 5, 2, 3, 1.

The highest whole body effective or equivalent (skin) dose is delivered by the conventional benchtop x-ray fluorescence system followed by the handheld Innov-X Delta unit. The lowest doses are delivered by the Innov-X Alpha 4000S handheld analyzer. Based simply on FOM or MDL, the optical focusing system returns the best performance. The x-ray beam size is largest with the conventional benchtop system. When quantifying arsenic in a subject's palm, it is best to interrogate over the largest possible surface area since that would be more representative of the intended *in vivo* measurement site. None of the other systems are able to offer such a beam irradiation area. The optical focusing system is superior despite a higher incident energy (~22.2 keV) than the conventional benchtop system (~17.5 keV), which reduces the arsenic (10.5 keV) photoelectric cross section. Also, on the optical system itself, the choice of SDD produces a lower MDL over the thicker Si(Li) detector. However, the SDD's superior FWHM and throughput capabilities and smaller footprint allow it to be placed closer to the phantom, than the Si(Li) detector, with the conventional system. Additionally, the SDD's system dead time is considerably lower and so, for a fixed real time (1800 seconds), the system live time is higher with this detector type.

By definition, the FOM is sensitive to varying levels of dose. The dose delivered is important and the range of dose readings reflects differences in systems' shielding, source output and acquisition times. The last two factors are affected by normalization, however shielding specific differences produce varying levels of dose from system to system. As mentioned in earlier chapters, in the dosimetry calculations, the shielding-specific differences are assumed to be built into the linear correction required in acquisition time. Non-linearity in this factor may result due to the secondary excitation source represented by the scatter from the shielding and this would affect the dose delivered. All localized or whole body effective doses (table 4.2a) are much lower than the ICRP limit. These may be more suitable for evaluation against ICRP limits since a subject's whole body will not be exposed to x-rays *in vivo*. With this in mind, a higher emphasis may be placed on detection limit than on dose delivered.

Populations exposed to arsenic have been have been reported to produce skin-scale concentrations of ~0.3-24 μg/g dry-weight (Das et al., 1995; Karim, 2000; Samanta, Sharma, Roychowdhury, & Chakraborti, 2004). The difference in the performance of the three approaches is not one full order of magnitude. This is important since all systems have reported phantom-based MDLs that are suitable for use with an exposed population. The systems are not likely to be sensitive enough to detect levels of arsenic in members of the general population in countries with low arsenic exposure. There are limitations to phantom-based MDLs. The calculations in this thesis are based on phantom-based calibration of each system. Improvements in MDL reported here, though small, are of use for the *in vivo* case. Unlike in phantoms, the distribution of arsenic in skin is not expected to be uniform. A correction factor must be incorporated in order to account for the skin's

inherent non-uniform distribution of arsenic. Under the assumption that keratinocytes increase in number moving up towards the surface of skin, previously published work used two models for the arsenic concentration: a) linearly decreasing from the surface and b) exponentially decreasing to 0.1 % from the surface. This was accomplished through the use of custom Monte Carlo simulations of arsenic in skin, using these models. Using each model, correction factors were then determined for phantom-based MDLs, based on the thickness of skin being interrogated (Studinski et al., 2005). The use of such models requires mention of depth-dependent detection limits, where the superficial depths are primarily being probed. This is consistent with knowledge that keratinocytes motion towards the surface of skin, where they die and form corneocytes. These are responsible for the barrier functions of skin. Thus, depth-corrected detection limits would be superficial detection limits comparable to skin-scale concentrations found in the literature from ex vivo studies. As per the above work performed previously, phantom-based MDLs would need to be scaled up depending on the thickness of the skin being measured and the model chosen. The work performed here towards improving MDLs is thus valuable, since the scaled up MDLs would indicate worse system performance.

Chapter 7 Ex vivo mapping of skin samples using μXRF:

7.1 Introduction to Article I

Article I describes the characterization of three elements in skin using micro-XRF (μXRF). The article describes the 2D surface mapping of skin samples acquired through a punch biopsy from cadavers donated to the Anatomy department at McMaster. Peak-fitting modeling and analysis, using MATLAB, and surface mapping, using IDL, were performed by the author of this thesis. Partial assistance in batch processing in MATLAB was kindly offered by Yicheng Liang. Statistical analysis of the IDL maps was provided by Dr. Alia-Al Ebraheem. Through consultation with Dr. Michael Farquharson, using cross-section data available through NIST XCOM, the results of the statistics were presented in layman's terms. Matching histology images and XRF maps was performed through extensive discussion with Dr. Bruce Wainman.

Incorrect amounts of micronutrients, in even very small concentrations, can be extremely detrimental to the body. Non-invasive assessment of micronutrient levels is crucial to understanding their accumulation in the human body. New in vivo techniques based on x-ray fluorescence (XRF) have been introduced to assess iron levels in skin. The technique has also been applied to other biometals and trace elements, including arsenic. Interpretation of ongoing research is complicated as these elements' depth distributions in skin are unknown. This work was intended to fill this gap in our understanding. With properly prepared samples of human skin, it would be possible to measure even very low concentrations of arsenic using a synchrotron radiation source. The samples were sectioned, along their depth starting at the skin surface and running straight down. Thus, a surface map of a sample would allow for a scan along the depth of skin starting at the skin surface and running straight down. Depth distributions could thus be obtained.

The first three scans were performed using an incident energy of 13 keV so as to excite arsenic, which has a K-edge just below 12 keV. These scans were performed for 20 second dwell times, per pixel, but did not reveal detectable levels of arsenic in the mounted skin samples. Samples were obtained from members of the general population and, thus, nominal levels of arsenic would be expected. Since occupational exposure is not present, detecting such levels was expected to be challenging with in vivo XRF but the higher signal intensity of a synchrotron may have presented at better possibility for this. The inability to detect such levels, using synchrotron μXRF, is motivation for the current overall research project (benchtop *in vivo* XRF) to specifically target individuals with known exposure to arsenic.

Nonetheless, while arsenic was not observed, it was still possible to perform scans of the samples for other elements at a beam energy of 12 keV and iron-targeted scans at a beam energy of 8 keV. Since cadavers were collected from Southern Ontario, Canada, the

WHO water limit may represent an estimate of the upper limit on the arsenic concentration in skin - ~ 0.01 ppm. For the thickest skin sample studied, sub-layers of the epidermis could be resolved on the raster scans and the corneum (outermost layer) showed opposing levels of calcium and zinc. Meanwhile, iron was consistently noted at the epidermal/dermal boundary, in agreement with studies in the literature. Statistically significant differences ($p<0.01$) in calcium and zinc levels were found between the epidermis and dermis. Further, we noted clear variations in the distributions, between samples extracted from the same cadaver. This shows the need for a depth distribution when interpreting results from *in vivo* quantification of trace elements in skin.

The sample preparation was performed by the author of this manuscript, in collaboration with Ibrahim Abu Atiya. Full sectioning of prepared samples and Hematoxylin and eosin (H&E) stained image slides – application of hemalum to stain cell nuclei blue followed by a counterstain to add a red/pink coloring to protein-composed structures - were performed by Mary Jo-Smith and Mary Bruni from the histology lab in the Department of Pathology and Molecular Medicine at McMaster University. A step-by-step protocol was prepared by the author of this thesis through email exchanges with the technicians in the histology lab. The manuscript was prepared by the author of this thesis and edited by Drs. Fiona McNeill, Michael Farquharson, David Fleming, Alia Al Ebraheem and also by Ibrahim Abu Atiya. The articles are not presented here in their order of publication as the emphasis of this thesis is on a comparison of XRF detection systems and, thus, this chapter presents a self-contained sub-project within the overall research project. This sub-project continues to be developed by Drs. Michael Farquharson, Bruce Wainman, David Fleming and Fiona McNeill, but is beyond the scope of work of the author of this thesis.

7.2 Contents of Article I

Reprinted from Applied Radiation and Isotopes, 77/July 2013, Elstan D. Desouza, Ibrahim Abu Atiya, Alia Al-Ebraheem, Bruce Wainman, David E. B. Fleming, Fiona E. McNeill, Michael J. Farquharson, Characterization of the depth distribution of Ca, Fe and Zn in skin samples, using synchrotron micro-x-ray fluorescence (SμXRF) to help quantify *in-vivo* measurements of elements in the skin / *Ex vivo* mapping of skin samples using μXRF, 68-75, Copyright (2013), with permission from Elsevier.

Applied Radiation and Isotopes 77 (2013) 68–75

Contents lists available at SciVerse ScienceDirect

Applied Radiation and Isotopes

journal homepage: www.elsevier.com/locate/apradiso

Characterization of the depth distribution of Ca, Fe and Zn in skin samples, using synchrotron micro-x-ray fluorescence (SμXRF) to help quantify *in-vivo* measurements of elements in the skin

Elstan D. Desouza [a,*], Ibrahim Abu Atiya [a], Alia Al-Ebraheem [a], Bruce C. Wainman [b], David E.B. Fleming [c], Fiona E. McNeill [a], Michael J. Farquharson [a]

[a] Department of Medical Physics and Applied Radiation Sciences, McMaster University, Canada
[b] Department of Pathology and Molecular Medicine, McMaster University, Canada
[c] Department of Physics, Mount Allison University, Canada

HIGHLIGHTS

- Micro x-ray fluorescence was performed on sectioned necropsy skin samples.
- Samples were extracted from members of the general population—various sites on body.
- Significant difference in trace element levels noted between epidermis and dermis.
- In thick skin sample, technique can differentiate levels in epidermal sub-layers.
- Decreasing trend of calcium, iron and zinc (in that order) is found to dominate.

ARTICLE INFO

Article history:
Received 22 October 2012
Received in revised form
20 February 2013
Accepted 21 February 2013
Available online 1 March 2013

Keywords:
Necropsy
Micro x-ray fluorescence
Depth-profile
Epidermis
Dermis

ABSTRACT

In vivo monitoring of trace and biometals in skin is normally quantified using phantoms that assume a constant elemental distribution within the skin. Layered calibration skin phantoms could potentially improve the reliability of *in vivo* calibration skin phantoms by better representing the actual *in vivo* distribution. This work investigates the micro-distribution of iron, calcium and zinc in prepared human skin samples taken from a number of locations on the body. Slices (orientation running from the skin surface into the dermis) were extracted from 18 formalin-fixed necropsy samples and scanned using the micro-XRF setup at the VESPERS beamline (Canadian Light Source). Elemental surface maps were produced using a $6 \times 6\ \mu m^2$ beam in steps of 10 μm. Microscope images of histology slides were obtained for comparison. Statistically significant differences ($p < 0.01$) were noted between the epidermal and dermal layers of skin for the elements examined (Ca, Fe and Zn), demonstrating the ability to clearly distinguish elemental content in each layer. Iron was consistently noted at the epidermal/dermal boundary. These results would indicate that when using phantoms to quantify elemental levels measured in the skin, note should be taken of the appropriate depth distribution.

© 2013 Elsevier Ltd. All rights reserved.

1. Introduction

The main function of skin is to serve as a barrier against microorganisms while preventing the loss of water. The two primary layers of the skin are the epidermis and dermis. The layers of the epidermis from the surface of skin are the stratum corneum, stratum lucidum, stratum granulosum, stratum spinosum and stratum basale (Forslind and Lindberg, 2004). The stratum corneum is approximately 10–40 μm thick (except the palms and soles) and consists of lipid bilayer of cells and corneocytes (Kertesz et al., 2005). The bulk layer following the stratum corneum, consisting of several sub-layers, is called the viable epidermis and consists of epithelial cells, neural stem cells and immune cells (Hanley et al., 2009). Trace elements are present in skin and the concentrations of some of these elements can be indicative of various diseases. As an example calcium is found in the skin and in the process of wound healing, when the epidermal barrier of skin is not normal, higher amounts of calcium are percutaneously absorbed through the skin (Hostynek et al., 1993). Epidermal calcium is comprised of intracellular organelles, extracellular fluid and intracellular fluid (Berridge et al., 2003),

* Correspondence to: Department of Medical Physics and Applied Radiation Sciences, McMaster University, Tandem Accelerator Building Room 104/D, 1280 Main Street West, Hamilton, Ontario, Canada L8S 4K1.
Tel.: +1 905 525 9140x21757.
E-mail address: desouze@mcmaster.ca (E.D. Desouza).

0969-8043/$ - see front matter © 2013 Elsevier Ltd. All rights reserved.
http://dx.doi.org/10.1016/j.apradiso.2013.02.019

with the former two making the largest contributions of calcium to the epidermal profile (Clapham, 2007). It has been suggested that the epidermal calcium profile is controlled by intracellular calcium because extracellular calcium is diffused into the viable layers of the epidermis (Adams et al., 2012). This intracellular calcium has been referred to as the source of mitosis, terminal cell differentiation and cell apoptosis (Lansdown, 1995). Calcium is not very well defined in the dermis (Kulesz-Martin et al., 1984).

Zinc is an element that skin depends on to perform its normal functions (Nelder, 1991). Zinc is present in all organs, tissues and fluids of the body with 20% located in the skin and appendages (Reeve et al., 1999), of which 6% is located in the skin alone (King et al., 2000). Zinc has been found to play a role as an antioxidant in protecting the skin (Rostan et al., 2002) and, in cultured skin fibroblasts exposed to UV A and UV B, it offers protection against cytotoxicity and lipid peroxidation (Leccia et al., 1999; Richard et al., 1993). Zinc proteins control cellular behavior and, together with zinc dependant enzymes, begin the transcription process of genes in the stratum basale layer of the epidermis (Tseng and Green, 1992). Zinc deficiencies directly impact skin health and can be due to dietary insufficiencies or genetic inability of the skin to absorb zinc (Wintergerst et al., 2006). The literature has examples of studies looking into the depth distribution of zinc in skin using various techniques. Neutron-activation analysis (NAA) has been used to estimate zinc levels in the dermis of healthy skin and showed that the epidermis contained a higher level of zinc than the dermis (Molokhia and Portnoy, 1969). A comparative study between normal and atopic skin types revealed that zinc content was highest in the stratum spinosum of normal skin, but it doubled in dry atopic skin, with the highest levels being found in the stratum corneum and stratum granulosum for this skin condition (Forslind, 2000).

In patients who suffer from iron overload as a result of thalassemia or hemochromatosis, iron can build up and is stored in the skin (Gorodetsky et al., 1990). In a study of trace elements relative to the various strata of the epidermis in normal skin, it has been found that iron is at the highest level in the stratum granulosum and decreases in content toward the surface of the skin (Boyce and Ham, 1983; Hennings et al., 1983). Elemental distributions in psoriatic skin revealed remarkably higher levels of iron in both quantity and distribution (Werner-Linde et al., 1998). Further comparative studies of trace elemental distributions in normal, psoriatic and dry atopic skin found that iron peaks in the stratum basale of the epidermis and decreases as it reaches the surface of the stratum corneum, in normal skin (Forslind et al., 1999).

One technique available for use in depth (line or area) mapping-based applications is synchrotron micro x-ray fluorescence (SμXRF). Radiation sources that can be used for XRF include radioactive isotopes, x-ray tubes or particle accelerators such as a synchrotron. There are numerous advantages of using synchrotron XRF: (a) reduced background, (b) superior spatial resolution, on the order of micrometers compared to conventional x-ray tube sources, is a consequence of excellent beam focusing, (c) good energy tunability, and (d) an intensity that is many orders of magnitude higher than that achievable with x-ray tubes. A combination of these advantages allows for a raster scan over a sample to be performed with micron spatial resolution in a short period of time. Elemental distributions across a set of specific locations on the surface of a sample, such as a depth-profile, can be obtained in this way (Grolimund et al., 2004; Mino et al., 2010). Techniques complementing μXRF depend on the sample type and include electron microprobe (Mcgee and Keil, 2001), micro-proton induced x-ray emission (micro-PIXE) (Karydas et al., 2007) and inductively coupled plasma mass spectrometry (Duval et al., 2011; Leng et al., 2011).

When applying XRF to *in vivo* studies of elemental content in skin, a challenge is that the thickness of the skin varies between individuals being monitored, and also between sites on the body. This could result in a variation in the skin volume for the element that is being probed and produce a range in the total fluorescence signal of that element, even if the underlying concentration of the element in the skin is the same. An effective means of accounting for this variation in skin thickness is thus of importance since the absence of such a correction factor could lead to calculation of bulk elemental concentrations based on an incorrect assumption of volume of skin being probed by the incident x-rays and subsequently to an inaccurate estimation of *in vivo* levels in skin. A second factor that needs to be considered is that elements may not be distributed homogenously within the different sub-layers in the skin. The calculation of a heterogeneously distributed *in vivo* signal from a homogenous calibration standard could lead to inaccurate estimates. Obviously, both the energy, and penetration depth of the incident x-ray beam, need to be considered, as well as the attenuation as a function of depth in skin of the resulting fluorescence signal as the detected signal is strongly dependent on these factors. As an example, when considering the measurement of iron, the mean free path of the resulting Kα x-rays is only approximately 0.5 mm in skin. For this reason the depth profile of the elements must be known for a given region of the body in order to develop and use appropriate calibration phantoms for quantification of concentration in terms of elemental mass per mass of tissue, in particular when fluorescence attenuation is comparable to skin thickness.

This study seeks to characterize trace element (calcium, iron and zinc) distributions in skin, from the epidermis and through the dermis, in necropsy skin samples obtained from various sites on the body. In the current work, the emphasis is on investigating the relative elemental distribution within skin, as opposed to quantifying concentration levels, in prepared skin samples. Furthermore, it also addresses the variation in this depth distribution for different skin locations on the body, providing a set of baseline results against which future work can be compared.

2. Method

2.1. Experimental procedure

Necropsy skin samples were extracted from cadavers donated for scientific research to the McMaster University Anatomy Department, after obtaining ethics approval. Samples were extracted from the cadavers using a Miltex circular biopsy punch that was 8 mm in diameter. Each extracted core was cylindrical in shape and 5 mm deep with its orientation perpendicular to the surface of the skin. This core was immediately frozen upon extraction. Before the samples were prepared for mounting, the section of fatty tissue that was extracted as part of the bulk core was removed. Each block was then placed in 10% neutral buffer formalin (VWR International LLC). After approximately 24 h, the core was removed, sliced into 2 semi-circular cylindrical blocks and then placed back in the formalin for 16–20 h. After this time, it was transferred to a 70% ethanol solution. With the original orientation noted (skin surface and bulk tissue), the sample was fixed in a paraffin block and microtomed into sectioned slices of 10 μm thickness. For each sliced block, one section was obtained and then floated onto ultralene XRF film (4 μm thickness) stretched across a plastic frame. A single glass slide with a hematoxylin and eosin stain (H&E stain) was also obtained for each sample, which is commonly used in histology. The stain changes the color of cell nuclei and protein-containing structures, thereby improving the contrast in a microscope image of the

sample. Samples were obtained from the feet, legs, arms, palms, chest and back. Prepared samples were then transported to the third generation Canadian Light Source (CLS) for analysis at the VESPERS (Very Sensitive Elemental and Structural Probe Employing Radiation from a Synchrotron) beamline (Feng et al., 2007). VESPERS is a hard x-ray microprobe beamline covering the energy range of 6–30 keV with 0.01%, 1.6% and 10% bandpass monochromatic beams, as well as a polychromatic beam. This facility has the capability of scanning samples with a beam of x-rays having a spot size of approximately 2 μm by 2 μm. Considering the high flux and low background requirements, a 1.6% monochromatic beam was chosen for the analysis. The beam had a spot size of 6 μm × 6 μm. This level of spatial resolution allows for detailed mapping of elemental levels in a single skin sample as a function of depth. An online beam microscope, in combination with a laser positioning system, was used for aligning the beam on the surface of the sample. The fluorescence spectrum was recorded with a 50 mm^2 active area single-element Vortex Silicon Drift Detector with a 400 μm thick Si wafer and a 12.5 μm Be entrance window (SII NanoTechnology, California, USA) which was placed 3 cm away from the sample, positioned 45° to the sample and to the incoming x-ray beam within the horizontal plane, in a geometry as shown in Fig. 1.

Raster scans were performed using an incident beam energy of 12 keV for 20–30 s per pixel, for between 400 and 900 pixels per map, in step sizes of 10 μm. This step size was chosen in order to map a region large enough to cover both the epidermis and a portion of the dermis to allow for a clear distinction between these two layers of skin. For the current work, a total of 18 raster scans (1 per sample) were collected. These were comprised of 14 samples with a clear difference between the epidermis and dermis: cadaver 1–left thigh, back; cadaver 2–left thigh; cadaver 3–back, chest, left arm; cadaver 4–left thigh, left palm, back, left arm; cadaver 5–back, chest; and cadaver 6–chest, left thigh. Thus, for these 14 samples, it was possible to define regions of interest (discussed later) and perform statistical analysis. Two of the 14 scans were specifically set up to probe for iron and so the beam energy was set to 8 keV to be as close to the iron absorption edge as possible, thereby maximizing the photoelectric cross section. One of the 14 scans was performed on a sample consisting of very thick skin (palm). In order to probe for other slightly higher energy elements (arsenic and selenium) this sample was scanned with a beam energy of 13 keV. Four of the 18 samples did not reveal a clear difference between the epidermis and dermis; thus these were not used in subsequent statistical analysis: 6–back, chest; 2–chest; and 3–left thigh. Finally, the H&E stained slides were examined under a microscope to examine the morphology of the samples for comparison with the element distribution (surface) maps.

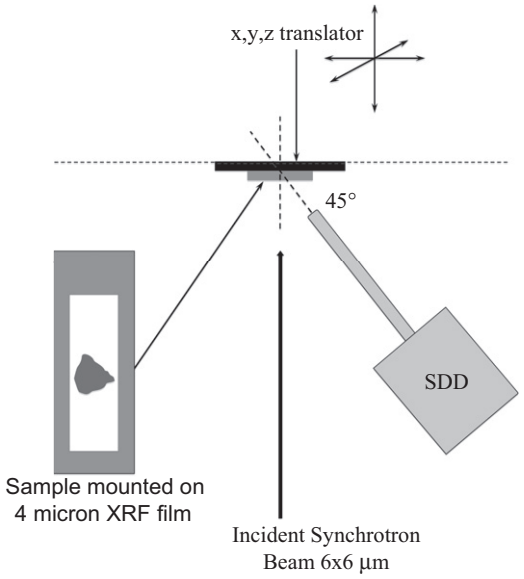

Fig. 1. Experimental setup utilized at the VESPERS microprobe, depicting sample, source and detector arrangement.

2.2. Data analysis

Data analysis consisted of peak fitting each pixel spectra using Mathworks Matrix Laboratory (MATLAB) R2012a with the non-linear least-square fitting routine available through the Curve-Fitting Toolbox (cftool) (Branch et al., 1999). Custom fitting equations consisting of a single or double Gaussian peak on a linear or exponential background were used to fit the Kα peaks corresponding to calcium, iron and zinc, with appropriate bounds set for the Kα peak's position and width. Line overlaps were taken into account, when present. The fitted Kα peak areas were normalized to scatter peaks (compton and coherent scatter contributions) in order to correct for beamline intensity reduction and for variations in detector dead time over the duration of a single scan. Finally, normalized data were then mapped in Exelis Interactive Data Language (IDL) version 6.2, providing a view of the elemental distribution within each sample, extending down from the skin surface, showing the mapped elemental distributions in various layers of skin. 1D line profiles (rectangular regions covering 3 pixels in the vertical direction and horizontally encompassing the entire length of a surface map) were extracted from the 2D maps in order to provide a 1D depth profile corresponding to the 2D surface map. These profiles are analogous to horizontal line scans–each horizontal line had a height of 3 pixels and a width that started from the left of the 2D map extending until the right end of it.

3. Results and discussion

3.1. Spectrum, surface maps, microscope (histology) images and 1D depth-profiles

The spectrum corresponding to one of the samples collected from the back (beam energy of 12 keV) is shown in Fig. 2. Eleven of the 14 samples were scanned at this incident energy. The SDD's resolution plays an important role in both the iron peak being resolved very well and the overlap of the incoherent and coherent scatter peaks. Energies beyond ~9.0 keV, if present, would lie under the incoherently scattered peak and thus are not observed.

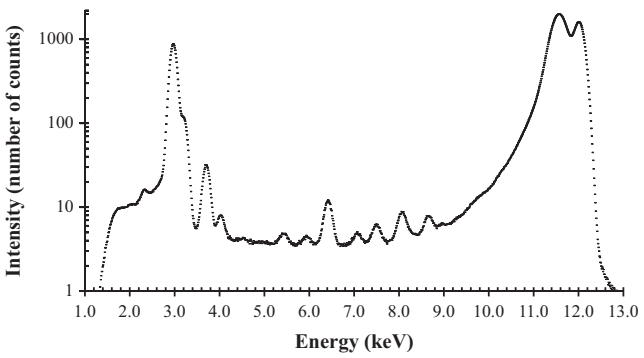

Fig. 2. Spectrum corresponding to sample collected from back (sample 3B), collected at the pre-dominantly used beam energy of 12 keV. The strong calcium peak and excellent separation of the iron Kα are noted.

This was also observed for a beam energy of 13 keV, indicating the absence of elements such as arsenic and selenium from the samples. The choice of 12 keV was made in order to maximize the counts under the zinc peak. By way of example, the H&E stained image, as viewed under a microscope, along with the corresponding 2D surface map for calcium is shown for two samples in Fig. 3. In each of these figures, highly detailed tissue-morphology can be visualized from the microscope images that show the structure of the epidermis–stratum corneum, stratum granulosum, stratum spinosum, basal layer of the epidermis and the dermis. The stratified squamous epithelium that is the epidermis is clearly visible in the microscope images, though the base membrane on which it sits is hard to see with an H&E stain. The variation in thickness of the bulk epidermis and its sub-layers, from site to site, is clearly visible in the microscope images. Fig. 4 shows the line profile as a function of depth for these two samples, for calcium. From both 1D and 2D maps, it can be seen that the sub-layers of the epidermis cannot be clearly distinguished from each other. It is thus not possible to identify which sub-layer contains the largest stores of zinc, iron and calcium. The patterns of elemental micro-distribution can nonetheless be discussed in the two bulk skin layers relative to the epidermal and dermal boundaries, by examining the 2D surface maps and the 1D plots. One observation is that iron is concentrated in a narrow range of depths located at the epidermal–dermal junction. All three elements are observed up until this boundary. Zinc and calcium are observed in the entire epidermal region. Iron was consistently observed deeper in the epidermis, relative to these two elements, in agreement with previous work as cited earlier. Variations in elemental levels were noted across different bodies and sites. Although literature has indicated opposing levels of calcium and zinc – high calcium and low zinc – in the outermost layer of the epidermis (Forslind, 2000; Forslind et al., 1997; Wickett and Visscher, 2006), such a sub-epidermal distribution cannot be established from the 2D surface maps. Previous work found stronger calcium content in the top and bottom most sub-layers of the epidermis, with a dip in level in the central layer. Within uncertainties, the presence of such a dip cannot be established from the 1D depth profiles, which prevents this elemental micro-distribution from being seen across the epidermis in most cases, the exception being where the epidermis is thickest in the palm (discussed later) and foot.

3.2. Statistical analysis

In order to establish whether the technique can clearly identify the presence of all three elements in the epidermis and dermis, regions of interest (ROIs) were defined for each map, with one defined in the epidermis (L1) and the other in the dermis (L2), for 14 of the 18 samples that were scanned. These regions were defined to include either the epidermis or the dermis individually, without selecting regions that included overlap of those two layers. Of the remaining four samples, either the raster scans were interrupted due to lack of a clear distribution in elemental levels across all three elemental maps or the completed set of maps did not show such a distribution for two of the three elements investigated. Thus ROIs could not be defined for the 2D maps created for these four samples. The results of statistical tests (such as Wilcoxon Signed Ranks test) performed on the two regions of interest – L1 and L2 – are shown in Table 1. These results revealed that calcium, iron and zinc levels in the epidermis were significantly different ($p < 0.01$) than their corresponding levels in the dermis with the percentage differences ranging from 0.06% to 297.18% (mean of 101.96%). In one of the 14 samples, the epidermal sub-layers were visible in the 2D maps and so this is treated separately later, with four ROIs instead of two. For the remaining 13 samples, calcium levels were found to be different between the dermis and epidermis at the $p < 0.01$ level of significance. The calcium percentage difference ranged from 73.18% to 297.18% with a mean difference ($\pm$ standard

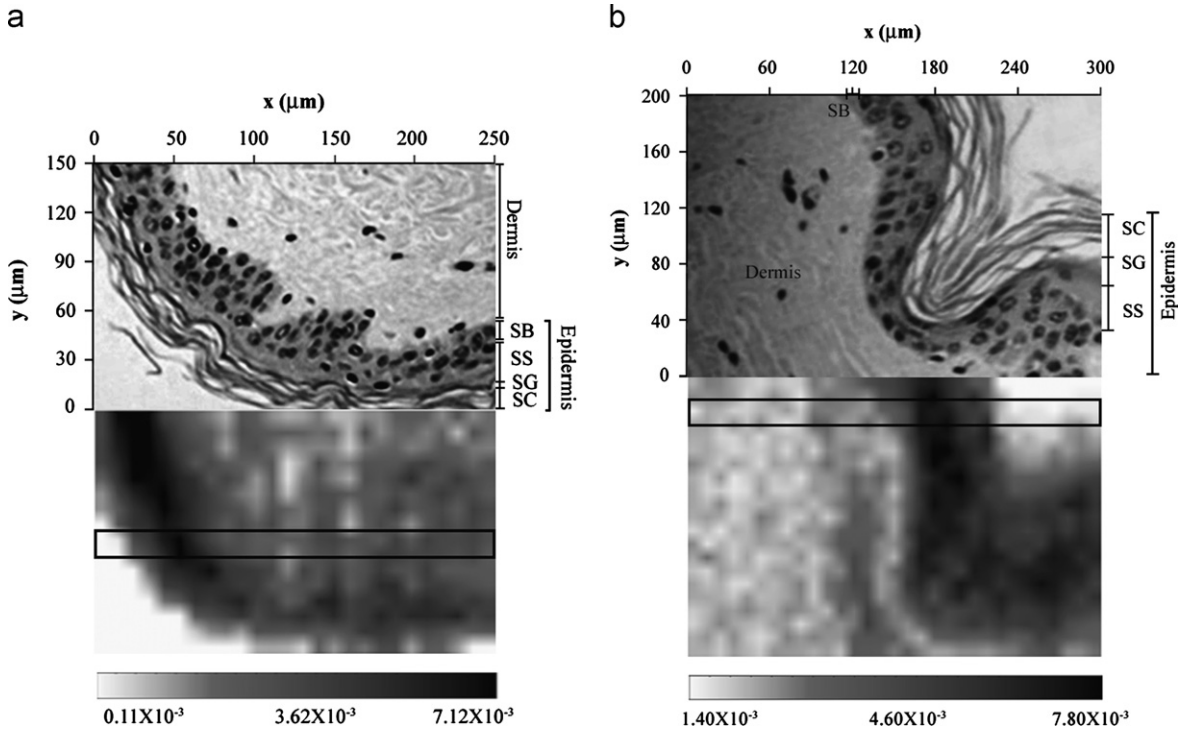

Fig. 3. Grayscale surface maps for calcium from two samples obtained from the left arm and left thigh respectively from the same body and the corresponding microscope image of H&E staining, in area where scan was performed. Horizontally oriented box (3 pixels in height) indicates region of 2D map over which associated depth profile was produced.

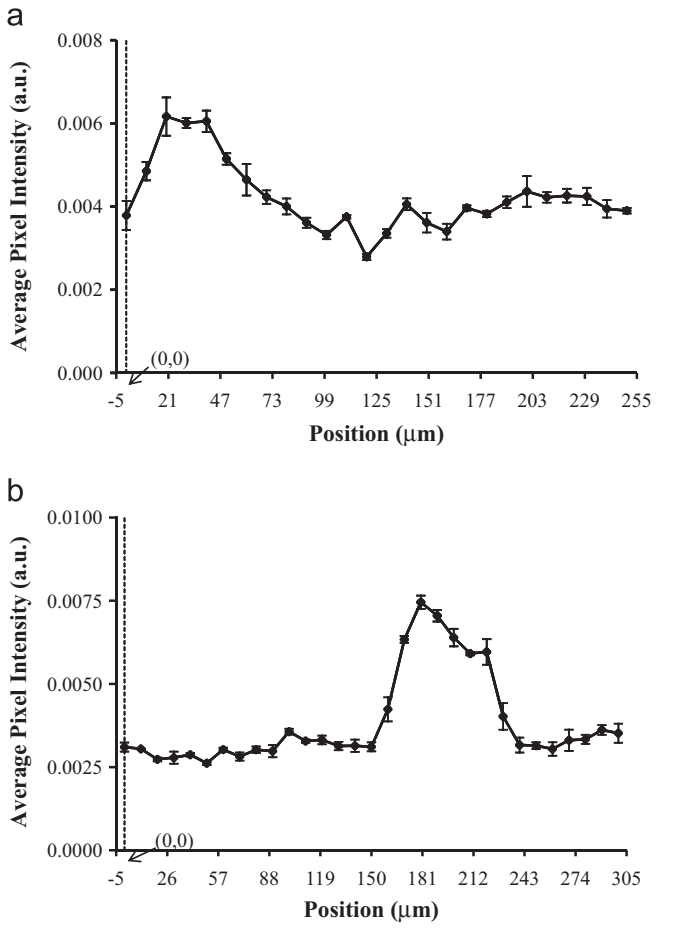

Fig. 4. Depth profile for samples obtained from (a) the left arm and (b) the left thigh respectively from the same body. Error bars in the 1D depth profiles correspond to mean ± SDOM, where SDOM = StdDev/$n^{1/2}$ and n is the number of points over which the mean was calculated.

Table 1
Results showing percentage differences between epidermis (L1) and dermis (L2) in 13 of the 14 samples.

Body #	Site on body	Element name	Difference between L1 and L2 (%)	*p* Value
1	Left Thigh	Ca	93.74	< 0.01
		Fe	2.22	0.504
		Zn	268.56	< 0.01
1	Back	Ca	91.63	< 0.01
		Fe	44.72	< 0.01
		Zn	250.36	< 0.01
4	Left Thigh	Ca	297.18	< 0.01
		Fe	37.89	< 0.01
		Zn	84.86	< 0.01
2	Left Thigh	Ca	249.14	< 0.01
		Fe	51.93	< 0.01
		Zn	166.02	< 0.01
3	Back	Ca	86.66	< 0.01
		Fe	44.24	< 0.01
		Zn	83.78	< 0.01
3	Chest	Ca	178.43	< 0.01
		Fe	7.36	< 0.01
		Zn	76.31	< 0.01
3	Left Arm	Ca	109.07	< 0.01
		Fe	13.06	< 0.01
		Zn	33.00	< 0.01
4	Back	Ca	116.96	< 0.01
		Fe	97.91	< 0.01
		Zn	141.14	< 0.01
4	Left Arm	Ca	214.91	< 0.01
		Fe	113.26	< 0.01
		Zn	60.04	< 0.01
5	Back	Ca	91.17	< 0.01
		Fe	93.80	< 0.01
		Ca	129.02	< 0.01
5	Chest	Fe	25.61	< 0.01
		Zn	75.62	< 0.01
6	Chest	Ca	90.32	< 0.01
		Fe	0.06	0.994
		Ca	73.18	< 0.01
6	Left Thigh	Fe	37.21	< 0.01
		Zn	142.08	< 0.01

The *t*-test or Wilcoxon Signed Ranks test was used to calculate the corresponding *p*-value and determine if this difference was significant. Note that the 14th sample is a special case where four regions were visible and so it is treated separately later.

deviation) of 140.11 ± 71.85%. Iron levels were found to be different between the dermis and epidermis at the $p < 0.01$ level of significance for 11 out of 13 samples. For all 13 samples, the iron percentage difference ranged from 0.06 to 113.26% with a mean difference (± standard deviation) of 43.79 ± 37.24%. Zinc levels were found to be different between the dermis and epidermis at the $p < 0.01$ level of significance for all 13 samples. The zinc percentage difference ranged from 32.99% to 268.56% with a mean difference (± standard deviation) of 125.62 ± 77.04%.

3.3. Results of scan on thick skin sample

In an attempt to examine the epidermal sub-layers, the scan performed on the thickest skin sample (palm) is considered. As expected, the calcium level in the outermost part of the epidermis is very high, while the zinc content here is much lower. This comparison was not possible in the thinner samples. Due to the enhanced morphology seen in the histology image, for this sample, and a clear variation in pixel intensities in the 2D surface maps, four ROIs were chosen for this sample based on the elemental 2D maps. The 2D distribution maps for the three elements are shown in Fig. 5 as well as the H&E stained image. The depth profiles for the three elements are shown in Fig. 6. The exact shape of the epidermal/dermal junction and dermal sub-structures such as collagen bundles or fibroblasts are not visible in the 2D surface maps. It is evident that calcium is present in the outermost layer of ROI1 – the stratum corneum – and in ROI3. In the case of this sample, ROI3 is believed to be a combination of the stratum spinosum, stratum granulosum, stratum lucidum (only noted in thick skin) and the stratum basale. Although a second ROI is defined within the stratum corneum, this region is devoid of calcium. While a small amount of zinc is found in ROI1, a much higher level is noted deeper in ROI3 (the hybrid epidermal sub-layer) in agreement with literature. From the 1D depth profile, it can be seen that the epidermis is estimated to be approximately 500 μm thick for this sample, which is comparable to the literature (International Commission on Radiological Protection, 1975). ROI4 is the dermis and, as found in other samples, stores the highest level of iron at its boundary with the stratum basale layer of the epidermis.

The results of statistical analysis to test the significance of the differences in the levels of elements within these regions are shown in Table 2. First, an evaluation of normality was performed using the Shapiro–Wilk test. All layers, except layer 1 for calcium and zinc, were found to be normally distributed. Accordingly for Fe, ANOVA was used to compare the mean of all four ROIs and the difference was found to be significant ($p < 0.01$). For the Ca and Zn layers, the Friedman test was used for the same comparison and a significant difference was also found here ($p < 0.01$). Finally post-hoc analysis was performed using pairwise comparisons in order

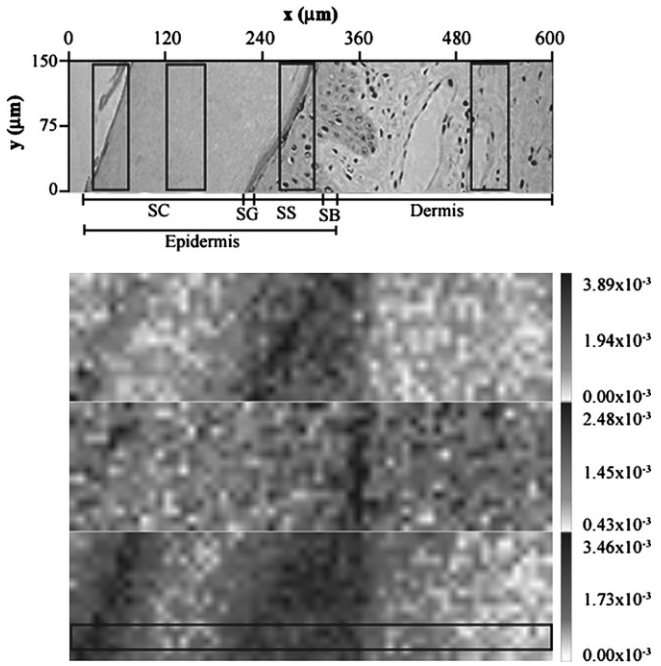

Fig. 5. Hematoxylin and eosin (H&E) stained image (upper) and 2D grayscale distribution maps (lower) for Zn (top), Fe (middle) and Ca (bottom) from a sample acquired from the left palm. Darker regions correspond to more intense levels of each element. Regions 1–4 are shown as vertical boxes in microscope image; regions are chosen using 2D maps. Horizontally oriented box (3 pixels in height) indicates region of 2D map over which associated depth profile was produced.

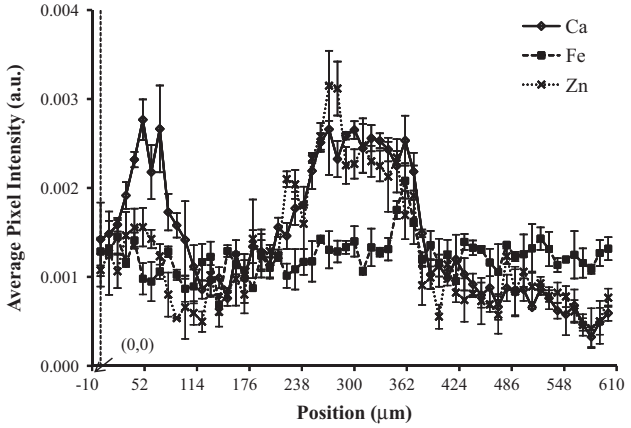

Fig. 6. 1D depth profile maps for Zn, Fe and Ca from a sample acquired from the left palm.

to test the difference between each pair of ROI means (e.g. means of ROIs 1 and 2, means of ROIs 1 and 3, etc.). This was done assuming unequal variances with Tamhane's T2 test. The *p*-values listed in Table 2(a) are produced by this test. For nearly all the comparisons, spanning all three elements, the difference between ROIs is significant, with the mean percentage difference being 43.52% and the lowest percentage difference being observed in the case of zinc, between the inner part of the stratum corneum (ROI2) and the dermis (ROI4). The highest percentage difference, over all three elements, is consistently noted for ROI3.

A more in-depth discussion of the results can be made from a biological point of view. Higher levels of iron were observed in the stratum basale of the sample, with the other epidermal layers not showing iron content as has been observed previously (Forslind et al., 1999). Skin iron arises from diet however iron absorption is highly variable depending on iron requirements and complex

Table 2
(a) Summary of statistics performed on various ROIs, indicating the level at which a significant difference was noted between mean pixel intensities in each pair of ROIs and (b) the corresponding percentage difference between the mean ROI values being compared (negative indicates a reduction).

ROI comparison	Ca	Fe	Zn
(a)			
ROI 1–ROI 2	< 0.01	0.25	< 0.01
ROI 1–ROI 3	0.28	< 0.01	< 0.01
ROI 1–ROI 4	< 0.01	0.21	< 0.01
ROI 2–ROI 3	< 0.01	< 0.01	< 0.01
ROI 2–ROI 4	< 0.01	< 0.01	1.00
ROI 3–ROI 4	< 0.01	< 0.01	< 0.01
(b)			
ROI 1–ROI 2	106.23	8.42	89.25
ROI 1–ROI 3	−6.65	−25.45	−37.81
ROI 1–ROI 4	215.26	−7.46	89.57
ROI 2–ROI 3	−54.74	−31.25	−67.14
ROI 2–ROI 4	52.87	−14.65	0.17
ROI 3–ROI 4	237.72	24.14	204.81

Statistical testing procedure explained in the text.

metabolic pathways which lead to skin deposition. Heme iron is easily absorbed by the body. Non-heme iron is not easily absorbed but is bound to transferrin (Tf) in the basolateral membrane (Beard et al., 1996) at the epidermal–dermal junction. Transferrin facilitates the transport of extracellular iron to keratinocytes in skin and the transferrin receptor (TR), located in the stratum basale (Gatter et al., 1983), regulates iron entering the keratinocytes (Milstone et al., 2006). As keratinocytes proliferate, they increase iron content in this layer. They are capable of holding excess iron in ferritin—an intracellular protein also found in the basal cell layer (Torti and Torti, 2002), which regulates iron content by storing and releasing iron to avoid overload or deficiency (Milstone et al., 2006). Thus, the body's metabolism of iron compensates for iron loss, via dietary iron intake that accumulates in ferritin (Andrews, 1999) from proliferation described above and leads to it being confined to the lowermost part of epidermis.

Calcium was found in elevated levels in the lower part of the epidermis, with almost none in the stratum corneum, as also seen by others (Forslind, 2000; Forslind et al., 1999). In terms of uptake, calcium is absorbed across the enterocyte brush border in the duodenem with a small amount entering the body percutaneously. Vitamin-D dependent calcium binding proteins (CaBP) along with a specific human brush border calcium-ion channel, identified as TRPV6 (Balesaria et al., 2009), are responsible for regulating intestinal calcium (Kamao et al., 2000; Wasserman et al., 1992). Absorbed Ca^{2+} ions are transported to the mitochondria and then calcium enters into blood circulation at the extremities through the basolateral membrane (Pansu et al., 1983). Functionally, as part of cell differentiation required to maintain skin structure, calcium ions pumped into keratinocytes in the basal layer are then released into extracellular fluid in the stratum granulosum until they disintegrate to almost negligible levels in the stratum corneum (Menon et al., 1985), as observed here via the hybrid ROI. In addition, the basal membrane also functions as a barrier, restricting intracellular calcium transfer into the dermis. Finally, in the stratum corneum the majority of keratinocytes are denucleated and so are devoid of calcium. They are surrounded by lipids produced during disintegration of lower epidermal layers, thus helping the stratum corneum regulate structure of skin (Wickett and Visscher, 2006).

The zinc distribution observed here peaked in the hybrid epidermal layer and decreased toward the stratum corneum, with the exception being along the outermost edge of the stratum corneum as have been documented previously (Forslind, 2000; Song et al., 2011). Zinc biomolecules include many characterized enzymes (Parisi and Vallee, 1969) including zinc finger proteins

(Miller et al., 1985). Specifically in skin, proliferating keratinocytes in the stratum basale hold 3 pairs of C2H2 zinc fingers in a nuclear protein called basonuclin, located in colonies in the stratum basale and in keratinocytes (Iuchi and Green, 1999; Tseng and Green, 1992), explaining its prevalence in the hybrid ROI. RNA and DNA are two of the most important of these proteins (Slater et al., 1971) and assist in epidermal keratinocyte proliferation. However, after cell mitosis, basonuclin mRNA levels are almost negligible resulting in differentiated keratinocytes, being heavily reduced in the suprabasal epidermis (Tseng and Green, 1994; Tseng et al., 1999). Functionally, it is the presence of corneocytes here that helps to facilitate this layer's regulation of skin's barrier functions, as mentioned earlier. Finally, in addition to oral zinc supplements, topically applied zinc compounds (e.g. ZnO) assist in wound healing (Agren, 1990; Rittenhouse, 1996; Stromberg and Agren, 1984) or for protection against UV-A/B induced damage (Leccia et al., 1993; Record et al., 1996) and this could explain the elevated level of zinc along the outermost part of the stratum corneum.

4. Conclusion

The present work investigated trace and biometal distributions in skin, using a synchrotron μXRF beamline. It should be noted that the use of biopsy samples can have its limitations. Biopsy tissue distortion and shrinkage have been observed post-excision and during sample preparation. This shrinkage has been documented to be as strong as 30% and can be hard to correct (Kerns et al., 2008). Different degrees of morphological change in skin can thus be expected with alterations in the overall thickness of the epidermis when viewed *in vitro*. Thus, in the current work, biopsy shrinkage must be considered as a factor that could contribute to the inability to distinguish sub-epidermal layers from each other, with the exception being in the thickest sample studied. Furthermore, the stratum corneum is estimated to be a 10th of the total thickness of the epidermis (International Commission on Radiological Protection, 1975), and the stratum lucidum is only present in the thickest of skin. Therefore, it is a combination of the other layers of the epidermis–stratum basale (bottom most layer), stratum granulosum (very thin, middle) and stratum corneum (top most) that would be visible in the non-thick skin maps obtained in this study, with their relative thicknesses being altered to an unknown degree by the sample extraction and preparation process. This limitation aside this study found that statistically significant differences ($p < 0.01$) in calcium and zinc levels between the epidermis and dermis were observed in all samples, and for iron in 12 out of 14 samples. Based on this, it can be seen that assumptions of distributions within the sub-layers of skin and thicknesses of these sub-layers being the same from site to site could indeed lead to an incorrect estimation of the *in vivo* quantification of toxic and biometals in skin. The results show the need to take depth distributions into account when developing and using calibration phantoms to mimic the skin and quantify the concentration of elements. Future studies are hoped to include developing and assessing the reliability of better *in vivo* calibration skin phantoms and potential studies involving patients suffering from various elemental over-exposure or deficiencies.

Acknowledgments

The authors would like to thank Mary-Jo Smith and Mary Bruni, from the histology lab at McMaster University, for help with histology preparation procedures and Glen Oomen, from the Anatomy Department at McMaster University, for assistance with handling the donated cadavers from which samples were extracted. The measurements were performed at the Canadian Light Source, which is supported by the Natural Sciences and Engineering Research Council of Canada, the National Research Council Canada, the Canadian Institutes of Health Research, the Province of Saskatchewan, Western Economic Diversification Canada and the University of Saskatchewan. The authors hold Discovery Grant funding from the Natural Sciences and Engineering Research Council of Canada which was used in partial support of this work. The authors would also like to thank Renfei Feng from the Canadian Light Source for technical assistance with the experiment at the beamline, Dr. Adam Hitchcock from the Department of Chemistry at McMaster University and the Canadian Light Source for providing student travel and accommodation funding that made this research possible, and Yicheng Liang for help with the MATLAB coding.

References

Adams, M.P., Mallet, D.G., Pettet, G.J., 2012. Active regulation of the epidermal calcium profile. J. Theor. Biol. 301, 112–121.
Agren, M.S., 1990. Percutaneous absorption of zinc from zinc oxide applied topically to intact skin in man. Dermatology 180, 36–39.
Andrews, N.C., 1999. Disorders of iron metabolism. N. Engl. J. Med. 341, 1986–1995.
Balesaria, S., Sangha, S., Walters, J.R.F., 2009. Human duodenum responses to vitamin D metabolites of TRPV6 and other genes involved in calcium absorption. Am. J. Physiol. Gastrointest. Liver Physiol. 297, G1193–G1197.
Beard, J.L., Dawson, H., Piñero, D.J., 1996. Iron metabolism: a comprehensive review. Nutr. Rev. 54, 295–317.
Berridge, M.J., Bootman, M.D., Roderick, H.L., 2003. Calcium signalling: dynamics, homeostasis and remodelling. Nat. Rev. Mol. Cell Biol. 4, 517–529.
Boyce, S.T., Ham, R.G., 1983. Calcium-regulated differentiation of normal human epidermal keratinocytes in chemically defined clonal culture and serum-free serial culture. J. Invest. Dermatol. 81, 33s–40s.
Branch, M., Coleman, T.F., Li, Y., 1999. A subspace, interior, and conjugate gradient method for large-scale bound-constrained minimization problems. SIAM J. Sci. Comput. 21, 1–23.
Clapham, D.E., 2007. Calcium signaling. Cell 131, 1047–1058.
Duval, M., Aubert, M., Hellstrom, J., Grün, R., 2011. High resolution LA-ICP-MS mapping of U and Th isotopes in an early pleistocene equid tooth from Fuente Nueva-3 (Orce, Andalusia, Spain). Quat. Geochronol. 6, 458–467.
Feng, R., Gerson, A., Ice, G., Reininger, R., Yates, B., McIntyre, S., 2007. VESPERS: a beamline for combined XRF and XRD measurements. In: AIP Conference Proceedings. AIP, pp. 872–874.
Forslind, B., 2000. The skin barrier: analysis of physiologically important elements and trace elements. Acta. Derm. Venereol. Suppl. (Stockholm) 208, 46–52.
Forslind, B., Lindberg, M. (Eds.), 2004. Skin, Hair, and Nails: Structure and Function. Marcel Dekker Inc., New York.
Forslind, B., Lindberg, M., Roomans, G.M., Pallon, J., Werner-Linde, Y., 1997. Aspects on the physiology of human skin: studies using particle probe analysis. Microsc. Res. Tech. 38, 373–386.
Forslind, B., Werner-Linde, Y., Lindberg, M., Pallon, J., 1999. Elemental analysis mirrors epidermal differentiation. Acta Derm. Venereol. 79, 12–17.
Gatter, K.C., Brown, G., Trowbridge, I.S., Woolston, R.E., Mason, D.Y., 1983. Transferrin receptors in human tissues: their distribution and possible clinical relevance. J. Clin. Pathol. 36, 539–545.
Gorodetsky, R., Loewenthal, E., Goldfarb, A.D.A., Rachmilewitz, E.A., 1990. Non-invasive evaluation of iron load and clearance in patients with B-thalassemia. Ann. NY. Acad. Sci. 612, 568–572.
Grolimund, D., Senn, M., Trottmann, M., Janousch, M., Bonhoure, I., Scheidegger, A.M., Marcus, M., 2004. Shedding new light on historical metal samples using micro-focused synchrotron X-ray fluorescence and spectroscopy. Spectrochim. Acta Part B 59, 1627–1635.
Hanley, C., Thurber, A., Hanna, C., Punnoose, A., Zhang, J., Wingett, D.G., 2009. The Influences of cell type and ZnO nanoparticle size on immune cell cytotoxicity and cytokine induction. Nanoscale Res. Lett. 4, 1409–1420.
Hennings, H., Holbrook, K.A., Yuspa, S.H., 1983. Potassium mediation of calcium-induced terminal differentiation of epidermal cells in culture. J. Invest. Dermatol. 81, 50s–55s.
Hostynek, J.J., Hinz, R.S., Lorence, C.R., Price, M., Guy, R.H., 1993. Metals and the skin. Crit. Rev. Toxicol. 23, 171–235.
International Commission on Radiological Protection, Publication 23, 1975. Report of the Task Group on Reference Man. Pergamon, Oxford, pp. 46–57.
Iuchi, S., Green, H., 1999. Basonuclin, a zinc finger protein of keratinocytes and reproductive germ cells, binds to the rRNA gene promoter. Proc. Natl. Acad. Sci. USA 96, 9628–9632.
Kamao, M., Tsugawa, N., Nakagawa, K., Kawamoto, Y., Fukui, K., Takamatsu, K., Kuwata, G., Imai, M., Okano, T., 2000. Absorption of calcium, magnesium, phosphorus, iron and zinc in growing male rats fed diets containing either

phytate-free soybean protein or soybean protein isolate or casein. J. Nutr. Sci. Vitaminol. 46, 34–41.
Karydas, A.-G., Sokaras, D., Zarkadas, C., Grlj, N., Pelicon, P., Žitnik, M., Schütz, R., Malzer, W., Kanngießer, B., 2007. 3D micro PIXE—a new technique for depth-resolved elemental analysis. J. Anal. At. Spectrom. 22, 1260–1265.
Kerns, M.J.J., Darst, M.A, Olsen, T.G., Fenster, M., Hall, P., Grevey, S., 2008. Shrinkage of cutaneous specimens: formalin or other factors involved? J. Cutan. Pathol. 35, 1093–1096.
Kertesz, Z., Szikszai, Z., Kiss, A.Z., 2005. Quality of Skin as a Barrier to Ultra-Fine Particles. Contribution of the IBA Group to the Nanoderm EU-5 Project in 2003–2004. ATOMKI Annual Report 2004. Debrecen, Hungary.
King, J.C., Shames, D.M., Woodhouse, L.R., 2000. Zinc homeostasis in humans. J. Nutr. 130, 1360s–1366s.
Kulesz-Martin, M.F., Fabian, D., Bertram, J.S., 1984. Differential calcium requirements for growth of mouse skin epithelial and fibroblast cells. Cell Tissue Kinet. 17, 525–533.
Lansdown, A.B., 1995. Physiological and toxicological changes in the skin resulting from the action and interaction of metal ions. Crit. Rev. Toxicol. 25, 397–462.
Leccia, M.T., Richard, M.J., Bean, J.C., Faure, H., Monjo, A.M., Cadet, J., Amblard, P., Favier, A., 1993. Protective effect of selenium and zinc on UV-A damage in human skin fibroblasts. Photochem. Photobiol. 58, 548–553.
Leccia, M.T., Richard, M.J., Favier, A., Béani, J.C., 1999. Zinc protects against ultraviolet A1-induced DNA damage and apoptosis in cultured human fibroblasts. Biol. Trace Elem. Res. 69, 177–190.
Leng, A., Xu, Q., Xie, M., Zhang, W., Bao, Y., Du, Y., Cheng, Z., Wang, H., Ying, X., Kang, T., 2011. ICP-MS determination of trace elements of different growth time in the leaves of *Crataegus pinnatifida* Bge. var. major. J. Med. Plant Res. 5, 4843–4850.
Mcgee, J.J., Keil, K., 2001. Application of electron probe microanalysis to the study of geological and planetary materials. Microsc. Microanal. 7, 200–210.
Menon, G.K., Grayson, S., Elias, P.M., 1985. Ionic calcium reservoirs in mammalian epidermis: ultrastructural localization by ion-capture cytochemistry. J. Invest. Dermatol. 84, 508–512.
Miller, J., McLachlan, A.D., Klug, A., 1985. Repetitive zinc-binding domains in the protein transcription factor IIIA from Xenopus oocytes. EMBO J. 4, 1609–1614.
Milstone, L.M., Adams, B.D., Zhou, J., Bruegel Sanchez, V.L., Shofner, J., 2006. Stratum-specific expression of human transferrin receptor increases iron in mouse epidermis. J. Invest. Dermatol. 126, 648–652.
Mino, L., Agostino, A., Codato, S., Lamberti, C., 2010. Study of epitaxial selective area growth $In_{1-x}Ga_xAs$ films by synchrotron μ-XRF mapping. J. Anal. At. Spectrom. 25, 831–836.
Molokhia, M., Portnoy, B., 1969. Neutron activation analysis of trace elements in skin. I. Copper in normal skin. Br. J. Dermatol. 81, 110–114.
Nelder, K.H., 1991. The biochemistry and physiology of zinc metabolism. In: Goldsmith, L.A. (Ed.), Physiology, Biochemistry, and Molecular Biology of the Skin, Second Ed. Oxford University Press, Oxford, UK, pp. 1329–1350.
Pansu, D., Bellaton, C., Roche, C., Bronner, F., 1983. Duodenal and ileal calcium absorption in the rat and effects of vitamin D. Am. J. Physiol. 244, G695–G700.
Parisi, A.F., Vallee, B.L., 1969. Zinc metalloenzymes: characteristics and significance in biology and medicine. Am. J. Clin. Nutr. 22, 1222–1239.
Record, I.R., Jannes, M., Dreosti, I.E., 1996. Protection by zinc against UVA- and UVB-induced cellular and genomic damage in vivo and in vitro. Biol. Trace Elem. Res. 53, 19–25.
Reeve, V.E., Nishimura, N., Bosnic, M., Choo, A.K., Michalska, A.E., 1999. Dietary zinc, photoimmunosuppression and metallothionein (MT). In: Klaassen, C.D. (Ed.), Metallothionein IV. Birkhäuser, Verlag, Basel, Switzerland, pp. 445–449.
Richard, M.J., Guiraud, P., Leccia, M.T., Beani, J.C., Favier, A., 1993. Effect of zinc supplementation on resistance of cultured human skin fibroblasts toward oxidant stress. Biol. Trace Elem. Res. 37, 187–199.
Rittenhouse, T., 1996. The management of lower-extremity ulcers with zinc-saline wet dressings versus normal saline wet dressings. Adv. Ther. 13, 88–94.
Rostan, E.F., DeBuys, H.V., Madey, D.L., Pinnell, S.R., 2002. Evidence supporting zinc as an important antioxidant for skin. Int. J. Dermatol. 41, 606–611.
Slater, J.P., Mildvan, A.S., Loeb, L.A., 1971. Zinc in DNA polymerases. Biochem. Biophys. Res. Commun. 44, 37–43.
Song, Z., Kelf, T.A., Sanchez, W.H., Roberts, M.S., Rička, J., Frenz, M., Zvyagin, A.V., 2011. Characterization of optical properties of ZnO nanoparticles for quantitative imaging of transdermal transport. Biomed. Opt. Express (2), 3321–3333.
Stromberg, H.-E., Agren, M.S., 1984. Topical zinc oxide treatment improves arterial and venous leg ulcers. Br. J. Dermatol. 111, 461–468.
Torti, F.M., Torti, S.V., 2002. Regulation of ferritin genes and protein. Blood 99, 3505–3516.
Tseng, H., Biegel, J.A., Brown, R.S., 1999. Basonuclin is associated with the ribosomal RNA genes on human keratinocyte mitotic chromosomes. J. Cell Sci. 112 (Pt 18), 3039–3047.
Tseng, H., Green, H., 1992. Basonuclin: a keratinocyte protein with multiple paired zinc fingers. Proc. Natl. Acad. Sci. USA 89, 10311–10315.
Tseng, H., Green, H., 1994. Association of basonuclin with ability of keratinocytes to multiply and with absence of terminal differentiation. J. Cell Biol. 126, 495–506.
Wasserman, R.H., Chandler, J.S., Meyer, S.A., Smith, C.A., Brindak, M.E., Fullmer, C.S., Penniston, J.T., Kumar, R., 1992. Intestinal calcium transport and calcium extrusion processes at the basolateral membrane. J. Nutr. 122, 662–671.
Werner-Linde, Y., Pallon, J., Forslind, B., 1998. Physiologically important trace elements of paralesional psoriatic skin. Scanning Microsc. 12, 599–608.
Wickett, R.R., Visscher, M.O., 2006. Structure and function of the epidermal barrier. Am. J. Infect. Control 34, S98–S110.
Wintergerst, E.S., Maggini, S., Hornig, D.H., 2006. Immune-enhancing role of vitamin C and zinc and effect on clinical conditions. Ann. Nutr. Metab. 50, 85–94.

Chapter 8 Conclusions and Future Work:

8.1 Conclusions:

Arsenic is an element whose toxicity is a known problem to populations in several parts of the world. Traditional methods of monitoring include using urine, nail or *ex vivo* biopsy skin samples. Being an organ of greater biological health consequence, skin is a more suitable choice for monitoring arsenic *in vivo*.

A potential non-invasive approach to this involves using an XRF detection system. This work continued development of a benchtop x-ray tube-based XRF detection system that was developed previously. The source was a polychromatic Mo anode x-ray tube that could be operated at maximum voltage-current settings of 50 kVp-1 mA. Modifications were made to the design of the system. These were found, with a regenerative monochromatic filter, to allow for a low As MDL of (0.499±0.002) ppm in ~1800 seconds (real time), essentially matching that achieved previously, but for a lower subject dose. This also helps to preserve tube life as the system does not need to be operated at high voltage-current settings. The associated gross Compton scatter normalized MDL was found to be (0.611±0.001) ppm – a normalization is required to correct for variations in dead time brought about by source strength fluctuations and skin phantom positioning. Using an array of Li(F) thermoluminiscent dosimetry (TLD) chips, the localized and whole body effective doses were found to be (0.14±0.04) μSv and (163±47) μSv respectively and the equivalent skin dose was (19±3) mSv.

Handheld x-ray analyzers from InnovX were also investigated, as these are becoming more and more commonly available commercially and offer the benefit of portability over benchtop systems. The main benefit of such portability is the ability to transport such an analyzer to the field and perform analysis in real time. The current use of either analyzer was in benchtop mode where the unit was fixed to a stand rather than being held in the hand. The InnovX Alpha4000 unit had a built-in polychromatic W anode x-ray tube with a fixed voltage-current of 40 kVp-20 μA. Fluorescence was collected with a PiN-diode detector and the system offered gross scatter-normalized MDLs of (1.649±0.002) ppm with nylon backing and (0.903±0.001) ppm without the backing, while delivering effective (localized) and equivalent doses of (6.38±1.51) $X10^{-3}$ μSv and (9.35±2.21) mSv respectively with backing and (11.35±2.97) $X10^{-3}$ μSv and (16.63±4.34) mSv respectively without backing, in 2 minute (real time) measurements. The associated direct MDLs were (1.651±0.002) ppm and (1.0105±0.0007) ppm with and without backing respectively. The whole body effective doses were (94±22) μSv and (166±44) μSv with and without backing respectively. The Delta model system contained a Au anode x-ray tube with an accelerating potential of 40kVp and variable current, ~ 17-37 μA were automatically chosen by the unit's software for phantom-based work. Gross normalized detection limits of (0.570±0.002) ppm and (0.4952±0.0004) ppm were

obtained in 120 seconds (real time), with and without backing respectively. The direct MDLs were (0.558±0.002) ppm and (0.462±0.004) ppm respectively. Dosimetry work was only performed with backing. The equivalent and whole body effective doses required to attain these detection limits were measured to be (19.0±9.0) mSv and (190±90) μSv respectively, with backing. The localized effective dose was (9.7±4.6) X 10^{-3} μSv.

Finally, an optically focused x-ray tube-based system was used. The source was a Ag target monochromatic x-ray tube that utilized a built-in DCC focusing method to pass only the Ag Kα energy, while simultaneously focusing the beam to a sub-mm spotsize at (30.0±0.2) cm away. The tube allowed a maximum voltage-current setting of 50 kVp-0.50 mA. An incident energy spread of ~300 eV was recorded with a 100 mm^2 SDD collimated to 80 mm^2 with a multi-element collimator material. The lowest MDL realizable with the system was found using a silicon drift detector to be (0.441±0.003) ppm in 1800 seconds (real time) while delivering equivalent and whole body effective doses of (11±2) mSv and (110±23) μSv respectively. The localized effective dose was (3.92±0.87) X10^{-3} μSv.

8.2 Future work:

Future work for this project consists of *in vivo* application of the various x-ray fluorescence systems and continued investigation of various questions and concerns that have been documented over the course of this thesis. *Ex vivo* work is also possible, but will likely prove to be beneficial with the SDD due to its superior resolution.

8.2.1 Conventional x-ray fluorescence system:

The *in vivo* capabilities of the conventional x-ray fluorescence bench-top system, at McMaster University, can be evaluated. The application procedure for the appropriate research ethics approval is under way. Depending on the scatter and dead time, the tube voltage and current will need to be altered. An accelerating voltage of ~30 kVp should be sufficient for the thicker (200-300 μm) filters, with additional adjustment possible with the tube's current setting. A change in dose delivered would be expected when the entire hand of a subject is inserted into the system, as shown in figure 8.1.

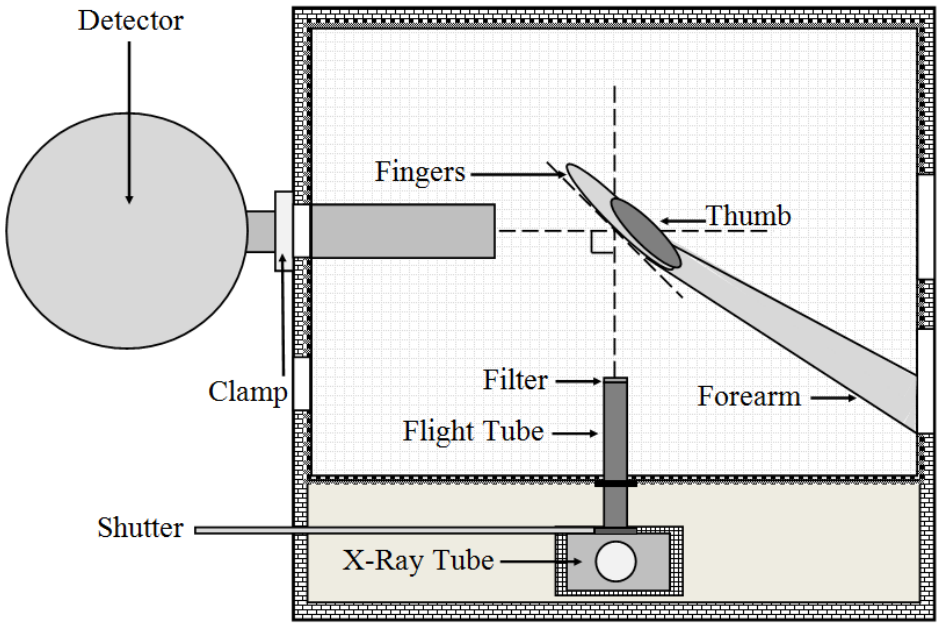

Figure 8.1: Schematic of interior of conventional x-ray tube-based detection system, showing subject's arm inserted into shielding cabinet through one of side entrances, with thumb, fingers and forearm labeled.

The increased scatter is because the subject's forearm is also fully inserted into the shielding cabinet *in vivo*, while a small palm phantom was used for the TLD work presented in chapter 2. An estimate of a change in dose, going from phantom to *in vivo*, can be obtained by casting resin in a plastic glove and letting it set. When it dries, the resulting mould assumes the shape of a human hand. An optional, though beneficial, step would include adding a plaster-of-paris mould in the center of the resin before casting so as to mimic human bone. This construct can be placed inside the system in the intended orientation for an *in vivo* measurement (see above figure). A considerably larger array of TLD chips, than that used in chapter 2, can be attached to the resin so as to track the dose delivered to the entire hand of a subject *in vivo*. In order to make a conservative estimate, the x-ray tube can be operated at full power settings, thereby delivering the maximum dose possible from a) the primary (incident) beam and b) scatter (secondary excitation source) off the shielding material. Such a resin mold has been built, without the plaster-of-paris bone-modeling insert, and it is available for use. The model extends from the fingers down to the elbow. A single mold was constructed for both the left and right hand, although only the palm of the right hand can be comfortably inserted into the cabinet under its current design. Two additional approaches to dosimetry will be discussed later.

With future work, including *in vivo* work, it would be best to shield the interior of the copper cabinet with several layers of aluminum foil. This may help reduce the intensity of the copper signal that is scattered. Elements with energies in the vicinity of

copper, such as iron or zinc can be studied without interference. The ability to extend the use of this system to energies beyond that of arsenic is limited by the tailing on the Mo Kα Compton scatter peak. Shielding the detector may also help to reduce scatter. This has the added benefit of reducing the system dead time since the scatter is blocked from interacting with the detector head in the area of the active element. A multi-material shield such as an inner layer of aluminum and an outer layer of plastic may be best. The plastic outer could help reduce additional scatter off the metal (aluminum), although it will not fully eliminate it. The presence of the gold contacts obstructs detection of the selenium (Se) Kα peak. Working at lower energies is almost certain to require substantial reduction of the copper signal from the spectrum as this interferes with zinc or iron characteristic x-rays (Abu Atiya, 2012).

The possibility of an external monochromator also exists. This would remove unwanted incident energies from the scattered spectrum – Mo Kβ, its Compton and coherent scatter and their respective escape peaks and tails. Examples are found in the literature of their use with x-ray tubes (Krol et al., 1997; Zhong et al., 2001, 1997). Intensity loss is to be expected with both filters or monochromators; however, these would offer an advantage over K-edge filters because the bending crystal used does not fluoresce x-rays in the range of energies covered by the Mo Kα scattered x-ray peaks. Saint-Gobain crystals in Quebec, CAN or Huber Diffraktionstechnik GmbH in Germany (ex. Graphite monochromator model 151) offer such crystals commercially and can be attached to the exterior of the x-ray tube.

There is also the possibility of re-designing the housing of the shielding cabinet. For the purposes of quantification of an arsenic signal in phantoms, or *in vivo*, the shielding cabinet is sufficient. However, a larger cabinet would allow scattered radiation to disperse before it reaches the detector. Also, the intensity of this radiation would be reduced. This would allow for a more reliable normalization since the scatter portion of the spectrum is currently fairly cluttered compared to the region of 10-12 keV, where the As Kα peak sits. A problem with such an approach is that the housing must be large enough to fully house the Si(Li) detector's dewar. This may also preclude the need for using copper as shielding material – if the intensity scatter is weak enough, it may not be necessary to use shielding and a simple plexiglass cabinet would suffice. This is a more cost effective approach than use of a large amount of copper to assemble a cabinet large enough to house the Si(Li) detector. Multiple phantom-detector geometries could be realized with such a modification. Additionally, ease of SDD usage with this system would also be facilitated with this modification. In order to use the SDD with the current layout, a change in the shape and size of the detector head opening would be needed. Since the opening required for the Si(Li) detector head is smaller, a customized additional shielding-block would then required when the Si(Li) detector is to be used. The disadvantage of such a modification is that the system will be unusable for an extended period of time. This approach should, thus, only be deployed after an *in vivo* study has been performed with the current layout.

8.2.2 Handheld x-ray fluorescence analyzers:

The possibility of modification of the handheld XRF units is limited since the unit is pre-assembled. However, dead time for the two units was fairly high. A tube filter could be used to address this by placing it on the kapton window, directly beneath the phantom. However, this would a) attenuate the incident signal and b) lead to increased backscatter from the filter itself.

For *in vivo* use, dead time can be easily reduced by holding the unit at some distance away from the subject. This might also require some override of an auto sample distance sensor on these devices. This would reduce backscatter reaching the detector and dose delivered. This is expected to be particularly beneficial for the Innov-X Delta handheld system where the skin dose is nearly 40 mSv. However, longer counting periods may be required due to the increased sample-detector distance. This would be most readily realized by removing the lid and attaching the unit directly under a custom built plexiglass cabinet, with an appropriate safety interlock system. With a hole drilled in the cabinet, the subject's hand can then be inserted for the measurement. Alternatively, two holes can be drilled into the shielding lid so as to facilitate insertion of the hand for a palm measurement site. Another option is to mount the nozzle of the unit in a floor or base-mounted stand and place it inside a plexiglass cabinet. Any of these modifications would, however, be subject to approval by the Ministry of Labour in Ontario or associated authority in New Brunswick. The handheld XRF approach is otherwise limited in system-modification capabilities.

8.2.3 Optical fousing system:

Filtered tube output should be further explored. In combination with changing backing material, this may re reveal the source of the non-zero intercept with the SDD data. Regardless of the source of the interference, a low concentration arsenic resin phantom would offer a means of evaluating the extent of the existing (unfiltered) interference. As seen from figure 8.2, the backing is quite close to adipose tissue that it was intended to replicate.

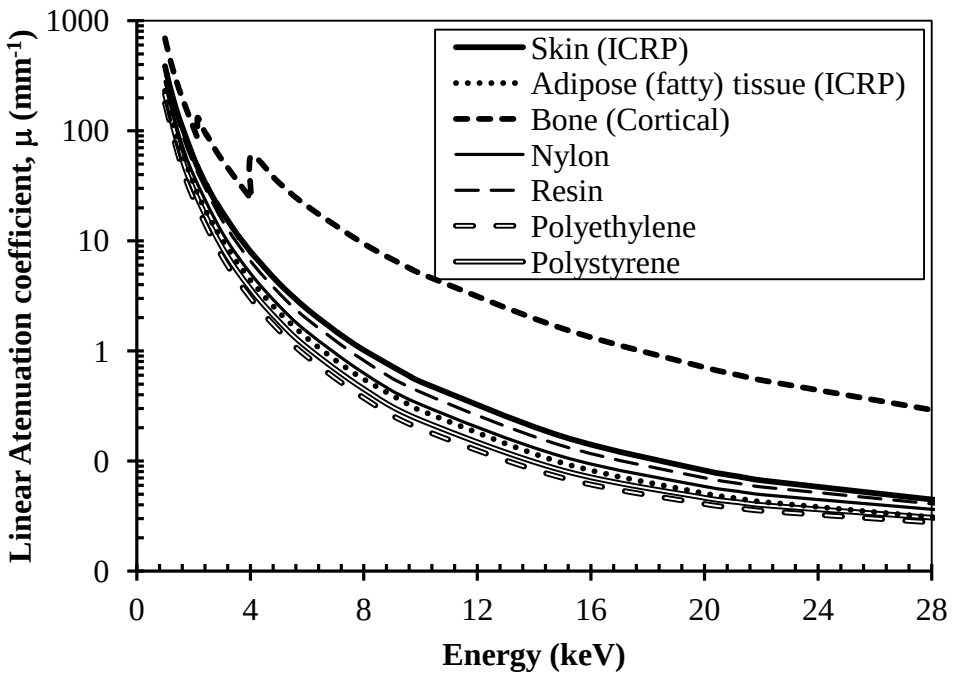

Figure 8.2: Linear attenuation coefficient of various materials that could be used to mimic scatter off bulk tissue behind skin.

However, there are other choices available that come close as well and polystyrene may be an alternative that is free of contaminants in the range of the arsenic energy. Including backscatter off a suitable material gives a more realistic estimate of what to expect in vivo than if such a contribution is ignored. Thus, the continued use of a backing material is recommended.

Additionally, if a suitable filter material can be chosen (i.e. one that does not interfere with peaks of interest), then a collimator may be placed at the focal length. The collimator opening would be of the same diameter as the focal spot, excluding any artifacts. This would guarantee that imperfect focusing is not present and that the source is in fact a point source at this source-phantom distance.

With the optical-focusing system, scatter is reduced relative to that observed with the conventional x-ray tube-based system. Thus, dosimetry using a resin-based hand mould is not required. An *in vivo* feasibility study can be performed with this detection system. As lowest MDLs do not differ by more than a factor of two, either detector type [Si(Li) or SDD] would be suitable in principle. However, the benefits of the SDD have been mentioned earlier – superior FWHM capabilities and a reduced phantom-detector separation. In a feasibility study, these may help to reduce the overall σ when it is calculated based on *in vivo* work, rather than on phantom work. An *in vivo* feasibility study is recommended to compare the performance of the two benchtop systems to each

other. If precedence is placed on the localized effective dose (with whole body skin volume correction applied), then the source strengths (depending on system dead time) or acquisition times can be increased for such work. This may represent a way of improving system performance during such an evaluation of system performance.

A multi-layer skin phantom with resin may be a more realistic description of the concentration of arsenic in skin. Several attempts at machining a 1.5-2 mm thin slice, using a lathe, revealed that the resin begins to bend as the thickness is reduced due to heat produced when it is being sliced. Ideally, individual sub-layers of the epidermis will be obtained separately and stacked together to produce a single phantom. Imperfections in the machining process mean that air gaps between each of the slices would be unavoidable. This would affect photon attenuation. Preparation of individual slices by pouring the resin into cylindrical moulds was also tested. This approach to preparing a resin slice was not found to give a consistent thickness across the entire surface of the slice. Although practically challenging, the impact of such a layered phantom on arsenic peak area can be examined using the EGS5 code for simulations. Overall skin thicknesses would not exceed 2 mm (ICRP) and individual sites on the body can be modeled using the EGS5 visualization tool CGView, as mentioned earlier. Various arsenic concentrations can be set for each layer. This can also be repeated for varying thicknesses of nylon backing material. Changes in the backing would affect the amount of backscatter that is detected and the location of the Compton scatter peak. Attempts at slicing the nylon backing (1.3 cm thick) showed similar heat-related bending of the material. As with the resin, this would result in air gaps. Estimations of the extent of backscatter to be expected *in vivo* can be obtained from such simulations.

Hardware modifications required for this system are minimal if the system is to be used for the current application or for work with *ex vivo* skin, bone or other biological tissue samples. Modifications would only be required if the x-ray tube needs to be elevated; this would require realignment of the beam. Such a modification would be necessary when working with a larger sample such as a painting. With software-programmed motion control capabilities incorporated into the lab-jacks and linear stages, the scanning of samples can be performed. The scans can be fully automated and unattended.

The Si(Li) detector cannot be used in a geometry approaching a backscatter (180^0 source-detector angle) arrangement without severely sacrificing count rate. This would be the result of larger phantom-detector distance because of the detector's bulkier footprint, as was seen earlier. However, this limitation can be lifted using a multi-detector arrangement where a single detector element is split into separate sensitive volumes, covering an angle of 360^0 with an opening in the center for the source radiation to pass through the detector housing and interact the closely placed sample in true backscatter geometry as shown, for the case of a 4-element arrangement, in figure 8.3.

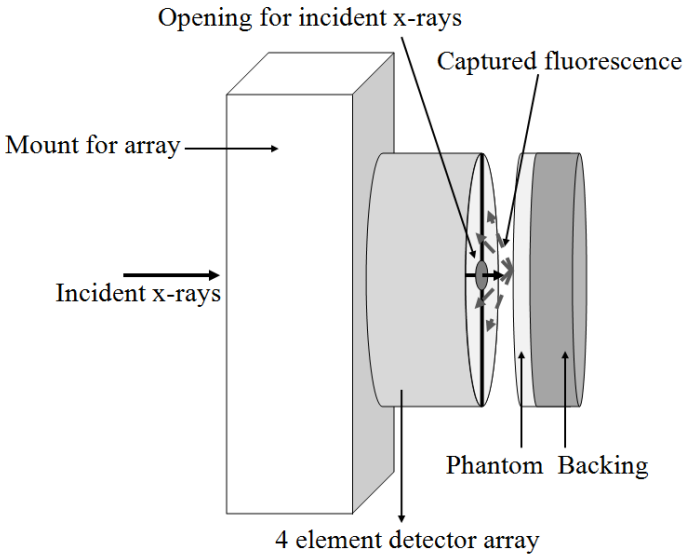

Figure 8.3: Possible layout of multi-element SDD.

Technological advances and new topology designs at PNDetector – a leading SDD manufacturer – have resulted in SDD arrays (Hansen, Reckleben, Diehl, and Klär, 2008; Hansen, Reckleben, Diehl, and Welter, 2008), maximizing efficiency and sensitivity via larger collection angles than a single SDD, improving efficiency which is vital for trace element analysis. For such an SDD's useful energy range, it could also be used for *in vivo* Fe or Cu analysis, which can be supported by the existing tube based XRF system. Simulations can be used to investigate the impact of a multi-element detector layout for the SDD by examining the percentage change in the As Kα/Compton ratio. The benefit of a multi-element layout is to allow for a truly backscatter geometry, which is not realizable currently. This would lead to nearly complete separation of the Compton and coherent scatter peaks even with tailing included. It would also allow for verification of the explanation of the shifted Compton scatter peak suggested in this work.

As a complementary approach, increasing the thickness of the SDD sensor will lower the Compton backscatter component inside the head of the SDD. This will help in cleaning up the scatter portion of the spectrum. Recently, a thicker SDD (Model VORTEX 90-EX) has become commercially available. It is manufactured by Hitachi-High Technologies Science America Inc. Whereas previously, ~70 % of incident Ag Kα photons will not deposit their energy in the active volume of the detector, a 1 mm thick Si detector will now reduce this to ~45%. A schematic depicting the increase in thickness is shown in figure 8.4.

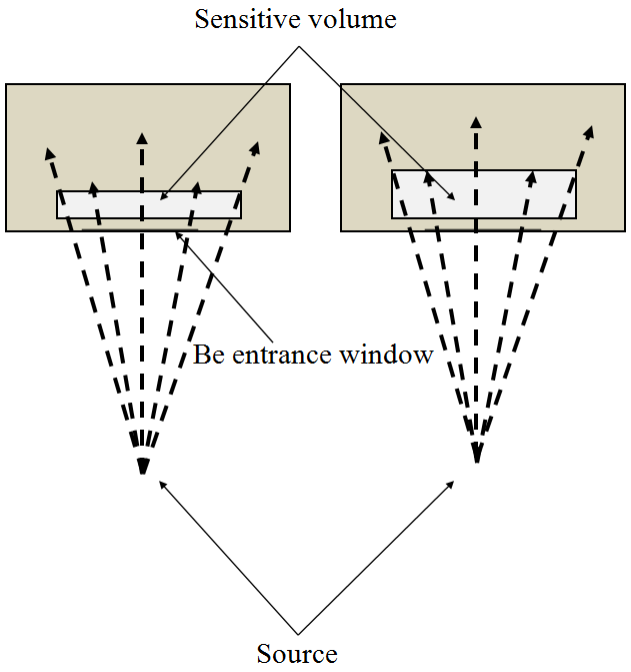

Figure 8.4: Overhead schematic of inside of head of SDD housing, showing thin and thick Si sensor.

The earlier difficulty experienced with backscatter off the internal housing of the head of the SDD is reduced and this will help with scatter de-convolution as the number of multiple Compton backscattered photons that interact with the SDD (from the back) will be preferentially reduced. A downside to this is that the active area is reduced from 80 mm^2 to 50 mm^2. This means that counting times of ~60% longer (~3000 seconds, or ~50 minutes) would theoretically be required to make up for this difference in active areas.

Higher throughput with such arrays prevents use of signal processors designed for traditional detectors, which cannot process SDD pulses fast enough. To maximize an array's effectiveness, new pulse-processing electronics are necessary, such as the DXP Mercury-4 pulse processor (XIA LLC). Each detector in the array can process the same count rate as a single detector. The resulting superior efficiency and statistics allows for more meaningful data to be collected. For example, in the case of bone Pb XRF system, a comparable HpGe array improved sensitivity by a factor of between 3 and 5 (Nie et al., 2004). A comparable improvement to the existing x-ray tube system (Studinski et al., 2006) would advance not just phantom but also *in vivo* As detection capabilities to the lower end of an occupationally exposed population. An array's higher precision will also allow for higher source strengths, reducing measurement times without compromising data quality through subject motion. This is also true for the other XRF applications, enabling use of a larger sample set – the detector can also be used for investigation of other elements in skin or bone – zinc, uranium, chromium, iron and selenium, to name a

few. This modification would maximize efficiency and statistical power because fluorescence over the largest range of backward scattering angles is detected.

The current means of imaging the beam is the gafchromic film. It takes several hours for a usable image to form, at the larger distances. An alternative to this would be to use a CCD camera to record the image of the beam directly out of the tube. Benefits include near instantaneous alignment of the setup and the realization of optical densitrometry capabilities allowing for micro-positioning of the sample with far superior control to the currently employed setup. The advantage is that the shadow of the beam observed with the optical system can be clearly visualized, quantified and fully shielded. Currently, this is not possible as the resolution of the film is not good enough to identify clearly the margins of the primary beam and the artifact. The non-zero contribution of the shadow cannot be fully ruled out as a source of the observed Compton shift. Simulating the effect of such an artifact is very challenging without extensive imaging of the beam since the film used is not of the appropriate resolution for this task. A digital x-ray camera would be of value to this end and can also be used with any similar XRF setup in the laboratory.

Finally, it should be noted that, with either benchtop system, a dedicated detector – either Si(Li) or SDD, is highly recommended unless a reliable normalization is established. Small changes in positioning of the detector relative to the source (90^0) were noted over the current work and were time-consuming to eliminate. Scatter, particularly with the conventional system, is strongly affected by changes in positioning of a metallic object such as the head of the detector. While scatter is unavoidable with a cabinet of such small dimensions, changes in it must be eliminated because of the appearance of additional interfering Compton scatter peaks. This can be done with a dedicated detector, as is the case with either of the handheld units.

8.2.4 Si(Li) detector pulse processing:

Pulse processing improvements can also be investigated with the aim of further elucidating the source of the tailing on the scatter peaks observed with the conventional x-ray fluorescence system. The interference of Ge characteristic x-ray peaks with the As x-ray peaks rules out the possibility of using Ge, rather than Si, as the active detector material. Thus, more detailed attention should be paid to the Si(Li) detector used in the current work. The use of a clover-leaf based Si(Li) detector was recommended in previous work and requires a small modification to the system's shielding. The aim of work to this end would involve cleaning up the scatter region of the spectrum so as to facilitate a reliable deconvolution. With regards to pulse processing and the existing single-element Si(Li) detector on the conventional system, optimization of pole zero and pile-up rejection were not investigated during the study of shaping times. The former could reduce the tail-peak area ratio with the system. The high tail-to-peak ratios, from preliminary work with the Si(Li) detector, suggest that a more advanced pile-up rejector may also be useful with that detector. The ORTEC DSPEC PLUS, used with the Si(Li) detector, has built-in pile-up rejection modes that were not investigated. Unfortunately, a

limitation of this MCA is that the pole-zero circuit is disconnected from the main pulse processing chain for a transistor reset preamplifier type.

Tailing is caused by charge collection inefficiencies in a few parts of or electron escape from the detection volume (Knoll, 1999). As mentioned in the introduction section, preamplifier output pulse undershoot is expected and depends on the decay time of the particular preamplifier used. A unipolar CR-RC response is thus a problem that can be remedied with a pole-zero cancellation (Robinson, 1961). In theory, the transistor reset preamplifier, coupled to the Si(Li) detector, should eliminate the need for this cancellation due to its infinite decay time. However, a non-ideal pole-zero circuitry may be caused by prolonged use of the DSP unit deployed with the SDD-based system. An analog approach to pulse processing, using a NIM rack, may be able to bear out this problem. This may be achieved by accessing the preamplifier output pulse directly using an analog amplifier NIM module and performing the pole zero adjustment manually until the output pulse is free of undershoot when viewed on an oscilloscope. Analog electronics have their limitations – gain drift is not observed with the DSP unit but may be expected as analog components heat up with extended use. Also, as more components are added to the NIM bin, non-linear performance of each additional unit may further add to the problem. A minimal number of components in the pulse processing chain would be best suited to evaluate the pole-zero cancellation performance of the DSP.

A fast and slow branch approach is typically used for pile-up rejection. In principle, by controlling the processing time of pulses in each branch, it is possible to collect spectra that are free of pulse pile-up. As with the pole-zero cancellation, a usage-related drop in performance may affect the efficiency of the rejection system used in the ORTEC DSPEC PLUS MCA unit. It should be noted that pile-up rejection may be expected to reduce higher-energy anomalies, such as sum peaks, and so improvement to the low-energy tail-like structure may not be dramatic. This would still, however, be useful to eliminate as it is a source of structure on the low-energy side of the Mo Kα Compton scatter peak. If successful, it may be possible to attribute low energy events to noise-triggered events that are piling up in combination with good x-ray events. The ORTEC DSP has an oscilloscope mode which displays the sampled amplifier pulse. This screen contains settings that can be fine-tuned to displays when pile-up is present and pulses are being rejected. These and other controls of logic gating functionality are adjustable. This was set to off in the current work but coincidence and anticoincidence modes exist and may be explored. If it is turned on, then it has to be present at a particular time in order for conversion to proceed.

The tail-peak area, for the arsenic Kα energy, with either detector, is ~10%. If this ratio does not greatly increase with energy, an 80% ratio for the Mo Kα Compton scatter peak, which was reported from preliminary analysis of this peak in chapter 2, is unrealistic. It also means that comparable tailing may be expected ideally for this Compton scatter energy. If the arsenic Kα tail-to-peak ratio is used as a gauge, then the pile-up rejector may have a greater impact on the tail-like feature on the low-energy side

of the Compton scatter peak than pole-zero optimization. The latter is nonetheless recommended as a means of verification of DSP performance.

8.2.5 SDD pulse processing:

With the SDD pulse processing system, the MCA software method for optimizing the pole-zero cancellation was found to be quite good as extensive As Kα low-energy tailing was not observed. Two parameters, besides shaping time, which can be changed are effective gain and conversion gain. As mentioned earlier, the effective gain was set to display the highest energy made accessible by the manufacturer – 40 keV and so a reduction would lower the highest energy that can be viewed with this detector. With a significant drop-off in absorption in the detector material at such high energies though, their benefit is greatly mitigated and so a lower effective gain (thereby expanding out the spectrum under current settings) would only be worthwhile for convenience. Unless the pulse processing system behavior is compromised for lower effective gain settings, a benefit is not expected to be realized by lowering this value. However, the number of channels (conversion gain) used with the DSA1000 may be reduced. This indicates the channel number in which the highest amplitude pulse detected will be stored, with the range of detected amplitudes covering this range of channels. The number of channels used ranges from 256 to 16384, in powers of 2, depending on the application requirements with a larger number of channels being used for work with high resolution requirements, thereby driving up the MCA dead time since extraction of a larger number of pulse heights and analog-to-digital conversions will be required (Knoll, 1999). In the case of an SDD, the dead time is already very low so a benefit from this point of view would not be much. A higher number of channels would allow the experimenter to better resolve closely spaced peaks since the overall shape will be more sensitive to changes in energy than for a smaller number of channels. If the number of channels is reduced this effect may be comparatively blurred out, however for an SDD the resolution is already good and so it may be possible to use a lower conversion gain. Thus, benefits of further SDD-specific pulse processing improvements aren't likely to be very significant.

8.2.6 Ex vivo based work:

The accuracy of our on-going work is impeded by the lack of knowledge of the micro distribution of the elements to be studied in skin. One way to account for the non-uniform depth distribution of arsenic, or any trace element, in skin is to use an XRF micro-probe such as the one utilized in the chapter describing the *ex vivo* synchrotron-based work. For a non uniform distribution it would be difficult to talk about concentrations but rather reference must be made to the concentration at the surface layer, which would represent skin scale levels instead. Furthermore, depending on the location from which the sample is taken, skin thicknesses range from approximately 50 to 2000 microns. These layers may be visible in the palm of the hand (recommended site) because it has very thick skin, however, the variation in the micro distribution between locations on the body is unknown and must also be determined. A spot-size of ~10 μm would be required in order to resolve the epidermal sub-layers. Arsenic located below ~2.5 mm of skin will not be detected due to the attenuation of As K-shell x-rays in skin. This is the

upper end of the expected range of skin thicknesses. Arsenic speciation is also possible, with x-ray absorption spectroscopy (XAS) at a synchrotron.

The *ex vivo* work performed demonstrates the capabilities of the μXRF mapping technique. Through University of Ottawa (Ottawa, ON, Canada) collaboration with researchers in Bangladesh is being explored and will be able to offer samples of interest. In addition to mapping and synchrotron work, this would allow for a quantification of arsenic in the bulk samples with the detection systems documented in this thesis. If it is known that arsenic will be present in necropsy skin samples in elevated concentrations, as would be expected for samples from such a population, then it is recommended that destructive analysis can also be performed. Collaboration with Dr. Patrick Parson's group in Albany, NY, USA is possible. This group is planning to perform just this analysis on arsenic nail clippings from an exposed population in Eastern Canada and a natural extension would be to contaminated arsenic skin samples. Finally, biopsy samples are collected from cadavers donated to the Anatomy department. Samples are extracted from 10 locations on the body. A handheld x-ray analyzer can be taken in to the cadaver storage area and, prior to extracting samples, the feasibility of a full body map can be performed. This requires a good resolution and the InnovX Delta's SDD would be ideal for such work. If obvious hot-spots are located, samples can be extracted from those sites. Ethics approval is not required as biological tissue is not being harvested.

8.2.7 Dosimetry approaches for exhaustive scatter dose monitoring:

Two additional ways of quantifying the effect of scatter produced by the shielding, are now discussed. The scatter off the shielding cabinet is a problem for deconvolution of scatter peaks in EDXRF spectra. However, it can also potentially contribute unwanted dose. Although the dose delivered over a 30-minute measurement is not very large, it may not be negligible. Additionally, correction factors applied in the dosimetry section may be underestimated because these assume well-known relationships between tube settings (voltage, current) and source strength. These relationships may break down if the scatter detected is strong enough. The aim of this is to assist in identifying the source and, more importantly, magnitude of the scatter. Since the applicability of this is to two of the three approaches documented here, such work is worth investigating. A careful characterization of dose as a function of source strength (varying x-ray tube voltage-current) is recommended as scatterers are introduced into the system (eg. entire human hand, detector shielding material, etc.).

8.2.7.1 Gafchromic EBT film:

One way to address this is to cover the inside of the cabinet with sheets of gafchromic film. The head of the detector is in the shape of a cylindrical tube and may be covered with smaller pieces of film. Image analysis can be performed on the film to extract intensity (optical density, OD). A potential disadvantage of this approach is that two setups will need to be tested: a) with the detector head inside the cabinet and b) without inserting the detector into the cabinet. Also, long exposures will need to be tested in order to pick up a sufficiently strong reading from the film. At the longer of the two

currently accessible source-phantom distances, approximately 7-10 hours of exposure are needed at 35 kVp, 0.5 mA in order to produce a usable image at the location of the phantom – direct output from tube. For a similar buildup of the scatter signal, a longer exposure time will be needed – likely 24-48 hours in order to see an image. Mapping the pixel intensity on a co-ordinate system will reveal the distribution of the scatter. Radiochromic film represents a convenient method to monitor significant amounts of spatial dosimetry results (Butson et al., 2006, 2005, 2004; Soares, 2006), in a more cost and time-effective manner than that realizable with TLDs (Muench, 1991). Gafchromic EBT film, such as the type used in the current work, is one type of radiochromic film. The first version of this film, for dosimetry purposes, has been studied for radiation therapy applications, where it is used for absorbed dose quality control related work (Martisíková et al., 2008; van Battum et al., 2008). Some positive results have been reported with the original EBT film. For 125 kVp, the film's sensitivity was found to be 0.05% higher than at 75 kVp, for a dose of 200 cGy and expressed as a function of dose at 6MV. A calculation of dose at 35 keV was performed here, using the calibration at 125 kVp because comparable half-value layers (HVL) were found. When this calculated dose was compared to ionization chamber measurements, only a 3% difference was noticed (Dugas et al., 2008). An MV calibration was also applied to EBT film, when used in determination of Compton backscatter factors, where <10% variation was expected between primary and backscatter x-rays (Mart et al., 2012). The Al HVL cannot be measured for the conventional XRF system in the current work unless an opening is created in the back wall of the shielding cabinet. With such a setup, a higher kVp source (x-ray tube) calibrator, for the film, may be feasible as an alternative to the ionization chamber measurements. In another study with the original EBT film, the sensitivity was found to be significantly lower at 35 keV than at 4MV, for doses from 50-150 cGy. The relative sensitivity of EBT2 film, by comparison, increased by ~4% over this range of doses delivered. A peak sensitivity was reported here for 30-35 keV, with lower sensitivity at 25 keV (Brown et al., 2012), in broad agreement with another study (Arjomandy et al., 2012). As with EBT2, EBT film has reported variations of ~20% at kVp energies (100 kVp) for doses in the range of 50-200 cGy (Oves et al., 2008; Richter et al., 2009). Here too (EBT), weak energy dependence has been reported (Butson et al., 2006; Chiu-Tsao et al., 2005) but confounding results have been reported for 20-34 kVp at various source-film distances. In the latter study, the small influence of dose rate on energy dependence (Rink et al., 2007), on the film's response, was eliminated by fixing the energy, or kVp setting, and changing the source-film distance, however such an assessment was found to have minimal impact on these results (Ebert et al., 2009).

The successor to this film, EBT2, was released in 2009, but homogeneity issues have been identified, thereby countering claims that enhanced accuracy would be possible (Hartmann et al., 2010; Micke et al., 2011). In the range of energies between 105 kVp and 6MV, an energy dependence of as much as 20% has been reported, depending on the particular batch of film used (Lindsay et al., 2010). This is in contrast to smaller variations: in the energy range of 50 kVp to 18 MV, including Cs-137 (662 keV) and Co-

60, an energy dependence of 4.5% (75 kVp to 18 MV) to 6.5% (50 kVp to 10 MV) have been reported (Arjomandy et al., 2010; Butson et al., 2010).

The newest version, EBT3, has been commercially available since 2011. The difference in this ratio decreases as the absorbed dose increases for 50kVp, as output by a 50 kVp, 1.4 mA with a W-anode x-ray tube (Massillon-JL, 2012). Comparable improvements were obtained in optical density versus dose for monochromatic 25-35 keV x-rays, with a decreasing dependence on energy shown from EBT to EBT2 to EBT3 film (Brown et al., 2012). In the case of the former work with EBT3 film, after about 25 Gy, the difference in the ratio of OD/dose starts to become negligible. For 1 Gy at 50 kVp, in this work, a difference in response compared to 6 MV x-rays was reported to be ~11%. Here, this variation was evaluated by examining the ratio of OD/dose at 50 kVp to that at 6MV. At energies on the scale of MV, the Compton scatter interaction dominates the photoelectric contribution and so the ratio of mass energy absorption coefficients would be unchanged here. Note that an Epson 10000 X: flatbed scanner was used at 75 and 300 dpi – the latter was found to exhibit a lower energy dependence at the higher spatial resolution. Procedures for handling and storage of such films is well documented (Lynch et al., 2006; Paelinck et al., 2007). The dependence of film readout on scanner position is easily accounted for by placing individual pieces of film at different positions on the scanner and repeating scans of the film (Hupe and Brunzendorf, 2006). Excellent results are generally obtained with Epson scanners and this would be recommended, if such work is to be undertaken. EBT3 film is recommended, however, caution is thus required when undertaking such work. Film can be obtained through Harpell Associates in Canada and the scanner required, for reading, is available at the Juravinski Cancer Center (JCC) affiliated with McMaster University.

8.2.7.2 Recomended use and exposure time estimations:

An approach to usage of this film for dosimetry with the conventional x-ray tube system is documented here. Either individual pieces or an entire sheet of exposed film may be used to measure separately the primary beam dose or the scattered dose from the copper shielding cabinet. Each piece/sheet of film used should be read 5 times using the same scanner, in the same position and orientation. An ROI at the center of each film is determined. For the same source strength, multiple pieces/sheets of film are exposed to the x-ray beam. An average of the mean pixel value of the ROI is calculated for all such films so as to establish reproducibility. This test should be performed for (a) accelerating voltages in the range of 20-50 kVp since lower voltage settings will not be practical, (b) with and without the detector head inserted into the shielding cabinet, for a fixed voltage and current and (c) with and without a shielding channel surrounding the head of the detector, for fixed voltage, current and detector head position. The ratio of optical density to dose is termed as the the sensitivity of the film and this quantity can be calculated and compared for varying beam energies (or kVp settings).

In the current application, dosimetry with EBT3 film requires longer exposures, with the conventional XRF benchtop system, so as to avoid sitting in the more volatile

region (low doses) of these curves for low energies. The dose delivered is higher, as was done with the TLD chips, and then scaled down to the equivalent in 30 minutes for *in vivo* scans. If such a dose is delivered to the film, with the conventional x-ray system, an extended exposure will be required, since ~250 cGy can be delivered in 17 hours, using the Mo 100 μm filter at 35 kVp, 0.5 mA. At full power (50 kVp, 1 mA), this would give ~13 Gy in 24 hours. This number drops to 635 cGy at 35 kVp and 1 mA. This means that ~2 days of exposure at maximum tube output or ~4 days at 35 kVp, 1 mA would be required to reach the dose regime where the dependence is sufficiently small that it can be ignored. However, such a long exposure is likely worth the time since it would offer the possibility of scaling down the dose recorded by the film to that delivered by a 30 minute exposure without encountering the low-dose regime of the film where the above ratio changes quite dramatically with dose. As per the aim of this work, the primary dose (phantom) and scattered dose contributions should be quantitatively investigated after such long exposures.

A limitation to these time calculations is that the dose used above (~250 cGy) includes scatter, which is expected to be higher with the thinner filter than with a thicker Mo filter. An accurate reading of the scattered dose may require a longer exposure time than those estimated above. Also, a linear correction against time may only be an estimate of the true correction required to the scatter contribution. The same disadvantage will enter the measurement of primary or scattered dose with a thicker filter. A way to address this would be to perform measurements at a series of exposure times, starting with shorter measurements and extending to longer ones and tracking the primary beam dose delivered and the scattered dose delivered. If a reliable estimate of dose can be obtained using an ionization chamber, such as the Radcal RC6M 6cm^3 parallel plate unsealed chamber, then a more accurate estimate of exposure time required may be obtained since the chamber will likely not require an extended exposure time to determine exposure rate in air, in mR/hr. Note that the Radcal ion chamber's energy dependence over 10-40 keV, is quoted as ±5%. By comparison, the ratio of mass-energy absorption coefficients at these two extreme energies is 70.85, in skin (ICRP), as per NIST (XCOM). With an opening drilled in the back of the shielding cabinet (see system setup in chapter 2), a HpGe detector can be inserted into the cabinet for measuring the output spectrum, which would include scatter. The superior efficiency of Ge, compared to Si (see Introduction for discussion of this and graphs), would make for Ge to be the preferred choice of detector material in the 10-40 keV range, barring interference from Ge escape peaks and Ge characteristic x-rays. As an alternative to the ionization chamber approach, an orthovoltage unit (130 kVp) is available at JCC. This assumes that the flat response of the film to energy between 50 and ~200 kVp can be trusted and may offer a rough estimate before proceeding to further work. The importance of knowing the average incident energy with this system, as a function of kVp, is crucial for such work. The validity of the constant response above 50 kVp can be evaluated with an ionization chamber.

8.2.7.3 Optically stimulated luminescence dosimeters (OSLDs):

A second approach would involve using a sparse array of Optically Stimulated Luminescent Dosimeters (OSLDs) instead of sheets of gafchromic film. Optically Stimulated Luminescence Dosimeters (OSLDs) have been extensively studied in radiotherapy applications, such as EBRT (Kerns et al., 2011; Mrčela et al., 2011; Schembri and Heijmen, 2007; Yukihara and McKeever, 2008). The phenomenon of optical stimulation is similar to that of thermoluminescence. The underlying principles governing OSLDs are known, and uses light to induce the luminescence (Jursinic, 2010; Viamonte et al., 2008; Yukihara and McKeever, 2008). Trace contaminants induce imperfections in the crystal structure of dielectric materials. Traps of electrons or holes are formed by the imperfections. When electrons and holes recombine, they are the point of origin of luminescence. The underlying mechanism is then electron or hole capture in the dosimetric traps within the structure of the crystal. An optical luminescence dosimetric trap was shown to maintain electrons for a period of 85 days (Bøtter-Jensen et al., 1997) and is similar in principle to a thermoluminescence trap (Bøtter-Jensen and McKeever, 1996). Although such traps are deep, they can be emptied with visible light (Markey et al., 1996). Stimulation and emission spectrum wavelengths are 400-700 nm and ~410 nm respectively (Markey et al., 1995). Continuous light can be used during the read out procedure (Gaza et al., 2005) and is commonly read out at a later time (Aznar et al., 2004; Edmund and Andersen, 2007).

A light emitting diode (LED) is used to stimulate the dosimeter material, with a bandpass filter. The luminescence signal is filtered with a bandpass filter and then detected with a photomultiplier tube. The straightforward repeatable readout process allows for a gradual measure of dose build-up and is a tremendous benefit over radiochromic films, where scanning and optical density calculations are required post-irradiation. As the optical stimulation process does not last long, the dosimeter's dose reading is not wiped out. It has been shown that 0.05-0.5% (high dose-low dose mode) of the signal is depleted (Al-Senan and Hatab, 2011; Jursinic, 2007). OSLDs are produced by Landauer Inc. (Glenwood, IL, USA) and are available as badges, each containing 4 dosimeters, or lose dosimeters called Dots or nanoDots (as was the case with TLDs used here), with the latter being offered with ±10% energy dependence and can be obtained with nanoDots calibrated against 80 kVp (Ding and Malcolm, 2013). Screened (2% accuracy) and regular (5%) are offered. Landauer's screened nanoDots are all similar to eachother. In this case, nanoDots within a single batch that read <2% of the required value are accepted. These assure the user that such sensitivity is to be expected 95% of the time. Aluminum oxide (Al_2O_3) is the chosen OSLD material (Akselrod et al., 1990a; McKeever et al., 1999) because of simple fabrication and high sensitivity.

For a single batch of dosimeters, Landauer quotes 2% variation in (screened) relative sensitivities. Practically, response has been found to show ~4% variation. Relative sensitivity was thus calculated, in one study, by comparing the average absorbed dose to an individual dosimeter reading, $Dose_{AVG}/Dose_{dosim}$. For an individual batch of n dosimeters, multiple readings are obtained per dosimeter and the average is calculated as

$Dose_{AVG}$. Multiple relative sensitivity factors for each of dosimeter were thus obtained, followed by irradiation to 0.5 Gy and then optical bleaching for ~24 hours with a 22 W fluorescence lamp in order to remove radiation effects of this exposure 0.5 Gy. The average sensitivity factor was found to vary by <1% at 1 StdDev, which is a substantial improvement over the manufacturer's quoted value (Reft, 2009).

OSLD studies at low energies are hard to come by and this study did not investigate kVp settings below 125 kVp. These authors did, however, notice a commonly observed phenomenon with OSLDs that a transient period exists in dose response to readout, after irradiation. Stabilization of the read-out signal after ~8 minutes post irradiation was found and stability to within 2% for the subsequent 2.5 days has been noted (Jursinic, 2007), although an even smaller 0.3% signal-loss per day was noted from 10 minutes to 11 days post-irradiation (Reft, 2009). It is postulated that OSLDs may have a transient period after irradiation, in this case due to unstable traps (Jursinic, 2007). This is a minimal waiting time before commencing the readout process and is considerably shorter than the time required to perform the full image analysis required for EBT film optical densitrometry. One research group waited 0.5 hours to 1 day before reading the nanoDot dosimeters post-irradiation (Al-Senan and Hatab, 2011).

Optical bleaching can be used to remove the effects of OSLD irradiation and is commonplace in OSLD dosimetry (Al-Senan and Hatab, 2011; Jursinic, 2007; Reft, 2009). Measurement uncertainty of <1% (net counts) has been reported regardless of whether a single use is deployed, after which the dosimeters are discarded, or multiple uses (Jursinic, 2007; Yukihara et al., 2005). Literature shows that up to 2 Gy absorbed dose, bleaching leaves relative sentitivity unchanged but removes the dosimeter's signal. For 8 Gy, bleaching reduced the radiation-induced signal to 2.7 times the pre-irradiation readings. Deeper energy traps are filled for higher dose exposures. The remaining signal was found to be removed by bleaching with a tungsten halogen lamp (Reft, 2009).

Good dose linearity has been demonstrated for nanoDot OSLDs in the CT, radiography, therapeutic and mammography energy ranges (Danzer et al., 2007; Jursinic, 2007). Reproducibility of <1% has been demonstrated at 6 MV (Jursinic, 2007). Here, the standard error given by $1/\sqrt{\text{counts}}$ was taken as an indication of reproducibility. At lower energies (25-120 kVp), reproducibility (COV) of counts read out was reported to be 2.9-3.6% over 13 dosimeters and relative standard deviations of 4.3-4.8% have been reported for 25-120 kVp settings over an entire batch (Al-Senan and Hatab, 2011). This is similar to 4.2% reported elsewhere, with 2.5% found for an individual dosimeter (Viamonte et al., 2008). The COV of a particular batch must be comparable to the variation of the incident radiation field.

For sufficiently low energies, Al_2O_3 does, however, over-respond to low-energy x-rays, including orthovoltage x-rays (200-500 keV) and superficial x-rays, when compared against MV energies. A comparison to gafchromic film will be shown later. Work with an Ir-192 source (average energy of ~380 keV), the sensitivity (counts/dose)

was 6% higher than that for MV photons (Jursinic, 2007), with comparable elevation reported elsewhere (Akselrod et al., 1990b). In the energy range of 29-62 keV, correction factors were calculated as ionization chamber reading to nanoDot readout. These were found to vary from 0.81 to 1.56 for 2.0-9.8 HVL Aluminum. It was, though, reassuring that the calculated values were found to be similar to those provided by the manufacturer, although the manufacturer's measurement details were not available. The authors' recommendation was that a well characterized energy measurement be in place before proceeding with OSLD work in this energy range (Al-Senan and Hatab, 2011). Note, that in this work, a comparison to the ratio of μ_{en}/ρ could have been made, but was not reported. This would have allowed for the efficiency of the scaling factor, as a first order correction, to be evaluated.

8.2.7.4 Preliminary work to demonstrate OSLDs usage at low energies and partial application:

A Landauer InLight^{TM} system was borrowed from University Health Network (UHN) in Toronto for evaluation. At this time, a brief test of the performance was performed with the intention of further commenting on the nature of the work recommended above.

As part of the InLight system, 4 separate OSL elements are placed side-by-side inside a single dosimeter badge. Each of the elements is placed under a different filter material (copper, aluminum, plastic or open) and thickness. The badges cannot be opened and hence the filters cannot be removed. Filtration is present above and below the four individual elements (Perks et al., 2007). Calibration was performed against a Cs-137 source, by the manufacturer and dosimeter badges at 0 amd 500 mrem (three badges each) were provided. The badges were contained in clear protective plastic cases.

As an evaluation of the performance of the InLight system, a Cd-109 source was used; it has dominant lines at the Ag Kα and Kβ energies of ~22 and 25 keV. Two dosimeter badges were removed from the clear plastic covers and placed in front of this source for 21.75 hours, at a source-dosimeter distance of ~10 cm. After exposure, the badges were stored in a light-tight cabinet for a period of 39 hours before reading, so as to avoid the transient period. Readouts were performed using a microStar Reader designed by Landauer with a slot into which the badge could be inserted. Two badges were used, placed side-by-side to eachother. Multiple readouts were performed for each badge, with readout of a single badge taking ~15 seconds, including time to record counts and doses.

A summary of the results is now discussed. The doses delivered to the Al_2O_3 elements were ~175 mrem over the ~22 hour exposures. Ideally, dosimeter elements would not be filtered since such low energies are heavily attenuated in particular by the copper and aluminum filters. Landauer's nanoDot dosimeters are bare sensitive elements and do not contain any added filtration. The COV (counts) for the 0 and 500 mrem calibrated dosimeter badges ranged from 5.19-8.39% and 1.98-2.91% respectively. This

was calculated by combining all 4 elements from all 3 chips, per dose setting, at 5 separate random readouts per chip. When the 4 elements were considered separately, the COVs ranged from 2.92-4.49%, 4.65-7.23% and 5.27-11.85% for the three 0 mrem badges. For the 500 mrem badges, these were 0.46-3.11%, 0.46-2.99% and 1.27-4.14%. If the Cd-109 irradiated badges are considered (4 elements kept separate), the ranges were 1.47-7.60% and 1.20-9.52% for badges 1 and 2 respectively. The number of counts registered in the last two elements was one order of magnitude lower than in the first two elements.

The standard error [1/sqrt(counts)] for a single reading was found to be 15.27-15.31% and 4.21-4.38% for 0 and 500 mrem respectively, for all 5 trials of all 3 chips per dose setting, when all the 4 elements were considered separately. For the Cd-109 irradiations, the standard errors were 2.75±0.02, 2.69±0.02, 14.86±0.02 and 12.83±0.51 for the first trial and 2.72±0.02, 2.65±0.02, 15.85±0.73 and 11.96±0.31 for the second trial, for the 4 elements respectively. The combined results are not shown for the source measurements here, due to the large variation for the last two elements. This is likely due to a stronger filter being used there than for the first two elements. This is also the likely explanation for the reduced counts in these elements. COVs of <4% were reported earlier with Landauer's nanoDot dosimeters, which are bare sensitive elements with no protecting housing and no filtration in front of or behind them. Standard errors of <1% were mentioned in literature results above, but the preliminary testing here indicates larger values. A very low dose was delivered here and this error would be expected to improve with better counting statistics. The filtered elements would require a longer exposure time in order to deliver a sufficiently strong dose that the number of counts is high enough to yield COVs that are comparable to those reported for the nanoDot dosimeters in the literature. Standard errors of <5% have been reported elsewhere and are in agreement with results of this testing.

The relative sensitivities (dose, in mrem) ranged from 0.64±0.46 to 0.70±0.46 and 1.00±0.03 to 1.00±0.04 for 0 and 500 mrem calibration badges respectively, when the 60 calibrated deep, shallow and lens absorbed dose readings were combined, per dose setting. No trends were seen in the relative sensitivity or individual dose readings (deep, shallow or lens). For Cd-109 exposed badges, the relative sensitivities ranged from 1.00±0.02 to 1.02±0.02 for the first trial and were equal at 1.00±0.01 for the second trial.

These preliminary results indicate the benefit of depositing a higher dose in the chips. Readings with the Cd-109 source were performed over ~22 hours at a source-dosimeter distance of ~10 cm. This preliminary work offers indications about future extensive dosimetry work that is possible with this project, particularly for scatter monitoring. However, the dose delivered by the Cd-109 source was not on the order of grays, even over ~22 hours, as most literature reports for OSLD-based work. Thus, trends in the above results would need to be investigated as a function of dose delivered, at this energy. However, this energy very close to what will be used in the proposed work and the results are quite encouraging if a sufficiently high dose can be delivered – approx.

100 mrem should be the minimum. Due to time constraints, a post-irradiation transient period, dose linearity at this energy and daily recommended QC testing of the microStar reader were not investigated. Optical bleaching is likely not possible with dosimeter badges since the badges would need to be physically opened and it appears that they were heat-sealed or sold as a single fully-enclosed unit without the possibility of removing the bare elements for direct unfiltered exposures. Finally, the influence of energy is not present in the above results; in particular COV and relative sensitivity would need careful monitoring as energy is changed. Cd-109 emits strong Ag K-shell lines, which will dominate the incident spectrum. This is substantially lower than the majority of results in the literature. With its durability, low-energy applications of OSLDs are likely to be found in the literature in coming years and should be monitored for this application.

A brief evaluation of various counting intervals on the Innov-X Delta unit was performed, in an attempt to illustrate the potential for investigating the scatter off the metallic shielding. For this investigation, the Innov-X delta handheld analyzer was used in benchtop mode. The badges were placed directly on the kapton window and beam 1 and beam 2 exposures were performed for various time intervals (combined results shown). Backing was not used for this test and, due to time constraints, a single exposure was performed per badge. The badges were counted ~10-15 minutes after each exposure and the following exposure was then performed. As with the calibration and Cd-109 badges, multiple readouts were performed per badge exposed with this system. The average net counts recorded (±StdDev) are shown for each element in the badge, in figure 8.5.

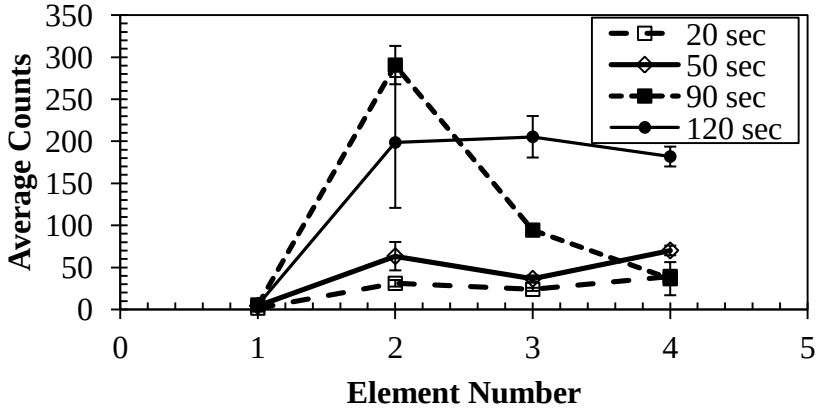

Figure 8.5: Plot of net counts registered for three counting intervals.

The error bars represent the standard deviation of 4 separate badge readouts. General, though not universal trends, are noted. More counts are collected as a function of time, except for 90 and 120 seconds for element 2, where the shorter duration has produced more counts. Also, for element 4, the same is true for 90 and 50 second exposures. At 90 seconds, elements #2 and 4 appear to be outliers although, except for a reading error, do not have an explanation. Badge positioning may be mainly attributable to this, since

uniformly distributed scatter off the metallic shielding lid would be expected as time is increased. The rate at which scatter appears to be growing, with time, is non-linear as evidenced from the readings for elements 2 and 4 for 20, 50 and 120 seconds. The increase from 50 – 120 seconds is much larger than the expected linear rise. The magnitude of the scatter may be growing with time but, if the same positioning is replicated for each exposure, the scatter distribution across the four badge elements is not expected to change greatly. This variation is, however, observed and, despite the large error bars, warrants further investigation. The first element has been filtered out sufficiently that net counts of nearly zero are registered for all counting times. The difficulty with positioning should be further investigated as a possible contributor to the jump from readings for 50-120 seconds. Note that dose readings could not be obtained here since an error message was repeatedly displayed for all attempted read outs performed with badges subjected to exposures with this system only. Similar problems were not encountered with the Cd-109 exposures. Manual conversion of the raw readings, in counts, to dose could not be performed since information required for this calculation was not available. Any dosimeter placed around the incident beam's isocenter would display the RAT error when reading. The error message is initiated when the ratio of readings between elements does not fall within the manufacturer's pre-programmed acceptable range. One solution to this would be to place a bolus in front of the dosimeter, however this is impractical for the current application.

The standard error (%), relative sensitivity and COV (%) are shown in table 8.1.

Table 8.1: List of (a) standard error (%), (b) relative sensitivity (using counts readings) and (c) COV (%) for four separate exposure times.

Time	Elem #1	Elem #2	Elem #3	Elem #4
20 sec	75 ± 24	18 ± 1	21 ± 1	16 ± 1
50 sec	51 ± 21	13 ± 1	17 ± 1	12 ± 0
90 sec	53 ± 25	6 ± 0	10 ± 0	18 ± 6
120 sec	46 ± 10	7 ± 1	7 ± 0	7 ± 0

(a)

Time	Elem #1	Elem #2	Elem #3	Elem #4
20 sec	0.30 ± 1.10	1.02 ± 0.15	1.00 ± 0.07	1.02 ± 0.16
50 sec	-0.17 ± 1.78	1.05 ± 0.23	1.01 ± 0.10	1.01 ± 0.08
90 sec	1.71 ± 1.68	1.00 ± 0.08	1.00 ± 0.05	1.33 ± 0.91
120 sec	1.14 ± 0.49	1.12 ± 0.43	1.01 ± 0.12	1.00 ± 0.07

(b)

Time	Elem #1	Elem #2	Elem #3	Elem #4
20 sec	117.38	12.58	7.70	16.74
50 sec	94.85	117.62	103.51	61.01
90 sec	64.12	37.79	91.11	146.68
120 sec	39.27	33.94	10.41	5.62

(c)

The COV and standard errors are substantially higher than that recorded with either the Cd-109 source or the calibration dosimeters. Like the absolute readout of counts, these may also be influenced by scatter off the shielding lid of system. The relative sensitivities are in general agreement with those reported in the literature and with the other dosimeters tested (calibration and Cd-109) but the standard deviations are consistently much larger than the values found with those dosimeters. Given the consistency in readouts obtained with the Cd-109 source and the fact that the average energy emitted by the handheld (beams 1 and 2) is ~ 22 keV, same as for Cd-109, similar results would be expected for both these quantities. The counts recorded were substantially lower, in general. This would explain the elevated standard error. However, the COV is much higher than earlier and is a direct result of the readout process. Exposures of the length performed for this evaluation are likely at the low end of what should be used with this dosimeter type. For such a small number of detected counts, the influence of the readout process and hardware inefficiencies may be attributable to as much as an ~30% increase in relative sensitivity and ~65% rise in standard error. The COV values are quite high and reflect the substantially larger standard deviations reported with this readout process, compared to the Cd-109 source or calibration dosimeters. If sufficient counts are recorded, then all three of these quantities should be <5%. These results will not change with correction for filtration but, given the low energies in use, the nanoDot (bare) OSLDs are recommended for future work.

The small number of measurements and single exposure per dosimeter are limitations of this work with the Innov-X Delta unit, but the reproducibility of the Cd-109 results (COV) is quite encouraging. Testing the linearity of the dosimeter material with dose, for a fixed energy, is achievable with this system since exposure times can be lengthened. A scatter-free test of the same can be performed using the Cd-109 source. This would allow for an estimate of role that scatter is playing in the total dose deliverd by this handheld unit.

8.2.7.5 Comparison of alternative dosimeter materials:

A direct comparison between these two materials, and a few others, is summarized in table 8.2.

Table 8.2: List of effective atomic number for various materials that can be used as dosimeters.

Mixture	Zeff (3.5)	Zeff (2.94)	Auto Zeff	Rel Zeff[1]	Ratio (avg±stdev)[2]
Al_2O_3	11.28	11.14	10.88	1.54	3.43 ± 0.04
CaSO4	15.62	15.22	14.17	2.13	10.31 ± 0.58
$Li_2B_4O_7$[3']	7.32	7.25	7.00	1.00	0.851 ± 0.002
CaF_2	16.91	16.54	15.47	2.30	12.89 ± 0.83
Li(F)[4']	8.31	8.20	7.62	1.13	1.20 ± 0.01
EBT2	7.18	6.96	6.08	0.92	0.85 ± 0.01
Water	7.51	7.42	5.78		
Tissue (ICRU-4	7.35	7.26	5.75		
Skin (ICRP)	7.34	7.18	5.68		
Tissue (ICRP)	7.39	7.22	5.67		
Tissue (ICRU-44)	7.63	11.24	5.92		
Adipose (ICRP)	6.38	6.23	4.76		

[1]calculated relative to Skin (ICRP), using Zeff with a = 3.5, [2]calculated over 15-30 keV, [3']used in previous work on Arsenic project, [4']used in current work on Arsenic project

where Z_{eff} was calculated using $Z_{eff} = \sqrt[m]{\sum_{i=1}^{n} a_i {Z_i}^m}$, where Z_i is the atomic number of element i and a_i is the electron fraction in the i_{th} element (Attix, 1986). Here, the ratio (15-20 keV) of mass-energy absorption coefficients (last column) is calculated with respect to skin (ICRP). The exact definition of Z_{eff} is debatable (Taylor et al., 2012), in particular regarding the value of the exponent m. Note that the composition of EBT2 was taken from a study in the literature (Ebert et al., 2009) and is the same as that for EBT3. This value was chosen as 3.5 for the purposes of this table, though a range of 3-4 is often suggested (Bos, 2001). A value of 2.94 has also been used (Khan, 2003). Auto Z_{eff} is a custom written software that was developed by researchers at the RMIT University in Melbourne, Australia. It is used here, with their permission. The software makes used of the total cross section, and hence energy, in the definition of Z_{eff}. A detailed description of the calculation is provided in published work (Taylor et al., 2012) and draws on spectra from various sources covering the energy range of a few keV to MeV. In terms of Z_{eff}, $Li_2B_4O_7$ is the best material, followed by EBT3 and Li(F). In terms of energy dependence in the energies of interest, which is characterized by the last column (ratio in the range of 15-20 keV), $Li_2B_4O_7$ and EBT3 have the superior ratio of μ_{en}/ρ (15% difference relative to skin), followed by Li(F). If Auto Z_{eff} results are used to calculate this ratio, then EBT3 is the best material, followed by $Li_2B_4O_7$ and then Li(F). Li(F) and $Li_2B_4O_7$ have already been used for the purposes of this project and the compact design of Li(F) TLD chips is found to be superior in terms of spatial resolution. Gafchromic film

and OSLDs (nanoDot: 5 mm diameter X 0.2 mm thick) are direct competitors to TLDs (3.2 X 3.2 X 0.89 mm – L X W X thick) in this regard, with the added benefit of read-out convenience which can be done on-site. OSLDs also offer re-usability. The ratio of μ_{en}/ρ is shown in figure 8.6 as a function of energy.

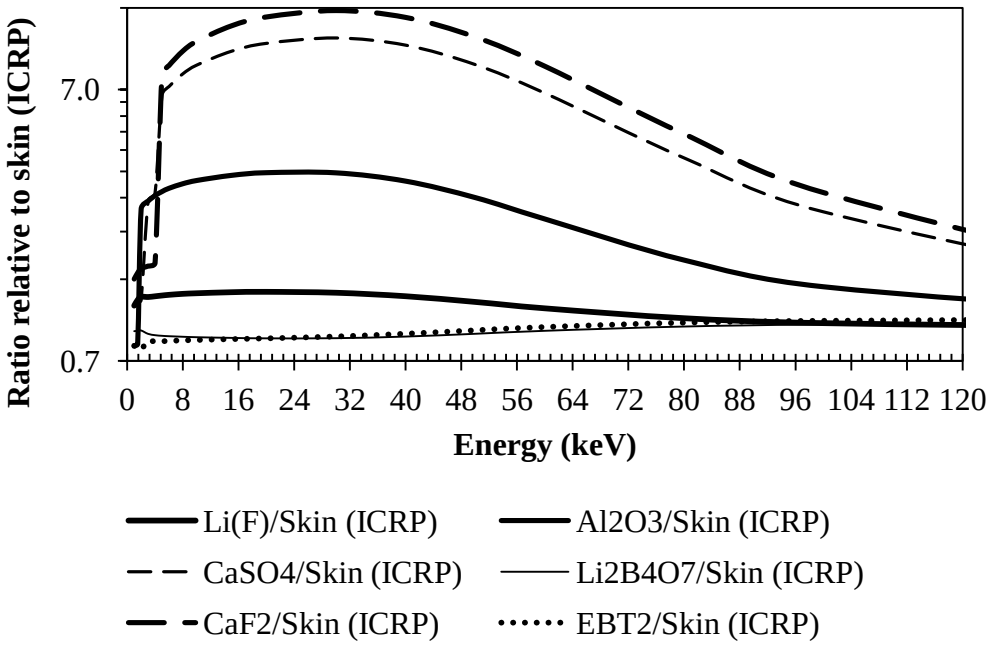

Figure 8.6: Ratio of mass-energy absorption coefficient in material to skin (ICRP) as a function of energy, covering the range of energies from 0-120 keV.

The flatness of the Li(F) and $Li_2B_4O_7$ curves are noted demonstrating their superior usefulness over the range of energies plotted. From this ratio it is seen why low energy kVp x-rays prefer TLD or radiochromic film to Al_2O_3. The kVp response (keV energies) of the OSLDs show an elevated response at lower energies, attributed to higher photoelectric cross-sections at these energies. The dosimeter's energy response is typically estimated from the ratio of μ_{en}/ρ in the dosimeter material to that in water (Reft, 2009) at a different energy because transient charge particle equilibrium is met (Attix, 1986).

The convenience of faster post-exposure analysis of gafchromic film or OSLDs are their advantages, over Li(F) TLDs, but do not appear quantitatively. For this application of scatter dose measurement, cost and particularly time effectiveness is superior for these two approaches due to the need for several exposures. The time savings mean that dosimetry under various configurations can be investigated in a very short period of time. Gafchromic EBT3 film comes with Film QA Pro 3.0 software, which allows for calibration and exposure in one scan and subsequent analysis. In the film's active component crystals, the rate of the polymerization decreases with time. Previously,

an extended waiting period was required between exposure and scanning, but this is reduced to >4 times the difference between scanning the first and last reference (calibration) films, making this process also very fast. If the calibration source used is able to deliver quickly the required dose to the film, then the calibration process should be performed after the application exposure which is likely to be several hours or days in length. All calibration films (calibrated against increasing dose up to the maximum expected dose) should be scanned at the same time as the application film so as to eliminate the error in dose due to the phenomenon described above. By comparison, after a long exposure (~16-24 hours or longer) TLDs need to be shipped back to the manufacturer for reading. The former can take several weeks, and so this is a rather lengthy process and can be quite expensive when used for an application such as tracking scatter content where frequent exposures are required. The usefulness of OSLDs are their instantaneous readout capabilities and reusability. Gafchromic film cannot be reused and data analysis is required post-exposure, as mentioned earlier. However, despite these benefits, the non-ideal low–energy response of either dosimetry material requires caution. Results with these dosimeters will reveal trends (relative results) that should not change with TLDs and, therefore, can be used as a pre-cursor to TLD exposures to verify their results. Use with a properly calibrated ionization chamber is thus strongly recommended.

The nanoDot OSLDs can be attached to the walls of the cabinet during exposures. They can then be read out with an immediate quantitative dose estimate. A benefit is that the experiment can be repeated multiple times, using different primary x-ray beam filters (with the conventional x-ray tube system) or voltage/current combinations. The other downside of using film is that an appropriate scanner is required to extract quantitative information from the film. Such a scanner is available in at least one of the University's Health Sciences facilities, however it cannot be transported to the x-ray laboratory. A benefit of the OSLD reader is it's smaller form factor, allowing for superior portability. OSLD exposure times may not be greatly reduced, compared to film exposures, as a minimum of ~100 mrem should be delivered to the dosimeters in order to rely on dose extraction. The exposures to either OSLD or film should be first tracked by sequentially ramping up the voltage and current and recording optical density or dose readings for each tube setting chosen. A direct comparison of TLD, OSLD and gafchromic film dosimetry is also possible.

References:

Abedin, M.J., Feldmann, J., Meharg, A.A., 2002. Uptake kinetics of arsenic species in rice plants. Plant Physiol. 128, 1120–8.

Abernathy, C.O., Liu, Y.P., Longfellow, D., Aposhian, H. V, Beck, B., Fowler, B., Goyer, R., Menzer, R., Rossman, T., Thompson, C., Waalkes, M., 1999. Arsenic: health effects, mechanisms of actions, and research issues. Environ. Health Perspect. 107, 593–7.

Abu Atiya, I., 2012. In-Vivo X-Ray Fluorescence Assessment of Iron Levels in the Skin for β-Thalassemia Patients. Open Access Diss. Theses.

Agency for Toxic Substances and Disease Registry (ATSDR), 2007. Toxicological Profile for Arsenic. Atlanta, GA, USA.

Ahlgren, L., Mattsson, S., 1981. Cadmium in man measured in vivo by x-ray fluorescence analysis. Phys. Med. Biol. 26, 19–26.

Ahmed, S.N., 2007. Physics and Engineering of Radiation Detection (Google eBook). Academic Press.

Ahsan, H., Chen, Y., Parvez, F., Zablotska, L., Argos, M., Hussain, I., Momotaj, H., Levy, D., Cheng, Z., Slavkovich, V., van Geen, A., Howe, G.R., Graziano, J.H., 2006. Arsenic exposure from drinking water and risk of premalignant skin lesions in Bangladesh: baseline results from the Health Effects of Arsenic Longitudinal Study. Am. J. Epidemiol. 163, 1138–1148.

Akselrod, M.S., Kortov, V.S., Kravetsky, D.J., Gotlib, V.I., 1990a. Highly Sensitive Thermoluminescent Anion-Defect Alpha-Al2O3:C Single Crystal Detectors. Radiat Prot. Dosim. 33, 119–122.

Akselrod, M.S., Kortov, V.S., Kravetsky, D.J., Gotlib, V.I., 1990b. Highly Sensitive Thermoluminescent Anion-Defective Alpha-Al203:C Single Crystal Detectors. Radiat Prot. Dosim. 32, 15–20.

Alain, G., Tousignant, J., Rozenfarb, E., 1993. Chronic Arsenic Toxicity. Int. J. Dermatol. 32, 899–901.

Alaluf, S., Heinrich, U., Stahl, W., Tronnier, H., Wiseman, S., 2002. Dietary Carotenoids Contribute to Normal Human Skin Color and UV Photosensitivity. J. Nutr. 132, 399–403.

Al-Senan, R.M., Hatab, M.R., 2011. Characteristics of an OSLD in the diagnostic energy range. Med. Phys. 38, 4396.

Amster, E., Tiwary, A., Schenker, M.B., 2007. Case report: potential arsenic toxicosis secondary to herbal kelp supplement. Environ. Health Perspect. 115, 606–8.

Andreae, M.O., 1979. Arsenic speciation in seawater and interstitial waters: the influence of biological-chemical interactions on the chemistry of a trace element. Limnol. Ocean. (United States) 24:3.

Antman, K.H., 2001. Introduction: The History of Arsenic Trioxide in Cancer Therapy. Oncologist 6, 1–2.

Argos, M., Kalra, T., Rathouz, P.J., Chen, Y., Pierce, B., Parvez, F., Islam, T., Ahmed, A., Rakibuz-Zaman, M., Hasan, R., Sarwar, G., Slavkovich, V., van Geen, A., Graziano, J., Ahsan, H., 2010. Arsenic exposure from drinking water, and all-cause and chronic-disease mortalities in Bangladesh (HEALS): a prospective cohort study. Lancet 376, 252–8.

Arjomandy, B., Tailor, R., Anand, A., Sahoo, N., Gillin, M., Prado, K., Vicic, M., 2010. Energy dependence and dose response of Gafchromic EBT2 film over a wide range of photon, electron, and proton beam energies. Med. Phys. 37, 1942.

Arjomandy, B., Tailor, R., Zhao, L., Devic, S., 2012. EBT2 film as a depth-dose measurement tool for radiotherapy beams over a wide range of energies and modalities. Med. Phys. 39, 912–21.

Attix, F.H., 1986. Introduction to Radiological Physics and Radiation Dosimetry. John Wiley & Sons.

Azcue, J.M., Mudroch, A., Rosa, F., Hall, G.E.M., 1994. Effects of abandoned gold mine tailings on the arsenic concentrations in water and sediments of jack of clubs lake, B.C. Environ. Technol. 15, 669–678.

Aznar, M.C., Andersen, C.E., Bøtter-Jensen, L., Bäck, S.Å.J., Mattsson, S., Kjær-Kristoffersen, F., Medin, J., 2004. Real-time optical-fibre luminescence dosimetry for radiotherapy: physical characteristics and applications in photon beams. Phys. Med. Biol. 49, 1655–1669.

Bae, D.-S., 2001. Toxicological Interactions among Arsenic, Cadmium, Chromium, and Lead in Human Keratinocytes. Toxicol. Sci. 63, 132–142.

Balakumar, P., Kaur, J., 2009. Arsenic exposure and cardiovascular disorders: an overview. Cardiovasc. Toxicol. 9, 169–76.

Barrett, H., Eskin, J., Barber, H., 1995. Charge Transport in Arrays of Semiconductor Gamma-Ray Detectors. Phys. Rev. Lett. 75, 156–159.

Barton, A., McLean, B., 2013. An unusual case of peripheral neuropathy possibly due to arsenic toxicity secondary to excessive intake of dietary supplements. Ann. Clin. Biochem. 50, 496–500.

Behinaein, S., Chettle, D.R., Atanackovic, J., Egden, L.M., Fleming, D.E.B., Nie, L.H., Richard, N., Stever, S., 2011. In vivo measurement of lead in the bones of smelter workers using the four-element "clover-leaf" geometry detector system. Phys. Med. Biol. 56, 653–665.

Berger, M.J., Coursey, J.S., Zucker, M.A., Chang, J., 2005. ESTAR, PSTAR, and ASTAR: Computer Programs for Calculating Stopping-Power and Range Tables for Electrons, Protons, and Helium Ions (version 1.2.3) (Gaithersburg,

MD: National Institute of Standards and Technology) [WWW Document]. URL http://www.nist.gov/pml/data/star/index.cfm
Berger, M.J., Hubbell, J.H., Seltzer, S.M., Chang, J., Coursey, J.S., Sukumar, R., Zucker, D.S., Olsen, K., 2010. XCOM: Photon Cross Section Database (version 1.5) National Institute of Standards and Technology, Gaithersburg, MD. Retrieved: January, 2010 from http://physics.nist.gov/xcom [WWW Document]. URL http://www.nist.gov/pml/data/xcom/index.cfm
Bernstam, L., Lan, C.-H., Lee, J., Nriagu, J.O., 2002. Effects of Arsenic on Human Keratinocytes: Morphological, Physiological, and Precursor Incorporation Studies. Environ. Res. 89, 220–235.
Biggs, M. Lou, Kalman, D.A., Moore, L.E., Hopenhayn-Rich, C., Smith, M.T., Smith, A.H., 1997. Relationship of urinary arsenic to intake estimates and a biomarker of effect, bladder cell micronuclei. Mutat. Res. Mutat. Res. 386, 185–195.
Bos, A.J.J., 2001. High sensitivity thermoluminescence dosimetry. Nucl. Instruments Methods Phys. Res. Sect. B 184, 3–28.
Bøtter-Jensen, L., Agersnap Larsen, N., Markey, B.G., McKeever, S.W.S., 1997. Al2O3:C as a sensitive OSL dosemeter for rapid assessment of environmental photon dose rates. Radiat. Meas. 27, 295–298.
Bøtter-Jensen, L., McKeever, S.W.S., 1996. Optically Stimulated Luminescence Dosimetry Using Natural and Synthetic Materials. Radiat. Prot. Dosimetry 65, 273–280.
Brown, L., Feynman, R., 1952. Radiative Corrections to Compton Scattering. Phys. Rev. 85, 231–244.
Brown, R.M., Newton, D., Pickford, C.J., Sherlock, J.C., 1990. Human Metabolism of Arsenobetaine Ingested with Fish. Hum. Exp. Toxicol. 9, 41–46.
Brown, T.A.D., Hogstrom, K.R., Alvarez, D., Matthews, K.L., Ham, K., Dugas, J.P., 2012. Dose-response curve of EBT, EBT2, and EBT3 radiochromic films to synchrotron-produced monochromatic x-ray beams. Med. Phys. 39, 7412–7.
Buchet, J.P., Lauwerys, R., Roels, H., 1981. Urinary excretion of inorganic arsenic and its metabolites after repeated ingestion of sodium metaarsenite by volunteers. Int. Arch. Occup. Environ. Health 48, 111–118.
Butson, M.J., Cheung, T., Yu, P.K.N., 2004. Radiochromic film: the new x-ray dosimetry and imaging tool. Australas. Phys. Eng. Sci. Med. 27, 230–230.
Butson, M.J., Cheung, T., Yu, P.K.N., 2005. XR type-R radiochromic film x-ray energy response. Phys. Med. Biol. 50, N195–9.
Butson, M.J., Cheung, T., Yu, P.K.N., 2006. Weak energy dependence of EBT gafchromic film dose response in the 50kVp–10MVp X-ray range. Appl. Radiat. Isot. 64, 60–62.
Butson, M.J., Yu, P.K.N., Cheung, T., Alnawaf, H., 2010. Technical Note: Energy response of the new EBT2 radiochromic film to x-ray radiation. Radiat. Meas. 45, 836–839.
Carvalho, M.L., Rodrigues Ferreira, F.E., Neves, M.C.M., Casaca, C., Cunha, A.S., Marques, J.P., Amorim, P., Marques, A.F., Marques, M.I., 2002. Arsenic detection in nineteenth century Portuguese Kingpost mortem tissues by energy-dispersive x-ray fluorescence spectrometry. X-Ray Spectrom. 31, 305–309.
Centeno, J.A., Mullick, F.G., Martinez, L., Page, N.P., Gibb, H., Longfellow, D., Thompson, C., Ladich, E.R., 2002. Pathology related to chronic arsenic exposure. Environ. Health Perspect. 110 Suppl , 883–6.
Ch'i, I.-C., Blackwell, R.Q., 1968. A controlled retrospective study of Blackfoot disease, an endemic peripheral gangrene disease in Taiwan. Am. J. Epidemiol. 88, 7–24.
Chen, C.-J., Chiou, H.-Y., Chiang, M.-H., Lin, L.-J., Tai, T.-Y., 1996. Dose-Response Relationship Between Ischemic Heart Disease Mortality and Long-term Arsenic Exposure. Arterioscler. Thromb. Vasc. Biol. 16, 504–510.
Chen, G., Djuric, Z., 2001. Carotenoids are degraded by free radicals but do not affect lipid peroxidation in unilamellar liposomes under different oxygen tensions. FEBS Lett. 505, 151–154.
Chiou, H.-Y., Huang, W.-I., Su, C.-L., Chang, S.-F., Hsu, Y.-H., Chen, C.-J., 1997. Dose-Response Relationship Between Prevalence of Cerebrovascular Disease and Ingested Inorganic Arsenic. Stroke 28, 1717–1723.
Chiou, P.W.-S., Chen, K.-L., Yu, B., 1997. Effects of Roxarsone on Performance, Toxicity, Tissue Accumulation and Residue of Eggs and Excreta in Laying Hens. J. Sci. Food Agric. 74, 229–236.
Chiu-Tsao, S.-T., Ho, Y., Shankar, R., Wang, L., Harrison, L.B., 2005. Energy dependence of response of new high sensitivity radiochromic films for megavoltage and kilovoltage radiation energies. Med. Phys. 32, 3350.
Cullen, W.R. (Ed.), 2008. Is Arsenic an Aphrodisiac?: The Sociochemistry of an Element. Royal Society of Chemistry.
Cullen, W.R., Reimer, K.J., 1989. Arsenic speciation in the environment. Chem. Rev. 89, 713–764.
Da Silva, E., Pejović-Milić, A., Heyd, D. V., 2008. The use of teeth as the site for the in vivo or ex vivo quantification of skeletal strontium by energy-dispersive X-ray fluorescence spectrometry: A feasibility study. J. Anal. At. Spectrom. 23, 527–534.
Danielson, C., Houseworth, J., Skipworth, E., Smith, D., McCarthy, L., Nanagas, K., 2006. Arsine toxicity treated with red blood cell and plasma exchanges. Transfusion 46, 1576–9.
Danzer, J., Dudney, C., Seibert, R., Robison, B., Harris, C., Ramsey, C., 2007. TH-C-M100E-02: Optically Stimulated Luminescence of Aluminum Oxide Detectors for Radiation Therapy Quality Assurance. Med. Phys. 34, 2628.

Das, D., Chatterjee, A, Mandal, B.K., Samanta, G., Chakraborti, D., Chanda, B., 1995. Arsenic in ground water in six districts of West bengal, India: the biggest arsenic calamity in the world. Part 2. Arsenic concentration in drinking water, hair, nails, urine, skin-scale and liver tissue (biopsy) of the affected people. Analyst 120, 917–24.
Ding, G.X., Malcolm, A.W., 2013. An optically stimulated luminescence dosimeter for measuring patient exposure from imaging guidance procedures. Phys. Med. Biol. 58, 5885–97.
Druwe, I.L., Vaillancourt, R.R., 2010. Influence of arsenate and arsenite on signal transduction pathways: an update. Arch. Toxicol. 84, 585–96.
Dugas, J.P., Oves, S.D., Sajo, E., Matthews, K.L., Ham, K., Hogstrom, K.R., 2008. Monochromatic beam characterization for Auger electron dosimetry and radiotherapy. Eur. J. Radiol. 68, S137–S141.
Duker, A.A., Carranza, E.J.M., Hale, M., 2005. Arsenic geochemistry and health. Environ. Int. 31, 631–641.
Ebert, M.A., Asad, A.H., Siddiqui, S.A., 2009. Suitability of radiochromic films for dosimetry of low energy X-rays. J. Appl. Clin. Med. Phys. 10, 232–240.
Edmund, J.M., Andersen, C.E., 2007. Temperature dependence of the Al2O3:C response in medical luminescence dosimetry. Radiat. Meas. 42, 177–189.
Enterline, P.E., Henderson, V.L., Marsh, G.M., 1987. Exposure to arsenic and respiratory cancer. A reanalysis. Am. J. Epidemiol. 125, 929–38.
Eskin, J.D., Barrett, H.H., Barber, H.B., Woolfenden, J.M., 1996. The effect of pixel geometry on spatial and spectral resolution in a CdZnTe imaging array. In: 1995 IEEE Nuclear Science Symposium and Medical Imaging Conference Record. IEEE, pp. 544–548.
Ettinger, A.S., Zota, A.R., Amarasiriwardena, C.J., Hopkins, M.R., Schwartz, J., Hu, H., Wright, R.O., 2009. Maternal arsenic exposure and impaired glucose tolerance during pregnancy. Environ. Health Perspect. 117, 1059–1064.
Feng, Z., Xia, Y., Tian, D., Wu, K., Schmitt, M., Kwok, R.K., Mumford, J.L., 2001. DNA damage in buccal epithelial cells from individuals chronically exposed to arsenic via drinking water in Inner Mongolia, China. Anticancer Res. 21, 51–7.
Finnegan, P.M., Chen, W., 2012. Arsenic toxicity: the effects on plant metabolism. Front. Physiol. 3, 182.
Fiorini, C., Lechner, P., 1999. Continuous charge restoration in semiconductor detectors by means of the gate-to-drain current of the integrated front-end JFET. IEEE Trans. Nucl. Sci. 46, 761–764.
Firestone, R., 2005. LBNL Isotopes Project Nuclear Data Dissemination Home Page. Ernest Orlando Lawrence Berkeley National Laboratory, Berkeley, U.S.A. Retrieved: October 2011 from http://ie.lbl.gov/toi.html [WWW Document].
Fleming, D.E.B., Gherase, M.R., 2007. A rapid, high sensitivity technique for measuring arsenic in skin phantoms using a portable x-ray tube and detector. Phys. Med. Biol. 52, N459–65.
Forslind, B., Lindberg, M. (Eds.), 2004. Skin, Hair, and Nails: Structure and Function. Marcel Dekker Inc., New York.
Francesconi, K.A., Kuehnelt, D., 2004. Determination of arsenic species: a critical review of methods and applications, 2000-2003. Analyst 129, 373–95.
Gadd, G.M., 1993. Microbial formation and transformation of organometallic and organometalloid compounds. FEMS Microbiol. Rev. 11, 297–316.
Gatti, E., Rehak, P., 1984. Semiconductor drift chamber — An application of a novel charge transport scheme. Nucl. Instruments Methods Phys. Res. 225, 608–614.
Gaza, R., McKeever, S.W.S., Akselrod, M.S., 2005. Near-real-time radiotherapy dosimetry using optically stimulated luminescence of Al[sub 2]O[sub 3]:C: Mathematical models and preliminary results. Med. Phys. 32, 1094.
Germolec, D.R., Yoshida, T., Gaido, K., Wilmer, J.L., Simeonova, P.P., Kayama, F., Burleson, F., Dong, W., Lange, R.W., Luster, M.I., 1996. Arsenic Induces Overexpression of Growth Factors in Human Keratinocytes. Toxicol. Appl. Pharmacol. 141, 308–318.
Gherase, M.R., Mader, J.E., Fleming, D.E.B., 2010. The radiation dose from a proposed measurement of arsenic and selenium in human skin. Phys. Med. Biol. 55, 5499–5514.
Gherase, M.R., Vallee, M.E., Fleming, D.E.B., 2010. Simultaneous detection of As and Se in polyester resin skin phantoms. Appl. Radiat. Isot. 68, 743–745.
Gorby, M.S., 1988. Arsenic poisoning. West. J. Med. 149, 308–15.
Guha Mazumder, D.N., 2008. Chronic arsenic toxicity & human health. Indian J. Med. Res. 128, 436–47.
Guha Mazumder, D.N., Haque, R., Ghosh, N., De, B.K., Santra, A., Chakraborty, D., Smith, A.H., 1998. Arsenic levels in drinking water and the prevalence of skin lesions in West Bengal, India. Int. J. Epidemiol. 27, 871–877.
Gulbrandsen, R.., 1966. Chemical composition of phosphorites of the Phosphoria Formation. Geochim. Cosmochim. Acta 30, 769–778.
Gulz, P.A., Gupta, S.-K., Schulin, R., 2005. Arsenic accumulation of common plants from contaminated soils. Plant Soil 272, 337–347.
Haack, S.K., Treccani, S.L., 2000. Arsenic concentration and selected geochemical characteristics for ground water and aquifer materials in southeastern Michigan.

Hansen, K., Reckleben, C., Diehl, I., Klär, H., 2008. A compact 7-cell Si-drift detector module for high-count rate X-ray spectroscopy. Nucl. Instruments Methods Phys. Res. Sect. A 589, 250–258.
Hansen, K., Reckleben, C., Diehl, I., Welter, E., 2008. Electrical and spectroscopic characterization of 7-cell Si-drift detectors. Nucl. Instruments Methods Phys. Res. Sect. A 585, 76–82.
Harris, D.C., 2006. Quantitative chemical analysis, 7th ed. W. H. Freeman, New York, USA.
Hartmann, B., Martišíková, M., Jäkel, O., 2010. Technical Note: Homogeneity of Gafchromic® EBT2 film. Med. Phys. 37, 1753.
Heirwegh, C.M., Chettle, D.R., Pejovic-Milic, A., 2012. Ex vivo evaluation of a coherent normalization procedure to quantify in vivo finger strontium XRS measurements. Med. Phys. 39, 832–41.
Hiller, E., Lalinská, B., Chovan, M., Jurkovič, Ľ., Klimko, T., Jankulár, M., Hovorič, R., Šottník, P., Fľaková, R., Ženišová, Z., Ondrejková, I., 2012. Arsenic and antimony contamination of waters, stream sediments and soils in the vicinity of abandoned antimony mines in the Western Carpathians, Slovakia. Appl. Geochemistry 27, 598–614.
Hindmarsh, J.T., McCurdy, R.F., 1986. Clinical and environmental aspects of arsenic toxicity. Crit. Rev. Clin. Lab. Sci. 23, 315–47.
Hirner, A. V, Feldmann, J., Krupp, E., Grümping, R., Goguel, R., Cullen, W.R., 1998. Metal(loid)organic compounds in geothermal gases and waters. Org. Geochem. 29, 1765–1778.
Holmgren, A., 1989. Thioredoxin and glutaredoxin systems. J. Biol. Chem. 264, 13963–6.
Hopenhayn, C., 2006. Arsenic in Drinking Water: Impact on Human Health. Elements 2, 103–107.
Hubbell, J.H., Seltzer, S.M., 2004. Tables of X-Ray Mass Attenuation Coefficients and Mass Energy-Absorption Coefficients (version 1.4) (Gaithersburg, MD: National Institute of Standards and Technology) [WWW Document]. URL http://www.nist.gov/pml/data/xraycoef/index.cfm
Hubbell, J.H., Veigele, W.J., Briggs, E.A., Brown, R.T., Cromer, D.T., Howerton, R.J., 1975. Atomic Form Factors, Incoherent Scattering Functions, and Photon Scattering Cross Sections. J. Phys. Chem. Ref. Data 4, 471–538.
Hughes, M.F., Beck, B.D., Chen, Y., Lewis, A.S., Thomas, D.J., 2011. Arsenic exposure and toxicology: a historical perspective. Toxicol. Sci. 123, 305–32.
Hupe, O., Brunzendorf, J., 2006. A novel method of radiochromic film dosimetry using a color scanner. Med. Phys. 33, 4085.
ICRU, 1989. Tissue substitutes in radiation dosimetry and measurement. ICRU Report No 44. (Bethesda, MD: ICRU).
Innov-X, 2005. Innov-X Systems Product Brochure (Woburn, MA: Innov-X Systems, Inc.).
International Commission on Radiological Protection, Publication 23, 1975. Rep. Task Gr. Ref. Man. Pergamon, Oxford, pp. 480.
International Commission on Radiological Protection, Publication 60, 1990. Recomm. Int. Comm. Radiol. Prot. Pergamon, Oxford.
Irgolic, K.J., H., G., Howard, A.G., 1995. The encyclopedia of analytical science. Academic Press.
Jenkins, R., 1995. Quantitative X-Ray Spectrometry, Second Edition,, 2nd ed. Marcel Dekker Inc., New York, USA.
Jha, S., Agarwal, V., 2008. Unusual features in a case of arsenic poisoning. J. Pediatr. Neurol. 6, 69–71.
Jonson, R., Mattsson, S., Unsgaard, B., 1988. A method for in vivo analysis of platinum after chemotherapy with cisplatin. Phys. Med. Biol. 33, 847–57.
Jursinic, P.A., 2007. Characterization of optically stimulated luminescent dosimeters, OSLDs, for clinical dosimetric measurements. Med. Phys. 34, 4594.
Jursinic, P.A., 2010. Changes in optically stimulated luminescent dosimeter (OSLD) dosimetric characteristics with accumulated dose. Med. Phys. 37, 132.
Kabata-Pendias, A., Pendias, H., 1984. Trace elements in soils and plants. CRC Press.
Kao, G., 1990. Arsenical keratosis and arsenical carcinoma. Precancerous lesions and carcinoma in situ. In: Farmer, E.R., Hood, A.F. (Eds.), Pathology of the Skin. Appleton & Lange, Norwalk, Conn, USA, p. 561.
Karim, M.M., 2000. Arsenic in groundwater and health problems in Bangladesh. Water Res. 34, 304–310.
Kasap, S.O., 2000. X-ray sensitivity of photoconductors: application to stabilized a-Se. J. Phys. D. Appl. Phys. 33, 2853–2865.
Kenyon, E.M., Hughes, M.F., 2001. A concise review of the toxicity and carcinogenicity of dimethylarsinic acid. Toxicology 160, 227–236.
Kerns, J.R., Kry, S.F., Sahoo, N., Followill, D.S., Ibbott, G.S., 2011. Angular dependence of the nanoDot OSL dosimeter. Med. Phys. 38, 3955.
Ketek, 2011. Vitus SDD Datasheet.
Khan, F.M., 2003. The Physics of Radiation Therapy. Lippincott Williams & Wilkins.
Kitchin, K.T., 2001. Recent Advances in Arsenic Carcinogenesis: Modes of Action, Animal Model Systems, and Methylated Arsenic Metabolites. Toxicol. Appl. Pharmacol. 172, 249–261.
Kitchin, K.T., Conolly, R., 2010. Arsenic-induced carcinogenesis--oxidative stress as a possible mode of action and future research needs for more biologically based risk assessment. Chem. Res. Toxicol. 23, 327–35.

Kitchin, K.T., Wallace, K., 2008. Evidence against the nuclear in situ binding of arsenicals–oxidative stress theory of arsenic carcinogenesis. Toxicol. Appl. Pharmacol. 232, 252–257.
Klein, O., Nishina, T., 1929. Uber die Streuung von Strahlung durch freie Elektronen nach der neuen relativistischen Quantendynamik von Dirac. Zeitschrift fur Phys. 52, 853–868.
Kleinman, D.A., 1956. The Forward Characteristic. Bell Syst. Tech. J. 35, 685–706.
Knoll, G.F., 1999. Radiation Detection and Measurement, 3rd ed. John Wiley & Sons Inc.
Kolker, A., Haack, S.K., Cannon, W.F., Westjohn, D.B., Kim, M.-J., Nriagu, J., Woodruff, L.G., 2003. Arsenic in southeastern Michigan. In: Welch, A.H., Stollenwerk, K.G. (Eds.), Arsenic in Ground Water. Kluwer Academic Publishers, Boston, pp. 281–294.
Kotulski, Z.A., 2010. Error Analysis with Applications in Engineering. Springer Science+Business Media B.V., Dordrecht.
Krieger, R.I., Krieger, W.C., Hodgson, E., Levi, P.E., 2001. Metabolism of Pesticides. In: Handbook of Pesticide Toxicology. pp. 531–562.
Krol, A., Ikhlef, A., Kieffer, J.C., Bassano, D.A., Chamberlain, C.C., Jiang, Z., Pépin, H., Prasad, S.C., 1997. Laser-based microfocused x-ray source for mammography: feasibility study. Med. Phys. 24, 725–32.
Kumagai, Y., Sumi, D., 2007. Arsenic: signal transduction, transcription factor, and biotransformation involved in cellular response and toxicity. Annu. Rev. Pharmacol. Toxicol. 47, 243–62.
Landis, D.A., Cork, C.P., Madden, N.W., Goulding, F.S., 1982. Transistor Reset Preamplifier for High Rate High Resolution Spectroscopy. IEEE Trans. Nucl. Sci. 29, 619–624.
Laverman, A., Blum, J., Schaefer, J., Phillips, E., Lovley, D., Oremland, R., 1995. Growth of Strain SES-3 with Arsenate and Other Diverse Electron Acceptors. Appl. Envir. Microbiol. 61, 3556–3561.
Lechner, P., Eckbauer, S., Hartmann, R., Krisch, S., Hauff, D., Richter, R., Soltau, H., Strüder, L., Fiorini, C., Gatti, E., Longoni, A., Sampietro, M., 1996. Silicon drift detectors for high resolution room temperature X-ray spectroscopy. Nucl. Instruments Methods Phys. Res. Sect. A Accel. Spectrometers, Detect. Assoc. Equip. 377, 346–351.
Lechner, P., Pahlke, A., Soltau, H., 2004. Novel high-resolution silicon drift detectors. X-Ray Spectrom. 33, 256–261.
Lee, R., Mathews-Roth, M.M., Pathak, M.A., Parrish, J.A., 1975. The detection of cartenoid pigments in human skin. J. Invest. Dermatol. 64, 175–77.
Lee-Feldstein, A., 1986. Cumulative exposure to arsenic and its relationship to respiratory cancer among copper smelter employees. J. Occup. Med. 28, 296–302.
Leslie, A.C.D., Smith, H., 1978. Napoleon Bonaparte's exposure to arsenic during 1816. Arch. Toxicol. 41, 163–167.
Lin, S., Cullen, W.R., Thomas, D.J., 1999. Methylarsenicals and Arsinothiols Are Potent Inhibitors of Mouse Liver Thioredoxin Reductase. Chem. Res. Toxicol. 12, 924–930.
Lindsay, P., Rink, A., Ruschin, M., Jaffray, D., 2010. Investigation of energy dependence of EBT and EBT-2 Gafchromic film. Med. Phys. 37, 571.
Liu, J., Zheng, B., Aposhian, H., Zhou, Y., Chen, M., Zhang, A., Waalkes, M., 2002. Chronic Arsenic Poisoning From Burning High-Arsenic-Containing Coal In Guizhou, China. J. Peripher. Nerv. Syst. 7, 208–208.
Luke, P.N., 1994. Single-polarity charge sensing in ionization detectors using coplanar electrodes. Appl. Phys. Lett. 65, 2884.
Lynch, B.D., Kozelka, J., Ranade, M.K., Li, J.G., Simon, W.E., Dempsey, J.F., 2006. Important considerations for radiochromic film dosimetry with flatbed CCD scanners and EBT GAFCHROMIC[sup ®] film. Med. Phys. 33, 4551.
Madison, K.C., 2003. Barrier function of the skin: "la raison d'être" of the epidermis. J. Invest. Dermatol. 121, 231–41.
Mandal, B.K., Suzuki, K.T., 2002. Arsenic round the world: a review. Talanta 58, 201–235.
Marafante, E., Bertolero, F., Edel, J., Pietra, R., Sabbioni, E., 1982. Intracellular interaction and biotransformation of arsenite in rats and rabbits. Sci. Total Environ. 24, 27–39.
Markey, B.G., Colyott, L.E., Mckeever, S.W.S., 1995. Time-resolved optically stimulated luminescence from α-Al2O3:C. Radiat. Meas. 24, 457–463.
Markey, B.G., McKeever, S.W.S., Akselrod, M.S., Botter-Jensen, L., Angersnap Larsen, N., Colyott, L.E., 1996. The Temperature Dependence of Optically Stimulated Luminescence From Alpha-Al2O3:C. Radiat. Prot. Dosimetry 65, 185–189.
Mart, C.J., Elson, H.R., Lamba, M.A.S., 2012. Measurement of low-energy backscatter factors using GAFCHROMIC film and OSLDs. J. Appl. Clin. Med. Phys. 13, 3832.
Martisíková, M., Ackermann, B., Jäkel, O., 2008. Analysis of uncertainties in Gafchromic EBT film dosimetry of photon beams. Phys. Med. Biol. 53, 7013–27.
Massillon-JL, G., 2012. Energy Dependence of the New Gafchromic EBT3 Film:Dose Response Curves for 50 KV, 6 and 15 MV X-Ray Beams. Int. J. Med. Physics,Clinical Eng. Radiat. Oncol. 01, 60–65.
Maud, J., Rumsby, P., 2008. A review of the toxicity of arsenic in air, Environmental Agency. Bristol, UK.
Mazumder, D.N.G., Steinmaus, C., Bhattacharya, P., von Ehrenstein, O.S., Ghosh, N., Gotway, M., Sil, A., Balmes, J.R., Haque, R., Hira-Smith, M.M., Smith, A.H., 2005. Bronchiectasis in persons with skin lesions resulting from arsenic in drinking water. Epidemiology 16, 760–5.

McGuigan, C.F., Hamula, C.L.A., Huang, S., Gabos, S., Le, X.C., 2010. A review on arsenic concentrations in Canadian drinking water. Environ. Rev. 18, 291–307.
McKeever, S.W.S., Akselrod, M.S., Colyott, L.E., Agersnap Larsen, N., Polf, J.C., Whitley, V., 1999. Characterisation of Al2O3 for Use in Thermally and Optically Stimulated Luminescence Dosimetry. Radiat. Prot. Dosimetry 84, 163–166.
Micke, A., Lewis, D.F., Yu, X., 2011. Multichannel film dosimetry with nonuniformity correction. Med. Phys. 38, 2523.
Milton, A.H., Rahman, M., 2002. Respiratory effects and arsenic contaminated well water in Bangladesh. Int. J. Environ. Health Res. 12, 175–9.
Mitra, S.R., Mazumder, D.N.G., Basu, A., Block, G., Haque, R., Samanta, S., Ghosh, N., Smith, M.M.H., von Ehrenstein, O.S., Smith, A.H., 2004. Nutritional factors and susceptibility to arsenic-caused skin lesions in West Bengal, India. Environ. Health Perspect. 112, 1104–9.
Moise, H., Adachi, J.D., Chettle, D.R., Pejović-Milić, A., 2012. Monitoring bone strontium levels of an osteoporotic subject due to self-administration of strontium citrate with a novel diagnostic tool, in vivo XRF: a case study. Bone 51, 93–97.
Mork, K., 1971. Radiative Corrections. II. Compton Effect. Phys. Rev. A 4, 917–927.
Mrčela, I., Bokulić, T., Izewska, J., Budanec, M., Fröbe, A., Kusić, Z., 2011. Optically stimulated luminescence in vivo dosimetry for radiotherapy: physical characterization and clinical measurements in (60)Co beams. Phys. Med. Biol. 56, 6065–82.
Muench, P.J., 1991. Photon energy dependence of the sensitivity of radiochromic film and comparison with silver halide film and LiF TLDs used for brachytherapy dosimetry. Med. Phys. 18, 769.
Mustacich, D., Powis, G., 2000. Thioredoxin reductase. Biochem. J. 346, 1–8.
Nachman, K.E., Raber, G., Francesconi, K.A., Navas-Acien, A., Love, D.C., 2012. Arsenic species in poultry feather meal. Sci. Total Environ. 417, 183–188.
Nagvi, S.M., Vaishnavi, C., Singh, H., 1994. Arsenic in the Environment. Part 2: Human Health and Ecosystem Effects. John Wiley & Sons Inc., New York, USA.
Nakajima, Y., Endo, Y., Inoue, Y., Yamanaka, K., Kato, K., Wanibuchi, H., Endo, G., 2006. Ingestion of Hijiki seaweed and risk of arsenic poisoning. Appl. Organomet. Chem. 20, 557–564.
Nevens, F., Fevery, J., Van Steenbergen, W., Sciot, R., Desmet, V., Groote, J.D., 1990. Arsenic and non-cirrhotic portal hypertension. J. Hepatol. 11, 80–85.
Nie, H., Chettle, D., Luo, L., O'Meara, J., 2006. In vivo investigation of a new 109Cd gamma-ray induced K-XRF bone lead measurement system. Phys. Med. Biol. 51, 351–60.
Nie, H., Chettle, D., Stronach, I., Arnold, M., Huang, S., McNeill, F., O'Meara, J., 2004. A study of MDL improvement for the in vivo measurement of lead in bone. Nucl. Instruments Methods Phys. Res. Sect. B Beam Interact. with Mater. Atoms 213, 579–583.
NIST, 2005a. Composition of Tissue, Soft (ICRP). National Institute of Standards and Technology, Gaithersburg, MD. Retrieved: February, 2012 from http://physics.nist.gov/cgi-bin/Star/compos.pl [WWW Document]. URL http://physics.nist.gov/cgi-bin/Star/compos.pl?matno=261
NIST, 2005b. Composition of Kapton Polymide Film. National Institute of Standards and Technology, Gaithersburg, MD. Retrieved: February, 2011 from http://physics.nist.gov/cgi-bin/Star/compos.pl [WWW Document]. URL http://physics.nist.gov/cgi-bin/Star/compos.pl?matno=179
Nordberg, J., Arnér, E.S.J., 2001. Reactive oxygen species, antioxidants, and the mammalian thioredoxin system1 1This review is based on the licentiate thesis "Thioredoxin reductase—interactions with the redox active compounds 1-chloro-2,4-dinitrobenzene and lipoic acid" by Jonas Nordberg,. Free Radic. Biol. Med. 31, 1287–1312.
O'Meara, J.M., Börjesson, J., Chettle, D.R., Mattsson, S., 2001. Normalisation with coherent scatter signal: improvements in the calibration procedure of the 57Co-based in vivo XRF bone-Pb measurement. Appl. Radiat. Isot. 54, 319–25.
Onishi, Y., 1969. Arsenic. In: Wedepohl, K.H. (Ed.), Handbook of Geochemistry, Volume I. Springer, p. 442.
Ouypornkochagorn, S., Feldmann, J., 2010. Dermal uptake of arsenic through human skin depends strongly on its speciation. Environ. Sci. Technol. 44, 3972–8.
Oves, S.D., Hogstrom, K.R., Ham, K., Sajo, E., Dugas, J.P., 2008. Dosimetry intercomparison using a 35-keV X-ray synchrotron beam. Eur. J. Radiol. 68, S121–S125.
Paelinck, L., De Neve, W., De Wagter, C., 2007. Precautions and strategies in using a commercial flatbed scanner for radiochromic film dosimetry. Phys. Med. Biol. 52, 231–42.
Palmer, C.N.A., Irvine, A.D., Terron-Kwiatkowski, A., Zhao, Y., Liao, H., Lee, S.P., Goudie, D.R., Sandilands, A., Campbell, L.E., Smith, F.J.D., O'Regan, G.M., Watson, R.M., Cecil, J.E., Bale, S.J., Compton, J.G., DiGiovanna, J.J., Fleckman, P., Lewis-Jones, S., Arseculeratne, G., Sergeant, A., Munro, C.S., El Houate, B., McElreavey, K., Halkjaer, L.B., Bisgaard, H., Mukhopadhyay, S., McLean, W.H.I., 2006. Common loss-of-function variants of the epidermal barrier protein filaggrin are a major predisposing factor for atopic dermatitis. Nat. Genet. 38, 441–6.

Parvez, F., Chen, Y., Yunus, M., Olopade, C., Segers, S., Slavkovich, V., Argos, M., Hasan, R., Ahmed, A., Islam, T., Akter, M.M., Graziano, J.H., Ahsan, H., 2013. Arsenic Exposure and Impaired Lung Function. Findings from a Large Population-based Prospective Cohort Study. Am. J. Respir. Crit. Care Med. 188, 813–9.
Patel, K.S., Shrivas, K., Brandt, R., Jakubowski, N., Corns, W., Hoffmann, P., 2005. Arsenic contamination in water, soil, sediment and rice of central India. Environ. Geochem. Health 27, 131–45.
Pejović-Milić, A., Stronach, I.M., Gyorffy, J., Webber, C.E., Chettle, D.R., 2004. Quantification of bone strontium levels in humans by in vivo x-ray fluorescence. Med. Phys. 31, 528–38.
Peng, Y.M., Peng, Y.S., Lin, Y., 1993. A nonsaponification method for the determination of carotenoids, retinoids, and tocopherols in solid human tissues. Cancer Epidemiol. Biomarkers Prev. 2, 139–44.
Perez, D.S., Armstrong-Lea, L., Fox, M.H., Yang, R.S.H., Campain, J.A., 2003. Arsenic and benzo[a]pyrene differentially alter the capacity for differentiation and growth properties of primary human epidermal keratinocytes. Toxicol. Sci. 76, 280–90.
Perks, C.A., Le Roy, G., Prugnaud, B., 2007. Introduction of the InLight monitoring service. Radiat. Prot. Dosimetry 125, 220–3.
Petrick, J.S., Jagadish, B., Mash, E.A., Aposhian, H.V., 2001. Monomethylarsonous Acid (MMA III) and Arsenite: LD 50 in Hamsters and In Vitro Inhibition of Pyruvate Dehydrogenase. Chem. Res. Toxicol. 14, 651–656.
Poumay, Y., Coquette, A., 2007. Modelling the human epidermis in vitro: tools for basic and applied research. Arch. Dermatol. Res. 298, 361–9.
Proksch, E., Brandner, J.M., Jensen, J.-M., 2008. The skin: an indispensable barrier. Exp. Dermatol. 17, 1063–1072.
Radeka, V., Rahek, P., Rescia, S., Gatti, E., Longoni, A., Sampietro, M., Bertuccio, G., Holl, P., Struder, L., Kemmer, J., 1989. Implanted silicon JFET on completely depleted high-resistivity devices. IEEE Electron Device Lett. 10, 91–94.
Rahman, M., Tondel, M., Ahmad, S.A., Axelson, O., 1998. Diabetes mellitus associated with arsenic exposure in Bangladesh. Am. J. Epidemiol. 148, 198–203.
Raie, R.M., 1996. Regional Variation in As, Cu, Hg, and Se and Interaction between Them. Ecotoxicol. Environ. Saf. 35, 248–252.
Ramírez-Jiménez, F.J., Mondragón-Contreras, L., Cruz-Estrada, P., 2006. Application of PIN diodes in Physics Research. AIP Conf. Proc. 857, 395–406.
Ratnaike, R.N., 2003. Acute and chronic arsenic toxicity. Postgrad. Med. J. 79, 391–396.
Razo, I., Carrizales, L., Castro, J., Díaz-Barriga, F., Monroy, M., 2004. Arsenic and Heavy Metal Pollution of Soil, Water and Sediments in a Semi-Arid Climate Mining Area in Mexico. Water, Air, Soil Pollut. 152, 129–152.
Reft, C.S., 2009. The energy dependence and dose response of a commercial optically stimulated luminescent detector for kilovoltage photon, megavoltage photon, and electron, proton, and carbon beams. Med. Phys. 36, 1690–9.
Rehak, P., Gatti, E., Longoni, A., Kemmer, J., Holl, P., Klanner, R., Lutz, G., Wylie, A., 1985. Semiconductor drift chambers for position and energy measurements. Nucl. Instruments Methods Phys. Res. Sect. A Accel. Spectrometers, Detect. Assoc. Equip. 235, 224–234.
Richter, C., Pawelke, J., Karsch, L., Woithe, J., 2009. Energy dependence of EBT-1 radiochromic film response for photon (10 kVp–15 MVp) and electron beams (6–18 MeV) readout by a flatbed scanner. Med. Phys. 36, 5506.
Rink, A., Vitkin, I.A., Jaffray, D.A., 2007. Intra-irradiation changes in the signal of polymer-based dosimeter (GAFCHROMIC EBT) due to dose rate variations. Phys. Med. Biol. 52, N523–9.
Robinson, J.W., 1991. Practical Handbook of Spectroscopy. CRC Press, Boca Raton, FL, USA.
Robinson, L.B., 1961. Reduction of Baseline Shift in Pulse-Amplitude Measurements. Rev. Sci. Instrum. 32, 1057.
Rodriguez-Lado, L., Sun, G., Berg, M., Zhang, Q., Xue, H., Zheng, Q., Johnson, C.A., 2013. Groundwater Arsenic Contamination Throughout China. Science (80-.). 341, 866–868.
Rossman, T.G., 2003. Mechanism of arsenic carcinogenesis: an integrated approach. Mutat. Res. 533, 37–65.
Roy, C.W., Gherase, M.R., Fleming, D.E.B., 2010. Simultaneous assessment of arsenic and selenium in human nail phantoms using a portable x-ray tube and a detector. Phys. Med. Biol. 55, N151–N159.
Rust, D.M., 2001. Risk/Benefit Profile of Arsenic Trioxide. Oncologist 6, 29–32.
Ruzin, A., Nemirovsky, Y., 1997. Statistical models for charge collection efficiency and variance in semiconductor spectrometers. J. Appl. Phys. 82, 2754.
Saha, J.C., Dikshit, A.K., Bandyopadhyay, M., Saha, K.C., 1999. A Review of Arsenic Poisoning and its Effects on Human Health. Crit. Rev. Environ. Sci. Technol. 29, 281–313.
Saha, K.C., 2003. Diagnosis of Arsenicosis. J. Environ. Sci. Heal. Part A 38, 255–272.
Salter, C., 2000. Error Analysis Using the Variance-Covariance Matrix. J. Chem. Educ. 77, 1239.
Saltikov, C.W., Olson, B.H., 2002. Homology of Escherichia coli R773 arsA, arsB, and arsC Genes in Arsenic-Resistant Bacteria Isolated from Raw Sewage and Arsenic-Enriched Creek Waters. Appl. Environ. Microbiol. 68, 280–288.
Samanta, G., Sharma, R., Roychowdhury, T., Chakraborti, D., 2004. Arsenic and other elements in hair, nails, and skin-scales of arsenic victims in West Bengal, India. Sci. Total Environ. 326, 33–47.

Savage, K.S., Bird, D.K., Ashley, R.P., 2000. Legacy of the California Gold Rush: Environmental Geochemistry of Arsenic in the Southern Mother Lode Gold District. Int. Geol. Rev. 42, 385–415.
Scheindlin, S., 2005. The duplicitous nature of inorganic arsenic. Mol. Interv. 5, 60–4.
Schembri, V., Heijmen, B.J.M., 2007. Optically stimulated luminescence (OSL) of carbon-doped aluminum oxide (Al[sub 2]O[sub 3]:C) for film dosimetry in radiotherapy. Med. Phys. 34, 2113.
Schoolmeester, W.L., White, D.R., 1980. Arsenic poisoning. South. Med. J. 73, 198–208.
Sekeres, M.A., 2007. New Data with Arsenic Trioxide in Leukemias and Myelodysplastic Syndromes. Clin. Lymphoma Myeloma 8, S7–S12.
Sherman, I.S., Roddick, R.G., 1970. Low Noise Preamplifier for Simultaneous High Resolution Energy & Time Measurement with Semiconductor Detectors. IEEE Trans. Nucl. Sci. 17, 252–259.
Shneidman, D., Belizaire, R., 1986. Arsenic exposure followed by the development of dermatofibrosarcoma protuberans. Cancer 58, 1585–1587.
Smedley, P.., Kinniburgh, D.., 2002. A review of the source, behaviour and distribution of arsenic in natural waters. Appl. Geochemistry 17, 517–568.
Smedley, P.L., Kinniburgh, D.G., Macdonald, D.M.J., Nicolli, H.B., Barros, A.J., Tullio, J.O., Pearce, J.M., Alonso, M.S., 2005. Arsenic associations in sediments from the loess aquifer of La Pampa, Argentina. Appl. Geochemistry 20, 989–1016.
Smith, A.H., Hopenhayn-Rich, C., Bates, M.N., Goeden, H.M., Hertz-Picciotto, I., Duggan, H.M., Wood, R., Kosnett, M.J., Smith, M.T., 1992. Cancer risks from arsenic in drinking water. Environ. Health Perspect. 97, 259–67.
Smith, A.H., Lingas, E.O., Rahman, M., 2000. Contamination of drinking-water by arsenic in Bangladesh: a public health emergency. Bull. World Health Organ. 78, 1093–103.
Soares, C.G., 2006. New developments in radiochromic film dosimetry. Radiat. Prot. Dosimetry 120, 100–6.
Somervaille, L.J., Chettle, D.R., Scott, M.C., 1985. In vivo measurement of lead in bone using x-ray fluorescence. Phys. Med. Biol. 30, 929–43.
Strüder, L., Soltau, H., 1995. High Resolution Silicon Detectors for Photons and Particles. Radiat Prot Dosim. 61, 39–46.
Studinski, R.C.N., 2005. Development of an in vivo method of measuring arsenic with radiation.
Studinski, R.C.N., McNeill, F.E., Chettle, D.R., O'Meara, J.M., 2005. Estimation of a method detection limit for an in vivo XRF arsenic detection system. Phys. Med. Biol. 50, 521–530.
Studinski, R.C.N., McNeill, F.E., O'Meara, J.M., Chettle, D.R., 2006. A method detection limit for potential in vivo arsenic measurements with a 50 W x-ray tube. Phys. Med. Biol. 51, N381–7.
Styblo, M., Del Razo, L.M., Vega, L., Germolec, D.R., LeCluyse, E.L., Hamilton, G.A., Reed, W., Wang, C., Cullen, W.R., Thomas, D.J., 2000. Comparative toxicity of trivalent and pentavalent inorganic and methylated arsenicals in rat and human cells. Arch. Toxicol. 74, 289–299.
Styblo, M., Serves, S. V, Cullen, W.R., Thomas, D.J., 1997. Comparative inhibition of yeast glutathione reductase by arsenicals and arsenothiols. Chem. Res. Toxicol. 10, 27–33.
Taylor, J.R., 1997. An Introduction Error Analysis: The Study of Uncertainties in Physical Measurements, 2nd ed. University Science Books, Sausalito, California, USA.
Taylor, M.L., Smith, R.L., Dossing, F., Franich, R.D., 2012. Robust calculation of effective atomic numbers: the Auto-Z(eff) software. Med. Phys. 39, 1769–78.
Tchounwou, P.B., Wilson, B., Ishaque, A., 1999. Important considerations in the development of public health advisories for arsenic and arsenic-containing compounds in drinking water. Rev. Environ. Health 14, 211–29.
Theodórsson, P., 1996. Measurements of weak radioactivity. World Scientific, River Edge, NJ, USA.
Todd, A.C., 2000. Coherent scattering and matrix correction in bone-lead measurements. Phys. Med. Biol. 45, 1953–63.
Tondel, M., Rahman, M., Magnuson, A., Chowdhury, I.A., Faruquee, M.H., Ahmad, S.A., 1999. The relationship of arsenic levels in drinking water and the prevalence rate of skin lesions in Bangladesh. Environ. Health Perspect. 107, 727–9.
Tourtelot, H.A., 1964. Minor-element composition and organic carbon content of marine and nonmarine shales of Late Cretaceous age in the western interior of the United States. Geochim. Cosmochim. Acta 28, 1579–1604.
Tseng, C.-H., Chong, C.-K., Chen, C.-J., Tai, T.-Y., 1996. Dose-response relationship between peripheral vascular disease and ingested inorganic arsenic among residents in blackfoot disease endemic villages in Taiwan. Atherosclerosis 120, 125–133.
Tseng, C.H., Tai, T.Y., Chong, C.K., Tseng, C.P., Lai, M.S., Lin, B.J., Chiou, H.Y., Hsueh, Y.M., Hsu, K.H., Chen, C.J., 2000. Long-term arsenic exposure and incidence of non-insulin-dependent diabetes mellitus: a cohort study in arseniasis-hyperendemic villages in Taiwan. Environ. Health Perspect. 108, 847–51.
Tseng, W.P., Chu, H.M., How, S.W., Fong, J.M., Lin, C.S., Yeh, S., 1968. Prevalence of Skin Cancer in an Endemic Area of Chronic Arsenicism in Taiwan. J Natl Cancer Inst 40, 453–463.
Tsoulfanidis, N., Ph.D., Landsberger, S., 2011. Measurement and Detection of Radiation. CRC Press.

Vahlquist, A., Lee, J.B., Michaelsson, G., Rollman, O., 1982. Vitamin A in Human Skin: II Concentrations of Carotene, Retinol and Dehydroretinol in Various Components of Normal Skin. J. Invest. Dermatol. 79, 94–97.
Vahter, M., Envall, J., 1983. In vivo reduction of arsenate in mice and rabbits. Environ. Res. 32, 14–24.
Vahter, M., Marafante, E., Dencker, L., 1984. Tissue distribution and retention of74As-dimethylarsinic acid in mice and rats. Arch. Environ. Contam. Toxicol. 13, 259–264.
Van Battum, L.J., Hoffmans, D., Piersma, H., Heukelom, S., 2008. Accurate dosimetry with GafChromic^{TM} EBT film of a 6 MV photon beam in water: What level is achievable? Med. Phys. 35, 704.
Van der Voet, G.B., Sarafanov, A., Todorov, T.I., Centeno, J.A., Jonas, W.B., Ives, J.A., Mullick, F.G., 2008. Clinical and analytical toxicology of dietary supplements: a case study and a review of the literature. Biol. Trace Elem. Res. 125, 1–12.
Van Dyck, P., Van Grieken, R., 1983. Automated matrix-correction of line ratios in energy-dispersive x-ray fluorescence spectrum deconvolution. X-Ray Spectrom. 12, 111–114.
Van Geen, A., Zheng, Y., Cheng, Z., He, Y., Dhar, R.K., Garnier, J.M., Rose, J., Seddique, A., Hoque, M.A., Ahmed, K.M., 2006. Impact of irrigating rice paddies with groundwater containing arsenic in Bangladesh. Sci. Total Environ. 367, 769–777.
Van Grieken, R.E., Markowicz, A.A., 2002. Handbook of X-Ray Spectrometry. Marcel Dekker Inc., New York, USA.
Vega, L., Styblo, M., Patterson, R., Cullen, W., Wang, C., Germolec, D., 2001a. Differential effects of trivalent and pentavalent arsenicals on cell proliferation and cytokine secretion in normal human epidermal keratinocytes. Toxicol. Appl. Pharmacol. 172, 225–32.
Vega, L., Styblo, M., Patterson, R., Cullen, W., Wang, C., Germolec, D., 2001b. Differential Effects of Trivalent and Pentavalent Arsenicals on Cell Proliferation and Cytokine Secretion in Normal Human Epidermal Keratinocytes. Toxicol. Appl. Pharmacol. 172, 225–232.
Viamonte, A., da Rosa, L.A.R., Buckley, L.A., Cherpak, A., Cygler, J.E., 2008. Radiotherapy dosimetry using a commercial OSL system. Med. Phys. 35, 1261.
Vincze, L., Janssens, K., Vekemans, B., Adams, F., 1999. Monte Carlo simulation of X-ray fluorescence spectra: Part 4. Photon scattering at high X-ray energies. Spectrochim. Acta Part B At. Spectrosc. 54, 1711–1722.
Vogt, B.L., 2001. Effects of arsenite on p53, p21 and cyclin D expression in normal human fibroblasts — a possible mechanism for arsenite's comutagenicity. Mutat. Res. Mol. Mech. Mutagen. 478, 159 – 168.
Wang, S., Mulligan, C.N., 2006. Occurrence of arsenic contamination in Canada: Sources, behavior and distribution. Sci. Total Environ. 366, 701–721.
Waxman, S., 2001. History of the Development of Arsenic Derivatives in Cancer Therapy. Oncologist 6, 3–10.
Wester, R.C., Hui, X., Barbadillo, S., Maibach, H.I., Lowney, Y.W., Schoof, R.A., Holm, S.E., Ruby, M. V, 2004. In vivo percutaneous absorption of arsenic from water and CCA-treated wood residue. Toxicol. Sci. 79, 287–95.
Wester, R.C., Maibach, H.I., Sedik, L., Melendres, J., Wade, M., 1993. In vivo and in vitro percutaneous absorption and skin decontamination of arsenic from water and soil. Fundam. Appl. Toxicol. 20, 336–40.
WHO, 2001. Arsenic and Arsenic Compounds, Environmental Health Criteria 224. World Health Organization, Geneva, Switzerland.
WHO, 2010. Exposure to arsenic: a major public health concern, WHO Press, Geneva, Switzerland. World Health Organization, Geneva, Switzerland.
WHO, 2011. Guidelines for drinking-water quality, fourth edition, WHO Press, Geneva, Switzerland. World Health Organization, Geneva, Switzerland.
Williams, P.N., Islam, M.R., Adomako, E.E., Raab, A., Hossain, S.A., Zhu, Y.G., Feldmann, J., Meharg, A.A., 2006. Increase in Rice Grain Arsenic for Regions of Bangladesh Irrigating Paddies with Elevated Arsenic in Groundwaters. Environ. Sci. Technol. 40, 4903–4908.
Wingerath, T., Sies, H., Stahl, W., 1998. Xanthophyll Esters in Human Skin. Arch. Biochem. Biophys. 355, 271–274.
Winship, K.A., 1984. Toxicity of inorganic arsenic salts. Adverse Drug React. Acute Poisoning Rev. 3, 129–60.
Winski, S.L., Barber, D.S., Rael, L.T., Carter, D.E., 1997. Sequence of toxic events in arsine-induced hemolysis in vitro: implications for the mechanism of toxicity in human erythrocytes. Fundam. Appl. Toxicol. 38, 123–8.
Yukihara, E.G., McKeever, S.W.S., 2008. Optically stimulated luminescence (OSL) dosimetry in medicine. Phys. Med. Biol. 53, R351–79.
Yukihara, E.G., Yoshimura, E.M., Lindstrom, T.D., Ahmad, S., Taylor, K.K., Mardirossian, G., 2005. High-precision dosimetry for radiotherapy using the optically stimulated luminescence technique and thin Al2O3:C dosimeters. Phys. Med. Biol. 50, 5619–28.
Zamburlini, M., Pejović-Milić, A., Chettle, D.R., 2006. Evaluation of geometries appropriate for 125I in vivo bone strontium X-ray fluorescence measurement. J. Radioanal. Nucl. Chem. 269, 625–629.
Zamburlini, M., Pejović-Milić, A., Chettle, D.R., 2008. Coherent normalization of finger strontium XRF measurements: feasibility and limitations. Phys. Med. Biol. 53, N307–13.
Zhang, X.-W., Yan, X.-J., Zhou, Z.-R., Yang, F.-F., Wu, Z.-Y., Sun, H.-B., Liang, W.-X., Song, A.-X., Lallemand-Breitenbach, V., Jeanne, M., Zhang, Q.-Y., Yang, H.-Y., Huang, Q.-H., Zhou, G.-B., Tong, J.-H., Zhang, Y., Wu, J.-H.,

Hu, H.-Y., de Thé, H., Chen, S.-J., Chen, Z., 2010. Arsenic trioxide controls the fate of the PML-RARalpha oncoprotein by directly binding PML. Science 328, 240–3.
Zhong, Z., Chapman, D., Menk, R., Richardson, J., Theophanis, S., Thomlinson, W., 1997. Monochromatic energy-subtraction radiography using a rotating anode source and a bent Laue monochromator. Phys. Med. Biol. 42, 1751–1762.
Zhong, Z., Dilmanian, F.A., Bacarian, T., Zhong, N., Chapman, D., Ren, B., Wu, X.Y., Weinmann, H.-J., 2001. Producing parallel x rays with a bent-crystal monochromator and an x-ray tube. Med. Phys. 28, 1931.

Appendix:

Error Analysis for calculation of dead time and dead time correction factor:

Error Analysis for Method 1:

The dead time in method 1 was given by

$$\tau = -\frac{z}{e^{y}} \tag{1}$$

where z and y are the slope and intercept of the straight line y = zx + y, so the uncertainty in the dead time would be given by

$$\delta\tau = \sqrt{\left(\frac{\partial\tau}{\partial z}\delta z\right)^{2} + \left(\frac{\partial\tau}{\partial y}\delta y\right)^{2}} \tag{2}$$

$$\delta\tau = \sqrt{\left(\frac{-1}{e^{y}}\delta z\right)^{2} + \left[\frac{ze^{y}}{(e^{y})^{2}}\delta y\right]^{2}} = \frac{1}{e^{y}}\sqrt{(\delta z)^{2} + (z\delta y)^{2}} \tag{3}$$

The dead time correction factor and its uncertainty are then given by

$$CF_{1} = e^{n\tau} \; and \; \delta CF_{1} = \sqrt{\left(\frac{\partial CF}{\partial n}\delta n\right)^{2} + \left(\frac{\partial CF}{\partial \tau}\delta\tau\right)^{2}} \tag{4}$$

respectively. Substituting in the appropriate expressions and taking the partial derivatives, the error is given by

$$\delta CF_{1} = \sqrt{(\tau e^{n\tau}\delta n)^{2} + (ne^{n\tau}\delta\tau)^{2}} \tag{5}$$

$$\delta CF_{1} = e^{n\tau}\sqrt{(\tau\delta n)^{2} + (n\delta\tau)^{2}} \tag{6}$$

Substituting equations 4 and 5 into equation 8 above, and simplifying, gives

$$\delta CF_1 = e^{n\tau}\sqrt{\left(\frac{z}{e^y}\delta n\right)^2 + \left[\frac{n}{e^b}\sqrt{(\delta z)^2 + (z\delta y)^2}\right]^2} \quad (7)$$

$$\delta CF_1 = e^{n\tau - y}\sqrt{(z\delta n)^2 + n^2[(z\delta y)^2 + (\delta z)^2]} \quad (8)$$

where n = ICR, z is the slope and y is the intercept.

Error Analysis for Method 2:

The dead time in method 2 was given by

$$\tau = -c \quad (9)$$

where c is the slope of the straight line y = cx + d, so the uncertainty in the dead time would be given by

$$\delta\tau = \frac{\partial\tau}{\partial c}\delta c = \delta c \quad (10)$$

The uncertainty in this dead time correction factor then is shown in equation 8 to be given by

$$\delta CF_2 = e^{n\tau}\sqrt{(\tau\delta n)^2 + (n\delta\tau)^2} \quad (11)$$

which can be written, by substituting in equations 14 and 17, as

$$\delta CF_2 = e^{n\tau}\sqrt{(c\delta n)^2 + (n\delta c)^2} \quad (12)$$

where n = ICR and c is the slope of the line obtained when $\ln(m_i)$ is plotted versus n_i.

Error Analysis for Method 2.1:

Equation 19 will still apply here, with n = ICR replaced by n = total recorded counts/live time and c' is the slope of the line obtained when $\ln(m_i)$ is plotted versus n_i.